Consistent Higher Order Accurate Time Discretization Methods for Inelastic Material Models

Bettina Anna Barbara Schröder

Publication Series
Institute of Mechanics and Dynamics
Prof. Dr.-Ing. Detlef Kuhl
Prof. Dr.-Ing. Jens Wackerfuß
University of Kassel

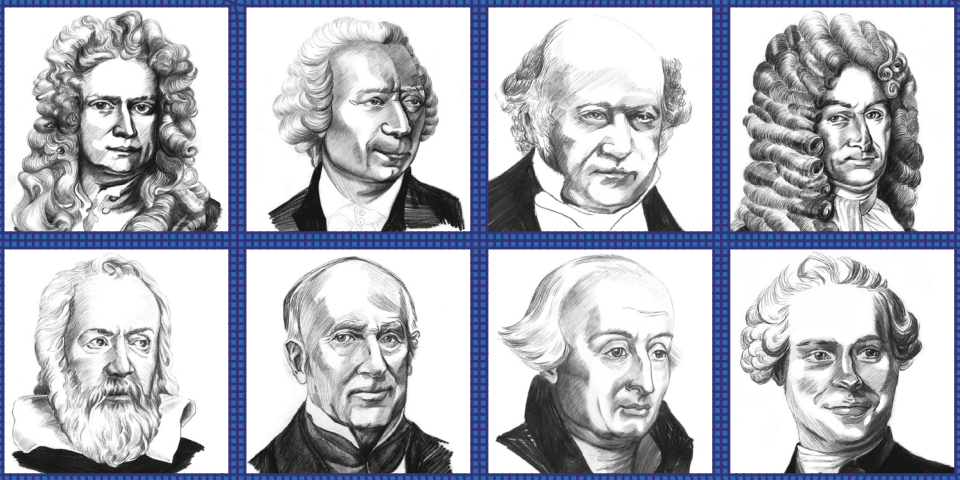

Series
Institute of Structural Mechanics
2019 – 2

Edited by
Prof. Dr.-Ing. habil. Detlef Kuhl
Prof. Dr.-Ing. Jens Wackerfuß
University of Kassel

Series Editor
Institute of Structural Mechanics

Chair of Mechanics and Dynamics
Prof. Dr.-Ing. Detlef Kuhl

Chair of Structural Analysis
Prof. Dr.-Ing. Jens Wackerfuß

University of Kassel
Department of Civil and Environmental Engineering

Mönchebergstraße 7
34109 Kassel
http://www.uni-kassel.de/fb14bau/en/institute/ibsd

Bettina Anna Barbara Schröder

Consistent Higher Order Accurate Time Discretization Methods for Inelastic Material Models

kassel
university
press

Series Institute of Structural Mechnics
Continuation of the Series Baumechanik/Baudynamik

(German title: Schriftenreihe Institut für Baustatik und Baudynamik, früher u. d. Titel
Schriftenreihe Baumechanik/Baudynamik (Vol. 2013-1 bis 2016-4))

This work has been accepted by the Faculty of Civil and Environmental Engineering of the University of Kassel as a thesis for acquiring the academic degree of Doktor der Ingenieurwissenschaften (Dr.-Ing.).

Supervisor: Prof. Dr.-Ing. habil. Detlef Kuhl, University of Kassel
Co-Supervisor: Prof. Dr.-Ing. habil. Jörg Schröder, University of Duisburg-Essen

Defense day: 15th May 2019

Bibliographic information published by Deutsche Nationalbibliothek
The Deutsche Nationalbibliothek lists this publication in the Deutsche Nationalbibliografie; detailed bibliographic data is available in the Internet at http://dnb.dnb.de.

Zugl.: Kassel, Univ., Diss. 2019
ISBN 978-3-7376-0772-8 (print)
ISBN 978-3-7376-0773-5 (e-book)
DOI: http://dx.medra.org/10.19211/KUP9783737607735
URN: https://nbn-resolving.org/urn:nbn:de:0002-407733

Printed and produced by: Print Management Logistics Solutions, Kassel
Printed in Germany

Explanation of the portraits on the cover

The cover of this work honors scientists whose discoveries and publications have laid the essential foundations of research and university teaching at the University of Kassel, Institute of Structural Mechanics. The following scientists are presented: Isaac Newton, Leonhard Euler, William Rowan Hamilton, Gottfried Wilhelm Leibniz, Galileo Galilei, Augustin-Louis Cauchy, Joseph-Louis Lagrange, Jean-Baptiste le Rond d'Alembert, Walter Ritz, Nathan Mortimore Newmark, Ray William Clough, Robert Leroy Taylor, Boris Grigorievich Galerkin, John Hadji Argyris, Olgierd Cecil Zienkiewicz and Thomas Joseph Robert Hughes.

The portraits were created in 2012 and 2013 by Stephanie Heike, student of the Art College of the University of Kassel.

Foreword

The present work was created during my work as a research assistant in the department of Civil and Environmental Engineering in the Institute of Mechanics and Dynamics at the University of Kassel. With the following few lines, I would like to thank all those who supported me all along.

First of all, I would like to thank my "boss" Professor Detlef Kuhl, who provided initial support as an expert for my diploma thesis. Then, he helped me to fulfill my dream of obtaining a doctorate. He encouraged me to strive for solutions, believed in me and my ideas, and guided me to find my own way. I am very grateful that I was able to be part of his team.

I would also like to express my special appreciation to Professor Jörg Schröder for his interest in my work and the willingness to give his expertise. Further, I would like to thank the two other members of the doctoral committee, Professor Andreas Meister and Professor Jens Wackerfuß, whose support also contributed to the success of the work.

My deepest gratitude belongs to my office neighbor and friend Tobias Gleim. Without his explanations, his proofreading, and our discussions, this thesis would not be as it is. Thank you also for your steady moral support and your encouraging words.

Of course, also my other colleagues - Sönke and Sandra Carstens, Daniela Gleim, Tobias Fritz, Matthias Weiland, Torsten Hartkorn, the SFB/ TR TRR 30 team and the FEM team of Volkswagen with Steffen Rothe, Christian Deubner, Juri Kniss, Matthias Rauchschwalbe and Georg Lührs - were indispensable for the completion of this thesis. I would not want to have gone without their assistance and technical support.

Furthermore, I want to thank Dorothee Knees, Stephanie Thomas, Stefan Kopecz, Andreas Meister, and Gunar Matthies who sacrificed many of their evenings to teach me maths. Without you, I would not have been able to accomplish my thesis in this way.

My final words of gratitude belong to my family and friends. Especially, I want to say thank you to my "husband" Marcus who accepted that a lot of my leisure time belonged to my thesis and who nonetheless stayed by my side with his patience and love to encourage and motivate me. Mum and Dad, thank you both for always having an open door for me, for trying to solve my problems and giving me new ideas to go on. Without you three, I would not be the person I am.

Kassel, November 2018 Bettina Schröder

Zusammenfassung

Die vorliegende Arbeit befasst sich mit der Anwendbarkeit höhergenauer Zeitintegrationsverfahren sowie den dazugehörigen Fehlerschätzern auf die dynamische (Visko)plastizität im Bereich kleiner und großer Deformationen. In diesem Zusammenhang wird ein allgemeines elasto(visko)plastisches Problem definiert, welches auf orts- und zeitabhängigen Variationsungleichungen und Variationsgleichungen basiert. Mit dieser Definition werden ganzheitliche Lösungsstrategien entwickelt, die die (Visko)plastizität bei großen und kleinen Deformationen als Ein- oder Mehrfeldproblem betrachten. Während für Variationsgleichungen ein Newton-Raphson Verfahren angewendet wird, werden für Variationsungleichungen die Vorteile halbglatter Newton Verfahren ausgenutzt. Beide Strategien benötigen jedoch spezielle Linearisierungstechniken. Zu diesem Zweck wird eine räumliche Diskretisierung, welche ein semidiskretes Gleichungssystem liefert, mittels der Finiten Elemente Methode unter Verwendung kontinuierlicher und diskontinuierlicher Ansätze durchgeführt. Danach findet das Konzept der Gâteaux Ableitung beziehungsweise das der generalisierten Gradienten Anwendung, um das allgemeine elasto(visko)pastische Problem in eine linearisierte semidiskrete Form zu überführen. Um daraus schließlich ein lineares Gleichungssystem zu generieren, muss zusätzlich noch eine Zeitdiskretisierung angewendet werden. Dazu werden verschiedene höhergenaue Zeitintegratoren wie zum Beispiel das Newmark Verfahren, voll und diagonal implizite Runge-Kutta Verfahren sowie kontinuierliche und diskontinuierliche Galerkin Methoden eingesetzt.

Des Weiteren wird in dieser Arbeit eine klassische Betrachtungsweise der dynamischen (Visko)plastizität im Bereich kleiner und großer Deformationen dargelegt und in das Lösungskonzept des allgemeinen elasto(visko)plastischen Problems eingebettet. Der konventionelle Ansatz basiert auf der Idee die Impulsbilanz schwach zu formulieren und die Materialgleichungen der (Visko)plastizität nur indirekt zu berücksichtigen. Das Verschiebungsfeld wird an Finiten Element Knoten bestimmt, während (visko)plastische Größen nur am Integrationspunkt ermittelt werden. Daher muss eine separate Zeitintegration des Beschleunigungsterms in der Impulsbilanz sowie der Materialgleichungen realisiert werden. Eine adequate Kopplung beider Ebenen erfolgt mittels des Radial Return Map Algorithmus. Damit geht jedoch die Limitierung auf gewisse Zeitintegratoren einher.

Im Gegensatz dazu wird eine alternative Mehrfeldformulierung hergeleitet. Zu diesem Zweck wird das Prinzip von Jourdain erweitert. Die Idee dahinter ist, die Energiebilanz bestehend aus der kinetischen, inneren und äußeren Energie sowie einem Potential, welches dissipativen Effekten Rechnung trägt, als ein Raten abhängiges Funktional anzunehmen. Die Gleichungen der Elasto(visko)plastizität bei kleinen und großen Deformationen stellen dann die stationäre Stelle dieses Funktionals dar. Demzufolge können die Materialgleichungen und die Bilanzgleichungen gleichzeitig an Finiten Element Knoten gelöst werden. Somit ist nur noch eine einzige Zeitintegration durchzuführen. Eine größere Freiheit bei der Wahl der Zeitintegratoren ist die Folge und die Anwendung höhergenauer Verfahren wird erleichtert.

Die Analyse und der Vergleich der klassischen und der Mehrfeldformulierung erfolgt im Zuge verschiedener Beispiele unter Berücksichtigung von großen und kleinen Deformationen. In diesem Kontext wird ein dynamisches Benchmarkproblem entwickelt, welches mit einer begrenzten Anzahl an räumlichen Freiheitsgraden auskommt und es so ermöglicht den Fokus auf die Effekte höhergenauer Zeitintegratoren zu legen. Für die damit einhergehenden Untersuchungen werden eine Vielzahl von verschiedenen Fehlerschätzern formuliert, ausgewertet und verglichen. Letztendlich werden die wichtigsten Ergebnisse zusammengefasst und offen gebliebene Fragestellungen werden thematisiert.

Abstract

The present thesis aims at investigating the applicability of higher order accurate time integration schemes together with appropriate error estimators in the context of small and finite strain dynamic (visco)plasticity. Therefore, a general elasto(visco)plastic problem is defined, whereby it is assumed that it is based on space and time-dependent variational equalities or inequalities. This definition serves as a basis to create closed-form solution strategies for small and finite strain (visco)plasticity as a single- or a multifield problem. While a NEWTON-RAPHSON scheme is applied to variational equalities, variational inequalities are treated taking advantage of a semi-smooth NEWTON scheme. Both approaches, however, require special linearization techniques. For this purpose, a spatial discretization is carried out with the help of the finite element method exploiting continuous or discontinuous approximations, leading to a semidiscrete system of equations. Afterwards, the concept of GÂTEAUX derivatives or rather generalized gradients is explored, before a linearized semidiscrete form of the general elasto(visco)plastic problem is obtained. In order to generate a linear system of equations, an appropriate time discretization has to be applied. Therefore, distinct higher order accurate schemes such as NEWMARK's method, fully implicit as well as diagonally implicit RUNGE-KUTTA schemes, and continuous as well as discontinuous GALERKIN methods are elaborated.

In the scope of this thesis, a classical access towards small and finite elasto(visco)plasticity is presented and integrated into the solution concept of the general elasto(visco)plastic problem. This approach is based on the idea, that the balance of linear momentum is formulated in a weak sense and the material laws of elasto(visco)plasticity are only included indirectly. The displacement field is determined at the finite element nodes, while (visco)plastic quantities are solved on integration point level. Thus, a separate time discretization is implemented - on the one hand for the acceleration term of the balance of linear momentum, and for the material equations on the other hand. An appropriate coupling of both discretization levels is created by means of the radial return map. Limitations for the usage of time integrators are the consequence.

In contrast, an alternative multifield formulation is derived. In order to do so, the principle of JOURDAIN is adapted. The idea is to assume that the balance of energy - taking into account the kinetic energy, the internal as well as the external energy, as well as a pseudopotential representing dissipative effects - resembles a rate-type functional, whose stationarity condition leads to the equations describing small or finite dynamic (visco)plasticity. Accordingly, the material laws and the balance of linear momentum can be solved on the same level at finite element nodes and only one single time discretization scheme has to be performed. A greater freedom in the choice of time discretization schemes is obtained and the application of higher order accurate schemes is facilitated.

An analysis and a comparison of the classical and the multifield formulation is accomplished by means of distinct examples in the small and the finite strain regime. In this context, a dynamic elasto(visco)plastic benchmark problem is developed as well, which comes along with a limited number of spatial degrees of freedom and, hence, allows to focus on the effect of different higher order accurate time integration methods. For this investigation, a variety of time discretization error estimators are formulated, evaluated, and compared. Last but not least, the main results are summarized and remaining questions are addressed.

Contents

List of Figures

List of Tables

List of Symbols

Scalar Values

$\bar{A}^e$	area of element e
A	surface area of a body in the reference configuration
a	surface area of a body in the current configuration
a_{ij}	RUNGE-KUTTA coefficients
b_i	RUNGE-KUTTA coefficients
C	nonlinear complementarity function
c	arbitrary constant
c_i	RUNGE-KUTTA coefficients
D	dissipation pseudopotential
D_{int}	internal dissipation
e_{n+1}	scalar value of the error estimator
E	free internal energy
e	volume specific free internal energy
f	yield function
f^{trial}	trial yield function
g	step size parameter
h	general function
J	deformation gradient's determinant
J_{t}	JACOBIAN in time
k	convex/concave function
K	kinetic energy
$\bar{N}$	discontinuous shape function
$\bar{N}_{\text{t}}$	shape function of the test function in the time domain
$\hat{N}$	general shape function
N	continuous shape function

N_t	shape function in the time domain
ND	number of dimensions
NE	number of elements
NEQ	number of equations
NG	number of integration points
NG_t	number of integration points in time
NN	number of nodes
NNS	total number of structural nodes
NT	number of time steps
P	total power
P^*	power of external forces
p	polynomial degree
$\bar{p}_\mathrm{t}$	polynomial degree of the test function in the time domain
p_t	polynomial degree of the shape function in the time domain
q	order of convergence
R	radial direction in the reference configuration
r	radial direction in the current configuration
r_2	general nonlinear scalar function
s	number of RUNGE-KUTTA stages
T	end point in time
t	time
t^n	element time
t_1	initial point in time
u	step size control parameter
$u_{\mathrm{Z}0}$	displacement amplitude
$\bar{V}^e$	volume of element e
V	volume of a body in the reference configuration
v	volume of a body in the current configuration
Z	axial direction in the reference configuration
z	axial direction in the current configuration

Bold Characters

$\mathbf{A}$	matrix of RUNGE-KUTTA coefficients a_{ij}
$\mathbf{A}_\mathrm{t}$	aggregated RUNGE-KUTTA coefficient matrix for distinct points in time
$\boldsymbol{b}$	left CAUCHY-GREEN tensor
$\check{\mathbf{b}}$	vector of RUNGE-KUTTA coefficients with reduced order
$\mathbf{b}$	vector of RUNGE-KUTTA coefficients
$\boldsymbol{C}$	right CAUCHY-GREEN tensor
$\tilde{\boldsymbol{C}}^{-1}_{\mathrm{p},ni}$	starting value of diagonally implicit RUNGE-KUTTA method
$\tilde{\boldsymbol{C}}^{-1}_{\mathrm{p},n}$	starting value of the NEWMARK method
$\mathbf{c}$	vector of RUNGE-KUTTA coefficients
$\bar{\mathbf{D}}_\mathrm{t}$	generalized jump terms matrix
$\bar{\mathbf{d}}^{ij}_\mathrm{t}$	jump terms time element matrix
$\mathbf{D}$	generalized damping matrix
$\mathbf{D}_\mathrm{t}$	generalized damping matrix of aggregated stage/node values
$\mathbf{d}^{eij}/\boldsymbol{d}^{eij}$	element tangential damping matrix/tensor
$\mathbf{d}^{ij}_\mathrm{t}$	time element damping matrix
$\boldsymbol{E}$	GREEN-LAGRANGE strain tensor
$\boldsymbol{e}$	EULER-ALMANSI strain tensor
$\mathbf{e}$	assembled error of distinct time steps
$\boldsymbol{F}$	material deformation gradient
$\boldsymbol{f}$	mass forces
$\boldsymbol{g}_i$	cartesian basis vector
$\boldsymbol{g}_\mathrm{R}$	cylindrical basis vector in radial direction for the reference configuration
$\boldsymbol{g}_\mathrm{r}$	cylindrical basis vector in radial direction for the current configuration
$\boldsymbol{g}_\Phi$	cylindrical basis vector in tangential direction for the reference configuration
$\boldsymbol{g}_\phi$	cylindrical basis vector in tangential direction for the current configuration
$\boldsymbol{g}_\mathrm{Z}$	cylindrical basis vector in axial direction for the reference configuration
$\boldsymbol{g}_\mathrm{z}$	cylindrical basis vector in axial direction for the current configuration
$\boldsymbol{I}$	second order unity tensor
$\mathbf{I}$	general unity matrix
$\boldsymbol{J}$	JACOBIAN matrix

$\boldsymbol{J}^{\mathrm{red}}$	reduced JACOBIAN matrix
$\mathbf{K}_{\mathrm{t}}$	generalized stiffness matrix of aggregated stage/node values
$\mathbf{K}_1$	generalized stiffness matrix
$\mathbf{K}_2$	generalized stiffness matrix
$\mathbf{K}_{\mathrm{eff}}$	effective generalized stiffness matrix
$\mathbf{k}^{eij}/\boldsymbol{k}^{eij}$	element tangential stiffness matrix/tensor
$\mathbf{k}_{\mathrm{t}}^{ij}$	time element stiffness matrix
$\mathbf{k}_2^{ei}/\boldsymbol{k}_2^{eij}$	element tangential stiffness matrix/tensor
$\boldsymbol{l}$	symmetric part of the deformation velocity tensor
$\mathbf{M}$	generalized mass matrix
$\mathbf{M}_{\mathrm{t}}$	generalized mass matrix of aggregated stage/node values
$\mathbf{m}^{eij}/\boldsymbol{m}^{eij}$	element tangential mass matrix/tensor
$\mathbf{m}_{\mathrm{t}}^{ij}$	time element mass matrix
$\boldsymbol{N}$	outward normal vector in the reference configuration
$\boldsymbol{n}$	outward normal vector in the current configuration
$\boldsymbol{P}$	first PIOLA-KIRCHHOFF stress tensor
$\boldsymbol{p}$	second PIOLA-KIRCHHOFF stress vector
$\bar{\mathbf{R}}_{\mathrm{t}}$	generalized jump terms time load vector
$\bar{\mathbf{r}}_{\mathrm{t}}^{i}$	jump terms time load vector
$\bar{\mathbf{R}}_{1\mathrm{t}}$	generalized jump terms time load vector
$\bar{\mathbf{r}}_{1\mathrm{t}}^{i}$	jump terms time load vector
$\bar{\mathbf{R}}_{2\mathrm{t}}$	generalized jump terms time load vector
$\bar{\mathbf{r}}_{2\mathrm{t}}^{i}$	jump terms time load vector
$\mathbf{R}_{\mathrm{t}}$	generalized internal load vector of aggregated stage/node values
$\mathbf{R}_{\mathrm{t}}^{*}$	generalized external load vector of aggregated stage/node values
$\mathbf{R}_1$	generalized internal load vector
$\mathbf{R}_1^{*}$	generalized external load vector
$\mathbf{R}_2$	generalized load vector
$\mathbf{r}_{\mathrm{eff}}$	effective generalized load vector
$\mathbf{r}^{*}$	general surface loads
$\mathbf{r}_{\mathrm{t}}^{*,i}$	external time element load vector
$\mathbf{r}_{\mathrm{t}}^{i}$	internal time element load vector

$\mathbf{r}_1$	general nonlinear vector-/tensor-valued function
$\mathbf{r}_1^{*,ei}/\boldsymbol{r}_1^{*,ei}$	external load vector/tensor
$\mathbf{r}_1^{ei}/\boldsymbol{r}_1^{ei}$	internal load vector/tensor
r_2^{ei}	element load
$\boldsymbol{S}$	second PIOLA-KIRCHHOFF stress tensor
$\boldsymbol{s}$	general variable
$\boldsymbol{T}$	first PIOLA-KIRCHHOFF stress vector
$\boldsymbol{t}$	CAUCHY stress vector
$\boldsymbol{T}^*$	external first PIOLA-KIRCHHOFF stress vector
$\boldsymbol{t}^*$	external CAUCHY stress vector
$\boldsymbol{u}$	displacement vector
$\mathbf{v}$	first time derivative of the vector of primary variables
$\mathbf{w}$	vector of primary variables
$\tilde{\mathbf{v}}_{ni}$	starting values for diagonally implicit RUNGE-KUTTA methods
$\tilde{\mathbf{w}}_{ni}$	starting values for diagonally implicit RUNGE-KUTTA methods
$\mathbf{v}_\mathrm{t}$	first time derivative of the vector of aggregated stage/node values
$\mathbf{w}_\mathrm{t}$	vector of aggregated stage/node values
$\boldsymbol{X}$	location vector in the reference configuration
$\boldsymbol{x}$	location vector in the current configuration
$\mathbf{y}$	vector of primary variables in the two-field setting
$\mathbf{y}_\mathrm{t}$	vector of aggregated stage/node values of primary variables in the two-field setting

Greak Symbols

α_r	RUNGE-KUTTA factor
α	integrational weight factors
β	NEWMARK parameter
β_r	RUNGE-KUTTA factor
Γ	boundary of domain Ω
γ	NEWMARK parameter
Γ_*	general NEUMANN boundary of domain Ω
$\Gamma_\mathbf{w}$	general DIRICHLET boundary of domain Ω

$\delta\mathbf{t}$	test function for the time domain
$\delta\mathbf{t}_1$	test function for the time domain
$\delta\mathbf{t}_2$	test function for the time domain
δW	general weak form
δW_t	virtual work for the time domain
$\delta\boldsymbol{C}$	test function related to the strain field
$\delta\boldsymbol{E}$	test function related to the strain field
$\delta\boldsymbol{F}$	test function related to the material deformation gradient
$\delta\boldsymbol{S}$	test function related to the stress field
$\delta\boldsymbol{u}$	test function related to the displacement field
$\delta\dot{\boldsymbol{\varepsilon}}_\mathrm{p}$	test function related to the rate of the plastic strain field
$\delta\dot{\boldsymbol{C}}_\mathrm{p}^{-1}$	test function related to the rate of the plastic strain field
$\delta\dot{\boldsymbol{u}}$	test function related to the rate of the displacement field
$\delta\dot{\mathbf{t}}$	time derivative of the test function in the time domain
$\delta\lambda$	test function related to the LAGRANGE multiplier
$\delta\boldsymbol{\sigma}$	test function related to the stress field
$\delta\boldsymbol{\varepsilon}$	test function related to the strain field
$\delta\mathbf{z}_1/\delta\boldsymbol{z}_1$	general test function
Δt	time step size
$\boldsymbol{\varepsilon}$	linearized strain tensor
$\tilde{\boldsymbol{\varepsilon}}_{\mathrm{p},ni}$	starting value of diagonally implicit RUNGE-KUTTA method
$\tilde{\boldsymbol{\varepsilon}}_{\mathrm{p},n}$	starting value of the NEWMARK method
κ	LAMÉ parameter
λ	primary variable / LAGRANGE multiplier
μ	LAMÉ parameter
η	prescribed termination criterion NEWTON-RAPHSON scheme
η_w	obtained termination criterion NEWTON-RAPHSON scheme
ξ	norm of the displacement gradient
$\boldsymbol{\xi}$	vector of natural coordinates
$\boldsymbol{\xi}_\mathrm{t}$	vector of integration points in the time domain
ξ_t	natural coordinate in the time domain
Θ	switching parameter for time integration

ρ	density of a body in the current configuration
ρ_0	density of a body in the reference configuration
$\boldsymbol{\sigma}$	CAUCHY stress tensor
σ_y	yield stress
τ	arbitrary monotonous function
Φ	tangential direction of the reference configuration
ϕ	tangential direction of the current configuration
χ	viscosity parameter
ψ	variation parameter
ψ_I	indicator function
$\bar{\Omega}^e$	domain of element e of the continuum mechanical body
Ω	domain of continuum mechanical body
ω	frequency
Ω^e	domain of standard element e

Caligraphic Quantities

$\mathcal{A}$	active set
$\mathcal{B}$	material body
$\mathcal{E}$	small material element
$\mathcal{I}$	inactive set
$\mathcal{L}$	LAGRANGE function
$\mathcal{O}$	LANDAU symbol
$\mathcal{P}$	material point
$\mathcal{S}$	set of admissible stresses

Fourth Order Tensors

$\mathbb{C}$	constitutive tensor
$\mathbb{G}$	algorithmic constitutive tensor
$\mathbb{I}$	fourth order unity tensor

Operators

$\bigcup$	assembly operator
$\mathbf{B}$	B-operator
$\circ$	conjunction operator
$\cdot$	dot product
$:$	double-dot product
Δ	difference operator
$\mathrm{DEV}\,(\bullet)$	deviator in the reference configuration
$\mathrm{dev}\,(\bullet)$	deviator
$\otimes$	dyadic product
$\lvert\,(\bullet)\,\rvert$	determinant
d	infinitesimal quantity
$\in$	element of operator
$[\![\bullet]\!]$	jump term
$\lVert\,(\bullet)\,\rVert$	FROBENIUS norm
$\lVert\,(\bullet)\,\rVert_{\max}$	maximum norm
$\bar{\mathrm{D}}_{\mathbf{s}}$	generalized derivative with respect to $\mathbf{s}$
$\mathrm{D}_{\mathbf{s}}$	GÂTEAUX derivative with respect to $\mathbf{s}$
$\frac{\partial}{\partial}$	partial derivative
$(\bullet)_{;i}$	derivative with respect to natural coordinate direction i
∂	sub- / superdifferential or generalized gradient depending on the context
$(\bullet)^{-1}$	inverse operator
inf	infimum operator
δ_{ik}	KRONECKER symbol
ln	natural logarithm function
max	maximum operator
∇	NABLA operator
$\langle\bullet,\bullet\rangle$	general scalar product
$\langle\bullet\rangle$	ramp function
$\mathrm{sgn}\,(\bullet)$	sign function
$\mathrm{sph}\,(\bullet)$	volumetric part

Σ	summation operator
sup	supremum operator
$\dot{(\bullet)}$	first time derivative
$\ddot{(\bullet)}$	second time derivative
$(\bullet)^{\mathrm{T}}$	transpose operator
$\mathrm{Tr}\,(\bullet)$	trace operator in the reference configuration
$\mathrm{tr}\,(\bullet)$	trace operator

Indices

$\check{(\bullet)}$	quantities associated to error estimations
$\hat{(\bullet)}$	quantities associated to the intermediate configuration
$(\bullet)^{*}$	boundary quantities
$(\bullet)^{+}$	right sided value of a variable in the case of discontinuities
$(\bullet)^{-}$	left sided value of a variable in the case of discontinuities
$(\bullet)_{\mathrm{e}}$	elastic quantity
$(\bullet)^{e}$	quantity related to an element e
$(\bullet)^{\mathrm{ex}}$	exact solution
$(\bullet)^{\mathrm{glob}}$	global error quantity
$(\bullet)^{\mathrm{max}}$	max error quantity
$(\bullet)^{\mathrm{mean}}$	mean error quantity
$(\bullet)_{\mathrm{emb}}$	embedded error quantity
$(\bullet)_{\mathrm{h}}$	h-error quantity
$(\bullet)_{\mathrm{r}}$	residual error quantity
$(\bullet)^{k}$	iteration index
$(\bullet)_{n}$	time step index
$(\bullet)_{ni}$	stage index
$(\bullet)_{\mathrm{p}}$	(visco)plastic quantity
$(\bullet)_{\mathrm{t}}$	quantity at distinct time nodes/stages
$(\bullet)_{\mathrm{R}}$	radial quantity in the reference configuration
$(\bullet)_{\mathrm{r}}$	radial quantity in the current configuration
$(\bullet)_{\Phi}$	tangential quantity in the reference configuration

$(\bullet)_{\phi}$	tangential quantity in the current configuration
$(\bullet)_{\mathrm{Z}}$	axial quantity in the reference configuration
$(\bullet)_{\mathrm{z}}$	axial quantity in the current configuration

1. Introduction

1.1. Motivation

Scientific research is often shaped by social and economic conditions as well as an environmental conscience. In the engineering field, this leads to high performance products with striking aspirations with regard to security aspects, lightweight constructions and resource efficient production strategies. Creating new multi-materials by cleverly combining existing ones in a single forming process step may be seen as a specific example, cf. (Fleischer, 2014). A different approach is to conceive hybrid materials by using joining techniques that are based on the exploitation of plastic deformations, cf. (Liewald, 2012). But there are also new fabrication scenarios in the regime of monomaterials, that lead to noteworthy results regarding the desired objectives. Thus, electromagnetic supported sheet metal deep drawing with different forming speeds leads to an optimized utilization of material as well as to an extended formability, cf. (Reese, 2008). Functionally graded structures for which material properties are adjusted in an application-oriented manner can be obtained by an integrated thermodynamical forming process, cf. (Steinhoff et al., 2009).

But apart from high demands in the context of production engineering, challenges concerning the simulation of these fabrication sequences as well as the simulation of the obtained products' application have to be overcome. The common ground within the previously described examples is that the manufacturing process or the products' application is characterized by both (visco)plastic deformations and dynamic effects. To demonstrate this, the integrated thermomechanical process of (Steinhoff et al., 2009) is analyzed explicitly. For metallic products, the production procedure is mainly characterized by three subsequent stages, see Figure 1.1.

Figure 1.1.: Integrated thermomechanical forming process, cf. (Steinhoff et al., 2009)

In the first step, a heterogenous temperature distribution is achieved throughout a local inductive heating. Afterwards, the workpiece is mechanically formed and simultaneously cooled due to the contact with the forming die. This is followed by a partial cooling with a high pressured air stream, whereby a further adjustment of the material characteristics is obtained, cf. (Steinhoff et al., 2009). The second task of this innovative fabrication sequence is considerably influenced by finite thermo(visco)plastic deformations and inertia effects due to the fast closing of the forming die. Hence, in order to simulate such a forming process, adequate models and implementation strategies have to be established.

Basic aspects for a continuum mechanical modeling of finite strains are provided by (Altenbach, 2012; Bonet and Wood, 2009; Haupt, 2000; Holzapfel, 2000; Wriggers, 2008). Therein, it is especially the balance equations that are necessary to describe the forming process mathematically

that are derived. Apart from field equations appropriate constitutive laws, characterizing elastic and (visco)plastic effects, have to be formulated. Within the finite strain regime, different kinematic relations have been formulated to describe elasto(visco)plastic behavior. A multiplicative split of the deformation gradient in a (visco)plastic and an elastic part was also considered as an additive split of the strain tensor, cf. (Lubliner, 2006; Naghdi, 1990; Simo and Ortiz, 1985). In the context of solid mechanics, it is customary to formulate the balance equations using quantities associated to the reference configuration, but there is no analogous concept for the material laws. Formulations in the reference configuration are just as common as a description in the current or even in a third, the intermediate configuration, cf. (Casey and Naghdi, 1988; Haupt, 2000; Lubliner, 2006; Miehe, 1995; Quint, 2011; Simo, 1998; Wriggers, 2008). If the considered deformation process is constituted by small strains, a geometric linearization can be carried out so that this distinction can be neglected and all configurations coincide, cf. (Altenbach, 2012; Haupt, 2000).

Concerning the modeling of metal plasticity, there are several approaches for small as well as for finite strains. While some models are based on phenomenological aspects, others acknowledge the microstructure as a starting point for a macroscopic modeling, cf. (Chaboche, 2008; Haupt, 2000; Mahnken et al., 2011, 2012; Ostwald et al., 2010). Furthermore, additional aspects such as directional-dependent material properties, hardening assumptions, or temperature dependencies are taken into account, cf. (Chaboche, 2008; Mahnken and Schneidt, 2009; Miehe, 1995; Schröder et al., 2002; Simo and Miehe, 1992; Svendsen, 2007; Tsakmakis, 1996*a*,*b*; Vladimirov et al., 2010).

There is a similar variety regarding the numerical realization. Since analytical solutions are only rarely available for elasto(visco)plastic behavior, numerical solution procedures experience an enhanced interest. They are generally based on nonlinear solution strategies together with spatial and temporal discretization methods. In the finite thermo(visco)plastic regime, for example, one attempt is to formulate the balance laws weakly, apply the finite element method using the displacement and the temperature field as primary variables, and to evaluate the material laws on integration point level, cf. (Dhondt, 2004; Hughes, 2000; Simo, 1998; Zienkiewicz and Taylor, 2000). Due to the often occurring volume preserving constraint of the plastic flow, and in the context of nearly incompressible materials, multifield approaches emerged, cf. (De Souza Neto et al., 2008; Simo and Miehe, 1992; Wriggers et al., 1992). Moreover, further independent fields like stresses or generalized forces came to attention through the explicit exploitation of the maximum principle of dissipation or of dissipational potentials, (Carstensen et al., 2002; Hackl, 1997; Halphen and Nguyen, 1975). These assessments also gained popularity in the context of small strain plasticity involving or disregarding thermal effects, cf. (Comi and Perego, 1995; De Borst and Mühlhaus, 1992; Miehe, 2011; Simo et al., 1989; Stainier, 2013). The common framework to derive these multifield settings within the finite and the small regime is an incremental variational formulation. The term dissipational potential may refer to different expressions - depending on the respective author. A mathematical analysis acknowledging some aspects of multifield plasticity is carried out in (Carstensen et al., 2002; Han and Reddy, 1999; Mielke, 2004; Reddy and Martin, 1994) and the references therein.

Apart from the spatial discretization, a temporal one has to be performed as well. In the scope of dynamic thermo(visco)plasticity, this is necessary due to two reasons. First, the heat conduction equation may take non-stationary effects into account, and the balance of linear momentum inherits an acceleration term, which is associated to the prevalent inertia effects. For high deformation speeds, these phenomena influence the resulting strain field and cannot be neglected. Hence, their temporal discretization plays an important role. However, they are often not taken into account and quasi-static circumstances are examined. The second argument for a time discretization is the modeling of (visco)plastic effects. They are often characterized by material laws which include constitutive as well as evolution equations. The

latter allow for mathematical descriptions of materials that possess a memory, thus linking their behavior to past events, cf. (Hartmann, 2008; Schreiber, 1997). This can be done using rate-dependent formulations where the strain rate influences the response of the material. If the same deformation state is obtained, despite considering distinct deformation speeds, rate-independent models are necessary, cf. (Hartmann, 2008; Haupt, 2000; Simo and Hughes, 1997).

Due to the various possible combinations of spatial and temporal discretizations, there are a lot of distinct numerical implementations. A commonly applied approach for the time discretization is the backward EULER scheme, cf. (Comi and Perego, 1995; Simo et al., 1989; Simo and Miehe, 1992; Zienkiewicz and Taylor, 2000), but also generalized midpoint rules, exponential time integrators, RUNGE-KUTTA methods, NEWMARK schemes, and GALERKIN methods are employed - either to discretize the evolution or the balance equations, cf. (Alberty and Carstensen, 2002; Auricchio and Taylor, 1999; Ellsiepen and Hartmann, 2001; Hager and Wohlmuth, 2009; Mohr et al., 2008; Simo, 1998; Simo and Hughes, 1997; Wriggers, 2008).

The important issue, with regard to dynamic plasticity, is that the time discretization of the material laws and the one of the balance equation are coupled appropriately. Furthermore, it must be assured that the yield condition is not violated at the calculated time step. In this context, a series of procedures has been developed. For conventional plasticity, where the displacement field is the only unknown, return mapping algorithms are established, cf. (Han and Reddy, 1999; Simo, 1998; Simo and Hughes, 1997). Therein, a trail state is defined for each integration point. This state is accepted if elastic behavior prevails, otherwise the yield condition is violated and a projection of the stress state back onto the yield surface is carried out. In (Ellsiepen and Hartmann, 2001; Hartmann, 2005) the link between the element and the integration point level and, hence, the fulfillment of the yield condition is obtained via a nested NEWTON method, a so called multilevel NEWTON algorithm. A further access towards the numerical implementation of plasticity is to use tools that are known from optimization. A reconsideration of the radial return map, leading to the application of sequential quadratic programming methods, is one consequence, cf. (Wieners, 2007). The numerical exploitation of variational inequalities by means of semi-smooth NEWTON methods is another, cf. (Christensen, 2002; Hager and Wohlmuth, 2009; Seitz et al., 2014). However, the actual realizations vary concerning the number and kind of considered primary variables. Hence, in this context, a variety of different multifield formulations prevails.

The algorithmic demands for dynamic viscoplasticity are different from those regarding the plastic case. Within viscoplasticity, the yield condition can be violated, since stress states outside the yield surface are permitted. Hence, the problem formulation loses its constraint, cf. (Hartmann et al., 1997). This behavior is often modeled using regularization techniques, whereby the limit case leads to the original formulation of plasticity, cf. (Alberty and Carstensen, 2000; Alberty et al., 1999; Ebobisse and Reddy, 2004). The consequence is that many classical algorithms can be applied to viscoplasticity and plasticity, cf. (Ellsiepen and Hartmann, 2001; Simo and Hughes, 1997). However, schemes known from optimization, for example semi-smooth NEWTON methods, are not necessary anymore. Nonetheless, the derivation of alternative methods like least-square formulations is enabled, cf. (Schwarz et al., 2009). However, an adequate coupling between the material laws and the balance equation is still an important aspect.

Despite the individuality of the previously described numerical schemes, all these methods are always accompanied by numerical errors. Apart from technically caused rounding errors, there are also approximation errors due to the spatial and temporal discretization. To assess the influence of the latter distinct error estimators are developed. In the context of (visco)plasticity, the spatial error estimation is analyzed in (Bangerth and Rannacher, 2003; Han and Reddy, 1999; Repin and Xanthis, 1996; Schmidt, 2001; Stein, 2003) using dual, residual, or recovery-based techniques. Specific plasticity-inherent procedures are taken into account as well. The

time discretization error of elastoplastic problems is examined in (Alberty and Carstensen, 2000; Eidel and Kuhn, 2015; Hartmann and Bier, 2007; Mielke et al., 2010). Thereby, theoretical as well as numerical investigations are performed.

In the following thesis, a selection of the previously mentioned topics will be outlined in detail. Motivated by the integrated thermomechanical forming process of (Steinhoff et al., 2009), two widespread models of elasto(visco)plasticity - one for the finite and one for the small strain regime - as well as their conventional implementations using the radial return map are presented, cf. (Simo, 1998; Simo and Hughes, 1997). Furthermore, a new approach and its consistent mathematical formulation towards these models is derived. The concept is to create a time-continuous variational multifield formulation which enables a simple implementation of a wide class of higher order accurate time integration schemes on balance and on material law level at the same time. Thus, lavish coupling algorithms can be disregarded. To achieve this, the ideas of a dissipational potential, cf. (Carstensen et al., 2002; Hackl, 1997; Halphen and Nguyen, 1975; Reddy and Martin, 1994), are interpreted in a broader sense and unified with the incremental multifield formulations of (Comi and Perego, 1995; Miehe, 2011). To simplify this way of proceeding, thermal effects will be neglected continuously. In the end, the classical and the variational procedure are compared. In order to do so, a dynamic benchmark problem with a viscoplastic and a plastic variant for the small and the finite strain regime is designed and implemented, and detailed results are provided. The distinct variants of the benchmark problem allow for a variety of numerical studies, including the analysis of distinct higher order accurate time integration schemes concerning their time discretization errors.

1.2. Outline

Chapter 2 is devoted to a short summary of the background of continuum mechanics, introducing all necessary kinematic and kinetic quantities as well as their meaning. Additionally, the crucial balance equations are depicted and explained. Furthermore, an insight into the topic of small strains derived by means of a linearization of finite deformation measurements is provided.

In **Chapter 3**, a general elasto(visco)plastic problem is defined. It is based on a nonlinear space- and time-dependent initial boundary value problem in its weak form. This general framework enables the mutual treatment of distinct model formulations as well as solution concepts. While the former are treated in **Chapter 4** and **Chapter 6**, the latter lie in the focus of this chapter. A classical ansatz employing only variational equalities is followed together with an approach that also takes inequalities into account. For the latter formulation, a semi-smooth Newton procedure is depicted, which rests on the notion to redraft the inequalities into equalities by using complementarity functions as well as creating active and inactive sets. In contrast, a Newton-Raphson scheme is presented for the classical approach. Both solution strategies, however, are founded on the idea of applying the finite element method for spatial discretization. Hence, important aspects including the parametrization, numerical integration, and the exploitation of both continuous and discontinuous approximations of primary variables are explored. The consequence is that the weak form of the nonlinear space- and time-dependent problem is transformed into a system of ordinary differential or differential algebraic equations. To solve this time-dependent problem, various time discretization schemes are employed. Hereby, only higher order accurate one-step time integration methods are considered, which are also appropriate for differential algebraic systems. This leads to fully or diagonally implicit Runge-Kutta schemes as well as to the Newmark class. A detailed description for distinct types of Galerkin time discretization methods is carried out, likewise. In the end, a system of linear equations has to be solved. Moreover, the reasons for errors appearing in the previously described solution schemes

are discussed, giving high priority to the time discretization error. Its quantification is depicted by means of three distinct procedures. Therefore, the h-, the residual as well as the embedded error estimation are explained and error characterizing quantities are defined.

Chapter 4 is concerned with the material modeling and the numerical implementation of small strain elasto(visco)plasticity. The first part of this chapter presents an introduction and a common known access towards the elasto(visco)plastic material laws. Additionally, their numerical realization is derived. In this context, the initial boundary value problem of **Chapter 3** is substantiated and the described solution procedures are augmented by the radial return mapping method. The latter aims at incorporating (visco)plastic effects into standard elastic computation schemes on integration point level by exploiting appropriate time integrators. In the second part of this chapter, an alternative derivation strategy for the already known elasto(visco)plastic material equations is depicted. It is based on the assumption that the virtual power reaches a stationary point. By exploiting aspects of functional analysis and optimization, a second initial boundary value problem describing elasto(visco)plastic phenomena is determined. Therein, the (visco)plastic quantities are changed into quantities on structural level, enabling a simple application of a wide range of higher order accurate time integrators to all unknowns. Again, the solution procedures of **Chapter 3** are elaborated to yield a numerical implementation strategy for the obtained variational approach.

In **Chapter 5**, numerical results for different model problems determined by the classical and the variational approach are presented. To start off with, a quasi-static benchmark problem from the literature is used to validate the implementation of the classical approach and the derivation as well as the numerical realization of the variational approach. Afterwards, a new dynamic benchmark problem with an adaptation for plasticity and viscoplasticity is established. In the first step, a quasi-static analysis of a displacement-driven deformation process of an axisymmetric shaft is carried out. Afterwards, the same model is investigated considering inertia effects. This allows to characterize distinct time integrators in the context of elasto(visco)plastic problems. On the one hand, the time discretization error of different field variables is estimated for the Newmark method as well as for some Galerkin and Runge-Kutta schemes. On the other hand, the orders of consistency and the orders of convergence are portrayed for the respective procedures.

Chapter 6 can be interpreted as the extension of **Chapter 4** with regard to the finite strain regime. A classical approach towards material modeling and numerical implementation of finite elasto(visco)plasticity is summed up together with the corresponding variational multifield approach exploiting the principle of Jordain. The latter procedure serves to enable a simple usage of higher order accurate time integrators, not only in the small but also in the finite strain regime.

The validation of the numerical realization of finite elasto(visco)plasticity within the classical and the variational approach is performed in **Chapter 7**. Therein, both variants of the newly created dynamic benchmark problem are studied in the finite strain regime. Again, various time integrators are analyzed concerning their resultant errors within distinct field variables. Moreover, the obtainable orders of convergence and consistency are estimated.

In **Chapter 8** and **Chapter 9**, the obtained results are summarized, and open questions are addressed - together with further research objectives.

2. Basic Aspects of Continuum Mechanics

The second fabrication step of the integrated thermomechanical forming process portrayed in **Chapter 1**, see Figure 1.1, is characterized by large thermo(visco)plastic deformations as well as by inertia effects. This aspect is to be seen as a motivation for this thesis. The idea is to develop new algorithms for an easy implementation of a wide range of higher order accurate time integration schemes taking plastic and viscoplastic deformations into account. To simplify the analysis, temperature effects will not be considered at all. This leads to a purely continuum mechanical framework, whose basic aspects are depicted in the proceeding chapter. Thereby, the integration of plastic phenomena is emphasized, bearing in mind that the same line of reasoning can be followed for viscoplastic effects. Furthermore, only three-dimensional cartesian coordinate systems are considered if not indicated otherwise. Important information concerning the tensor calculus can be found in **Appendix A**. For more detailed explanations concerning continuum mechanical theory and tensor calculus see (Altenbach, 2012; De Boer, 1982; Grinfeld, 2013; Haupt, 2000; Holzapfel, 2000; Kelly, 2015; Talpaert, 2002; Wriggers, 2008).

2.1. Kinematics and Kinetics of a Continuum

In order to describe the deformation process of a continuum mechanical object, adequate kinematical as well as kinetical quantities have to be defined. Considering a general body $\mathcal{B}$ - consisting of different material points and possessing the volume V, the surface area A, as well as the density ρ_0 - then the variable $\boldsymbol{X}$ denotes the location vector of one specific material point $\mathcal{P}$ at time t_1, see Figure 2.1. The unambiguous differentiable assignment of position vectors to all material points at this time is called reference configuration, cf. (Altenbach, 2012). If, furthermore, an imposed movement or deformation process of this body $\mathcal{B}$ is assumed, $\boldsymbol{x}$ indicates the new position vector of point $\mathcal{P}$ at time t. This yields the current configuration. The possibly resulting new properties like volume, surface area, and density are denoted by v, a, and ρ, respectively. The difference between both location vectors of point $\mathcal{P}$ is defined as the displacement vector

$$\boldsymbol{u}(\boldsymbol{X},t) = \boldsymbol{x}(\boldsymbol{X},t) - \boldsymbol{X} \qquad \text{or} \qquad \boldsymbol{u}(\boldsymbol{x},t) = \boldsymbol{x} - \boldsymbol{X}(\boldsymbol{x},t), \tag{2.1}$$

which can be expressed in dependence of the current or the reference configuration. The corresponding designation will be kept within the forthcoming analysis, due to its importance. For all other quantities defined further on, the spatial and temporal dependencies will be dropped in favor of a shorter notation. In order to describe the changes of size and shape of a material body, the transformation of an infinitesimal line element $d\boldsymbol{X}$ of the reference configuration into the current configuration $d\boldsymbol{x}$ is examined. Due to the unambiguous differentiable relationship between the current position vector $\boldsymbol{x}$ and the reference location vector $\boldsymbol{X}$, a total differential

$$d\boldsymbol{x} = \frac{\partial \boldsymbol{x}(\boldsymbol{X},t)}{\partial \boldsymbol{X}} \cdot d\boldsymbol{X} = \boldsymbol{F} \cdot d\boldsymbol{X} \qquad \text{with} \qquad \det \boldsymbol{F} = J > 0 \tag{2.2}$$

can be formulated, leading to the material deformation gradient $\boldsymbol{F}$ and its determinant J, cf. (Altenbach, 2012; Haupt, 2000). With the help of the deformation gradient, a variety of strain measures can be derived. The basic idea is to evaluate the difference between the squared lengths of line elements of the current and the reference configuration, cf. (Hartmann, 1993; Haupt, 2000;

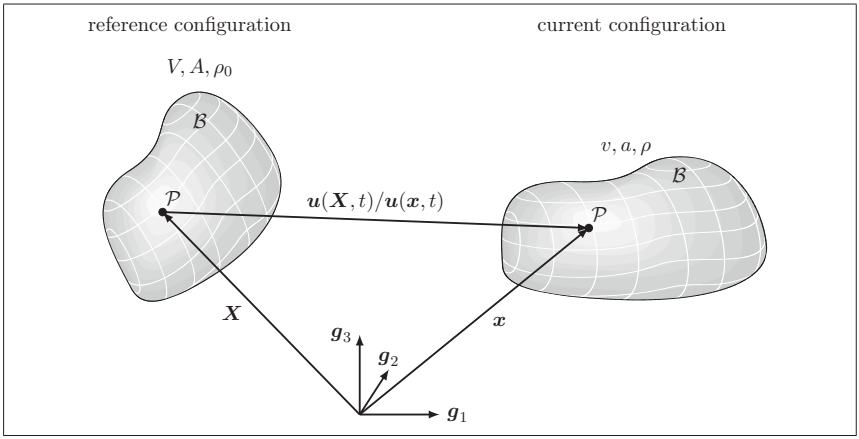

Figure 2.1.: Definition of the displacement vector $\boldsymbol{u}(\boldsymbol{X}, t)$

Holzapfel, 2000). Hence, the right CAUCHY-GREEN tensor $\boldsymbol{C}$ and the GREEN-LAGRANGE strain tensor $\boldsymbol{E}$ can be defined by

$$\boldsymbol{C} = \boldsymbol{F}^{\mathrm{T}} \cdot \boldsymbol{F}, \qquad \boldsymbol{E} = \frac{1}{2}\left[\boldsymbol{C} - \boldsymbol{I}\right], \tag{2.3}$$

exploiting the second order unity tensor $\boldsymbol{I} = \delta_{ij}\, \boldsymbol{g}_i \otimes \boldsymbol{g}_j$ with the KRONECKER symbol δ_{ij} and the cartesian basis vectors $\boldsymbol{g}_i$ with $i, j = 1, ..., 3$. Both measurements operate on line elements of the reference configuration and are thus associated to the latter. In contrast, the left CAUCHY-GREEN tensor $\boldsymbol{b}$ and the EULER-ALMANSI strain tensor $\boldsymbol{e}$

$$\boldsymbol{b} = \boldsymbol{F} \cdot \boldsymbol{F}^{\mathrm{T}}, \qquad \boldsymbol{e} = \frac{1}{2}\left[\boldsymbol{I} - \boldsymbol{b}^{-1}\right] \tag{2.4}$$

operate on the current configuration. If (visco)plastic effects are taken into account for the continuum mechanical modeling as well, the kinematic relations have to be extended. A classical approach is to consider a further, intermediate configuration, which is associated to an unstressed state in which only (visco)plastic deformations prevail. This state is obtained by cutting the body $\mathcal{B}$ into small elements $\mathcal{E}$ and removing all applied stresses instantly, leading to elastic deformations described by $\boldsymbol{F}_{\mathrm{e}}$ as well as to residual ones represented by $\boldsymbol{F}_{\mathrm{p}}$, cf. (Haupt, 2000; Lee and Liu, 1967; Lubliner, 2006; Simo and Ortiz, 1985). Hence, the material deformation gradient $\boldsymbol{F}$ is split multiplicatively into

$$\boldsymbol{F} = \boldsymbol{F}_{\mathrm{e}} \cdot \boldsymbol{F}_{\mathrm{p}}, \tag{2.5}$$

with the corresponding determinants

$$J = J_{\mathrm{e}} J_{\mathrm{p}}, \qquad J_{\mathrm{e}} = \det(\boldsymbol{F}_{\mathrm{e}}), \qquad J_{\mathrm{p}} = \det(\boldsymbol{F}_{\mathrm{p}}).$$

Due to the local unloading, the different elements $\mathcal{E}$ change their shape and can thus not be fitted together to form the body $\mathcal{B}$ again. Accordingly, the individual parts of the deformation gradient cannot be determined by gradients of corresponding elastic and (visco)plastic displacement fields, cf. (Lee and Liu, 1967). From a micromechanical point of view, the elastic part $\boldsymbol{F}_{\mathrm{e}}$ represents the lattice distortion, whereas the (visco)plastic part $\boldsymbol{F}_{\mathrm{p}}$ is linked to the dislocation flow, cf. (Simo, 1998).

Alternative points of departure to describe plastic or viscoplastic effects are presented in (Casey and Nagdhi, 1980; Green and Nagdhi, 1965; Kleiber, 1975; Lee, 1969; Lee and Liu, 1967; Naghdi, 1990; Nemat-Nasser, 1982; Xiao et al., 2006), where, for example, an additive decomposition of the GREEN-LAGRANGE strain tensor or the deformation velocity tensor into an elastic and a (visco)plastic part is proposed. A unifying concept of these approaches is established in (Simo and Ortiz, 1985). A similar strategy is followed here, drawing on information provided in (Xiao et al., 2006).

The multiplicative split leads to a number of further strain measures characterizing elastic and (visco)plastic effects. Operating on the reference configuration, the (visco)plastic right CAUCHY-GREEN tensor $\boldsymbol{C}_\mathrm{p}$ and the (visco)plastic GREEN-LAGRANGE tensor $\boldsymbol{E}_\mathrm{p}$

$$\boldsymbol{C}_\mathrm{p} = \boldsymbol{F}_\mathrm{p}^\mathrm{T} \cdot \boldsymbol{F}_\mathrm{p}, \qquad \boldsymbol{E}_\mathrm{p} = \frac{1}{2}\left[\boldsymbol{C}_\mathrm{p} - \boldsymbol{I}\right] \tag{2.6}$$

can be defined. Formally, also an elastic GREEN-LAGRANGE tensor $\boldsymbol{E}_\mathrm{e}$ can be constructed by

$$\boldsymbol{E}_\mathrm{e} = \frac{1}{2}\left[\boldsymbol{C} - \boldsymbol{C}_\mathrm{p}\right] = \boldsymbol{E} - \boldsymbol{E}_\mathrm{p}. \tag{2.7}$$

Hence, with a multiplicative decomposition of the deformation gradient an additive decomposition of the GREEN-LAGRANGE strain tensor can be obtained too. Similar expressions can be acquired if the quantities associated to the current configuration are enhanced. If the elastic left CAUCHY-GREEN tensor is denoted by

$$\boldsymbol{b}_\mathrm{e} = \boldsymbol{F}_\mathrm{e} \cdot \boldsymbol{F}_\mathrm{e}^\mathrm{T}, \tag{2.8}$$

the (visco)plastic as well as the elastic EULER-ALMANSI strain tensors result in

$$\boldsymbol{e}_\mathrm{p} = \frac{1}{2}\left[\boldsymbol{b}_\mathrm{e}^{-1} - \boldsymbol{b}^{-1}\right], \qquad \boldsymbol{e}_\mathrm{e} = \boldsymbol{e} - \boldsymbol{e}_\mathrm{p} = \frac{1}{2}\left[\boldsymbol{I} - \boldsymbol{b}_\mathrm{e}^{-1}\right]. \tag{2.9}$$

Moreover, if the intermediate configuration is introduced, additional measures like the (visco)-plastic left CAUCHY-GREEN tensor $\hat{\boldsymbol{b}}_\mathrm{p}$ and the elastic right CAUCHY-GREEN tensor $\hat{\boldsymbol{C}}_\mathrm{e}$ are obtained

$$\hat{\boldsymbol{b}}_\mathrm{p} = \boldsymbol{F}_\mathrm{p} \cdot \boldsymbol{F}_\mathrm{p}^\mathrm{T}, \qquad \hat{\boldsymbol{C}}_\mathrm{e} = \boldsymbol{F}_\mathrm{e}^\mathrm{T} \cdot \boldsymbol{F}_\mathrm{e}.$$

Associated strain measurements are the consequence

$$\hat{\boldsymbol{E}} = \frac{1}{2}\left[\hat{\boldsymbol{C}}_\mathrm{e} - \hat{\boldsymbol{b}}_\mathrm{p}^{-1}\right], \qquad \hat{\boldsymbol{E}}_\mathrm{p} = \frac{1}{2}\left[\boldsymbol{I} - \hat{\boldsymbol{b}}_\mathrm{p}^{-1}\right], \qquad \hat{\boldsymbol{E}}_\mathrm{e} = \hat{\boldsymbol{E}} - \hat{\boldsymbol{E}}_\mathrm{p} = \frac{1}{2}\left[\hat{\boldsymbol{C}}_\mathrm{e} - \boldsymbol{I}\right].$$

For the explicit transformation between these quantities and their link to the configurations see Figure 2.2. A detailed embedding of these relationships in the context of dual variables is performed in (Hartmann, 1993; Haupt, 2000), whereas a connection to tensor calculus aspects is noted in (Holzapfel, 2000). Apart from having to establish strain tensors, adequate stress measurements have to be formulated as well. Within this thesis, only the reference and the current configuration are of importance. For the corresponding stress tensor formulations in the intermediate configuration see (Haupt, 2000; Simo, 1998).

It is assumed that arbitrary volume or surface loads are applied on the continuum mechanical body $\mathcal{B}$. In order to analyze their effects on a material point $\mathcal{P}$ a cut through this is performed in order to disclose the internal forces. By determining the quotient of the latter and the corresponding surface element of the cutting plane in the current configuration, the CAUCHY stress vector $\boldsymbol{t}$ can be defined. The first PIOLA-KIRCHHOFF stress vector $\boldsymbol{T}$ results from the actual

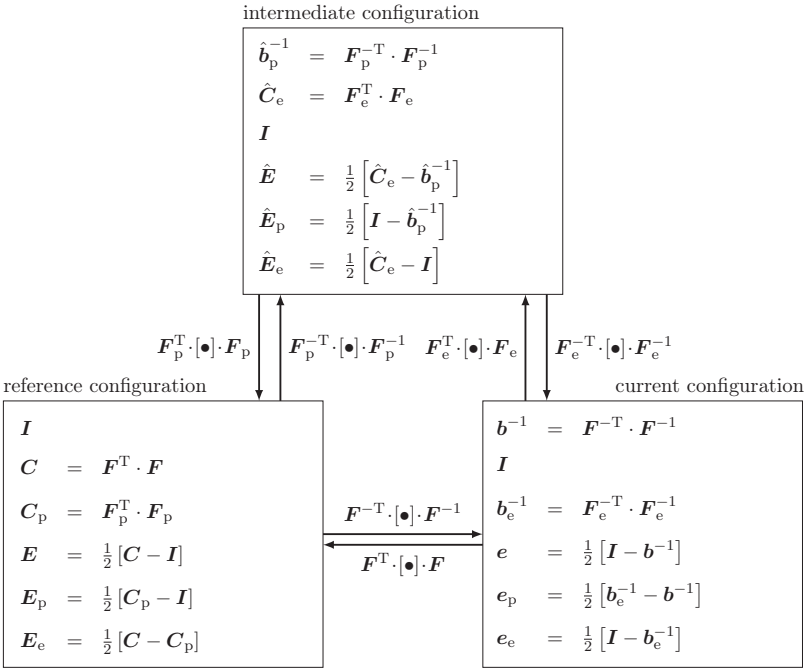

Figure 2.2.: Overview of strain measures at distinct configurations

force vector and an appropriate surface element associated to the reference configuration. An alternative Piola-Kirchhoff stress vector $\boldsymbol{p}$ can be generated by relating the surface element in the reference configuration to a fictitious force vector, whereby the latter is obtain by transforming the actual force vector into the reference configuration using Equation (2.2), cf. (Altenbach, 2012). Furthermore, the outward normal vector $\boldsymbol{n}$, perpendicular to the cutting plane in the current configuration is determined. Its analogue related to the reference configuration is denoted as $\boldsymbol{N}$. If now three distinct cuts with non-coplanar normal vectors are performed, the stress state in point $\mathcal{P}$ is uniquely defined. It can be described by the Cauchy stress tensor $\boldsymbol{\sigma}$ related to the Cauchy stress vector $\boldsymbol{t}$, the first Piola-Kirchhoff stress tensor $\boldsymbol{P}$ linked to the first Piola-Kirchhoff stress vector $\boldsymbol{T}$, or the second Piola-Kirchhoff stress tensor $\boldsymbol{S}$ connected to the second Piola-Kirchhoff stress vector $\boldsymbol{p}$ via

$$\boldsymbol{t} = \boldsymbol{\sigma} \cdot \boldsymbol{n}, \qquad \boldsymbol{T} = \boldsymbol{P} \cdot \boldsymbol{N}, \qquad \boldsymbol{p} = \boldsymbol{S} \cdot \boldsymbol{N}. \tag{2.10}$$

The transformations between the distinct stress tensors read as follows:

$$\boldsymbol{S} = \boldsymbol{F}^{-1} \cdot J\boldsymbol{\sigma} \cdot \boldsymbol{F}^{-\mathrm{T}} = \boldsymbol{F}^{-1} \cdot \boldsymbol{P}. \tag{2.11}$$

With the presented quantities at hand, it is possible to describe the mechanical behavior of a continuum mechanical body. This is done by means of balance equations, which will be presented in the next section.

2.2. Balance Equations

Balance equations represent material-independent laws which describe the effects of external influences on continuum mechanical properties, cf. (Altenbach, 2012). For the mass in a closed system, this means that it is conserved over time. Using terms associated to the reference configuration yields

$$\rho_0 = \rho J. \tag{2.12}$$

In contrast, the balance of angular momentum equilibrates the temporal change of the rotational momentum and the applied torques. The resulting key statement concerning the continuum mechanical theory is the symmetry of the CAUCHY stress tensor $\boldsymbol{\sigma} = \boldsymbol{\sigma}^{\mathrm{T}}$, (Holzapfel, 2000). For problems involving (visco)plastic effects, the balance of linear momentum is of great importance. It can be expressed in terms of quantities operating on the reference configuration

$$\rho_0 \ddot{\boldsymbol{u}}(\boldsymbol{X}, t) = \nabla_X \cdot \boldsymbol{P} + \rho_0 \boldsymbol{f}, \tag{2.13}$$

where $\ddot{\boldsymbol{u}}(\boldsymbol{X}, t)$ denotes the second time derivative of the displacement vector and $\boldsymbol{f}$ embodies the mass forces. The nabla operator $\nabla_X = \frac{\partial}{\partial \boldsymbol{X}}$ represents the derivatives with respect to the reference configuration. The equivalent equation expressed by measures associated to the current configuration is formulated as follows:

$$\rho \ddot{\boldsymbol{u}}(\boldsymbol{x}, t) = \nabla_x \cdot \boldsymbol{\sigma} + \rho \boldsymbol{f}.$$

Therein, $\nabla_x = \frac{\partial}{\partial \boldsymbol{x}}$ represents the spatial derivative with respect to the current configuration. For the definitions of the nabla operators and their interrelations see **Appendix A**. Generally, the balance of linear momentum states that the change of translational momentum equals the sum of all applied forces. For detailed derivations see (Altenbach, 2012; Haupt, 2000; Holzapfel, 2000; Kelly, 2015). Moreover, (visco)plastic phenomena are accompanied by dissipative effects which influence the energy in the analyzed system. Consequently, also the first and second law of thermodynamics, in form of the dissipation inequality, have to be considered. This implies that the difference between the stress power $\boldsymbol{S} : \dot{\boldsymbol{C}}$ or $J\boldsymbol{\sigma} : \boldsymbol{l}$ and the rate of energy per volume $\dot{e}$ has to be non-negative, cf. (Haupt, 2000; Simo and Hughes, 1997). In terms of quantities of the reference configuration

$$D_{\mathrm{int}} = \frac{1}{2} \boldsymbol{S} : \dot{\boldsymbol{C}} - \dot{e} \geq 0 \tag{2.14}$$

is obtained. As an appropriate reformulation into the current configuration

$$D_{\mathrm{int}} = J\boldsymbol{\sigma} : \boldsymbol{l} - \dot{e} \geq 0$$

can be derived (Simo, 1998), wherein $\boldsymbol{l}$ denotes the symmetric part of the deformation velocity tensor, determined by

$$\boldsymbol{l} = \frac{1}{2} \left[\dot{\boldsymbol{F}} \cdot \boldsymbol{F}^{-1} + \left[\dot{\boldsymbol{F}} \cdot \boldsymbol{F}^{-1} \right]^{\mathrm{T}} \right].$$

2.3. Reduction to Small Strains

The continuum mechanical aspects presented so far are universally applicable and, thus, take the appearance of large deformations into account. In the following chapters, the first step is to derive specific methodologies based on small strains - later to be adapted to finite strains. This practice requires a simplification of the continuum mechanical theory. This is done following the ideas of (Altenbach, 2012; Casey, 1985; Hartmann, 1993; Holzapfel, 2000; Lee and Liu, 1967).

2.3.1. Kinematics and Kinetics

In order to determine the size of prevailing deformations, the spatial change of the displacement vector has to be estimated. Therefore, the norm of the displacement gradient ξ

$$\xi = \left\| \frac{\partial \boldsymbol{u}(\boldsymbol{X},\boldsymbol{t})}{\partial \boldsymbol{X}} \right\| = \sqrt{\frac{\partial \boldsymbol{u}(\boldsymbol{X},\boldsymbol{t})}{\partial \boldsymbol{X}} : \frac{\partial \boldsymbol{u}(\boldsymbol{X},\boldsymbol{t})}{\partial \boldsymbol{X}}} = \|\boldsymbol{F} - \boldsymbol{I}\| \ll 1 \tag{2.15}$$

is evaluated. Small deformations are predominant if the deformation gradient differs only slightly from the identity tensor or rather the norm of the material displacement gradient is essentially smaller than one, cf. (Altenbach, 2012; Haupt, 2000). The consequence is that the gradients of the displacement field connected to the reference and the current configuration

$$\frac{\partial \boldsymbol{u}(\boldsymbol{X},t)}{\partial \boldsymbol{X}} \approx \frac{\partial \boldsymbol{u}(\boldsymbol{x},t)}{\partial \boldsymbol{x}} \qquad \text{with} \qquad \frac{\partial \boldsymbol{x}}{\partial \boldsymbol{X}} \approx \boldsymbol{I} \tag{2.16}$$

are identical, cf. (Altenbach, 2012). The aim is now to reformulate the quantities in Equations (2.3) and (2.4) in such a way that all terms of order $\mathcal{O}(\xi^{\mathrm{n}})$ with $\mathrm{n} \geq 2$ are neglected, cf. (Altenbach, 2012). For the right Cauchy-Green tensor

$$\boldsymbol{C} = \boldsymbol{I} + \left[\frac{\partial \boldsymbol{u}(\boldsymbol{X},t)}{\partial \boldsymbol{X}} + \left[\frac{\partial \boldsymbol{u}(\boldsymbol{X},t)}{\partial \boldsymbol{X}} \right]^{\mathrm{T}} \right] + \mathcal{O}(\xi^2) = \boldsymbol{I} + 2\boldsymbol{\varepsilon} + \mathcal{O}(\xi^2) \tag{2.17}$$

is obtained, wherein $\boldsymbol{\varepsilon}$ represents the linearized strain tensor. An analogous expression can be obtained for the left Cauchy-Green tensor, whereas its inverse leads to

$$\boldsymbol{b}^{-1} = \boldsymbol{I} - \left[\frac{\partial \boldsymbol{u}(\boldsymbol{x},t)}{\partial \boldsymbol{x}} + \left[\frac{\partial \boldsymbol{u}(\boldsymbol{x},t)}{\partial \boldsymbol{x}} \right]^{\mathrm{T}} \right] + \mathcal{O}(\xi^2). \tag{2.18}$$

Inserting Equations (2.17) as well as (2.18) in $(2.3)_2$ and $(2.4)_2$ and exploiting Equation (2.16) yields

$$\boldsymbol{E} \approx \boldsymbol{e} \approx \boldsymbol{\varepsilon} = \frac{1}{2} \left[\frac{\partial \boldsymbol{u}(\boldsymbol{X},t)}{\partial \boldsymbol{X}} + \left[\frac{\partial \boldsymbol{u}(\boldsymbol{X},t)}{\partial \boldsymbol{X}} \right]^{\mathrm{T}} \right]. \tag{2.19}$$

Accordingly, in the small strain regime, both the Green-Lagrange and the Euler-Almansi tensor are equivalent and the linearized strain tensor $\boldsymbol{\varepsilon}$ can be derived. A similar line of reasoning can be followed if (visco)plastic effects are considered and both elastic as well as (visco)plastic strains are small. For the sake of argument, it is assumed that an infinitely small material element $\mathcal{E}$ is analyzed - which undergoes successive homogeneous deformations as depicted in Figure 2.3, cf. (Lee, 1969; Lubliner, 2006; Simo and Hughes, 1997). Hence, the occurring mappings are postulated to be continuous and differentiable and the displacement field is additively decomposed, cf. (Backman, 1964; Bonet and Wood, 2009; Kleiber, 1975; Lee, 1969; Lee and Liu, 1967),

$$\boldsymbol{u}(\boldsymbol{X},t) = \boldsymbol{u}_{\mathrm{e}}(\boldsymbol{X},t) + \boldsymbol{u}_{\mathrm{p}}(\boldsymbol{X},t). \tag{2.20}$$

These properties are surely true in two cases: either if a purely elastic deformation prevails, or if a complete and instantaneous (visco)plastic process is carried out. Considering the latter instance

$$\boldsymbol{F}_{\mathrm{e}} = \boldsymbol{I}, \qquad \hat{\boldsymbol{x}} = \boldsymbol{x}, \qquad \boldsymbol{u}(\boldsymbol{X},t) = \boldsymbol{u}_{\mathrm{p}}(\boldsymbol{X},t)$$

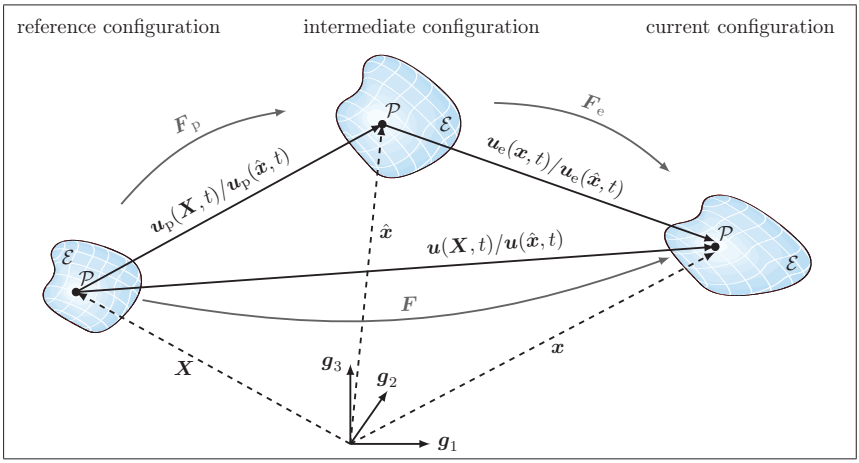

Figure 2.3.: Hypothetical homogeneous deformation of a small material element $\mathcal{E}$

holds and

$$\boldsymbol{F} = \boldsymbol{F}_\mathrm{p} = \frac{\partial \hat{\boldsymbol{x}}}{\partial \boldsymbol{X}} = \frac{\partial \boldsymbol{u}_\mathrm{p}(\boldsymbol{X},t)}{\partial \boldsymbol{X}} + \boldsymbol{I} \tag{2.21}$$

is obtained. Following the ideas in (Casey, 1985; Hartmann, 1993), both elastic as well as (visco)plastic strains are considered as small if the analogous formulation to Equation (2.15)

$$\xi_\mathrm{e/p} = \max\left(\sup\left\|\frac{\partial \boldsymbol{u}_\mathrm{p}(\boldsymbol{X},t)}{\partial \boldsymbol{X}}\right\|, \sup\left\|\frac{\partial \boldsymbol{u}_\mathrm{e}(\hat{\boldsymbol{x}},t)}{\partial \hat{\boldsymbol{x}}}\right\|\right) \ll 1 \tag{2.22}$$

for the appropriate gradients is fulfilled. This yields for the (visco)plastic right Cauchy-Green tensor

$$\boldsymbol{C}_\mathrm{p} = \boldsymbol{I} + \left[\frac{\partial \boldsymbol{u}_\mathrm{p}(\boldsymbol{X},t)}{\partial \boldsymbol{X}} + \left[\frac{\partial \boldsymbol{u}_\mathrm{p}(\boldsymbol{X},t)}{\partial \boldsymbol{X}}\right]^\mathrm{T}\right] + \mathcal{O}(\xi_\mathrm{e/p}^2) = \boldsymbol{I} + 2\boldsymbol{\varepsilon}_\mathrm{p} + \mathcal{O}(\xi_\mathrm{e/p}^2). \tag{2.23}$$

The identification of the linearized (visco)plastic strain tensor $\boldsymbol{\varepsilon}_\mathrm{p}$ ensues the concept of Equation (2.19). Neglecting terms of $\mathcal{O}(\xi_\mathrm{e/p}^\mathrm{n})$ with $\mathrm{n} \geq 2$ and inserting Relations (2.19), (2.23) in Equations $(2.6)_2$ as well as (2.7) together with (2.20) and $(2.16)_2$ results in

$$\boldsymbol{E}_\mathrm{p} = \boldsymbol{\varepsilon}_\mathrm{p}, \qquad \boldsymbol{E}_\mathrm{e} = \frac{1}{2}\left[\frac{\partial \boldsymbol{u}_\mathrm{e}(\boldsymbol{X},t)}{\partial \boldsymbol{X}} + \left[\frac{\partial \boldsymbol{u}_\mathrm{e}(\boldsymbol{X},t)}{\partial \boldsymbol{X}}\right]^\mathrm{T}\right] = \boldsymbol{\varepsilon} - \boldsymbol{\varepsilon}_\mathrm{p} = \boldsymbol{\varepsilon}_\mathrm{e} = \boldsymbol{0}.$$

Acknowledging a purely elastic deformation, leads to:

$$\boldsymbol{F}_\mathrm{p} = \boldsymbol{I}, \qquad \hat{\boldsymbol{x}} = \boldsymbol{X}, \qquad \boldsymbol{u} = \boldsymbol{u}_\mathrm{e}$$

together with

$$\boldsymbol{F}^{-1} = \boldsymbol{F}_\mathrm{e}^{-1} = \frac{\partial \hat{\boldsymbol{x}}}{\partial \boldsymbol{x}} = \boldsymbol{I} - \frac{\partial \boldsymbol{u}_\mathrm{e}(\boldsymbol{x},t)}{\partial \boldsymbol{x}}. \tag{2.24}$$

The inverse elastic left CAUCHY-GREEN tensor can then be recast into

$$\boldsymbol{b}_{\mathrm{e}}^{-1} = \boldsymbol{I} - \left[\frac{\partial \boldsymbol{u}_{\mathrm{e}}(\boldsymbol{x},t)}{\partial \boldsymbol{x}} + \left[\frac{\partial \boldsymbol{u}_{\mathrm{e}}(\boldsymbol{x},t)}{\partial \boldsymbol{x}}\right]^{\mathrm{T}}\right] + \mathcal{O}(\xi_{\mathrm{e/p}}^2) = \boldsymbol{I} - 2\boldsymbol{\varepsilon}_{\mathrm{e}} + \mathcal{O}(\xi_{\mathrm{e/p}}^2), \tag{2.25}$$

exploiting Equations (2.22) and $(2.16)_2$. If again terms of $\mathcal{O}(\xi_{\mathrm{e/p}}^{\mathrm{n}})$ with $\mathrm{n} \geq 2$ are disregarded and Relations (2.25) as well as (2.19) are inserted in (2.9)

$$\boldsymbol{e}_{\mathrm{e}} = \boldsymbol{\varepsilon}_{\mathrm{e}}, \qquad \boldsymbol{E}_{\mathrm{p}} = \frac{1}{2}\left[\frac{\partial \boldsymbol{u}_{\mathrm{p}}(\boldsymbol{x},t)}{\partial \boldsymbol{x}} + \left[\frac{\partial \boldsymbol{u}_{\mathrm{p}}(\boldsymbol{x},t)}{\partial \boldsymbol{x}}\right]^{\mathrm{T}}\right] = \boldsymbol{\varepsilon} - \boldsymbol{\varepsilon}_{\mathrm{e}} = \boldsymbol{\varepsilon}_{\mathrm{p}} = \boldsymbol{0}.$$

can be derived, taking (2.20) and $(2.16)_2$ into account.

Hence, if either completely elastic or purely (visco)plastic deformations prevail in the small strain regime, the two limits are characterized by

$$\boldsymbol{E}_{\mathrm{e}} = \boldsymbol{\varepsilon}_{\mathrm{e}} = \boldsymbol{e}_{\mathrm{e}}, \qquad \boldsymbol{E}_{\mathrm{p}} = \boldsymbol{\varepsilon}_{\mathrm{p}} = \boldsymbol{e}_{\mathrm{p}}$$

and one of the terms is equal to zero. In these cases, the respective quantities of the current and the reference configuration are identical to the linearized strain measurements, and the additive decomposition

$$\boldsymbol{\varepsilon} = \boldsymbol{\varepsilon}_{\mathrm{e}} + \boldsymbol{\varepsilon}_{\mathrm{p}} \tag{2.26}$$

can be established. For a general material body $\mathcal{B}$ with non-homogeneous deformations it cannot be assumed that the mappings towards the intermediate configuration are continuous and differentiable due to the lack of material continuity, (Haupt, 2000; Lee and Liu, 1967; Lubliner, 2006; Simo and Hughes, 1997). Accordingly, the elastic and (visco)plastic deformation gradients can only be considered as linear transformations between line elements and not as partial derivatives as in (2.21) and (2.24), cf. (Kleiber, 1975; Lee and Germain, 1974; Lee and Liu, 1967). For small strains, in analogy to the previously mentioned limiting cases, it seems to be appropriate to identify the GREEN-LAGRANGE and the EULER-ALMANSI tensors with their linearized counterparts, although they might not be interpreted as gradients of a displacement field. The resulting additive decomposition in (2.26) is furthermore experimentally motivated and generates the kinematic basis for small strain (visco)plasticity models, cf. (Chaboche, 2008; De Souza Neto et al., 2008; Lubliner, 2006; Simo and Hughes, 1997). For a thermodynamic derivation of the additive decomposition see (Reddy and Martin, 1994).

2.3.2. Balance Equations

The geometric linearization of the kinematic quantities in Section 2.3.1 influences the notion of the balance equations derived in Section 2.2. From Equation $(2.16)_2$ it can be followed, that the current and the reference configuration are almost identical, cf. (Altenbach, 2012). Hence, for a stress-free reference configuration, there is no need to distinguish between the different stress measurements as is done in Equation (2.11), cf. (Hartmann, 1993). Moreover, Relation (2.15) indicates that for the deformation gradient's determinant $J \approx 1$ holds. This leads, following Equation (2.12), to the correspondence of the density in both configurations. For small strains, the balance of linear momentum and the dissipation inequality can thus be stated as:

$$\rho_0 \ddot{\boldsymbol{u}}(\boldsymbol{X},t) = \nabla_X \cdot \boldsymbol{\sigma} + \rho_0 \boldsymbol{f}, \qquad D_{\mathrm{int}} = \boldsymbol{\sigma} : \dot{\boldsymbol{\varepsilon}} - \dot{e} \geq 0, \tag{2.27}$$

where also small strain rates in the sense of (2.15) are assumed.

2.4. Summary

As a starting point to introduce the substantial ideas of continuum mechanics, the term configuration is defined and two different types - the reference and the current configuration - are characterized. This distinction is realized with the help of the deformation gradient and allows to model large deformations. The incorporation of (visco)plastic aspects in addition to elastic ones is achieved using a multiplicative split of the deformation gradient. Thus, a third intermediate configuration is generated. With these three configurations at hand, it is possible to define distinct quantities, that describe the motion of continuum mechanical bodies and take elasto(visco)plastic characteristics into account. For the specification of the appearing internal forces, distinct types of stress tensors are established. In order to reflect the physics of a general continuum mechanical body, the law of conservation of mass, the balance of angular and linear momentum, as well as the dissipation inequality are formulated. Apart from large deformations, small ones are of interest as well. Hence, a linearization strategy is portrayed that incorporates this reduction step. The result is that the multiplicative split of the deformation tensor turns into an additive split of the linearized strain tensor and the balance equations as well as the dissipation inequality can be simplified.

3. Numerical Realization of Multifield Problems

Investigations involving small elasto(visco)plastic strains are characterized by material nonlinearities. If finite strains are considered as well, geometric nonlinearities play an important role too. For both cases, analytical solutions are only rarely at hand, so that it is inevitable to develop and apply numerical strategies. First approaches in that direction were made by (Marcal and King, 1967; Zienkiewicz, 1984; Zienkiewicz et al., 1969), who calculated the displacement field and, thereafter, estimated the variables determining plastic effects using different incremental procedures. Recent advances for example from (Carstensen et al., 2002; Comi and Perego, 1995; Miehe, 2011; Simo and Hughes, 1997) follow a different ansatz. They introduce plastic or viscoplastic measurements as additional unknown field quantities apart from the displacements. In order to establish a common framework for these different solution procedures as well as for the distinct model formulations, it is assumed that a general elasto(visco)plastic problem can be defined by

$$\delta W_1 \coloneqq \int_{\Omega} \delta \boldsymbol{z}_1(\boldsymbol{X}) \circ \boldsymbol{r}_1(\ddot{\mathbf{w}}(\boldsymbol{X},t), \dot{\mathbf{w}}(\boldsymbol{X},t), \mathbf{w}(\boldsymbol{X},t), \nabla_X \mathbf{w}(\boldsymbol{X},t))\, dV - \int_{\Gamma_{\mathbf{r}^*}} \delta \boldsymbol{z}_1(\boldsymbol{X}) \circ \boldsymbol{r}^*(\boldsymbol{X},t)\, dA = 0, \quad (3.1)$$

$$\delta W_2 \coloneqq \int_{\Omega} [\delta\lambda(\boldsymbol{X}) - \lambda(\boldsymbol{X},t)]\; r_2(\mathbf{w}(\boldsymbol{X},t))\, dV \leq 0 \quad (3.2)$$

with $\lambda(\boldsymbol{X},t) \in \mathbf{w}(\boldsymbol{X},t)$ as well as $\delta\lambda(\boldsymbol{X}), \lambda(\boldsymbol{X},t) \geq 0$ and the initial conditions

$$\mathbf{w}_1 = \mathbf{w}(\boldsymbol{X},t_1), \qquad \dot{\mathbf{w}}_1 = \dot{\mathbf{w}}(\boldsymbol{X},t_1). \quad (3.3)$$

It includes a description of a general three-dimensional continuum mechanical body occupying the domain Ω and its elasto(visco)plastic behavior in the small or finite strain regime obeying the nonlinear tensor- or vector-valued function $\boldsymbol{r}_1(\ddot{\mathbf{w}}(\boldsymbol{X},t), \dot{\mathbf{w}}(\boldsymbol{X},t), \mathbf{w}(\boldsymbol{X},t), \nabla_X \mathbf{w}(\boldsymbol{X},t))$. The expression $\mathbf{w}(\boldsymbol{X},t)$ denotes the vector of primary variables, depending on the spatial coordinate $\boldsymbol{X}$ as well as on time t. The underlying coordinate system is assumed to be of cartesian type, so that the gradient of the vector of primary variables is symbolized by $\nabla_X \mathbf{w}(\boldsymbol{X},t)$, see **Chapter A**. The terms $\dot{\mathbf{w}}(\boldsymbol{X},t)$ as well as $\ddot{\mathbf{w}}(\boldsymbol{X},t)$ represent the corresponding first and second time derivatives. Possibly applied surface loads on $\Gamma_{\mathbf{r}^*}$ are characterized by $\boldsymbol{r}^*(\boldsymbol{X},t)$ and labeled as NEUMANN type boundary conditions. In contrast, inhomogeneous DIRICHLET boundary conditions with $\mathbf{w}(\boldsymbol{X},t) = \mathbf{w}^* \; \forall \boldsymbol{X}$ on $\Gamma_{\mathbf{w}}$ are considered directly within the vector of primary variables. Hence, for the domain's boundary $\Gamma = \Gamma_{\mathbf{w}} \cap \Gamma_{\mathbf{r}^*}$ holds.

By introducing the variational inequality in (3.2) the modeling of an elastoplastic material behavior by means of inequality constraints is considered as well. In this context, a nonlinear scalar-valued convex or concave function $r_2(\mathbf{w}(\boldsymbol{X},t))$ is assumed together with a LAGRANGE multiplier field $\lambda(\boldsymbol{X},t)$. Apart from the described functions and variables the conjunction operator '$\circ$' is established. It represents the necessary mathematical operator needed to link the respective variables and functions with distinct valencies appropriately.

The expression $\delta\boldsymbol{z}_1(\boldsymbol{X})$ represents arbitrary infinitely small tensor-, vector- or scalar-valued test functions. The test function $\delta\lambda(\boldsymbol{X})$ however is assumed to be scalar-valued. While $\delta\boldsymbol{z}_1(\boldsymbol{X})$ is generally supposed to be non zero, $\delta\lambda(\boldsymbol{X}) \geq 0$ has to hold. Only for DIRICHLET type boundaries $\delta\boldsymbol{z}_1 = \mathbf{0} \; \forall \boldsymbol{X}$ on $\Gamma_{\mathbf{w}}$ is adapted.

Furthermore, it is emphasized that the integral representation of the general elasto(visco)plastic problem in (3.1)-(3.2) is especially useful for numerical solution procedures. Some of them are presented in the consecutive sections, highlighting the applicability of different time integration schemes. For explicit examples of generating weak forms in the context of arbitrary physical problems see (Euler, 1894; Finlayson and Scriven, 1966; Hamilton, 1834, 1835; Lagrange, 1894; Lambermont and Lebon, 1972; Lemaitre and Chaboche, 1990; Tonti, 1984; Zienkiewicz and Taylor, 2000). For the considered general elasto(visco)plastic problem distinct derivation strategies will be presented in **Chapter 4** and **Chapter 6**.

3.1. The Finite Element Method for Space Discretization

In order to solve the initial boundary value problem in (3.1)-(3.3) it is necessary to approximate the spatial and temporal course of the primary variable and its time and space derivatives. In the scope of this thesis, the spatial discretization will always be done by means of the finite element method. This scheme is based on the idea of splitting the considered domain into small non-overlapping subdomains, which are spanned and characterized by nodal quantities as well as by shape functions, cf. (Hughes, 2000; Zienkiewicz and Taylor, 2000). Moreover, it is assumed that the initial boundary value problem in (3.1)-(3.3) has to be fulfilled at each of these segments. Hence, a semidiscrete form can be derived.

An overview of the most important steps needed for the numerical implementation of elasto-(visco)plastic problems is drawn in the following sections. Therein, always a fix cartesian coordinate system with ND dimensions will be assumed together with the space and time-independent unit basis vectors $\boldsymbol{g}_i$ with $i = 1, ..., ND$. Additionally, basic aspects of the finite element method in terms of mathematical analysis and application can be found in (Ciarlet, 1978; Turner et al., 1956; Wriggers, 2008; Zienkiewicz, 1984; Zienkiewicz and Taylor, 2000). Other aspects like the consideration of multifield formulations are treated in (Arnold et al., 2007; Braess, 2010; Brezzi and Bathe, 1990; Brezzi and Fortin, 1991; Han and Reddy, 1999; Miehe, 2011; Zienkiewicz and Taylor, 2000).

3.1.1. General Application

For the application of the finite element method a material body $\mathcal{B}$ is examined, whose elasto-(visco)plastic behavior is described by the nonlinear expressions in (3.1)-(3.2) and the initial conditions in (3.3). In the context of the spatial discretization, this continuum with domain Ω is divided into a number NE of non-overlapping elements $\mathcal{E}$ with domain $\bar{\Omega}^e$ with $e = 1, ..., NE$, so that for the union of all elements

$$\Omega = \bigcup_{e=1}^{NE} \bar{\Omega}^e, \qquad \text{with} \qquad \bar{\Omega}^i \cap \bar{\Omega}^j = \emptyset \quad \text{for} \quad i, j \in [1, NE] \tag{3.4}$$

holds, see Figure 3.1. The geometry of each subdomain can be approximated by a number NN of special material position vectors $\boldsymbol{X}^{ei}$, so-called nodes, and by mapping functions $\hat{N}^i(\boldsymbol{\xi})$. Likewise, spatial location vectors $\boldsymbol{x}^{ei}$ can be used to describe the deformed configuration, yielding

$$\boldsymbol{X}^e \approx \sum_{i=1}^{NN} \boldsymbol{X}^{ei} \hat{N}^i(\boldsymbol{\xi}), \qquad \boldsymbol{x}^e \approx \sum_{i=1}^{NN} \boldsymbol{x}^{ei} \hat{N}^i(\boldsymbol{\xi}). \tag{3.5}$$

The consequence is that any finite element is transformed into a standard element with domain Ω^e based on natural coordinates $\boldsymbol{\xi}$, where $\xi_j \in [-1, 1]$ with $j = 1, ..., ND$ represents the j-th

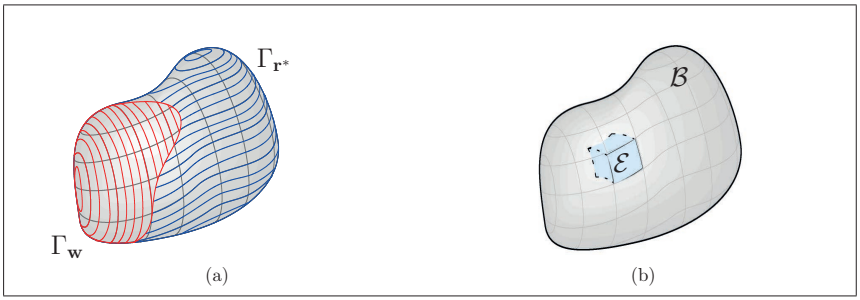

Figure 3.1.: (a) Material body with boundary conditions, (b) Element $\mathcal{E}$ of a continuum

component of $\boldsymbol{\xi}$ for ND dimensions. The relation between both configurations is established via the deformation gradient in (2.2). In order to derive a proper approximation rule, the gradient of Expression $(3.5)_2$ is calculated - and it is beneficial that the nodal quantities $\boldsymbol{x}^{ei}$ with $i = 1, ..., NN$ and the included unit basis vectors $\boldsymbol{g}_i$ with $i = 1, ..., ND$ are constant. This leads to:

$$\boldsymbol{F}^e \approx \sum_{i=1}^{NN} \boldsymbol{x}^{ei} \otimes \nabla_X \hat{N}^i(\boldsymbol{\xi}), \tag{3.6}$$

with $\nabla_X \hat{N}^i(\boldsymbol{\xi})$ as the gradient of the respective mapping function. In an isoparametric setting, the primary variables and their derivatives

$$\mathbf{w}^e \approx \sum_{i=1}^{NN} \mathbf{w}^{ei} \hat{N}^i(\boldsymbol{\xi}), \qquad \nabla_X \mathbf{w}^e \approx \sum_{i=1}^{NN} \mathbf{w}^{ei} \otimes \nabla_X \hat{N}^i(\boldsymbol{\xi}), \tag{3.7}$$

$$\dot{\mathbf{w}}^e \approx \sum_{i=1}^{NN} \dot{\mathbf{w}}^{ei} \hat{N}^i(\boldsymbol{\xi}), \qquad \ddot{\mathbf{w}}^e \approx \sum_{i=1}^{NN} \ddot{\mathbf{w}}^{ei} \hat{N}^i(\boldsymbol{\xi}) \tag{3.8}$$

are approximated in the same manner, cf.(Wriggers, 2008). Thereby, it is again taken into account that the nodal quantities and the included unit basis vectors do not depend on the spatial coordinate. Thus, the mapping functions do not only transfer physical quantities into natural ones, but are also implemented to describe the primary variables themselves. Therefore, they are also called shape functions, cf. (Szabó and Babuška, 1991). If additionally also the test functions $\delta \boldsymbol{z}_1$ and $\delta\lambda$ are interpreted element-wise and assumed to be approximated by

$$\delta \boldsymbol{z}_1^e \approx \sum_{i=1}^{NN} \delta \boldsymbol{z}_1^{ei} \hat{N}^i(\boldsymbol{\xi}), \qquad \delta\lambda^e \approx \sum_{i=1}^{NN} \delta\lambda^{ei} \hat{N}^i(\boldsymbol{\xi}), \tag{3.9}$$

then the finite element method in question is known as a Bubnov-Galerkin scheme, (Hughes, 2000). On the contrary, a distinct approximation of the test function compared to the primary variables results in a Petrov-Galerkin method, cf. (Eriksson et al., 2005; Gleim and Kuhl, 2013; Matthies and Schieweck, 2011). The latter approach will not be considered for spatial discretization, but it will play an important role within the context of Galerkin time integration schemes, see Section 3.4.3.

Apart from the division of the continuum mechanical body $\mathcal{B}$ into elements $\mathcal{E}$ and the approximation of the characterizing quantities, the finite element method states

$$\delta W_1 = \bigcup_{e=1}^{NE} \delta W_1^e \qquad \text{and} \qquad \delta W_2 = \bigcup_{e=1}^{NE} \delta W_2^e. \quad (3.10)$$

Hence, it is assumed that the weak forms in (3.1)-(3.2) do not only apply to the whole material body $\mathcal{B}$ but also to each element $\mathcal{E}$. The consequence is the following reformulation:

$$\int_{\bar{\Omega}^e} \delta \boldsymbol{z}_1^e(\boldsymbol{X}^e) \circ \boldsymbol{r}_1(\ddot{\mathbf{w}}^e(\boldsymbol{X}^e,t), \dot{\mathbf{w}}^e(\boldsymbol{X}^e,t), \mathbf{w}^e(\boldsymbol{X}^e,t), \nabla_X \mathbf{w}^e(\boldsymbol{X}^e,t))\, d\bar{V}^e - \int_{\bar{\Gamma}^e} \delta \boldsymbol{z}_1^e(\boldsymbol{X}^e) \circ \boldsymbol{r}^*(\boldsymbol{X}^e,t)\, d\bar{A}^e = 0, \quad (3.11)$$

$$\int_{\bar{\Omega}^e} [\delta\lambda^e(\boldsymbol{X}^e) - \lambda^e(\boldsymbol{X}^e,t)]\; r_2(\mathbf{w}^e(\boldsymbol{X}^e,t))\, d\bar{V}^e \leq 0, \quad (3.12)$$

where the primary variables and the test functions are substituted by their finite dimensional counterparts of Equations (3.5)-(3.9). Besides, the observed volume $\bar{V}^e$ and the area $\bar{A}^e$ refer to the respective element quantities.

Unlike to the discontinuous spatial finite element method, where the element boundary terms are approximated in each element by fluxes, the element boundary terms here are only considered if they belong to the boundary of the outer domain Ω, cf. (Cockburn et al., 2000; Hesthaven and Wartburton, 2000). Otherwise, they are neglected.

3.1.2. Shape Functions and their Derivatives

The remaining issue of the spatial discretization is the qualification of the general shape functions and the related derivatives. Their determination has a significant influence on the quality of the spatial discretization. This is the reason why a variety of distinct approaches exists. Generally, shape functions form a nodal basis associated to a set of degrees of freedom on a standard element which, in the isoparametric approach, allows to approximate the geometry, the primary variables, and the test functions, cf. (Braess, 2010; Ciarlet, 1978; Szabó and Babuška, 1991). In the non-isoparametric setting, additional mapping functions have to be introduced to establish the link between the standard element and the actually considered finite element's geometry, cf. (Boffi et al., 2013; Szabó and Babuška, 1991).

The choice of appropriate shape and mapping functions and the accompanying degrees of freedom often depends on the physical problem under consideration. For a general introduction to the derivation of elements see (Boffi et al., 2013; Ciarlet, 1978). Saddle point problems, where the election of element conception may influence the stability of the numerical scheme are treated in (Boffi et al., 2013; Braess, 2010). Thereby, attention is also given to nonconforming and mixed methods. While the first approach considers finite element spaces which are not included in the space of the variational problem, the latter enables the usage of distinct approximation ansatzes for different field variables. In the context of electromagnetic analysis, special care has to be taken concerning the primary variables' tangential components. This is achieved, for example, by using Nédélec elements or formulations which are based on special hierarchical shape functions, cf. (Monk, 1993; Schöberl and Zaglmayr, 2005). A different type of the latter can be applied for structural computations. All kinds of hierarchical elements exploit Legendre polynomials for their construction and consider nodal values as well as additional modes as their related degrees of freedom, cf. (Kuhl, 2004; Szabó and Babuška, 1991; Zienkiewicz and Taylor, 2000). Other commonly used elements in the structural mechanical regime are Lagrange and Serendipity elements. Their shape functions are based on Lagrange

polynomials, and the degrees of freedom are only affiliated to the points of support of these functions, cf. (Hughes, 2000; Kuhl, 2004; Szabó and Babuška, 1991; Zienkiewicz and Taylor, 2000). Another difference appears if the elements' geometry is investigated. In the two-dimensional case, both quadrilateral and triangular elements are commonly used. Within the three-dimensional case, tetrahedra, hexahedra, and pentahedra are widespread, cf.(Macneal, 1994; Szabó and Babuška, 1991; Zienkiewicz and Taylor, 2000).

In the course of this work, a diversity of formulations involving elasto(visco)plastic effects is investigated based on the general problem definition in (3.1)-(3.2). While some of them will be embedded in the isoparametric setting, others may be included in a mixed finite element framework. Nevertheless, only two distinct types of quadrilateral or hexahedral LAGRANGE elements will be considered for spatial discretization. Hence, the general shape function $\hat{N}$ can be selected as N yielding continuous or as $\bar{N}$ leading to discontinuous approximations. The actual choice is made in the context of the individual formulation. The mapping function, however, is always assumed to rest on a continuous material distribution.

3.1.2.1. Continuous inter-elemental LAGRANGE Approximations

In the one-dimensional case, LAGRANGE shape functions of polynomial degree p can be determined by

$$N^i(\xi_1) = \prod_{\substack{k=1 \\ k \neq i}}^{NN} \frac{\xi_1^k - \xi_1}{\xi_1^k - \xi_1^i}, \qquad \xi_1^j = \frac{2\,[j-1]}{p} - 1 \quad \text{with} \quad i,j = 1,...,NN. \tag{3.13}$$

Therein, NN embodies the number of points of support needed to generate the shape function $N^i(\xi_1)$. The variable ξ_1^i is the coordinate of a specific node for which the shape function is generated, and ξ_1^k represents the coordinates of all other element nodes. The consequence of this construction rule is that each shape function fulfills the interpolation property

$$N^i(\xi_1^k) = \delta_{ik} \qquad \text{with} \qquad i,k = 1,...,NN. \tag{3.14}$$

Hence, the shape function associated to node i is one at this node, while it is zero at all other element nodes. The determination rule in $(3.13)_2$ for ξ_1^j governs the position of the points of support and ensures their uniform distribution. Additionally, it is crucial for establishing continuous approximations. These nodes are connected to the element's geometry and its degrees of freedom. As an example for polynomial degree $p = 1$ see Figure 3.2. Since not only the

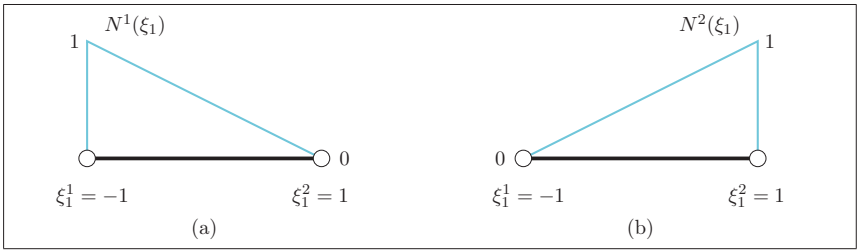

Figure 3.2.: (a) One-dimensional linear LAGRANGE shape function associated to node 1,
(b) One-dimensional linear LAGRANGE shape function associated to node 2

geometry can be approximated by these shape functions but also the primary variable and its gradient, the first derivative of Relation (3.13) is also employed here:

$$\frac{\partial N^i(\xi_1)}{\partial \xi_1} = N^i_{;1}(\xi_1) = \sum_{\substack{l=1 \\ l \neq i}}^{NN} \frac{-1}{\xi_1^l - \xi_1^i} \prod_{\substack{k=1 \\ k \neq i \\ k \neq l}}^{NN} \frac{\xi_1^k - \xi_1}{\xi_1^k - \xi_1^i}. \tag{3.15}$$

This derivative, however, is no longer continuous, and it leads to jumps over element boundaries. Figure 3.3 shows the result for polynomial degree $p = 1$.

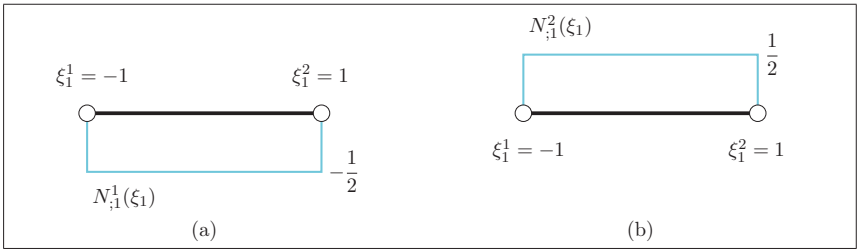

Figure 3.3.: (a) Derivative of one-dimensional LAGRANGE shape function associated to node 1, (b) Derivative of one-dimensional LAGRANGE shape function associated to node 2

Multidimensional LAGRANGE shape functions can now be formulated by exploiting the fact that Equation (3.13) holds for each direction ξ_j with $j = 1, ..., ND$. For the most general three-dimensional case, a multiplication of these one-dimensional approaches leads to

$$N^i(\xi_1, \xi_2, \xi_3) = N^k(\xi_1) N^l(\xi_2) N^m(\xi_3) \qquad \text{with} \qquad i = 1, ..., NN, \tag{3.16}$$

where $k = 1, ..., NN_1, l = 1, ..., NN_2$ and $m = 1, ..., NN_3$ represent the number of nodes in the individual direction and $NN = NN_1\, NN_2\, NN_3$ depicts the number of total element nodes. In this manner, for each spatial direction a distinct polynomial degree can be used for approximation. The interpolation property of Equation (3.14) remains unaffected and is only extended to

$$N^i(\boldsymbol{\xi}^k) = \delta_{ik} \qquad \text{with } i, k = 1, ..., NN \tag{3.17}$$

for the three-dimensional case. Analogous considerations as for multi-dimensional shape functions can be performed to obtain multi-dimensional derivatives. For the most general three-dimensional case,

$$\frac{\partial N^i(\xi_1, \xi_2, \xi_3)}{\partial \xi_d} = N^i_{;d}(\xi_1, \xi_2, \xi_3) = \frac{\partial (N^k(\xi_1) N^l(\xi_2) N^m(\xi_3))}{\partial \xi_d} \qquad d = 1, ..., 3 \tag{3.18}$$

is obtained, whereby the derivative in the respective direction can be calculated using Equation (3.15). For the two-dimensional case, it is possible to reformulate (3.16) and (3.18) by neglecting the third dimension.

If these shape functions are used to determine the field variable's gradient $\nabla_X \mathbf{w}^e(\boldsymbol{X}^e, t)$, which might even be discontinuous, an additional step has to be carried out. A link between the derivatives in natural coordinates to those in physical ones has to be constituted. Therefore,

Equation $(3.5)_1$ is differentiated with respect to natural coordinates, providing the JACOBIAN matrix

$$\boldsymbol{J}^e = \frac{\partial \boldsymbol{X}^e}{\partial \boldsymbol{\xi}} \approx \sum_{i=1}^{NN} \boldsymbol{X}^{ei} \otimes \nabla_\xi N^i(\boldsymbol{\xi}). \tag{3.19}$$

Accordingly,

$$\nabla_{\boldsymbol{X}} N^i(\boldsymbol{\xi}) = \frac{\partial N^i\left(\boldsymbol{\xi}\left(\boldsymbol{X}^e\right)\right)}{\partial \boldsymbol{X}^e} = \frac{\partial N^i\left(\boldsymbol{\xi}\left(\boldsymbol{X}^e\right)\right)}{\partial \boldsymbol{\xi}} \cdot \frac{\partial \boldsymbol{\xi}}{\partial \boldsymbol{X}^e} = \boldsymbol{J}^{e-\mathrm{T}} \cdot \nabla_\xi N^i(\boldsymbol{\xi})$$

is obtained.

In order to evaluate the weak forms in (3.11)-(3.12), the only missing aspect is the transformation of the finite element's volume and the area to amounts of the standard element. This is achieved by adapting the limits of the integrals with respect to the regime of natural coordinates $\boldsymbol{\xi}$ and by taking advantage of the JACOBIAN matrix's determinant.

$$d\bar{V}^e = |\boldsymbol{J}^e| dV^e, \qquad d\bar{A}^e = |\boldsymbol{J}^{e,\mathrm{red}}| dA^e. \tag{3.20}$$

Herein, it is assumed that the boundary integral of Equation (3.11) is approximated by an element whose dimension is one less than the one used to model the volumetric part. For the three-dimensional case, this means that a two-dimensional element is considered and that the reduced JACOBIAN matrix $\boldsymbol{J}^{e,\mathrm{red}}$ is obtained by taking only the transformation of the respective plane into account. An alternative approach is described in (Gleim, 2016; Ottosen and Petersson, 1992).

3.1.2.2. Discontinuous inter-elemental LAGRANGE Approximations

LAGRANGE shape functions as described in Section 3.1.2.1 lead to continuous approximations at common nodes of neighboring elements. This characteristic is appropriate for the geometry's description. For other quantities contained in the vector of primary variables, it may be an advantage to allow jumps between element boundaries. In the one-dimensional case, this can be acknowledged by Equation $(3.13)_1$. However, the determination rule in $(3.13)_2$ has to be modified so that elemental nodes and the respective degrees of freedom are not allowed to lie at the boundaries. Selecting GAUSS-LEGENDRE points as points of support ξ_1^j is one possibility, see Section 3.3.1. In Figure 3.4, as an example, the linear case - where $\xi_1^1 = -1/\sqrt{3}$ and $\xi_1^2 = 1/\sqrt{3}$ are chosen - is analyzed for two elements, including a comparison to the continuous approach. In the continuous case, the unknowns are calculated at three different positions - while four positions are significant for the discontinuous case and, thus, jumps over the element boundary are modeled. Nevertheless, the interpolation property in (3.14) stays fulfilled. The extension to multi-dimensional shape functions is equally stated by Equation (3.16), except that again only nodes which are not situated at the boundary are taken into account.

3.2. Nonlinear Solution Strategies

By applying the finite element method to the general elasto(visco)plastic problem in (3.1)-(3.2), it is converted into a semidiscrete form consisting of solely time-dependent equations and inequalities. In a further step, this nonlinear form has to be solved. Thus, widespread methods are NEWTON schemes, cf. (Alt, 2011; Geiger and Kanzow, 2002; Luenberger, 1973; Zienkiewicz and Taylor, 2000). Their basic idea is to generate an iterative procedure by guessing a solution, linearizing the nonlinear equations and inequalities at this point, solving them, and taking the

obtained result as a new starting value. This procedure is carried out until a user-defined criterion is reached. The incorporation of the semidiscrete forms in (3.11)-(3.12) in such a solution strategy is derived in the next sections.

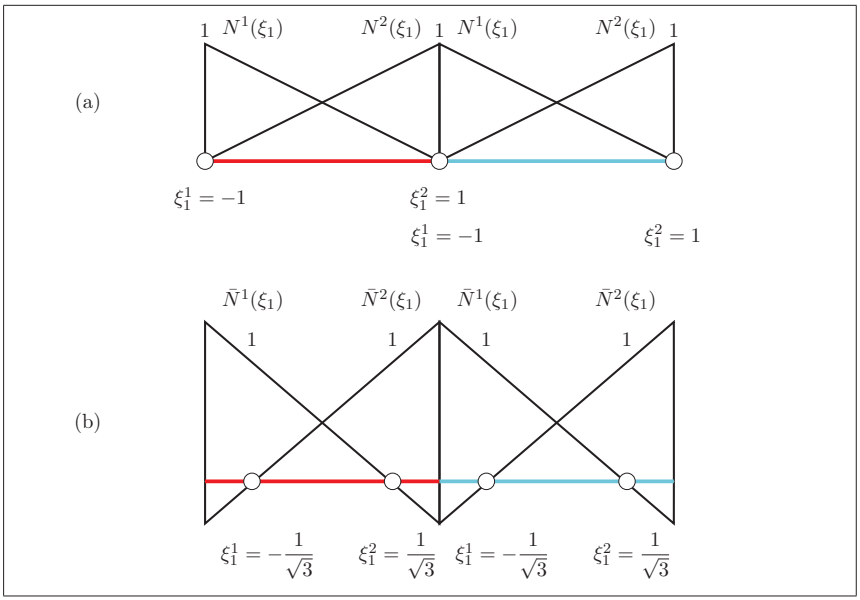

Figure 3.4.: (a) Continuous linear approach for two one-dimensional elements, (b) Discontinuous linear approach for two one-dimensional elements

3.2.1. The Newton-Raphson Scheme

In a first step, it is assumed that there are formulations which model elasto(visco)plastic problems solely by equations of the kind (3.11). In order to solve this nonlinear system of equations, it is linearized with respect to the vector of unknowns $\mathbf{w}^e(\boldsymbol{X}^e, t)$, its time derivatives $\dot{\mathbf{w}}^e(\boldsymbol{X}^e, t)$, $\ddot{\mathbf{w}}^e(\boldsymbol{X}^e, t)$, as well as its gradient $\nabla_X \mathbf{w}^e(\boldsymbol{X}^e, t)$. Therefore, a Taylor series expansion, which is aborted after the linear term, is carried out around the points $\mathbf{w}^{e,k}(\boldsymbol{X}^e, t)$, $\dot{\mathbf{w}}^{e,k}(\boldsymbol{X}^e, t)$, $\ddot{\mathbf{w}}^{e,k}(\boldsymbol{X}^e, t)$ and $\nabla_X \mathbf{w}^{e,k}(\boldsymbol{X}^e, t)$. Hence, summands of higher order are neglected. For better clarity, the spatial and temporal dependencies are dropped in what follows, yielding

$$\begin{aligned}
\delta W_1^e &= \delta W_1^{e,k} + \Delta \delta W_1^e = \\
&= \int_{\Omega^e} \delta \boldsymbol{z}_1^e \circ \boldsymbol{r}_1 \left(\ddot{\mathbf{w}}^{e,k}, \dot{\mathbf{w}}^{e,k}, \mathbf{w}^{e,k}, \nabla_X \mathbf{w}^{e,k} \right) |\boldsymbol{J}^e| dV^e - \int_{\Gamma^e} \delta \boldsymbol{z}_1^e \circ \boldsymbol{r}^{*,k} |\boldsymbol{J}^{e,\mathrm{red}}| dA^e + \\
&+ \int_{\Omega^e} \delta \boldsymbol{z}_1^e \circ \left[\mathrm{D}^k_{\ddot{\mathbf{w}}^e} \boldsymbol{r}_1 + \mathrm{D}^k_{\dot{\mathbf{w}}^e} \boldsymbol{r}_1 + \mathrm{D}^k_{\mathbf{w}^e} \boldsymbol{r}_1 + \mathrm{D}^k_{\nabla \mathbf{w}^e} \boldsymbol{r}_1 \right] |\boldsymbol{J}^e| dV^e = 0,
\end{aligned} \tag{3.21}$$

where the abbreviation

$$\mathrm{D}^k_{\mathbf{s}^e}\boldsymbol{r}_1 = \frac{d}{d\psi}\boldsymbol{r}_1\left(\mathbf{s}^{e,k}+\psi\Delta\mathbf{s}^e\right)\Big|_{\psi=0} = \left.\frac{\partial \boldsymbol{r}_1(\mathbf{s}^e)}{\partial \mathbf{s}^e}\right|_k \circ \Delta\mathbf{s}^e \quad \text{with} \quad \Delta\mathbf{s}^e = \mathbf{s}^{e,k+1}-\mathbf{s}^{e,k} \tag{3.22}$$

stands for the GÂTEAUX derivative of the respective general variable $\mathbf{s}^e$, while all other quantities are assumed to be constant. Hence, the main ingredient for the applicability of this NEWTON-RAPHSON scheme is the GÂTEAUX differentiability of the nonlinear vector- or tensor-valued function $\boldsymbol{r}_1$.

Expanding the approximations in (3.7)-(3.9) to the respective increments and inserting them together with $(3.9)_1$ into (3.21) results in the linearized semidiscrete form

$$\sum_{i=1}^{NN}\sum_{j=1}^{NN}\delta\boldsymbol{z}_1^{ei}\circ\left[\boldsymbol{m}^{eij}\circ\Delta\ddot{\mathbf{w}}^{ej}+\boldsymbol{d}^{eij}\circ\Delta\dot{\mathbf{w}}^{ej}+\boldsymbol{k}^{eij}\circ\Delta\mathbf{w}^{ej}\right]=\sum_{i=1}^{NN}\delta\boldsymbol{z}_1^{ei}\circ\left[\boldsymbol{r}_1^{*,ei}-\boldsymbol{r}_1^{ei}\right]$$

on element level. The terms therein embody suitable tangent matrices $\boldsymbol{m}^{eij},\boldsymbol{d}^{eij},\boldsymbol{k}^{eij}$, the external load vector $\boldsymbol{r}_1^{*,ei}$, and the internal load vector $\boldsymbol{r}_1^{ei}$. They are defined by

$$\boldsymbol{k}^{eij}=\int_{\Omega^e}\hat{N}^i\hat{N}^j\left.\frac{\partial\mathbf{r}_1}{\partial\mathbf{w}^e}\right|_k|\boldsymbol{J}^e|dV^e+\int_{\Omega^e}\hat{N}^i\left.\frac{\partial\mathbf{r}_1}{\partial\nabla_X\mathbf{w}^e}\right|_k\cdot\nabla_X\hat{N}^j\,|\boldsymbol{J}^e|dV^e, \tag{3.23}$$

$$\begin{aligned}
\boldsymbol{m}^{eij}&=\int_{\Omega^e}\hat{N}^i\hat{N}^j\left.\frac{\partial\mathbf{r}_1}{\partial\ddot{\mathbf{w}}^e}\right|_k|\boldsymbol{J}^e|dV^e, & \boldsymbol{d}^{eij}&=\int_{\Omega^e}\hat{N}^i\hat{N}^j\left.\frac{\partial\mathbf{r}_1}{\partial\dot{\mathbf{w}}^e}\right|_k|\boldsymbol{J}^e|dV^e,\\
\boldsymbol{r}_1^{*,ei}&=\int_{\Gamma^e}\hat{N}^i\,\boldsymbol{r}^*|\boldsymbol{J}^{e,\mathrm{red}}|dA^e, & \boldsymbol{r}_1^{ei}&=\int_{\Omega^e}\hat{N}^i\,\boldsymbol{r}_1^k\,|\boldsymbol{J}^e|dV^e,
\end{aligned} \tag{3.24}$$

wherein all arguments of functions are abandoned. A GAUSS-LEGENDRE quadrature is used for the explicit calculation of the integrals, as explained in Section 3.3.

The partition of the continuum mechanical body $\mathcal{B}$ into finite elements in Section 3.1 enables a local evaluation of the nonlinear Equation (3.1) as well as the finite-dimensional approximation of the quantities that characterize the problem. The engineering issue, however, is to determine the primary variables of the entire material body. By exploiting the fact that Equation (3.10) holds, assembly operators can be established, sorting all quantities in respective matrices and vectors. Thereby, inherent connectivities are taken into account. For the test function, the primary variable, its derivatives, and the load vectors, this is formulated by

$$\begin{aligned}
\Delta\ddot{\mathbf{w}}&=\bigcup_{e=1}^{NE}\bigcup_{j=1}^{NN}\Delta\ddot{\mathbf{w}}^{ej}, & \Delta\dot{\mathbf{w}}&=\bigcup_{e=1}^{NE}\bigcup_{j=1}^{NN}\Delta\dot{\mathbf{w}}^{ej}, & \Delta\mathbf{w}&=\bigcup_{e=1}^{NE}\bigcup_{j=1}^{NN}\Delta\mathbf{w}^{ej},\\
\delta\mathbf{z}_1&=\bigcup_{e=1}^{NE}\bigcup_{i=1}^{NN}\delta\boldsymbol{z}_1^{ei}, & \mathbf{R}_1^*&=\bigcup_{e=1}^{NE}\bigcup_{i=1}^{NN}\boldsymbol{r}_1^{*,ei}, & \mathbf{R}_1&=\bigcup_{e=1}^{NE}\bigcup_{i=1}^{NN}\boldsymbol{r}_1^{ei}.
\end{aligned} \tag{3.25}$$

If now only continuous inter-elemental approximations are considered, see Section 3.1.2.1, common nodes of distinct elements are only considered once in the assembly process. Hence, their

associated degrees of freedom only appear once in the assembled quantities in (3.25), cf. (Hughes, 2000; Zienkiewicz and Taylor, 2000). For discontinuous approximations, see Section 3.1.2.2, there are no common nodes, so that no special care has to be taken. An analogous assembly procedure has to be carried out for the tangential matrices in (3.23)-(3.24), with

$$\mathbf{M} = \bigcup_{\substack{i=1\\j=1\\e=1}}^{\substack{NE\\NN\\NN}} \boldsymbol{m}^{eij}, \qquad \mathbf{D} = \bigcup_{\substack{i=1\\j=1\\e=1}}^{\substack{NE\\NN\\NN}} \boldsymbol{d}^{eij}, \qquad \mathbf{K}_1 = \bigcup_{\substack{i=1\\j=1\\e=1}}^{\substack{NE\\NN\\NN}} \boldsymbol{k}^{eij}. \tag{3.26}$$

Here, a combination of the entries at common nodes has to be performed for continuous inter-elemental approximations, while the discontinuous case does not require a distinction between the individual nodes. Exploiting the fact that the test function's nodal values are arbitrary but non-zero, the linearized semidiscrete equation

$$\mathbf{M}\Delta\ddot{\mathbf{w}} + \mathbf{D}\Delta\dot{\mathbf{w}} + \mathbf{K}_1\Delta\mathbf{w} = \mathbf{R}_1^* - \mathbf{R}_1 \tag{3.27}$$

is obtained. Together with Equation (3.3), it forms the initial boundary value problem. Therein, the variable $\mathbf{M}$ represents the generalized mass matrix, $\mathbf{D}$ the generalized damping matrix, $\mathbf{K}_1$ the generalized stiffness matrix, $\mathbf{R}_1$ the generalized load vector of internal, and $\mathbf{R}_1^*$ the generalized load vector of external forces.

The last step in solving Equation (3.27) is the temporal discretization, where a relationship between the primary variable vector $\Delta\mathbf{w}$ and its time derivatives is stated. Different methods concerning this topic are described in Section 3.4. In the subsequent passage, it is assumed that this interdependence is known and Equation (3.27) can be reformulated into

$$\mathbf{K}_{\text{eff}}\Delta\mathbf{w} = \mathbf{r}_{\text{eff}}, \tag{3.28}$$

$$\mathbf{w}^{k+1} = \Delta\mathbf{w} + \mathbf{w}^k,$$

where $\mathbf{K}_{\text{eff}}$ embodies the effective generalized stiffness matrix and $\mathbf{r}_{\text{eff}}$ the effective generalized load vector. In the context of the Newton-Raphson scheme, Equation (3.28) is solved with respect to the increment, which in return is used to update the primary variable vector. The latter, though, is employed to determine a new effective generalized stiffness matrix. This iterative process is carried out until a certain termination criterion, for example

$$\eta_{\text{w}} = \frac{\|\Delta\mathbf{w}\|}{\|\mathbf{w}^{k+1} - \mathbf{w}^{k=1}\|} \leq \eta,$$

is matched. Hence, the discrepancy between successive iteration steps is related to the change with regard to the first iteration. If the starting value is chosen to be near the solution, a quadratic rate of convergence can be obtained, cf. (Geiger and Kanzow, 2002). Alternative types of termination criteria and adaptations of the Newton-Raphson procedure can be found in the literature, cf. (Carstens, 2013; Wriggers, 2008; Zienkiewicz and Taylor, 2000). Eventually, an algorithmic scheme for this local Newton-Raphson scheme can be established, see Figure 3.5.

3.2.2. A Semi-Smooth Newton Method

An alternative solution procedure has to be followed if the most general elasto(visco)plastic problem in (3.11)-(3.12) is considered. The idea is to reformulate the included variational inequality

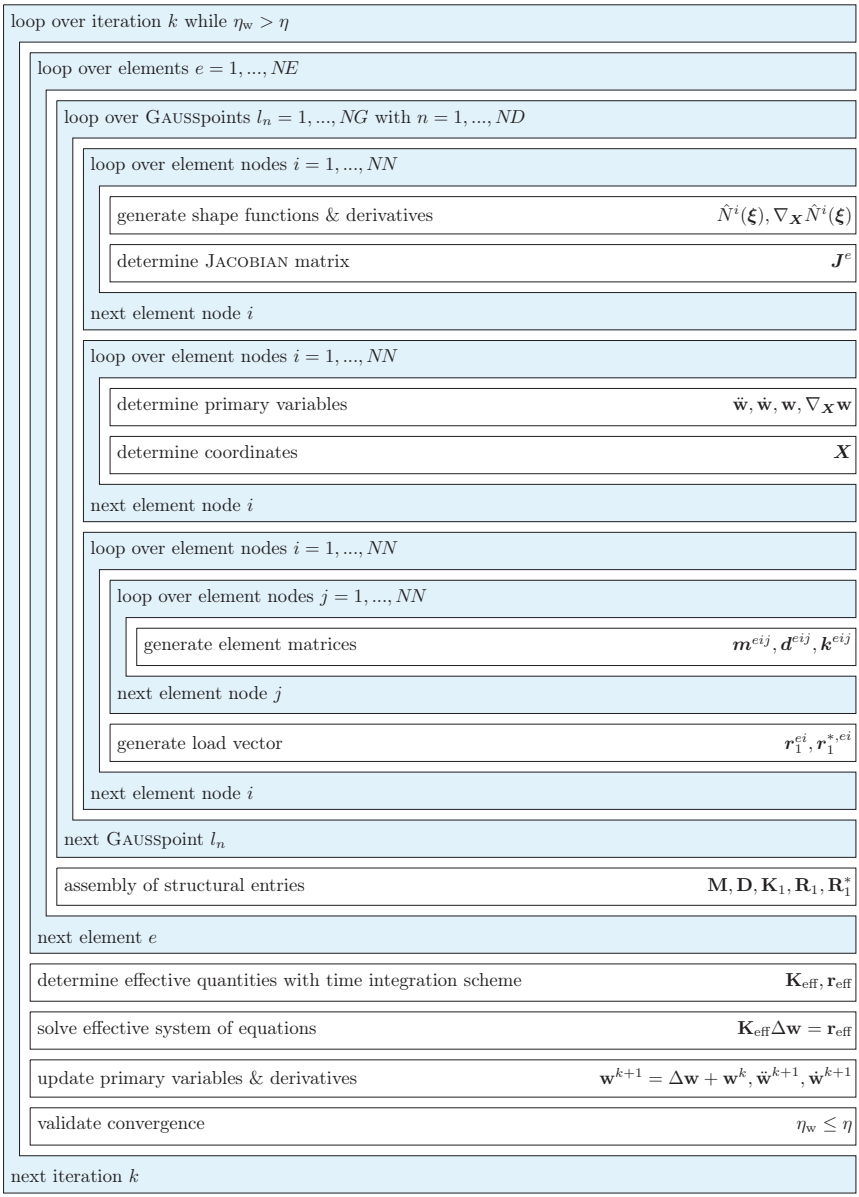

Figure 3.5.: Algorithm scheme for a NEWTON-RAPHSON method

into an equality and to enable the application of a NEWTON scheme similar to the one described in Section 3.2.1, cf. (Facchinei and Pang, 2003; Geiger and Kanzow, 2002; Hintermüller et al., 2003; Popp et al., 2009). Therefore, in the first step, the Inequality (3.12) is transferred to the standard element and the approximations in (3.7)-(3.9) are inserted, leading to

$$\sum_{i=1}^{NN} \left[\delta\lambda^{ei} - \lambda^{ei}\right] \, r_2^{ei} \leq 0 \qquad \text{with} \qquad \lambda^{ei} \in \mathbf{w}^{ei} \qquad \text{and} \qquad \delta\lambda^{ei}, \lambda^{ei} \geq 0. \tag{3.29}$$

The abbreviation therein is defined by

$$r_2^{ei} = \int_{\Omega^e} \hat{N}^i \, r_2 \, |\boldsymbol{J}^e| dV^e,$$

whereby the function's dependencies are dropped for better clarity. For the explicit calculation of the integral, a GAUSS-LEGENDRE quadrature is used as described in Section 3.3.

Following the approach in (Geiger and Kanzow, 2002), it can be shown that the solutions λ^{ei} of the variational inequality in (3.29) solve the nonlinear complementarity problem

$$\lambda^{ei} \geq 0, \qquad r_2^{ei} \leq 0, \qquad \lambda^{ei} r_2^{ei} = 0 \tag{3.30}$$

at each element node i. A similar way of proceeding is performed in Equations (4.63)-(4.64). The terms in Equation (3.30) are also known as Karush-Kuhn-Tucker conditions. They can be restated into a non-smooth nonlinear complementarity function of the following kind

$$C^i\left(\lambda^{ei}, \mathbf{w}^e\right) = 0 \qquad \text{with} \qquad C^i\left(\lambda^{ei}, \mathbf{w}^e\right) = \lambda^{ei} - \max\left(0, \lambda^{ei} + c \, r_2^{ei}\right), \tag{3.31}$$

where $c > 0$ holds for an arbitrary constant. The constant's influence is analyzed in (Hüeber and Wohlmuth, 2005; Popp et al., 2009) in the context of contact problems. Therein, it is emphasized that it is a purely algorithmic constant which does not affect the accuracy of the result. In (Schröder and Kuhl, 2016), this statement is reinforced and the constant's influence on the number of iterations within an example of elastoplasticity is investigated. In the context of other plasticity problems, completely different complementarity functions are exploited together with additional stabilization parameters, cf. (Hager and Wohlmuth, 2009; Seitz et al., 2014). Further examples for nonlinear complementarity functions can be taken from (Facchinei and Pang, 2003; Geiger and Kanzow, 2002).

A closer look at the apparent complementarity function in (3.31) reveals a case distinction due to the maximum operator. Its evaluation leads directly to the discrete Karush-Kuhn-Tucker Conditions (3.30). Instead of dealing with an inequality, the nonlinear Equation (3.31) can be added to Equation (3.11).

Since the complementarity function is continuous but non-smooth, due to the maximum operator, it is not possible to carry out a simple linearization as in Section 3.2.1. As a remedy, advantage is taken of the concept of a generalized JACOBIAN, which aims at extending the notion of differentiability to non-smooth functions, cf. (Clarke, 1990; Hintermüller, 2010; Qi and Sun, 1993). Following the approach in (Hintermüller, 2010; Qi and Sun, 1993), picking out one specific element of this generalized JACOBIAN is sufficient to construct a semi-smooth NEWTON method. For the present case, this means that a generalized gradient ∂h of the maximum operator $h = \max(0, s)$ depending on an arbitrary variable s

$$\partial_s h(s) \coloneqq \begin{cases} 0 & \text{if } s \leq 0 \\ 1 & \text{if } s > 0 \end{cases} \tag{3.32}$$

is defined, cf. (Popp et al., 2009). The linearization of the complementarity function in (3.31) can then be accomplished similarly to Section 3.2.1 by a TAYLOR series expansion, which is aborted after the linear term

$$\bar{\mathrm{D}}^k_{\lambda^{ei}} C^i + \bar{\mathrm{D}}^k_{\mathbf{w}^e} C^i + C^i \left(\lambda^{ei,k}, \mathbf{w}^{e,k} \right) = 0 \tag{3.33}$$

with a kind of generalized derivative $\bar{\mathrm{D}}^k_{\mathbf{s}} C^i$ of the respective variable $\mathbf{s}$ and the increment $\Delta\mathbf{s} = \mathbf{s}^{k+1} - \mathbf{s}^k$. For an explicit determination of the quantities in Equation (3.33), the case distinction of the maximum operator's generalized gradient in (3.32) has to be considered. Thus, for

$$\lambda^{ei,k} + c\, r_2^{ei,k} \leq 0 \qquad \Longrightarrow \qquad \lambda^{ei,k+1} = 0$$

is obtained, while for

$$\lambda^{ei,k} + c\, r_2^{ei,k} > 0 \qquad \Longrightarrow \qquad \boldsymbol{k}_2^{eij} \circ \Delta\mathbf{w}^{ej} = r_2^{ei} \qquad \text{with} \qquad \boldsymbol{k}_2^{eij} = -\int_{\Omega^e} \hat{N}^i \hat{N}^j \left. \frac{\partial r_2}{\partial \mathbf{w}^e} \right|_k |\boldsymbol{J}^e| dV^e$$

holds. Thus, the argument in the maximum operator serves as criterion to decide whether the node i has to be considered in the solution process and belongs to the active set $\mathcal{A}$ - or whether it can be neglected and is associated to the set of inactive nodes $\mathcal{I}$. This distinction has to be made in each iteration step k. Apart from the Inequality (3.29), the weak form in (3.11) is linearized. This is done as shown in Section 3.2.1.

In order to describe the behavior of the complete general elasto(visco)plastic body $\mathcal{B}$, the elemental quantities are assembled on structural level. Therefore, the expressions in Equations (3.25)-(3.26) are extended to:

$$\boldsymbol{\lambda} = \bigcup_{\substack{j=1 \\ e=1}}^{\substack{NE \\ NN}} \lambda^{ej}, \qquad \mathbf{R}_2 = \bigcup_{\substack{i=1 \\ e=1}}^{\substack{NE \\ NN}} r_2^{ei}, \qquad \mathbf{K}_2 = \bigcup_{\substack{i=1 \\ j=1 \\ e=1}}^{\substack{NE \\ NN \\ NN}} \boldsymbol{k}_2^{eij}, \tag{3.34}$$

whereby $\boldsymbol{\lambda} \in \mathbf{w}$ is assumed to hold. This leads to the system

$$\mathbf{M}\Delta\ddot{\mathbf{w}} + \mathbf{D}\Delta\dot{\mathbf{w}} + \mathbf{K}_1\Delta\mathbf{w} = \mathbf{R}_1^* - \mathbf{R}_1, \tag{3.35}$$

$$\mathbf{K}_2\Delta\mathbf{w} = -\mathbf{R}_2, \tag{3.36}$$

$$\lambda^{i,k+1} = 0 \qquad \forall i \in \mathcal{I}^k, \tag{3.37}$$

$$\mathcal{A}^{k+1} := \{ i \leq NNS | \lambda^{ei,k+1} + c\, r_2^{ei,k+1} > 0 \}, \tag{3.38}$$

$$\mathcal{I}^{k+1} := \{ i \leq NNS | \lambda^{ei,k+1} + c\, r_2^{ei,k+1} \leq 0 \}. \tag{3.39}$$

Equation (3.35) is already known from the NEWTON-RAPHSON approach in Section 3.2.1. Equations (3.36)-(3.39) form the counterpart of Equation (3.33) on structural level with the additional tangential matrix $\mathbf{K}_2$ and the corresponding internal load vector $\mathbf{R}_2$. Hence, Equation (3.36) only refers to nodes belonging to the active set $\mathcal{A}^k$, while (3.37) is linked to the inactive set $\mathcal{I}^k$. The maximum number of nodes included in a set is limited to the number of total structural nodes NNS.

The last step before the vector of primary variables can be determined is to create a link between itself and its time derivatives. This is accomplished by corresponding time integration schemes as depicted in Section 3.4. Thus, the system of Equations (3.35)-(3.37) can be reformulated to

$$\mathbf{K}_{\text{eff}}\Delta\mathbf{w} = \mathbf{r}_{\text{eff}}, \tag{3.40}$$

$$\lambda^{i,k+1} = 0 \qquad \forall i \in \mathcal{I}^k, \tag{3.41}$$

$$\mathbf{w}^{k+1} = \Delta\mathbf{w} + \mathbf{w}^k, \tag{3.42}$$

$$\mathcal{A}^{k+1} \coloneqq \{i \leq NNS | \lambda^{ei,k+1} + c\, r_2^{ei,k+1} > 0\}, \tag{3.43}$$

$$\mathcal{I}^{k+1} \coloneqq \{i \leq NNS | \lambda^{ei,k+1} + c\, r_2^{ei,k+1} \leq 0\}. \tag{3.44}$$

Therein $\mathbf{K}_{\text{eff}}$ embodies the effective generalized stiffness matrix and $\mathbf{r}_{\text{eff}}$ depicts the effective generalized load vector. In the context of a semi-smooth NEWTON scheme, the system of Equations (3.40)-(3.41) is solved with respect to the increment, exploiting a starting guess of the primary variable vector $\mathbf{w}^k$ and of the active and inactive sets $\mathcal{A}^k$ as well as $\mathcal{I}^k$. Afterwards, an update of all these quantities is performed. This iterative process is carried out until a specific termination criterion is matched. Therefore,

$$\eta_{\text{w}} = \frac{\|\Delta\mathbf{w}\|}{\|\mathbf{w}^{k+1} - \mathbf{w}^{k=1}\|} \leq \eta$$

could be taken into account. Hence, the discrepancy between successive iteration steps is related to the change with regard to the first iteration.

In contrast to the NEWTON-RAPHSON scheme, the semi-smooth NEWTON method is not always characterized by a quadratic convergence rate, even though the starting value is chosen to be near the solution. Depending on the characteristics of the Equations (3.1) and (3.2), the outcome can be a linear, superlinear, or quadratic convergence, cf. (Facchinei and Pang, 2003; Geiger and Kanzow, 2002; Hager and Wohlmuth, 2009; Hintermüller et al., 2003). Eventually, an algorithmic scheme for this local semi-smooth NEWTON scheme can be elaborated, see Figure 3.6.

3.3. Quadrature Rules

The general elasto(visco)plastic problem is defined by the weak forms in (3.1)-(3.2). Due to the application of the finite element method as described in Section 3.1, the integrals of these terms are transferred to unit integrals, where for each spatial direction $\xi_i \in [-1, 1]$ with $i = 1, ..., ND$ is assumed. To be able to apply a nonlinear solution procedure as shown in Section 3.2, the distinct integrals have to be evaluated. This is done numerically by using a quadrature rule:

$$\int_{-1}^{1} h(\xi_1)\, d\xi_1 \approx \sum_{i=1}^{NG_1} \alpha_1^i\, h(\xi_1^i). \tag{3.45}$$

It approximates the integral of an arbitrary function $h(\xi_1)$ by a sum of integrands evaluated at the points ξ_1^i and weighted by factors α_1^i, where $i = 1, .., NG_1$ represents the number of quadrature points. For an integration in ND spatial directions, an adequate extension of the one-dimensional case (3.45) has to be carried out. For the most complicated three-dimensional case, this means

$$\int_{\Omega^e} h(\xi_1, \xi_2, \xi_3)\, d\xi_1 d\xi_2 d\xi_3 \approx \sum_{i=1}^{NG_1} \sum_{j=1}^{NG_2} \sum_{k=1}^{NG_3} \alpha_1^i \alpha_2^j \alpha_3^k\, h(\xi_1^i, \xi_2^j, \xi_3^k).$$

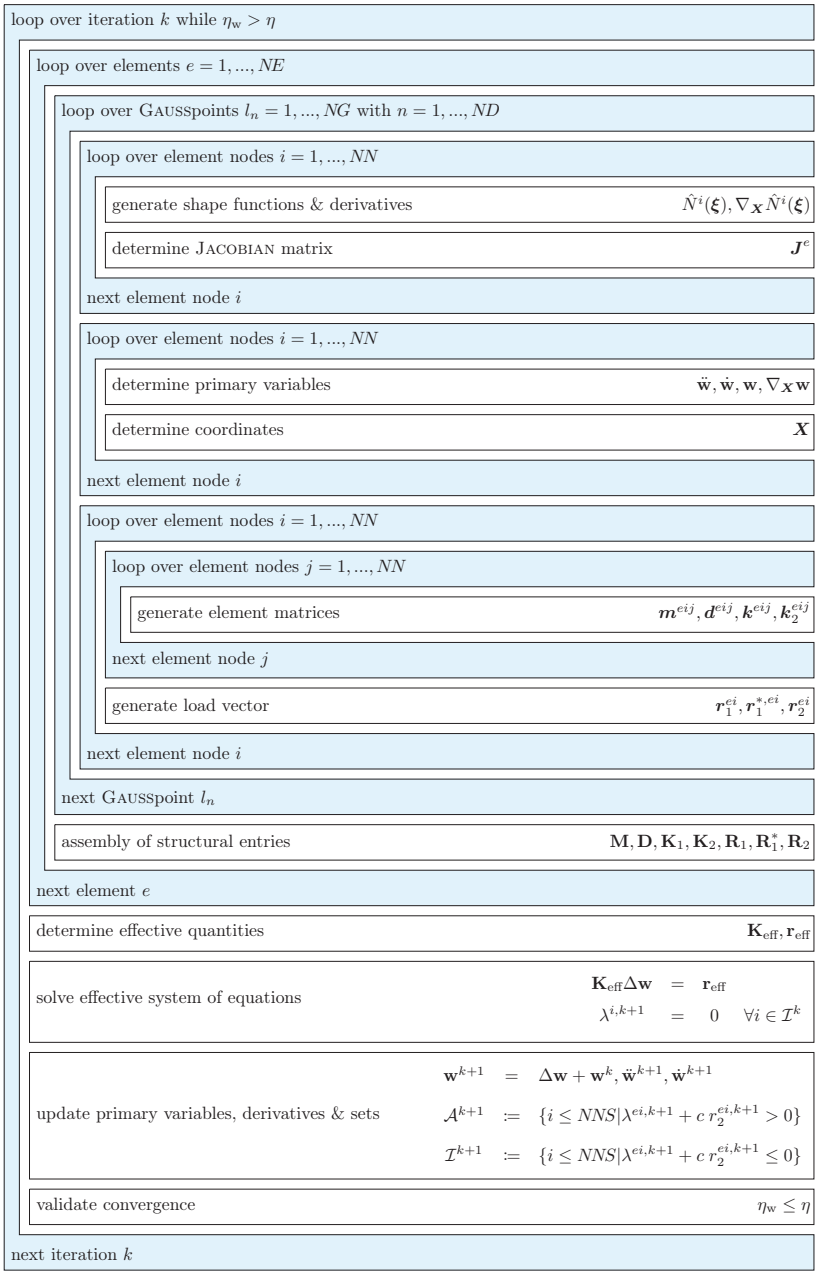

Figure 3.6.: Algorithm scheme for a semi-smooth NEWTON method

The integral of the arbitrary function $h(\xi_1, \xi_2, \xi_3)$ is now estimated by three sums, where NG_d with $d = 1, ..., 3$ embodies the number of quadrature points in the respective spatial direction. The latter and the weighting coefficients are identical to those used in the one-dimensional case. The two-dimensional case is treated similarly. Depending on the choice of weighting constants and quadrature points, different integration accuracies can be obtained. Hence, different types of quadrature rules exist and can be applied.

3.3.1. Gauss-Legendre

The idea of the Gauss-Legendre quadrature is to choose weighting coefficients and nodal points in such a way that polynomials of order p are approximated as well as possible. This is achieved if the considered nodal points ξ_d^i with $i = 1, ..., NG_d$ and $d = 1, ..., ND$ are the roots of the Legendre polynomials, while the weighting coefficients are determined by the integral of the corresponding Lagrange interpolants, cf. (Meister, 2010). For NG_d nodal points, a polynomial of order $p \leq 2NG_d - 1$ can be approximated exactly. The following Table 3.1 shows an exemplary list of the Gauss-Legendre quadrature parameters. For further values see (Abramowitz and Stegun, 1972; Casio Computer Co. LTD, 2016; Szabó and Babuška, 1991).

3.3.2. Radau

The nodal points of the Gauss-Radau quadrature are also related to the Legendre polynomials. The same is true for the weighting factors, cf. (Abramowitz and Stegun, 1972; Gautschi, 1999; Rose, 2007; Stroud, 1974; Weisstein, 2016). The difference to the Gauss-Legendre quadrature, however, is that one nodal point is prescribed beforehand. Here, only the case $\xi_d^{NG_d} = 1$ with $d = 1, ..., ND$ is considered. Due to this, for NG_d nodal points only a polynomial of order $p \leq 2NG_d - 2$ can thus be approximated exactly, (Matthies and Schieweck, 2011; Ueberhuber, 1997). A few quadrature parameters are listed in Table 3.2, cf. (Matthies and Schieweck, 2011; Weisstein, 2016).

3.3.3. Lobatto

The Gauss-Lobatto quadrature is also based on Legendre polynomials, and it is characterized by the fact that the two nodal points $\xi_d^1 = -1$ as well as $\xi_d^{NG_d} = 1$ with $d = 1, ..., ND$ are always considered, cf. (Abramowitz and Stegun, 1972). Accordingly, for NG_d nodal points only a polynomial of order $p \leq 2NG_d - 3$ can be approximated exactly, (Matthies and Schieweck, 2011; Ueberhuber, 1997). Table 3.3 depicts a list of quadrature parameters, cf. (Casio Computer Co. LTD, 2016; Szabó and Babuška, 1991).

3.4. Time Discretization

The nonlinear solution strategies of Section 3.2 yield a set of linearized semidiscrete equations, which are characterized by the primary variable vector $\mathbf{w}$ and its time derivatives $\dot{\mathbf{w}}$ and $\ddot{\mathbf{w}}$. At a certain step of the solution procedure a link between these quantities has to be established. This is achieved by time discretization schemes.

To be able to start from a common ground Equations (3.27) and (3.35)-(3.36) are aggregated in

$$\mathbf{M}\Delta\ddot{\mathbf{w}} + \mathbf{D}\Delta\dot{\mathbf{w}} + \mathbf{K}\Delta\mathbf{w} = \mathbf{R}^* - \mathbf{R}. \tag{3.46}$$

Therein, $\mathbf{M}$ represents the linearized generalized mass matrix and $\mathbf{D}$ the generalized damping matrix. The generalized stiffness matrix $\mathbf{K}$ is identical to the matrix $\mathbf{K}_1$ if the problem formulation is only identified by equalities - otherwise, the matrix $\mathbf{K}_2$ is incorporated as well. A similar course of action is followed concerning the generalized load vectors $\mathbf{R}$ and $\mathbf{R}^*$.

Subsequently, different approaches will be presented to solve the generalized Equation (3.46) in time. As a starting point for all methods, it is assumed that the time period of interest of the general elasto(visco)plastic lies between $[t_1, T]$. In the next step, this interval is subdivided into a number NT of time steps $[t_n, t_{n+1}]$ with $n = 1, ..., NT$. The time step size is denoted as $\Delta t = t_{n+1} - t_n$. Hence, Equation (3.46) is exclusively evaluated at discrete points in time, which are dictated by the chosen time discretization technique. Another analogy of the consecutive schemes is that they all belong to the class of implicit one-step methods. Thus, the time derivatives of the primary variable vector only depend on quantities of the currently analyzed time step.

Table 3.1.: Gauss-Legendre parameters

NG_d	ξ_d^i	α_d^i
2	$-\frac{1}{\sqrt{3}}$	1
	$\frac{1}{\sqrt{3}}$	1
3	$-\sqrt{\frac{3}{5}}$	$\frac{5}{9}$
	0	$\frac{8}{9}$
	$\sqrt{\frac{3}{5}}$	$\frac{5}{9}$
4	$-\sqrt{\frac{3}{7}+\frac{2}{7}\sqrt{\frac{6}{5}}}$	$\frac{18-\sqrt{30}}{36}$
	$-\sqrt{\frac{3}{7}-\frac{2}{7}\sqrt{\frac{6}{5}}}$	$\frac{18+\sqrt{30}}{36}$
	$\sqrt{\frac{3}{7}-\frac{2}{7}\sqrt{\frac{6}{5}}}$	$\frac{18+\sqrt{30}}{36}$
	$\sqrt{\frac{3}{7}+\frac{2}{7}\sqrt{\frac{6}{5}}}$	$\frac{18-\sqrt{30}}{36}$

Table 3.2.: Radau parameters

NG_d	ξ_d^i	α_d^i
2	$-\frac{1}{3}$	$\frac{3}{2}$
	1	$\frac{1}{2}$
3	$-\frac{1}{5}\left(1+\sqrt{6}\right)$	$\frac{1}{18}\left(16-\sqrt{6}\right)$
	$-\frac{1}{5}\left(1-\sqrt{6}\right)$	$\frac{1}{18}\left(16+\sqrt{6}\right)$
	1	$\frac{2}{9}$
4	−0.822824	0.440924
	−0.181066	0.776387
	0.575319	0.657689
	1	0.125

Table 3.3.: Lobatto parameters

NG_d	ξ_d^i	α_d^i
2	−1	1
	1	1
3	−1	$\frac{1}{3}$
	0	$\frac{4}{3}$
	1	$\frac{1}{3}$
4	−1	$\frac{1}{6}$
	−0.447213	$\frac{5}{6}$
	0.447213	$\frac{5}{6}$
	1	$\frac{1}{6}$

3.4.1. The Newmark Method

Originally, the Newmark method was derived for structural dynamics considering forces and displacements, cf. (Newmark, 1959). The time discretization is based on the idea of determining the unknown velocity at the end of a time step by means of a weighted linear combination of

the accelerations at the beginning and at the end of the time step. The unknown displacements are treated analogously. Transforming this concept to the general elasto(visco)plastic problem in (3.46) with the vector of unknowns $\mathbf{w}$ yields the approximations

$$\mathbf{M}_{n+1}\Delta\ddot{\mathbf{w}}_{n+1} + \mathbf{D}_{n+1}\Delta\dot{\mathbf{w}}_{n+1} + \mathbf{K}_{n+1}\Delta\mathbf{w}_{n+1} = \mathbf{R}^*_{n+1} - \mathbf{R}_{n+1}, \tag{3.47}$$

$$\mathbf{w}_{n+1} = \mathbf{w}_n + \Delta t\dot{\mathbf{w}}_n + \frac{\Delta t^2}{2}\left[[1-2\beta]\,\ddot{\mathbf{w}}_n + 2\beta\ddot{\mathbf{w}}_{n+1}\right], \tag{3.48}$$

$$\dot{\mathbf{w}}_{n+1} = \dot{\mathbf{w}}_n + \Delta t\left[[1-\gamma]\,\ddot{\mathbf{w}}_n + \gamma\ddot{\mathbf{w}}_{n+1}\right], \tag{3.49}$$

whereby the indices represent the points in time where the respective quantity is calculated, e.g. $\mathbf{w}_{n+1} = \mathbf{w}(t_{n+1})$. The variables β and γ resemble the NEWMARK parameters and influence the stability as well as the accuracy of the method. For details on these topics and an in-depth analysis concerning the NEWMARK method see (Bathe, 2002; Hughes, 1983; Neundorf, 2013; Newmark, 1959; Strehmel et al., 2012). In this thesis, Equation (3.47) is to be solved with respect to the vector of primary variables $\mathbf{w}_{n+1}$, which is why Equations (3.48)-(3.49) have to be reformulated. To obtain a term for the second time derivative, Equation (3.48) is rearranged. Afterwards, the resulting expression is inserted in (3.49), leading to

$$\dot{\mathbf{w}}_{n+1} = \frac{\gamma}{\beta\Delta t}\left[\mathbf{w}_{n+1} - \mathbf{w}_n\right] - \frac{\gamma-\beta}{\beta}\dot{\mathbf{w}}_n - \frac{\gamma-2\beta}{2\beta}\Delta t\ddot{\mathbf{w}}_n, \tag{3.50}$$

$$\ddot{\mathbf{w}}_{n+1} = \frac{1}{\beta\Delta t^2}\left[\mathbf{w}_{n+1} - \mathbf{w}_n\right] - \frac{1}{\beta\Delta t}\dot{\mathbf{w}}_n - \frac{1-2\beta}{2\beta}\ddot{\mathbf{w}}_n. \tag{3.51}$$

Therein, only quantities of the last time step are included. For the first time step t_1 the primary variable vector $\mathbf{w}_1$ and its first derivative $\dot{\mathbf{w}}_1$ are given, due to the initial conditions in (3.3). The generalized accelerations $\ddot{\mathbf{w}}_1$ have to be determined in a preprocessing step by solving the general elasto(visco)plastic problem in (3.1)–(3.2) at t_1 directly.

Inserting the linearizations of Expressions (3.50)- (3.51) in Equation (3.47) yields the linear system of equations

$$\begin{aligned} \mathbf{K}_{\text{eff}}\Delta\mathbf{w}_{n+1} &= \mathbf{r}_{\text{eff}}, \\ \mathbf{K}_{\text{eff}} &= \frac{1}{\beta\Delta t^2}\mathbf{M}_{n+1} + \frac{\gamma}{\beta\Delta t}\mathbf{D}_{n+1} + \mathbf{K}_{n+1}, \\ \mathbf{r}_{\text{eff}} &= \mathbf{R}^*_{n+1} - \mathbf{R}_{n+1}, \end{aligned} \tag{3.52}$$

which is represented by Equation (3.28) or (3.40) in Section 3.2. In the following, the nonlinear solution strategies can thus be carried out to determine the unknown quantities. The time derivatives can be updated in each iteration by utilizing Equations (3.50)-(3.51).

For a potential choice of the numerical parameters β, γ, and the respective analysis see (Bathe, 2002; Chung and Hulbert, 1993; Hilber et al., 1977; Hughes, 1983; Newmark, 1959; Wood et al., 1980). In the examples investigated in the course of this thesis, only

$$\beta = \frac{1}{4}, \qquad \gamma = \frac{1}{2} \tag{3.53}$$

are taken into account, leading to a second order accurate time discretization scheme. For the accompanying algorithmic implementation scheme see Figure 3.7. Further combinations of parameters are listed in (Gleim, 2016; Kuhl, 2004).

To enable a better control of the amount of numerical dissipation and dispersion, enhancements of the NEWMARK time integration scheme are developed in (Hilber et al., 1977; Wood et al.,

1980) by introducing additional numerical parameters. Further abstractions and investigations of these time integration schemes are performed in (Chung and Hulbert, 1993) emanating in the generalized NEWMARK-α method.

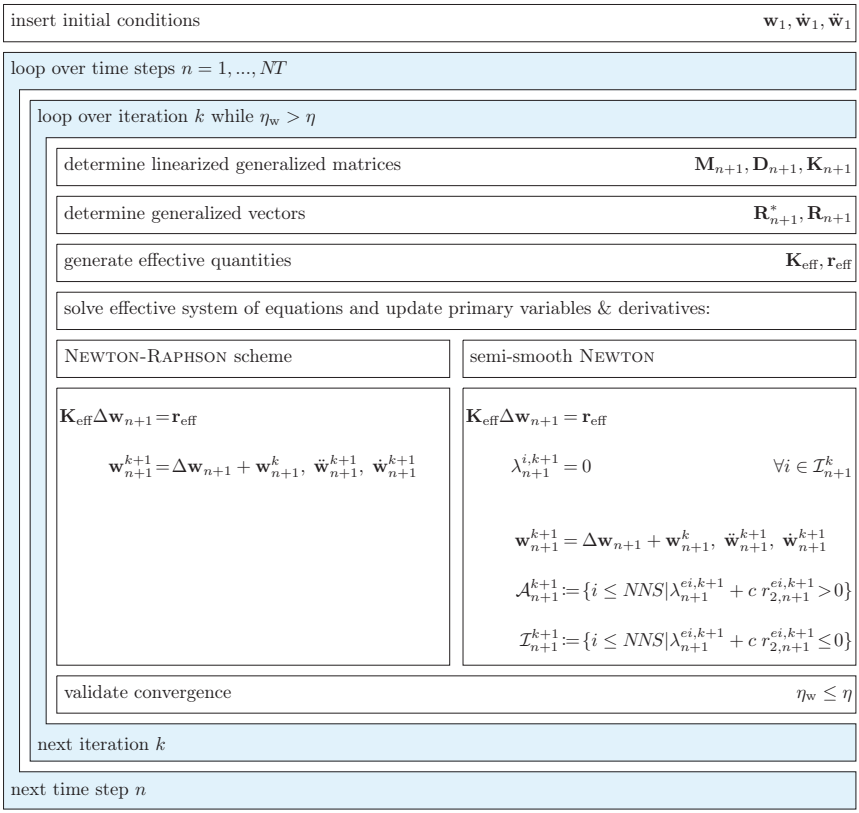

Figure 3.7.: Algorithm scheme for the NEWMARK method

3.4.2. RUNGE-KUTTA Schemes

One of the oldest classes of time integration schemes are the RUNGE-KUTTA methods. Their beginning rests on the idea of solving first order differential equations by a reformulation into corresponding integral counterparts. To obtain higher orders of convergence, these integrals are approximated by a linear combination of trapezoidal rules, cf. (Butcher, 1996; Runge, 1895). In a next step, this rather inductive approach is generalized by assuming an arbitrary quadrature rule, whose coefficients and supporting points are determined using a TAYLOR series expansion to obtain a prescribed order of convergence, cf. (Butcher and Wanner, 1996; Heun, 1900). Todays RUNGE-KUTTA procedures include a further modification exploiting additional parameters to generate greater flexibility in their design, cf. (Butcher and Wanner, 1996;

Kutta, 1901). While the original schemes were solely of explicit nature, the search for even higher orders of convergence led to the creation of implicit schemes. Because of their advantageous stability issues, they gained further popularity, despite their greater computational effort, cf. (Alexander, 1977; Butcher, 1963, 1964, 2008; Butcher and Wanner, 1996; Cash, 1979; Hairer and Wanner, 2002; Prothero and Robinson, 1974; Strehmel et al., 2012). Additionally, the possibility to determine the time discretization error efficiently is of great practical interest. Hence, schemes using incorporated error estimates resemble useful tools. For their derivation and investigation see (Cash, 1979; Dormand and Prince, 1980; Fehlberg, 1970).

Due to the different numerical demands - such as efficiency, order of convergence, stability, or error quantification - a variety of RUNGE-KUTTA schemes emerged. In the following sections, only a few special cases from this range of methods are treated in detail.

3.4.2.1. Stiffly Accurate Fully Implicit RUNGE-KUTTA Methods (IRK)

Apart from a few exceptions, e.g. the NYSTRÖM schemes cf. (Hairer et al., 2008), RUNGE-KUTTA methods were originally derived for first order ordinary differential equations. Thus, Equation (3.46) is transformed into

$$\mathbf{M}_{ni}\Delta\dot{\mathbf{v}}_{ni} + \mathbf{D}_{ni}\Delta\mathbf{v}_{ni} + \mathbf{K}_{ni}\Delta\mathbf{w}_{ni} = \mathbf{R}^{*}_{ni} - \mathbf{R}_{ni}, \tag{3.54}$$

$$\dot{\mathbf{w}}_{ni} = \mathbf{v}_{ni}, \tag{3.55}$$

whereby the indices represent the points in time where the respective quantity is calculated, e.g. $\mathbf{w}_{ni} = \mathbf{w}(t_{ni})$. These specific moments lie within the time step $[t_n, t_{n+1}]$ and are denoted as stages. They are determined by

$$t_{ni} = t_n + c_i\Delta t,$$

with the coefficients $c_i \in [0, 1]$ and $i = 1, ..., s$, where s embodies the maximum number of stages. Hence, the general elasto(visco)plastic problem in (3.46) is not only solved at the end of the time step, but also in-between. The link between the primary variable vectors $\mathbf{w}, \mathbf{v}$, and their time derivatives is established by exploiting the fundamental theorem of calculus

$$\mathbf{w}_{n+1} = \mathbf{w}_n + \int_{t_n}^{t_{n+1}} \dot{\mathbf{w}}(t)\, dt, \qquad \mathbf{v}_{n+1} = \mathbf{v}_n + \int_{t_n}^{t_{n+1}} \dot{\mathbf{v}}(t)\, dt \tag{3.56}$$

as well as by approximating the appearing integrals in Equation (3.56) using the particular quadrature rules

$$\mathbf{w}_{n+1} = \mathbf{w}_n + \Delta t \sum_{i=1}^{s} b_i\, \dot{\mathbf{w}}_{ni}, \qquad \mathbf{v}_{n+1} = \mathbf{v}_n + \Delta t \sum_{i=1}^{s} b_i\, \dot{\mathbf{v}}_{ni}, \tag{3.57}$$

with weighting coefficients b_i. To figure out the new unknowns $\dot{\mathbf{w}}_{ni}, \dot{\mathbf{v}}_{ni}$, further quadratures

$$\mathbf{w}_{ni} = \mathbf{w}_n + \Delta t \sum_{j=1}^{s} a_{ij}\, \dot{\mathbf{w}}_{nj}, \qquad \mathbf{v}_{ni} = \mathbf{v}_n + \Delta t \sum_{j=1}^{s} a_{ij}\, \dot{\mathbf{v}}_{nj}, \tag{3.58}$$

with weighting coefficients a_{ij} are applied, emanating in a fully coupled system of linear equations for the stage values $\mathbf{w}_{ni}, \mathbf{v}_{ni}$. The concept behind these nested quadrature rules is to obtain a variety of parameters which enable the creation of time integration methods with relatively arbitrary orders of convergence. The actual determination of these coefficients can be carried out by comparing the TAYLOR series expansion of the method with the one of the exact solution,

cf. (Butcher, 2008; Hairer et al., 2008). But apart from accuracy, these parameters also influence the stability of the method, cf. (Butcher, 2008; Hairer et al., 2008; Hairer and Wanner, 2002; Kutta, 1901). To provide a better overview of the chosen quadrature parameters, they are conventionally sorted into a Butcher tableau, see Figure 3.8.

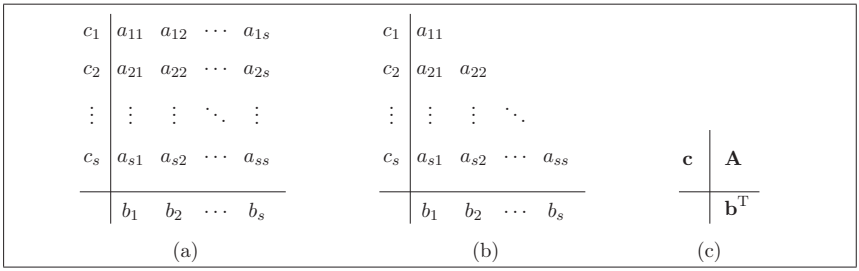

Figure 3.8.: (a) Implicit Runge-Kutta method, (b) Diagonally implicit Runge-Kutta scheme, (c) Short notation of the Butcher tableau

The classification of Runge-Kutta schemes is mainly performed by the form of the coefficient matrix $\mathbf{A}$ consisting of entries a_{ij}. If this matrix has a lower triangular structure, a diagonally implicit method is obtained, which will be described in detail in Section 3.4.2.2. In contrast, a completely dense structure leads to fully implicit Runge-Kutta procedures. Moreover, in this thesis, only Runge-Kutta schemes will be considered, where

$$a_{si} = b_i \tag{3.59}$$

holds. This results in the correspondence of Equations (3.57) and (3.58) for the last stage. Hence, the last stage equals the end of the time step $t_{ns} = t_{n+1}$. These methods are denoted as stiffly accurate. This property is especially important if algebraic equations are included in Equation (3.46), as it is the case for the model problem in (3.35)-(3.39). Nevertheless, this characteristic will also play an important role for the general elasto(visco)plastic scheme in (3.27). Condition (3.59) enforces the algebraic equations to be fulfilled at the end of the time step. For an arbitrary choice of Runge-Kutta parameters b_i, this is not ensured, cf. (Ellsiepen and Hartmann, 2001; Hairer and Wanner, 2002). With these assumptions, each stage value is represented by a linear combination of all respective time derivatives at the different stages, see Figure 3.9.

Aggregating the stage values in the vector $\mathbf{w}_\mathrm{t} = [\mathbf{w}_{n1}, ..., \mathbf{w}_{ns}]$, the corresponding time derivatives in $\dot{\mathbf{w}}_\mathrm{t} = [\dot{\mathbf{w}}_{n1}, ..., \dot{\mathbf{w}}_{ns}]$ and enhancing the vector $\mathbf{w}_{\mathrm{t},n}$ by s copies of $\mathbf{w}_n$, leads to a reformulation of the equations in (3.58) into

$$\mathbf{w}_\mathrm{t} = \mathbf{w}_{\mathrm{t},n} + \Delta t\ \mathbf{A}_\mathrm{t}\dot{\mathbf{w}}_\mathrm{t}, \qquad \mathbf{v}_\mathrm{t} = \mathbf{v}_{\mathrm{t},n} + \Delta t\ \mathbf{A}_\mathrm{t}\dot{\mathbf{v}}_\mathrm{t}, \tag{3.60}$$

if the variables connected to $\mathbf{v}$ are treated analogously. The matrix $\mathbf{A}_\mathrm{t}$ consists of an extension of the coefficient matrix $\mathbf{A}$

$$\mathbf{A}_\mathrm{t} = \begin{bmatrix} a_{11} & \cdots & a_{11} & a_{12} & \cdots & a_{12} & \cdots & a_{1s} & \cdots & a_{1s} \\ a_{21} & \cdots & a_{21} & a_{22} & \cdots & a_{22} & \cdots & a_{2s} & \cdots & a_{2s} \\ \vdots & & \vdots & \vdots & & \vdots & & \vdots & \ddots & \vdots \\ a_{s1} & \cdots & a_{s1} & a_{s2} & \cdots & a_{s2} & \cdots & a_{ss} & \cdots & a_{ss} \end{bmatrix},$$

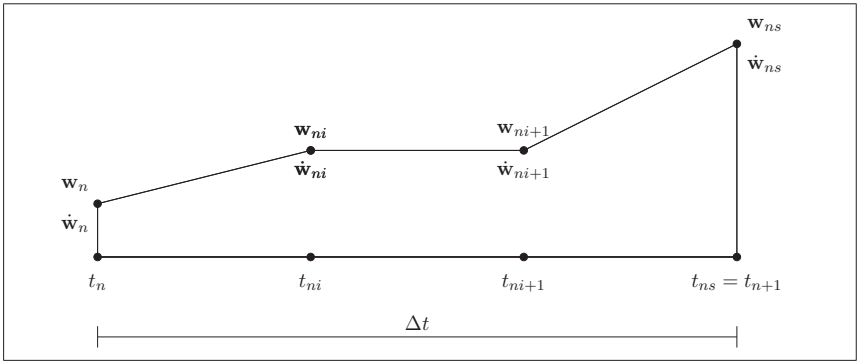

Figure 3.9.: Stage value location for stiffly accurate RUNGE-KUTTA schemes

where the individual entries are duplicated to take the sizes of the vectors $\mathbf{w}_\mathrm{t}, \dot{\mathbf{w}}_\mathrm{t}, \mathbf{v}_\mathrm{t}, \dot{\mathbf{v}}_\mathrm{t}$ into account. Transferring these ideas to the first order system of Equations (3.54)-(3.55) yields

$$\mathbf{M}_\mathrm{t}\Delta\dot{\mathbf{v}}_\mathrm{t} + \mathbf{D}_\mathrm{t}\Delta\mathbf{v}_\mathrm{t} + \mathbf{K}_\mathrm{t}\Delta\mathbf{w}_\mathrm{t} = \mathbf{R}_\mathrm{t}^* - \mathbf{R}_\mathrm{t}, \tag{3.61}$$

$$\Delta\dot{\mathbf{w}}_\mathrm{t} = \Delta\mathbf{v}_\mathrm{t}. \tag{3.62}$$

Analogously, the linearizations

$$\Delta\mathbf{w}_\mathrm{t} = \Delta t\ \mathbf{A}_\mathrm{t}\Delta\dot{\mathbf{w}}_\mathrm{t}, \qquad \Delta\mathbf{v}_\mathrm{t} = \Delta t\ \mathbf{A}_\mathrm{t}\Delta\dot{\mathbf{v}}_\mathrm{t}, \tag{3.63}$$

are determined, if $\Delta\mathbf{w}_{\mathrm{t},n} = \mathbf{0}$ and $\Delta\mathbf{v}_{\mathrm{t},n} = \mathbf{0}$ are exploited as well. In the following, it will always be assumed, that the coefficient matrix $\mathbf{A}$ is invertible and, hence, also its extension $\mathbf{A}_\mathrm{t}$. By taking advantage of the aforementioned properties, Equations (3.61)-(3.63) can be combined to derive the linear system of equations

$$\begin{aligned}
\mathbf{K}_\mathrm{eff}\Delta\mathbf{w}_\mathrm{t} &= \mathbf{r}_\mathrm{eff},\\
\mathbf{K}_\mathrm{eff} &= \frac{1}{\Delta t^2}\mathbf{M}_\mathrm{t}\mathbf{A}_\mathrm{t}^{-1}\mathbf{A}_\mathrm{t}^{-1} + \frac{1}{\Delta t}\mathbf{D}_\mathrm{t}\mathbf{A}_\mathrm{t}^{-1} + \mathbf{K}_\mathrm{t},\\
\mathbf{r}_\mathrm{eff} &= \mathbf{R}_\mathrm{t}^* - \mathbf{R}_\mathrm{t},
\end{aligned}$$

depending only on the vector of unknowns $\mathbf{w}_\mathrm{t}$. Thus, the system of equations is reduced, a direct solution with regard to the only primary variable vector $\mathbf{w}_\mathrm{t}$ is enabled, and the nonlinear solution strategies described in Section 3.2 can be carried out. The time derivatives can be updated in each iteration by utilizing reformulated forms of the equations in (3.60). Due to the stiff accuracy, evaluations of the corresponding expressions in (3.57) are obsolete. The solution at the end of the time step is already contained in the vector $\mathbf{w}_\mathrm{t}$.

While a system of *NEQ* number of equations has to be solved in the NEWMARK method, the system of equations for the fully implicit RUNGE-KUTTA schemes is s-times bigger - as a result of the additional stage values. However, the latter possess the ability to be constructed as procedures of an arbitrary order of convergence q, cf. (Butcher, 2008; Hairer et al., 2008; Hairer and Wanner, 2002). In the examples investigated in the course of this thesis, only the parameter constellations in Figure 3.10 and Figure 3.11 are considered. For the accompanying algorithmic implementation scheme see Figure 3.12.

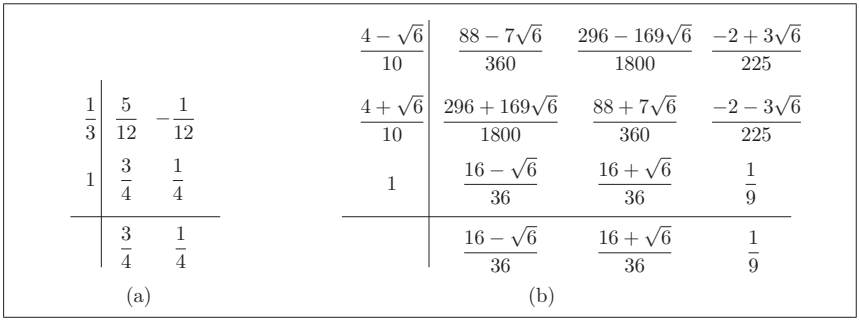

Figure 3.10.: (a) RADAU IIA(2) ($q = 3$), (b) RADAU IIA(3) ($q = 5$)

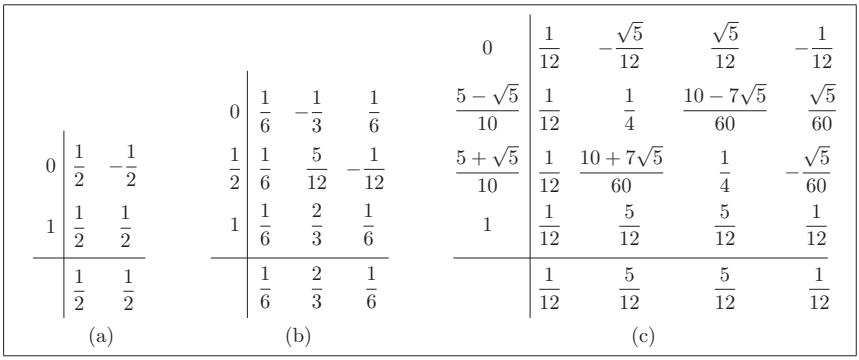

Figure 3.11.: (a) LOBATTO IIIC(2) ($q = 2$), (b) LOBATTO IIIC(3) ($q = 4$), (c) LOBATTO IIIC(4) ($q = 6$)

3.4.2.2. Stiffly Accurate Diagonally Implicit RUNGE-KUTTA Schemes (DIRK)

A special class of stiffly accurate fully implicit RUNGE-KUTTA schemes are those with a lower triangular matrix $\mathbf{A}$. They are denoted as stiffly accurate diagonal implicit RUNGE-KUTTA methods. If the coefficient matrix $\mathbf{A}$ remains invertible, the time discretization of Equation (3.46) can be carried out as described in the previous Section 3.4.2.1. Alternatively, the decoupling property of $\mathbf{A}$ can be exploited. Due to the lower triangular structure, each stage value only depends on its own and on previous stage derivatives, see the equations in (3.58). Therefore, it is not necessary to solve a system of equations consisting of $s \cdot NEQ$ equations. Instead, a system of equations with NEQ equations can be solved s-times. This leads to slight changes in the algorithmic treatment compared to the fully implicit case. The equations in (3.58) can be reformulated to

$$\mathbf{w}_{ni} = \tilde{\mathbf{w}}_{ni} + \Delta t \; a_{ii} \; \dot{\mathbf{w}}_{ni}, \qquad \mathbf{v}_{ni} = \tilde{\mathbf{v}}_{ni} + \Delta t \; a_{ii} \; \dot{\mathbf{v}}_{ni}, \quad (3.64)$$

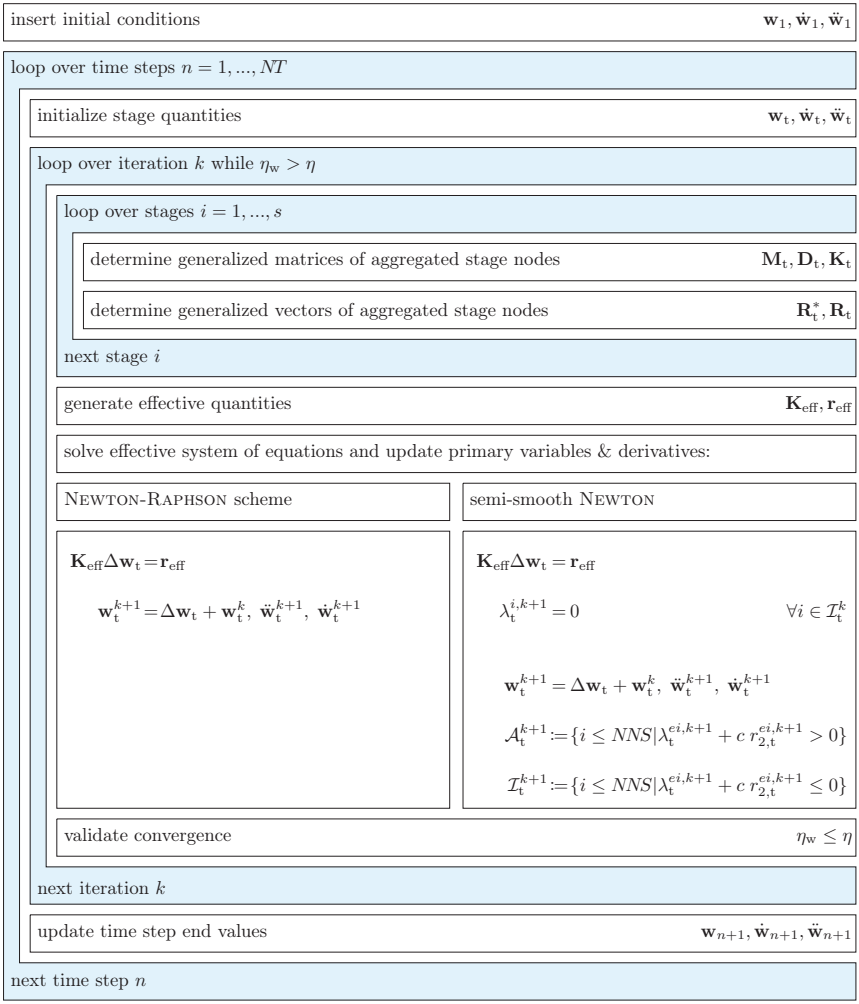

Figure 3.12.: Algorithm scheme for fully implicit RUNGE-KUTTA methods

with

$$\tilde{\mathbf{w}}_{ni} = \mathbf{w}_n + \Delta t \sum_{j=1}^{i-1} a_{ij}\ \dot{\mathbf{w}}_{nj}, \qquad \tilde{\mathbf{v}}_{ni} = \mathbf{v}_n + \Delta t \sum_{j=1}^{i-1} a_{ij}\ \dot{\mathbf{v}}_{nj}. \quad (3.65)$$

Linearizing the expressions in (3.64) and taking advantage of $\Delta\tilde{\mathbf{w}}_{ni} = \mathbf{0}$ as well as $\Delta\tilde{\mathbf{v}}_{ni} = 0$ yields

$$\Delta\mathbf{w}_{ni} = \Delta t\ a_{ii}\Delta\dot{\mathbf{w}}_{ni}, \qquad \Delta\mathbf{v}_{ni} = \Delta t\ a_{ii}\Delta\dot{\mathbf{v}}_{ni}, \quad (3.66)$$

as counterparts to the equations in (3.63). Hence, the equations in (3.66) can be combined with the Relationships (3.54)-(3.55) to derive the linear system of equations

$$\begin{aligned} \mathbf{K}_{\text{eff}}\Delta\mathbf{w}_{ni} &= \mathbf{r}_{\text{eff}}, \\ \mathbf{K}_{\text{eff}} &= \frac{1}{a_{ii}^2\Delta t^2}\mathbf{M}_{ni} + \frac{1}{a_{ii}\Delta t}\mathbf{D}_{ni} + \mathbf{K}_{ni}, \\ \mathbf{r}_{\text{eff}} &= \mathbf{R}^*_{ni} - \mathbf{R}_{ni}, \end{aligned} \tag{3.67}$$

which corresponds to Equation (3.28) or (3.40). Hence, the nonlinear solution strategies described in Section 3.2 can be carried out to determine the unknown quantities. The time derivatives can be updated in each iteration by utilizing reformulated forms of the equations in (3.64). The quantities at the end of the time step are obtained automatically, due to the stiff accuracy. Correspondingly, the equations in (3.57) are obsolete. Compared to the NEWMARK method, these methods have a s-times higher computational effort, because the solution procedure has to be carried out for all s stages. The benefit, however, is that higher orders of convergence can be achieved. In contrast to the fully implicit RUNGE-KUTTA schemes, the computational costs per solution procedure are reduced, since the number of equations is s-times less. However, at least s-times more iterations have to be performed.

In the examples investigated in the course of this thesis, only the parameter constellations in Figure 3.13 are considered:

$\alpha_r = 0.4358665215$

(a)

1	1
	1

(b)

$\frac{2-\sqrt{2}}{2}$	$\frac{2-\sqrt{2}}{2}$	
1	$\frac{\sqrt{2}}{2}$	$\frac{2-\sqrt{2}}{2}$
	$\frac{\sqrt{2}}{2}$	$\frac{2-\sqrt{2}}{2}$

(c)

α_r	α_r		
$\frac{1+\alpha_r}{2}$	$\frac{1-\alpha_r}{2}$	α_r	
1	$-\frac{6\alpha_r^2-16\alpha_r+1}{4}$	$\frac{6\alpha_r^2-20\alpha_r+5}{4}$	α_r
	$-\frac{6\alpha_r^2-16\alpha_r+1}{4}$	$\frac{6\alpha_r^2-20\alpha_r+5}{4}$	α_r

Figure 3.13.: (a) DIRK(1) ($q = 1$), (b) DIRK(2) ($q = 2$), (c) DIRK(3) ($q = 3$)

For the accompanying algorithmic implementation scheme see Figure 3.14.

3.4.3. GALERKIN Time Discretization Scheme

Another class of time discretization schemes are the GALERKIN time integrators. They are based on the idea of adapting the concept of the finite element method for space discretizations to the time domain. Hence, the differential equation, which has to be solved in time, is reformulated into a corresponding weak form by a premultiplication with a test function and an integration over the time domain. The primary variables as well as the test functions are then approximated using appropriate interpolations. Carrying out a numerical integration allows to determine the required unknowns in the time domain. Early approaches in this context are performed in (Argyris and Scharpf, 1969; Fried, 1969; Oden, 1969). Further applications consider the heat conduction equation, linear elastodynamics, rigid body movements, and optimal control

problems with algebraic constraints as the target of investigation, cf. (Aziz and Monk, 1989; Borri et al., 1990; Botasso and Ragazzi, 2000; Huang and Costanzo, 2002; Hulber and Hughes, 1990; Hulbert, 1992). By utilizing distinct shape functions and quadrature rules to estimate the appearing integrals, a whole bundle of parameterizations of GALERKIN integrators can be generated. For RUNGE-KUTTA procedures, an analogous influence within the variation of the numerical integration scheme is perceptible, see Section 3.4.2. These similarities between both RUNGE-KUTTA and GALERKIN methods as well as their link to collocation methods are considered in (Ascher and Petzold, 1998; Aziz and Monk, 1989; Botasso, 1997; Estep and Stuart, 2001; Hulme, 1972*a*; Matthies and Schieweck, 2011; Zhao and Wei, 2013).

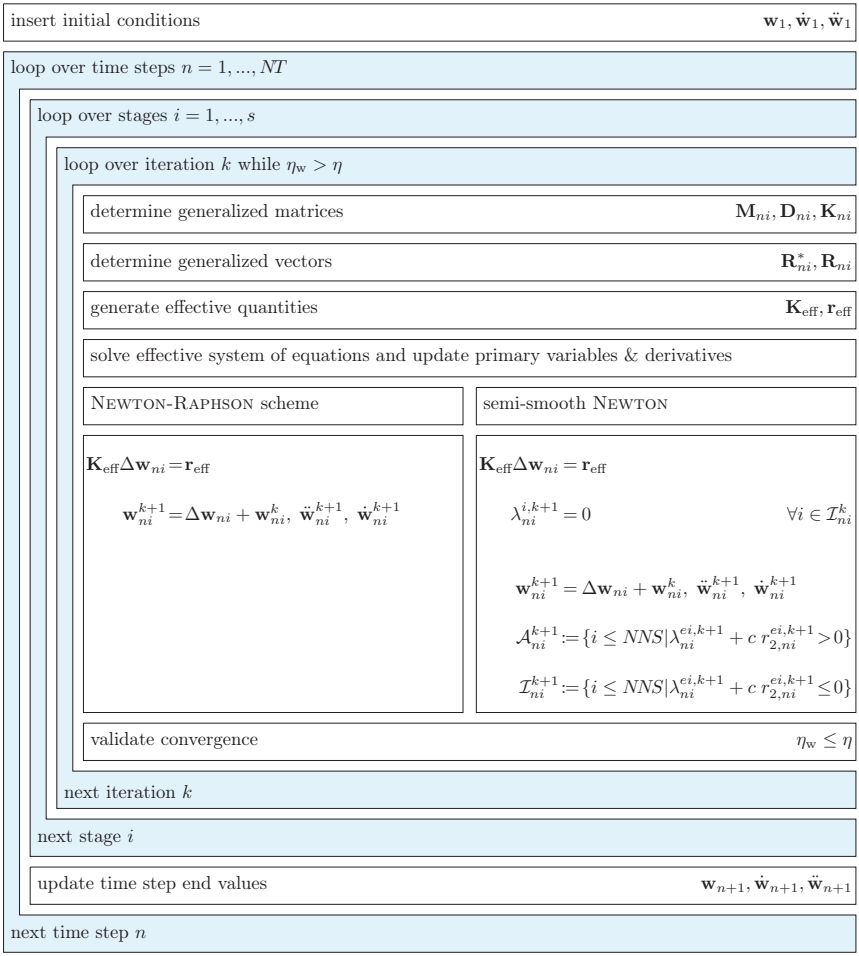

Figure 3.14.: Algorithm scheme for diagonally implicit RUNGE-KUTTA methods

Due to these connections, it is obvious, that since the family of RUNGE-KUTTA schemes can be derived in principle for arbitrary orders, this also has to hold for the class of GALERKIN time discretization schemes. Mathematical investigations concerning these convergence rates and in terms of error estimates as well as stability aspects are performed in (Aziz and Monk, 1989; Eriksson et al., 2005; Hulme, 1972*a*,*b*; Matthies and Schieweck, 2011; Schieweck, 2009; Thomée, 1997). In the following sections, only selected combinations of quadrature rules and interpolatory functions are treated in detail.

3.4.3.1. Continuous GALERKIN Two-Field Setting (cG$_2(p_\mathrm{t})$)

There are various possibilities to solve Equation (3.46) by applying the finite element method in the time domain. Since a large number of analyses has been carried out with regard to systems of first order in time, cf. (Eriksson et al., 2005; Matthies and Schieweck, 2011; Thomée, 1997), this approach is considered here as well. Therefore, Equation (3.46) is transformed to

$$\mathbf{M}\Delta\dot{\mathbf{v}} + \mathbf{D}\Delta\mathbf{v} + \mathbf{K}\Delta\mathbf{w} = \mathbf{R}^* - \mathbf{R}, \tag{3.68}$$

$$\Delta\dot{\mathbf{w}} - \Delta\mathbf{v} = \mathbf{v}^k - \dot{\mathbf{w}}^k, \tag{3.69}$$

taking into account that the linearization of $\dot{\mathbf{w}} = \mathbf{v}$ is included as an additional velocity constraint. In the next step, a temporal weak form is generated by multiplying Equations (3.68)-(3.69) with arbitrary vector-valued test functions $\delta\mathbf{t}_1, \delta\mathbf{t}_2$ and carrying out an integration over one time step for each equation, cf. (Matthies and Schieweck, 2011; Thomée, 1997). In general, identical test functions $\delta\mathbf{t}_1$ and $\delta\mathbf{t}_2$ could be chosen. Here, the distinction is made in order to take differences concerning physical units into account. Furthermore, a weighting of both equations is not considered in contrast to the approaches in (Carstens, 2013; Gleim, 2016). Adding up the resulting equations yields the relationship

$$\begin{aligned} \delta W_\mathrm{t} &= \int_{t_n}^{t_{n+1}} \delta\mathbf{t}_1 \quad [\mathbf{M}\Delta\dot{\mathbf{v}} + \mathbf{D}\Delta\mathbf{v} + \mathbf{K}\Delta\mathbf{w} - \mathbf{R}^* + \mathbf{R}] \quad dt^n \quad + \\ &+ \int_{t_n}^{t_{n+1}} \delta\mathbf{t}_2 \quad \mathbf{I} \quad \left[\Delta\dot{\mathbf{w}} - \Delta\mathbf{v} - \mathbf{v}^k + \dot{\mathbf{w}}^k\right] \quad dt^n \quad = \quad 0. \end{aligned} \tag{3.70}$$

Therein, the unity matrix $\mathbf{I}$ is of the size of the considered number of degrees of freedom. In the next step, it is assumed that the primary variables are approximated continuously using shape functions $N_\mathrm{t}^i(\xi_\mathrm{t})$ with $i = 1, ..., p_\mathrm{t} + 1$, where $p_\mathrm{t} \geq 2$ represents the polynomial degree. The test functions, however, are approximated discontinuously by functions $\bar{N}_\mathrm{t}^i(\xi_\mathrm{t})$ with $i = 1, ..., \bar{p}_\mathrm{t} + 1$ but of polynomial degree $\bar{p}_\mathrm{t} = p_\mathrm{t} - 1$. Thus, following the wording in (Matthies and Schieweck, 2011) a continuous PETROV-GALERKIN method in the two-field setting is derived.

As in the spatial finite element analysis, see Section 3.1, for GALERKIN type time integrators a parametrization of every time element $[t_n, t_{n+1}]$ with $n = 1, ..., NT$ is realized to form a standard time element based on natural coordinates $\xi_\mathrm{t} \in [-1, 1]$. The element time t^n is hence approximated analogously to Equation $(3.5)_1$ by

$$t^n \approx \sum_{i=1}^{p_\mathrm{t}+1} t^{ni} N_\mathrm{t}^i(\xi_\mathrm{t}), \tag{3.71}$$

where t^{ni} represents the respective time element node i and $N_\mathrm{t}^i(\xi_\mathrm{t})$ the corresponding shape function, cf. (Gleim and Kuhl, 2013; Kuhl, 2004; Stangenberg et al., 2009). Due to the one-dimensional character and the proportional positioning of the arbitrary and the standard finite

element nodes, Equation (3.71) can be simplified to the linear relation

$$t^n \approx \frac{\Delta t}{2}\xi_\mathrm{t} + \frac{t_n + t_{n+1}}{2}. \tag{3.72}$$

The primary variables, their time derivatives, their increments, and the test functions, however, are treated as follows

$$\begin{aligned}
\mathbf{w} &\approx \sum_{i=1}^{p_\mathrm{t}+1} \mathbf{w}^i N_\mathrm{t}^i(\xi_\mathrm{t}), \quad & \dot{\mathbf{w}} &\approx \sum_{i=1}^{p_\mathrm{t}+1} \mathbf{w}^i N_{\mathrm{t,t}}^i(\xi_\mathrm{t}), \quad & \Delta\mathbf{w} &\approx \sum_{i=1}^{p_\mathrm{t}+1} \Delta\mathbf{w}^i N_\mathrm{t}^i(\xi_\mathrm{t}), \quad & \Delta\dot{\mathbf{w}} &\approx \sum_{i=1}^{p_\mathrm{t}+1} \Delta\mathbf{w}^i N_{\mathrm{t,t}}^i(\xi_\mathrm{t}), \\
\mathbf{v} &\approx \sum_{i=1}^{p_\mathrm{t}+1} \mathbf{v}^i N_\mathrm{t}^i(\xi_\mathrm{t}), \quad & \dot{\mathbf{v}} &\approx \sum_{i=1}^{p_\mathrm{t}+1} \mathbf{v}^i N_{\mathrm{t,t}}^i(\xi_\mathrm{t}), \quad & \Delta\mathbf{v} &\approx \sum_{i=1}^{p_\mathrm{t}+1} \Delta\mathbf{v}^i N_\mathrm{t}^i(\xi_\mathrm{t}), \quad & \Delta\dot{\mathbf{v}} &\approx \sum_{i=1}^{p_\mathrm{t}+1} \Delta\mathbf{v}^i N_{\mathrm{t,t}}^i(\xi_\mathrm{t}), \\
\delta\mathbf{t}_1 &\approx \sum_{i=1}^{\bar{p}_\mathrm{t}+1} \delta\mathbf{t}_1^i \bar{N}_\mathrm{t}^i(\xi_\mathrm{t}), \quad & \delta\mathbf{t}_2 &\approx \sum_{i=1}^{\bar{p}_\mathrm{t}+1} \delta\mathbf{t}_2^i \bar{N}_\mathrm{t}^i(\xi_\mathrm{t}).
\end{aligned} \tag{3.73}$$

Thereby, the abbreviation $N_{\mathrm{t,t}}^i(\xi_\mathrm{t})$ with

$$N_{\mathrm{t,t}}^i(\xi_\mathrm{t}) = \frac{\partial N_\mathrm{t}^i(\xi_\mathrm{t})}{\partial \xi_\mathrm{t}} \frac{\partial \xi_\mathrm{t}}{\partial t^n} = N_{\mathrm{t;t}}^i(\xi_\mathrm{t}) J_\mathrm{t}^{-1} \tag{3.74}$$

illustrates the derivative of the shape function with respect to the physical time. The derivative with respect to the natural coordinate is denoted as $N_{\mathrm{t;t}}^i(\xi_\mathrm{t})$, while J_t embodies the Jacobian in time. The latter can be determined as

$$J_\mathrm{t} \approx \sum_{i=1}^{p_\mathrm{t}+1} N_{\mathrm{t;t}}^i(\xi_\mathrm{t}) t^{ni} = \frac{\Delta t}{2}, \tag{3.75}$$

with the Simplification (3.72). Furthermore, the generalization of the Galerkin time marching process is carried out by transforming the integrals of arbitrary time elements in Equation (3.70) into standard ones

$$\begin{aligned}
\delta W_\mathrm{t} &= \int_{-1}^{1} \delta\mathbf{t}_1 \quad [\mathbf{M}\Delta\dot{\mathbf{v}} + \mathbf{D}\Delta\mathbf{v} + \mathbf{K}\Delta\mathbf{w} - \mathbf{R}^* + \mathbf{R}] \quad J_\mathrm{t}\, d\xi_\mathrm{t} \quad + \\
&+ \int_{-1}^{1} \delta\mathbf{t}_2 \quad \mathbf{I} \quad \left[\Delta\dot{\mathbf{w}} - \Delta\mathbf{v} - \mathbf{v}^k + \dot{\mathbf{w}}^k\right] \qquad\qquad J_\mathrm{t}\, d\xi_\mathrm{t} \quad = \quad 0.
\end{aligned} \tag{3.76}$$

Inserting the approximations of (3.73) in Equation (3.76) yields the fully discrete form

$$\sum_{i=1}^{\bar{p}_\mathrm{t}+1} \sum_{j=2}^{p_\mathrm{t}+1} \delta\mathbf{t}^i \left[\mathbf{d}_\mathrm{t}^{ij} + \mathbf{k}_\mathrm{t}^{ij}\right] \Delta\mathbf{y}^j = \sum_{i=1}^{\bar{p}_\mathrm{t}+1} \delta\mathbf{t}^i \left[\mathbf{r}_\mathrm{t}^{*,i} - \mathbf{r}_\mathrm{t}^i\right].$$

Therein, it is taken into consideration that the quantities at the first time node $j = 1$ are known and, thus, their respective increments are zero. The primary variables as well as the test functions are summarized in

$$\Delta\mathbf{y} = \begin{bmatrix} \Delta\mathbf{w} \\ \Delta\mathbf{v} \end{bmatrix}, \qquad \delta\mathbf{t} = \begin{bmatrix} \delta\mathbf{t}_1 \\ \delta\mathbf{t}_2 \end{bmatrix} \tag{3.77}$$

and the other terms are defined by:

$$\begin{aligned}
\mathbf{d}_\mathrm{t}^{ij} &= \int_{-1}^{1} \bar{N}_\mathrm{t}^i(\xi_\mathrm{t}) N_{\mathrm{t,t}}^j(\xi_\mathrm{t}) \begin{bmatrix} \mathbf{0} & \mathbf{M} \\ \mathbf{I} & \mathbf{0} \end{bmatrix} J_\mathrm{t}\, d\xi_\mathrm{t}, \qquad \mathbf{k}_\mathrm{t}^{ij} = \int_{-1}^{1} \bar{N}_\mathrm{t}^i(\xi_\mathrm{t}) N_\mathrm{t}^j(\xi_\mathrm{t}) \begin{bmatrix} \mathbf{K} & \mathbf{D} \\ \mathbf{0} & -\mathbf{I} \end{bmatrix} J_\mathrm{t}\, d\xi_\mathrm{t}, \\
\mathbf{r}_\mathrm{t}^{*,i} &= \int_{-1}^{1} \bar{N}_\mathrm{t}^i(\xi_\mathrm{t}) \begin{bmatrix} \mathbf{R}^* \\ \mathbf{0} \end{bmatrix} J_\mathrm{t}\, d\xi_\mathrm{t}, \qquad \mathbf{r}_\mathrm{t}^i = \int_{-1}^{1} \bar{N}_\mathrm{t}^i(\xi_\mathrm{t}) \begin{bmatrix} \mathbf{R} \\ \mathbf{v}^k - \dot{\mathbf{w}}^k \end{bmatrix} J_\mathrm{t}\, d\xi_\mathrm{t}.
\end{aligned} \tag{3.78}$$

The assembly of the quantities in (3.77)-(3.78) into respective hypermatrices or vectors results in

$$\begin{aligned}
\Delta\mathbf{y}_{\mathrm{t}} &= \bigcup_{i=2}^{p_{\mathrm{t}}+1} \Delta\mathbf{y}^i, & \delta\mathbf{t}_{\mathrm{t}} &= \bigcup_{i=1}^{\bar{p}_{\mathrm{t}}+1} \delta\mathbf{t}^i, & \mathbf{K}_{\mathrm{t}} &= \bigcup_{\substack{i=1\\j=2}}^{\substack{p_{\mathrm{t}}+1\\ \bar{p}_{\mathrm{t}}+1}} \mathbf{k}_{\mathrm{t}}^{ij},\\
\mathbf{D}_{\mathrm{t}} &= \bigcup_{\substack{i=1\\j=2}}^{\substack{p_{\mathrm{t}}+1\\ \bar{p}_{\mathrm{t}}+1}} \mathbf{d}_{\mathrm{t}}^{ij}, & \mathbf{R}_{\mathrm{t}}^{*} &= \bigcup_{i=1}^{\bar{p}_{\mathrm{t}}+1} \mathbf{r}_{\mathrm{t}}^{*,i}, & \mathbf{R}_{\mathrm{t}} &= \bigcup_{i=1}^{\bar{p}_{\mathrm{t}}+1} \mathbf{r}_{\mathrm{t}}^{i},
\end{aligned} \tag{3.79}$$

wherein the entries associated to $j = 1$ are dropped, since the linked increments of the primary variables $\Delta\mathbf{y}^1$ are zero. Thus, the linear system of equations

$$\begin{aligned}
\mathbf{K}_{\mathrm{eff}}\Delta\mathbf{y}_{\mathrm{t}} &= \mathbf{r}_{\mathrm{eff}},\\
\mathbf{K}_{\mathrm{eff}} &= \mathbf{D}_{\mathrm{t}} + \mathbf{K}_{\mathrm{t}},\\
\mathbf{r}_{\mathrm{eff}} &= \mathbf{R}_{\mathrm{t}}^{*} - \mathbf{R}_{\mathrm{t}}
\end{aligned}$$

is established and the nonlinear solution strategies described in Section 3.2 can be performed. The necessary time derivatives are determined in each iteration by evaluating the forms in (3.73) at $\xi_{\mathrm{t}} = 1$. However, due to the two-field setting, the solution vector automatically covers the first time derivative of the primary variable vector $\dot{\mathbf{w}}$.

To eventually characterize the previously described continuous Galerkin two-field setting completely, appropriate shape functions and corresponding quadrature rules to calculate the appearing integrals have to be chosen, see Section 3.3. As in the case of the spatial finite element method, various realizations exist. Concerning the shape functions, isogeometric approaches can be used just as well as Hermite or Lagrange interpolants, cf. (Fried, 1969; Gleim and Kuhl, 2013; Kuhl, 2004; Matthies and Schieweck, 2011; Schäuble, 2013). With respect to numerical integrations, Gauss-Legendre, Radau or Lobatto quadrature rules are applied in the time finite element context, cf. (Carstens, 2013; Gleim, 2016; Matthies and Schieweck, 2011; Schieweck, 2009).

In the course of this thesis, a specific Radau quadrature together with specific Lagrange shape functions will be used for all examples based on the continuous Galerkin two-field setting. The necessary quadrature parameters are depicted in Table 3.2 in Section 3.3. The idea is to choose the number of quadrature points as $NG_{\mathrm{t}} = p_{\mathrm{t}}$ and to form the vector $\bar{\boldsymbol{\xi}}_{\mathrm{t}} = [\xi_{\mathrm{t}}^1, ..., \xi_{\mathrm{t}}^{NG_{\mathrm{t}}}]$ containing the corresponding Radau nodes. Furthermore, the vector $\boldsymbol{\xi}_{\mathrm{t}} = [-1, \bar{\boldsymbol{\xi}}_{\mathrm{t}}]$ is established. The Lagrange approaches are now formulated in such a way that, for the test functions, the entries of $\bar{\boldsymbol{\xi}}_{\mathrm{t}}$ are considered as interpolation points, since $\bar{p}_{\mathrm{t}} = p_{\mathrm{t}} - 1$ holds. For the approximation of the primary variables, their derivatives and increments, however, the quantities of $\boldsymbol{\xi}_{\mathrm{t}}$ are taken into account. This leads to the formulations

$$N_{\mathrm{t}}^i(\xi_{\mathrm{t}}) = \prod_{\substack{k=1\\k\neq i}}^{p_{\mathrm{t}}+1} \frac{\xi_{\mathrm{t}}^k - \xi_{\mathrm{t}}}{\xi_{\mathrm{t}}^k - \xi_{\mathrm{t}}^i} \qquad \xi_{\mathrm{t}}^j \in \boldsymbol{\xi}_{\mathrm{t}} \quad \text{with} \quad j = 1, ..., NG_{\mathrm{t}} + 1, \tag{3.80}$$

$$\bar{N}_{\mathrm{t}}^i(\xi_{\mathrm{t}}) = \prod_{\substack{k=1\\k\neq i}}^{\bar{p}_{\mathrm{t}}+1} \frac{\xi_{\mathrm{t}}^k - \xi_{\mathrm{t}}}{\xi_{\mathrm{t}}^k - \xi_{\mathrm{t}}^i} \qquad \xi_{\mathrm{t}}^j \in \bar{\boldsymbol{\xi}}_{\mathrm{t}} \quad \text{with} \quad j = 1, ..., NG_{\mathrm{t}}, \tag{3.81}$$

$$N_{\mathrm{t;t}}^i(\xi_{\mathrm{t}}) = \sum_{\substack{l=1\\l\neq i}}^{p_{\mathrm{t}}+1} \frac{-1}{\xi_{\mathrm{t}}^l - \xi_{\mathrm{t}}^i} \prod_{\substack{k=1\\k\neq i\\k\neq l}}^{p_{\mathrm{t}}+1} \frac{\xi_{\mathrm{t}}^k - \xi_{\mathrm{t}}}{\xi_{\mathrm{t}}^k - \xi_{\mathrm{t}}^i} \qquad \xi_{\mathrm{t}}^j \in \boldsymbol{\xi}_{\mathrm{t}} \quad \text{with} \quad j = 1, ..., NG_{\mathrm{t}} + 1. \tag{3.82}$$

For the derivative of the shape functions $N^i_{\mathrm{t,t}}(\xi_\mathrm{t})$ with respect to the physical coordinates, the evaluation of the JACOBIAN in time is needed as well. Although the application of RADAU quadrature points as interpolation points yields to non-equidistant nodes, Equation (3.71) can be formulated as the affine linear relationship in (3.72) between the physical time t and the natural time ξ_t so that $J_\mathrm{t} = \Delta t/2$ still has to hold (Babuška and Strouboulis, 2001; Matthies and Schieweck, 2011; Szabó and Babuška, 1991).

Due to the dependency of the selected number of RADAU quadrature points on the polynomial degree, the entries of the generalized time damping matrix $\mathbf{D}_\mathrm{t}$ are integrated exactly. For the generalized time stiffness matrix $\mathbf{K}_\mathrm{t}$ this is, because of the integration accuracy of RADAU schemes, not the case. Nevertheless, this strategy has the benefit that the points in time where the spatial quantities are evaluated, are identical to the time nodes. This is especially important if algebraic equations have to be considered, as it is the case within the semi-smooth NEWTON method in Section 3.2.2. Otherwise, these equations would not necessarily be fulfilled at the time nodes. Hence, the semi-smooth NEWTON method is evaluated at each time node. This argument is similar to the necessity of stiffly accurate RUNGE-KUTTA methods, see Section 3.4.2 and (Hairer and Wanner, 2002). Another analogy to the RUNGE-KUTTA schemes is that the order of convergence is not limited to two as in the NEWMARK case. Within the continuous GALERKIN two-field setting, it can be increased by varying the polynomial degree of the shape functions, cf. (Matthies and Schieweck, 2011; Thomée, 1997). But because of this enhancement and the two-field formulation, the linear system of equations which has to be solved is $2(\bar{p}_\mathrm{t}+1)$-times bigger as in the NEWMARK case and two-times bigger as for a fully implicit RUNGE-KUTTA scheme with $s = \bar{p}_\mathrm{t} + 1$ stages. For the accompanying algorithmic implementation scheme see Figure 3.16.

3.4.3.2. Discontinuous GALERKIN Two-Field Setting ($\mathrm{dG}_2(\bar{p}_\mathrm{t})$)

An alternative approach towards solving the respective first order reformulations in (3.68)-(3.69) of Equation (3.46) by means of GALERKIN time discretization schemes is to permit the primary variables to be discontinuous at the beginning of each time step t_n. This is described by

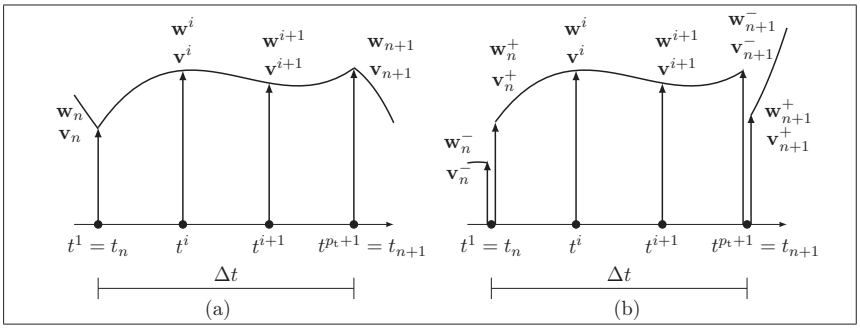

Figure 3.15.: (a) Continuous GALERKIN time integrator, (b) Discontinuous GALERKIN time integrator

introducing the jump terms

$$[\![\mathbf{w}]\!] = \mathbf{w}_n^+ - \mathbf{w}_n^- = 0, \qquad [\![\mathbf{v}]\!] = \mathbf{v}_n^+ - \mathbf{v}_n^- = 0, \quad (3.83)$$

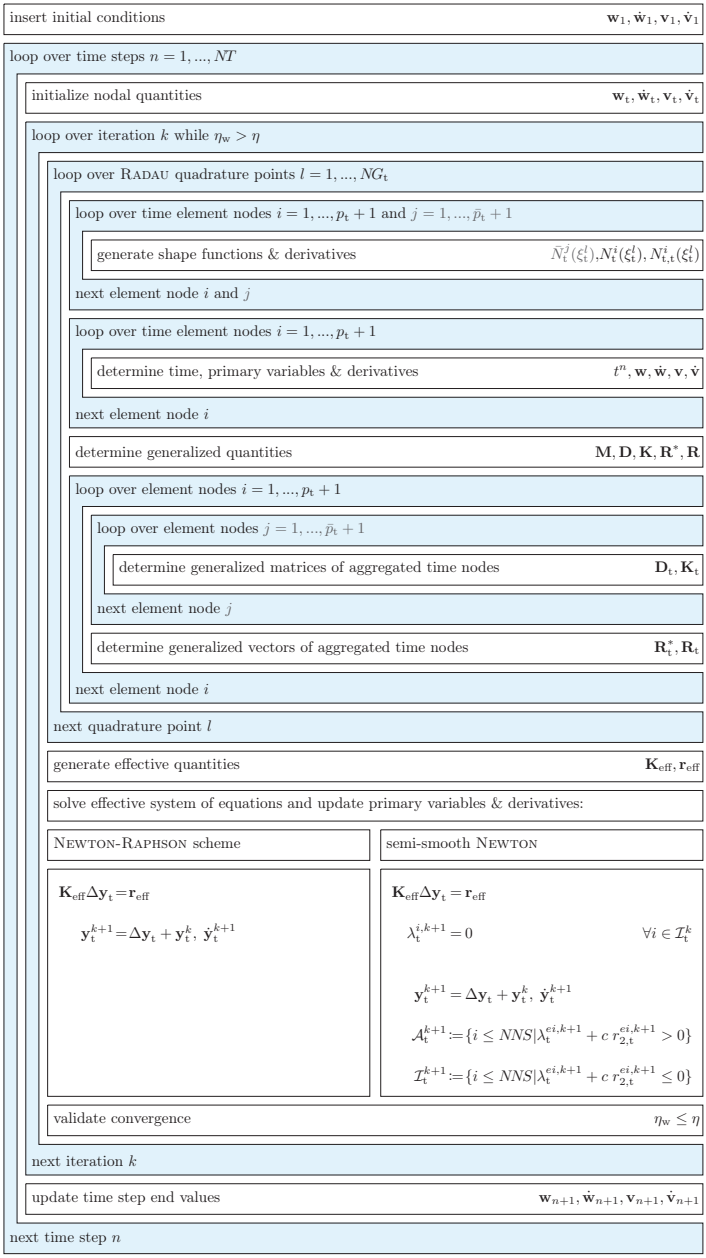

Figure 3.16.: Algorithm scheme for the continuous GALERKIN two-field setting

which embody the difference between the primary variables at the end of the last $\mathbf{w}_n^-, \mathbf{v}_n^-$ and at the beginning of the current time step $\mathbf{w}_n^+, \mathbf{v}_n^+$, see Figure 3.15. These continuity conditions can be weighted and linearized to obtain

$$\mathbf{M}\Delta\mathbf{v}^+ + \mathbf{M}[\![\mathbf{v}^k]\!] = 0, \qquad \mathbf{I}\Delta\mathbf{w}^+ + \mathbf{I}[\![\mathbf{w}^k]\!] = 0. \tag{3.84}$$

The weighting matrices are chosen as in (Matthies and Schieweck, 2011) and assumed to be constant. Other possibilities are described in (Gleim and Kuhl, 2013; Thomée, 1997).

If the temporal weak form of Equations (3.68)-(3.69) is now generated as described in Section 3.4.3.1, the discontinuities of the primary variables have to be considered. This is achieved by including the expressions of (3.84) in the extended temporal weak form

$$\begin{aligned}
\delta W_{\mathrm{t}} \;=\; & \int_{t_n}^{t_{n+1}} \delta\mathbf{t}_1 \quad \left[\mathbf{M}\Delta\dot{\mathbf{v}} + \mathbf{D}\Delta\mathbf{v} + \mathbf{K}\Delta\mathbf{w} - \mathbf{R}^* + \mathbf{R}\right] \; dt^n \; + \\
+ \; & \int_{t_n}^{t_{n+1}} \delta\mathbf{t}_2 \quad \left[\mathbf{I}\Delta\dot{\mathbf{w}} - \mathbf{I}\Delta\mathbf{v} - \mathbf{v}^k + \dot{\mathbf{w}}^k\right] \qquad dt^n \; + \\
+ \; & \delta\mathbf{t}_1^+ \quad \mathbf{M}\Delta\mathbf{v}^+ + \delta\mathbf{t}_1^+ \; \mathbf{M}[\![\mathbf{v}^k]\!] \qquad + \\
+ \; & \delta\mathbf{t}_2^+ \quad \mathbf{I} \; \Delta\mathbf{w}^+ + \delta\mathbf{t}_2^+ \; \mathbf{I}[\![\mathbf{w}^k]\!] \qquad = \; 0,
\end{aligned} \tag{3.85}$$

where $\delta\mathbf{t}_1^+, \delta\mathbf{t}_2^+$ represent the evaluated test functions at the beginning of the time step t_n. In this case, both the primary variables and the test functions are approximated by shape functions $\bar{N}^i(\xi_{\mathrm{t}})$ with $i = 1, ..., \bar{p}_{\mathrm{t}} + 1$ where $\bar{p}_{\mathrm{t}} \geq 1$ represents the polynomial degree. The result is a discontinuous Bubnov-Galerkin method in the two-field setting, cf. (Gleim and Kuhl, 2013; Kuhl, 2004; Matthies and Schieweck, 2011; Thomée, 1997; Zhao and Wei, 2013). Again, identical test functions $\delta\mathbf{t}_1$ and $\delta\mathbf{t}_2$ could be chosen - but the distinction in this case only serves to take differences concerning physical units into account.

To generalize the weak form in (3.85) to a standard time finite element, the procedure in Section 3.4.3.1 is followed and a parametrization of the arbitrary time element is carried out according to Equation (3.72). The approximations in Equation (3.73) are changed slightly, since in the discontinuous method the same shape functions are used for all quantities:

$$\begin{aligned}
&\mathbf{w} \approx \sum_{i=1}^{\bar{p}_{\mathrm{t}}+1} \mathbf{w}^i \bar{N}_{\mathrm{t}}^i(\xi_{\mathrm{t}}), \quad \dot{\mathbf{w}} \approx \sum_{i=1}^{\bar{p}_{\mathrm{t}}+1} \mathbf{w}^i \bar{N}_{\mathrm{t,t}}^i(\xi_{\mathrm{t}}), \quad \Delta\mathbf{w} \approx \sum_{i=1}^{\bar{p}_{\mathrm{t}}+1} \Delta\mathbf{w}^i \bar{N}_{\mathrm{t}}^i(\xi_{\mathrm{t}}), \quad \Delta\dot{\mathbf{w}} \approx \sum_{i=1}^{\bar{p}_{\mathrm{t}}+1} \Delta\mathbf{w}^i \bar{N}_{\mathrm{t,t}}^i(\xi_{\mathrm{t}}), \\
&\mathbf{v} \approx \sum_{i=1}^{\bar{p}_{\mathrm{t}}+1} \mathbf{v}^i \bar{N}_{\mathrm{t}}^i(\xi_{\mathrm{t}}), \quad \dot{\mathbf{v}} \approx \sum_{i=1}^{\bar{p}_{\mathrm{t}}+1} \mathbf{v}^i \bar{N}_{\mathrm{t,t}}^i(\xi_{\mathrm{t}}), \quad \Delta\mathbf{v} \approx \sum_{i=1}^{\bar{p}_{\mathrm{t}}+1} \Delta\mathbf{v}^i \bar{N}_{\mathrm{t}}^i(\xi_{\mathrm{t}}), \quad \Delta\dot{\mathbf{v}} \approx \sum_{i=1}^{\bar{p}_{\mathrm{t}}+1} \Delta\mathbf{v}^i \bar{N}_{\mathrm{t,t}}^i(\xi_{\mathrm{t}}), \\
&t^n \approx \sum_{i=1}^{\bar{p}_{\mathrm{t}}+1} t^{ni} \bar{N}_{\mathrm{t}}^i(\xi_{\mathrm{t}}), \quad \delta\mathbf{t}_1 \approx \sum_{i=1}^{\bar{p}_{\mathrm{t}}+1} \delta\mathbf{t}_1^i \bar{N}_{\mathrm{t}}^i(\xi_{\mathrm{t}}), \quad \delta\mathbf{t}_2 \approx \sum_{i=1}^{\bar{p}_{\mathrm{t}}+1} \delta\mathbf{t}_2^i \bar{N}_{\mathrm{t}}^i(\xi_{\mathrm{t}}), \\
&\delta\mathbf{t}_1^+ \approx \sum_{i=1}^{\bar{p}_{\mathrm{t}}+1} \delta\mathbf{t}_1^i \bar{N}_{\mathrm{t}}^i(-1), \quad \delta\mathbf{t}_2^+ \approx \sum_{i=1}^{\bar{p}_{\mathrm{t}}+1} \delta\mathbf{t}_2^i \bar{N}_{\mathrm{t}}^i(-1), \quad \Delta\mathbf{w}^+ \approx \sum_{i=1}^{\bar{p}_{\mathrm{t}}+1} \Delta\mathbf{w}^i \bar{N}_{\mathrm{t}}^i(-1), \quad \Delta\mathbf{v}^+ \approx \sum_{i=1}^{\bar{p}_{\mathrm{t}}+1} \Delta\mathbf{v}^i \bar{N}_{\mathrm{t}}^i(-1).
\end{aligned} \tag{3.86}$$

The Term (3.74) has to be adjusted analogously:

$$\bar{N}_{\mathrm{t,t}}^i(\xi_{\mathrm{t}}) = \frac{\partial \bar{N}_{\mathrm{t}}^i(\xi_{\mathrm{t}})}{\partial \xi_{\mathrm{t}}} \frac{\partial \xi_{\mathrm{t}}}{\partial t^n} = \bar{N}_{\mathrm{t;t}}^i(\xi_{\mathrm{t}}) J_{\mathrm{t}}^{-1}, \tag{3.87}$$

while the Jacobian remains as $J_{\mathrm{t}} = \Delta t/2$, as before. Inserting the Approximations (3.86) together with the Abbreviations (3.77) and exploiting the transformation to a standard finite

element in time yields the fully discrete form

$$\sum_{i=1}^{\bar{p}_\mathrm{t}+1}\sum_{j=1}^{\bar{p}_\mathrm{t}+1}\delta\mathbf{t}^i\left[\mathbf{d}_\mathrm{t}^{ij}+\mathbf{k}_\mathrm{t}^{ij}+\bar{\mathbf{d}}_\mathrm{t}^{ij}\right]\Delta\mathbf{y}^j=\sum_{i=1}^{\bar{p}_\mathrm{t}+1}\delta\mathbf{t}^i\left[\mathbf{r}_\mathrm{t}^{*,i}-\mathbf{r}_\mathrm{t}^i-\bar{\mathbf{r}}_\mathrm{t}^i\left[\!\left[\mathbf{y}^k\right]\!\right]\right],$$

where

$$\begin{aligned}
\mathbf{d}_\mathrm{t}^{ij} &= \int_{-1}^{1}\bar{N}_\mathrm{t}^i(\xi_\mathrm{t})\bar{N}_{\mathrm{t},\mathrm{t}}^j(\xi_\mathrm{t})\begin{bmatrix}\mathbf{0}&\mathbf{M}\\ \mathbf{I}&\mathbf{0}\end{bmatrix}J_\mathrm{t}\,d\xi_\mathrm{t}, & \mathbf{k}_\mathrm{t}^{ij} &= \int_{-1}^{1}\bar{N}_\mathrm{t}^i(\xi_\mathrm{t})\bar{N}_\mathrm{t}^j(\xi_\mathrm{t})\begin{bmatrix}\mathbf{K}&\mathbf{D}\\ \mathbf{0}&-\mathbf{I}\end{bmatrix}J_\mathrm{t}\,d\xi_\mathrm{t},\\
\mathbf{r}_\mathrm{t}^{*,i} &= \int_{-1}^{1}\bar{N}_\mathrm{t}^i(\xi_\mathrm{t})\begin{bmatrix}\mathbf{R}^*\\ \mathbf{0}\end{bmatrix}J_\mathrm{t}\,d\xi_\mathrm{t}, & \mathbf{r}_\mathrm{t}^i &= \int_{-1}^{1}\bar{N}_\mathrm{t}^i(\xi_\mathrm{t})\begin{bmatrix}\mathbf{R}\\ \mathbf{v}^k-\dot{\mathbf{w}}^k\end{bmatrix}J_\mathrm{t}\,d\xi_\mathrm{t},\\
\bar{\mathbf{d}}_\mathrm{t}^{ij} &= \bar{N}_\mathrm{t}^i(-1)\bar{N}_\mathrm{t}^j(-1)\begin{bmatrix}\mathbf{0}&\mathbf{M}\\ \mathbf{I}&\mathbf{0}\end{bmatrix}, & \bar{\mathbf{r}}_\mathrm{t}^i &= \bar{N}_\mathrm{t}^i(-1)\begin{bmatrix}\mathbf{0}&\mathbf{M}\\ \mathbf{I}&\mathbf{0}\end{bmatrix}
\end{aligned} \tag{3.88}$$

holds. Therein, the quantities with the superscript $(\bullet)^+$ are replaced by the linear combination of their nodal counterparts evaluated at the left boundary of the time element $\xi_\mathrm{t}=-1$. The assembly of the distinct parts

$$\begin{aligned}
\Delta\mathbf{y}_\mathrm{t} &= \bigcup_{i=1}^{\bar{p}_\mathrm{t}+1}\Delta\mathbf{y}^i, & \delta\mathbf{t} &= \bigcup_{i=1}^{\bar{p}_\mathrm{t}+1}\delta\mathbf{t}^i, & \mathbf{D}_\mathrm{t} &= \bigcup_{\substack{i=1\\ j=1}}^{\substack{\bar{p}_\mathrm{t}+1\\ \bar{p}_\mathrm{t}+1}}\mathbf{d}_\mathrm{t}^{ij},\\
\mathbf{K}_\mathrm{t} &= \bigcup_{\substack{i=1\\ j=1}}^{\substack{\bar{p}_\mathrm{t}+1\\ \bar{p}_\mathrm{t}+1}}\mathbf{k}_\mathrm{t}^{ij}, & \mathbf{R}_\mathrm{t}^* &= \bigcup_{i=1}^{\bar{p}_\mathrm{t}+1}\mathbf{r}_\mathrm{t}^{*,i}, & \mathbf{R}_\mathrm{t} &= \bigcup_{i=1}^{\bar{p}_\mathrm{t}+1}\mathbf{r}_\mathrm{t}^i,\\
\bar{\mathbf{D}}_\mathrm{t} &= \bigcup_{\substack{i=1\\ j=1}}^{\substack{\bar{p}_\mathrm{t}+1\\ \bar{p}_\mathrm{t}+1}}\bar{\mathbf{d}}_\mathrm{t}^{ij}, & \bar{\mathbf{R}}_\mathrm{t} &= \bigcup_{i=1}^{\bar{p}_\mathrm{t}+1}\bar{\mathbf{r}}_\mathrm{t}^i,
\end{aligned} \tag{3.89}$$

results in the linear system of equations

$$\begin{aligned}
\mathbf{K}_\mathrm{eff}\Delta\mathbf{y}_\mathrm{t} &= \mathbf{r}_\mathrm{eff},\\
\mathbf{K}_\mathrm{eff} &= \mathbf{D}_\mathrm{t}+\mathbf{K}_\mathrm{t}+\bar{\mathbf{D}}_\mathrm{t},\\
\mathbf{r}_\mathrm{eff} &= \mathbf{R}_\mathrm{t}^*-\mathbf{R}_\mathrm{t}-\bar{\mathbf{R}}_\mathrm{t}.
\end{aligned}$$

Since this is almost identical to Equation (3.28) or (3.40), the nonlinear solution strategies described in Section 3.2 can be carried out to deduce the unknown quantities. Their time derivatives can be updated in each iteration by utilizing the forms in (3.86). However, due to the two-field setting, the solution vector automatically covers the first time derivative of the primary variable vector $\dot{\mathbf{w}}$.

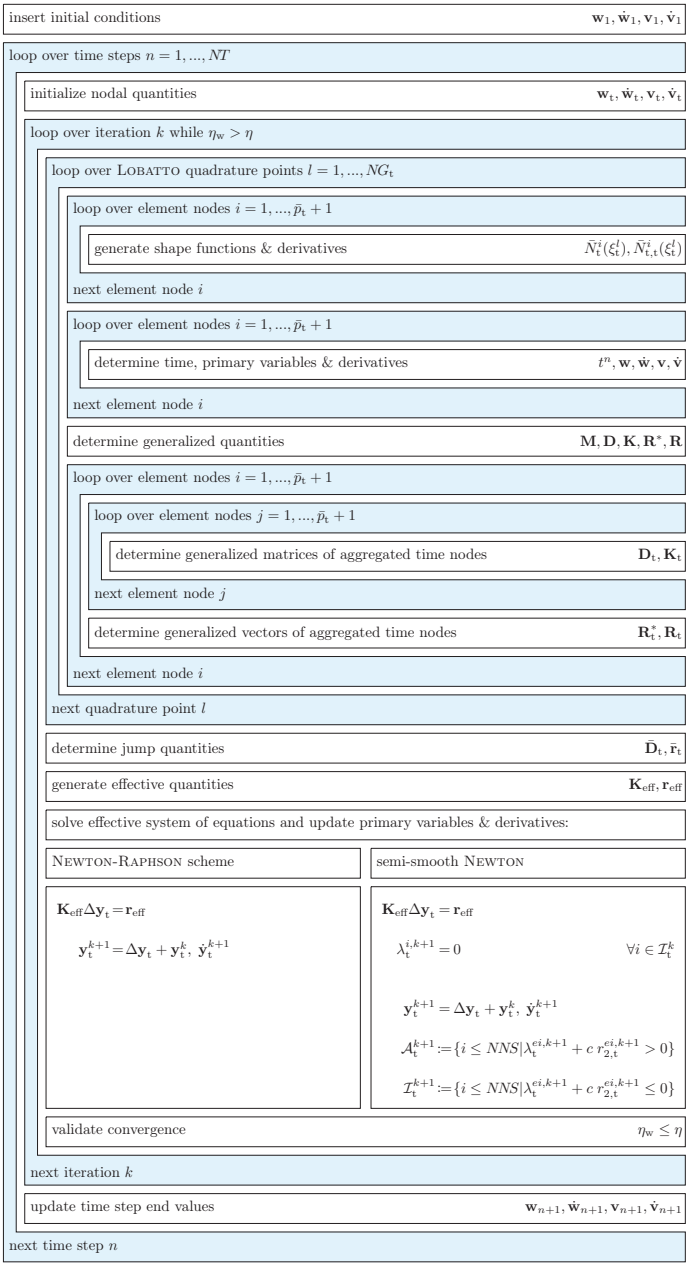

Figure 3.17.: Algorithm scheme for the discontinuous Galerkin two-field setting

The last step to completely describe this discontinuous GALERKIN approach is to define the shape functions and to choose a suitable quadrature rule to determine the integrals in (3.88) numerically. Following the course of action in Section 3.4.3.1, only LAGRANGE shape functions will be taken into account. However, in contrast to the continuous GALERKIN two-field setting, a LOBATTO quadrature with the parameters listed in Table 3.3 is applied. Moreover, the number of considered quadrature points is fixed to $NG_\mathrm{t} = \bar{p}_\mathrm{t} + 1$ and the corresponding supporting points are summarized in the vector $\bar{\boldsymbol{\xi}}_\mathrm{t} = [\xi_\mathrm{t}^1, ..., \xi_\mathrm{t}^{NG_\mathrm{t}}]$. The entries of this vector serve as the interpolatory nodes of the LAGRANGE shape functions. Thus, similar to Equations (3.80) and (3.82), these can be formulated by

$$\bar{N}_\mathrm{t}^i(\xi_\mathrm{t}) = \prod_{\substack{k=1 \\ k \neq i}}^{\bar{p}_\mathrm{t}+1} \frac{\xi_\mathrm{t}^k - \xi_\mathrm{t}}{\xi_\mathrm{t}^k - \xi_\mathrm{t}^i} \qquad \xi_\mathrm{t}^j \in \bar{\boldsymbol{\xi}}_\mathrm{t} \quad \text{with} \quad j = 1, ..., NG_\mathrm{t}, \tag{3.90}$$

$$\bar{N}_{\mathrm{t};\mathrm{t}}^i(\xi_\mathrm{t}) = \sum_{\substack{l=1 \\ l \neq i}}^{\bar{p}_\mathrm{t}+1} \frac{-1}{\xi_\mathrm{t}^l - \xi_\mathrm{t}^i} \prod_{\substack{k=1 \\ k \neq i \\ k \neq l}}^{\bar{p}_\mathrm{t}+1} \frac{\xi_\mathrm{t}^k - \xi_\mathrm{t}}{\xi_\mathrm{t}^k - \xi_\mathrm{t}^i} \qquad \xi_\mathrm{t}^j \in \bar{\boldsymbol{\xi}}_\mathrm{t} \quad \text{with} \quad j = 1, ..., NG_\mathrm{t}. \tag{3.91}$$

The derivative of the shape functions with respect to physical coordinates $\bar{N}_{\mathrm{t},\mathrm{t}}^i(\xi_\mathrm{t})$ is determined by exploiting the JACOBIAN to be $J_\mathrm{t} = \Delta t/2$ - presuming that the same arguments as in Section 3.4.3.1 hold.

Due to the accuracy of the applied LOBATTO quadrature and the limitation of the quadrature points by the polynomial degree, the entries of the generalized time damping matrix $\mathbf{D}_\mathrm{t}$ are integrated exactly. For the generalized time stiffness matrix $\mathbf{K}_\mathrm{t}$ no exact integration is performed - and a similar presumption also applies to the continuous GALERKIN method. In both cases, the discrepancy is supposed to serve as a basis for a strategy that benefits from the characteristic that the quadrature points where the spatial quantities are evaluated are identical to the time nodes. Within the discontinuous GALERKIN two-field setting the order of accuracy can be increased by varying the polynomial degree of the shape functions, cf. (Matthies and Schieweck, 2011; Thomée, 1997). However, due to this enhancement and the two-field formulation, the linear system of equations which has to be solved is $2(\bar{p}_\mathrm{t} + 1)$-times bigger as in the NEWMARK case and two-times bigger as for a fully implicit RUNGE-KUTTA scheme with $s = \bar{p}_\mathrm{t} + 1$ stages. For the accompanying algorithmic implementation scheme see Figure 3.17.

3.4.3.3. Continuous GALERKIN Single-Field Setting ($\mathrm{cG}_1(p_\mathrm{t})$)

In order to reduce the size of the system of linear equations which has to be solved in the end, the knowledge about the continuous and discontinuous GALERKIN two-field settings is used to construct a continuous GALERKIN scheme in the one-field setting. Once again, test functions $\bar{N}^i(\xi_\mathrm{t})$ with $i = 1, ..., \bar{p}_\mathrm{t} + 1$ with polynomial degree $\bar{p}_\mathrm{t} \geq 1$ are therefore assumed. The primary variables, in contrast, are approximated by shape functions $N^i(\xi_\mathrm{t})$ for $i = 1, ..., p_\mathrm{t} + 1$ with polynomial degree $p_\mathrm{t} = \bar{p}_\mathrm{t} + 1$. The resulting continuity assumption, however, is not necessarily fulfilled for the first time derivative, see Figure 3.18.

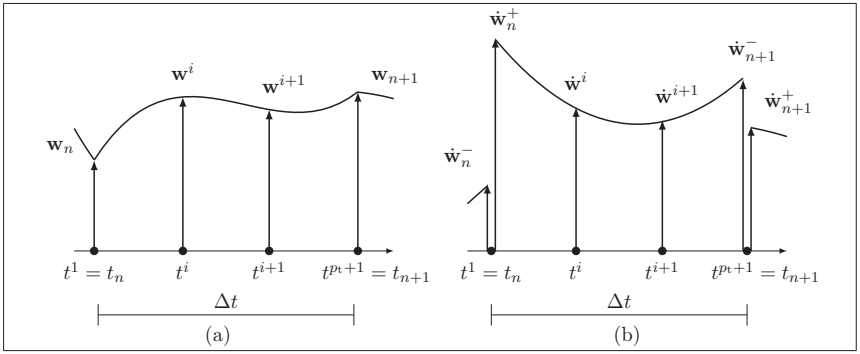

Figure 3.18.: (a) Continuous course of the primary variable $\mathbf{w}$, (b) Discontinuous course of the first derivative of the primary variable $\dot{\mathbf{w}}$

Analogously to Section 3.4.3.2, the appearing discontinuities are considered by allowing the first derivative of the primary variable to jump at the beginning of each time step. Thus, the term

$$[\![\dot{\mathbf{w}}]\!] = \dot{\mathbf{w}}_n^+ - \dot{\mathbf{w}}_n^- = 0 \tag{3.92}$$

is established similar to Equation (3.83). Performing a linearization and a weighting as in (3.84) results in

$$\mathbf{M}\Delta\dot{\mathbf{w}}^+ + \mathbf{M}[\![\dot{\mathbf{w}}^k]\!] = 0. \tag{3.93}$$

If now Equation (3.46) is formulated in a weak sense, Equation (3.93) has to be accounted for properly. This leads to the temporal weak form

$$\begin{aligned} \delta W_{\mathrm{t}} &= \int_{-1}^{1} \delta\mathbf{t}\ [\mathbf{M}\Delta\ddot{\mathbf{w}} + \mathbf{D}\Delta\dot{\mathbf{w}} + \mathbf{K}\Delta\mathbf{w} - \mathbf{R}^* + \mathbf{R}]\ J_{\mathrm{t}} d\xi_{\mathrm{t}} + \\ &+ \delta\mathbf{t}^+\ \mathbf{M}\Delta\dot{\mathbf{w}}^+ + \delta\mathbf{t}^+\mathbf{M}[\![\dot{\mathbf{w}}^k]\!] = 0, \end{aligned} \tag{3.94}$$

with the test function $\delta\mathbf{t}$ and its at the beginning of the time step t_n evaluated counterpart $\delta\mathbf{t}^+$. The parametrization, the approximation of the time and the determination of the JACOBIAN are carried out as described in Section 3.4.3.1. Alternative formulations and further derivation strategies can be found in (Gleim and Kuhl, 2013; Gleim et al., 2015; Hughes and Hulbert, 1988; Matthies and Schieweck, 2011; Thomée, 1997).

To derive the fully discrete system of equations, the primary variables, their time derivatives, and their increments have to be approximated

$$\begin{aligned} \mathbf{w} &\approx \sum_{i=1}^{p_{\mathrm{t}}+1} \mathbf{w}^i N_{\mathrm{t}}^i(\xi_{\mathrm{t}}), & \dot{\mathbf{w}} &\approx \sum_{i=1}^{p_{\mathrm{t}}+1} \mathbf{w}^i N_{\mathrm{t,t}}^i(\xi_{\mathrm{t}}), & \ddot{\mathbf{w}} &\approx \sum_{i=1}^{p_{\mathrm{t}}+1} \Delta\mathbf{w}^i N_{\mathrm{t,tt}}^i(\xi_{\mathrm{t}}), \\ \Delta\mathbf{w} &\approx \sum_{i=1}^{p_{\mathrm{t}}+1} \Delta\mathbf{w}^i N_{\mathrm{t}}^i(\xi_{\mathrm{t}}), & \Delta\dot{\mathbf{w}} &\approx \sum_{i=1}^{p_{\mathrm{t}}+1} \Delta\mathbf{w}^i N_{\mathrm{t,t}}^i(\xi_{\mathrm{t}}), & \Delta\ddot{\mathbf{w}} &\approx \sum_{i=1}^{p_{\mathrm{t}}+1} \Delta\mathbf{w}^i N_{\mathrm{t,tt}}^i(\xi_{\mathrm{t}}), \\ \delta\mathbf{t} &\approx \sum_{i=1}^{\bar{p}_{\mathrm{t}}+1} \delta\mathbf{t}^i \bar{N}_{\mathrm{t}}^i(\xi_{\mathrm{t}}), & \delta\mathbf{t}^+ &\approx \sum_{i=1}^{\bar{p}_{\mathrm{t}}+1} \delta\mathbf{t}^i \bar{N}_{\mathrm{t}}^i(-1), & \Delta\dot{\mathbf{w}}^+ &\approx \sum_{i=1}^{p_{\mathrm{t}}+1} \Delta\mathbf{w}^i N_{\mathrm{t,t}}^i(-1). \end{aligned} \tag{3.95}$$

These terms are similar to those in Equation (3.73), except that in this case, due to the one-field setting, second derivatives appear and jump terms are taken into account instead of a further primary variable $\mathbf{v}$. Hence, apart from Equations (3.74) as well as (3.75), the connection between the natural and physical second derivative must be formulated:

$$N^i_{\mathrm{t,tt}}(\xi_\mathrm{t}) = \frac{\partial N^i_{\mathrm{t,t}}(\xi_\mathrm{t})}{\partial \xi_\mathrm{t}} \frac{\partial \xi_\mathrm{t}}{\partial t^n} = N^i_{\mathrm{t;tt}}(\xi_\mathrm{t}) \left[J_\mathrm{t}^{-1}\right]^2 + N^i_{\mathrm{t;t}}(\xi_\mathrm{t}) \left[J_\mathrm{t}^{-1}\right]_{,\mathrm{t}} . \tag{3.96}$$

Finally, inserting the quantities of (3.95) into (3.94) results in the system of linear equations

$$\sum_{i=1}^{\bar{p}_\mathrm{t}+1} \sum_{j=2}^{p_\mathrm{t}+1} \delta\mathbf{t}^i \left[\mathbf{m}^{ij}_\mathrm{t} + \mathbf{d}^{ij}_\mathrm{t} + \mathbf{k}^{ij}_\mathrm{t} + \bar{\mathbf{d}}^{ij}_\mathrm{t}\right] \Delta\mathbf{w}^j = \sum_{i=1}^{\bar{p}_\mathrm{t}+1} \delta\mathbf{t}^i \left[\mathbf{r}^{*,i}_\mathrm{t} - \mathbf{r}^i_\mathrm{t} - \bar{\mathbf{r}}^i_\mathrm{t}[\![\dot{\mathbf{w}}^k]\!]\right],$$

where

$$\begin{aligned}
\mathbf{m}^{ij}_\mathrm{t} &= \int_{-1}^{1} \bar{N}^i_\mathrm{t}(\xi_\mathrm{t}) N^j_{\mathrm{t,tt}}(\xi_\mathrm{t})\ \mathbf{M}\ J_\mathrm{t}\ d\xi_\mathrm{t}, & \mathbf{d}^{ij}_\mathrm{t} &= \int_{-1}^{1} \bar{N}^i_\mathrm{t}(\xi_\mathrm{t}) N^j_{\mathrm{t,t}}(\xi_\mathrm{t})\ \mathbf{D}\ J_\mathrm{t}\ d\xi_\mathrm{t},\\
\mathbf{k}^{ij}_\mathrm{t} &= \int_{-1}^{1} \bar{N}^i_\mathrm{t}(\xi_\mathrm{t}) N^j_\mathrm{t}(\xi_\mathrm{t})\ \mathbf{K}\ J_\mathrm{t}\ d\xi_\mathrm{t}, & \mathbf{r}^{*,i}_\mathrm{t} &= \int_{-1}^{1} \bar{N}^i_\mathrm{t}(\xi_\mathrm{t})\ \mathbf{R}^*\ J_\mathrm{t}\ d\xi_\mathrm{t},\\
\mathbf{r}^i_\mathrm{t} &= \int_{-1}^{1} \bar{N}^i_\mathrm{t}(\xi_\mathrm{t})\ \mathbf{R}\ J_\mathrm{t}\ d\xi_\mathrm{t},\\
\bar{\mathbf{d}}^{ij}_\mathrm{t} &= \bar{N}^i_\mathrm{t}(-1) N^j_{\mathrm{t,t}}(-1)\ \mathbf{M}, & \bar{\mathbf{r}}^i_\mathrm{t} &= \bar{N}^i_\mathrm{t}(-1)\ \mathbf{M}
\end{aligned}$$

holds. The quantities with the superscript $(\bullet)^+$ are replaced by the linear combination of their nodal counterparts evaluated at the left boundary $\xi_\mathrm{t} = -1$ of the time element. The assembly of the distinct parts is implemented by exploiting the respective terms in (3.79) augmented by

$$\mathbf{M}_\mathrm{t} = \bigcup_{\substack{i=1\\ j=2}}^{\substack{p_\mathrm{t}+1\\ \bar{p}_\mathrm{t}+1}} \mathbf{m}^{ij}_\mathrm{t}, \qquad \bar{\mathbf{D}}_\mathrm{t} = \bigcup_{\substack{i=1\\ j=2}}^{\substack{p_\mathrm{t}+1\\ \bar{p}_\mathrm{t}+1}} \bar{\mathbf{d}}^{ij}_\mathrm{t}, \qquad \bar{\mathbf{R}}_\mathrm{t} = \bigcup_{i=1}^{\bar{p}_\mathrm{t}+1} \bar{\mathbf{r}}^i_\mathrm{t}, \qquad \Delta\mathbf{w}_\mathrm{t} = \bigcup_{i=2}^{p_\mathrm{t}+1} \Delta\mathbf{w}^i.$$

Again, the quantities linked to $j = 1$ are neglected since the associated increments $\Delta\mathbf{w}^1$ are zero. The effective quantities can thus be determined, yielding the linear system of equations

$$\begin{aligned}
\mathbf{K}_\mathrm{eff}\Delta\mathbf{w}_\mathrm{t} &= \mathbf{r}_\mathrm{eff},\\
\mathbf{K}_\mathrm{eff} &= \mathbf{M}_\mathrm{t} + \mathbf{D}_\mathrm{t} + \mathbf{K}_\mathrm{t} + \bar{\mathbf{D}}_\mathrm{t},\\
\mathbf{r}_\mathrm{eff} &= \mathbf{R}^*_\mathrm{t} - \mathbf{R}_\mathrm{t} - \bar{\mathbf{R}}_\mathrm{t},
\end{aligned}$$

which can be solved using the nonlinear solution strategies described in Section 3.2. The respective time derivatives can be updated in each iteration by utilizing the forms in (3.95).

The last step in constructing this continuous Galerkin one-field setting is to choose a quadrature rule and adequate shape functions. Here again, like in the continuous Galerkin two-field approach in Section 3.4.3.1, a Radau quadrature is applied and, hence, the Lagrange shape functions as well as their first derivatives are used as formulated in (3.80)-(3.82). Additionally, the second derivative is stated by

$$N^i_{\mathrm{t;tt}}(\xi_\mathrm{t}) = \sum_{\substack{m=1\\ m\neq i}}^{p_\mathrm{t}+1} \frac{-1}{\xi^m_\mathrm{t} - \xi^i_\mathrm{t}} \sum_{\substack{l=1\\ l\neq i\\ l\neq m}}^{p_\mathrm{t}+1} \frac{-1}{\xi^l_\mathrm{t} - \xi^i_\mathrm{t}} \prod_{\substack{k=1\\ k\neq i\\ k\neq l\\ k\neq m}}^{p_\mathrm{t}+1} \frac{\xi^k_\mathrm{t} - \xi_\mathrm{t}}{\xi^k_\mathrm{t} - \xi^i_\mathrm{t}} \quad \xi^j_\mathrm{t} \in \boldsymbol{\xi}_\mathrm{t} \quad \text{with} \quad j = 1, ..., NG_\mathrm{t} + 1.$$

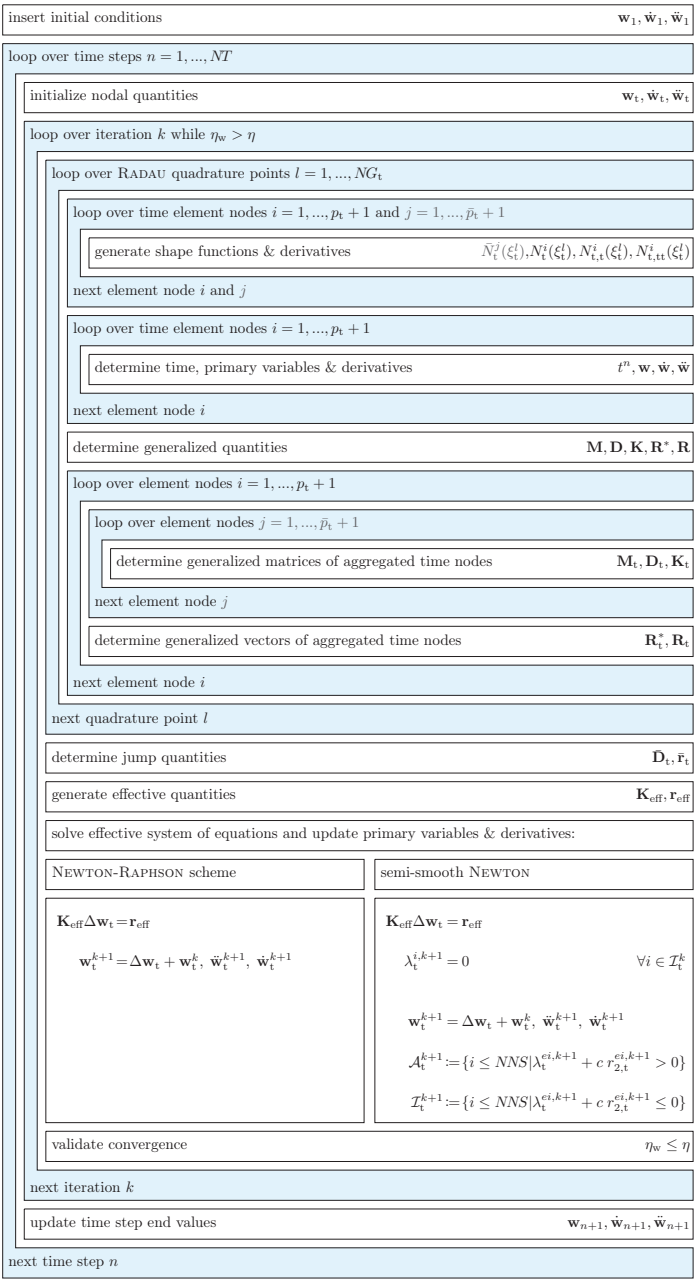

Figure 3.19.: Algorithm scheme for the continuous GALERKIN one-field setting

In order to calculate the corresponding derivatives with respect to physical coordinates, Equation (3.96) has to be evaluated. Here, it is possible to take advantage of the fact that Equation (3.72) leads to the constant JACOBIAN $J_\mathrm{t} = \Delta t/2$, cf.(Babuška and Strouboulis, 2001; Matthies and Schieweck, 2011; Szabó and Babuška, 1991). Hence, to transform the second derivatives from natural to physical coordinates, only a multiplication with the square of the inverse JACOBIAN has to be performed.

Apart from one exception, the properties of the developed continuous GALERKIN one-field procedure are identical to those of its two-field counterpart, see Section 3.4.3.1. The resulting system of linear equations is half the size as in the two-field case. Hence, it is only $\bar{p}_\mathrm{t} + 1$ times bigger than the NEWMARK scheme, and it is identical to a fully implicit RUNGE-KUTTA method with $s = \bar{p}_\mathrm{t} + 1$ stages. For the accompanying algorithmic implementation scheme see Figure 3.19.

3.4.3.4. Discontinuous GALERKIN Single-Field Setting ($\mathrm{dG}_1(\bar{p}_\mathrm{t})$)

Analogously to the previous Section 3.4.3.3, also the discontinuous GALERKIN two-field setting is reworded to a one-field approach. As in the discontinuous GALERKIN two-field setting, see Section 3.4.3.2, it is again assumed that both the test functions and the primary variables are approximated using functions $\bar{N}^i(\xi_\mathrm{t})$ with $i = 1, ..., \bar{p}_\mathrm{t}+1$, where $\bar{p}_\mathrm{t} \geq 2$ represents the polynomial degree. The discontinuities of the primary variable have to be accounted for by introducing jump terms, cf. (Gleim and Kuhl, 2013; Matthies and Schieweck, 2011; Thomée, 1997). This is done as in Equations (3.83) and (3.92) by

$$[\![\mathbf{w}]\!] = \mathbf{w}_n^+ - \mathbf{w}_n^- = 0, \qquad [\![\dot{\mathbf{w}}]\!] = \dot{\mathbf{w}}_n^+ - \dot{\mathbf{w}}_n^- = 0. \tag{3.97}$$

The linearization and weighting of (3.97) in accordance to (3.84) results in

$$\mathbf{M}\Delta\dot{\mathbf{w}}^+ + \mathbf{M}[\![\dot{\mathbf{w}}^k]\!] = 0, \qquad \mathbf{D}\Delta\mathbf{w}^+ + \mathbf{D}[\![\mathbf{w}^k]\!] = 0.$$

To obtain convergence, the relationship

$$\mathbf{M}\Delta\mathbf{w}^+ + \mathbf{M}[\![\mathbf{w}^k]\!] = 0$$

is considered additionally. With these supplementary and modified expressions, the discontinuous GALERKIN two-field temporal weak form in (3.85) can be adapted to its single-field counterpart

$$\begin{aligned}
\delta W_\mathrm{t} \;=\; & \int_{-1}^{1} \delta\mathbf{t} \quad [\mathbf{M}\Delta\ddot{\mathbf{w}} + \mathbf{D}\Delta\dot{\mathbf{w}} + \mathbf{K}\Delta\mathbf{w} - \mathbf{R}^* + \mathbf{R}] \quad J_\mathrm{t} d\xi_\mathrm{t} \quad + \\
& + \quad \delta\mathbf{t}^+ \quad \mathbf{M}\Delta\dot{\mathbf{w}}^+ + \delta\mathbf{t}^+\mathbf{M}[\![\dot{\mathbf{w}}^k]\!] \quad + \\
& + \quad \delta\mathbf{t}^+ \quad \mathbf{D}\Delta\mathbf{w}^+ \; + \delta\mathbf{t}^+\mathbf{D}[\![\mathbf{w}^k]\!] \quad + \\
& - \quad \delta\dot{\mathbf{t}}^+ \quad \mathbf{M}\Delta\mathbf{w}^+ - \delta\dot{\mathbf{t}}^+\mathbf{M}[\![\mathbf{w}^k]\!] \quad = \; 0.
\end{aligned} \tag{3.98}$$

While the test function is indicated by $\delta\mathbf{t}$, the variable $\delta\mathbf{t}^+$ represents the test function evaluated at the beginning $\xi_\mathrm{t} = -1$ of the time step t_n. Its time derivative is denoted by $\delta\dot{\mathbf{t}}^+$. The terms involving this time derivative are inserted to obtain convergence. This choice is founded on the approaches in (Botasso, 1997; Botasso and Ragazzi, 2000), where the connection between RUNGE-KUTTA and GALERKIN schemes is treated, since in the linear case and for a polynomial degree of $\bar{p}_\mathrm{t} = 2$ the discontinuous GALERKIN scheme degenerates into the fully implicit RUNGE-KUTTA LOBATTO IIIC(3) method. The parametrization, the approximation of the time, and the

determination of the JACOBIAN are carried out as described in Section 3.4.3.2. An alternative discontinuous one-field strategy with different weighting factors is depicted in (Gleim and Kuhl, 2013; Hulber and Hughes, 1990). All further quantities in (3.98) are approximated by

$$\begin{aligned}
\mathbf{w} &\approx \sum_{i=1}^{\bar{p}_\mathrm{t}+1} \mathbf{w}^i \bar{N}_\mathrm{t}^i(\xi_\mathrm{t}), & \dot{\mathbf{w}} &\approx \sum_{i=1}^{\bar{p}_\mathrm{t}+1} \mathbf{w}^i \bar{N}_{\mathrm{t},\mathrm{t}}^i(\xi_\mathrm{t}), & \ddot{\mathbf{w}} &\approx \sum_{i=1}^{\bar{p}_\mathrm{t}+1} \Delta\mathbf{w}^i \bar{N}_{\mathrm{t},\mathrm{tt}}^i(\xi_\mathrm{t}), \\
\Delta\mathbf{w} &\approx \sum_{i=1}^{\bar{p}_\mathrm{t}+1} \Delta\mathbf{w}^i \bar{N}_\mathrm{t}^i(\xi_\mathrm{t}), & \Delta\dot{\mathbf{w}} &\approx \sum_{i=1}^{\bar{p}_\mathrm{t}+1} \Delta\mathbf{w}^i \bar{N}_{\mathrm{t},\mathrm{t}}^i(\xi_\mathrm{t}), & \Delta\ddot{\mathbf{w}} &\approx \sum_{i=1}^{\bar{p}_\mathrm{t}+1} \Delta\mathbf{w}^i \bar{N}_{\mathrm{t},\mathrm{tt}}^i(\xi_\mathrm{t}), \\
\delta\mathbf{t} &\approx \sum_{i=1}^{\bar{p}_\mathrm{t}+1} \delta\mathbf{t}^i \bar{N}_\mathrm{t}^i(\xi_\mathrm{t}), & \delta\dot{\mathbf{t}} &\approx \sum_{i=1}^{\bar{p}_\mathrm{t}+1} \delta\mathbf{t}^i \bar{N}_{\mathrm{t},\mathrm{t}}^i(\xi_\mathrm{t}), & \delta\mathbf{t}^+ &\approx \sum_{i=1}^{\bar{p}_\mathrm{t}+1} \delta\mathbf{t}^i \bar{N}_{\mathrm{t},\mathrm{t}}^i(-1), \\
\delta\dot{\mathbf{t}}^+ &\approx \sum_{i=1}^{\bar{p}_\mathrm{t}+1} \delta\mathbf{t}^i \bar{N}_{\mathrm{t},\mathrm{t}}^i(-1), & \Delta\mathbf{w}^+ &\approx \sum_{i=1}^{\bar{p}_\mathrm{t}+1} \Delta\mathbf{w}^i \bar{N}_\mathrm{t}^i(-1), & \Delta\dot{\mathbf{w}}^+ &\approx \sum_{i=1}^{\bar{p}_\mathrm{t}+1} \Delta\mathbf{w}^i \bar{N}_{\mathrm{t},\mathrm{t}}^i(-1).
\end{aligned} \tag{3.99}$$

Some of the approximations herein are already known from (3.86). They are only repeated for a better understanding and to yield a closed-form description of the method.

The terms of Equation (3.99) contain, as for the continuous GALERKIN one-field setting, second order derivatives. Hence, apart from the relationships between the natural and physical first derivatives in (3.87), the connection between the second derivatives in (3.96) has to be taken into account. Finally, inserting the quantities of (3.99) in (3.98) results in the system of linear equations

$$\sum_{i=1}^{\bar{p}_\mathrm{t}+1} \sum_{j=1}^{\bar{p}_\mathrm{t}+1} \delta\mathbf{t}^i \left[\mathbf{m}_\mathrm{t}^{ij} + \mathbf{d}_\mathrm{t}^{ij} + \mathbf{k}_\mathrm{t}^{ij} + \bar{\mathbf{d}}_\mathrm{t}^{ij} \right] \Delta\mathbf{w}^j = \sum_{i=1}^{\bar{p}_\mathrm{t}+1} \delta\mathbf{t}^i \left[\mathbf{r}_\mathrm{t}^{*,i} - \mathbf{r}_\mathrm{t}^i - \bar{\mathbf{r}}_{1\mathrm{t}}^i [\![\dot{\mathbf{w}}^k]\!] - \bar{\mathbf{r}}_{2\mathrm{t}}^i [\![\mathbf{w}^k]\!] \right],$$

where

$$\begin{aligned}
\mathbf{m}_\mathrm{t}^{ij} &= \int_{-1}^{1} \bar{N}_\mathrm{t}^i(\xi_\mathrm{t}) \bar{N}_{\mathrm{t},\mathrm{tt}}^j(\xi_\mathrm{t})\, \mathbf{M}\, J_\mathrm{t}\, d\xi_\mathrm{t}, & \mathbf{d}_\mathrm{t}^{ij} &= \int_{-1}^{1} \bar{N}_\mathrm{t}^i(\xi_\mathrm{t}) \bar{N}_{\mathrm{t},\mathrm{t}}^j(\xi_\mathrm{t})\, \mathbf{D}\, J_\mathrm{t}\, d\xi_\mathrm{t}, \\
\mathbf{k}_\mathrm{t}^{ij} &= \int_{-1}^{1} \bar{N}_\mathrm{t}^i(\xi_\mathrm{t}) \bar{N}_\mathrm{t}^j(\xi_\mathrm{t})\, \mathbf{K}\, J_\mathrm{t}\, d\xi_\mathrm{t}, & \mathbf{r}_\mathrm{t}^{*,i} &= \int_{-1}^{1} \bar{N}_\mathrm{t}^i(\xi_\mathrm{t})\, \mathbf{R}^*\, J_\mathrm{t}\, d\xi_\mathrm{t}, \\
\mathbf{r}_\mathrm{t}^i &= \int_{-1}^{1} \bar{N}_\mathrm{t}^i(\xi_\mathrm{t})\, \mathbf{R}\, J_\mathrm{t}\, d\xi_\mathrm{t}, & & \\
\bar{\mathbf{d}}_\mathrm{t}^{ij} &= \bar{N}_\mathrm{t}^i(-1) \bar{N}_{\mathrm{t},\mathrm{t}}^j(-1)\mathbf{M} + \bar{N}_\mathrm{t}^i(-1) \bar{N}_\mathrm{t}^j(-1)\mathbf{D} - \bar{N}_{\mathrm{t},\mathrm{t}}^i(-1) \bar{N}_\mathrm{t}^j(-1)\mathbf{M}, & & \\
\bar{\mathbf{r}}_{1\mathrm{t}}^i &= \bar{N}_\mathrm{t}^i(-1)\mathbf{M}, & \bar{\mathbf{r}}_{2\mathrm{t}}^i &= \bar{N}_\mathrm{t}^i(-1)\mathbf{D} - \bar{N}_{\mathrm{t},\mathrm{t}}^i(-1)\mathbf{M}
\end{aligned}$$

hold. The quantities with the superscript $(\bullet)^+$ are replaced by the linear combination of their nodal counterparts evaluated at the left boundary $\xi_\mathrm{t} = -1$ of the time element t_n. The assembly of the distinct parts is achieved by exploiting the respective terms in (3.89) augmented by

$$\mathbf{M}_\mathrm{t} = \bigcup_{\substack{i=1 \\ j=1}}^{\substack{p_\mathrm{t}+1 \\ \bar{p}_\mathrm{t}+1}} \mathbf{m}_\mathrm{t}^{ij}, \qquad \bar{\mathbf{R}}_{1\mathrm{t}} = \bigcup_{i=1}^{\bar{p}_\mathrm{t}+1} \bar{\mathbf{r}}_{1\mathrm{t}}^i, \qquad \bar{\mathbf{R}}_{2\mathrm{t}} = \bigcup_{i=1}^{\bar{p}_\mathrm{t}+1} \bar{\mathbf{r}}_{2\mathrm{t}}^i, \qquad \Delta\mathbf{w}_\mathrm{t} = \bigcup_{i=1}^{\bar{p}_\mathrm{t}+1} \Delta\mathbf{w}^i.$$

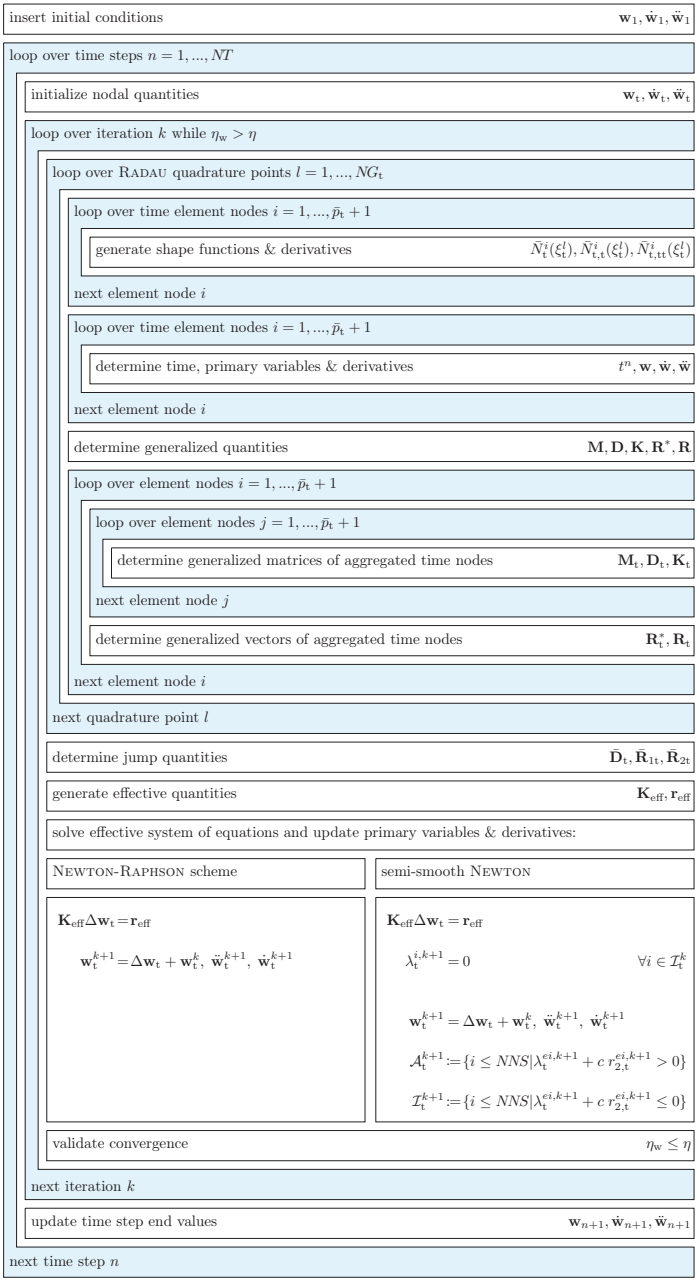

Figure 3.20.: Algorithm scheme for the discontinuous GALERKIN one-field setting

The effective quantities can thus be determined, yielding the linear system of equations

$$\begin{aligned} \mathbf{K}_{\text{eff}}\Delta\mathbf{w}_{\text{t}} &= \mathbf{r}_{\text{eff}}, \\ \mathbf{K}_{\text{eff}} &= \mathbf{M}_{\text{t}} + \mathbf{D}_{\text{t}} + \mathbf{K}_{\text{t}} + \bar{\mathbf{D}}_{\text{t}}, \\ \mathbf{r}_{\text{eff}} &= \mathbf{R}^{*}_{\text{t}} - \mathbf{R}_{\text{t}} - \bar{\mathbf{R}}_{1\text{t}} - \bar{\mathbf{R}}_{2\text{t}}. \end{aligned}$$

Since this is almost identical to Equation (3.28) or (3.40), the nonlinear solution strategies described in Section 3.2 can be carried out to deduce the unknown quantities. The respective time derivatives can be updated in each iteration by utilizing the forms in (3.99).

The last step in constructing this discontinuous GALERKIN one-field setting is the choice of a quadrature rule and of shape functions. Here again, like in the discontinuous GALERKIN two-field approach in Section 3.4.3.2, a LOBATTO quadrature is applied and, hence, the LAGRANGE shape functions as well as their first derivatives are used as formulated in (3.90)-(3.91). Additionally, the second derivative is stated by

$$\bar{N}^{i}_{\text{t;tt}}(\xi_{\text{t}}) = \sum_{\substack{m=1 \\ m\neq i}}^{\bar{p}_{\text{t}}+1} \frac{-1}{\xi^{m}_{\text{t}} - \xi^{i}_{\text{t}}} \sum_{\substack{l=1 \\ l\neq i \\ l\neq m}}^{\bar{p}_{\text{t}}+1} \frac{-1}{\xi^{l}_{\text{t}} - \xi^{i}_{\text{t}}} \prod_{\substack{k=1 \\ k\neq i \\ k\neq l \\ k\neq m}}^{\bar{p}_{\text{t}}+1} \frac{\xi^{k}_{\text{t}} - \xi_{\text{t}}}{\xi^{k}_{\text{t}} - \xi^{i}_{\text{t}}} \quad \xi^{j}_{\text{t}} \in \bar{\boldsymbol{\xi}}_{\text{t}} \quad \text{with} \quad j = 1, ..., NG_{\text{t}}.$$

In order to calculate the corresponding derivatives with respect to physical coordinates, Equation (3.96) has to be evaluated as described, for example, in Section 3.4.3.3. The computational properties of the developed discontinuous GALERKIN one-field procedure are similar to those of the two-field counterpart, see Section 3.4.3.2. The only exception is that the resulting system of linear equations is half the size as in the two-field case. Hence, it is only $\bar{p}_{\text{t}} + 1$ times bigger than the NEWMARK scheme and identical to a fully implicit RUNGE-KUTTA method with $s = \bar{p}_{\text{t}} + 1$ stages. For the accompanying algorithmic implementation scheme see Figure 3.20.

3.5. Time Discretization Error

In the context of the numerical implementations of elasto(visco)plastic problems, the estimation of appearing errors is one key ingredient. In fact, the occurrence of errors within the simulations of real life processes is manifold. While first deviations are already induced in the modeling phase, imprecisions in the identification of necessary parameters lead to even more discrepancies. Last but not least, the numerical realization leads to additional errors. Contributions to this category stem from the spatial as well as the temporal discretization, the application of numerical quadratures, solver tolerances and round off errors, cf. (Eriksson et al., 2005; Schmidt, 2001). While the influence of the latter aspects is out of the scope of this thesis, the main focus lies on estimating errors caused by the time discretization and the related time integration schemes. Discrepancies due to the spatial discretization are analyzed by mesh refinement.

For an overview and a classification of further error estimators in this field see (Ainsworth and Oden, 1997; Braess, 2010; Zienkiewicz and Taylor, 2000). A supplementary analysis on recovery-based error estimators in the context of spatial discretization is presented in (Ainsworth and Craig, 1997; Grätsch and Bathe, 2005), while goal-oriented error estimators are discussed in (Bangerth and Rannacher, 2003; Grätsch and Bathe, 2005). For topics concerning residual error estimates see (Babuška and Miller, 1987; Babuška and Rheinboldt, 1978; Eriksson et al., 2005), and a special treatment of elastoplasticity related to purely spatial discretization errors is performed in (Alberty et al., 1999; Repin and Xanthis, 1996; Schmidt, 2001; Schröder

and Wiedemann, 2011; Wiberg et al., 1996). Approaches taking the time discretization error additionally into account can be found in (Alberty and Carstensen, 2000; Mielke et al., 2010).

While the spatial discretization in this thesis is always performed using the finite element method, a variety of schemes is used for time integration, see Section 3.4. This diversity is also represented by the different types of estimates for the time discretization error. In this thesis, three kinds of estimators are treated. While the h-error estimation is applicable to all procedures, embedded ones are only applied to diagonally implicit RUNGE-KUTTA schemes. The residual error estimator, however, is reserved for GALERKIN time integration schemes.

A similar picture is drawn in the literature, where individual error estimates are formulated for specific schemes. For example for NEWMARK time integration methods, the error may be determined by assuming a linear combination of acceleration quantities at different points in time, cf. (Kuhl, 2004; Li et al., 1993; Zienkiewicz and Xie, 1991). A mathematical analysis of error estimates linked to GALERKIN schemes is outlined in (Johnson, 1988; Matthies and Schieweck, 2011), while optimal error estimates for space-time finite elements are predicted in (Hughes and Hulbert, 1988). For an application of the dual weighted residual method in the context of time finite elements see (Kizio, 2008).

3.5.1. h-Error Estimation

In order to motivate the current error quantity, the linearized semidiscrete form of the general elasto(visco)plastic problem in (3.46) is considered. Due to the already performed spatial discretization, only a system of ordinary differential equations is left, which is characterized by the time-dependent primary variable vector $\mathbf{w}$. Now, it is assumed that the exact solution $\mathbf{w}_{n+1}^{\mathrm{ex}}$ and a numerically calculated solution $\mathbf{w}_{n+1}$ at the point in time t_{n+1} are known. Thus, the local error $\mathbf{e}_{\mathrm{h},n+1}$ can be stated as

$$\mathbf{e}_{\mathrm{h},n+1} = \mathbf{w}_{n+1}^{\mathrm{ex}}(\mathbf{w}_n) - \mathbf{w}_{n+1}(\mathbf{w}_n). \tag{3.100}$$

The term local time discretization error implies the determination of the numerical solution be means of the exact initial condition $\mathbf{w}_n^{\mathrm{ex}}$. Hence, the quantity in (3.100) refers to the error within one single time step. Moreover, it is supposed that the norm of the local error can be linked to the time step size by

$$\|\mathbf{e}_{\mathrm{h},n+1}\| \leq C\Delta t^{q+1}, \tag{3.101}$$

whereby C denotes an arbitrary constant. The variable q embodies the order of consistency. For detailed explanations and necessary conditions see (Eriksson et al., 2005; Hairer et al., 2008; Strehmel et al., 2012). Equation (3.100), however, cannot be evaluated since for general cases the exact solution is unknown. Hence, a proper approximation has to be found. Since, Inequality (3.101) states that the error gets smaller with decreasing time step size, the local h-error can be estimated as

$$\mathbf{e}_{\mathrm{h},n+1} \approx \mathbf{w}_{n+1}^{\Delta t/m}(\mathbf{w}_n) - \mathbf{w}_{n+1}(\mathbf{w}_n). \tag{3.102}$$

Therein, the numerical comparative solution $\mathbf{w}_{n+1}^{\Delta t/m}$ is computed by using the time step size Δt, reduced by an arbitrary factor $m = 2, 3, ...$, cf. (Gleim, 2016; Kuhl, 2004). To estimate the local time discretization error of the simulation performed with the time step size Δt within one time step, Equation (3.102) is evaluated. If, afterwards, the solution obtained using the bigger time step size is passed as an initial condition to the simulation performed with the time step size $\Delta t/m$ to determine the next comparative solution, the local time discretization error of the simulation performed with the time step size Δt can be estimated for the next time step. Hence,

a series of local time discretization error estimates is created. Figure 3.21 shows a schematic implementation. The usage of Equation (3.102) enables a numerical estimation of the local time discretization error for all presented time integration procedures of Section 3.4.

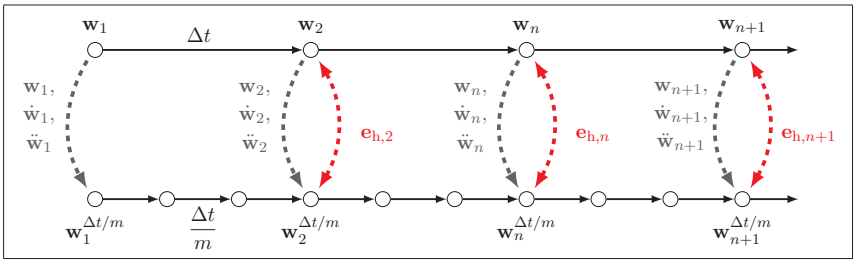

Figure 3.21.: Illustration of the h-error estimator with m= 3

Opposed to the local error, a global error can be formulated. Therein, the exact solution is compared to a numerical one at an arbitrary point in time,

$$\mathbf{e}_{\mathrm{h},n+1}^{\mathrm{glob}} = \mathbf{w}_{n+1}^{\mathrm{ex}}(\mathbf{w}_0) - \mathbf{w}_{n+1}(\mathbf{w}_0), \tag{3.103}$$

whereby the initial condition is only fulfilled at the beginning, see Figure 3.22. Differences may appear within intermediate time steps, cf. (Gleim, 2016; Strehmel et al., 2012). Thus, a link between the global error and the time step size can be established

$$\left\| \mathbf{e}_{\mathrm{h},n+1}^{\mathrm{glob}} \right\|_{\max} \leq c\Delta t^q,$$

whereby c denotes an arbitrary constant and q denotes the order of convergence. Assuming that the preconditions defined in (Strehmel et al., 2012) are valid, the order of convergence can be determined exploiting the order of consistency. However, as already known from the local

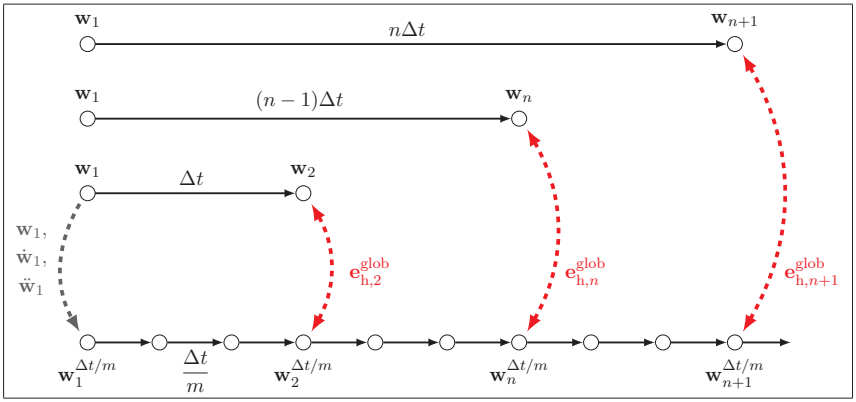

Figure 3.22.: Illustration of the global h-error estimator with m= 3

error definition, Equation (3.103) cannot be evaluated since the exact solution is not known for

general cases. Analogously to Equation (3.102), the approximation

$$\mathbf{e}_{\mathrm{h},n+1}^{\mathrm{glob}} \approx \mathbf{w}_{n+1}^{\Delta t/m}(\mathbf{w}_0) - \mathbf{w}_{n+1}(\mathbf{w}_0)$$

is settled. The differences between both definitions are, firstly, that only the initial condition is passed for the global h-error, while the results of various intermediate time steps are transferred for the local h-error, and, secondly, that the considered comparative solution $\mathbf{w}_{n+1}^{\Delta t/m}(\mathbf{w}_0)$ is identical for all analyzed vectors $\mathbf{w}_{n+1}(\mathbf{w}_0)$. The drawback of both the local and the global h-error estimation is the high computational effort, since two simulations with or without interchanging data after each time step have to be carried out simultaneously, see Figure 3.21 or Figure 3.22. To reduce the costs, procedure-dependent estimates are introduced.

3.5.2. Embedded Error Estimation

The h-error estimation is based on the influence of the time step size on the error. Following Inequality (3.101), the error can also be manipulated by the order parameter q. This fact can easily be exploited in the context of diagonally implicit Runge-Kutta schemes, see Section 3.4.2. They are based on performing the time integration of the linearized semidiscrete form of the general elasto(visco)plastic problem in (3.46) by applying distinct quadrature rules, see Equations (3.57)-(3.58). The choice of quadrature parameters, however, determines the order of the procedure and, hence, affects the variable q in (3.101), cf. (Butcher, 2008; Strehmel et al., 2012). The idea is now to construct two Runge-Kutta schemes with an identical coefficient matrix $\mathbf{A}$, but with different parameter vectors $\mathbf{b}$ and $\check{\mathbf{b}}$ leading to distinct orders q as well as $\check{q}$, cf. (Butcher, 2008; Cash, 1979; Ellsiepen and Hartmann, 2001; Strehmel et al., 2012). Throughout this procedure, the calculated stage variables of the two schemes remain identical but the time step end values vary. Therefore, these schemes are denoted as embedded Runge-Kutta methods. The local error can thus be defined by

$$\mathbf{e}_{\mathrm{em},n+1} \approx \check{\mathbf{w}}_{n+1} - \mathbf{w}_{n+1} = \Delta t \sum_{i=1}^{s} \left[\check{b}_i - b_i\right] \mathbf{w}_{ni}, \tag{3.104}$$

wherein the solution $\check{\mathbf{w}}_{n+1}$ is obtained with the scheme of order $\check{q}$ and $\mathbf{w}_{n+1}$ is determined by the procedure with accuracy q. The dominant order of the error in (3.104) in the sense of (3.101) is always the lower one, see (Strehmel et al., 2012).

$$\begin{array}{c|cc} \frac{2-\sqrt{2}}{2} & \frac{2-\sqrt{2}}{2} & \\ 1 & \frac{\sqrt{2}}{2} & \frac{2-\sqrt{2}}{2} \\ \hline & \frac{\sqrt{2}}{2} & \frac{2-\sqrt{2}}{2} \\ \hline & \frac{-4+5\sqrt{2}}{4} & \frac{8-5\sqrt{2}}{4} \end{array}$$

(a)

$$\begin{array}{c|cc} \alpha_{\mathrm{r}} & \alpha_{\mathrm{r}} & \\ \frac{1+\alpha_{\mathrm{r}}}{2} & \frac{1-\alpha_{\mathrm{r}}}{2} & \alpha_{\mathrm{r}} \\ 1 & -\frac{6\alpha_{\mathrm{r}}^2-16\alpha_{\mathrm{r}}+1}{4} & \frac{6\alpha_{\mathrm{r}}^2-20\alpha_{\mathrm{r}}+5}{4} \quad \alpha_{\mathrm{r}} \\ \hline & -\frac{6\alpha_{\mathrm{r}}^2-16\alpha_{\mathrm{r}}+1}{4} & \frac{6\alpha_{\mathrm{r}}^2-20\alpha_{\mathrm{r}}+5}{4} \quad \alpha_{\mathrm{r}} \\ \hline & \frac{1/2-\beta_{\mathrm{r}}}{\alpha_{\mathrm{r}}-\beta_{\mathrm{r}}} & \frac{\alpha_{\mathrm{r}}-1/2}{\alpha_{\mathrm{r}}-\beta_{\mathrm{r}}} \quad 0 \end{array}$$

$\alpha_{\mathrm{r}} = 0.4358665215$
$\beta_{\mathrm{r}} = [1+\alpha_{\mathrm{r}}]/2$

(b)

Figure 3.23.: (a) DIRK(2) ($q = 2, \check{q} = 1$), (b) DIRK(3) ($q = 3, \check{q} = 2$)

The computational effort compared to the h-error estimation is clearly lower, since no simultaneous calculation has to be performed solely a weighted sum has to be evaluated. In the course of this thesis, the parameter constellations in Figure 3.23 are analyzed. The last rows of the schemes in Figure 3.23 represent the entries of the parameter vector $\check{\mathbf{b}}$, yielding a RUNGE-KUTTA scheme of order $\check{q} = q-1$. It can be observed that, while the reference method is stiffly accurate, this is not true for the error estimating procedure. A schematic implementation of this error estimation is depicted in Figure 3.24.

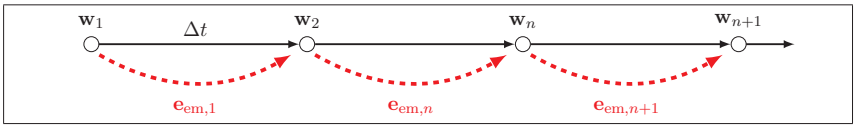

Figure 3.24.: Illustration of the embedded error estimator

3.5.3. Residual Error Estimation

While the embedded and the h-error estimator are both based on defining the local error by subtracting approximated versions of the primary variable vector, the residual error estimator rests on a distinct principle. Originally, the linearized semidiscrete form of the general elasto(visco)plastic problem in (3.46) has to be fulfilled at each point in time. By introducing a time discretization scheme, this assumption is weakened by demanding only a point-wise accomplishment. The residual error estimator takes advantage of this discrepancy by being stated as:

$$\mathbf{e}_{\mathrm{r},n+1} \approx \int_{t_n}^{t_{n+1}} [\mathbf{R}^* - \mathbf{R}]\, dt, \tag{3.105}$$

whereby it is assumed that a converged NEWTON-RAPHSON or semi-smooth NEWTON scheme is based on equilibrated internal and external forces. The local deviations from the point-wise fulfillment can be measured by evaluating the integral over one time step. Typical applications of this kind of error estimation are GALERKIN type time integrators. There, Equation (3.105) degenerates to a weighted sum of residua, which can be determined with low computational effort, cf. (Gleim, 2010, 2016; Gleim et al., 2015). A comparative calculation as in the case of the h-error estimator is not needed. The implementation is schematically depicted in Figure 3.25. The motivation for Equation (3.105) stems from the field of spatial error estimates, and it can be considered in the widest sense as a numerical evaluation of an adaptation of the approach in (Babuška and Rheinboldt, 1978). For further aspects on residual estimators within space discretization see (Ainsworth and Oden, 1997; Babuška and Miller, 1987) and the references therein. Moreover, it should be noted here that, to the best knowledge of the author, no coherence between the order of consistency of the residual error in time and GALERKIN time integration schemes has been mathematically proven.

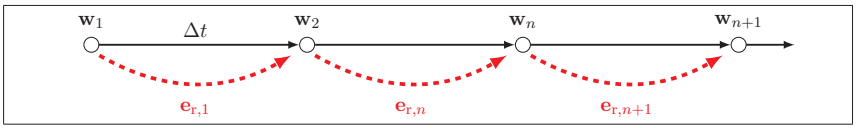

Figure 3.25.: Illustration of the residual error estimator

3.5.4. Error Characterizing Quantities

Apart from defining the time discretization errors, it is necessary to establish error characterizing quantities that allow to evaluate the error course, the order of consistency, and the order of convergence for a given problem. There are many possibilities to do so. In (Eidel and Kuhn, 2015), a weighted global error estimator is determined at specific points in time. (Grafenhorst et al., 2017) examine the maximum value of a global error estimator, and (Gleim, 2016) analyses the mean value of a local error estimator. In the present thesis, similar error quantities are investigated.

In order to be able to make a statement regarding the total time discretization error of distinct unknowns, the norm of the respective error vector is evaluated for various time step sizes at common points in time. Correspondingly, the following quantity is established and can be calculated for the previously described h-error, the embedded error, and the residual error estimator

$$e_{n+1} = \|\mathbf{e}_{n+1}\| \,. \tag{3.106}$$

An assembly of the quantity in (3.106) at distinct time steps yields the corresponding vector

$$\mathbf{e} = [e_1, ..., e_{n+1}] \,. \tag{3.107}$$

Sometimes, it may also be useful to generate relative errors by correlating the obtained quantities of Equation (3.106) to some reference values. One example would be the maximum of the primary variable vector $\|\mathbf{w}\|_{\max}$ or the sum over all residual errors $\sum_{n=1}^{NT} \|\mathbf{e}_{\mathrm{r},n+1}\|$. For further options see (Gleim, 2016; Kuhl, 2004).

To estimate the order of consistency or the order of convergence numerically, a measure has to be defined to characterize the temporal evolution of the error estimates in (3.107), so that a relation to a fixed time step size can be established. For this purpose, three different methods are developed, which can be taken into account for all described local and global error estimators

$$q^{\max} = \text{linear fit}\left(\log(\Delta t), \log\left(\max\left(\mathbf{e}(\Delta t)\right)\right)\right), \tag{3.108}$$

$$q^{\text{mean}} = \text{linear fit}\left(\log(\Delta t), \log\left(\text{mean}\left(\mathbf{e}(\Delta t)\right)\right)\right), \tag{3.109}$$

$$q = \text{mean}\left(\text{linear fit}\left(\log(\Delta t), \log\left(e_{n+1}(\Delta t)\right)\right)\right). \tag{3.110}$$

The idea behind the approaches in (3.108)-(3.110) is to calculate the respective error estimator for a variety of time step sizes, install a link to the latter by choosing a specific error characterizing value, and to identify the resulting slope by a linear regression in the logarithmic space as the order of consistency or convergence. The only difference between the three Equations (3.108)-(3.110) is the selected error-characterizing quantity. While the maximum is taken into account in Equation (3.108), as it is done by (Grafenhorst et al., 2017) for the global error, (3.109) exploits the mean value as it is followed in (Gleim, 2016). The method in (3.110) is adapted in (Eidel and Kuhn, 2015). Therein, however, the global h-error is estimated at distinct points in time - and the order of convergence is investigated only at those points. Here, the mean value over all considered points in time is chosen.

In this thesis, the expression order of consistency will always refer to the accuracy of a procedure estimated using a local error formulation. In contrast, the order of convergence is determined directly by a global error estimator.

3.6. Summary

Elasto(visco)plastic problems are characterized by a diversity of distinct types of material formulations and implementation schemes. Hence, one of the main ingredients of this chapter is to establish a common variational framework which is capable of taking these different aspects into account. In this context, the general elasto(visco)plastic problem is defined. In addition to nonlinear space- and time-dependent variational equalities, it even acknowledges inequalities and, thus, allows for a mutual treatment of dynamic finite as well as small strain plasticity and viscoplasticity. In addition, single or multifield formulations can be examined.

Due to the definition of this general elasto(visco)plastic problem, a sound solution process can be developed. It is based on a sequential space-time discretization. In the first step, the spatial discretization is carried out using the finite element method. For the primary variables' discretization, LAGRANGE polynomials with arbitrary polynomial degree and arbitrarily chosen supporting points are employed. Accordingly, continuous and discontinuous inter-elemental approximations can be constructed for the distinct unknowns, as required. The established triangulation is applicable to problems of arbitrary spatial dimension, and it is founded on LAGRANGE elements with arbitrary polynomial degrees as well.

In the next step, the nonlinear characteristic of the obtained semidiscrete form of the general elasto(visco)plastic problem is faced. This is done by deriving NEWTON-type algorithms. If solely variational equalities persist, a classical NEWTON-RAPHSON scheme is performed. This is based on the idea of creating an iterative process where the semidiscrete form is linearized at a guessed starting point. Afterwards, the resulting system of linear equations is solved and the obtained result is taken as a new point for linearization. This procedure is carried out until a user-defined criterion is reached. If variational inequalities prevail, an extension of this strategy, a semi-smooth NEWTON method, is adapted. Its concept is to recast all inequalities into equalities, so that the solution process can be carried out following the NEWTON-RAPHSON scheme. To obtain this modification, complementarity functions are constructed which possess the same solutions as the corresponding variational inequalities, but consist only of combinations of active and inactive equations. The resulting drawback is that they inherit a non-smooth character and cannot be differentiated easily. A special linearization treatment, taking the case distinction between active and inactive sets into account, is the consequence. If this is considered, an iterative solution procedure based on updated linearizations as within the NEWTON-RAPHSON scheme is gained. Hence, variational equalities and inequalities can be solved jointly.

After performing the linearization, and before the linear system of equations can be solved, two more issues have to be considered. First, the spatial integrals included in the linearized semidiscrete form have to be evaluated. This is achieved by utilizing a GAUSS-LEGENDRE quadrature rule. Therein, the integrals are converted into weighted sums, whereby the integrants are determined at specific points in space.

Secondly, the linearized semidiscrete form has to be discretized in time. This means that the time period of interest is divided into time steps, a link between the primary variable vector and its time derivatives is established, and the linearized semidiscrete form is evaluated only at discrete points in time dictated by the chosen time integrator. A further central point within this chapter is the generation and application of distinct classes of higher order accurate implicit time discretization schemes to the general elasto(visco)plastic problem. All of them are capable of treating differential algebraic systems, since the linearized semidiscrete form may contain algebraic equations.

The second order accurate NEWMARK scheme formulates the primary variable vector in dependence of distinct linear combinations of its corresponding first and second time derivatives of the last and the current time step. Hence, the general elasto(visco)plastic problem is solved at

the end of the time step, and all included algebraic equations are fulfilled.

Arbitrary orders of convergence can be obtained employing RUNGE-KUTTA methods. In this thesis, stiffly accurate diagonally implicit RUNGE-KUTTA methods are analyzed together with stiffly accurate fully implicit RUNGE-KUTTA schemes. The core goals of all these procedures are to recast differential equations into their integral counterpart and to approximate these integrals using quadrature rules whose coefficients as well as supporting points are chosen in such a way that prescribed orders of convergence are obtained. The stiffly accurate behavior ensures that all equations, including algebraic ones, are fulfilled at the end of each time step.

This property is also preserved in the class of continuous and discontinuous GALERKIN time integrators. Their functioning is founded on the idea of formulating the linearized semidiscrete form weakly in the time domain - and approximating the test functions, the primary variable vector, and its time derivatives using shape functions. Depending on the selection of the quadrature rule for the resulting time integral and the choice of the approximations, continuous or discontinuous, one-field or two-field settings are obtained. In this chapter, the procedures to derive the distinct schemes are constructed. The main focus is to create reliable schemes with arbitrary orders of convergence, which are able to treat algebraic equations intrinsically. This is achieved by adapting specially deduced combinations of LOBATTO and RADAU quadrature rules together with specific LAGRANGE polynomials in time.

An essential feature within this chapter is the natural implementation of different higher order accurate time discretization schemes to the general elasto(visco)plastic problem. Various error estimators are defined in order to assess the quality of the applied time integration schemes. While the time-step-based local and global h-error estimator can be employed for the NEWMARK, the RUNGE-KUTTA, and the GALERKIN schemes, the latter two methods come along with individual error estimators. Diagonally implicit RUNGE-KUTTA schemes can possess an embedded error estimator. It exploits the fact that varying orders of convergence can be obtained by employing different weighting coefficients. The computational effort is drastically lower than within the h-error estimation, since only an additional summation has to be carried out - instead of a simultaneous computation with a smaller time step. For the GALERKIN methods a residual error estimator can be established. Therein, the integral of the residuum within one time step is evaluated using the quadrature rule implemented in the GALERKIN scheme. Again, the computational effort is lower than for the h-error estimator since only a weighted sum has to be determined. With these error estimates at hand, it is possible to specify error-characterizing quantities that allow to determine the order of consistency and convergence.

4. Small Strain Elastoplasticity and Viscoplasticity

As is apparent from Figure 1.1, the integrated thermomechanical forming process is founded on the deformation of a metal steel shaft. Its material behavior is characterized by elastic, plastic, or viscoplastic properties. Purely elastic behavior is based on a reversible process, whereby an applied load leads to deformations which disappear after unloading. Hence, the strain is completely determined by the stress, cf. (Han and Reddy, 1999). Microscopically, this can be explained by the atomistic structure of most metals. In general, metallic materials consist of an aggregate of crystal grains, forming a polycrystalline structure in which the atoms are placed at specific lattice positions, cf. (Hill, 1983). If the lattice experiences only small shear deformations, an elastic behavior is the consequence. Otherwise, irreversible plastic or viscoplastic deformations occur, cf. (Bargel and Schulze, 2005). Lattice defects such as dislocations, point defects, and grain, or phase boundaries tend to promote this effect. While dislocations represent the main reason for plastic behavior, point defects and grain or phase boundaries result in viscous properties, cf. (Kröner and Teodosiu, 1974). Mostly, however, all three material states prevail simultaneously, cf. (Kröner and Teodosiu, 1974).

In order to perform specific numerical simulations of elasto(visco)plastically influenced processes, these characteristics have to be described mathematically. Some approaches considering the actual microstructure of the specimen are itemized in (El Hajj et al., 2009; Mahnken et al., 2009; Mahnken and Wilmanns, 2011) and the references therein. Another approach towards plastic and viscoplastic features is the idea that the microstructure has to be considered only by its influence on the specimen itself. Thus, a homogenization to the macroscopic scale is accomplished. The plasticity is then defined by the existence of a stress threshold which distinguishes between elastic and plastic effects. Furthermore, viscous properties are included by taking into account the distance to this threshold in the inelastic regime, cf. (Maugin, 1992). This rather standard course of action can be found e.g. in (Han and Reddy, 1999; Haupt, 2000; Simo, 1998; Simo and Hughes, 1997; Wriggers, 2008). Due to the drastically reduced modeling and implementation effort, this is the way elasto(visco)plasticity will be treated in the scope of this thesis. Moreover, in a first approach only small elastic as well as inelastic deformations will be considered. The extension to the finite strain regime is performed in **Chapter 6**.

4.1. Classical Approach

To specify the equations of the general elasto(visco)plastic problem, a continuum mechanical body $\mathcal{B}$ with spatial domain Ω in the time domain $[t_1, T]$ is considered. Its displacement field $\boldsymbol{u}(\boldsymbol{X}, t)$ and the corresponding strain tensor $\boldsymbol{\varepsilon}$ are defined by Equations (2.1) and (2.19), respectively. The occurring stresses are denoted by $\boldsymbol{\sigma}$. Hence, the body's boundary $\Gamma = \Gamma_{\mathrm{u}} \cup \Gamma_{\mathrm{t}^*}$ can be divided into a part Γ_{u}, where the displacements are prescribed, and a part Γ_{t^*}, where the stresses are known

$$\boldsymbol{u}(\boldsymbol{X}, t) = \boldsymbol{u}^* \qquad \forall \boldsymbol{X} \in \Gamma_{\mathrm{u}}, \qquad\qquad \boldsymbol{\sigma}(\boldsymbol{X}, t) \cdot \boldsymbol{n}(\boldsymbol{X}, t) = \boldsymbol{t}^* \qquad \forall \boldsymbol{X} \in \Gamma_{\mathrm{t}^*}. \tag{4.1}$$

These boundary conditions and possibly applied volume forces $\rho_0 \boldsymbol{f}$ lead to the deformation process described by Equation $(2.27)_1$ for $\boldsymbol{X} \in \Omega$, supplemented by the initial conditions

$$\boldsymbol{u}_1 = \boldsymbol{u}(\boldsymbol{X}, t_1) \qquad \forall \boldsymbol{X} \in \Omega, \qquad\qquad \dot{\boldsymbol{u}}_1 = \dot{\boldsymbol{u}}(\boldsymbol{X}, t_1) \qquad \forall \boldsymbol{X} \in \Omega. \tag{4.2}$$

Equations $(2.27)_1$, (4.1) and (4.2) form the basis of the strong, local initial boundary value problem. The remaining issue is the determination of the stress-strain relationship considering elasto(visco)plastic effects. Hence, two distinct cases, the elastoplastic and the elastoviscoplastic one, have to be accounted for. In what follows, the temporal and spatial dependencies are dropped for the sake of simplicity.

4.1.1. Elastoplasticity

Macroscopically, metal plasticity is characterized in the stress space by an elastic region $\mathcal{S}_\mathrm{e}$ and a plastic domain $\mathcal{S}_\mathrm{p}$. Both areas are separated by a stress-dependent threshold. Due to the physical behavior most metals show after passing this brink, it is commonly denoted as yield surface. Thus, the elastic domain

$$\mathcal{S}_\mathrm{e} \coloneqq \{\boldsymbol{\sigma} | f(\boldsymbol{\sigma}) < 0\} \tag{4.3}$$

is constrained by the yield function $f(\boldsymbol{\sigma})$ defining the corresponding plane. The plastic domain, however, is restricted to the boundary of $\mathcal{S}_\mathrm{e}$ and is therefore identical to the yield surface

$$\mathcal{S}_\mathrm{p} \coloneqq \{\boldsymbol{\sigma} | f(\boldsymbol{\sigma}) = 0\}.$$

Stress states outside both domains are prohibited in classical elastoplasticity, cf. (Han and Reddy, 1999; Simo, 1998; Simo and Hughes, 1997). Thus, the union $\mathcal{S} = \mathcal{S}_\mathrm{e} \cup \mathcal{S}_\mathrm{p}$ depicts the area of admissible stresses. For the examples treated in the course of this thesis, only the VON MISES yield surface

$$f(\boldsymbol{\sigma}) = \|\mathrm{dev}\,(\boldsymbol{\sigma})\| - \sqrt{\frac{2}{3}}\sigma_\mathrm{y} \qquad \text{with} \qquad \sigma_\mathrm{y} > 0 \tag{4.4}$$

will be taken into account. It is continuous as well as convex, (Simo and Hughes, 1997). The variable σ_y, therein represents a material-dependent yield stress and

$$\mathrm{dev}\,(\boldsymbol{\sigma}) = \boldsymbol{\sigma} - \frac{1}{3}\mathrm{tr}\,(\boldsymbol{\sigma})\,\boldsymbol{I},$$

denotes the deviatoric part of the CAUCHY stress tensor with the trace operator $\mathrm{tr}\,(\bullet)$. In general, the yield stress could depend on the loading history. This is achieved by introducing additional hardening or softening parameters, cf. (Haupt, 2000; Maugin, 1992; Simo and Hughes, 1997; Tsakmakis, 1994). For the sake of simplicity, these aspects are neglected herein and only ideal elastoplasticity is considered. In (Wieners, 2007), this approach is denoted as PRANDTL-REUSS plasticity.

To characterize the elastic as well as the plastic regime, proper kinematic quantities have to be considered. Therefore, the additive decomposition of the strain tensor into an elastic $\boldsymbol{\varepsilon}_\mathrm{e}$ and a plastic part $\boldsymbol{\varepsilon}_\mathrm{p}$ as in Equation (2.26) is exploited. Assuming that the internal energy of the continuum mechanical body only depends on elastic quantities, cf. (De Souza Neto et al., 2008; Halphen and Nguyen, 1975; Maugin, 1992; Simo and Hughes, 1997), it can be determined by

$$e = \frac{1}{2}\left[\boldsymbol{\varepsilon} - \boldsymbol{\varepsilon}_\mathrm{p}\right] : \mathbb{C}_\mathrm{e} : \left[\boldsymbol{\varepsilon} - \boldsymbol{\varepsilon}_\mathrm{p}\right]. \tag{4.5}$$

The variable $\mathbb{C}_\mathrm{e}$ represents the isotropic constitutive tensor representing linear elasticity. It can be calculated by

$$\mathbb{C}_\mathrm{e} = \kappa\, \boldsymbol{I} \otimes \boldsymbol{I} + 2\mu\, \mathbb{I}, \tag{4.6}$$

using the LAMÉ parameters κ, μ as well as the fourth order unity tensor

$$\mathbb{I} = \frac{1}{2}[\delta_{ik}\delta_{jl} + \delta_{il}\delta_{jk}]\, \boldsymbol{g}_i \otimes \boldsymbol{g}_j \otimes \boldsymbol{g}_k \otimes \boldsymbol{g}_l \qquad \text{with} \qquad i,j,k,l = 1,...,3.$$

A strategy to derive Equation (4.5) without considering the dependence on purely elastic terms is described in (Han and Reddy, 1999). To ensure thermodynamical consistency, the constitutive equations describing elastoplastic material properties are determined, taking advantage of the dissipation inequality in $(2.27)_2$. Equation (4.5) is differentiated with respect to time and inserted together with (2.26) in $(2.27)_2$ leading to

$$D_{\text{int}} = \left[\boldsymbol{\sigma} - \frac{\partial e}{\partial \boldsymbol{\varepsilon}_{\text{e}}}\right] : \dot{\boldsymbol{\varepsilon}}_{\text{e}} + \boldsymbol{\sigma} : \dot{\boldsymbol{\varepsilon}}_{\text{p}} \geq 0. \tag{4.7}$$

Exploiting the fact that Inequality (4.7) is fulfilled if the term in brackets is equal to zero, the constitutive equation

$$\boldsymbol{\sigma} = \frac{\partial e}{\partial \boldsymbol{\varepsilon}_{\text{e}}} = \mathbb{C}_{\text{e}} : [\boldsymbol{\varepsilon} - \boldsymbol{\varepsilon}_{\text{p}}] \tag{4.8}$$

is defined. To determine the evolution equation of the plastic strains, the postulate of maximum plastic work or maximum plastic dissipation

$$D_{\text{int}} = \sup_{\boldsymbol{\sigma}} \{\boldsymbol{\sigma} : \dot{\boldsymbol{\varepsilon}}_{\text{p}} \big| f(\boldsymbol{\sigma}) \leq 0\} \tag{4.9}$$

is considered. Hence, it is assumed that, from among all admissible stresses, the state of maximal stresses $\boldsymbol{\sigma}$ is the preferable one - and that the dissipation in the material reaches a maximum. The models obtained in this context are referred to as associative plasticity, cf. (Han and Reddy, 1999; Miehe, 2011; Simo and Miehe, 1992). An explanation of this postulate concerning the microstructure is given in (Bishop and Hill, 1951). Alternative postulates forming the starting point for the derivation of the evolution equation are mentioned in (Junker et al., 2013; Lubliner, 2006; Reddy and Martin, 1994). Following the approach in (Simo and Hughes, 1997), Equation (4.9) can be reformulated using ideas associated to optimization. This results in the LAGRANGE function

$$\mathcal{L} = \boldsymbol{\sigma} : \dot{\boldsymbol{\varepsilon}}_{\text{p}} - \lambda f(\boldsymbol{\sigma}), \tag{4.10}$$

with the LAGRANGE multiplier $\lambda \geq 0$ and the yield function $f(\boldsymbol{\sigma}) \leq 0$ as a considered inequality constraint, cf. (Geiger and Kanzow, 2002; Luenberger, 1973). The necessary optimality conditions for a stationary point

$$\frac{\partial \mathcal{L}}{\partial \boldsymbol{\sigma}} = 0 \qquad \text{and} \qquad \lambda f(\boldsymbol{\sigma}) = 0$$

with $\text{dev}\,(\boldsymbol{\sigma}) \neq \mathbf{0}$, yield

$$\dot{\boldsymbol{\varepsilon}}_{\text{p}} = \lambda \frac{\partial f(\boldsymbol{\sigma})}{\partial \boldsymbol{\sigma}} = \lambda \frac{\text{dev}\,(\boldsymbol{\sigma})}{\|\text{dev}\,(\boldsymbol{\sigma})\|} \qquad \text{with} \qquad \lambda \geq 0,\ f(\boldsymbol{\sigma}) \leq 0,\ \lambda f(\boldsymbol{\sigma}) = 0. \tag{4.11}$$

Therein, Equation $(4.11)_1$ resembles the evolution equation characterizing plastic strains as purely deviatoric. This fact is related to the observation that in metal plasticity the volume change is only linked to elastic deformations. Plastic ones are assumed to be volume insensitive, cf. (Han and Reddy, 1999; Hartmann, 2008). On the contrary, Equation $(4.11)_2$ comprises the KARUSH-KUHN-TUCKER conditions. If purely elastic deformations prevail, they state that $f < 0$ and $\lambda = 0$ hold. For plastic deformations, the examined stress state has to be on the yield

surface $f = 0$, and the LAGRANGE multiplier is $\lambda \geq 0$. If $\lambda = 0$ endures, elastic unloading or neutral loading can pertain. Plastic loading takes place for $\lambda > 0$. In order to prove that these choices always lead to a fulfilled dissipation inequality (4.7), Equation $(4.11)_1$ is inserted and the condition for the LAGRANGE multiplier in $(4.11)_2$ is applied.

In general, the standard optimality conditions and, thus, Equation (4.11) are only valid for continuous differentiable functions $f(\boldsymbol{\sigma})$, cf. (Geiger and Kanzow, 2002). For an extension to the non-differentiable case, the derivative of $f(\boldsymbol{\sigma})$ is exchanged by the subdifferential, cf. (Clarke, 1990). Here, this generalization is not needed, although the yield function is differentiable everywhere - except for the zero stress state $\|\mathrm{dev}\,(\boldsymbol{\sigma})\| = 0$. But at that point, due to the yield function in (4.4), only elastic properties prevail and the rate of plastic strains has to disappear anyway. An alternative possibility to derive Equation (4.11) using convex analysis is done in in (Eve et al., 1990; Reddy and Martin, 1994).

To be able to solve Equation (4.11), a proper initial condition

$$\boldsymbol{\varepsilon}_{\mathrm{p},1} = \boldsymbol{\varepsilon}_{\mathrm{p}}(t_1) \tag{4.12}$$

has to be chosen. To complete the material model for elastoplasticity, only the equation needed to determine the LAGRANGE multiplier is missing. Therefore, the consistency condition

$$\lambda \dot{f} = 0 \tag{4.13}$$

is elaborated, (Simo and Hughes, 1997). For the current model formulation, Equation (4.13) is evaluated. In the case of plastic loading $\lambda > 0$, the yield function's time derivative is calculated and set to zero. After inserting (4.8) as well as (4.11), the LAGRANGE multiplier

$$\lambda = \frac{\dfrac{\partial f(\boldsymbol{\sigma})}{\partial \boldsymbol{\sigma}} : \mathbb{C}_{\mathrm{e}} : \dot{\boldsymbol{\varepsilon}}}{\dfrac{\partial f(\boldsymbol{\sigma})}{\partial \boldsymbol{\sigma}} : \mathbb{C}_{\mathrm{e}} : \dfrac{\partial f(\boldsymbol{\sigma})}{\partial \boldsymbol{\sigma}}}$$

is determined. Hence, the stress-strain rate relationship can be formulated to

$$\begin{aligned} \dot{\boldsymbol{\sigma}} &= \mathbb{C}_{\mathrm{p}} : \dot{\boldsymbol{\varepsilon}}, \\ \mathbb{C}_{\mathrm{p}} &:= \begin{cases} \mathbb{C}_{\mathrm{e}} & \text{for} \quad \lambda = 0 \\ \mathbb{C}_{\mathrm{e}} - \dfrac{\left[\mathbb{C}_{\mathrm{e}} : \dfrac{\partial f(\boldsymbol{\sigma})}{\partial \boldsymbol{\sigma}}\right] \otimes \left[\mathbb{C}_{\mathrm{e}} : \dfrac{\partial f(\boldsymbol{\sigma})}{\partial \boldsymbol{\sigma}}\right]}{\dfrac{\partial f(\boldsymbol{\sigma})}{\partial \boldsymbol{\sigma}} : \mathbb{C}_{\mathrm{e}} : \dfrac{\partial f(\boldsymbol{\sigma})}{\partial \boldsymbol{\sigma}}} & \text{for} \quad \lambda > 0. \end{cases} \end{aligned} \tag{4.14}$$

For the case $\lambda = 0$, it is identical to the purely elastic case. In the plastic case, because of the linear dependence on the strain rate in (4.14), the time variable can be exchanged by any other monotonously increasing function, cf. (Hartmann, 2008; Simo and Hughes, 1997). This is the reason why this kind of model is also referred to as rate-independent plasticity.

4.1.2. Viscoplasticity

In cyclic experiments performed with different strain rates, it can be observed that some metals show a rate-dependent stress-strain behavior, cf. (Haupt, 2000). This characteristic is termed viscoplasticity, and it can be seen as an enhancement of the previously described elastoplastic theory. For other approaches towards modeling viscoplastic effects see the references in (Haupt, 2000). In the viscoplastic model formulation of this thesis, the stress state again embodies an

elastic region (4.3) which is bounded by the yield function in (4.4). In contrast to the elastoplastic model of Section 4.1.1, the viscous states are not enforced to lie on the yield surface. Stress states beyond this are also permitted. Thus, the whole stress space constitutes admissible stresses. The additive decomposition of the strain tensor in (2.26) is preserved, as well as the corresponding energy in (4.5) with the elastic constitutive tensor in (4.6). But the index $_{\mathrm{p}}$ therein now refers to viscous relations. The constitutive equation in (4.8) is maintained too. The postulate of maximum plastic dissipation, however, has to be adapted. It is still assumed that, from among all admissible stresses, the state of maximal stresses $\boldsymbol{\sigma}$ is the preferable one. Yet, due to the fact that the region outside the yield surface contributes admissible stresses as well, the inequality constraint imposed by the yield function can be weakened. This is achieved by following the approach in (Simo and Hughes, 1997) and by introducing a penalization term

$$D_{\mathrm{int}} = \sup_{\boldsymbol{\sigma}} \left\{ \boldsymbol{\sigma} : \dot{\boldsymbol{\varepsilon}}_{\mathrm{p}} - \frac{1}{\chi} h\left(f(\boldsymbol{\sigma})\right) \right\}. \tag{4.15}$$

The former Lagrange multiplier as well as the inequality constraint are now replaced by a continuous differentiable function

$$h\left(f(\boldsymbol{\sigma})\right) := \begin{cases} \dfrac{1}{2}\left[f(\boldsymbol{\sigma})\right]^2 & \text{for} \quad f(\boldsymbol{\sigma}) \geq 0 \\ 0 & \text{for} \quad f(\boldsymbol{\sigma}) < 0. \end{cases} \tag{4.16}$$

and the viscosity parameter $\chi > 0$. Hence, stress states outside the yield surface are penalized according to their distance and with respect to the viscosity parameter χ. The smaller this parameter, the greater its penalization. If it tends to zero, $\chi \to 0$, the rate-dependent elastoviscoplastic problem degenerates to the rate-independent elastoplastic problem, cf. (Simo and Hughes, 1997). For basic aspects and proofs of general penalty methods see (Alt, 2011; Luenberger, 1973). For an alternative approach towards plasticity as a limit of viscoplasticity see (Haupt, 2000).

By taking into account (4.15) as well as (4.16), the Lagrange function in (4.10) can be modified to

$$\mathcal{L} = \boldsymbol{\sigma} : \dot{\boldsymbol{\varepsilon}}_{\mathrm{p}} - \frac{1}{\chi} h\left(f(\boldsymbol{\sigma})\right).$$

The stationarity condition

$$\frac{\partial \mathcal{L}}{\partial \boldsymbol{\sigma}} = 0$$

results with

$$\frac{\partial\, h\left(f(\boldsymbol{\sigma})\right)}{\partial (f(\boldsymbol{\sigma}))} = \langle f(\boldsymbol{\sigma}) \rangle := \begin{cases} f(\boldsymbol{\sigma}) & \text{for} \quad f(\boldsymbol{\sigma}) \geq 0 \\ 0 & \text{for} \quad f(\boldsymbol{\sigma}) < 0. \end{cases} \tag{4.17}$$

in the evolution equation with the prescribed Lagrange multiplier

$$\dot{\boldsymbol{\varepsilon}}_{\mathrm{p}} = \lambda \frac{\partial f(\boldsymbol{\sigma})}{\partial \boldsymbol{\sigma}} = \lambda \frac{\operatorname{dev}(\boldsymbol{\sigma})}{\|\operatorname{dev}(\boldsymbol{\sigma})\|} \qquad \text{with} \qquad \lambda = \frac{1}{\chi} \langle f(\boldsymbol{\sigma}) \rangle. \tag{4.18}$$

As an initial condition to solve Equation (4.18), the Term (4.12) is chosen as in the elastoplastic case.

Because of the extension of the domain of admissible stresses to the exterior of the yield surface, the consistency condition in (4.13) is obsolete. The stress-strain rate relationship can now be formulated to

$$\dot{\boldsymbol{\sigma}} = \mathbb{C}_\mathrm{p} : \dot{\boldsymbol{\varepsilon}},$$

$$\mathbb{C}_\mathrm{p} := \begin{cases} \mathbb{C}_\mathrm{e} & \text{for} \quad \lambda = 0 \\ \mathbb{C}_\mathrm{e} - \dfrac{1}{\chi} \langle f(\boldsymbol{\sigma}) \rangle \, \mathbb{C}_\mathrm{e} : \dfrac{\partial f(\boldsymbol{\sigma})}{\partial \boldsymbol{\sigma}} : \dot{\boldsymbol{\varepsilon}}^{-1} & \text{for} \quad \lambda > 0. \end{cases} \tag{4.19}$$

For the case $\lambda = 0$, it is identical to the purely elastic situation. If viscoplastic effects prevail and $\lambda > 0$ holds, there is apparently no longer a linear dependence on the strain rate in (4.19). This stands in contrast to the elastoplastic case defined in Equation (4.14) and, hence, underlines the rate-dependence of the material model.

4.1.3. Numerical Realization

A general elastoplastic or elastoviscoplastic problem consists of the balance equation in $(2.27)_1$, the constitutive equation in (4.8), the evolution equations in (4.11) or (4.18) together with the yield function in (4.4) and the appropriate boundary (4.1) as well as initial conditions (4.2), (4.12). The corresponding scheme is depicted in Figure 4.1.

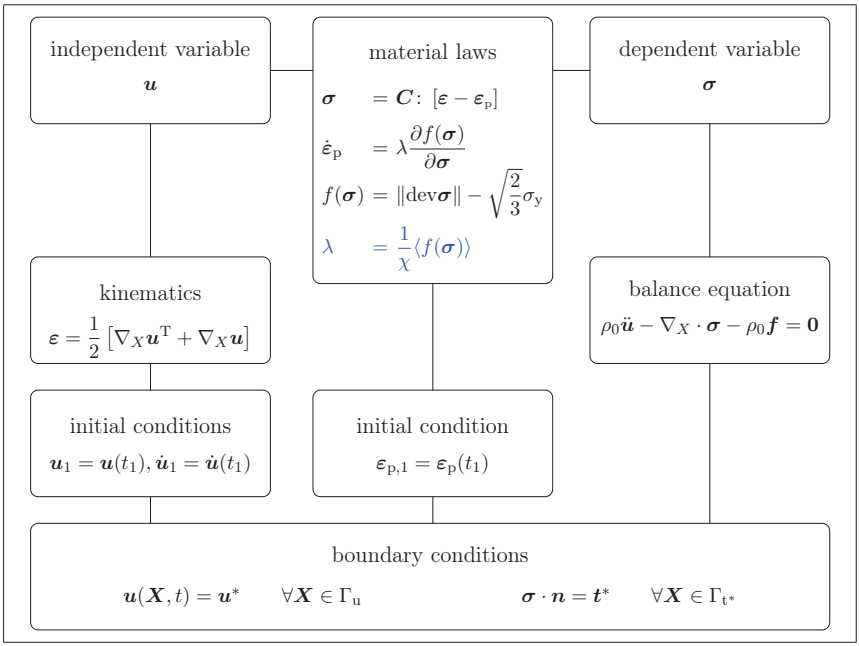

Figure 4.1.: Initial boundary value problem of the classical approach in the small strain regime with entries in blue referring to expressions needed only in the viscoplastic case

It can be observed that, due to the yield function a differential algebraic system is obtained. This

requires a special numerical treatment concerning the time discretization methods, cf. (Büttner and Simeon, 2002; Hairer and Wanner, 2002; Strehmel et al., 2012). A more detailed explanation is given in Section 4.1.3.4.

In order to solve this initial boundary value problem for arbitrarily shaped continuum mechanical bodies with distinct kinds of dead-loads, a numerical solution scheme has to be derived as well as applied. Therefore, the numerical strategies of **Chapter 3** are considered and specified. It has to be emphasized that, in this context, a fix cartesian coordinate system will always be assumed - with the space- and time-independent unit basis vectors $\boldsymbol{g}_i$ with $i = 1, ..., 3$.

4.1.3.1. Generation of the Weak Formulation

The methods in **Chapter 3** are based on the general weak forms in (3.1)-(3.2). Hence, the first step to solve the classical elasto(visco)plastic initial boundary value problem is to generate a corresponding weak formulation - for which the principle of virtual work is exploited, cf. (Finlayson, 1972; Holzapfel, 2000; Kelly, 2015; Lagrange, 1788; Wriggers, 2008). The idea therein is to multiply the balance of linear momentum in $(2.27)_1$ with an arbitrary vector-valued test function $\delta\boldsymbol{u} \neq \boldsymbol{0}$ with $\delta\boldsymbol{u} = \boldsymbol{0}$ only on Γ_u and to integrate the resulting expression over the domain Ω of the investigated continuum mechanical body $\mathcal{B}$. The NEUMANN boundary condition in $(4.1)_2$ is treated analogously, except that the integration is performed over the boundary Γ_{t^*} of $\mathcal{B}$. An addition of both terms yields

$$\delta W = \int_\Omega \delta\boldsymbol{u} \cdot [\rho_0 \ddot{\boldsymbol{u}} - \nabla_X \cdot \boldsymbol{\sigma} - \rho_0 \boldsymbol{f}] \; dV + \int_{\Gamma_{\mathrm{t}^*}} \delta\boldsymbol{u} \cdot [\boldsymbol{\sigma} \cdot \boldsymbol{n} - \boldsymbol{t}^*] \; dA = 0. \tag{4.20}$$

By applying the product rule

$$\delta\boldsymbol{u} \cdot [\nabla_X \cdot \boldsymbol{\sigma}] = \nabla_X \cdot [\delta\boldsymbol{u} \cdot \boldsymbol{\sigma}] - \nabla_X \delta\boldsymbol{u} \colon \boldsymbol{\sigma}, \tag{4.21}$$

the divergence theorem

$$\int_\Omega \nabla_X \cdot [\delta\boldsymbol{u} \cdot \boldsymbol{\sigma}] \; dV = \int_{\Gamma_{\mathrm{t}^*}} \delta\boldsymbol{u} \cdot \boldsymbol{\sigma} \cdot \boldsymbol{n} \; dA \tag{4.22}$$

and the relationship

$$\nabla_X \delta\boldsymbol{u} \colon \boldsymbol{\sigma} = \delta \nabla_X \boldsymbol{u} \colon \boldsymbol{\sigma} = \delta\boldsymbol{\varepsilon} \colon \boldsymbol{\sigma}$$

with $\boldsymbol{\sigma} = \boldsymbol{\sigma}^\mathrm{T}$, Equation (4.20) can be reformulated into

$$\delta W = \int_\Omega \delta\boldsymbol{u} \cdot \rho_0 \ddot{\boldsymbol{u}} \; dV + \int_\Omega \delta\boldsymbol{\varepsilon} \colon \boldsymbol{\sigma} \; dV - \int_\Omega \delta\boldsymbol{u} \cdot \rho_0 \boldsymbol{f} \; dV - \int_{\Gamma_{\mathrm{t}^*}} \delta\boldsymbol{u} \cdot \boldsymbol{t}^* \; dA = 0. \tag{4.23}$$

The DIRICHLET boundary conditions are considered in a strong sense. Because the test functions are arbitrary but non zero, the fundamental lemma of variational calculus states that the weak and the strong forms are equivalent, cf. (Holzapfel, 2000). By comparing Equation (4.23) to the general weak forms in (3.1)-(3.2), it can be recognized that if

$$\delta\mathbf{z}_1 = \begin{bmatrix} \delta\boldsymbol{u} \\ \delta\boldsymbol{\varepsilon} \end{bmatrix} = \begin{bmatrix} \delta\boldsymbol{u} \\ \delta\nabla_X\boldsymbol{u} \end{bmatrix}, \qquad \mathbf{r}_1 = \begin{bmatrix} \rho_0\ddot{\boldsymbol{u}} - \rho_0\boldsymbol{f} \\ \boldsymbol{\sigma} \end{bmatrix}, \qquad \mathbf{r}^* = \begin{bmatrix} \mathbf{t}^* \\ \mathbf{0} \end{bmatrix}, \qquad \mathbf{w} = \boldsymbol{u} \tag{4.24}$$

is set and the variational inequality is neglected, they are identical. Nonetheless, some attention has to be paid to the second entries of $\delta\boldsymbol{z}_1$ and $\boldsymbol{r}_1$, since they are not vector-valued but tensors of second order. Furthermore, the primary variable vector $\mathbf{w}$ only consists of the displacement field $\boldsymbol{u}$ as the solely unknown quantity. With these definitions, the numerical realization of **Chapter 3** can be applied one-to-one to the weak form in (4.23).

4.1.3.2. Linearized Spatially Discrete System of Equations on Structural Level

The first step towards solving the weak form in (4.23) according to **Chapter 3** is the spatial discretization by means of the finite element method. Therefore, the continuum mechanical body's domain Ω is partitioned following (3.4) into small elements $\bar{\Omega}^e$, and the geometry is approximated by (3.5). The approximation of the primary variable $\boldsymbol{u}$ and related terms is performed exploiting Equations (3.7)-(3.8). Equation (3.9) is applied for the test function. Here, it is necessary to take care - since, in agreement with (4.24), the vector of test functions $\delta \boldsymbol{z}_1$ contains a gradient expression which has to be acknowledged properly. The appearing shape functions are assumed to be of LAGRANGE type leading to continuous approximations, so that they can be determined by Equation (3.16) together with (3.13). Their derivatives are obtained by evaluating (3.18) together with Relation (3.15). Thus, only rectangular or hexahedra elements of arbitrary polynomial degree are admitted for the two- and three-dimensional case. By exploiting Equation (3.10), the weak form in (4.23) is transferred to the element level analogously to Equation (3.11). For a better understanding, the spatial and temporal dependencies are introduced in this reformulation.

$$\begin{aligned} \delta W^e = & \int_{\bar{\Omega}^e} \delta \boldsymbol{u}^e(\boldsymbol{X}^e) \cdot \rho_0 \ddot{\boldsymbol{u}}^e(\boldsymbol{X}^e, t)\, d\bar{V}^e + \int_{\bar{\Omega}^e} \delta \boldsymbol{\varepsilon}^e(\boldsymbol{X}^e) \colon \boldsymbol{\sigma}(\boldsymbol{\varepsilon}^e(\boldsymbol{X}^e, t))\, d\bar{V}^e - \\ & - \int_{\bar{\Omega}^e} \delta \boldsymbol{u}^e(\boldsymbol{X}^e) \cdot \rho_0 \boldsymbol{f}(\boldsymbol{X}^e, t)\, d\bar{V}^e - \int_{\bar{\Gamma}^e_{t^*}} \delta \boldsymbol{u}^e(\boldsymbol{X}^e) \cdot \boldsymbol{t}^*(\boldsymbol{X}^e, t)\, d\bar{A}^e \qquad = 0. \end{aligned} \tag{4.25}$$

Since the stresses are not considered as primary variables, they can only be approximated indirectly. Section 4.1.3.4 addresses the question how this is done in an explicit manner.

The next step towards the linearized semidiscrete system of equations is the application of the NEWTON-RAPHSON scheme, which serves to convert the nonlinear Equation (4.25) on element level into a series of linear equations on structural level, see Section 3.2.1. It is not necessary to consider a semi-smooth NEWTON method, because no inequalities are taken into account. Consequently, the linearization in terms of (3.21) and (3.22) is performed, leading to

$$\sum_{i=1}^{NN} \sum_{j=1}^{NN} \delta \boldsymbol{u}^{ei} \cdot \left[\boldsymbol{m}^{eij} \cdot \Delta \ddot{\boldsymbol{u}}^{ej} + \boldsymbol{k}^{eij} \cdot \Delta \boldsymbol{u}^{ej} \right] = \sum_{i=1}^{NN} \delta \boldsymbol{u}^{ei} \cdot \left[\boldsymbol{r}_1^{*,ei} - \boldsymbol{r}_1^{ei} \right] \tag{4.26}$$

with the suitable tangent matrices and load vectors

$$\begin{aligned} \boldsymbol{m}^{eij} &= \int_{\Omega^e} \rho_0 N^i N^j\, \boldsymbol{I}\, |\boldsymbol{J}^e|\, dV^e, \\ \boldsymbol{k}^{eij} &= \int_{\Omega^e} \nabla_X N^i \cdot \left. \frac{\partial \boldsymbol{\sigma}}{\partial \boldsymbol{\varepsilon}^e} \right|_k \cdot \nabla_X N^j\, |\boldsymbol{J}^e|\, dV^e, \\ \boldsymbol{r}_1^{*,ei} &= \int_{\Omega^e} N^i\, \rho_0 \boldsymbol{f}^k\, |\boldsymbol{J}^e| dV^e + \int_{\Gamma^e_{t^*}} N^i\, \boldsymbol{t}^{*,k}\, |\boldsymbol{J}^e|\, dA^e, \\ \boldsymbol{r}_1^{ei} &= \int_{\Omega^e} N^i\, \rho_0 \ddot{\boldsymbol{u}}^{e,k}\, |\boldsymbol{J}^e| dV^e + \int_{\Omega^e} \boldsymbol{\sigma}^k \cdot \nabla_X N^i\, |\boldsymbol{J}^e|\, dV^e. \end{aligned}$$

Furthermore, the Relationship (3.20) together with (3.19) and the symmetry of the stress tensor $\boldsymbol{\sigma} = \boldsymbol{\sigma}^{\mathrm{T}}$ are employed. The appearing integrals are numerically determined using the Gauss-Legendre quadrature. Afterwards, the individual constituents of (4.26) are assembled according to (3.25) as well as (3.26), yielding the spatial semidiscrete equation on structural level

$$\mathbf{M}\Delta\ddot{\mathbf{u}} + \mathbf{K}_1\Delta\mathbf{u} = \mathbf{R}_1^* - \mathbf{R}_1. \tag{4.27}$$

4.1.3.3. Time Discretization on Structural Level

In order to be able to solve the presented elasto(visco)plastic problem, two issues remain. On the one hand, a temporal integration of the semidiscrete Equation (4.27) has to be performed, and on the other hand, the material laws have to be included. But these aspects can only partly be treated separately, since the evolution equation demands a time discretization too. Hence, an appropriate coupling with special requirements concerning the time integration method is needed. This will be addressed in Section 4.1.3.4.

In the literature, this challenge is often circumvented by considering a quasi-static elasto(visco)-plastic problem. Therein, the forces of inertia are neglected and the second time derivative of the primary variable vector in Equation (4.27) is dropped, cf. (Christensen, 2002; De Souza Neto et al., 2008; Ellsiepen and Hartmann, 2001; Lubliner, 2006; Simo, 1998; Simo et al., 1988, 1989; Wieners, 2007). As a result, only the time integration of the evolution equation is left. In contrast, examples where dynamic effects are treated can be found in (Hager and Wohlmuth, 2009; Ortiz et al., 1983). In (Hager and Wohlmuth, 2009), a Newmark scheme is applied to the balance equation and an implicit Euler to the evolution equation, while in (Ortiz et al., 1983) the implicit Euler as well as the trapezoidal rule are exploited for all equations at the same time - and this concept is pursued in this thesis as well. Here, however, only the Newmark scheme of Section 3.4.1 and the stiffly accurate diagonally implicit Runge-Kutta methods of Section 3.4.2.2 are utilized. With the latter schemes, Equation (4.27) can be recast similar to (3.67) into

$$\begin{aligned} \mathbf{K}_{\mathrm{eff}}\Delta\mathbf{u}_{ni} &= \mathbf{r}_{\mathrm{eff}}, \\ \mathbf{K}_{\mathrm{eff}} &= \frac{1}{a_{ii}^2\Delta t^2}\mathbf{M}_{ni} + \mathbf{K}_{1,ni}, \\ \mathbf{r}_{\mathrm{eff}} &= \mathbf{R}_{1,ni}^* - \mathbf{R}_{1,ni}, \end{aligned} \tag{4.28}$$

where the parameters are chosen as depicted in Figure 3.13. Consequently, the weak form of the balance equation has to be evaluated at each Runge-Kutta stage. Applying the Newmark method leads to a reformulation

$$\begin{aligned} \mathbf{K}_{\mathrm{eff}}\Delta\mathbf{u}_{n+1} &= \mathbf{r}_{\mathrm{eff}}, \\ \mathbf{K}_{\mathrm{eff}} &= \frac{1}{\beta\Delta t^2}\mathbf{M}_{n+1} + \mathbf{K}_{1,n+1}, \\ \mathbf{r}_{\mathrm{eff}} &= \mathbf{R}_{1,n+1}^* - \mathbf{R}_{1,n+1}, \end{aligned} \tag{4.29}$$

as in (3.52) with the parameters in (3.53). Thus, the evaluation is only performed at the end of the time step. The benefits of these two time integration schemes will be explained in the context of the radial return map in the next section.

4.1.3.4. Radial Return Map

The last step within the numerical realization is the incorporation of elastoplastic or viscoplastic effects. Despite the differences in their physical interpretation and their mathematical formula-

tion, the numerical implementation of both phenomena is similar. The corresponding material laws have to be linked to the weak form of the balance of linear momentum. This is achieved by means of the tangential stiffness matrix and the internal load vector in Equation (4.26). Both require the stress state to be determined in dependence of the strains, which is achieved by the constitutive equation in (4.8). Nevertheless, the (visco)plastic strains contained therein have to be calculated beforehand. Therefore, on the one hand, it has to be decided whether (visco)plastic flow prevails while, on the other hand, its evolution has to be calculated by discretizing Equations (4.11) or (4.18) in time.

These two aspects are classically covered within the radial return mapping algorithm, also denoted as closest point projection, cf. (Büttner and Simeon, 2002; Christensen, 2002; De Souza Neto et al., 2008; Krieg and Krieg, 1977; Simo, 1998; Simo and Hughes, 1997; Wieners, 2007; Wilkins, 1963). A generalization of this method in terms of product formulas, where an elastic and a plastic operator are defined to yield a solution strategy, is introduced in (Ortiz et al., 1983; Simo and Hughes, 1997). Alternative approaches towards the solution of elastoplastic problems implying facets from convex analysis are analyzed in (Alberty et al., 1999; Carstensen, 1997; Wieners, 2007), while the application of non-smooth NEWTON methods is described in (Christensen, 2002; Hager and Wohlmuth, 2009). In (Ellsiepen and Hartmann, 2001; Wriggers, 2008) a multi-level NEWTON procedure is performed to couple the material laws to the balance equation. The time discretization schemes included in all these distinct procedures range from the most frequently used backward EULER over the trapezoidal rule to various RUNGE-KUTTA methods, cf. (Büttner and Simeon, 2002; De Souza Neto et al., 2008; Eidel and Kuhn, 2015; Ellsiepen and Hartmann, 2001; Hager and Wohlmuth, 2009; Ortiz et al., 1983; Simo and Govindjee, 1991; Simo and Hughes, 1997).

Within the course of this thesis, the classical approach will always embody the radial return map, and the same time integration method is applied to the balance law as well as to the evolution equation. Hence, in accordance to Equations (4.28) and (4.29), the closest point projection is derived for stiffly accurate diagonally implicit RUNGE-KUTTA schemes as well as for the NEWMARK method. This course of action is adapted from the literature, cf. (Ellsiepen and Hartmann, 2001; Simo and Hughes, 1997), and, because of its wide dispersal, it will serve as a reference scheme for numerical validation.

4.1.3.4.1. Elastoplasticity: NEWMARK's method and DIRK Schemes

Due to the high amount of similarities between the radial return map for stiffly accurate DIRK schemes and for the NEWMARK method, both approaches are treated simultaneously. The distinct indices indicate the evaluated point in time for the respective procedure.

To derive the radial return map in a first step, the constitutive equation in (4.8) is reformulated together with (4.6) to obtain a split of the stress tensor in a spherical and a deviatoric part

$$\begin{aligned} \boldsymbol{\sigma}^{k}_{ni/n+1} &= \frac{3\kappa+2\mu}{3}\mathrm{tr}\left(\boldsymbol{\varepsilon}^{e,k}_{ni/n+1}\right)\boldsymbol{I} + \mathrm{dev}\left(\boldsymbol{\sigma}^{k}_{ni/n+1}\right), \\ \mathrm{dev}\left(\boldsymbol{\sigma}^{k}_{ni/n+1}\right) &= 2\mu\,\mathrm{dev}\left(\boldsymbol{\varepsilon}^{e,k}_{ni/n+1} - \boldsymbol{\varepsilon}_{\mathrm{p},ni/n+1}\right). \end{aligned} \tag{4.30}$$

The evaluation of Equation (4.30) is performed for every iteration k of the NEWTON-RAPHSON procedure at each RUNGE-KUTTA stage or at the end of the time step for the NEWMARK method. The stress states are required at those points in time to determine the tangential stiffness matrix and the load vector. Since the plastic strains are not updated within this global iteration scheme, the index k is thereby dropped. Furthermore, it is emphasized that, due to the numerical integration, the stress state is determined only at GAUSS-LEGENDRE quadrature points.

In the next step, the evolution equation in (4.11) has to be appraised. Applying a stiffly accurate diagonally implicit RUNGE-KUTTA scheme yields

$$\boldsymbol{\varepsilon}_{\mathrm{p},ni} = \tilde{\boldsymbol{\varepsilon}}_{\mathrm{p},ni} + \Delta t\; a_{ii}\; \dot{\boldsymbol{\varepsilon}}_{\mathrm{p},ni} \qquad \text{with} \qquad \tilde{\boldsymbol{\varepsilon}}_{\mathrm{p},ni} = \boldsymbol{\varepsilon}_{\mathrm{p},n} + \Delta t \sum_{j=1}^{i-1} a_{ij}\; \dot{\boldsymbol{\varepsilon}}_{\mathrm{p},nj}, \tag{4.31}$$

analogously to Equation (3.64) with (3.65). Using Equation (3.50) of the NEWMARK method, whereby the included second time derivatives are neglected, results in

$$\boldsymbol{\varepsilon}_{\mathrm{p},n+1} = \tilde{\boldsymbol{\varepsilon}}_{\mathrm{p},n} + \Delta t\; \frac{\beta}{\gamma}\; \dot{\boldsymbol{\varepsilon}}_{\mathrm{p},n+1} \qquad \text{with} \qquad \tilde{\boldsymbol{\varepsilon}}_{\mathrm{p},n} = \boldsymbol{\varepsilon}_{\mathrm{p},n} + \Delta t \frac{\gamma - \beta}{\gamma}\; \dot{\boldsymbol{\varepsilon}}_{\mathrm{p},n}. \tag{4.32}$$

Comparing Equations $(4.31)_1$ and $(4.32)_1$ yields the general formulation

$$\boldsymbol{\varepsilon}_{\mathrm{p},ni/n+1} = \tilde{\boldsymbol{\varepsilon}}_{\mathrm{p},ni/n} + \Delta t\; \Theta\; \dot{\boldsymbol{\varepsilon}}_{\mathrm{p},ni/n+1} \qquad \text{with} \qquad \Theta = \begin{cases} a_{ii} & \text{for DIRK} \\ \dfrac{\beta}{\gamma} & \text{for NEWMARK.} \end{cases} \tag{4.33}$$

Inserting the general Relationship (4.33) in (4.30) leads to the definition of the trial state

$$\operatorname{dev}\left(\boldsymbol{\sigma}^{k,\mathrm{trial}}_{ni/n+1}\right) \coloneqq 2\mu\, \operatorname{dev}\left(\boldsymbol{\varepsilon}^{e,k}_{ni/n+1} - \tilde{\boldsymbol{\varepsilon}}_{\mathrm{p},ni/n}\right) = \operatorname{dev}\left(\boldsymbol{\sigma}^{k}_{ni/n+1}\right) + 2\mu\; \Delta t\; \Theta\; \dot{\boldsymbol{\varepsilon}}_{\mathrm{p},ni/n+1}. \tag{4.34}$$

It depends on the actual total strains, but only on plastic strains from previous stages or time steps. Its norm can be derived by exploiting the evolution equation in (4.11) together with the fact that the time integration parameter Θ, the time increment Δt, and the material property μ are always positive

$$\begin{aligned} \left\|\operatorname{dev}\left(\boldsymbol{\sigma}^{k,\mathrm{trial}}_{ni/n+1}\right)\right\| &= \left\|\operatorname{dev}\left(\boldsymbol{\sigma}^{k}_{ni/n+1}\right) + 2\mu\; \Delta t\; \Theta\; \dot{\boldsymbol{\varepsilon}}_{\mathrm{p},ni/n+1}\right\| = \\ &= \left\| \frac{\operatorname{dev}\left(\boldsymbol{\sigma}^{k}_{ni/n+1}\right)}{\left\|\operatorname{dev}\left(\boldsymbol{\sigma}^{k}_{ni/n+1}\right)\right\|} \left[\left\|\operatorname{dev}\left(\boldsymbol{\sigma}^{k}_{ni/n+1}\right)\right\| + 2\mu\; \Delta t\; \Theta \lambda_{ni/n+1}\right] \right\| = \\ &= \left\|\operatorname{dev}\left(\boldsymbol{\sigma}^{k}_{ni/n+1}\right)\right\| + 2\mu\; \Delta t\; \Theta \lambda_{ni/n+1}. \end{aligned} \tag{4.35}$$

Additionally, Equation (4.34) is recast into

$$\begin{aligned} \operatorname{dev}\left(\boldsymbol{\sigma}^{k,\mathrm{trial}}_{ni/n+1}\right) &= \left[\left\|\operatorname{dev}\left(\boldsymbol{\sigma}^{k}_{ni/n+1}\right)\right\| + 2\mu\; \Delta t\; \Theta \lambda_{ni/n+1}\right] \frac{\operatorname{dev}\left(\boldsymbol{\sigma}^{k}_{ni/n+1}\right)}{\left\|\operatorname{dev}\left(\boldsymbol{\sigma}^{k}_{ni/n+1}\right)\right\|} = \\ &= \left\|\operatorname{dev}\left(\boldsymbol{\sigma}^{k,\mathrm{trial}}_{ni/n+1}\right)\right\| \frac{\operatorname{dev}\left(\boldsymbol{\sigma}^{k}_{ni/n+1}\right)}{\left\|\operatorname{dev}\left(\boldsymbol{\sigma}^{k}_{ni/n+1}\right)\right\|} \end{aligned} \tag{4.36}$$

using the evolution equation in (4.11) and the link between the norms in (4.35), to obtain the definition

$$\boldsymbol{n}^{k}_{\mathrm{p}} \coloneqq \frac{\operatorname{dev}\left(\boldsymbol{\sigma}^{k}_{ni/n+1}\right)}{\left\|\operatorname{dev}\left(\boldsymbol{\sigma}^{k}_{ni/n+1}\right)\right\|} = \frac{\operatorname{dev}\left(\boldsymbol{\sigma}^{k,\mathrm{trial}}_{ni/n+1}\right)}{\left\|\operatorname{dev}\left(\boldsymbol{\sigma}^{k,\mathrm{trial}}_{ni/n+1}\right)\right\|}. \tag{4.37}$$

Hence, the plastic strains do not only evolve normal to the yield surface - as the trial state lies in that direction too. For a further geometric interpretation see (Han and Reddy, 1999; Simo and Hughes, 1997). By computing the yield function in (4.4) at the trial state

$$f^{\text{trial}}(\boldsymbol{\sigma}^{k,\text{trial}}_{ni/n+1}) = \left\| \text{dev}\left(\boldsymbol{\sigma}^{k,\text{trial}}_{ni/n+1}\right)\right\| - \sqrt{\frac{2}{3}}\sigma_{\text{y}} \qquad \text{with} \qquad \sigma_{\text{y}} > 0 \quad (4.38)$$

a criterion for the switching point between elastic and plastic behavior is established. If the difference between the current total strains and the previous plastic strains leads to a negative value of the trial yield function $f^{\text{trial}}(\boldsymbol{\sigma}^{k,\text{trial}}_{ni/n+1}) < 0$, elastic properties prevail. Thus, the plastic strains, their rates, the stress state, and the algorithmic constitutive tensor can be determined by

$$\begin{aligned}
\dot{\boldsymbol{\varepsilon}}_{\text{p},ni/n+1} &= \mathbf{0}, \\
\boldsymbol{\varepsilon}_{\text{p},ni/n+1} &= \tilde{\boldsymbol{\varepsilon}}_{\text{p},ni/n}, \\
\text{dev}\left(\boldsymbol{\sigma}^{k}_{ni/n+1}\right) &= \text{dev}\left(\boldsymbol{\sigma}^{k,\text{trial}}_{ni/n+1}\right), \\
\boldsymbol{\sigma}^{k}_{ni/n+1} &= \frac{3\kappa + 2\mu}{3}\text{tr}\left(\boldsymbol{\varepsilon}^{e,k}_{ni/n+1}\right)\boldsymbol{I} + \text{dev}\left(\boldsymbol{\sigma}^{k}_{ni/n+1}\right), \\
\mathbb{G} := \left.\frac{\partial \boldsymbol{\sigma}_{ni/n+1}}{\partial \boldsymbol{\varepsilon}_{ni/n+1}}\right|_{k} &= \mathbb{C}_{\text{e}}.
\end{aligned} \quad (4.39)$$

For values of the trial yield function that are greater or equal to zero $f^{\text{trial}}(\boldsymbol{\sigma}^{k,\text{trial}}_{ni/n+1}) \geq 0$, the real stress state is calculated by projecting the trial state back onto the yield surface, cf. (Simo and Hughes, 1997). Consequently, the current stress state $\boldsymbol{\sigma}^{k}_{ni/n+1}$ is situated on the yield function. Taking advantage of the connection between the distinct stress state norms in (4.35) leads to the relationship

$$f(\boldsymbol{\sigma}^{k}_{ni/n+1}) = \left\| \text{dev}\left(\boldsymbol{\sigma}^{k,\text{trial}}_{ni/n+1}\right)\right\| - 2\mu\ \Delta t\ \Theta\lambda_{ni/n+1} - \sqrt{\frac{2}{3}}\sigma_{\text{y}} = 0. \quad (4.40)$$

The Lagrange multiplier can, henceforth, be denoted in the explicit form

$$\lambda_{ni/n+1} = \frac{\left\| \text{dev}\left(\boldsymbol{\sigma}^{k,\text{trial}}_{ni/n+1}\right)\right\| - \sqrt{\frac{2}{3}}\sigma_{\text{y}}}{2\mu\ \Delta t\ \Theta}. \quad (4.41)$$

Accordingly, it is assured that at each stage t_{ni} or at each time step t_{n+1}, where the semidiscrete balance equation in (4.28) or (4.29) is assessed, the resulting stress state is an admissible one included in the set $\mathcal{S}$, cf. (Ellsiepen and Hartmann, 2001). It should be remarked that the last stage of the applied stiffly accurate diagonally implicit Runge-Kutta schemes is identical to the end of the time step. In the case of a more complicated yield function, Equation (4.40) might be solved using a local Newton-Raphson scheme, cf. (Simo, 1998; Simo and Hughes, 1997). Ultimately, the plastic strains, their time derivatives, the stress state, and the algorithmic

constitutive tensor can be determined by

$$
\begin{aligned}
\dot{\boldsymbol{\varepsilon}}_{\mathrm{p},ni/n+1} &= \lambda_{ni/n+1}\, \boldsymbol{n}_{\mathrm{p}}^{k},\\
\boldsymbol{\varepsilon}_{\mathrm{p},ni/n+1} &= \tilde{\boldsymbol{\varepsilon}}_{\mathrm{p},ni/n} + \Delta t\, \Theta \dot{\boldsymbol{\varepsilon}}_{\mathrm{p},ni/n+1},\\
\operatorname{dev}\left(\boldsymbol{\sigma}_{ni/n+1}^{k}\right) &= \operatorname{dev}\left(\boldsymbol{\sigma}_{ni/n+1}^{k,\mathrm{trial}}\right) - 2\mu\, \Delta t\, \Theta \lambda_{ni/n+1} \boldsymbol{n}_{\mathrm{p}}^{k},\\
\boldsymbol{\sigma}_{ni/n+1}^{k} &= \frac{3\kappa + 2\mu}{3} \operatorname{tr}\left(\boldsymbol{\varepsilon}_{ni/n+1}^{e,k}\right) \boldsymbol{I} + \operatorname{dev}\left(\boldsymbol{\sigma}_{ni/n+1}^{k}\right),\\
\mathbb{G} &= \frac{3\kappa + 2\mu}{3}\, \boldsymbol{I} \otimes \boldsymbol{I} + \left[2\mu - \frac{4\mu^2\, \Delta t\, \Theta \lambda_{ni/n+1}}{\left\| \operatorname{dev}\left(\boldsymbol{\sigma}_{ni/n+1}^{k,\mathrm{trial}}\right)\right\|}\right] \left[\mathbb{I} - \frac{1}{3}\boldsymbol{I} \otimes \boldsymbol{I} - \boldsymbol{n}_{\mathrm{p}}^{k} \otimes \boldsymbol{n}_{\mathrm{p}}^{k}\right].
\end{aligned}
$$

4.1.3.4.2. Viscoplasticity: Newmark's method and DIRK Schemes

If viscoplastic effects are considered instead of elastoplastic ones, Equations (4.30)-(4.38) can be applied identically. In the elastic case for negative values of the trial yield function $f^{\mathrm{trial}}(\boldsymbol{\sigma}_{ni/n+1}^{k,\mathrm{trial}})$, even Equation (4.39) remains valid. However, for the case $f^{\mathrm{trial}}(\boldsymbol{\sigma}_{ni/n+1}^{k,\mathrm{trial}}) \geq 0$, the Lagrange multiplier has to be determined following Equation $(4.18)_2$. Exploiting the connection between the different stress state norms in (4.35) results in

$$
\lambda_{ni/n+1} = \frac{\left\| \operatorname{dev}\left(\boldsymbol{\sigma}_{ni/n+1}^{k,\mathrm{trial}}\right)\right\| - \sqrt{\frac{2}{3}}\sigma_{\mathrm{y}}}{\chi + 2\mu\, \Delta t\, \Theta}. \tag{4.42}
$$

With the Lagrange multiplier in (4.42), stress states outside the yield surface are permitted, as is common in the scope of the viscoplastic theory. Furthermore, it can be recognized that for $\chi = 0$ the elastoplastic multiplier in (4.41) is obtained. Ultimately, the viscoplastic strains, their time derivatives, the stress state, and the algorithmic constitutive tensor can be determined by

$$
\begin{aligned}
\dot{\boldsymbol{\varepsilon}}_{\mathrm{p},ni/n+1} &= \lambda_{ni/n+1}\, \boldsymbol{n}_{\mathrm{p}}^{k},\\
\boldsymbol{\varepsilon}_{\mathrm{p},ni/n+1} &= \tilde{\boldsymbol{\varepsilon}}_{\mathrm{p},ni/n} + \Delta t\, \Theta \dot{\boldsymbol{\varepsilon}}_{\mathrm{p},ni/n+1},\\
\operatorname{dev}\left(\boldsymbol{\sigma}_{ni/n+1}^{k}\right) &= \operatorname{dev}\left(\boldsymbol{\sigma}_{ni/n+1}^{k,\mathrm{trial}}\right) - 2\mu\, \Delta t\, \Theta \lambda_{ni/n+1} \boldsymbol{n}_{\mathrm{p}}^{k},\\
\boldsymbol{\sigma}_{ni/n+1}^{k} &= \frac{3\kappa + 2\mu}{3} \operatorname{tr}\left(\boldsymbol{\varepsilon}_{ni/n+1}^{e,k}\right) \boldsymbol{I} + \operatorname{dev}\left(\boldsymbol{\sigma}_{ni/n+1}^{k}\right),\\
\mathbb{G} &= \frac{3\kappa + 2\mu}{3}\, \boldsymbol{I} \otimes \boldsymbol{I} + \left[2\mu - \frac{4\mu^2\, \Delta t\, \Theta \lambda_{ni/n+1}}{\left\| \operatorname{dev}\left(\boldsymbol{\sigma}_{ni/n+1}^{k,\mathrm{trial}}\right)\right\|}\right] \left[\mathbb{I} - \frac{1}{3}\boldsymbol{I} \otimes \boldsymbol{I}\right] -\\
&\quad - 2\mu \left[\frac{2\mu \Delta t\, \Theta}{\chi + 2\mu \Delta t\, \Theta} + \frac{2\mu\, \Delta t\, \Theta \lambda_{ni/n+1}}{\left\| \operatorname{dev}\left(\boldsymbol{\sigma}_{ni/n+1}^{k,\mathrm{trial}}\right)\right\|}\right] \boldsymbol{n}_{\mathrm{p}}^{k} \otimes \boldsymbol{n}_{\mathrm{p}}^{k}.
\end{aligned} \tag{4.43}
$$

Figure 4.2 shows an algorithmic implementation of the general elastoplastic and viscoplastic problem concerning stiffly accurate diagonally implicit Runge-Kutta schemes or the Newmark method.

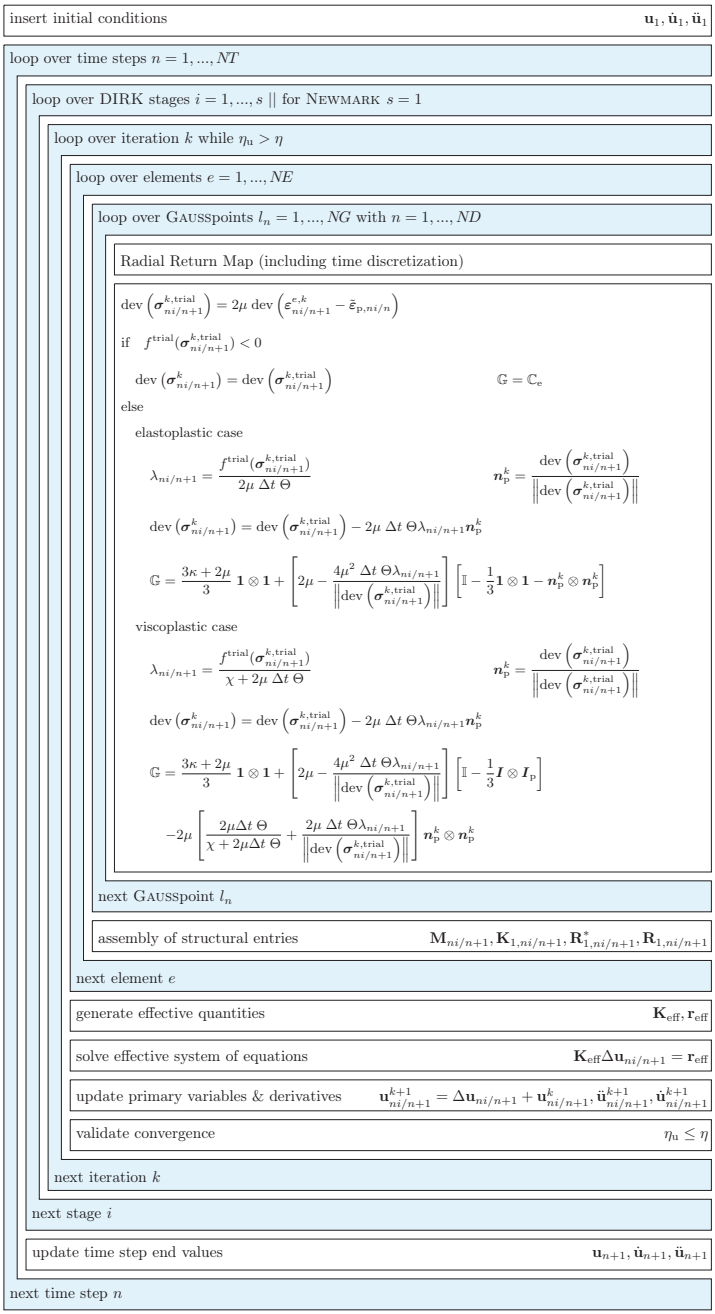

Figure 4.2.: Classical algorithm scheme involving DIRK schemes or the NEWMARK method

4.1.4. Elastoplasticity vs. Viscoplasticity

For a better understanding of elastoplastic and viscoplastic phenomena as well as their differences, the previously described material models and their classical implementations are analyzed with the help of a one-dimensional example. Both material models are compared concerning their local material behavior without considering the balance of linear momentum. This can be done since the balance of linear momentum describes the movement of all continuum mechanical bodies in general. For its evaluation, an arbitrary link between stresses and strains can be considered. The difficulty arising in the implementation of both models is that, due to the idea of defining a material that has a memory, non-smooth or rate-type equations have to be taken into account. Hence, strategies to transform these equations into adequate stress-strain relations have to be employed. For the comparison, a uniaxial stress state with the LAMÉ parameter $\kappa = 0$ is assumed. Thus, the stress, the strain, and the plastic strain tensor have the following structure, cf. (Schreiber, 1997)

$$\boldsymbol{\sigma} = \begin{bmatrix} \sigma_{11} & 0 & 0 \\ 0 & 0 & 0 \\ 0 & 0 & 0 \end{bmatrix} \qquad \boldsymbol{\varepsilon} = \begin{bmatrix} \varepsilon_{11} & 0 & 0 \\ 0 & \varepsilon_{22} & 0 \\ 0 & 0 & \varepsilon_{33} \end{bmatrix} \qquad \boldsymbol{\varepsilon}_{\mathrm{p}} = \begin{bmatrix} \varepsilon_{\mathrm{p},11} & 0 & 0 \\ 0 & -\frac{1}{2}\varepsilon_{\mathrm{p},11} & 0 \\ 0 & 0 & -\frac{1}{2}\varepsilon_{\mathrm{p},11} \end{bmatrix}.$$

With these simplifications, the VON MISES yield function in Equation (4.4) can be recast into

$$f(\sigma_{11}) = \sqrt{\frac{2}{3}}|\sigma_{11}| - \sqrt{\frac{2}{3}}\sigma_{\mathrm{y}} \qquad \text{with} \qquad \sigma_{\mathrm{y}} > 0.$$

Additionally, the internal energy can be reformulated into

$$e = \mu \left[\varepsilon_{11} - \varepsilon_{\mathrm{p},11}\right]^2.$$

Evaluating the dissipation inequality in (4.7) for the one-dimensional case leads to the material laws

$$\sigma_{11} = 2\mu \left[\varepsilon_{11} - \varepsilon_{\mathrm{p},11}\right] \qquad \dot{\varepsilon}_{\mathrm{p},11} = \sqrt{\frac{2}{3}}\lambda \,\mathrm{sgn}\left(\sigma_{11}\right), \quad (4.44)$$

where $\mathrm{sgn}\left(\bullet\right)$ refers to the sign function. In the elastoplastic case, the KARUSH-KUHN-TUCKER conditions

$$\lambda \geq 0, \qquad f(\sigma_{11}) \leq 0, \qquad \lambda f(\sigma_{11}) = 0$$

have to be fulfilled and the LAGRANGE multiplier is determined to

$$\lambda = \sqrt{\frac{3}{2}}\mathrm{sgn}\left(\sigma_{11}\right)\dot{\varepsilon}_{11}, \quad (4.45)$$

using the consistency condition in (4.13). In contrast, in the viscoplastic case, the LAGRANGE multiplier is prescribed explicitly by

$$\lambda = \frac{1}{\chi}\langle f(\sigma_{11})\rangle, \quad (4.46)$$

based on Equation $(4.18)_2$. Inserting Equations (4.45) as well as (4.46) into the material laws or the respective time derivative in (4.44) serves as a basis for the comparison in Table 4.1. Therein, two main aspects become apparent. First, as was already shown for the general three-dimensional case in Sections 4.1.1 and 4.1.2, the rate-type constitutive equation for the elastoplastic model

shows no dependency on the strain rate within the constitutive factor $C_\mathrm{p} \neq C_\mathrm{p}(\dot{\varepsilon}_{11})$. In this case, the time can hence be replaced by any other monotonous function τ

$$\frac{d\sigma_{11}}{dt} = \frac{\partial\sigma_{11}}{\partial\tau}\frac{\partial\tau}{\partial t} = C_\mathrm{p}\frac{\partial\varepsilon_{11}}{\partial\tau}\frac{\partial\tau}{\partial t} \qquad => \qquad \frac{\partial\sigma_{11}}{\partial\tau} = C_\mathrm{p}\frac{\partial\varepsilon_{11}}{\partial\tau}\,.$$

This is the reason why elastoplasticity is also denoted as rate-independent plasticity. In the viscoplastic case, $C_\mathrm{p} = C_\mathrm{p}(\dot{\varepsilon}_{11})$ holds and, thus, the included time derivatives pertain their physical meaning. The result is a rate-dependent model.

Table 4.1.: Comparison of elastoplastic and elastoviscoplastic characteristics

	elastoplasticity	elastoviscoplasticity
evolution equation	$\dot{\varepsilon}_{\mathrm{p},11} = \dot{\varepsilon}_{11}$	$\dot{\varepsilon}_{\mathrm{p},11} = \sqrt{\frac{2}{3}}\frac{\operatorname{sgn}(\sigma_{11})}{\chi}\langle f(\sigma_{11})\rangle$
rate-type constitutive equation	$\dot{\sigma}_{11} = C_\mathrm{p}\,\dot{\varepsilon}_{11}$	
constitutive factor	$C_\mathrm{p} \coloneqq \begin{cases} 2\mu & \text{for} \quad \lambda = 0 \\ 0 & \text{for} \quad \lambda > 0 \end{cases}$	$C_\mathrm{p} \coloneqq \begin{cases} 2\mu & \text{for} \quad \lambda = 0 \\ 2\mu\left[1 - \sqrt{\frac{2}{3}}\frac{\operatorname{sgn}(\sigma_{11})}{\chi}\frac{\langle f(\sigma_{11})\rangle}{\dot{\varepsilon}_{11}}\right] & \text{for} \quad \lambda > 0 \end{cases}$

The second difference between plasticity and viscoplasticity, which can be observed within the one-dimensional example, is that the stress rate is zero in the plastic case. Accordingly, for ideal plasticity an increase in the stresses is not possible after yielding. In the viscoplastic regime, this is not the case. There, the stresses may grow after yielding, because of the fact that stress states beyond the yield surface are permitted but penalized by the parameter χ. The same behavior can be observed in the three-dimensional case if the symmetry of the elastic constitutive tensor $\mathbb{C}_\mathrm{e}$ is taken into account.

Table 4.2.: Comparison of the radial return map implementation of plasticity and viscoplasticity

	elastoplasticity	elastoviscoplasticity
(visco)plastic strain	$\varepsilon_{\mathrm{p},11,n+1} = \dot{\varepsilon}_{\mathrm{p},11,n+1}\Delta t + \varepsilon_{\mathrm{p},11,n} = \sqrt{\frac{2}{3}}\lambda_{n+1}\frac{\sigma_{11,n+1}}{\lvert\sigma_{11,n+1}\rvert}\Delta t + \varepsilon_{\mathrm{p},11,n}$	
trial state	$\lvert\sigma^{\mathrm{trial}}_{11,n+1}\rvert = \lvert\sigma_{11,n+1}\rvert + 2\mu\sqrt{\frac{2}{3}}\Delta t\lambda_{n+1}$	
(visco)plastic strain direction	$\frac{\sigma^{\mathrm{trial}}_{11,n+1}}{\lvert\sigma^{\mathrm{trial}}_{11,n+1}\rvert} = \frac{\sigma_{11,n+1}}{\lvert\sigma_{11,n+1}\rvert}$	
Lagrange multiplier	$\lambda_{n+1} = \frac{\lvert\sigma^{\mathrm{trial}}_{11,n+1}\rvert - \sigma_\mathrm{y}}{2\mu\sqrt{\frac{2}{3}}\Delta t}$	$\lambda_{n+1} = \frac{\lvert\sigma^{\mathrm{trial}}_{11,n+1}\rvert - \sigma_\mathrm{y}}{\sqrt{\frac{3}{2}}\chi + 2\mu\sqrt{\frac{2}{3}}\Delta t}$

In order to investigate not only the rates involved in elastoplasticity and viscoplasticity but also their discrete counterparts, the radial return map presented in Section 4.1.3.4 is elaborated

using the backward EULER scheme. Equations (4.31), (4.34), (4.35), (4.37), (4.38), (4.41), and (4.42) are adapted to fit the one-dimensional case. The main results are depicted in Table 4.2, where the rate-independence of elastoplasticity becomes apparent again. Inserting the LAGRANGE multiplier into the plastic strain relation yields a formulation that is independent of the time increment in the plastic case. Within viscoplasticity, however, the time increment cannot be cancelled out in the viscoplastic strain formulation due to the parameter χ. However, if this parameter is small, the elastoplastic formulation is retrieved. Figure 4.3 shows the resulting differences between the models for a one-dimensional example where the LAMÉ parameter $\mu = 1 \cdot 10^5$ N/mm^2 and the yield stress $\sigma_y = 900$ N/mm^2 are set. Moreover, the strain $\varepsilon_{11} = 0.08 \sin(\omega t)$ is prescribed, whereby the parameter ω is varied to simulate distinct strain rates. As initial condition for the plastic strain $\varepsilon_{p,11,1} = 0$ is assumed. For all cases, a time step size of $\Delta t = 1 \cdot 10^{-6}$ s is chosen and a time span $T = 0.005$ s is computed.

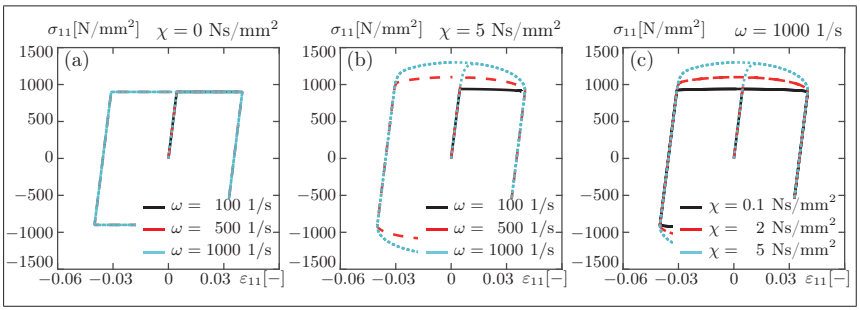

Figure 4.3.: Discrepancies between plasticity and viscoplasticity in the stress-strain curve: (a) Variation of the strain rate in plasticity, (b) Variation of the strain rate in viscoplasticity, (c) Variation of the viscosity parameter in viscoplasticity

Figure 4.3 (a) depicts stress-strain curves for the plasticity model with various strain rates. Since the same time span is simulated for all strain rates, the graphs end at distinct strains. Nevertheless, there are apparently no further discrepancies apart from these deviations. This is due to the rate-independence of the formulation. Analogously, Figure 4.3 (b) depicts stress-strain curves for the viscoplastic model with a viscosity parameter $\chi = 5$ Ns/mm^2. Here, differences can be seen in the viscoplastic zone. Higher strain rates lead to higher stresses well above the yield stress, and it is only for increasing strains that the curves tend to fall back to reach the yield stress. In Figure 4.3 (c), the viscoplastic approach is again applied for a constant strain rate $\omega = 1000$ 1/s, and the viscosity parameter is varied. As predicted, if the viscosity parameter decreases the stress-strain curves assimilate to the elastoplastic case.

4.2. Variational Multifield Approach

Section 4.1 focuses on a classical approach towards elasto(visco)plasticity. Therein, the principle of virtual work is exploited to generate a purely displacement-based weak form of the balance of linear momentum. The material laws, accounting for elasto(visco)plastic properties, are considered implicitly via the evaluation of the appearing integrals on GAUSS-LEGENDRE point level. Thus, the standard solution procedure covers the structural as well as the integral level, each characterized by appropriate methods and time integration schemes. Here, the difficulty is to establish a proper coupling between the two levels of time integration.

In contrast, this section is devoted to derive a novel approach that enables the usage of a wide class of higher order accurate time integration schemes for the balance of linear momentum and the material laws within one single-level time integration scheme. Therefore, a variational procedure is developed where the displacements form only one part of the unknown field variables.

Variational principles rest on the idea that a physical system can be described by a specific functional and its stationary conditions achieved by differentiating this functional, cf. (Euler, 1894; Finlayson and Scriven, 1966; Hamilton, 1834, 1835; Jeltsch-Fricker, 2007; Lagrange, 1894; Tonti, 1984; Zeidler, 1985). In the scope of plasticity-related considerations, these properties are taken into account to different degrees. In (Mosler and Bruhns, 2010; Ortiz and Stainier, 1999; Stainier, 2013) minimization principles are established to construct update procedures for the material laws. On the structural level, stationarity conditions can be exploited to generate weak forms. Equation (4.23) of the classical approach can be seen as one example of HAMILTON's variational principle. If the considered functional depends on multiple variables and, hence, its variation involves distinct stationary conditions, a variety of further weak forms can be deduced. For plasticity or viscoplasticity, this is performed in (Comi and Perego, 1991, 1995; Hackl, 1997; Miehe, 2011; Simo and Hughes, 1997; Simo et al., 1989). Such extended weak forms have also been used for mathematical analysis concerning error estimates or solvability aspects, cf. (Anzellotti and Luckhaus, 1987; Capurso and Maier, 1970; Chelmiński, 2001; Duvaut and Lions, 1972; Johnson, 1976; Schröder and Wiedemann, 2011; Suquet, 1978). Moreover, due to their consideration of multiple variables, variational principles build the framework for multifield finite element applications, where on the structural level more than one field variable is taken into account as unknown, cf. (Christensen, 2002; Hager and Wohlmuth, 2009; Miehe, 2011; Schröder and Wiedemann, 2011; Welschinger, 2011). In the following section, a physically motivated variational principle will be presented and extended to the elastoplastic as well as to the viscoplastic case, respectively. The resulting weak form will be exploited to derive a new numerical solution scheme for ideal elasto(visco)plasticity, enabling the simple usage of higher order accurate time integrators.

4.2.1. The Principle of JOURDAIN

In 1909, in the context of the analysis of point masses, JOURDAIN established a principle to fill the gap between D'ALEMBERT's principle of virtual work and GAUSS' principle of least constraints, cf. (Bremer, 1993; Jourdain, 1909; Piedbœuf, 1993). This principle is therefore often denoted as principle of JOURDAIN or principle of virtual power, cf. (Moon, 1998; Piedbœuf, 1993). Its adaptation to problems of continuum mechanics is performed in (Germain, 1972, 1973; Maugin, 1980), where the virtual power is generally defined by a continuous linear form consisting of forces and virtual velocities. Furthermore, it is assumed that the virtual power of all internal, external, and inertia forces is zero. As examples for the principle's application, micromorphic structures, higher order gradient continua, and electromagnetic continua are outlined. A distinct extension of the principle of JOURDAIN is carried out in (Yunt, 2014), where rigid body systems in conjunction with dissipative processes are investigated. Further, dissipative mechanisms in the regime of plasticity for continua are analyzed in (Miehe, 2011; Simo and Hughes, 1997; Simo et al., 1989), although only time-discrete variants of the principle of virtual power are evaluated there. In contrast to that, the next sections are devoted to deducing elasto(visco)plastic models by directly exploiting the principle of JOURDAIN and its rate-type characteristic. At the same time, this course of action allows to consider inertia effects together with a natural formulation of dissipative behavior. Thus, an altered initial boundary value problem is obtained, which facilitates the application of higher order accurate time discretization methods. First approaches in that direction are already presented in (Gleim et al., 2017; Schröder and Kuhl, 2015*a*,*b*).

4.2.1.1. The Principle of Virtual Power for Elastoplasticity

In order to construct the principle of JOURDAIN for dissipative continua, the first step is to consider the balance of energy

$$P(\dot{\boldsymbol{u}}, \dot{\boldsymbol{\varepsilon}}_{\mathrm{p}}, \boldsymbol{\sigma}, \lambda) = \dot{K} + \dot{E} + P^{*} + D = 0,$$

indicating that the total power P of a body $\mathcal{B}$ with domain Ω is zero, cf. (Altenbach, 2012; Yunt, 2014). The included variable K denotes the kinetic energy, the term E the internal energy, and P^{*} the power due to external forces. The quantity D represents a pseudopotential embodying dissipative effects, characterizing plastic deformations, amongst other things, cf. (Miehe, 2011; Yunt, 2014). Additionally, it is assumed that the total power P reaches a stationary point, whereby at the same time the prevalent stress state lies within the VON MISES yield surface of Equation (4.4). This approach is similar to the one followed in (Miehe, 2012), enhanced by acknowledging inertia effects. Hence, the stationarity problem

$$\operatorname*{stat}_{\dot{\boldsymbol{u}}, \dot{\boldsymbol{\varepsilon}}_{\mathrm{p}}} \sup_{\boldsymbol{\sigma}} \inf_{\lambda \geq 0} P(\dot{\boldsymbol{u}}, \dot{\boldsymbol{\varepsilon}}_{\mathrm{p}}, \boldsymbol{\sigma}, \lambda), \tag{4.47}$$

with the balance of energy as a rate-type functional, is postulated to hold. In the case of a general elastoplastic continuum, the listed quantities are specified by

$$\dot{K} = \int_{\Omega} \rho_0 \ddot{\boldsymbol{u}} \cdot \dot{\boldsymbol{u}} \, dV, \tag{4.48}$$

$$\dot{E} = \int_{\Omega} \dot{e}(\boldsymbol{\varepsilon}, \boldsymbol{\varepsilon}_{\mathrm{p}}) \, dV = \int_{\Omega} [\dot{\boldsymbol{\varepsilon}} \colon \mathbb{C}_{\mathrm{e}} \colon [\boldsymbol{\varepsilon} - \boldsymbol{\varepsilon}_{\mathrm{p}}] + \dot{\boldsymbol{\varepsilon}}_{\mathrm{p}} \colon \mathbb{C}_{\mathrm{e}} \colon [\boldsymbol{\varepsilon}_{\mathrm{p}} - \boldsymbol{\varepsilon}]] \, dV, \tag{4.49}$$

$$P^{*} = -\int_{\Omega} \rho_0 \dot{\boldsymbol{u}} \cdot \boldsymbol{f} \, dV - \int_{\Gamma} \dot{\boldsymbol{u}} \cdot \boldsymbol{t}^{*} \, dA, \tag{4.50}$$

$$D = \int_{\Omega} \boldsymbol{\sigma} \colon \dot{\boldsymbol{\varepsilon}}_{\mathrm{p}} \, dV - \int_{\Omega} \lambda f(\boldsymbol{\sigma}) \, dV \qquad \text{with } \lambda \geq 0. \tag{4.51}$$

Thereby, the used volume-specific energy e in (4.49) is identical to the one formulated in Equation (4.5) of the classical approach. A closer look at the expression D reveals that it includes the yield function as a sort of inequality constraint within the LAGRANGE multiplier theory, cf. (Burger, 2003; Dür and Martin, 2005; Ito and Kunisch, 2008; Zeidler, 1985). Furthermore, it possesses a respective analogue within the conventional procedure. It is the integral version of the postulate of maximum plastic work (4.9). Hence, for ideal associative elastoplasticity, the depicted pseudopotential actually serves as a measure for the internal dissipation of a system in the context of the dissipation inequality $(2.27)_2$. For further details on this topic see (Hildebrand, 2013; Miehe, 2002; Miehe et al., 2002).

The concept of formulating the dissipation pseudopotential in this way is also followed in (Eve et al., 1990; Han and Reddy, 1999; Miehe, 2011; Reddy and Martin, 1994; Simo and Miehe, 1992; Welschinger, 2011). Additional pseudopotential assumptions are discussed in (Eve et al., 1990; Han and Reddy, 1999; Reddy and Martin, 1994) to derive a variety of formulations within elastoplasticity. Even in (Halphen and Nguyen, 1975; Moreau, 1970), the idea of using potential functions for plastic and viscoplastic effects is already prevalent.

In the next step, a reformulation of (4.47) into

$$\underset{\dot{\boldsymbol{u}},\dot{\boldsymbol{\varepsilon}}_\mathrm{p}}{\mathrm{stat}}\ \sup_{\boldsymbol{\sigma}}\ \inf_{\lambda\geq 0}\ P(\dot{\boldsymbol{u}},\dot{\boldsymbol{\varepsilon}}_\mathrm{p},\boldsymbol{\sigma},\lambda)=\underset{\dot{\boldsymbol{u}},\dot{\boldsymbol{\varepsilon}}_\mathrm{p}}{\mathrm{stat}}\ \sup_{\boldsymbol{\sigma}}\ \inf_{\lambda}\left[\dot{K}+\dot{E}+P^*+\int_\Omega \boldsymbol{\sigma}\colon\dot{\boldsymbol{\varepsilon}}_\mathrm{p}\,dV-\int_\Omega[\lambda f(\boldsymbol{\sigma})-\psi_\mathrm{I}(\lambda)]\,dV\right], \tag{4.52}$$

is carried out, cf. (Burger, 2003; Zeidler, 1985), exploiting the indicator function

$$\psi_\mathrm{I}(\lambda)=\begin{cases}0 & \text{for } \lambda\geq 0\\ \infty & \text{for } \lambda<0.\end{cases} \tag{4.53}$$

In order to determine the solution of Problem (4.52), the course of action in (Burger, 2003; Rockafellar, 1970; Zeidler, 1985) is followed defining the stationarity condition

$$0\in\partial P\,(\dot{\boldsymbol{u}},\dot{\boldsymbol{\varepsilon}}_\mathrm{p},\boldsymbol{\sigma},\lambda)\coloneqq\partial_{\dot{\boldsymbol{u}}}P+\partial_{\dot{\boldsymbol{\varepsilon}}_\mathrm{p}}P+\partial_{\boldsymbol{\sigma}}P+\partial_{\lambda}P \tag{4.54}$$

of the virtual power ∂P. The operator $\partial_{(\bullet)}$ represents the subdifferential or superdifferential with regard to the respective quantity. The search for an infimum or a supremum and, hence, the treatment of convex or concave functions is the difference between both formulations, cf. (Rockafellar, 1970). For the cases in (4.54) where only stationarity is required, the functionals are Gâteaux differentiable with respect to the necessary quantity and, hence, no distinction between the super- and subdifferential has to be made.

An alternative interpretation of the inclusions in (4.54) can be given by considering the impressions in (Germain, 1973; Maugin, 1980). There, the virtual power of a system is directly stated and assumed to be zero. Thus, an evaluation of the stationary conditions of a rate-type functional is not necessary. Although inertia effects are taken into account in this approach, dissipative mechanisms are neglected. For the isothermal case of linear elasticity, the similarity between both procedures is shown in (Germain, 1973). Special care has to be taken in non-isothermal processes, cf. (Germain, 1973; Maugin, 1980). Adaptations in that direction as well as extensions to dissipative media are considered in (Junker et al., 2013; Stainier, 2013). Therein, material laws are deduced using optimization strategies on local level. The quasi-static balance laws are treated separately. However, such thermal modifications are out of the scope of this thesis.

Before the virtual power is determined, the subdifferential of an arbitrary, convex functional $k(x)$ on the space X is defined by

$$\partial k(x)=\{x^*\in X'\colon k(y)\geq k(x)+\langle x^*,y-x\rangle\quad\forall\, y\in X\}, \tag{4.55}$$

where X is assumed to be a proper normed vector space with its topological dual X' with the corresponding scalar product $\langle\bullet,\bullet\rangle$. If the functional $k(x)$ is now considered to be concave, the superdifferential can be established analogously to Inequality (4.55), but reversing the inequality sign, cf. (Rockafellar, 2001). For detailed explanations on sub- and superdifferentials and related topics see (Han and Reddy, 1999; Rockafellar, 1970; Zeidler, 1985). In the following, it will be assumed that the necessary conditions for Definition (4.55) are fulfilled. Hence, the spaces can be chosen appropriately and the functionals possess the demanded properties. If, furthermore, the Gâteaux Derivative (3.22) of the functional $k(x)$ exists, then

$$\partial k(x)=\{\mathrm{D}_x k(x)\}=:\delta k(x) \tag{4.56}$$

has to hold, cf. (Han and Reddy, 1999; Zeidler, 1985). The application of (4.55)-(4.56) to the

rate-type functional in (4.52) yields in a first step

$$\int_\Omega \rho_0 \delta\dot{\boldsymbol{u}} \cdot \ddot{\boldsymbol{u}}\, dV + \int_\Omega [\delta\dot{\boldsymbol{\varepsilon}} : \mathbb{C}_\mathrm{e} : [\boldsymbol{\varepsilon} - \boldsymbol{\varepsilon}_\mathrm{p}]]\, dV - \int_\Omega \rho_0 \delta\dot{\boldsymbol{u}} \cdot \boldsymbol{f}\, dV - \int_{\Gamma_{t^*}} \delta\dot{\boldsymbol{u}} \cdot \boldsymbol{t}^*\, dA = 0, \tag{4.57}$$

$$\int_\Omega [\delta\dot{\boldsymbol{\varepsilon}}_\mathrm{p} : \mathbb{C}_\mathrm{e} : [\boldsymbol{\varepsilon}_\mathrm{p} - \boldsymbol{\varepsilon}] + \delta\dot{\boldsymbol{\varepsilon}}_\mathrm{p} : \boldsymbol{\sigma}]\, dV = 0, \tag{4.58}$$

$$\int_\Omega [\lambda\, f(\delta\boldsymbol{\sigma}) - \lambda\, f(\boldsymbol{\sigma})]\, dV - \int_\Omega \dot{\boldsymbol{\varepsilon}}_\mathrm{p} : [\delta\boldsymbol{\sigma} - \boldsymbol{\sigma}]\, dV \geq 0, \tag{4.59}$$

$$\int_\Omega [\psi_\mathrm{I}(\delta\lambda) - \psi_\mathrm{I}(\lambda)]\, dV - \int_\Omega f(\boldsymbol{\sigma})\, [\delta\lambda - \lambda]\, dV \geq 0, \tag{4.60}$$

whereby the symmetry of the elastic constitutive tensor $\mathbb{C}_\mathrm{e}$ is exploited together with the interchangeability of variation and differentiation. For a better numerical treatment, the obtained variational inequalities are reformulated. Therefore, their strong counterparts are derived. Applying the definition of the superdifferential following (4.55) to the Inequality (4.59) yields the inclusion

$$\dot{\boldsymbol{\varepsilon}}_\mathrm{p} \in \lambda\, \partial f(\boldsymbol{\sigma}), \tag{4.61}$$

while exploiting the properties of the indicator function in (4.53) and the subdifferential in (4.55) in the context of Inequality (4.60) leads to the abbreviated version

$$\int_\Omega f(\boldsymbol{\sigma})\, [\delta\lambda - \lambda]\, dV \leq 0 \qquad \forall \delta\lambda \geq 0, \lambda \geq 0. \tag{4.62}$$

Dividing the elastoplastic region Ω into a plastic subsection $\Omega_\mathrm{p} := \{\boldsymbol{X} | \lambda > 0\}$ and an elastic one $\Omega_\mathrm{e} := \{\boldsymbol{X} | \lambda = 0\}$, admits the two conclusions

$$\forall \delta\lambda \geq 0 \,\text{with}\, \delta\lambda = \lambda \,\text{on}\, \Omega_\mathrm{p} : \int_{\Omega_\mathrm{e}} f(\boldsymbol{\sigma}) \delta\lambda \leq 0, \tag{4.63}$$

$$\forall \delta\lambda \geq 0 \,\text{with}\, \delta\lambda = \lambda \,\text{on}\, \Omega_\mathrm{e} : \int_{\Omega_\mathrm{p}} f(\boldsymbol{\sigma})\, [\delta\lambda - \lambda] \leq 0. \tag{4.64}$$

From (4.63) it can be followed that $f(\boldsymbol{\sigma}) \leq 0$, $\lambda = 0$ and $\lambda f(\boldsymbol{\sigma}) = 0$ has to hold on Ω_e. On the contrary, (4.64) results in $f(\boldsymbol{\sigma}) = 0$, $\lambda > 0$ as well as $f(\boldsymbol{\sigma})\lambda = 0$ on Ω_p. Hence, the Karush-Kuhn-Tucker conditions $f(\boldsymbol{\sigma}) \leq 0$, $\lambda = 0, \lambda f(\boldsymbol{\sigma}) = 0$ are valid on the entire domain Ω. Their characteristics can be used to recast the Relationship (4.61) into

$$\dot{\boldsymbol{\varepsilon}}_\mathrm{p} := \begin{cases} \lambda \dfrac{\partial f(\boldsymbol{\sigma})}{\partial \boldsymbol{\sigma}} & \text{for } \|\mathrm{dev}\,(\boldsymbol{\sigma})\| \neq 0 \\ \{\boldsymbol{0}\} & \text{for } \|\mathrm{dev}\,(\boldsymbol{\sigma})\| = 0 \end{cases} \tag{4.65}$$

and, thus, transform the variational inequality in (4.59) into a variational equality. Finally, the

general elastoplastic problem can be described by

$$\int_\Omega \rho_0 \delta\dot{\boldsymbol{u}} \cdot \ddot{\boldsymbol{u}}\, dV + \int_\Omega [\delta\dot{\boldsymbol{\varepsilon}} : \mathbb{C}_\mathrm{e} : [\boldsymbol{\varepsilon} - \boldsymbol{\varepsilon}_\mathrm{p}]]\, dV - \int_\Omega \rho_0 \delta\dot{\boldsymbol{u}} \cdot \boldsymbol{f}\, dV - \int_{\Gamma_{t^*}} \delta\dot{\boldsymbol{u}} \cdot \boldsymbol{t}^*\, dA = 0, \tag{4.66}$$

$$\int_\Omega [\delta\dot{\boldsymbol{\varepsilon}}_\mathrm{p} : \mathbb{C}_\mathrm{e} : [\boldsymbol{\varepsilon}_\mathrm{p} - \boldsymbol{\varepsilon}] + \delta\dot{\boldsymbol{\varepsilon}}_\mathrm{p} : \boldsymbol{\sigma}]\, dV = 0, \tag{4.67}$$

$$\int_\Omega \left[\delta\boldsymbol{\sigma} : \dot{\boldsymbol{\varepsilon}}_\mathrm{p} - \lambda\delta\boldsymbol{\sigma} : \frac{\partial f(\boldsymbol{\sigma})}{\partial \boldsymbol{\sigma}}\right] dV = 0, \tag{4.68}$$

$$\int_\Omega f(\boldsymbol{\sigma})\, [\delta\lambda - \lambda]\, dV \leq 0, \tag{4.69}$$

with $\delta\lambda \geq 0, \lambda \geq 0$ and $\|\mathrm{dev}\,(\boldsymbol{\sigma})\| \neq 0$, if for $\mathrm{dev}\,(\boldsymbol{\sigma}) = \mathbf{0}$ the LAGRANGE multiplier λ is simply set to zero. To demonstrate the identity of the models derived by the principle of virtual power and those established in the classical approach, the weak forms in (4.66)-(4.69) are recast into their strong counterparts. This was already performed for (4.68)-(4.69), resulting in the Karush-Kuhn-Tucker conditions and the evolution equation in (4.65). They are equal to those settled within the classical approach in (4.11). Equation (4.67) can be recast by taking into account that the variations $\delta\dot{\boldsymbol{\varepsilon}}_\mathrm{p}$ are arbitrary as well as non zero. Applying the lemma of variational calculus yields the constitutive law in (4.8). Inserting this relationship into Equation (4.66), performing some tensor calculus and exploiting the divergence theorem

$$\int_\Omega \nabla_X \cdot [\boldsymbol{\sigma} \cdot \delta\dot{\boldsymbol{u}}]\, dV = \int_{\Gamma_{t^*}} \delta\dot{\boldsymbol{u}} \cdot \boldsymbol{\sigma} \cdot \boldsymbol{n}\, dA$$

results, together with the symmetry $\boldsymbol{\sigma} = \boldsymbol{\sigma}^\mathrm{T}$, in

$$\int_\Omega \rho_0 \delta\dot{\boldsymbol{u}} \cdot \ddot{\boldsymbol{u}}\, dV - \int_\Omega \delta\dot{\boldsymbol{u}} \cdot [\nabla_X \cdot \boldsymbol{\sigma}] + \int_{\Gamma_{t^*}} \delta\dot{\boldsymbol{u}} \cdot [\boldsymbol{\sigma} \cdot \boldsymbol{n} - \boldsymbol{t}^*]\, dA - \int_\Omega \rho_0 \delta\dot{\boldsymbol{u}} \cdot \boldsymbol{f}\, dV = 0.$$

Utilizing the lemma of variational calculus and considering that the variations $\delta\dot{\boldsymbol{u}}$ are arbitrary as well as non zero leads to the balance of linear momentum in $(2.27)_1$ and the NEUMANN boundary condition in $(4.1)_2$. Hence, identical strong formulations are obtained, although the weak forms of the classical and the variational multifield approach are completely different. In the latter, not only the balance of linear momentum is enforced in a weak sense, but also the material laws as well as the KARUSH-KUHN-TUCKER conditions. Thereby, the plastic strains, the stresses, and the LAGRANGE multiplier are introduced as additional unknown field quantities which have to be determined. Since this is achieved by exploiting variational methods, this alternative ansatz is denoted as the variational multifield approach.

The idea of demanding only a weak fulfillment of the yield condition was already applied to gradient plasticity, cf. (De Borst and Mühlhaus, 1992; Mühlhaus and Aifantis, 1991; Pamin, 1994). The weak consideration of further equations such as material laws or even hardening aspects in an incremental fashion is performed in (Comi and Perego, 1991, 1995; Miehe, 2011, 2012; Simo and Hughes, 1997; Simo et al., 1989; Welschinger, 2011) and the references therein. A time-continuous procedure containing rates is presented in (Hackl, 1997), but inertia terms are neglected there. Another approach to determine the weak forms in (4.66)-(4.69) could be an extension of HAMILTON'S principle. In (Kim et al., 2013), a RAYLEIGH dissipation term is

added. A proper redefinition of this addition could enable the derivation of the viscoplastic Equations (4.70)-(4.72) of the next chapter. Ways to consider variational inequalities or inclusions within HAMILTON'S principle are discussed in (Buliga, 2009; Leine and Aeberhard, 2008). These approaches could lead to an alternative derivation strategy compared to the principle of JOURDAIN.

However, in this thesis, the principle of virtual power will be followed up due to its intuitive evaluation process. The sole input argument for this variational approach is the formulation of the rate-type functional, all other equations or inequalities result automatically. A judgement concerning mathematical properties concerning distinct variational approaches is out of the scope of this thesis. Here, the focus lies on a systematic derivation strategy that takes dynamic effects into account. By choosing this rate-type formulation, the material laws are elevated on structural level. Thus, all sorts of equations containing time derivatives can be temporally discretized simultaneously, enabling a straightforward application of higher order accurate time integrators. The numerical realization can be carried out as described in **Chapter 3**. Special care has to be taken because of the introduced variational inequality, which is at the same time an algebraic inequality. Before this topic is treated in detail in Section 4.2.2, the next step is to find a viscoplastic extension of the multifield approach.

4.2.1.2. The Principle of Virtual Power for Elastoviscoplasticity

In the classical approach in Section 4.1.2, viscoplastic effects are considered by a regularization of the postulate of maximum plastic work. Thereby, the constraint established by the yield function is weakened by introducing a penalization term, leading to the internal dissipation in (4.15). A similar procedure is performed in the context of the variational multifield approach. As in the elastoplastic case, the stationarity problem in (4.47) is taken into account, whereby the kinetic energy, the internal energy, and the power due to external forces are formulated identical to Equations (4.48)-(4.50). The dissipative pseudopotential in (4.51), however, is adapted to

$$D = \int_{\Omega} \boldsymbol{\sigma} : \dot{\boldsymbol{\varepsilon}}_{\mathrm{p}} - \frac{1}{\chi} h(f(\boldsymbol{\sigma}))\, dV,$$

including the continuous differentiable function $h(f(\boldsymbol{\sigma}))$ as described in Equation (4.16) and the viscosity parameter χ. In the next step, it is again assumed that the physical state where the power within the elastoviscoplastic continuum reaches a stationary point is the preferable one, cf. (Miehe, 2011, 2012). Hence, the stationarity condition

$$0 \in \partial P\left(\dot{\boldsymbol{u}}, \dot{\boldsymbol{\varepsilon}}_{\mathrm{p}}, \boldsymbol{\sigma}\right) \coloneqq \partial_{\dot{\boldsymbol{u}}} P + \partial_{\dot{\boldsymbol{\varepsilon}}_{\mathrm{p}}} P + \partial_{\boldsymbol{\sigma}} P$$

is obtained. Due to the regularization in the pseudopotential, a smoothening effect is introduced - and the evaluation of a subdifferential with respect to λ as in the elastoplastic case becomes superfluous. The results are the weak forms

$$\int_{\Omega} \rho_0 \delta\dot{\boldsymbol{u}} \cdot \ddot{\boldsymbol{u}}\, dV + \int_{\Omega} \delta\dot{\boldsymbol{\varepsilon}} : \mathbb{C}_{\mathrm{e}} : \left[\boldsymbol{\varepsilon} - \boldsymbol{\varepsilon}_{\mathrm{p}}\right] dV - \int_{\Omega} \rho_0\, \delta\dot{\boldsymbol{u}} \cdot \boldsymbol{f}\, dV - \int_{\Gamma_{\mathrm{t}^*}} \delta\dot{\boldsymbol{u}} \cdot \boldsymbol{t}^*\, dA = 0, \tag{4.70}$$

$$\int_{\Omega} \left[\delta\dot{\boldsymbol{\varepsilon}}_{\mathrm{p}} : \mathbb{C}_{\mathrm{e}} : \left[\boldsymbol{\varepsilon}_{\mathrm{p}} - \boldsymbol{\varepsilon}\right] + \delta\dot{\boldsymbol{\varepsilon}}_{\mathrm{p}} : \boldsymbol{\sigma}\right] dV = 0, \tag{4.71}$$

$$\int_{\Omega} \left[\delta\boldsymbol{\sigma} : \dot{\boldsymbol{\varepsilon}}_{\mathrm{p}} - \delta\boldsymbol{\sigma} : \frac{1}{\chi} \left\langle f(\boldsymbol{\sigma}) \right\rangle \frac{\partial f(\boldsymbol{\sigma})}{\partial \boldsymbol{\sigma}}\right] dV = 0, \tag{4.72}$$

where $\langle f(\boldsymbol{\sigma})\rangle$ denotes the ramp function in (4.17). The critical point $\|\mathrm{dev}\,(\boldsymbol{\sigma})\| = 0$, where the superdifferential $\partial_\sigma f(\boldsymbol{\sigma})$ would actually be multivalued, is ruled out by the differentiability condition of the function $h(f(\boldsymbol{\sigma}))$ and the positivity of the yield stress $\sigma_\mathrm{y} > 0$.

In order to prove that the obtained model is identical to that of the classical approach, the weak forms in (4.70)-(4.72) are reformulated into their strong counterparts by following the same procedure as in Section 4.2.1.1. Equation (4.70) yields the balance of linear momentum in $(2.27)_1$ and the NEUMANN boundary condition in $(4.1)_2$. Equation (4.71) leads to the constitutive law in (4.8), and the Relationship (4.72) embodies the evolution equation in (4.18). Despite the distinct proceedings, the same strong forms are derived in the classical and the variational approach. The weak forms, however, are completely different.

4.2.2. Implementation Strategy for Multifield Elastoplasticity

By generalizing the principle of virtual power in order to include dissipative effects and by demanding that it results from the stationarity of a rate-type functional, a physically sound basis for the multifield formulation is created, cf. (Germain, 1973; Maugin, 1980; Miehe, 2012; Yunt, 2014). The consequent maintaining of the power type structure enables the treatment of material laws as balance equations, leading to an altered initial boundary value problem, see Figure 4.4. A changed numerical implementation is the consequence.

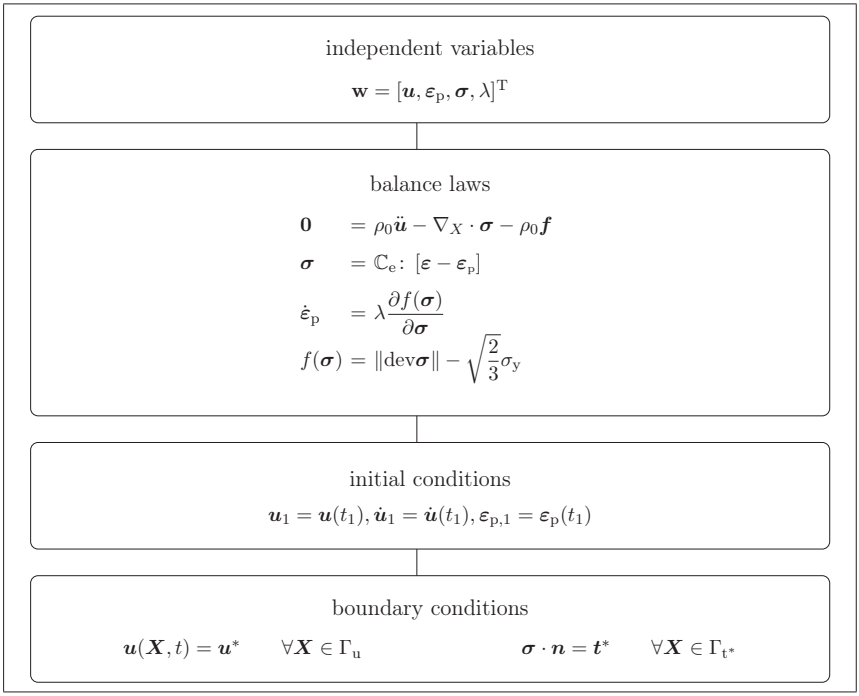

Figure 4.4.: Initial boundary value problem of the variational approach for elastoplasticity in the small strain regime

4.2.2.1. Weak Formulation of Multifield Elastoplasticity

In the classical approach for small strain elastoplasticity, depicted in Section 4.1.1, the point of departure is the formulation of the material laws and the balance of linear momentum in a strong sense. Only within the context of numerical realization, the balance equation is transformed into its weak counterpart to enable a finite element analysis. The material laws, however, remain unchanged. Their spatial discretization is only performed indirectly, due to the numerical integration applied to the weak form of the balance of linear momentum. Hence, it is mandatory that the material laws are fulfilled point-wise at the GAUSS-LEGENDRE quadrature points. An approximation of the plastic quantities by means of nodal values and associated shape functions is not carried out. In contrast, the multifield approach follows a completely different strategy. Therein, a variational principle is taken as the point of departure, directly creating a weak form of the balance of linear momentum and the material laws. Thus, concerning the numerical realization, no additional step has to be performed - and Equations (4.66)-(4.69) can immediately be integrated into the solution procedures described in **Chapter 3**. If, moreover, the relations

$$\delta \mathbf{z}_1 = \begin{bmatrix} \delta \dot{\boldsymbol{u}} \\ \delta \dot{\boldsymbol{\varepsilon}} \\ \delta \dot{\boldsymbol{\varepsilon}}_\mathrm{p} \\ \delta \boldsymbol{\sigma} \end{bmatrix}, \quad \mathbf{r}_1 = \begin{bmatrix} \rho_0 \ddot{\boldsymbol{u}} - \rho_0 \boldsymbol{f} \\ \mathbb{C}_\mathrm{e} : [\boldsymbol{\varepsilon} - \boldsymbol{\varepsilon}_\mathrm{p}] \\ \mathbb{C}_\mathrm{e} : [\boldsymbol{\varepsilon}_\mathrm{p} - \boldsymbol{\varepsilon}] + \boldsymbol{\sigma} \\ \dot{\boldsymbol{\varepsilon}}_\mathrm{p} - \lambda \dfrac{\partial f(\boldsymbol{\sigma})}{\partial \boldsymbol{\sigma}} \end{bmatrix}, \quad \mathbf{r}^* = \begin{bmatrix} \mathbf{t}^* \\ \mathbf{0} \\ \mathbf{0} \\ \mathbf{0} \end{bmatrix}, \quad \mathbf{w} = \begin{bmatrix} \boldsymbol{u} \\ \boldsymbol{\varepsilon}_\mathrm{p} \\ \boldsymbol{\sigma} \\ \lambda \end{bmatrix}, \quad r_2 = f(\boldsymbol{\sigma})$$

are taken into account, the identity to the general weak form in (3.1)-(3.2) becomes apparent. It is to be kept in mind that the quantities of the general weak form consist of a mixture of tensor-, vector-, and scalar-valued functions. Hence, the connection in between these terms must be defined properly. Additionally, further aspects have to be considered. Due to the inequality constraint, a semi-smooth NEWTON procedure is necessary and, as Figure 4.4 illustrates, the material laws do not possess boundary terms, cf. (Miehe, 2011). This is founded in the fact that they are algebraic equations or first order differential equations in time but not in space.

4.2.2.2. Linearized Spatial Semidiscrete System of Equations

The first step to solve the elastoplastic problem defined by Equations (4.66)-(4.69), following the solution procedure in **Chapter 3**, is the spatial discretization. Its realization will subsequently be demonstrated with the help of the most general case of a three-dimensional continuum mechanical body $\mathcal{B}$. By means of the finite element method, a partition of the body's domain into subdomains $\bar{\Omega}^e$ characterized by Equation (3.4) is carried out. The resulting geometry can then be approximated exploiting the relations in (3.5) together with LAGRANGE shape functions derived in (3.16) as well as (3.13). The same shape functions are chosen to interpolate the displacement field, its time derivatives, and the corresponding test function following Equations (3.7)-(3.9). Due to the symmetry of the elastic constitutive tensor, the strain tensor and the respective test function are approximated by $(3.7)_2$ together with the derivatives of the LAGRANGE shape functions (3.18) and (3.15). The plastic strains, their time derivatives, the stresses, the LAGRANGE multiplier, and the associated test functions are approximated by $(3.7)_1$, but taking special LAGRANGE shape functions into account here. They are generated using Equations $(3.13)_1$ as well as (3.16), however, the supporting points are chosen in dependence of the polynomial degree so that they match the GAUSS-LEGENDRE quadrature points listed in Table 3.1. Thus, the interpolation property (3.17) is fulfilled at each quadrature point and the quantities may jump between neighboring elements. The shape functions

generating continuous approximations are denoted as N^i, while those leading to discontinuous inter-elemental approximations are characterized by $\bar{N}^i$. With this choice of finite element grid, the same spatial discretization as in the classical approach is obtained. Other choices of shape functions are presented in (Comi and Perego, 1991, 1995; Pinsky, 1987; Simo et al., 1989) and the references therein.

In the next step, the semi-smooth NEWTON method is applied and all appearing equalities are linearized as within the standard NEWTON-RAPHSON procedure, see Section 3.2.1. The included inequality is first transformed into an equality by means of the nonlinear complementarity function in (3.31). Afterwards, a special kind of linearization is performed, introducing an active set strategy, see Section 3.2.2. The result is the following system of equations at iteration k on element level, whereby the '$\circ$'-operator is implied to embody a proper product operator for the distinct entries:

$$\begin{aligned}
\sum_{\substack{i,j=1\\ l,n\in\mathcal{A}^k}}^{NN}
\begin{bmatrix} \delta\dot{\boldsymbol{u}}^{ei} \\ \delta\dot{\boldsymbol{\varepsilon}}_{\mathrm{p}}^{ei} \\ \delta\boldsymbol{\sigma}^{ei} \\ \delta\lambda^{el} \end{bmatrix} \circ
\left[\begin{bmatrix} \boldsymbol{m}_{\mathrm{uu}}^{eij} & \mathbf{0} & \mathbf{0} & \mathbf{0} \\ \mathbf{0} & \mathbf{0} & \mathbf{0} & \mathbf{0} \\ \mathbf{0} & \mathbf{0} & \mathbf{0} & \mathbf{0} \\ \mathbf{0} & \mathbf{0} & \mathbf{0} & 0 \end{bmatrix} \circ
\begin{bmatrix} \Delta\ddot{\boldsymbol{u}}^{ej} \\ \Delta\ddot{\boldsymbol{\varepsilon}}_{\mathrm{p}}^{ej} \\ \Delta\ddot{\boldsymbol{\sigma}}^{ej} \\ \Delta\ddot{\lambda}^{en} \end{bmatrix} +
\begin{bmatrix} \mathbf{0} & \mathbf{0} & \mathbf{0} & \mathbf{0} \\ \mathbf{0} & \mathbf{0} & \mathbf{0} & \mathbf{0} \\ \mathbf{0} & \boldsymbol{d}_{\mathrm{sp}}^{eij} & \mathbf{0} & \mathbf{0} \\ \mathbf{0} & \mathbf{0} & \mathbf{0} & 0 \end{bmatrix} \circ
\begin{bmatrix} \Delta\dot{\boldsymbol{u}}^{ej} \\ \Delta\dot{\boldsymbol{\varepsilon}}_{\mathrm{p}}^{ej} \\ \Delta\dot{\boldsymbol{\sigma}}^{ej} \\ \Delta\dot{\lambda}^{en} \end{bmatrix} + \right. \\
\left. + \begin{bmatrix} \boldsymbol{k}_{\mathrm{uu}}^{eij} & \boldsymbol{k}_{\mathrm{up}}^{eij} & \mathbf{0} & \mathbf{0} \\ \boldsymbol{k}_{\mathrm{pu}}^{eij} & \boldsymbol{k}_{\mathrm{pp}}^{eij} & \boldsymbol{k}_{\mathrm{ps}}^{eij} & \mathbf{0} \\ \mathbf{0} & \mathbf{0} & \boldsymbol{k}_{\mathrm{ss}}^{eij} & \boldsymbol{k}_{\mathrm{s}\lambda}^{ein} \\ \mathbf{0} & \mathbf{0} & \boldsymbol{k}_{\lambda\mathrm{s}}^{elj} & 0 \end{bmatrix} \circ
\begin{bmatrix} \Delta\boldsymbol{u}^{ej} \\ \Delta\boldsymbol{\varepsilon}_{\mathrm{p}}^{ej} \\ \Delta\boldsymbol{\sigma}^{ej} \\ \Delta\lambda^{en} \end{bmatrix} \right] &= \sum_{\substack{i=1\\ l\in\mathcal{A}^k}}^{NN}
\begin{bmatrix} \delta\dot{\boldsymbol{u}}^{ei} \\ \delta\dot{\boldsymbol{\varepsilon}}_{\mathrm{p}}^{ei} \\ \delta\boldsymbol{\sigma}^{ei} \\ \delta\lambda^{el} \end{bmatrix} \circ
\begin{bmatrix} \boldsymbol{r}_{\mathrm{u}}^{*,ei} - \boldsymbol{r}_{\mathrm{u}}^{ei} \\ -\boldsymbol{r}_{\mathrm{p}}^{ei} \\ -\boldsymbol{r}_{\mathrm{s}}^{ei} \\ -r_{\lambda}^{el} \end{bmatrix}, \\
\lambda^{en,k+1} &= 0 \qquad\qquad \forall\, n \in \mathcal{I}^k.
\end{aligned} \tag{4.73}$$

The indices l, n therein are introduced to distinguish between element nodes characterized by plastic or elastic effects. Nodes inheriting plastic properties are gathered in the active set $\mathcal{A}^k$, while the inactive set $\mathcal{I}^k$ contains all elastic nodes. These sets are updated after each iteration k with

$$\begin{aligned}
\mathcal{A}^{k+1} &:= \{l | \lambda^{el,k+1} + c\, r_{\lambda}^{el,k+1} > 0\}, \\
\mathcal{I}^{k+1} &:= \{l | \lambda^{el,k+1} + c\, r_{\lambda}^{el,k+1} \leq 0\},
\end{aligned}$$

where $c > 0$ is assumed. The individual entries in (4.73) are defined by:

$$\boldsymbol{m}_{\mathrm{uu}}^{eij} = \int_{\Omega^e} \rho_0 N^i N^j\, \boldsymbol{I}\, |\boldsymbol{J}^e| dV^e, \qquad \boldsymbol{d}_{\mathrm{sp}}^{eij} = \int_{\Omega^e} \bar{N}^i\, \mathbb{I}\, \bar{N}^j\, |\boldsymbol{J}^e| dV^e,$$

$$\boldsymbol{k}_{\mathrm{uu}}^{eij} = \int_{\Omega^e} \nabla_X N^i \cdot \mathbb{C}_{\mathrm{e}} \cdot \nabla_X N^j\, |\boldsymbol{J}^e| dV^e, \qquad \boldsymbol{k}_{\mathrm{up}}^{eij} = -\int_{\Omega^e} \nabla_X N^i \cdot \mathbb{C}_{\mathrm{e}}\, \bar{N}^j\, |\boldsymbol{J}^e| dV^e,$$

$$\boldsymbol{k}_{\mathrm{pu}}^{eij} = -\int_{\Omega^e} \bar{N}^i\, \mathbb{C}_{\mathrm{e}} \cdot \nabla_X N^j\, |\boldsymbol{J}^e| dV^e, \qquad \boldsymbol{k}_{\mathrm{pp}}^{eij} = \int_{\Omega^e} \bar{N}^i\, \mathbb{C}_{\mathrm{e}}\, \bar{N}^j\, |\boldsymbol{J}^e| dV^e,$$

$$\boldsymbol{k}_{\mathrm{ss}}^{eij} = -\int_{\Omega^e} \bar{N}^i \lambda^{e,k} \frac{\partial^2 f(\boldsymbol{\sigma}^e)}{\partial [\boldsymbol{\sigma}^e]^2}\bigg|_k \bar{N}^j\, |\boldsymbol{J}^e| dV^e, \qquad \boldsymbol{k}_{\lambda\mathrm{s}}^{elj} = -\int_{\Omega^e} \bar{N}^l \frac{\partial f(\boldsymbol{\sigma}^e)}{\partial \boldsymbol{\sigma}^e}\bigg|_k \bar{N}^j\, |\boldsymbol{J}^e| dV^e,$$

$$\boldsymbol{k}_{\mathrm{s}\lambda}^{ein}=-\int_{\Omega^e}\bar{N}^i\frac{\partial f(\boldsymbol{\sigma}^e)}{\partial\boldsymbol{\sigma}^e}\bigg|_k\bar{N}^n\,|\boldsymbol{J}^e|dV^e, \qquad \boldsymbol{k}_{\mathrm{ps}}^{eij}=\int_{\Omega^e}\bar{N}^i\,\mathbb{I}\,\bar{N}^j\,|\boldsymbol{J}^e|dV^e,$$

$$\boldsymbol{r}_{\mathrm{p}}^{ei}=\int_{\Omega^e}\bar{N}^i\left[\boldsymbol{\sigma}^{e,k}+\mathbb{C}_{\mathrm{e}}\colon\left[\boldsymbol{\varepsilon}_{\mathrm{p}}^{e,k}-\boldsymbol{\varepsilon}^{e,k}\right]\right]|\boldsymbol{J}^e|dV^e, \qquad r_{\lambda}^{el}=-\int_{\Omega^e}\bar{N}^l\,f(\boldsymbol{\sigma}^{e,k})|\boldsymbol{J}^e|dV^e,$$

$$\boldsymbol{r}_{\mathrm{u}}^{*,ei}=\int_{\Omega^e}N^i\,\rho_0\boldsymbol{f}^k\,|\boldsymbol{J}^e|dV^e+\int_{\Gamma_{t^*}^e}N^i\,\boldsymbol{t}^{*,k}\,|\boldsymbol{J}^e|dA^e, \qquad \boldsymbol{r}_{\mathrm{s}}^{ei}=\int_{\Omega^e}\bar{N}^i\left[\boldsymbol{\varepsilon}_{\mathrm{p}}^{e,k}-\lambda^{e,k}\frac{\partial f(\boldsymbol{\sigma}^e)}{\partial\boldsymbol{\sigma}^e}\bigg|_k\right]|\boldsymbol{J}^e|dV^e,$$

$$\boldsymbol{r}_{\mathrm{u}}^{ei}=\int_{\Omega^e}N^i\,\rho_0\ddot{\boldsymbol{u}}^k\,|\boldsymbol{J}^e|dV^e+\int_{\Omega^e}\nabla_X N^i\cdot\left[\mathbb{C}_{\mathrm{e}}\colon\left[\boldsymbol{\varepsilon}^{e,k}-\boldsymbol{\varepsilon}_{\mathrm{p}}^{e,k}\right]\right]|\boldsymbol{J}^e|dV^e.$$

The included integrals are determined numerically as in the classical approach by means of the Gauss-Legendre quadrature. In order to create a solvable system of equations on structural level, the tensor-valued entries have to be sorted. The unknown tensors of second order, such as the plastic strains and the stresses, are rearranged in a vector. The tensors of third as well as fourth order are recast into matrices. Then, the assembly operators in (3.25) - (3.26) and (3.34) can be applied, resulting in

$$\mathbf{M}\Delta\ddot{\mathbf{w}}+\mathbf{D}\Delta\dot{\mathbf{w}}+\mathbf{K}\Delta\mathbf{w}\;=\mathbf{R}_1^*-\mathbf{R}_1, \tag{4.74}$$

$$\mathbf{w}^{k+1}=\Delta\mathbf{w}+\mathbf{w}^k, \tag{4.75}$$

$$\lambda^{i,k+1}\;=0 \qquad\qquad \forall i\in\mathcal{I}^k, \tag{4.76}$$

$$\mathcal{A}^{k+1}:=\{i|\lambda^{ei,k+1}+c\,r_{\lambda}^{ei,k+1}>0\}, \tag{4.77}$$

$$\mathcal{I}^{k+1}:=\{i|\lambda^{ei,k+1}+c\,r_{\lambda}^{ei,k+1}\leq 0\}. \tag{4.78}$$

For explicit realizations of the sorting see Sections 5.1.2 as well as 5.2.2. Furthermore, it is emphasized that in Equation (4.74) only the active entries of the assembled parts of $\boldsymbol{k}_{\lambda\mathrm{s}}^{elj}$, $\boldsymbol{k}_{\mathrm{s}\lambda}^{ein}$ and r_{λ}^{el} are taken into account. Thereby, it is emphasized that, as a result of the choice of shape functions, one node may only be part of one element. An alternative solution procedure in the context of a predictor corrector multifield method is presented in (Comi and Perego, 1995).

4.2.2.3. Time discretization on Structural Level

Equations (4.74)-(4.78) represent the linearized semidiscrete form of an arbitrary three-dimensional elastoplastic problem. The last step towards their solution is the time discretization of Equation (4.74) and the evaluation of Equations (4.75)-(4.78) at the respective points in time. Due to the identity of Equation (4.74) and Equation (3.46), all time integration schemes of Section 3.4 can be applied directly without further adaptation. However, the utilization of completely arbitrary time integration schemes is only partly possible. If Equation (4.67) as well as Inequality (4.69) are examined closer, it becomes apparent that these are algebraic constituents. Thus, Equation (4.74) illustrates a differential-algebraic system which has to be solved. This is the explanation for the choice of time integration schemes presented in Section 3.4. In all methods, the weak forms in (4.66)-(4.69), including the algebraic ones, are fulfilled at the end of the time step. For the application of Runge-Kutta schemes in the context of differential-algebraic systems see the explanations in (Hairer and Wanner, 2002). Moreover, within the Galerkin schemes, the quadrature points in time are chosen to be identical to the temporal nodes. Hence,

the algebraic equations are automatically fulfilled at the time nodes and no projection steps for the determination of the active sets have to be performed. In contrast to the classical approach towards elastoplasticity in Section 4.1.3.3, only one single time discretization has to be carried out. In the multifield approach, an explicit coupling between the material laws and the balance of linear momentum exists, so that the radial return map with its separate time integration scheme and the projection step is completely superfluous.

4.2.3. Implementation Strategy for Multifield Viscoplasticity

A similar but simpler way compared to the numerical realization of multifield plasticity can be accomplished for multifield viscoplasticity. The big and only difference between both models is that the LAGRANGE multiplier is not determined within the solution process of the latter, but prescribed at the beginning. Hence, the corresponding initial boundary value problem depicted in Figure 4.5 shows only small changes compared to the scheme in Figure 4.4. The classical approach towards viscoplasticity, however, is characterized by a completely distinct structure, see Figure 4.1. Therein, the only unknown quantity is the displacement field. Within the variational ansatz, the plastic strains and the stresses are considered as additional primary variables. Consequently, a totally new structure is obtained, leading to a distinct numerical realization characterized by a single time discretization.

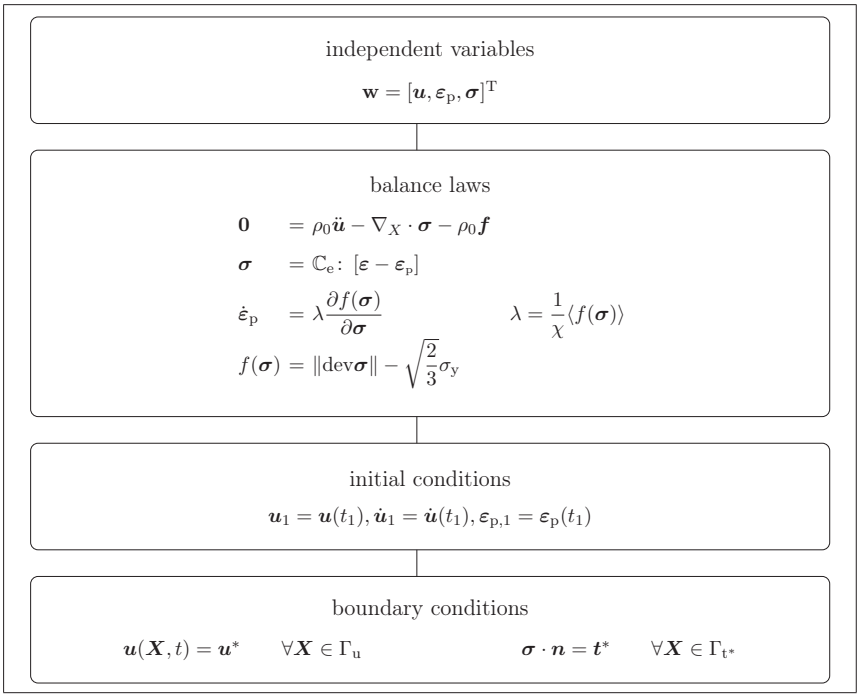

Figure 4.5.: Initial boundary value problem of the variational approach for viscoplasticity in the small strain regime

4.2.3.1. Weak Formulation of Multifield Viscoplasticity

Analogously to the multifield elastoplastic approach, the modeling of viscoplastic effects is based on a variational concept. Accordingly, the weak forms in (4.70)-(4.72) are automatically obtained and can be incorporated directly into the solution procedure of **Chapter 3**. To accomplish the general weak form in (3.1), the following definitions

$$\delta\mathbf{z}_1 = \begin{bmatrix} \delta\dot{\boldsymbol{u}} \\ \delta\dot{\boldsymbol{\varepsilon}} \\ \delta\dot{\boldsymbol{\varepsilon}}_\mathrm{p} \\ \delta\boldsymbol{\sigma} \end{bmatrix}, \qquad \mathbf{r}_1 = \begin{bmatrix} \rho_0\ddot{\boldsymbol{u}} - \rho_0\boldsymbol{f} \\ \mathbb{C}_\mathrm{e}\colon [\boldsymbol{\varepsilon} - \boldsymbol{\varepsilon}_\mathrm{p}] \\ \mathbb{C}_\mathrm{e}\colon [\boldsymbol{\varepsilon}_\mathrm{p} - \boldsymbol{\varepsilon}] + \boldsymbol{\sigma} \\ \dot{\boldsymbol{\varepsilon}}_\mathrm{p} - \dfrac{1}{\chi}\langle f(\boldsymbol{\sigma})\rangle \dfrac{\partial f(\boldsymbol{\sigma})}{\partial \boldsymbol{\sigma}} \end{bmatrix}, \qquad \mathbf{r}^* = \begin{bmatrix} \mathbf{t}^* \\ \mathbf{0} \\ \mathbf{0} \\ \mathbf{0} \end{bmatrix}, \qquad \mathbf{w} = \begin{bmatrix} \boldsymbol{u} \\ \boldsymbol{\varepsilon}_\mathrm{p} \\ \boldsymbol{\sigma} \end{bmatrix}$$

are settled. Thereby, it is important to know that the test function $\delta\mathbf{z}_1$ consists of a mixture of tensor- and vector-valued functions. Hence, the connection to the nonlinear function $\mathbf{r}_1$ must be defined properly. Again, the material laws do not possess boundary terms as in the elastoplastic formulation depicted in Figure 4.4, cf. (Miehe, 2011).

4.2.3.2. Spatial Semidiscrete Linearized System of Equations

In order to solve the weak forms in (4.70)-(4.72), a spatial discretization has to be carried out. For the sake of simplicity, the subsequent sections consistently address the most general case of a three-dimensional continuum mechanical body. On the one hand, it is assumed that the analyzed viscoplastic body's domain can be partitioned, following (3.4), into a finite number of elements. On the other hand, Equation (3.10) yields the validity of the weak forms (4.70)-(4.72) on element level. These subdomains enable the description of the body's geometry exploiting Equation (3.5). The included shape functions are supposed to be of LAGRANGE type, derived by the Terms (3.16) as well as (3.13). Hence, a continuous approximation of the geometry is carried out. The identical ansatz is pursued for the displacement field, its time derivatives, and the corresponding test function following Equations (3.7)-(3.9). Due to the symmetry of the elastic constitutive tensor, the strain tensor and the respective test function are approximated by $(3.7)_2$ together with the derivatives of the LAGRANGE shape functions (3.18) and (3.15). For the evolution of the other primary variables, a spatially discontinuous course is permitted. Thus, they are approximated as in the elastoplastic multifield approach by $(3.7)_1$ using LAGRANGE shape functions, which are constructed in such a way that the interpolation property (3.17) is fulfilled, depending on the polynomial degree, at the GAUSS-LEGENDRE quadrature points listed in Table 3.1. The shape functions generating continuous approximations are denoted as N^i, while those leading to discontinuous inter-elemental approximations are characterized by $\bar{N}^i$. By adopting this procedure, it is possible to obtain the same spatial discretization explicitly as it is implicitly available in the classical approach.

The next step is to extend the nonlinear semidiscrete forms to the structural level and to solve the resulting system. Since there are only variational equalities in the viscoplastic case, a conventional NEWTON-RAPHSON procedure can by applied as described in Section 3.2.1. The

result is the following system of equations at iteration k on element level:

$$\sum_{i,j=1}^{NN} \begin{bmatrix} \delta\dot{\boldsymbol{u}}^{ei} \\ \delta\dot{\boldsymbol{\varepsilon}}_{\mathrm{p}}^{ei} \\ \delta\boldsymbol{\sigma}^{ei} \end{bmatrix} \circ \left(\begin{bmatrix} \boldsymbol{m}_{\mathrm{uu}}^{eij} & \mathbf{0} & \mathbf{0} \\ \mathbf{0} & \mathbf{0} & \mathbf{0} \\ \mathbf{0} & \mathbf{0} & \mathbf{0} \end{bmatrix} \circ \begin{bmatrix} \Delta\ddot{\boldsymbol{u}}^{ej} \\ \Delta\ddot{\boldsymbol{\varepsilon}}_{\mathrm{p}}^{ej} \\ \Delta\ddot{\boldsymbol{\sigma}}^{ej} \end{bmatrix} + \begin{bmatrix} \mathbf{0} & \mathbf{0} & \mathbf{0} \\ \mathbf{0} & \mathbf{0} & \mathbf{0} \\ \mathbf{0} & \boldsymbol{d}_{\mathrm{sp}}^{eij} & \mathbf{0} \end{bmatrix} \circ \begin{bmatrix} \Delta\dot{\boldsymbol{u}}^{ej} \\ \Delta\dot{\boldsymbol{\varepsilon}}_{\mathrm{p}}^{ej} \\ \Delta\dot{\boldsymbol{\sigma}}^{ej} \end{bmatrix} + \right.$$
$$\left. + \begin{bmatrix} \boldsymbol{k}_{\mathrm{uu}}^{eij} & \boldsymbol{k}_{\mathrm{up}}^{eij} & \mathbf{0} \\ \boldsymbol{k}_{\mathrm{pu}}^{eij} & \boldsymbol{k}_{\mathrm{pp}}^{eij} & \boldsymbol{k}_{\mathrm{ps}}^{eij} \\ \mathbf{0} & \mathbf{0} & \boldsymbol{k}_{\mathrm{ss}}^{eij} \end{bmatrix} \circ \begin{bmatrix} \Delta\boldsymbol{u}^{ej} \\ \Delta\boldsymbol{\varepsilon}_{\mathrm{p}}^{ej} \\ \Delta\boldsymbol{\sigma}^{ej} \end{bmatrix} \right] = \sum_{i=1}^{NN} \begin{bmatrix} \delta\dot{\boldsymbol{u}}^{ei} \\ \delta\dot{\boldsymbol{\varepsilon}}_{\mathrm{p}}^{ei} \\ \delta\boldsymbol{\sigma}^{ei} \end{bmatrix} \circ \begin{bmatrix} \boldsymbol{r}_{\mathrm{u}}^{*,ei} - \boldsymbol{r}_{\mathrm{u}}^{ei} \\ -\boldsymbol{r}_{\mathrm{p}}^{ei} \\ -\boldsymbol{r}_{\mathrm{s}}^{ei} \end{bmatrix}. \tag{4.79}$$

The 'o'-operator therein embodies a proper product operator for the distinct vector- and tensor-valued entries. The differences between the included quantities can be recognized by considering the respective definitions:

$$\boldsymbol{m}_{\mathrm{uu}}^{eij} = \int_{\Omega^e} \rho_0 N^i N^j \; \boldsymbol{I} \; |\boldsymbol{J}^e| dV^e, \qquad \boldsymbol{d}_{\mathrm{sp}}^{eij} = \int_{\Omega^e} \bar{N}^i \, \mathbb{I} \, \bar{N}^j \; |\boldsymbol{J}^e| dV^e,$$

$$\boldsymbol{k}_{\mathrm{uu}}^{eij} = \int_{\Omega^e} \nabla_X N^i \cdot \mathbb{C}_{\mathrm{e}} \cdot \nabla_X N^j \; |\boldsymbol{J}^e| dV^e, \qquad \boldsymbol{k}_{\mathrm{up}}^{eij} = -\int_{\Omega^e} \nabla_X N^i \cdot \mathbb{C}_{\mathrm{e}} \, \bar{N}^j \; |\boldsymbol{J}^e| dV^e,$$

$$\boldsymbol{k}_{\mathrm{pu}}^{eij} = -\int_{\Omega^e} \bar{N}^i \, \mathbb{C}_{\mathrm{e}} \cdot \nabla_X N^j \; |\boldsymbol{J}^e| dV^e, \qquad \boldsymbol{k}_{\mathrm{pp}}^{eij} = \int_{\Omega^e} \bar{N}^i \, \mathbb{C}_{\mathrm{e}} \, \bar{N}^j \; |\boldsymbol{J}^e| dV^e,$$

$$\boldsymbol{k}_{\mathrm{ss}}^{eij} = -\int_{\Omega^e} \bar{N}^i \frac{\partial}{\partial \boldsymbol{\sigma}^e} \left[\frac{1}{\chi} \langle f(\boldsymbol{\sigma}^e) \rangle \frac{\partial f(\boldsymbol{\sigma}^e)}{\partial \boldsymbol{\sigma}^e} \right] \Big|_k \bar{N}^j \; |\boldsymbol{J}^e| dV^e, \qquad \boldsymbol{k}_{\mathrm{ps}}^{eij} = \int_{\Omega^e} \bar{N}^i \, \mathbb{I} \, \bar{N}^j \; |\boldsymbol{J}^e| dV^e,$$

$$\boldsymbol{r}_{\mathrm{p}}^{ei} = \int_{\Omega^e} \bar{N}^i \Big[\boldsymbol{\sigma}^{e,k} + \mathbb{C}_{\mathrm{e}} : \Big[\boldsymbol{\varepsilon}_{\mathrm{p}}^{e,k} - \boldsymbol{\varepsilon}^{e,k} \Big] \Big] |\boldsymbol{J}^e| dV^e,$$

$$\boldsymbol{r}_{\mathrm{s}}^{ei} = \int_{\Omega^e} \bar{N}^i \left[\boldsymbol{\varepsilon}_{\mathrm{p}}^{e,k} - \frac{1}{\chi} \langle f(\boldsymbol{\sigma}^{e,k}) \rangle \frac{\partial f(\boldsymbol{\sigma}^e)}{\partial \boldsymbol{\sigma}^e} \Big|_k \right] |\boldsymbol{J}^e| dV^e,$$

$$\boldsymbol{r}_{\mathrm{u}}^{*,ei} = \int_{\Omega^e} N^i \, \rho_0 \boldsymbol{f}^k \, |\boldsymbol{J}^e| dV^e + \int_{\Gamma_{t^*}^e} N^i \; \boldsymbol{t}^{*,k} \; |\boldsymbol{J}^e| dA^e,$$

$$\boldsymbol{r}_{\mathrm{u}}^{ei} = \int_{\Omega^e} N^i \; \rho_0 \ddot{\boldsymbol{u}}^k \; |\boldsymbol{J}^e| dV^e + \int_{\Omega^e} \nabla_X N^i \cdot \Big[\mathbb{C}_{\mathrm{e}} : \Big[\boldsymbol{\varepsilon}^{e,k} - \boldsymbol{\varepsilon}_{\mathrm{p}}^{e,k} \Big] \Big] \; |\boldsymbol{J}^e| dV^e.$$

Similar to the handling described in Section 4.2.2.2 for the variational elastoplastic approach, the included integrals are determined numerically by means of the Gauss-Legendre quadrature, and a matrix vector product form is created by an appropriate realignment of the distinct tensor-valued quantities. Thus, the assembly operators in (3.25) - (3.26) and (3.34) can be employed to generate the linearized semidiscrete form

$$\mathbf{M}\Delta\ddot{\mathbf{w}} + \mathbf{D}\Delta\dot{\mathbf{w}} + \mathbf{K}\Delta\mathbf{w} = \mathbf{R}_1^* - \mathbf{R}_1,$$
$$\mathbf{w}^{k+1} = \Delta\mathbf{w} + \mathbf{w}^k$$

of the viscoplastic model within the multifield approach. For an explicit realization of the sorting see Section 5.1.2 and 5.2.2.

4.2.3.3. Time Discretization on Structural Level

The last step within the solution procedure described in **Chapter 3** is the time discretization. Due to the variational multifield setting, the material laws are transferred to structural level so that their time discretization can be performed simultaneously to the one of the balance of linear momentum. A return mapping procedure as in the classical approach in Section 4.1 is not necessary. Hence, all time integration schemes presented in Section 3.4 can be employed directly. Nevertheless, an extension to include further time discretization schemes has to be carried out with care. A closer look at Equations (4.70)-(4.72) reveals that an algebraic equation is included. This has to be taken into account within the choice of time discretization schemes. The ones presented in Section 3.4 exhibit the special characteristics that all considered equations, even the algebraic ones, are fulfilled at the end of the time step. For a discussion on the application of RUNGE-KUTTA schemes to differential algebraic systems see (Hairer and Wanner, 2002).

4.3. Summary

In this chapter, the previously defined general elasto(visco)plastic problem is specified for the small strain regime. Therefore, a macroscopic point of view for material modeling is adapted and two distinct approaches are followed.

The classical ansatz is widespread, so that the aim of its presentation is to enable the generation of reference solutions. The starting point of the classical approach is the balance of linear momentum with inherent inertia effects. This ansatz derives the mathematical formulations for plasticity as well as viscoplasticity in a strong sense, based on the dissipation inequality. Thereby, strain rate-dependent viscoplasticity results from a regularization of rate-independent plasticity. To integrate the classical approach in the solution process of the general elasto(visco)plastic problem, the balance of linear momentum is formulated weakly. The material laws, however, stay in their strong form. Hence, their coupling to the balance of linear momentum requires an additional step to the general procedure depicted in **Chapter 3**. The incorporation of the material laws is carried out using the radial return map. On integration point level, this determines whether elastic or (visco)plastic properties will prevail, and a time discretization of the evolution equations is performed if needed. With the prevalent external conditions of this thesis, this supplementary step reduces the applicable time integrators to diagonally implicit RUNGE-KUTTA schemes and the NEWMARK method. Furthermore, two levels of time integration are introduced. The balance of linear momentum is temporally discretized on structural level, while the evolution equations are temporally discretized on integration point level.

To counteract these phenomena, a novel variational multifield approach is generated. Therefore, the principle of JOURDAIN is extended to dissipative continua, creating a rate-type functional whose stationarity conditions yield the weak formulations of the balance of linear momentum and the material laws of elasto(visco)plasticity in a natural fashion. On the one hand, this strategy neutralizes the distinction between balance equations as well as material formulations. On the other hand, it enables a mutual time integration of all contributors due to its time continuous property. Thus, the utilization of higher order accurate time discretization schemes within dynamic elasto(visco)plasticity is standardized, substantially simplifying the application of distinct classes of time integrators. However, with this approach, an altered initial boundary value problem with more unknown field variables is derived, despite the fact that the material behavior is identical to the classical approach. The multifield form can be integrated one-to-one into the context of the general elasto(visco)plastic problem, leading to the numerical realization as portrayed in **Chapter 3**.

5. Numerical Examples for Small Strain Elasto(visco)plasticity

For a numerical analysis of the algorithmic implementations of small strain elasto(visco)plasticity, described in **Chapter 4**, different examples are treated. They serve, on the one hand, to verify the applicability of the classical and the variational approach, and, on the other hand, allow for a comparison between both procedures in terms of solution accuracy as well as of convergence properties.

5.1. Rectangular Strip with a Hole in the Plane Strain Case

The first numerical example in this thesis is based on a benchmark problem extensively studied in (Stein, 2003). Therein, the quasi-static elastic-perfectly plastic behavior of a quadratic plate with a central circular hole under a uniformly applied distributed load is analyzed, see Figure 5.1. Here, the focus lies on the evolution of the displacements and the stress field at certain specific points of the geometry. Due to the two-dimensional character of the plate and the uniaxial loading a plane strain state

$$\boldsymbol{\varepsilon} = \begin{bmatrix} \varepsilon_{11} & 0 & \varepsilon_{13} \\ 0 & 0 & 0 \\ \varepsilon_{13} & 0 & \varepsilon_{33} \end{bmatrix} = \begin{bmatrix} \dfrac{\partial u_1}{\partial X} & 0 & \dfrac{1}{2}\left[\dfrac{\partial u_3}{\partial X_1} + \dfrac{\partial u_1}{\partial X_3}\right] \\ 0 & 0 & 0 \\ \dfrac{1}{2}\left[\dfrac{\partial u_3}{\partial X_1} + \dfrac{\partial u_1}{\partial X_3}\right] & 0 & \dfrac{\partial u_3}{\partial X_3} \end{bmatrix}$$

with the displacement field $\boldsymbol{u}(\boldsymbol{X}) = [u_1, u_3]$ can be assumed, resulting in the corresponding three-dimensional stress state

$$\boldsymbol{\sigma} = \begin{bmatrix} \sigma_{11} & 0 & \sigma_{13} \\ 0 & \sigma_{22} & 0 \\ \sigma_{13} & 0 & \sigma_{33} \end{bmatrix}.$$

The necessary dimensions, the loading path, and the simulation parameters can be inferred from Figure 5.1. With the help of the presented benchmark, a validation of the classical and the variational approach in the quasi-static case is performed.

5.1.1. Classical Approach towards Elastoplasticity

A conventional model for perfect von Mises elastoplasticity is derived in Section 4.1.1, while its general three-dimensional numerical implementation is presented in Section 4.1.3. The identical model is now taken into account in the context of the example depicted in Figure 5.1. However, because of the plane strain condition and the quasi-static analysis, the numerical realization can be simplified. In order to do so, the tangential quantities in (4.26) are modified. The second order stress and strain tensors are rearranged in vectors of the same length, and the fourth order

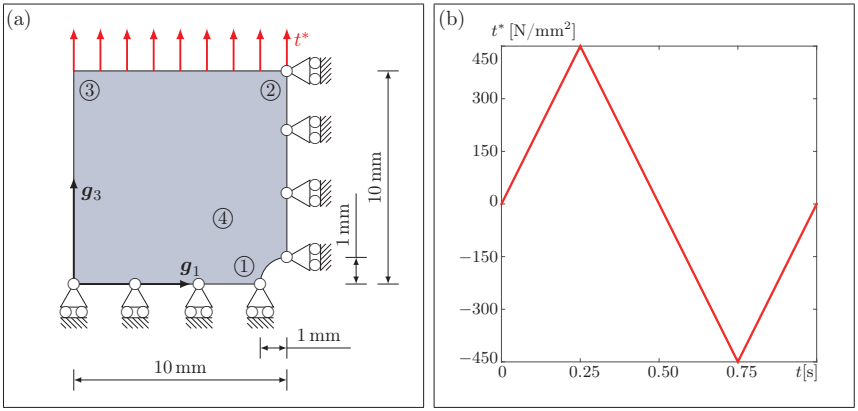

(c)

κ	μ	σ_y	ρ_0	Δt	T
$1.1074 \cdot 10^5\,\mathrm{N/mm^2}$	$8.0194 \cdot 10^4\,\mathrm{N/mm^2}$	$450\,\mathrm{N/mm^2}$	$0\,\mathrm{kg/mm^3}$	$1/288\,\mathrm{s}$	$1\,\mathrm{s}$

Figure 5.1.: (a) Plate geometry and evaluation points.
①:$X_1 = 9\,\mathrm{mm}$, $X_3 = 0\,\mathrm{mm}$, ②:$X_1 = 10\,\mathrm{mm}$, $X_3 = 10\,\mathrm{mm}$, ③:$X_1 = 0\,\mathrm{mm}$, $X_3 = 10\,\mathrm{mm}$,
④:$X_1 = 6.1953\,\mathrm{mm}$, $X_3 = 3.8047\,\mathrm{mm}$, (b) Loading path, (c) Simulation parameters

algorithmic constitutive tensor is rewritten in matrix representation

$$\overline{\overline{\boldsymbol{\varepsilon}}} = \begin{bmatrix} \varepsilon_{11} \\ 0 \\ \varepsilon_{33} \\ \varepsilon_{13} \end{bmatrix}, \qquad \overline{\overline{\boldsymbol{\sigma}}} = \begin{bmatrix} \sigma_{11} \\ \sigma_{22} \\ \sigma_{33} \\ 2\sigma_{13} \end{bmatrix}, \qquad \overline{\overline{\mathbf{G}}} = \begin{bmatrix} G_{1111} & G_{1122} & G_{1133} & 2G_{1113} \\ G_{2211} & G_{2222} & G_{2233} & 2G_{2213} \\ G_{3311} & G_{3322} & G_{3333} & 2G_{3313} \\ 2G_{1311} & 2G_{1322} & 2G_{1333} & 4G_{1313} \end{bmatrix}. \tag{5.1}$$

Additionally, the spatially discrete connection between the displacement field $\boldsymbol{u}(\boldsymbol{X}) = [u_1, u_3]$ and the strain tensor is expressed via a matrix vector multiplication, exploiting the $\mathbf{B}$-operator

$$\overline{\overline{\boldsymbol{\varepsilon}}} = \sum_{i=1}^{NN} \mathbf{B}^i \boldsymbol{u}^i, \qquad \mathbf{B}^i = \begin{bmatrix} \dfrac{\partial N^i}{\partial X_1} & 0 & 0 & \dfrac{1}{2}\dfrac{\partial N^i}{\partial X_3} \\ 0 & 0 & \dfrac{\partial N^i}{\partial X_3} & \dfrac{1}{2}\dfrac{\partial N^i}{\partial X_1} \end{bmatrix}^{\mathrm{T}}. \tag{5.2}$$

Furthermore, the density is set to zero, and the mass matrix as well as the respective parts in the load vector can be neglected. Thus, for Equation (4.26) the adapted tangential quantities

$$\mathbf{k}^{eij} = \int_{\Omega^e} \left[\mathbf{B}^i\right]^{\mathrm{T}} \overline{\overline{\mathbf{G}}}^k \mathbf{B}^j \, |\boldsymbol{J}^e| dV^e,$$

$$\mathbf{r}_1^{*,ei} = \int_{\Gamma^e} N^i \, \boldsymbol{t}^{*,k} \, |\boldsymbol{J}^e| dA^e, \qquad \mathbf{r}_1^{ei} = \int_{\Omega^e} \left[\mathbf{B}^i\right]^{\mathrm{T}} \overline{\overline{\boldsymbol{\sigma}}}^k \, |\boldsymbol{J}^e| dV^e$$

are obtained.

5.1.2. Multifield Approach towards Elastoplasticity

Another approach towards solving the benchmark problem is described in Section 4.2. A distinct derivation strategy of the material model presented in Section 4.1.1 is offered, accompanied by an alternative numerical realization. A three-dimensional point of view is followed in this context. Concerning the benchmark problem, similar simplifications as portrayed in Section 5.1.1 can be performed, regarding the tangential quantities in the system of Equations (4.73). But apart from the rearrangement of the strain and stress tensors in (5.1), the plastic strain tensor as well as the derivative of the yield function have to be resorted together with a diversity of fourth order tensors

$$\overline{\overline{\boldsymbol{\varepsilon}}}_{\mathrm{p}} = \begin{bmatrix} \varepsilon_{\mathrm{p},11} \\ \varepsilon_{\mathrm{p},22} \\ \varepsilon_{\mathrm{p},33} \\ \varepsilon_{\mathrm{p},13} \end{bmatrix}, \qquad \overline{\overline{\mathbf{C}}}_{\mathrm{e}} = \begin{bmatrix} C_{\mathrm{e},1111} & C_{\mathrm{e},1122} & C_{\mathrm{e},1133} & 2C_{\mathrm{e},1113} \\ C_{\mathrm{e},2211} & C_{\mathrm{e},2222} & C_{\mathrm{e},2233} & 2C_{\mathrm{e},2213} \\ C_{\mathrm{e},3311} & C_{\mathrm{e},3322} & C_{\mathrm{e},3333} & 2C_{\mathrm{e},3313} \\ 2C_{\mathrm{e},1311} & 2C_{\mathrm{e},1322} & 2C_{\mathrm{e},1333} & 4C_{\mathrm{e},1313} \end{bmatrix}, \qquad \overline{\overline{\mathbf{I}}} = \begin{bmatrix} I_{1111} & I_{1122} & I_{1133} & 2I_{1113} \\ I_{2211} & I_{2222} & I_{2233} & 2I_{2213} \\ I_{3311} & I_{3322} & I_{3333} & 2I_{3313} \\ 2I_{1311} & 2I_{1322} & 2I_{1333} & 4I_{1313} \end{bmatrix},$$

$$\overline{\overline{\mathbf{f}}} = \begin{bmatrix} \dfrac{\partial f(\boldsymbol{\sigma})}{\partial \sigma_{11}} \\ \dfrac{\partial f(\boldsymbol{\sigma})}{\partial \sigma_{22}} \\ \dfrac{\partial f(\boldsymbol{\sigma})}{\partial \sigma_{33}} \\ 2\dfrac{\partial f(\boldsymbol{\sigma})}{\partial \sigma_{13}} \end{bmatrix}, \qquad \overline{\overline{\mathbf{F}}} = \begin{bmatrix} \dfrac{\partial^2 f(\boldsymbol{\sigma})}{\partial \sigma_{11}\partial \sigma_{11}} & \dfrac{\partial^2 f(\boldsymbol{\sigma})}{\partial \sigma_{11}\partial \sigma_{22}} & \dfrac{\partial^2 f(\boldsymbol{\sigma})}{\partial \sigma_{11}\partial \sigma_{33}} & 2\dfrac{\partial^2 f(\boldsymbol{\sigma})}{\partial \sigma_{11}\partial \sigma_{13}} \\ \dfrac{\partial^2 f(\boldsymbol{\sigma})}{\partial \sigma_{22}\partial \sigma_{11}} & \dfrac{\partial^2 f(\boldsymbol{\sigma})}{\partial \sigma_{22}\partial \sigma_{22}} & \dfrac{\partial^2 f(\boldsymbol{\sigma})}{\partial \sigma_{22}\partial \sigma_{33}} & 2\dfrac{\partial^2 f(\boldsymbol{\sigma})}{\partial \sigma_{22}\partial \sigma_{13}} \\ \dfrac{\partial^2 f(\boldsymbol{\sigma})}{\partial \sigma_{33}\partial \sigma_{11}} & \dfrac{\partial^2 f(\boldsymbol{\sigma})}{\partial \sigma_{33}\partial \sigma_{22}} & \dfrac{\partial^2 f(\boldsymbol{\sigma})}{\partial \sigma_{33}\partial \sigma_{33}} & 2\dfrac{\partial^2 f(\boldsymbol{\sigma})}{\partial \sigma_{33}\partial \sigma_{13}} \\ 2\dfrac{\partial^2 f(\boldsymbol{\sigma})}{\partial \sigma_{13}\partial \sigma_{11}} & 2\dfrac{\partial^2 f(\boldsymbol{\sigma})}{\partial \sigma_{13}\partial \sigma_{22}} & 2\dfrac{\partial^2 f(\boldsymbol{\sigma})}{\partial \sigma_{13}\partial \sigma_{33}} & 4\dfrac{\partial^2 f(\boldsymbol{\sigma})}{\partial \sigma_{13}\partial \sigma_{13}} \end{bmatrix}.$$

The Relationship (5.2) between the displacement field and the strain tensor remains valid. Hence, the tangential quantities in (4.73) can be recast into

$$\mathbf{d}_{\mathrm{sp}}^{eij} = \int_{\Omega^e} \bar{N}^i \overline{\overline{\mathbf{I}}}\, \bar{N}^j \, |\boldsymbol{J}^e| dV^e = \left[\mathbf{k}_{\mathrm{ps}}^{eij}\right]^{\mathrm{T}},$$

$$\mathbf{k}_{\mathrm{uu}}^{eij} = \int_{\Omega^e} \left[\mathbf{B}^i\right]^{\mathrm{T}} \overline{\overline{\mathbf{C}}}_{\mathrm{e}} \mathbf{B}^j \, |\boldsymbol{J}^e| dV^e, \qquad \mathbf{k}_{\mathrm{up}}^{eij} = -\int_{\Omega^e} \left[\mathbf{B}^i\right]^{\mathrm{T}} \overline{\overline{\mathbf{C}}}_{\mathrm{e}}\, \bar{N}^j \, |\boldsymbol{J}^e| dV^e = \left[\mathbf{k}_{\mathrm{pu}}^{eij}\right]^{\mathrm{T}},$$

$$\mathbf{k}_{\mathrm{pp}}^{eij} = \int_{\Omega^e} \bar{N}^i \overline{\overline{\mathbf{C}}}_{\mathrm{e}}\, \bar{N}^j \, |\boldsymbol{J}^e| dV^e, \qquad \mathbf{k}_{\mathrm{ss}}^{eij} = -\int_{\Omega^e} \bar{N}^i \lambda^{e,k} \overline{\overline{\mathbf{F}}}^{e,k} \bar{N}^j \, |\boldsymbol{J}^e| dV^e,$$

$$\mathbf{k}_{\lambda\mathrm{s}}^{elj} = -\int_{\Omega^e} \bar{N}^{l/i} \left[\overline{\overline{\mathbf{f}}}^{e,k}\right]^{\mathrm{T}} \bar{N}^{j/n} |\boldsymbol{J}^e| dV^e = \left[\mathbf{k}_{\mathrm{s}\lambda}^{ein}\right]^{\mathrm{T}}, \qquad \mathbf{r}_{\mathrm{s}}^{ei} = \int_{\Omega^e} \bar{N}^i \left[\overline{\overline{\boldsymbol{\varepsilon}}}_{\mathrm{p}}^{e,k} - \lambda^{e,k} \overline{\overline{\boldsymbol{f}}}^{e,k}\right] |\boldsymbol{J}^e| dV^e,$$

$$\mathbf{r}_{\mathrm{p}}^{ei} = \int_{\Omega^e} \bar{N}^i \left[\overline{\overline{\boldsymbol{\sigma}}}^{e,k} + \overline{\overline{\mathbf{C}}}_{\mathrm{e}} \left[\overline{\overline{\boldsymbol{\varepsilon}}}_{\mathrm{p}}^{e,k} - \overline{\overline{\boldsymbol{\varepsilon}}}^{e,k}\right]\right] |\boldsymbol{J}^e| dV^e, \qquad r_{\lambda}^{el} = -\int_{\Omega^e} \bar{N}^l \, f(\boldsymbol{\sigma}^{e,k}) |\boldsymbol{J}^e| dV^e,$$

$$\mathbf{r}_{\mathrm{u}}^{*,ei} = \int_{\Gamma_{t^*}^e} N^i \, \boldsymbol{t}^{*,k} \, |\boldsymbol{J}^e| dA^e, \qquad \mathbf{r}_{\mathrm{u}}^{ei} = \int_{\Omega^e} \left[\mathbf{B}^i\right]^{\mathrm{T}} \left[\overline{\overline{\mathbf{C}}}_{\mathrm{e}} \left[\overline{\overline{\boldsymbol{\varepsilon}}}^{e,k} - \overline{\overline{\boldsymbol{\varepsilon}}}_{\mathrm{p}}^{e,k}\right]\right] |\boldsymbol{J}^e| dV^e,$$

whereby the terms including the density are neglected due to the quasi-static characteristic of the benchmark problem. Furthermore, different shape functions are chosen for the distinct fields. While N^i lead to continuous inter-elemental approximations, $\bar{N}^i$ characterize discontinuous ones as specified in Section 4.2.2.2.

5.1.3. Classical vs. Variational Approach

With the help of the implementation schemes of the classical and the variational approach presented in Sections 5.1.1 as well as 5.1.2, the quasi-static benchmark problem of a plate with a circular hole introduced in Section 5.1 can be calculated. For both proposals, a fixed spatial discretization of the geometry consisting of $NE = 1504$ second order LAGRANGE elements is applied. For the displacement field, biquadratic approximations are used, likewise. For the stresses, the plastic strains and the LAGRANGE multiplier in the variational approach discontinuous approximations are established. Therefore, biquadratic LAGRANGE shape functions, with the GAUSS-LEGENDRE quadrature points listed in Table 3.1 as supporting points, are chosen. The temporal discretization is carried out using the second order accurate diagonally implicit RUNGE-KUTTA scheme depicted in Figure 3.13 (b) together with a constant time step size of $\Delta t = 1/288$ s. For the multifield ansatz, the exemplary VON MISES stress distributions depicted in Figure 5.2 are obtained.

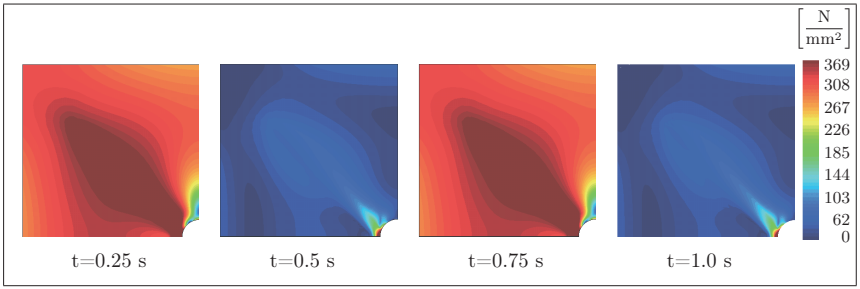

Figure 5.2.: Contour plots of the VON MISES stress at distinct points in time

It can be observed that, due to the intrinsic hole, an inhomogeneous stress distribution is apparent in all demonstrated points in time. For the case where the maximal tensional or compressional load is applied, the middle part of the plate is characterized by plastic effects. Meanwhile, an elastic spot is formed near the hole. In contrast, the plate behaves predominantly elastically in the depicted unloading steps - except for a small plastic region near the hole. The corresponding deformed states are shown in Figure 5.3. As can be seen here, and in Figure 5.2, the plasticity depends on the history. Although no external loads are applied at the points in time $t = 0.5$ s and $t = 1$ s, there are deformed states characterized by VON MISES stresses that are not zero.

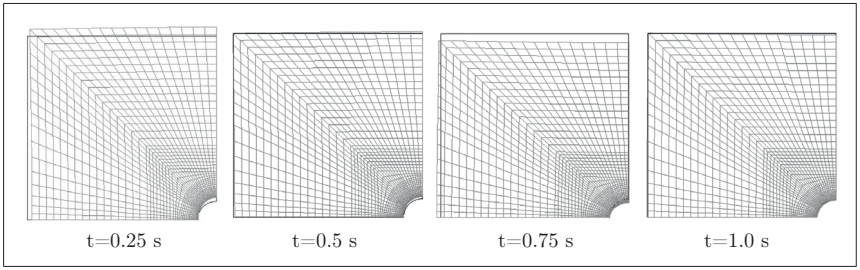

Figure 5.3.: Deformation states at distinct points in time scaled by factor 20

For the conventional approach, identical results are obtained. In order to quantify the appearing errors, the stress and displacement evolution at the selected points ① -④ of Figure 5.1 of the classical and the multifield procedure are compared to the reference solution provided by (Stein, 2003). The respective developments are shown in Figure 5.4.

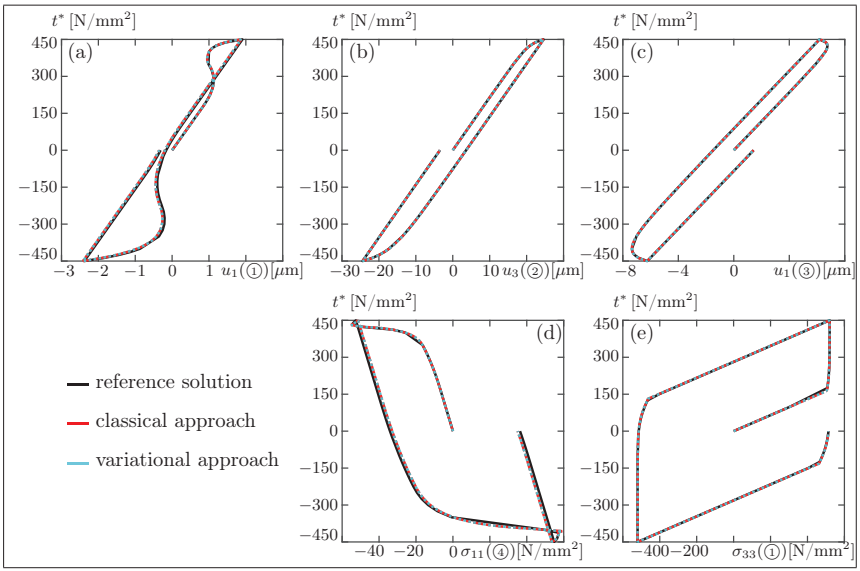

Figure 5.4.: Comparison of the solutions of the classical/variational approach to the reference solution at the evaluation points ①-④: (a)-(c) Displacement-load diagrams, (d)-(e) Stress-load diagrams

Therein, it can be seen that the conventional and the variational approach yield identical graphs. If the maximal absolute discrepancy between both is determined and compared to the result of the classical procedure, the biggest value does not exceed $4 \cdot 10^{-4}\%$. Performing the same analysis concerning the reference solutions, larger deviations are retrieved. For a detailed review see **Appendix D**. While the difference in the evolution of the stress $\sigma_{33}(①)$ is of about 0.6%, the stress $\sigma_{11}(④)$ already varies around 3.5%. For the distinct displacement courses $u_1(③)$, $u_3(②)$ as well as $u_1(①)$, errors of circa 0.2%, 0.04% and even 10.0% prevail. These comparably huge disagreements stem from the poorly chosen spatial discretization. While, due to the high computational effort of the variational approach, only $NE = 1504$ elements are considered in the present example, the reference solution in (Stein, 2003) is derived using $NE = 65\,536$ elements. Nevertheless, the gathered results demonstrate that the classical and the multifield approach are suitable to determine appearing displacement and stress fields involving plastic effects in the context of a quasi-static analysis. With this benchmark problem, the derived algorithms and their implementations are validated. In the next step, a second benchmark problem is formulated to extend the analysis towards dynamic (visco)plasticity and to enable the investigation of corresponding time discretization schemes.

5.2. Displacement Driven Deformation of an Axisymmetric Steel Shaft

While Section 5.1 is based on a static benchmark problem, which aims at validating the derived algorithms, the following passage focuses on a new example that aims to examine dynamic aspects of plastic and viscoplastic phenomena. First studies with this example are already published in (Schröder and Kuhl, 2018), since it enables a deep analysis on the occurring effects and permits to investigate different time discretization schemes. The background for the creation of the dynamic benchmark problem is in the widest sense guided by the integrated thermomechanical forming process depicted in Figure 1.1 in **Chapter 1**. Correspondingly, an appropriate model of the steel shaft is derived whereby the appearing thermal effects are neglected.

Motivated by the shaft's rotational symmetry, a polar coordinate system with the basis vector $\boldsymbol{g}_{\mathrm{R}}$ in radial, $\boldsymbol{g}_{\mathrm{Z}}$ in axial, and $\boldsymbol{g}_{\Phi}$ in tangential direction is introduced, see Figure 5.5. For a better

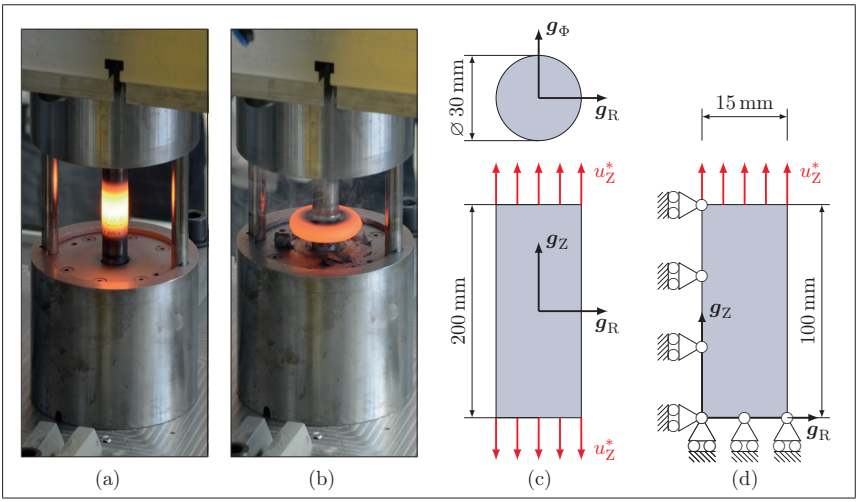

Figure 5.5.: (a) Steel shaft in the reference configuration, (b) Deformed steel shaft, (c) Sketch of the steel shaft and its dimensioning, (d) Axisymmetric model of the steel shaft and its dimensioning

distinction between cartesian and polar coordinates, the indices referring to spatial directions are now determined by letters instead of numbers. Additionally, it is assumed that there is only a symmetrically applied displacement-based load u_{Z}^{*} pointing in the shaft's longitudinal direction $\boldsymbol{g}_{\mathrm{Z}}$. Due to both, the workpiece geometry as well as its load state, the displacement field is solely characterized by its radial and axial components $\boldsymbol{u}(\boldsymbol{X}) = [u_{\mathrm{R}}, u_{\mathrm{Z}}]$, cf. (Göldner et al., 1991; Kreißig and Benedix, 2002). Furthermore, these two aspects lead to the fact that an arbitrary meridian half plane with $\Phi = \text{const.}$ can be taken into account to describe the steel shaft's properties. Hence, for all derivatives $\partial(\bullet)/\partial\Phi = 0$ has to hold and the location vector reduces to $\boldsymbol{X} = [R, Z]$. These modifications cause small adaptations of the formerly introduced continuum mechanical theory and its numerical realization. The result is an axisymmetric strain

state

$$\boldsymbol{\varepsilon} = \begin{bmatrix} \varepsilon_{\mathrm{RR}} & 0 & \varepsilon_{\mathrm{RZ}} \\ 0 & \varepsilon_{\Phi\Phi} & 0 \\ \varepsilon_{\mathrm{RZ}} & 0 & \varepsilon_{\mathrm{ZZ}} \end{bmatrix} = \begin{bmatrix} \dfrac{\partial u_{\mathrm{R}}}{\partial R} & 0 & \dfrac{1}{2}\left[\dfrac{\partial u_{\mathrm{Z}}}{\partial R} + \dfrac{\partial u_{\mathrm{R}}}{\partial Z}\right] \\ 0 & \dfrac{u_{\mathrm{R}}}{R} & 0 \\ \dfrac{1}{2}\left[\dfrac{\partial u_{\mathrm{Z}}}{\partial R} + \dfrac{\partial u_{\mathrm{R}}}{\partial Z}\right] & 0 & \dfrac{\partial u_{\mathrm{Z}}}{\partial Z} \end{bmatrix}. \tag{5.3}$$

For a detailed derivation and further aspects concerning polar coordinates see **Appendix C**. Together with the material laws in **Chapter 4**, an axisymmetric stress state

$$\boldsymbol{\sigma} = \begin{bmatrix} \sigma_{\mathrm{RR}} & 0 & \sigma_{\mathrm{RZ}} \\ 0 & \sigma_{\Phi\Phi} & 0 \\ \sigma_{\mathrm{RZ}} & 0 & \sigma_{\mathrm{ZZ}} \end{bmatrix} \tag{5.4}$$

is generated, cf. (Kreißig and Benedix, 2002). Exploiting the symmetry with respect to the $\boldsymbol{g}_{\mathrm{R}}$ - axis yields the axisymmetric model of the steel shaft, consisting of one quarter of a meridian plane equipped with appropriate boundary conditions, see Figure 5.5. Thus, the number of unknowns can be reduced drastically compared to a general three-dimensional case.

5.2.1. Classical Approach towards Elastoplasticity

In order to be able to apply the classical approach of small strain elastoplasticity of Section 4.1 to the described axisymmetric example, modifications of the tangential quantities in (4.26) have to be performed. In the first step, the fact that there are zero entries in the stress (5.4) and strain tensor (5.3) is exploited for a rearrangement into

$$\overline{\overline{\boldsymbol{\varepsilon}}} = \begin{bmatrix} \varepsilon_{\mathrm{RR}} \\ \varepsilon_{\Phi\Phi} \\ \varepsilon_{\mathrm{ZZ}} \\ \varepsilon_{\mathrm{RZ}} \end{bmatrix}, \qquad \overline{\overline{\boldsymbol{\sigma}}} = \begin{bmatrix} \sigma_{\mathrm{RR}} \\ \sigma_{\Phi\Phi} \\ \sigma_{\mathrm{ZZ}} \\ 2\sigma_{\mathrm{RZ}} \end{bmatrix}, \qquad \overline{\overline{\mathbf{G}}} = \begin{bmatrix} G_{\mathrm{RRRR}} & G_{\mathrm{RR\Phi\Phi}} & G_{\mathrm{RRZZ}} & 2G_{\mathrm{RRRZ}} \\ G_{\Phi\Phi\mathrm{RR}} & G_{\Phi\Phi\Phi\Phi} & G_{\Phi\Phi\mathrm{ZZ}} & 2G_{\Phi\Phi\mathrm{RZ}} \\ G_{\mathrm{ZZRR}} & G_{\mathrm{ZZ\Phi\Phi}} & G_{\mathrm{ZZZZ}} & 2G_{\mathrm{ZZRZ}} \\ 2G_{\mathrm{RZRR}} & 2G_{\mathrm{RZ\Phi\Phi}} & 2G_{\mathrm{RZZZ}} & 4G_{\mathrm{RZRZ}} \end{bmatrix}. \tag{5.5}$$

Consequently, the algorithmic constitutive tensor $\mathbb{G}$ is recast too. Furthermore, it is taken into account that the dimension of the tangential mass matrix is reduced, compared to the general three-dimensional case, since the axisymmetric displacement vector only consists of the two unknowns $\boldsymbol{u}(\boldsymbol{X}) = [u_{\mathrm{R}}, u_{\mathrm{Z}}]$. The displacement-based load leads to the fact that the volume forces and the surface forces within the load vector can be neglected. But the greatest change has to be carried out within the tangential stiffness matrix. Due to the introduction of polar coordinates and their position-dependent basis vectors, an additional term has to be considered concerning gradient impaired quantities, see **Appendix C**. This is achieved by expressing the strains using the **B**-operator in conjunction with the displacement vector $\boldsymbol{u}$

$$\overline{\overline{\boldsymbol{\varepsilon}}} = \sum_{i=1}^{NN} \mathbf{B}^i \boldsymbol{u}^i, \qquad \mathbf{B}^i = \begin{bmatrix} \dfrac{\partial N^i}{\partial R} & \dfrac{N^i}{R} & 0 & \dfrac{1}{2}\dfrac{\partial N^i}{\partial Z} \\ 0 & 0 & \dfrac{\partial N^i}{\partial Z} & \dfrac{1}{2}\dfrac{\partial N^i}{\partial R} \end{bmatrix}^{\mathrm{T}}. \tag{5.6}$$

Thus, for Equation (4.26) the adapted tangential quantities

$$\mathbf{m}^{eij} = \int_{\Omega^e} \rho_0 N^i N^j \, \mathbf{I} \, |\boldsymbol{J}^e| dV^e, \tag{5.7}$$

$$\mathbf{k}^{eij} = \int_{\Omega^e} \left[\mathbf{B}^i\right]^{\mathrm{T}} \overline{\overline{\mathbf{G}}}^k \mathbf{B}^j \, |\boldsymbol{J}^e| dV^e, \tag{5.8}$$

$$\mathbf{r}_1^{ei} = \int_{\Omega^e} N^i \, \rho_0 \ddot{\boldsymbol{u}}^{e,k} \, |\boldsymbol{J}^e| dV^e + \int_{\Omega^e} \rho_0 \left[\mathbf{B}^i\right]^{\mathrm{T}} \overline{\overline{\boldsymbol{\sigma}}}^k \, |\boldsymbol{J}^e| dV^e \tag{5.9}$$

are obtained, whereby the included element volume is specified as $dV^e = 2\pi R^e dR^e dZ^e$. For the realization of the previously described axisymmetric implementation strategy, the simulation parameters in Figure 5.6 (b) are exploited, unless stated otherwise. The prescribed displacement u_{Z}^* is characterized by a time-dependent sinusoidal function with frequency ω, see Figure 5.6 (c). The obtained simulation results are investigated on various levels. While the complete set of field variables is needed for the time discretization analysis, the spatial discretization will mainly be examined by considering the discrete points ① and ② or the horizontal and vertical sections a-a and b-b in Figure 5.6 (a).

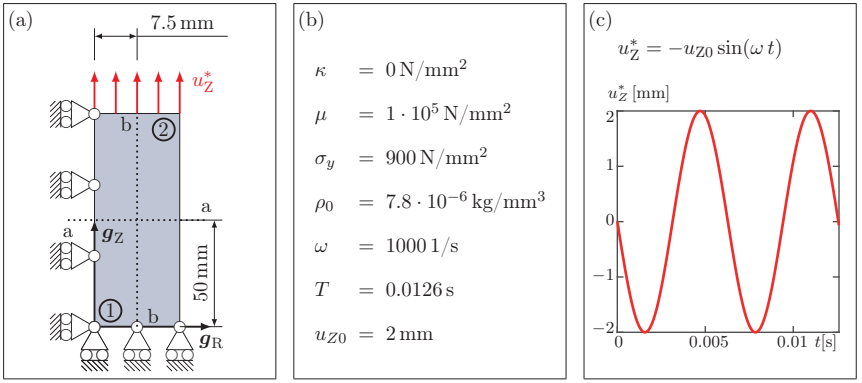

Figure 5.6.: (a) Evaluation cuts and points of the axisymmetric model:
①: $R = 1\,\mathrm{mm}$, $Z = 1\,\mathrm{mm}$, ②: $R = 14\,\mathrm{mm}$, $Z = 99\,\mathrm{mm}$, (b) Simulation parameter, (c) Prescribed displacement u_Z^*

5.2.1.1. Quasi-Static Analysis

Generally, an elastoplastic problem is influenced by two kinds of dynamic effects. On the one hand, the plastic strains are described by means of an evolution equation - while, on the other hand, inertia effects are considered in the balance of linear momentum. In a first step towards a proper access to the axisymmetric ideal elastoplastic benchmark problem the latter phenomena are neglected. This will facilitate the classification of the appearing effects in dynamic elastoplasticity later on. Within the numerical implementation, this is achieved by setting the density of the entire elastoplastic body to zero $\rho_0 = 0\,\mathrm{kg/mm^3}$. Hence, the time included in the inhomogeneous boundary condition u_{Z}^* can be regarded as a pseudotime, exchangeable by any other monotonous function, cf. (Hartmann, 2008; Stein, 2003). The time increments can then

be interpreted as a kind of load factor. However, because of the extension to the dynamic and the viscoplastic case later on, the terminus time and time increment will be preserved. For an exemplary mesh consisting of $NE_{\mathrm{R}} = 1$ and $NE_{\mathrm{Z}} = 10$ bilinear continuous LAGRANGE elements in the $\boldsymbol{g}_{\mathrm{R}}$ and the $\boldsymbol{g}_{\mathrm{Z}}$-direction, Figure 5.7 shows the temporal progress of the model characterizing quantities at the evolution points ① /②. For the time discretization, the backward EULER scheme is used with a time step size of $\Delta t = 1 \cdot 10^{-5}$ s.

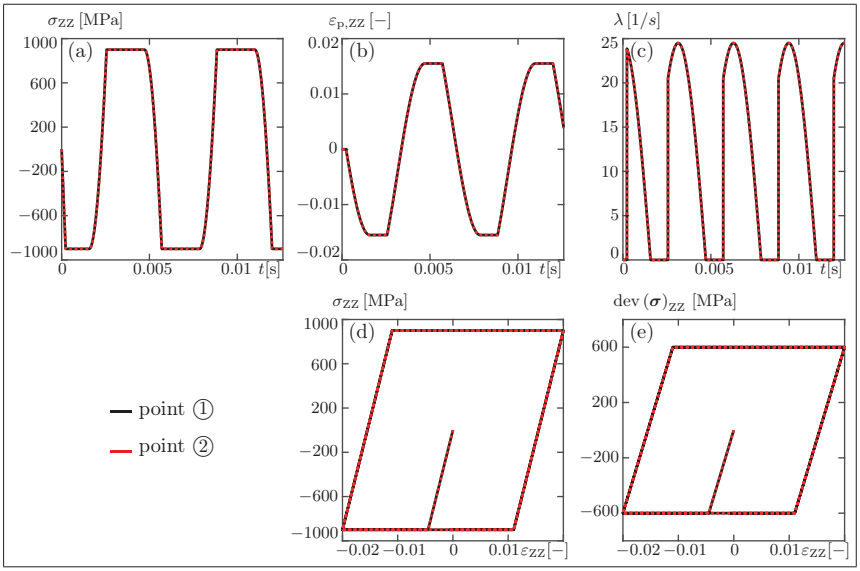

Figure 5.7.: Evaluation for $NE_{\mathrm{R}} = 1, NE_{\mathrm{Z}} = 10$ at points ①/②: (a) Stress-time diagram, (b) Plastic strain-time diagram, (c) LAGRANGE multiplier-time diagram, (d) Stress-strain diagram, (e) Deviatoric stress-strain diagram

Additionally, to improve convergence, a step size control is applied, following the strategy described in (Kanzow, 2007). It is based on the ARMIJO rule, stating that in each NEWTON-RAPHSON iteration the inequality

$$\frac{1}{2}\left\|\mathbf{r}_{\mathrm{eff}}(\mathbf{u}_{ni}^{k} + u\Delta\mathbf{u}_{ni})\right\|^{2} \leq \frac{1}{2}\left\|\mathbf{r}_{\mathrm{eff}}(\mathbf{u}_{ni}^{k})\right\| - u\, g\left[\mathbf{r}_{\mathrm{eff}}(\mathbf{u}_{ni}^{k})^{\mathrm{T}}\mathbf{K}_{\mathrm{eff}}(\mathbf{u}_{ni}^{k})\right]\Delta\mathbf{u}_{ni} \tag{5.10}$$

has to be fulfilled. The included parameters are in a first step chosen in an echo of (Kanzow, 2007) as $u = 0.8$ and $g = 10^{-2}$. While the variable g is held constant, u is halved as long as Inequality (5.10) is violated.

Figure 5.7 (a)-(c) show the evolution of the σ_{ZZ} component of the stress tensor, the $\varepsilon_{\mathrm{p,ZZ}}$ component of the plastic strain tensor, and the LAGRANGE multiplier over time. Figure 5.7 (d)-(e) demonstrate the stress-strain diagram as well as the deviatoric stress-strain diagram. Due to the sinusoidally applied displacement boundary condition u_{Z}^{*}, a cyclic deformation process is induced, which can be seen in Figure 5.7 (a)-(e). By considering the sign of the stress component σ_{ZZ} in Figure 5.7 (a), a clear distinction of the tension and compression state can be realized. The switching point between elastic and plastic behavior is apparent from Figure 5.7 (c). If

the LAGRANGE multiplier is zero, purely elastic behavior prevails. In these regimes, the plastic strain component $\varepsilon_{\mathrm{p,ZZ}}$ remains constant, see Figure 5.7 (b). The graph in the stress-strain diagram Figure 5.7 (d) reveals that the yield stress of $\sigma_{\mathrm{y}} = 900\ \mathrm{N/mm^2}$ is reached in the entire plastic regime. This indicates that, despite the axisymmetric modeling, a uniaxial stress state in the $\boldsymbol{g}_{\mathrm{Z}}$-direction is obtained, cf. (Hartmann, 2008). The same conclusion can be drawn from Figure 5.7 (e). Another important aspect becomes apparent if the curves in evaluation point ① and ② are compared. Although both points are situated on opposite sides of the model, the graphs are identical throughout the deformation process. This suggests that a homogeneous stress state exists at any point in time.

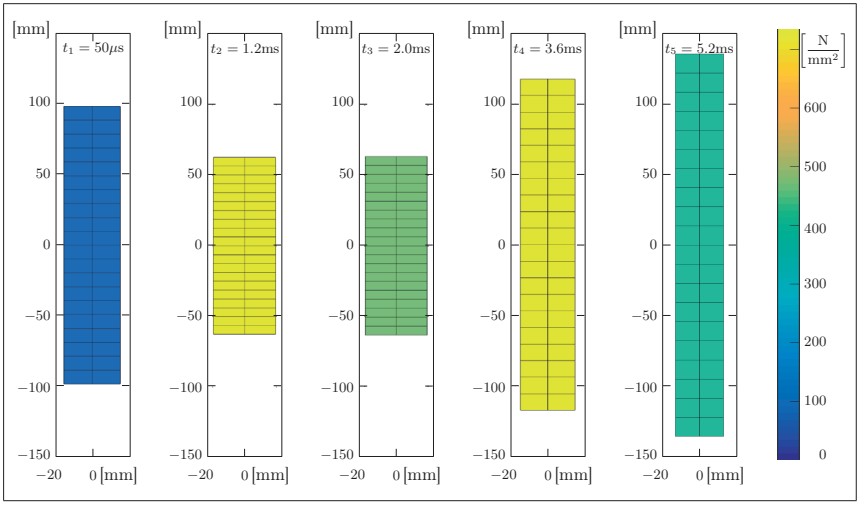

Figure 5.8.: Contour plot of the VON MISES stress for $NE_{\mathrm{R}} = 1, NE_{\mathrm{Z}} = 10$

The contour plots of the von MISES stress at various points in time in Figure 5.8 confirm this. Therein, the results of the entire steel shaft are depicted by mirroring. While the stress states at t_1, t_3, t_5 exhibit a purely elastic behavior, all elements at t_2, t_4 deform purely plastically. Furthermore, Figure 5.8 shows the simulated displacement field, scaled by the factor 20, highlighting the instantaneous deformation of the whole elastoplastic body if the applied load is changed. This phenomenon can be attributed to the lack of inertia effects.

In order to determine the influence of the spatial discretization, the number of elements in the $\boldsymbol{g}_{\mathrm{R}}$- as well as in the $\boldsymbol{g}_{\mathrm{Z}}$-direction is varied. The consequences with respect to the model-characterizing quantities are analyzed in Figure 5.9. Since Figure 5.7 demonstrates that there is no difference between the evaluation points ① /②, only point ① is investigated. Moreover, it suffices to consider the stress-strain relationship and the evolution of the plastic strains, because their course is decisive for ideal plastic effects. In Figure 5.9 (a)-(b), the number of elements in the radial direction is varied, while the discretization in axial direction is held constant. Neither the stress-strain diagram nor the plastic strain-time diagram show discrepancies between the distinct element variations. Figure 5.9 (c)-(d) show identical results, although they contain alterations in the number of elements in $\boldsymbol{g}_{\mathrm{Z}}$-direction. Hence, the spatial discretization has no importance at all.

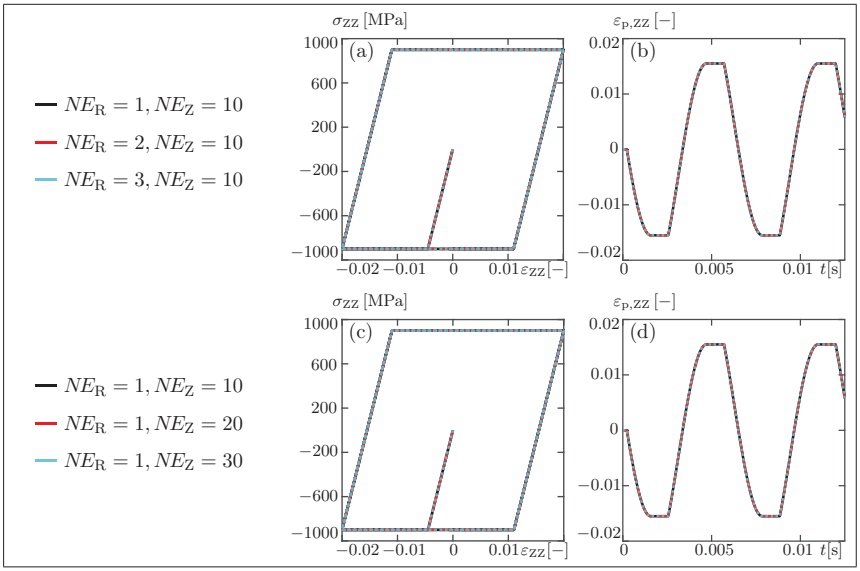

Figure 5.9.: Evaluation point ①: (a) Stress-strain diagram and (b) Plastic strain-time diagram with varying NE_R, (c) Stress-strain diagram and (d) Plastic strain-time diagram with varying NE_Z

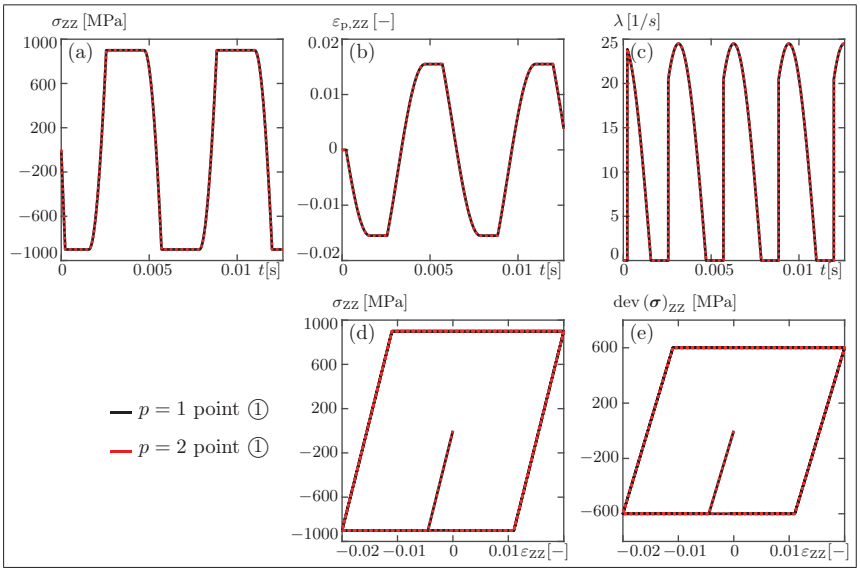

Figure 5.10.: Evaluation for $NE_R = 1, NE_Z = 10, p = 1/NE_R = 1, NE_Z = 5, p = 2$ at point ①: (a) Stress-time diagram, (b) Plastic strain-time diagram, (c) Lagrange multiplier-time diagram. (d) Stress-strain diagram, (e) Deviatoric stress-strain diagram

To illustrate the influence of the polynomial degree p of the applied LAGRANGE elements, an exemplary biquadratic mesh with about the same number of nodes as the standard bilinear mesh with $NE_{\mathrm{R}} = 1$ and $NE_{\mathrm{Z}} = 10$ is used for the axisymmetric elastoplastic continuum. A selection of results obtained by exploiting the biquadratic mesh with $NE_{\mathrm{R}} = 1$,$NE_{\mathrm{Z}} = 5$ and $p = 2$ is depicted in Figure 5.10. Thereby, the stresses, the strains, the LAGRANGE multiplier and the displacement field of the linear and the quadratic approach are interrelated at evaluation point ①. Regardless of the material state, whether elastic or plastic behavior prevails, the graphs for the polynomial degrees $p = 1$ and $p = 2$ in Figure 5.10 are identical. Thus, in this example, also the polynomial degree of the considered LAGRANGE shape functions has no impact. Due to the spatial analysis of the quasi-static axisymmetric model, a mesh dependence of the solutions is ruled out. Furthermore, the occurrence of a homogeneous uniaxial stress state is elaborated. The problematic nature of ideal elastoplasticity concerning localization effects can thus be neglected, cf. (Ebobisse and Reddy, 2004; Moreau, 1976; Pamin, 1994; Suquet, 1978). The next step is to investigate the influence of the employed backward EULER scheme as time discretization method of the evolution equation. In order to do so, the local h-error of Equation (3.102) is determined for the displacement field, the stress field, and the plastic strain field for three distinct time step sizes. Figure 5.11 shows the respective error evolutions over time for the standard linear mesh with $NE_{\mathrm{R}} = 1$ and $NE_{\mathrm{Z}} = 10$ elements.

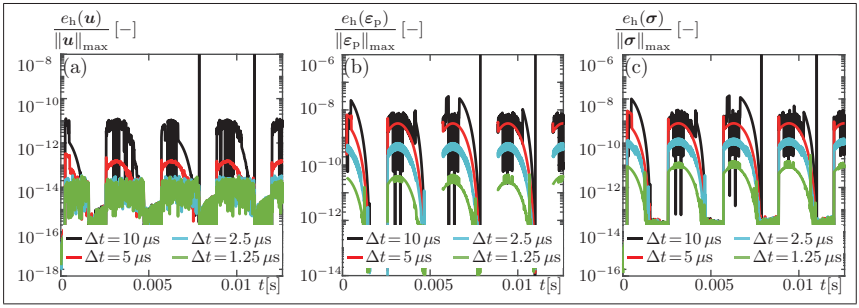

Figure 5.11.: Evaluation of the displacement, the stress and the LAGRANGE multiplier time discretization error for $NE_{\mathrm{R}} = 1, NE_{\mathrm{Z}} = 10$: (a) Displacement error-time diagram, (b) Plastic strain error-time diagram, (c) Stress error-time diagram

In Figure 5.11 (a) it can be seen that the local displacement error increases during plastic behavior and decreases in the elastic regime. Furthermore, it decreases with decreasing time step sizes. For a time step size of 5μs, it oscillates around the order of $1 \cdot 10^{-13}$ - while smaller time step sizes cause the error curves to lie on top of each other. The local plastic strain error diagram in Figure 5.11 (b) reveals greater differences between the distinct time step sizes - but, once again, decreasing time step sizes also lead to a decrease in the error. Since the plastic strain field is necessary to determine the stress tensor, strong similarities between the two local error curves in Figure 5.11 (b)-(c) can be recognized. Due to these generally small errors, the backward EULER scheme with the chosen time step size of $\Delta t = 1 \cdot 10^{-5}$s can be seen as a possibility to obtain adequate results in the quasi-static subproblem of the dynamic elastoplastic benchmark. With this analysis, fundamental impressions of the axisymmetric model's behavior are obtained and can serve as preliminary considerations. From now on the original dynamic problem formulation will be investigated together with an analysis of the higher order accurate schemes presented in Section 3.4.

5.2.1.2. Dynamic Analysis

While the previous paragraph is concerned with the quasi-static case of ideal elastoplasticity, inertia effects will be treated in what follows. Once more, the axisymmetric model of the steel shaft in Figure 5.6 forms the foundation of the analysis. This time, however, it is necessary to also define appropriate initial conditions. At the beginning, the displacement field is set to zero in the entire shaft. In contrast, the velocity field varies linearly in the shaft's longitudinal direction, whereby the course depicted in Figure 5.17 is applied to the outer nodes. First, the spatial discretization is analyzed - again based on the exemplary mesh consisting of $NE_{\mathrm{R}} = 1$ and $NE_{\mathrm{Z}} = 10$ bilinear elements in $\boldsymbol{g}_{\mathrm{R}}$ as well as $\boldsymbol{g}_{\mathrm{Z}}$-direction. For the time discretization, the backward EULER scheme with a time step size $\Delta t = 1 \cdot 10^{-5}$s is applied. As an initial approach to evaluate the obtained results, the temporal progress of the material characterizing quantities in the evaluation points ① /② are depicted in Figure 5.12.

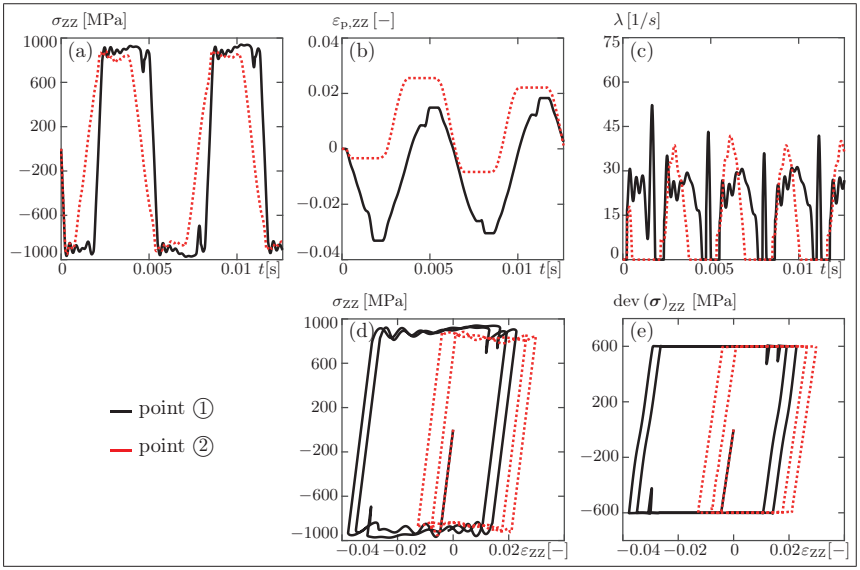

Figure 5.12.: Evaluation for $NE_{\mathrm{R}} = 1, NE_{\mathrm{Z}} = 10$ at points ①/②:
(a) Stress-time diagram, (b) Plastic strain-time diagram, (c) LAGRANGE multiplier-time diagram, (d) Stress-strain diagram, (e) Deviatoric stress-strain diagram

Figure 5.12 (a) shows the evolution of the stress component σ_{ZZ} over time. It reveals a similar characteristic as in Figure 5.7 (a), where the quasi-static case is analyzed. However, in Figure 5.12 (a) differences between the stress evolution at the evaluation points ① /② are perceptible, and for both points the ideal plastic regime is marked by oscillations. The temporal progress of the plastic strain $\varepsilon_{\mathrm{p,ZZ}}$ and the LAGRANGE multiplier in Figure 5.12 (b)-(c) have even less common ground with their quasi-static counterparts in Figure 5.7 (b)-(c). The discrepancies between the graphs at evolution point ① and the ones at evolution point ② increase too. Figure 5.12 (d) portrays the stress-strain diagram of the ZZ-components, whereby the ideal plastic regime is characterized by oscillations. Moreover, it can be recognized that the switching point between elastic and plastic behavior clearly depends on the analyzed spatial position.

This effect is also to be seen in Figure 5.12 (e), where the evolution of the ZZ-component of the stress deviator is depicted over the ZZ-component of the strain tensor. Therein, even jumps from the plastic into the elastic regime can be observed, if evolution point ① is considered. The corresponding diagrams of the quasi-static case in Figure 5.7 (d)-(e) do not show equivalent phenomena. In order to analyze these aspects further on, the spatial discretization is varied.

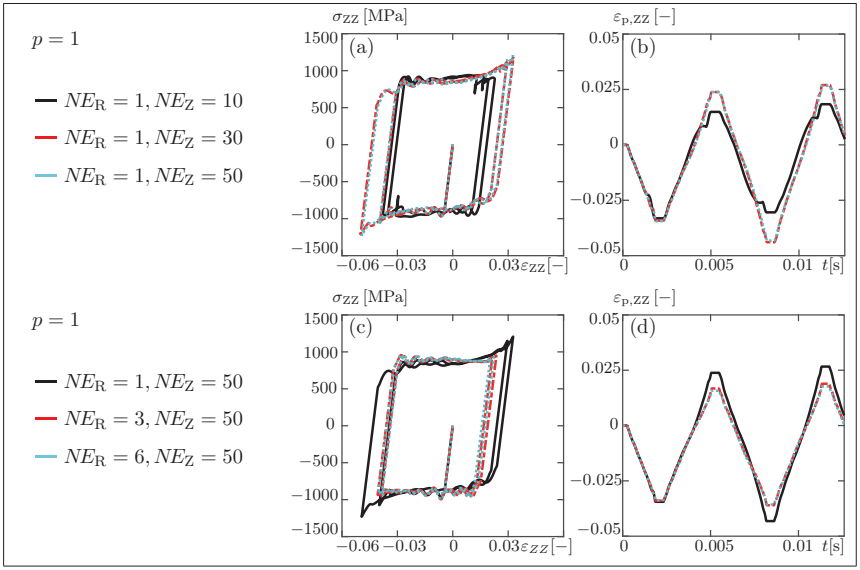

Figure 5.13.: Evaluation point ①:
(a) Stress-strain diagram, (b) Plastic strain-time diagram for varying NE_Z,
(c) Stress-strain diagram, (d) Plastic strain-time diagram for varying NE_R

Figure 5.13 shows the stress-strain diagram of the ZZ-components as well as the evolution of the ZZ-component of the plastic strain over time at the evolution point ① for a varying number of elements in $\boldsymbol{g}_R$- as well as $\boldsymbol{g}_Z$-direction. Similar results are obtained for evaluation point ②. In Figure 5.13 (a), it can be recognized that the jumps from the plastic into the elastic regime are caused by the spatial discretization. By increasing the number of elements in $\boldsymbol{g}_Z$-direction, these jumps disappear and only small oscillations in the plastic region remain. However, extending only the number of elements in $\boldsymbol{g}_Z$-direction leads to an increased stress σ_{ZZ}. If the number of elements in $\boldsymbol{g}_R$-direction is increased at the same time, this phenomenon is counteracted. This can be seen in Figure 5.13 (c). A similar effect is perceptible concerning the evolution of the plastic strain $\varepsilon_{p,ZZ}$. While the diagrams in Figure 5.13 are based on simulations involving bilinear elements, biquadratic LAGRANGE shape functions are taken into account in Figure 5.14. In the latter, again the stress-strain diagram of the ZZ-components and the evolution of the ZZ-component of the plastic strain over time are depicted for a varying number of elements. A comparison of Figure 5.14 (a) and Figure 5.13 (c) shows that the result for a bilinear mesh with $NE_R = 6$ and $NE_Z = 50$ elements is alike to a biquadratic mesh with $NE_R = 1$ and $NE_Z = 10$ elements. However, the number of nodes changes from $NN = 357$ to $NN = 22$. Moreover, Figure 5.14 (a) does not show an increase in the stress if the number of elements

is extended in $\boldsymbol{g}_{\mathrm{Z}}$-direction, as it is the case in Figure 5.13 (a). A variation of the number of elements in $\boldsymbol{g}_{\mathrm{R}}$-direction results in only small changes in the stress-strain diagram as well as in the plastic strain-time diagram, see Figure 5.14 (c)-(d). Hence, the investigated biquadratic meshes represent a good spatial discretization. For a further analysis, the horizontal section a-a and the vertical section b-b of Figure 5.6 (a) are considered for a variety of biquadratic meshes.

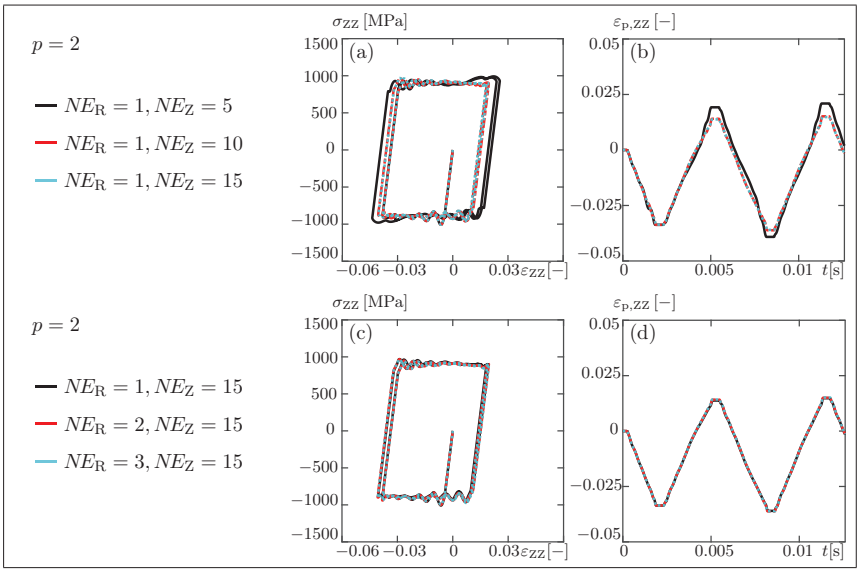

Figure 5.14.: Evaluation point ①:
(a) Stress-strain diagram, (b) Plastic strain-time diagram for varying NE_{Z},
(c) Stress-strain diagram, (d) Plastic strain-time diagram for varying NE_{R}

Figure 5.15 and Figure 5.16 represent the courses of the normed axial displacement as well as the normed radial displacement in these sections at two arbitrarily chosen points in time $t = 1.2$ms and $t = 2.8$ms. Figure 5.15 (a) as well as Figure 5.16 (a) demonstrate the expected result that the equally applied inhomogeneous boundary condition leads to a constant axial displacement in section a-a. The radial displacement in this section follows a linear behavior at both points in time, see Figure 5.15 (c) and Figure 5.16 (c). Within the section b-b, however, nonlinearities are perceptible which can be attributed to the prevalent inertia effects, see Figure 5.15 (b)/(d) and Figure 5.16 (b)/(d). Nevertheless, the influence of the spatial discretization on the results obtained in sections a-a and b-b is negligible. Together with the results depicted in Figure 5.13 and Figure 5.14 it can be seen that a biquadratic mesh containing $NE_{\mathrm{R}} = 2$ as well as $NE_{\mathrm{Z}} = 15$ elements leads to a spatially convergent solution. Hence, only this spatial configuration will be investigated in the following.

In order to emphasize the differences between the quasi-static and the dynamic analysis, a series of contour plots for 16 selected points in time is displayed. These points are marked by black circles in Figure 5.17, where the applied inhomogeneous boundary condition and its time derivatives can be observed. Thus, it can be recognized that $t_1 - t_3$ and $t_{10} - t_{11}$ coincide with a compression of the steel shaft, whereas $t_5 - t_8$ embody a tensional deformation. The points t_4 as well as t_9 are reversal points.

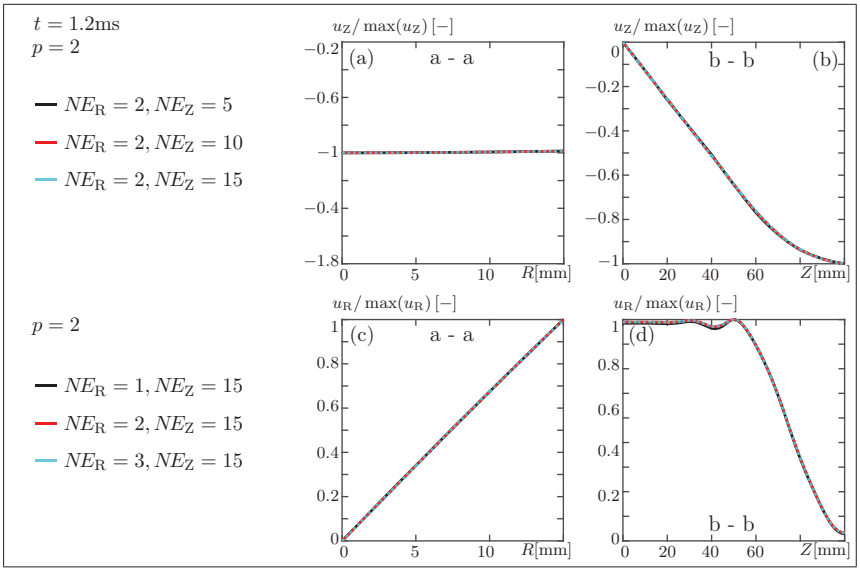

Figure 5.15.: Point in time $t = 1.2$ms: (a) Axial displacement over radius, (b) Axial displacement in axial direction, (c) Radial displacement over radius, (d) Radial displacement in axial direction

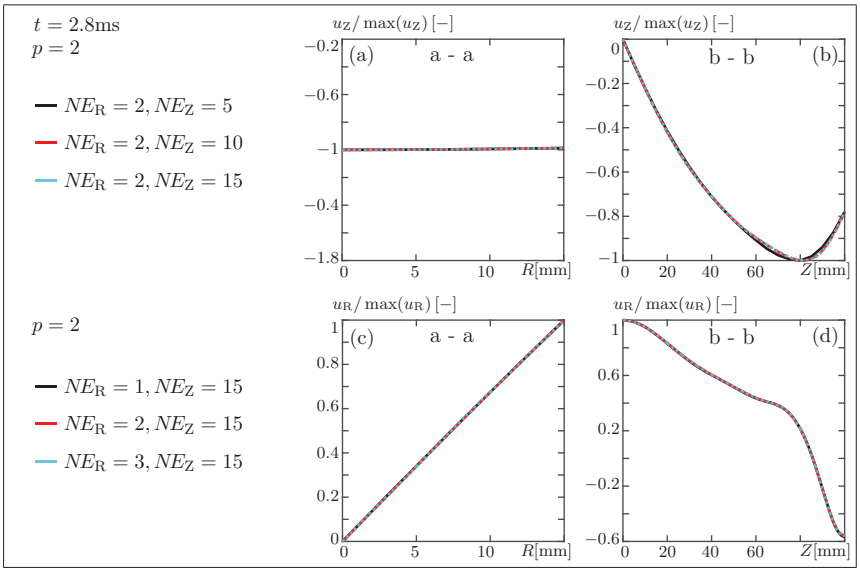

Figure 5.16.: Point in time $t = 2.8$ms: (a) Axial displacement over radius, (b) Axial displacement in axial direction, (c) Radial displacement over radius, (d) Radial displacement in axial direction

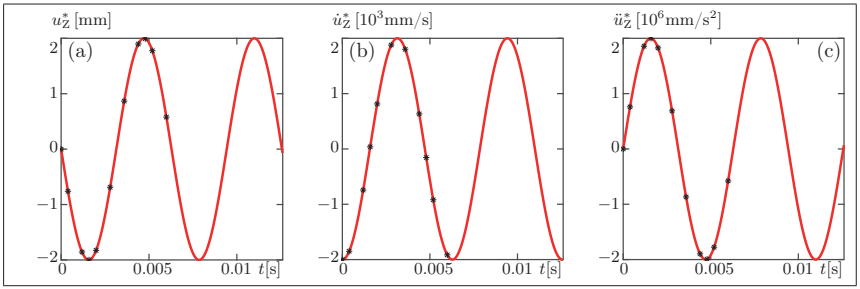

Figure 5.17.: Temporal course of the applied boundary condition and its time derivatives

Figure 5.18 (a) shows the corresponding deformation process of the steel shaft over time, scaled by the factor 20, together with the contour plots of the VON MISES stress. While at the beginning of the simulation at t_1 a purely elastic behavior can be observed, the point in time t_2 is already characterized exclusively by plastic effects. Such homogeneous stress distributions can be recognized in Figure 5.8 within the quasi-static case as well. The contour plot at the point in time t_3, however, clearly portrays an inhomogeneous stress distribution. Despite the continuously performed compression, a local unloading within the steel shaft can be observed. This phenomenon occurs because inertia effects are considered. Due to the high frequency of $\omega = 1000$ 1/s included in the boundary condition and the linked inertia forces, an elastic wave front is induced to move through the shaft. When the reversal point of the applied boundary condition t_4 is reached and the shaft's deformation is characterized by elongation, a repeated plastification takes place - leading to homogeneous plastic VON MISES stress states in the points $t_6 - t_7$. By approaching the next reversal point t_9 of the boundary condition, the formation of another elastic wave arises. In contrast, the point in time t_{11} is again coined by homogeneous plastic effects. This interaction of elastic and plastic phenomena decreases if the frequency included in the applied boundary condition is reduced. Figure 5.18 (b) shows contour plots of the resulting VON MISES stress distribution at the points in time where the amplitudes of the displacement boundary condition are identical to those assigned at the points in time of Figure 5.18 (a). However, the frequency under consideration is changed to $\omega = 200$ 1/s, leading to almost entirely homogeneous stress distributions. To demonstrate that these unloading and reloading phenomena are not induced by the spatial discretization, the contour plot of Figure 5.18 (a) at t_4 is examined in detail. In Figure 5.19, different spatial discretizations are compared, constituting that the width of the elastic zone is not influenced by the mesh size. This stands in strong contrast to the localization aspects known from static ideal elastoplasticity, cf. (Pamin, 1994). The variation of the time step size results in similar effects. The position and the width of the elastic regime remains unaffected.

Thus, due to the application of high-frequency dependent boundary conditions, local unloading and reloading effects can be recognized, which do not lead to mesh or time step size dependencies. Similar circumstances concerning the generation and the evolution of plastic and elastic wave fronts and the corresponding effects are analyzed in (Chakrabarty, 2000; Cristescu, 1967; Kolsky, 1963; Lubliner, 2006; Wood, 1952). Therein, large parts of the investigations are linked to different types of wave fronts resulting, for example, from impulsive loads, which are connected to impact problems of elastoplastic solids.

After the analysis of the spatial discretization and the explanation of the appearing effects within the benchmark problem of dynamic elastoplasticity, the time discretization schemes described in Section 4.1.3.3 are investigated. For this purpose, the quadratic mesh consisting of $NE_R = 2$

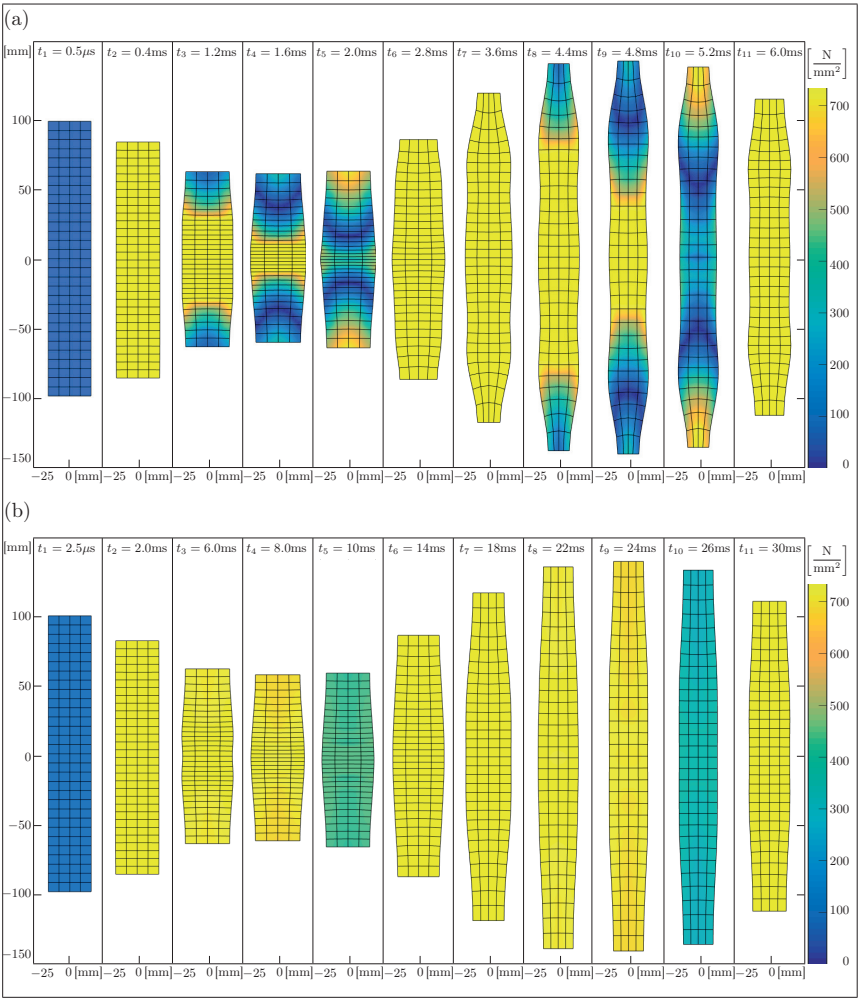

Figure 5.18.: Contour plot of the VON MISES stress for $NE_R = 2, NE_Z = 15, p = 2$,
(a) $\omega = 1000\,1/s$, (b) $\omega = 200\,1/s$

as well as $NE_Z = 15$ elements constitutes the basis for a series of simulations, wherein the DIRK(1), DIRK(2), DIRK(3), and the NEWMARK scheme are applied for distinct time step sizes. Exemplary solutions for the displacements, the stresses, the plastic strains, and the LAGRANGE multiplier for the DIRK(3) method with a time step size of $\Delta t = 1 \cdot 10^{-5}$s are listed in **Appendix E**. In order to evaluate the accuracy of the time integration methods, the local error estimators defined in Section 3.5.1 and 3.5.2 are exploited. Figure 5.20 demonstrates the obtained results for the local h-error estimator concerning the displacement, the plastic strain,

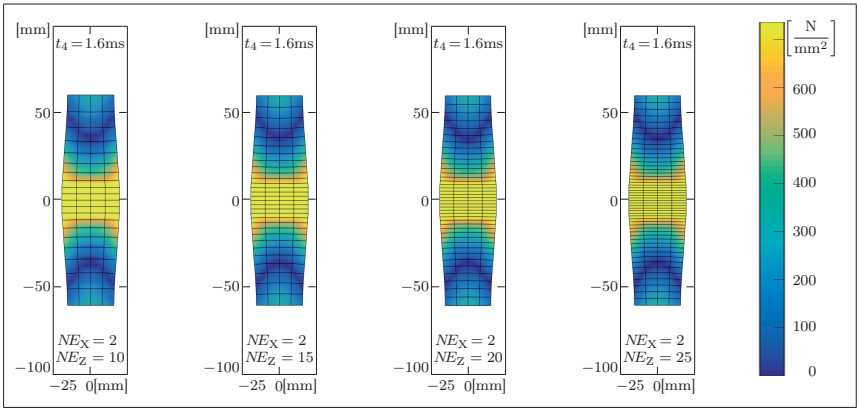

Figure 5.19.: Contour plot of the VON MISES stress for different spatial discretizations at time t_4, $p = 2$, $\omega = 1000$ 1/s

and the stress field for four distinct time step sizes. Figure 5.20 (a)-(c) can be assigned to the backward EULER scheme, while Figure 5.20 (d)-(f) represent the DIRK(2) method. The graphs in Figure 5.20 (g)-(i) are obtained exploiting the DIRK(3) method, and Figure 5.20 (k)-(m) characterize the NEWMARK scheme. It can be seen that for all time integrators a decreasing time step size leads to a decreasing local h-error of the respective field variable. Furthermore, a decrease of the local h-error can be identified if the error curves for the DIRK(1)-DIRK(3) methods are compared for a constant time step size. The local h-error of the NEWMARK approach for the same time step size lies in between the DIRK(1) and the DIRK(2) method. Generally, it can be stated that the local h-error of the stress field is higher than the one of the plastic strains. The latter, however, is greater than the one of the displacement field. Similar properties are observed for the local embedded error estimator portrayed in Figure 5.21 (a)-(d). Thereby, Figure 5.21 (a)-(b) are connected to the DIRK(2) scheme, while Figure 5.21 (c)-(d) correspond to the DIRK(3) method and the respective field variables. For the other two schemes, no embedded error estimator can be established, see Section 3.5.2. Since within the conventional approach towards elastoplasticity the stress field is not temporally differentiated, an embedded error estimator cannot be evaluated. For the displacement and the plastic strain field, the embedded error estimator shows that a decreasing time step size yields a decreasing error. Moreover, the local embedded error of the plastic strains is greater than the one of the displacement field. Additionally, the local embedded errors for the DIRK(3) method are smaller than those for the DIRK(2) scheme for a constant time step size.

The results depicted in Figure 5.20-5.21 can now be exploited to estimate the orders of convergence of the respective procedures. In order to do so, the possibilities described in Section 3.5.4 based on (Eidel and Kuhn, 2015; Grafenhorst et al., 2017) are taken into account. The obtained quantities founded on the local error are listed in Table 5.1. A comparison of the values of the distinct measurements in the individual columns shows that the way the order of consistency is determined influences the result - no matter whether the embedded or the h-error estimator is considered. For the displacement field, the calculated quantities are still similar. The backward EULER scheme almost reaches the theoretical order of one, and the DIRK(2) as well as the NEWMARK method reach roughly the theoretical order of two. Just the DIRK(3) scheme is scarcely above order two, although its theoretical order is three. Huge discrepancies, however,

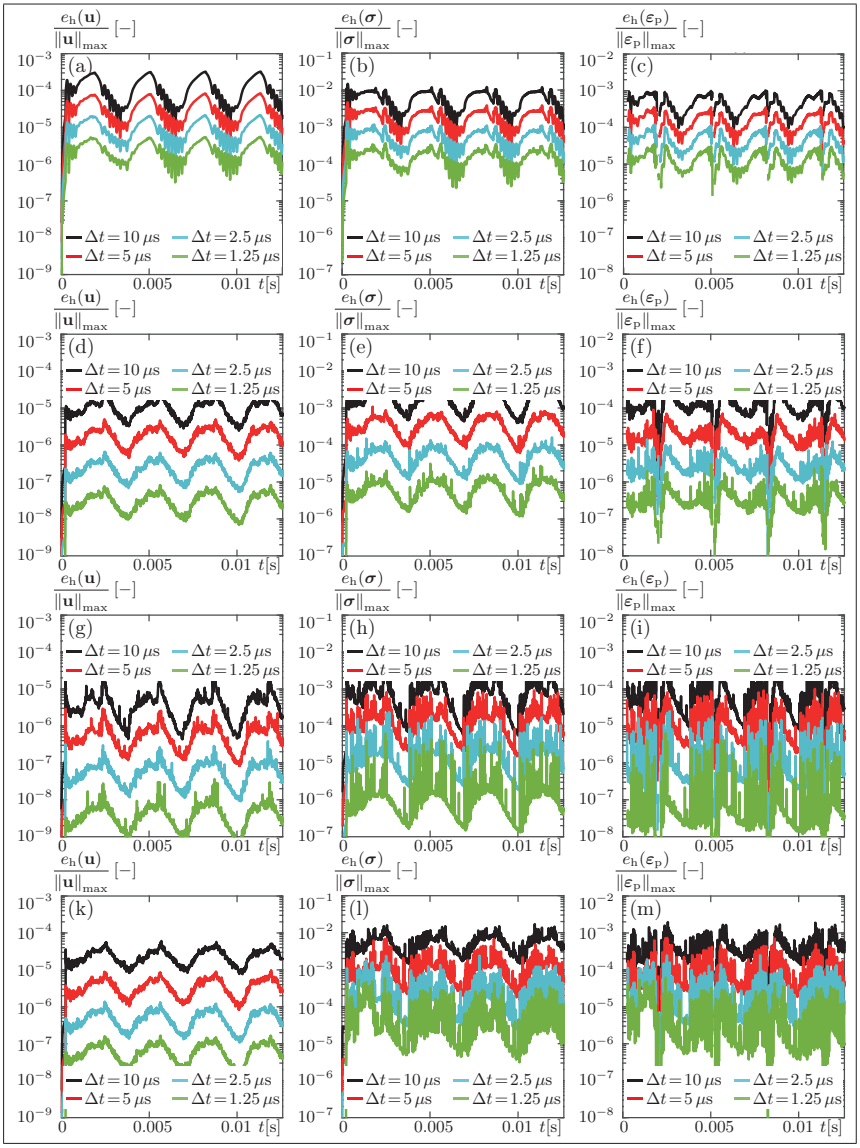

Figure 5.20.: Local time discretization error of the h-method for the displacement, the plastic strain, and the stress field for distinct time integration methods within the classical approach: (a)-(c) DIRK(1), (d)-(f) DIRK(2), (g)-(i) DIRK(3), (k)-(m) NEWMARK

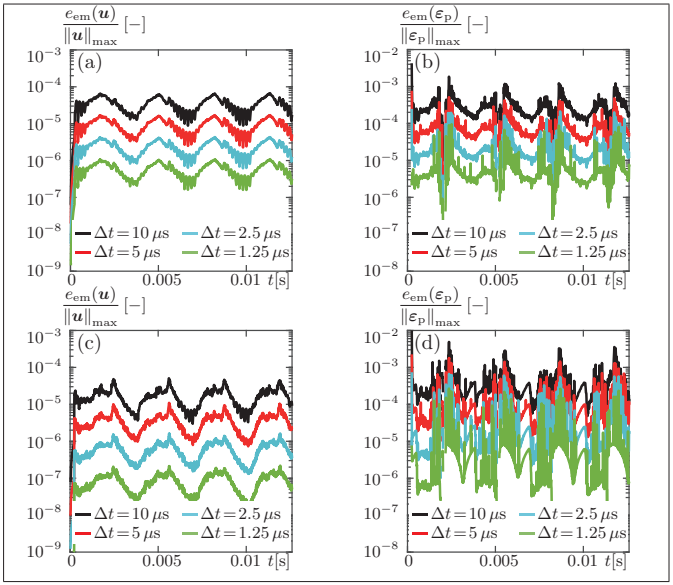

Figure 5.21.: Local embedded time discretization error for the displacement and the plastic strain field for distinct time integration methods within the classical approach: (a)-(b) DIRK(2), (c)-(d) DIRK(3)

appear for the different measurements concerning the plastic strain and the stress field. While their mean orders of consistency behave like those of the displacement field, the maximum measure leads, in the worst case, to a reduction of more than one order. A similar performance can be observed for the local embedded error estimator. However, this is an additional order below the corresponding h-error estimator, due to the fact that the embedded schemes possess by construction an order lower, see Section 3.5.2.

On the other hand, the orders of convergence are estimated directly by means of the global error, see Table 5.2. The obtained results are comparable to the values included in Table 5.1. Again, discrepancies between the two calculation procedures can be recognized, although they are smaller than within the local considerations. Concerning the achievement of the theoretical order, the global estimations turn out analogous to their local counterparts, except for the DIRK(3) method. In the global framework, the difference regarding the theoretical order for the plastic strain and the stress field is smaller. For a discussion on the possible sources for these order deviations see Section 5.2.2.

In order to reduce the expenditure for the evaluations in the following sections, only the mean consistency as well as the mean convergence order are treated. This decision can be justified by analyzing Figure 5.20, where it can be seen that increasing stage orders cause the error level to get smaller and to decrease faster. This observation is not represented by $q_{\mathrm{h}}^{\max}$. Thus, this quantity seems to be too strict to compare the particular time integrators, since it focusses on a single value. A similar argumentation holds for the respective embedded and global quantities. At best, the estimators q_{h} as well as q_{em} seem to reflect the properties depicted in the graphs in Figure 5.20-5.21. Hence, for the following examples, the order of consistency or convergence will only be determined using Equation (3.110).

Table 5.1.: Estimation of the order of consistency using distinct measurements

	$q_{\mathrm{h}}(\mathbf{u})$	$q_{\mathrm{h}}(\boldsymbol{\varepsilon}_{\mathrm{p}})$	$q_{\mathrm{h}}(\boldsymbol{\sigma})$	$q_{\mathrm{h}}^{\max}(\mathbf{u})$	$q_{\mathrm{h}}^{\max}(\boldsymbol{\varepsilon}_{\mathrm{p}})$	$q_{\mathrm{h}}^{\max}(\boldsymbol{\sigma})$	$q_{\mathrm{em}}(\mathbf{u})$	$q_{\mathrm{em}}(\boldsymbol{\varepsilon}_{\mathrm{p}})$	$q_{\mathrm{em}}^{\max}(\mathbf{u})$	$q_{\mathrm{em}}^{\max}(\boldsymbol{\varepsilon}_{\mathrm{p}})$
DIRK(1)	0.84	0.73	0.74	0.96	0.66	0.75	–	–	–	–
DIRK(2)	1.86	1.91	1.82	1.88	1.33	1.40	0.98	0.96	0.98	0.65
DIRK(3)	2.46	2.59	2.36	2.12	1.09	1.06	1.68	1.36	1.73	0.73
NEWMARK	1.91	1.30	1.38	1.88	0.66	0.62	–	–	–	–

Table 5.2.: Estimation of the order of convergence for different field variables

	$q_{\mathrm{h}}^{\mathrm{glob}}(\mathbf{u})$	$q_{\mathrm{h}}^{\mathrm{glob}}(\boldsymbol{\varepsilon}_{\mathrm{p}})$	$q_{\mathrm{h}}^{\mathrm{glob}}(\boldsymbol{\sigma})$	$q_{\mathrm{h}}^{\mathrm{glob,max}}(\mathbf{u})$	$q_{\mathrm{h}}^{\mathrm{glob,max}}(\boldsymbol{\varepsilon}_{\mathrm{p}})$	$q_{\mathrm{h}}^{\mathrm{glob,max}}(\boldsymbol{\sigma})$
DIRK(1)	1.04	0.97	0.83	0.93	0.91	0.84
DIRK(2)	1.91	1.73	1.48	1.88	1.61	1.31
DIRK(3)	2.47	2.31	2.09	2.43	2.09	1.91
NEWMARK	1.92	1.69	1.34	1.96	1.60	1.16

5.2.2. Variational Approach towards Dynamic Elastoplasticity

In the context of the classical approach, a profound investigation of the displacement-driven deformation of an axisymmetric steel shaft is carried out. Now, this knowledge is used to validate the variational multifield approach for elastoplasticity derived in Section 4.2. The equivalence between the classical and the multifield approach concerning quasi-static aspects was already demonstrated in the scope of the benchmark problem in Section 5.1. To investigate the differences if inertia effects are considered, the dynamic benchmark problem in Section 5.2 is taken into account. For a simulation using the variational approach, the tangential quantities in the system of Equations (4.73) have to be simplified in analogy to the classical approach in Section 5.2.1, taking the axisymmetric properties of the example into account. Accordingly, the expressions for the axisymmetric strain and stress state in Equations (5.3) and (5.4) remain as valid as their respective reformulations into vector-valued quantities in $(5.5)_1$ and $(5.5)_2$. The relation between the strain field vector and the displacement field established in Equation (5.6) prevails too. Additionally, the following recasts

$$\overline{\overline{\boldsymbol{\varepsilon}}}_{\mathrm{p}} = \begin{bmatrix} \varepsilon_{\mathrm{p,RR}} \\ \varepsilon_{\mathrm{p,\Phi\Phi}} \\ \varepsilon_{\mathrm{p,ZZ}} \\ \varepsilon_{\mathrm{p,RZ}} \end{bmatrix}, \qquad \overline{\overline{\mathbf{C}}}_{\mathrm{e}} = \begin{bmatrix} C_{\mathrm{e,RRRR}} & C_{\mathrm{e,RR\Phi\Phi}} & C_{\mathrm{e,RRZZ}} & 2C_{\mathrm{e,RRRZ}} \\ C_{\mathrm{e,\Phi\PhiRR}} & C_{\mathrm{e,\Phi\Phi\Phi\Phi}} & C_{\mathrm{e,\Phi\PhiZZ}} & 2C_{\mathrm{e,\Phi\PhiRZ}} \\ C_{\mathrm{e,ZZRR}} & C_{\mathrm{e,ZZ\Phi\Phi}} & C_{\mathrm{e,ZZZZ}} & 2C_{\mathrm{e,ZZRZ}} \\ 2C_{\mathrm{e,RZRR}} & 2C_{\mathrm{e,RZ\Phi\Phi}} & 2C_{\mathrm{e,RZZZ}} & 4C_{\mathrm{e,RZRZ}} \end{bmatrix}, \tag{5.11}$$

$$\overline{\overline{\mathbf{f}}} = \begin{bmatrix} \dfrac{\partial f(\boldsymbol{\sigma})}{\partial \sigma_{\mathrm{RR}}} \\ \dfrac{\partial f(\boldsymbol{\sigma})}{\partial \sigma_{\Phi\Phi}} \\ \dfrac{\partial f(\boldsymbol{\sigma})}{\partial \sigma_{\mathrm{ZZ}}} \\ 2\dfrac{\partial f(\boldsymbol{\sigma})}{\partial \sigma_{\mathrm{RZ}}} \end{bmatrix}, \qquad \overline{\overline{\mathbf{I}}} = \begin{bmatrix} I_{\mathrm{RRRR}} & I_{\mathrm{RR}\Phi\Phi} & I_{\mathrm{RRZZ}} & 2I_{\mathrm{RRRZ}} \\ I_{\Phi\Phi\mathrm{RR}} & I_{\Phi\Phi\Phi\Phi} & I_{\Phi\Phi ZZ} & 2I_{\Phi\Phi\mathrm{RZ}} \\ I_{\mathrm{ZZRR}} & I_{\mathrm{ZZ}\Phi\Phi} & I_{\mathrm{ZZZZ}} & 2I_{\mathrm{ZZRZ}} \\ 2I_{\mathrm{RZRR}} & 2I_{\mathrm{RZ}\Phi\Phi} & 2I_{\mathrm{RZZZ}} & 4I_{\mathrm{RZRZ}} \end{bmatrix}, \tag{5.12}$$

$$\overline{\overline{\mathbf{F}}} = \begin{bmatrix} \dfrac{\partial^2 f(\boldsymbol{\sigma})}{\partial \sigma_{\mathrm{RR}} \partial \sigma_{\mathrm{RR}}} & \dfrac{\partial^2 f(\boldsymbol{\sigma})}{\partial \sigma_{\mathrm{RR}} \partial \sigma_{\Phi\Phi}} & \dfrac{\partial^2 f(\boldsymbol{\sigma})}{\partial \sigma_{\mathrm{RR}} \partial \sigma_{\mathrm{ZZ}}} & 2\dfrac{\partial^2 f(\boldsymbol{\sigma})}{\partial \sigma_{\mathrm{RR}} \partial \sigma_{\mathrm{RZ}}} \\ \dfrac{\partial^2 f(\boldsymbol{\sigma})}{\partial \sigma_{\Phi\Phi} \partial \sigma_{\mathrm{RR}}} & \dfrac{\partial^2 f(\boldsymbol{\sigma})}{\partial \sigma_{\Phi\Phi} \partial \sigma_{\Phi\Phi}} & \dfrac{\partial^2 f(\boldsymbol{\sigma})}{\partial \sigma_{\Phi\Phi} \partial \sigma_{\mathrm{ZZ}}} & 2\dfrac{\partial^2 f(\boldsymbol{\sigma})}{\partial \sigma_{\Phi\Phi} \partial \sigma_{\mathrm{RZ}}} \\ \dfrac{\partial^2 f(\boldsymbol{\sigma})}{\partial \sigma_{\mathrm{ZZ}} \partial \sigma_{\mathrm{RR}}} & \dfrac{\partial^2 f(\boldsymbol{\sigma})}{\partial \sigma_{\mathrm{ZZ}} \partial \sigma_{\Phi\Phi}} & \dfrac{\partial^2 f(\boldsymbol{\sigma})}{\partial \sigma_{\mathrm{ZZ}} \partial \sigma_{\mathrm{ZZ}}} & 2\dfrac{\partial^2 f(\boldsymbol{\sigma})}{\partial \sigma_{\mathrm{ZZ}} \partial \sigma_{\mathrm{RZ}}} \\ 2\dfrac{\partial^2 f(\boldsymbol{\sigma})}{\partial \sigma_{\mathrm{RZ}} \partial \sigma_{\mathrm{RR}}} & 2\dfrac{\partial^2 f(\boldsymbol{\sigma})}{\partial \sigma_{\mathrm{RZ}} \partial \sigma_{\Phi\Phi}} & 2\dfrac{\partial^2 f(\boldsymbol{\sigma})}{\partial \sigma_{\mathrm{RZ}} \partial \sigma_{\mathrm{ZZ}}} & 4\dfrac{\partial^2 f(\boldsymbol{\sigma})}{\partial \sigma_{\mathrm{RZ}} \partial \sigma_{\mathrm{RZ}}} \end{bmatrix}.$$

have to be performed to yield the modified tangential quantities

$$\mathbf{m}_{\mathrm{uu}}^{eij} = \int_{\Omega^e} N^i N^j \, \mathbf{I} \, \rho_0 \, |\boldsymbol{J}^e| dV^e, \qquad \mathbf{d}_{\mathrm{sp}}^{eij} = \int_{\Omega^e} \bar{N}^i \overline{\overline{\mathbf{I}}} \, \bar{N}^j \, |\boldsymbol{J}^e| dV^e = \left[\boldsymbol{k}_{\mathrm{ps}}^{eij}\right]^{\mathrm{T}},$$

$$\mathbf{k}_{\mathrm{uu}}^{eij} = \int_{\Omega^e} \left[\mathbf{B}^i\right]^{\mathrm{T}} \overline{\overline{\mathbf{C}}}_{\mathrm{e}} \mathbf{B}^j \, |\boldsymbol{J}^e| dV^e, \qquad \mathbf{k}_{\mathrm{up}}^{eij} = -\int_{\Omega^e} \left[\mathbf{B}^i\right]^{\mathrm{T}} \overline{\overline{\mathbf{C}}}_{\mathrm{e}} \bar{N}^j \, |\boldsymbol{J}^e| dV^e = \left[\boldsymbol{k}_{\mathrm{pu}}^{eij}\right]^{\mathrm{T}},$$

$$\mathbf{k}_{\mathrm{pp}}^{eij} = \int_{\Omega^e} \bar{N}^i \overline{\overline{\mathbf{C}}}_{\mathrm{e}} \bar{N}^j \, |\boldsymbol{J}^e| dV^e, \qquad \mathbf{k}_{\mathrm{ss}}^{eij} = -\int_{\Omega^e} \bar{N}^i \lambda^{e,k} \, \overline{\overline{\mathbf{F}}}^{e,k} \, \bar{N}^j \, |\boldsymbol{J}^e| dV^e,$$

$$\mathbf{k}_{\mathrm{s}\lambda}^{elj} = -\int_{\Omega^e} \bar{N}^{l/i} \left[\overline{\overline{\mathbf{f}}}^{e,k}\right]^{\mathrm{T}} \bar{N}^{j/n} |\boldsymbol{J}^e| dV^e = \left[\mathbf{k}_{\mathrm{s}\lambda}^{ein}\right]^{\mathrm{T}}, \qquad \mathbf{r}_{\mathrm{s}}^{ei} = \int_{\Omega^e} \bar{N}^i \left[\overline{\overline{\boldsymbol{\varepsilon}}}_{\mathrm{p}}^{e,k} - \lambda^{e,k} \overline{\overline{\mathbf{f}}}^{e,k}\right] |\boldsymbol{J}^e| dV^e,$$

$$\mathbf{r}_{\mathrm{p}}^{ei} = \int_{\Omega^e} \bar{N}^i \left[\overline{\overline{\boldsymbol{\sigma}}}^{e,k} + \overline{\overline{\mathbf{C}}}_{\mathrm{e}} \left[\overline{\overline{\boldsymbol{\varepsilon}}}_{\mathrm{p}}^{e,k} - \overline{\overline{\boldsymbol{\varepsilon}}}^{e,k}\right]\right] |\boldsymbol{J}^e| dV^e, \qquad r_{\lambda}^{el} = -\int_{\Omega^e} \bar{N}^i \, f(\boldsymbol{\sigma}^{e,k}) |\boldsymbol{J}^e| dV^e,$$

$$\mathbf{r}_{\mathrm{u}}^{ei} = \int_{\Omega^e} N^i \, \rho_0 \ddot{\boldsymbol{u}}^{e,k} \, |\boldsymbol{J}^e| dV^e + \int_{\Omega^e} \left[\mathbf{B}^i\right]^{\mathrm{T}} \left[\overline{\overline{\mathbf{C}}}_{\mathrm{e}} \left[\overline{\overline{\boldsymbol{\varepsilon}}}^{e,k} - \overline{\overline{\boldsymbol{\varepsilon}}}_{\mathrm{p}}^{e,k}\right]\right] |\boldsymbol{J}^e| dV^e.$$

It is emphasized that the included unity matrix $\mathbf{I}$ is a two-dimensional one, and the parts of the load vector related to volume or surface loads are neglected due to their irrelevance. Different shape functions are chosen for the distinct fields. While N^i represent continuous approximations, $\bar{N}^i$ characterize discontinuous ones as specified in Section 4.2.2.2. A similar approach is followed in (Schröder and Kuhl, 2015*a*). With these expressions at hand, the dynamic benchmark problem depicted in Figure 5.6 can be solved.

Therefore, again a biquadratic mesh consisting of $NE_{\mathrm{R}} = 2$ elements in radial and $NE_{\mathrm{Z}} = 15$ elements in axial direction is taken into account. As discussed in Section 5.2.1, this spatial discretization - together with biquadratic LAGRANGE shape functions for the displacement field - leads to a convergent spatial solution within the conventional approach. Hence, these aspects are taken into account for the variational ansatz as well. Additionally, the other unknown field

variables are approximated discontinuously by using biquadratic LAGRANGE shape functions with the GAUSS-LEGENDRE quadrature points listed in Table 3.1 as supporting points. For the time integration, the first step is to apply a backward EULER scheme with a time step size of $\Delta t = 1 \cdot 10^{-5}$ s. Figure 5.22 shows a comparison between the classical and the variational method concerning the evolution of the stress, the plastic strain, and the LAGRANGE multiplier over time for the evaluation point ①. Furthermore, the stress-strain and the deviatoric stress-strain diagram are represented therein.

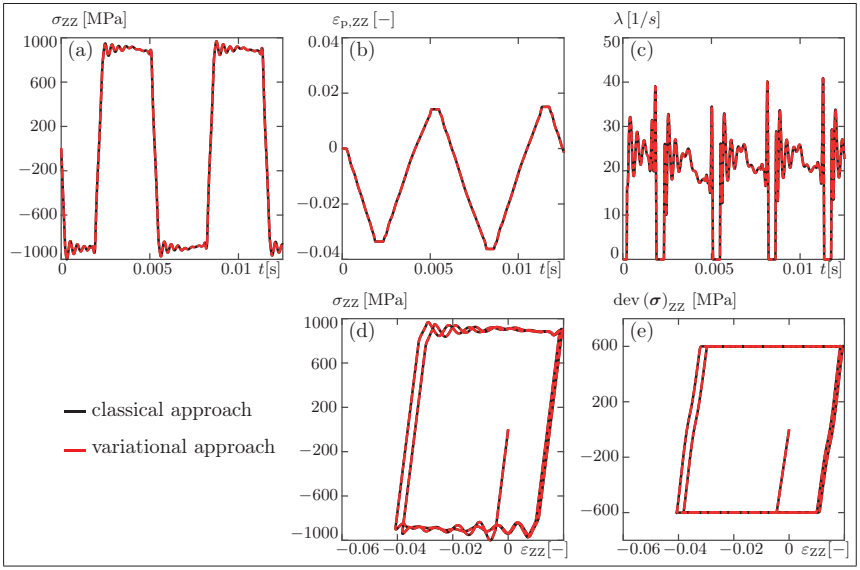

Figure 5.22.: Comparison of the classical and the variational approach at evaluation point ①: (a) Stress-time diagram, (b) Plastic strain-time diagram, (c) LAGRANGE multiplier-time diagram, (d) Stress-strain diagram, (e) Deviatoric stress-strain diagram

It can be seen that the curves for the classical and the variational approach overlay exactly. Moreover, the solutions for the entire displacement field, the stress field, the plastic strain field, and the LAGRANGE multiplier are compared at each point in time. Thereby, the maximal absolute deviation is determined and related to the corresponding result of the conventional approach. The greatest obtained value does not exceed $3 \cdot 10^{-3}$%. Identical contour plots with equivalent phenomena to those depicted in Figure 5.18 (a) are the consequence. Thus, it can be concluded that the chosen mesh contributes also within the multifield ansatz to a spatially convergent solution and, consequently, a variation in the spatial discretization leads to identical results as within the classical method in Section 5.2.1.

The same line of reasoning can be drawn with respect to the time discretization error. To prove this, the time discretization studies performed in Section 5.2.1 are repeated for the variational approach, resulting in identical curves as depicted in Figure 5.20-5.21 as well as in the same quantities as listed in Table 5.1-Table 5.2. To confirm this, local orders of consistency at discrete points in time are shown in Figure 5.23. It can be observed that the graphs for the conventional and the multifield approach lie above each other. Hence, for identical underlying conditions,

both approaches can be considered as coincident, despite the necessarily higher computational costs needed for the variational ansatz.

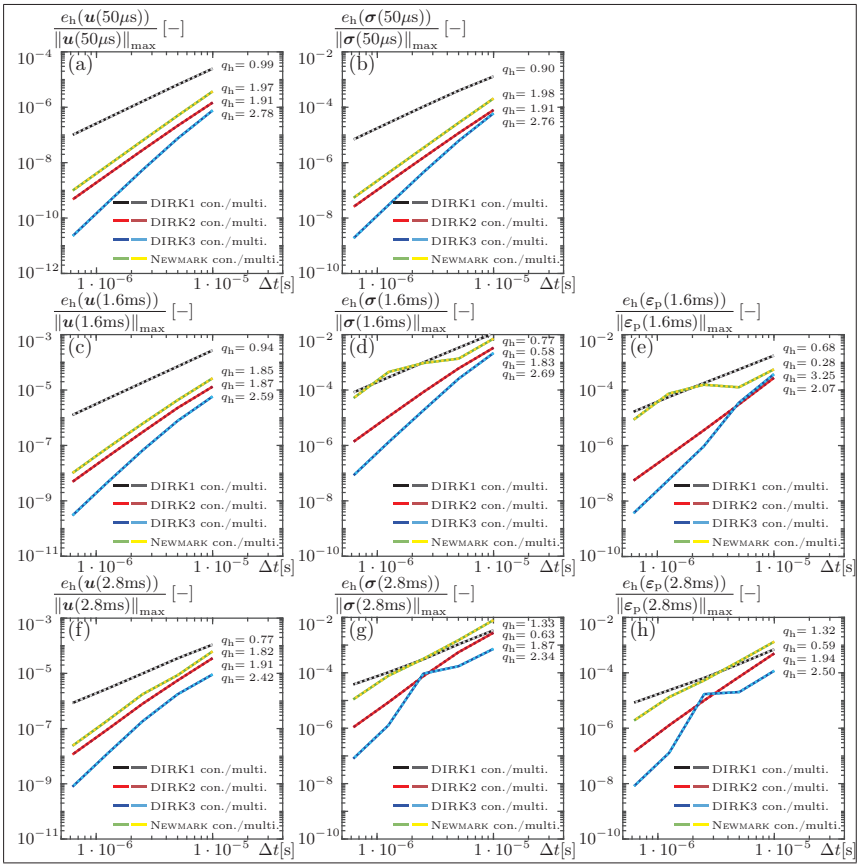

Figure 5.23.: Local orders of consistency for the h-method at distinct points in time

The first evaluated point in time at 50μs in Figure 5.23 resembles a purely elastic state of the deformation process, the point in time 1.6ms represents a mixed elastoplastic state, and the point in time 2.8ms embodies a homogeneously plastic state. If purely elastic properties prevail, the DIRK(1), DIRK(2) and the Newmark method almost achieve the ideal order of consistency. The DIRK(3) scheme with about $q_h = 2.7$ is further away. Within the mixed and the purely plastic case, the orders of consistency decrease for all schemes. Additionally, for the plastic strain field and the stress field, non-uniform consistency curves appear. Similar effects are already documented in (Büttner and Simeon, 2002; Eidel and Kuhn, 2011, 2015; Ellsiepen, 1999; Ellsiepen and Hartmann, 2001; Grafenhorst et al., 2017; Hartmann and Bier, 2007; Wieners, 1999). In (Eidel and Kuhn, 2015) three explanations are given in the context of fully coupled Runge-Kutta schemes. Therein, the phenomenon is linked to an error founded in an incon-

sistent interpolation of the strains before the plastic quantities on spatial integration point level are determined. Since Figure 5.23 refers to solutions which are determined by DIRK methods - where the stages are calculated consecutively leading to proper predictions for the strains - this is not an adequate answer within the present context. The second reason given in (Eidel and Kuhn, 2015) is supported by (Ellsiepen and Hartmann, 2001; Grafenhorst et al., 2017; Wieners, 1999), stating that the lack of non-smoothness or regularity in ideal elastoplasticity leads to the order reduction. In (Eidel and Kuhn, 2015) this is demonstrated by contrasting distinct hardening assumptions. Depending on the hardening law, the strain curve is smoothed, favoring higher orders of convergence. However, none of the authors gives a proof - and while (Eidel and Kuhn, 2015; Ellsiepen and Hartmann, 2001; Grafenhorst et al., 2017) observe an order reduction to second order, (Wieners, 1999) elaborates one to first order. Additionally, in (Hartmann and Bier, 2007) order reduction is detected within viscoplasticity even though the mathematical structure of the problem is a different one. The last argument formulated in (Eidel and Kuhn, 2015) is that an overstepping of the switching point between elastic and plastic behavior deteriorates the order of consistency. A similar line of reasoning is also followed in (Büttner and Simeon, 2002). Another analysis of this argument is performed in (Schröder and Kuhl, 2018), where the order of consistency and convergence are determined for an elasto(visco)plastic example assuming a yield stress close to zero. With this supposition, an instantaneous (visco)plastic deformation is achieved, and the switching point disappears virtually. However, an order reduction can be observed for this case as well. Furthermore, even discrepancies between the locally determined order of consistency and the globally calculated order of convergence prevail. To circumvent the switching point dilemma, (Bär and Groß, 2016) follow an endochronic approach, resulting in a convergence rate of four if hardening is considered as well. The idea behind this is, to model the elastic region already using a plasticity model. Hence, there is, per definition, no switching point. As a side effect, the problem is smoothed automatically. Concerning the current problem's order reduction, the discussion above gives only hints. A final answer cannot be given at all, and it is necessary to carry out further investigations.

As part of this, the next step is to analyze higher order accurate time integration schemes within the multifield approach. Their applicability to the classical ansatz is to some extend demonstrated in (Eidel and Kuhn, 2015). However, due to the additional effort concerning various implementation aspects, this possibility is not followed here. Figure 5.24 depicts the local h-error curves obtained for different time step sizes for the displacement field, the plastic strains and the stresses within four distinct fully implicit Runge-Kutta procedures. The first row depicts the results for the Lobatto IIIC(2) method, followed by those achieved using the Lobatto IIIC(3) scheme. Row three is linked to the Radau IIA(2) method, while the last row inherits results for the Radau IIA(3) scheme. What all procedures have in common is that the error of the respective field variables decreases with decreasing time step size. Furthermore, the methods based on three stages are characterized by smaller error heights than those consisting of two stages. If schemes with identical stage orders are compared, Radau IIA is the preferable choice concerning the error level. For the achieved orders of consistency and convergence of the individual procedures see Table 5.3. Considering the local estimates, it becomes apparent that the Lobatto IIIC(2) method is quite far away from its theoretical order of two. In contrast, the Lobatto IIIC(3) schemes almost reaches its theoretical order of four for all field variables. A similar behavior can be recognized within the Radau IIA schemes. The three-stage approach tends to the theoretical order of five, while the Radau IIA(2) method hardly achieves order three. Analyzing the corresponding global measurements in Table 5.3, however, yields a deviating picture. Apart from the Lobatto IIIC(2) scheme, all methods are estimated to reach orders well above two but not more. However, the Lobatto IIIC(2) scheme is the only method where the order of convergence is in some cases higher than the order of consistency.

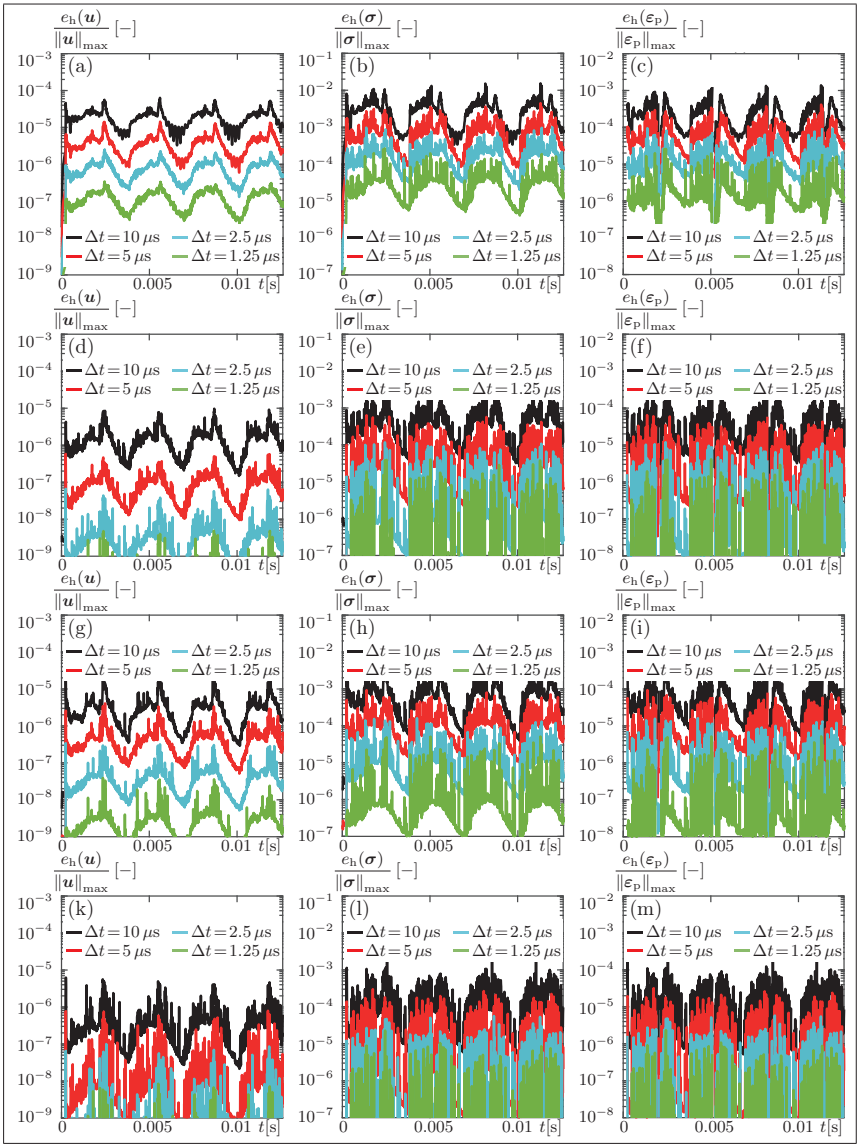

Figure 5.24.: Local time discretization error of the h-method for the displacement, the plastic strain, and the stress field for distinct time integration methods within the elasto-plastic multifield approach: (a)-(c) Lobatto IIIC(2), (d)-(f) Lobatto IIIC(3), (g)-(i) Radau IIA(2), (k)-(m) Radau IIA(3)

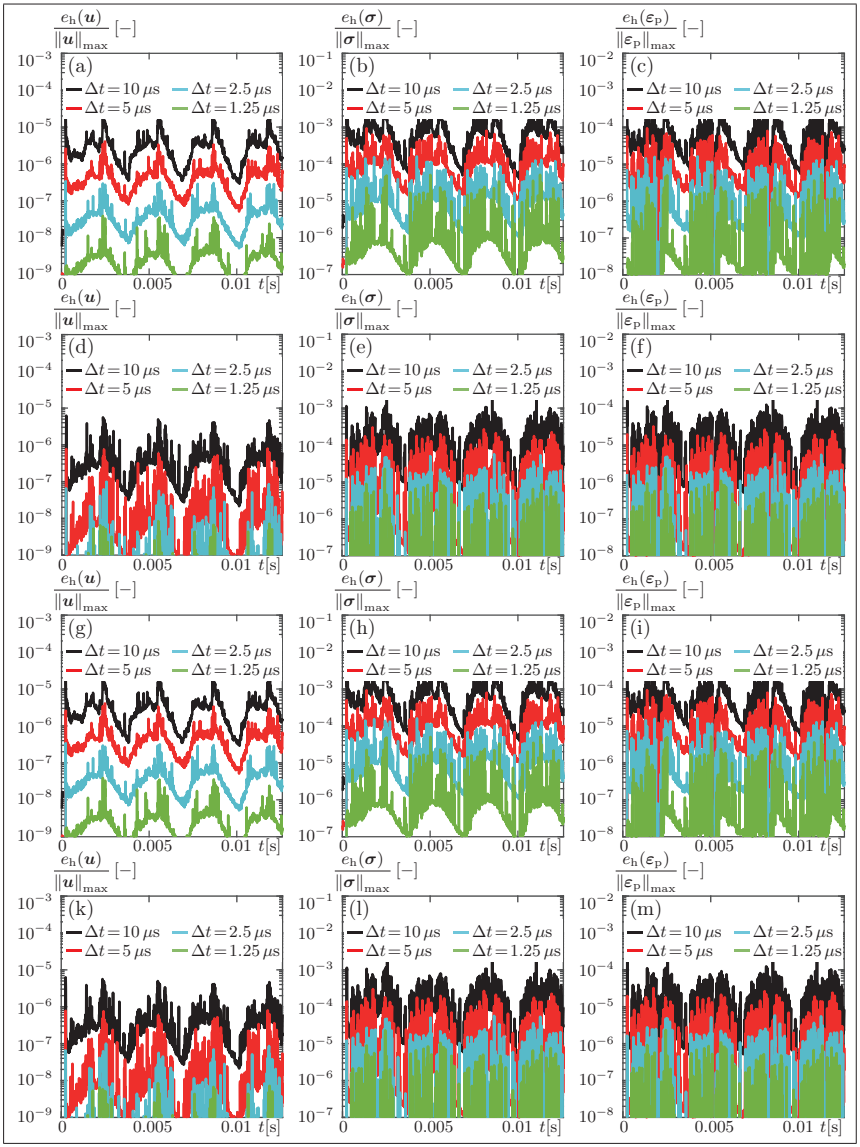

Figure 5.25.: Local time discretization error of the h-method for the displacement, the plastic strain, and the stress field for distinct time integration methods within the elastoplastic multifield approach: (a)-(c) $cG_1(2)$, (d)-(f) $cG_1(3)$, (g)-(i) $cG_2(2)$, (k)-(m) $cG_2(3)$

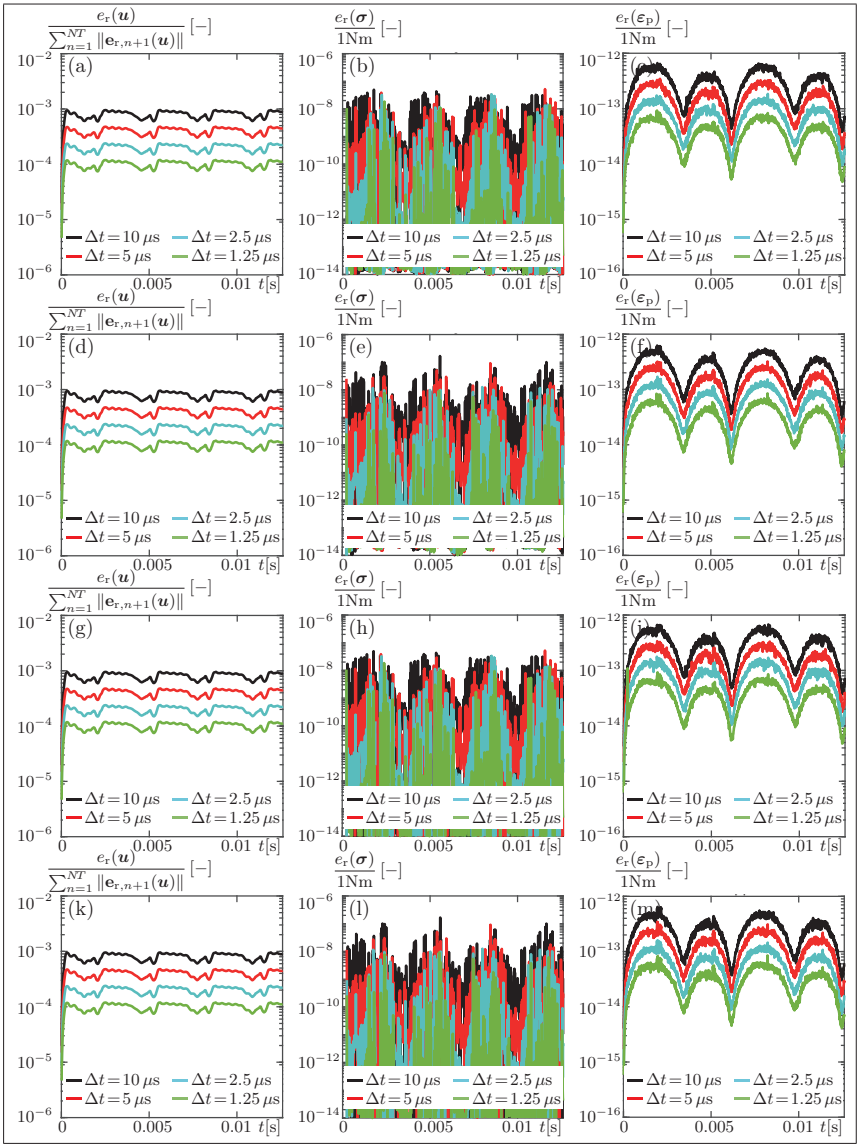

Figure 5.26.: Local residual time discretization error for the displacement, the plastic strain, and the stress field for distinct time integration methods within the elastoplastic multifield approach: (a)-(c) $cG_1(2)$, (d)-(f) $cG_1(3)$, (g)-(i) $cG_2(2)$, (k)-(m) $cG_2(3)$

In addition to the RUNGE-KUTTA schemes, also GALERKIN procedures are adapted to the multifield approach of ideal elastoplasticity. The resultant h-error curves for the displacement, the plastic strain, and the stress field for some continuous representatives are portrayed in Figure 5.25. While the first row therein is connected to a one-field setting of polynomial degree two, based on LAGRANGE shape functions with RADAU sampling points, the second row is characterized by a polynomial degree of three. For all graphs in Figure 5.25 (a)-(f), it can be observed that the error decreases with decreasing time step size. Furthermore, an increase in the polynomial degree results in a decrease of the error level, although augmented oscillations are prevalent. Figure 5.25 (g)-(m) represent the corresponding two-field formulations with similar error curves as depicted in Figure 5.25 (a)-(f). Small differences can only be recognized if the orders of consistency and convergence are compared, see Table 5.3. Both the continuous one-field and the two-field setting with polynomial degree two, roughly reach the order of three. In contrast, the two continuous GALERKIN approaches with polynomial degree three almost reach a local order of five. The coincidence between the orders of the continuous GALERKIN schemes and the implicit RADAU IIA methods might be attributed to the matching quadrature points. Additional parallelisms between both time integration families can be drawn concerning the globally determined order of convergence. The continuous GALERKIN procedures also attain orders well above two - but not more. A dissimilarity, however, is that it is possible to formulate a residual error estimator for the GALERKIN approach. The corresponding graphs for the four previously described GALERKIN schemes are portrayed in Figure 5.26. While again with decreasing time step size a decreasing error can be observed for all cases, the curves' characteristics vary drastically. Nevertheless, the orders of consistency gathered in Table 5.3 deviate only slightly. Surprisingly, the order of consistency determined by the residual error of the displacement and the plastic strain field is about one for all schemes. An order of around two is estimated for the stress field. This stands in strong contrast to the results obtained in (Gleim, 2016), where a correlation between the polynomial degree and the residual error is obtained. Therein, however, the GALERKIN procedures are assumed to be built on distinct shape functions, no inhomogeneous boundary conditions are taken into account, and the errors of the different field variables are summed up.

The last analyzed time integration class in this thesis is based on discontinuous GALERKIN schemes with LOBATTO sampling points. Similar to the continuous GALERKIN context, the one-field and the two-field setting for polynomial degrees two and three are investigated. The accompanying local h-error curves for the displacement, the plastic strain, and the stress field are illustrated in Figure 5.27. While the first two rows are associated to the one-field setting, the last two represent the two-field setting. The correlation between the first and the third row, as well as between the second and the fourth row, stems from choosing the identical polynomial degree of two or rather three. Apart from these agreements, it can be observed that for a decreasing time step size the error decreases disregarding the field variable and the time integration scheme. However, with increasing polynomial degree, oscillations become apparent. Moreover, the error of the plastic strains and the stress field tends to higher oscillations than the one of the displacement field. The numerically estimated orders of convergence are listed in Table 5.3. Comparing the results for the one and the two-field discontinuous GALERKIN setting yields the insight that the two-field approach performs slightly better. Between the various field variables, however, almost no difference can be recognized. The locally estimated orders of consistency lie in the range of four for polynomial degree two and of five for polynomial degree three. To reach such orders with the implicit RUNGE-KUTTA LOBATTO IIIC methods, at least a three-stage scheme is necessary. But if a LOBATTO IIIC(4) RUNGE-KUTTA procedure is chosen, a theoretical order of six should be obtained. Hence, despite that the discontinuous GALERKIN approach and the LOBATTO IIIC(4) scheme are based on identical supporting points, the reached orders deviate. Considering the global orders of convergence of the discontinuous GALERKIN

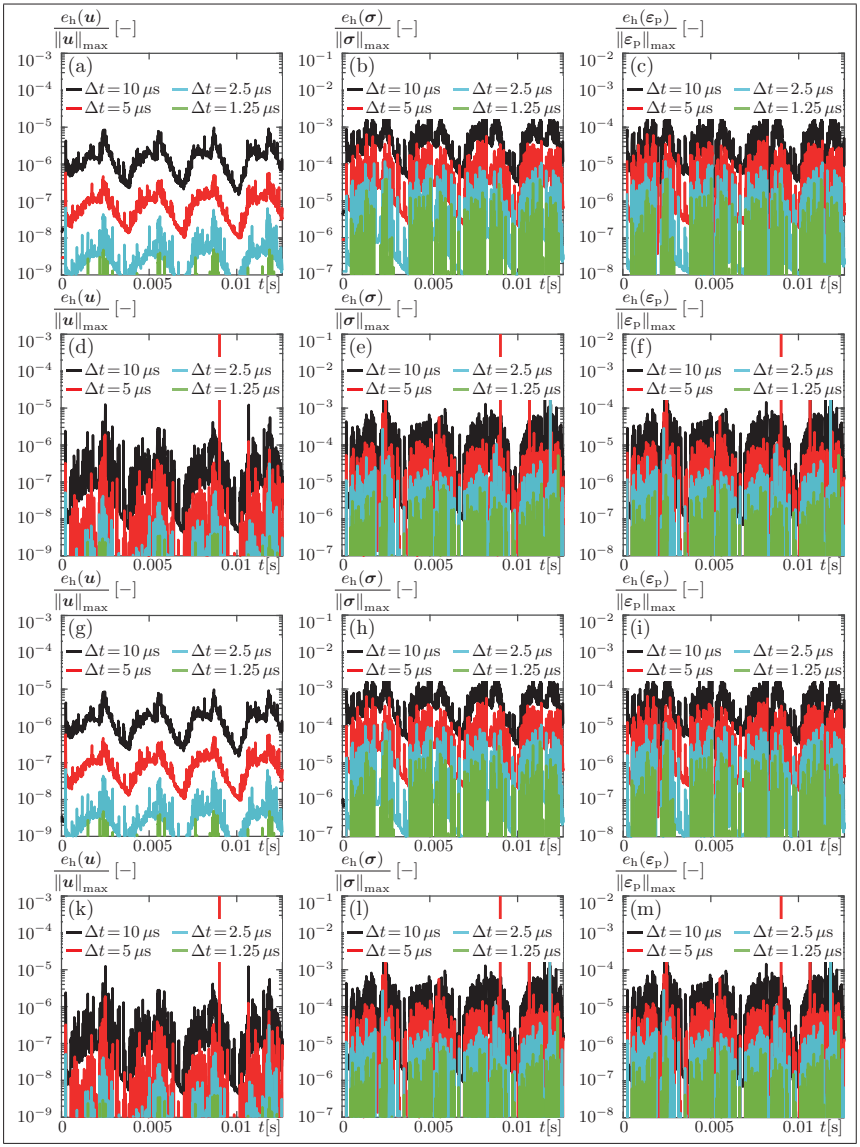

Figure 5.27.: Local time discretization error of the h-method for the displacement, the plastic strain, and the stress field for distinct time integration methods within the elastoplastic multifield approach: (a)-(c) $dG_1(2)$, (d)-(f) $dG_1(3)$, (g)-(i) $dG_2(2)$, (k)-(m) $dG_2(3)$

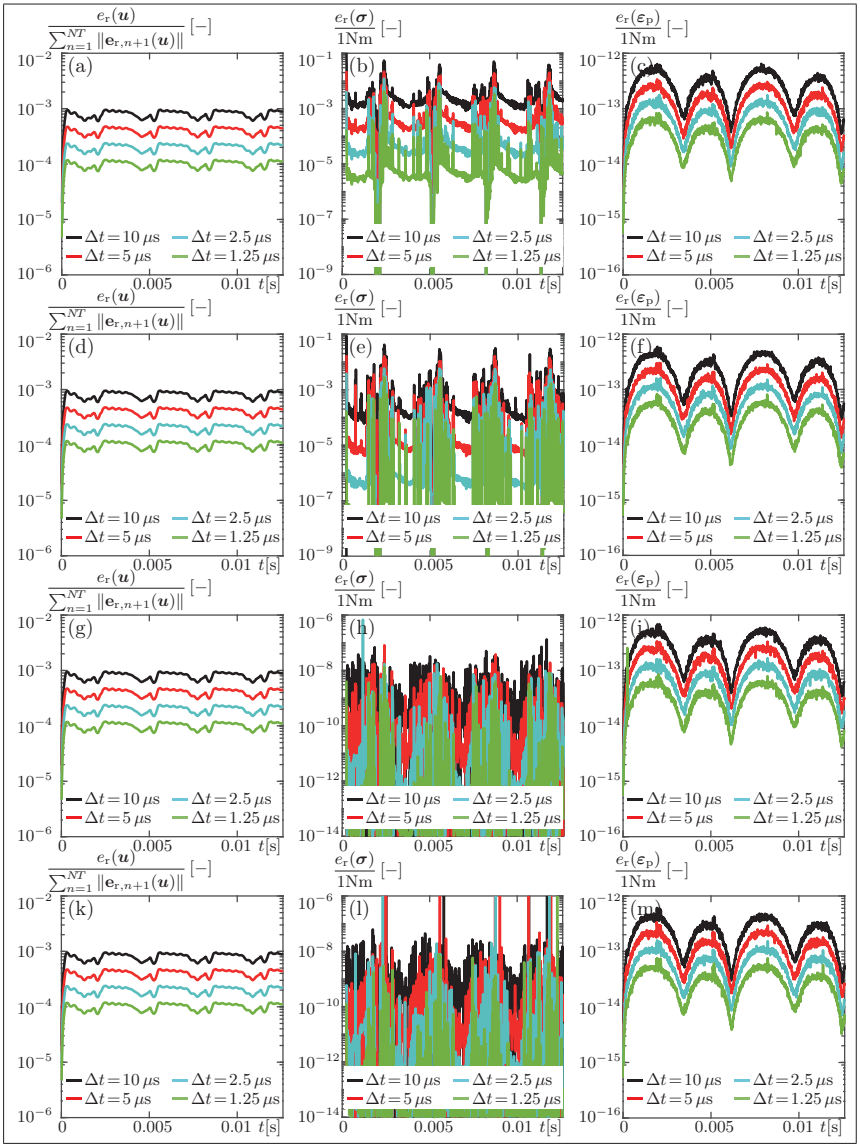

Figure 5.28.: Local residual time discretization error for the displacement, the plastic strain, and the stress field for distinct time integration methods within the elastoplastic multifield approach: (a)-(c) $dG_1(2)$, (d)-(f) $dG_1(3)$, (g)-(i) $dG_2(2)$, (k)-(m) $dG_2(3)$

Table 5.3.: Estimation of the order of consistency/convergence for small strain plasticity

	$q_\mathrm{h}(\mathbf{u})$	$q_\mathrm{h}(\boldsymbol{\varepsilon}_\mathrm{p})$	$q_\mathrm{h}(\boldsymbol{\sigma})$	$q_\mathrm{r}(\mathbf{u})$	$q_\mathrm{r}(\boldsymbol{\varepsilon}_\mathrm{p})$	$q_\mathrm{r}(\boldsymbol{\sigma})$	$q_\mathrm{h}^\mathrm{glob}(\mathbf{u})$	$q_\mathrm{h}^\mathrm{glob}(\boldsymbol{\varepsilon}_\mathrm{p})$	$q_\mathrm{h}^\mathrm{glob}(\boldsymbol{\sigma})$
Lobatto IIIC(2)	1.54	1.51	1.38	–	–	–	1.89	1.76	1.22
Lobatto IIIC(3)	3.76	3.87	3.65	–	–	–	2.33	2.34	2.84
Radau IIA(2)	2.58	2.69	2.48	–	–	–	2.51	2.40	2.24
Radau IIA(3)	4.77	4.98	4.71	–	–	–	2.22	2.19	2.48
$\mathrm{cG}_1(2)$	2.58	2.60	2.48	1.00	1.00	2.13	2.51	2.40	2.24
$\mathrm{cG}_1(3)$	4.51	4.66	4.59	1.00	1.00	2.36	2.20	2.19	2.46
$\mathrm{cG}_2(2)$	2.58	2.53	2.48	1.00	1.00	2.28	2.51	2.36	2.24
$\mathrm{cG}_2(3)$	4.74	4.73	4.71	1.00	1.02	2.61	2.23	2.15	2.48
$\mathrm{dG}_1(2)$	3.42	3.49	3.33	1.00	1.00	2.87	2.28	2.34	2.79
$\mathrm{dG}_1(3)$	4.49	4.79	4.75	1.00	0.99	3.92	1.16	1.04	1.49
$\mathrm{dG}_2(2)$	3.76	3.78	3.65	1.00	1.02	2.45	2.33	2.30	2.84
$\mathrm{dG}_2(3)$	5.19	5.22	5.32	1.00	1.00	2.73	1.22	1.03	1.54

methods, a variation between one and two can be recognized. Thereby, it is emphasized that the discontinuous procedures with polynomial degree three inherit the lower order. In addition to the local h-error, the residual error is examined. The results are depicted in Figure 5.28. It can once again be seen that decreasing time step sizes lead to a decreasing error. However, in contrast to the h-error curves, almost no differences can be detected between the schemes. Deviations are only seen for the stress field. A similar picture can be drawn for the corresponding orders of consistency. Apart from those linked to the stresses, all measurements indicate an order of one, as it is the case for the continuous Galerkin schemes. The identical residual error formulation is adapted in (Gleim, 2016) in the electromagnetic context. Therein, however, a link between the error and the polynomial degree is concluded, which cannot be confirmed here. The reason may be founded in the differences within the model problem and the analyzed Galerkin approaches. There are however still open questions concerning the theoretically obtainable orders of convergence of both the continuous and discontinuous Galerkin schemes regarding the h-error estimation. In (Gleim, 2016) the order of convergence for Galerkin procedures using Lagrange shape functions and a Gauss-Legendre quadrature rule are determined numerically to be equal to the applied polynomial degree. In (Matthies and Schieweck, 2011) a mathematical proof is given for the error estimation taking Lobatto quadratures for continuous and Radau quadratures for discontinuous Galerkin schemes into account. Further mathematical estimations are depicted in (Aziz and Monk, 1989). Another approach to ascertain the order of convergence is followed in (Botasso, 1997; Carstens, 2013; Hulme, 1972*b*; Zhao and Wei, 2013). Therein, the similarities between Runge-Kutta schemes and Galerkin procedures are exploited. Some of these relationships would most probably hold for the methods analyzed in this thesis as well.

All in all, it can be summarized that introducing the multifield approach of elastoplasticity, is an elegant way to incorporate higher order accurate schemes, like fully implicit Runge-Kutta or Galerkin methods. Due to their application, local orders of consistency of about five can be obtained and the error level is reduced drastically. Nevertheless, an order of convergence greater than three could not be numerically determined on global level. In the scope of this thesis, it can

not be ascertained whether it is simple not measurable or whether it is not reached due to special characteristics of the elastoplastic problem. For further aspects see Section 5.2.3. Moreover, the applicability of embedded and residual error estimators can be deduced by the previous studies. While the embedded schemes can be used for a time adaptive simulation strategy to judge the accuracy within and in between DIRK procedures, the residual error estimator can't serve to draw conclusions about the polynomial degree in question. However, both variants clearly have lower computational costs compared to the h-error estimator.

5.2.3. Classical Approach to Dynamic Elastoviscoplasticity

An alternative way to model the steel shaft's behavior within the integrated thermomechanical forming process depicted in Figure 1.1 in **Chapter 1** is to account for viscoplastic effects. Apart from a change in the considered physical phenomena, this modification implies a regularization of the material model's mathematical structure, see Section 4.1.2. To elucidate the appearing influences, the dynamic benchmark problem of the ideal elastoplastic case is adapted. Since only the constitutive laws on integration point level are changed within the viscoplastic modeling, Equations (5.3)-(5.9) pertain their validity to describe an axisymmetric problem appropriately. Only the entries of the algorithmic constitutive tensor and of the stress tensor have to be modified taking Equations (4.42)-(4.43) into account. Furthermore, the geometry and the parameters are chosen as depicted in Figure 5.6. Initially, the viscosity parameter χ is varied to demonstrate its influence. The simulation is carried out with the same biquadratic spatial mesh consisting of $NE_{\mathrm{R}} = 2$ as well as $NE_{\mathrm{Z}} = 15$ elements as within the elastoplastic model. For the time discretization, a backward EULER scheme with a time step size $\Delta t = 1 \cdot 10^{-5}\,\mathrm{s}$ is applied. Figure 5.29 shows the evolution of the axial component of the stress and the plastic strain for the distinct models over time at evaluation point ①. Additionally, the deviatoric stress-strain diagram is illustrated. It can be seen that a growth in χ causes the stress state to increasingly leave the yield surface. Hence, the corresponding plastic strains decrease. To ensure comparability between the elastoplastic and the viscoplastic approach concerning the analysis of time integration schemes, the viscosity parameter $\chi = 0.001\ \mathrm{Ns/mm^2}$ is selected.

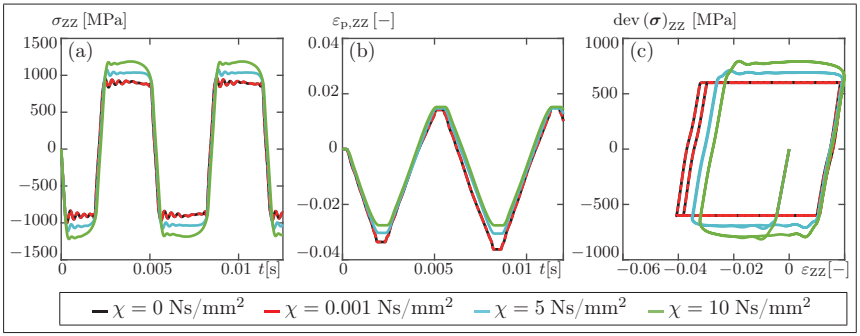

Figure 5.29.: Comparison of the elastoplastic and the viscoplastic model at evaluation point ①: (a) Stress-time diagram, (b) Plastic strain-time diagram, (c) Deviatoric stress-strain diagram

In a more precise look the maximal absolute deviations of the stress, the displacement as well as the plastic strain field are determined. Their relation to the elastoplastic approach reveals that values greater than 0.7% are not reached. Hence, this kind of spatial discretization is

not only adequate to yield a comparable solution to the elastoplastic case, but it can also be assumed to embody a convergent spatial solution of the viscoplastic problem with the chosen parameter setting. In the forthcoming analysis also the multifield approach will be presented in the viscoplastic context and different time integration schemes are examined. All other necessary parameters will be held constant, so that a further influence of the viscosity parameter on the model formulation is not investigated. A possible interrelation between its choice and the spatial as well as the temporal discretization is not investigated either.

5.2.4. Multifield Approach to Dynamic Elastoviscoplasticity

Apart from the ideal elastoplastic behavior, the multifield approach of Section 4.2 is also able to take viscoplastic properties into account. To confirm this, the dynamic benchmark problem of Section 5.2 is modified to reflect viscoplastic effects by including the viscosity parameter $\chi = 0.001\,\mathrm{Ns/mm^2}$. Additionally, the implementation strategy of the viscoplastic variational approach of Section 4.2.3 has to be modified to suffice the demands of an axisymmetric problem. In this context, the tangential quantities in the system of Equations (4.79) are simplified exploiting the relations in Equations (5.3) and (5.4) together with the rearrangements in $(5.5)_1$, $(5.5)_2$ as well as (5.11)-(5.12). To determine the approximated strains, the matrix vector relation of the displacement field and the shape functions derivatives in (5.6) are used. Furthermore, the additional statement

$$\overline{\overline{\mathbf{F}}} = \begin{bmatrix} \frac{\partial f(\boldsymbol{\sigma})}{\partial \sigma_{\mathrm{RR}}}\Big[\lambda \frac{\partial f(\boldsymbol{\sigma})}{\partial \sigma_{\mathrm{RR}}}\Big] & \frac{\partial f(\boldsymbol{\sigma})}{\partial \sigma_{\mathrm{RR}}}\Big[\lambda \frac{\partial f(\boldsymbol{\sigma})}{\partial \sigma_{\Phi\Phi}}\Big] & \frac{\partial f(\boldsymbol{\sigma})}{\partial \sigma_{\mathrm{RR}}}\Big[\lambda \frac{\partial f(\boldsymbol{\sigma})}{\partial \sigma_{\mathrm{ZZ}}}\Big] & 2\frac{\partial f(\boldsymbol{\sigma})}{\partial \sigma_{\mathrm{RR}}}\Big[\lambda \frac{\partial f(\boldsymbol{\sigma})}{\partial \sigma_{\mathrm{RZ}}}\Big] \\ \frac{\partial f(\boldsymbol{\sigma})}{\partial \sigma_{\Phi\Phi}}\Big[\lambda \frac{\partial f(\boldsymbol{\sigma})}{\partial \sigma_{\mathrm{RR}}}\Big] & \frac{\partial f(\boldsymbol{\sigma})}{\partial \sigma_{\Phi\Phi}}\Big[\lambda \frac{\partial f(\boldsymbol{\sigma})}{\partial \sigma_{\Phi\Phi}}\Big] & \frac{\partial f(\boldsymbol{\sigma})}{\partial \sigma_{\Phi\Phi}}\Big[\lambda \frac{\partial f(\boldsymbol{\sigma})}{\partial \sigma_{\mathrm{ZZ}}}\Big] & 2\frac{\partial f(\boldsymbol{\sigma})}{\partial \sigma_{\Phi\Phi}}\Big[\lambda \frac{\partial f(\boldsymbol{\sigma})}{\partial \sigma_{\mathrm{RZ}}}\Big] \\ \frac{\partial f(\boldsymbol{\sigma})}{\partial \sigma_{\mathrm{ZZ}}}\Big[\lambda \frac{\partial f(\boldsymbol{\sigma})}{\partial \sigma_{\mathrm{RR}}}\Big] & \frac{\partial f(\boldsymbol{\sigma})}{\partial \sigma_{\mathrm{ZZ}}}\Big[\lambda \frac{\partial f(\boldsymbol{\sigma})}{\partial \sigma_{\Phi\Phi}}\Big] & \frac{\partial f(\boldsymbol{\sigma})}{\partial \sigma_{\mathrm{ZZ}}}\Big[\lambda \frac{\partial f(\boldsymbol{\sigma})}{\partial \sigma_{\mathrm{ZZ}}}\Big] & 2\frac{\partial f(\boldsymbol{\sigma})}{\partial \sigma_{\mathrm{ZZ}}}\Big[\lambda \frac{\partial f(\boldsymbol{\sigma})}{\partial \sigma_{\mathrm{RZ}}}\Big] \\ 2\frac{\partial f(\boldsymbol{\sigma})}{\partial \sigma_{\mathrm{RZ}}}\Big[\lambda \frac{\partial f(\boldsymbol{\sigma})}{\partial \sigma_{\mathrm{RR}}}\Big] & 2\frac{\partial f(\boldsymbol{\sigma})}{\partial \sigma_{\mathrm{RZ}}}\Big[\lambda \frac{\partial f(\boldsymbol{\sigma})}{\partial \sigma_{\Phi\Phi}}\Big] & 2\frac{\partial f(\boldsymbol{\sigma})}{\partial \sigma_{\mathrm{RZ}}}\Big[\lambda \frac{\partial f(\boldsymbol{\sigma})}{\partial \sigma_{\mathrm{ZZ}}}\Big] & 4\frac{\partial f(\boldsymbol{\sigma})}{\partial \sigma_{\mathrm{RZ}}}\Big[\lambda \frac{\partial f(\boldsymbol{\sigma})}{\partial \sigma_{\mathrm{RZ}}}\Big] \end{bmatrix} \quad \text{with} \quad \lambda = \frac{1}{\chi}\langle f(\boldsymbol{\sigma})\rangle$$

is established to yield the modified tangential quantities

$$\mathbf{m}_{\mathrm{uu}}^{eij} = \int_{\Omega^e} N^i N^j\, \mathbf{I}\, \rho_0\, |\boldsymbol{J}^e| dV^e, \qquad \mathbf{d}_{\mathrm{sp}}^{eij} = \int_{\Omega^e} \bar{N}^i \overline{\overline{\mathbf{I}}}\, \bar{N}^j\, |\boldsymbol{J}^e| dV^e = \big[\boldsymbol{k}_{\mathrm{ps}}^{eij}\big]^{\mathrm{T}},$$

$$\mathbf{k}_{\mathrm{uu}}^{eij} = \int_{\Omega^e} \big[\mathbf{B}^i\big]^{\mathrm{T}}\, \overline{\overline{\mathbf{C}}}_{\mathrm{e}} \mathbf{B}^j\, |\boldsymbol{J}^e| dV^e, \qquad \mathbf{k}_{\mathrm{up}}^{eij} = -\int_{\Omega^e} \big[\mathbf{B}^i\big]^{\mathrm{T}}\, \overline{\overline{\mathbf{C}}}_{\mathrm{e}}\, \bar{N}^j\, |\boldsymbol{J}^e| dV^e = \big[\boldsymbol{k}_{\mathrm{pu}}^{eij}\big]^{\mathrm{T}},$$

$$\mathbf{k}_{\mathrm{pp}}^{eij} = \int_{\Omega^e} \bar{N}^i\, \overline{\overline{\mathbf{C}}}_{\mathrm{e}}\, \bar{N}^j\, |\boldsymbol{J}^e| dV^e, \qquad \mathbf{k}_{\mathrm{ss}}^{eij} = -\int_{\Omega^e} \bar{N}^i\, \overline{\overline{\mathbf{F}}}^{e,k}\, \bar{N}^j\, |\boldsymbol{J}^e| dV^e,$$

$$\mathbf{r}_{\mathrm{p}}^{ei} = \int_{\Omega^e} \bar{N}^i \Big[\overline{\overline{\boldsymbol{\sigma}}}^{e,k} + \overline{\overline{\mathbf{C}}}_{\mathrm{e}}\Big[\overline{\overline{\boldsymbol{\varepsilon}}}_{\mathrm{p}}^{e,k} - \overline{\overline{\boldsymbol{\varepsilon}}}^{e,k}\Big]\Big] |\boldsymbol{J}^e| dV^e, \qquad \mathbf{r}_{\mathrm{s}}^{ei} = \int_{\Omega^e} \bar{N}^i \Big[\overline{\overline{\boldsymbol{\varepsilon}}}_{\mathrm{p}}^{e,k} - \lambda^{e,k} \overline{\overline{\mathbf{f}}}^{e,k}\Big]\, |\boldsymbol{J}^e| dV^e,$$

$$\mathbf{r}_{\mathrm{u}}^{ei} = \int_{\Omega^e} N^i\, \rho_0 \ddot{\boldsymbol{u}}^{e,k}\, |\boldsymbol{J}^e| dV^e + \int_{\Omega^e} \big[\mathbf{B}^i\big]^{\mathrm{T}} \Big[\overline{\overline{\mathbf{C}}}_{\mathrm{e}}\, \Big[\overline{\overline{\boldsymbol{\varepsilon}}}^{e,k} - \overline{\overline{\boldsymbol{\varepsilon}}}_{\mathrm{p}}^{e,k}\Big]\Big]\, |\boldsymbol{J}^e| dV^e.$$

Therein, the variable $\mathbf{I}$ represents a two-dimensional unity matrix, and the parts of the load vector related to volume or surface loads are neglected due to their irrelevance. Different shape functions are chosen for the distinct fields. While N^i represent continuous approximations, $\bar{N}^i$ characterize discontinuous ones - as specified in Section 4.2.3.2.

5.2.5. Classical vs. Variational Approach for Viscoplasticity

The viscoplastic variant of the dynamic benchmark problem can be simulated using the previously determined quantities. In order to ensure comparability between the time discretization results between the classical and the variational approach, the identical spatial discretization consisting of a quadratic mesh with $NE_{\mathrm{R}} = 2$ and $NE_{\mathrm{Z}} = 15$ elements is considered. For both approaches, the displacement field is approximated continuously with the help of biquadratic LAGRANGE shape functions. In the variational ansatz, the stresses and the plastic strains are approximated discontinuously. Therefore, biquadratic LAGRANGE shape functions, with GAUSS-LEGENDRE quadrature points as supporting points, are exploited. This yields for a multifield simulation implying the DIRK(3) method, together with a time step size of $\Delta t = 1 \cdot 10^{-5}$ s, to a maximum deviation in the displacement, the stress, and the plastic strain field of about 0.02% in relation to the results obtained by the classical approach. Due to the small deviations between the classical and the variational approach as well as between the elastoplastic and the viscoplastic model for the distinct field variables, a spatially convergent solution can be assumed for the multifield approach as well. In the next step, particular attention is paid to the time discretization error. Therefore, distinct time integrators are applied together with distinct time step sizes.

Figure 5.30 (a)-(f) show the h-error curves of the displacement, the stress, as well as the plastic strain field for the DIRK(3) scheme within the conventional and the multifield approach. Figure 5.30 (g)-(m) demonstrate the corresponding courses of the embedded error. A portrait of the stress field's embedded error in the conventional approach is missing, since no time discretization of the stress field is performed. For all error estimations, it can be observed that for a decreasing time step size the error always decreases. By comparing the graphs of the classical and the variational procedure, an agreement between both can be identified. Identical results are stated for the matching error curves in the elastoplastic context in Figure 5.20 and Figure 5.21. Comparing the results of the elastoplastic and the viscoplastic approach reveals corresponding characteristics, too.

Table 5.4.: Estimation of the order of consistency/convergence for small strain viscoplasticity

	$q_{\mathrm{h}}(\mathbf{u})$	$q_{\mathrm{h}}(\boldsymbol{\varepsilon}_{\mathrm{p}})$	$q_{\mathrm{h}}(\boldsymbol{\sigma})$	$q_{\mathrm{r}}(\mathbf{u})/$ $q_{\mathrm{emb}}(\mathbf{u})$	$q_{\mathrm{r}}(\boldsymbol{\varepsilon}_{\mathrm{p}})/$ $q_{\mathrm{emb}}(\boldsymbol{\varepsilon}_{\mathrm{p}})$	$q_{\mathrm{r}}(\boldsymbol{\sigma})/$ $q_{\mathrm{emb}}(\boldsymbol{\sigma})$	$q_{\mathrm{h}}^{\mathrm{glob}}(\mathbf{u})$	$q_{\mathrm{h}}^{\mathrm{glob}}(\boldsymbol{\varepsilon}_{\mathrm{p}})$	$q_{\mathrm{h}}^{\mathrm{glob}}(\boldsymbol{\sigma})$
DIRK(3) CON	2.47	2.36	2.23	1.68	1.37	–	2.44	2.32	2.10
DIRK(3) MULTI	2.47	2.36	2.23	1.68	1.37	1.08	2.24	2.11	2.07
LOBATTO IIIC(2)	1.55	1.52	1.39	–	–	–	1.91	1.78	1.24
RADAU IIA(2)	2.58	2.59	2.40	–	–	–	2.52	2.43	2.25
$\mathrm{cG}_1(2)$	2.57	2.50	2.40	1.00	1.00	2.71	2.52	2.43	2.25
$\mathrm{dG}_1(2)$	3.43	3.33	3.12	1.00	1.00	2.86	2.25	2.33	2.79

In addition to the diagonally implicit RUNGE-KUTTA schemes, fully implicit RUNGE-KUTTA schemes and GALERKIN methods are analyzed within the multifield approach in the viscoplastic regime. However, only a small extent of the time discretization methods used in the elastoplastic benchmark problem is analyzed. The respective h-error or residual error curves for the displacement, the stress and the plastic strain field are shown in Figure 5.32 as well as in Figure 5.31. If again a comparison to the elastoplastic analogues in Figure 5.24-Figure 5.28 is performed, huge similarities between the viscoplastic and elastoplastic time discretization errors can be observed.

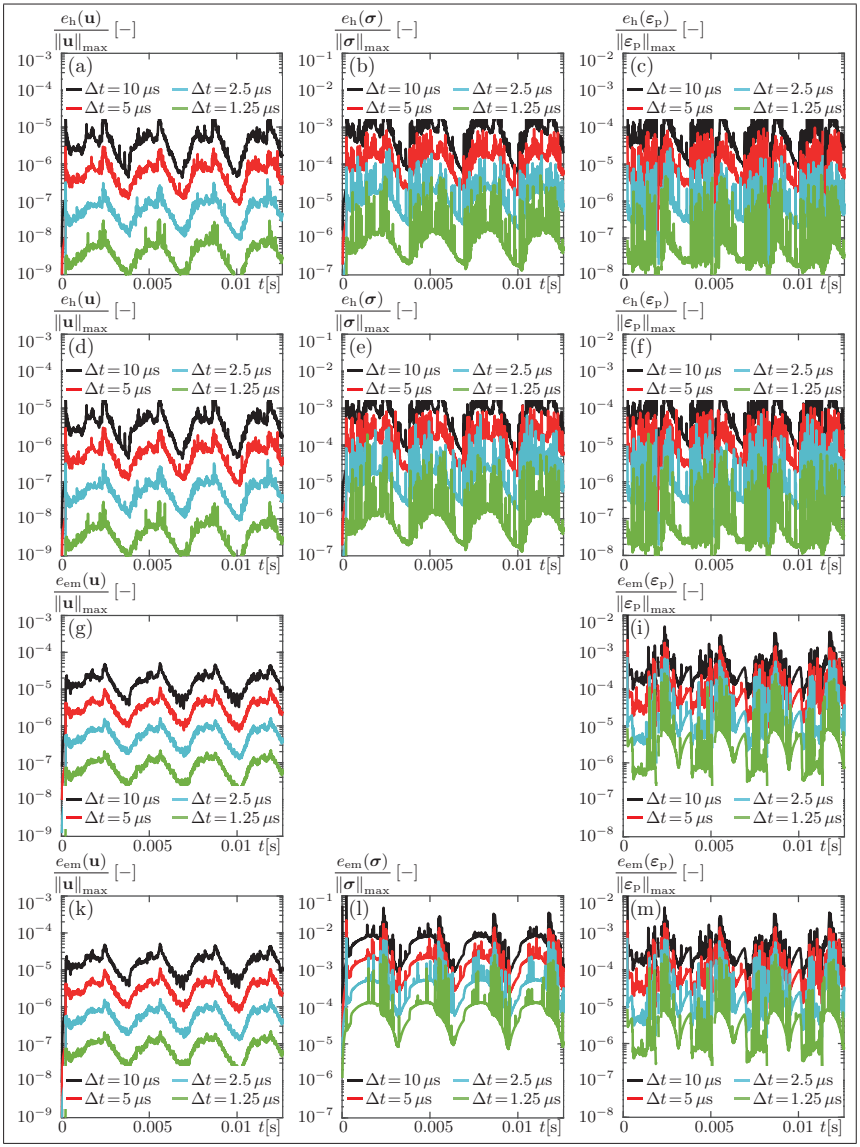

Figure 5.30.: Local time discretization error of the h- and the embedded method for the displacement, the viscoplastic strain, and the stress field within conventional and multifield elastoviscoplasticity: (a)-(c) h-error DIRK(3) conventional, (d)-(f) h-error DIRK(3) multifield, (g)-(i) embedded error DIRK(3) conventional, (k)-(m) embedded error DIRK(3) multifield

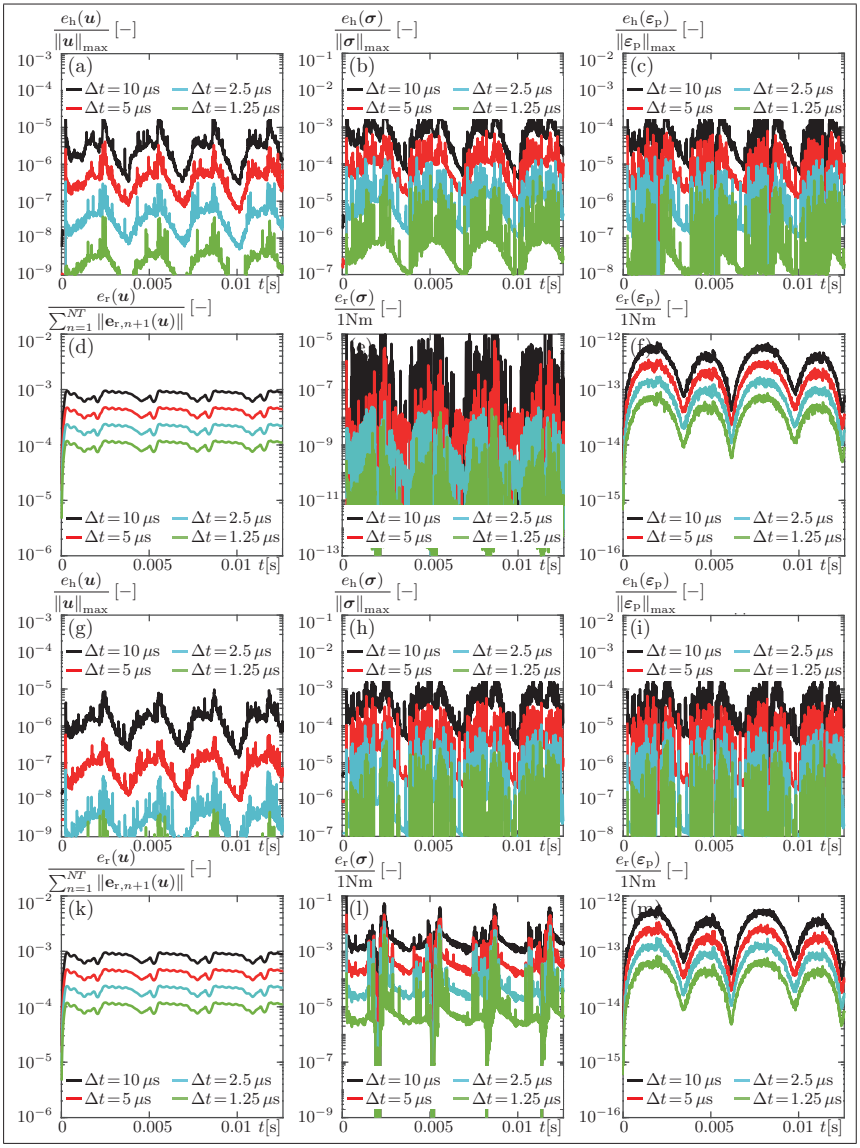

Figure 5.31.: Local time discretization error of the h- and the residual method for the displacement, the viscoplastic strain, and the stress field for distinct time integration methods within multifield elastoviscoplasticity: (a)-(c) h-error $\mathrm{cG}_1(2)$, (d)-(f) residual error $\mathrm{cG}_1(2)$, (g)-(i) h-error $\mathrm{dG}_1(2)$, (k)-(m) residual error $\mathrm{dG}_1(2)$

This is also represented by the order of consistency or the order of convergence. For the viscoplastic example problem, the estimates are listed in Table 5.4, while for the elastoplastic approach Table 5.1-Table 5.3 have to be accounted for. Examining the distinct entries shows that only slight differences prevail. Even in the viscoplastic adaptation of the benchmark problem global orders above 2.5 are not obtained, although, locally orders well above three are achieved. Obviously, the regularization and, thus, the smoothening of the problem does not cure the effect of global order reduction. In (Hartmann and Bier, 2007), this phenomenon is observed for DIRK methods. Thus, it is necessary to carry out a profound mathematical analysis of dynamic elasto(visco)plasticity to clarify why the theoretical orders of convergence cannot be obtained, although this is possible for similar problems, cf. (Butcher, 2008; Eidel and Kuhn, 2015; Hairer and Wanner, 2002). This, however, is beyond the scope of this thesis. Although not all time integrators of the elastoplastic benchmark problem are applied in the viscoplastic context, the previous statements suggest that identical results are obtainable also for the unrealized schemes.

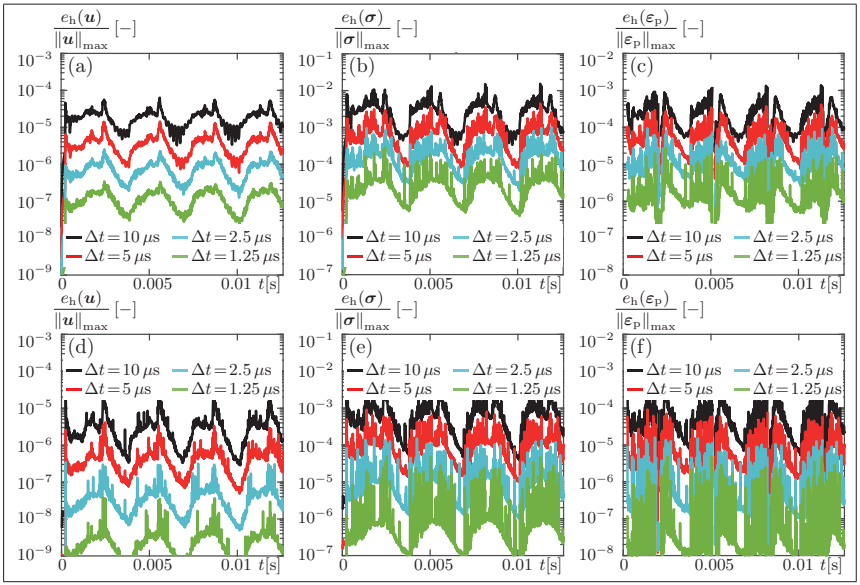

Figure 5.32.: Local time discretization error of the h-method for the displacement, the viscoplastic strain, and the stress field for distinct time integration methods within multifield elastoviscoplasticity: (a)-(c) Lobatto IIIC(2), (d)-(f) Radau IIA(2)

5.3. Summary

In order to check the programming of the classical approach, a standard benchmark problem from small strain quasi-static ideal elastoplasticity, the rectangular strip with a hole in the plain strain case, is investigated. Additionally, the variational approach is applied to this problem and both strategies are compared to the reference solution of (Stein, 2003). The deviations between the classical and the variational multifield approach are smaller than $10^{-3}\%$. The differences with respect to the reference solution lie between $0.04\% - 10\%$ depending on the evaluated

quantity. Since a 40 times higher number of spatial elements is used to determine the reference solution, these relative errors are acceptable. Hence, the classical and the variational approach are able to adequately represent small strain quasi-static ideal elastoplastic problems.

For the analysis of distinct time discretization schemes in the context of small strain dynamic ideal elasto(visco)plasticity, an additional benchmark problem is developed. As motivation, the displacement-driven deformation of an axisymmetric steel shaft is taken into account. The aim of this new benchmark problem is to model a highly dynamic process which makes it possible to concentrate on time integrators and, at the same time, to create a problem consisting of relatively few degrees of freedom.

To gain a better understanding of this novel benchmark problem, a quasi-static investigation is performed within small strain ideal elastoplasticity using the classical approach. A homogeneous stress distribution within the steel shaft is the result. Moreover, a variation of the spatial discretization concerning the number of elements and the polynomial degree has no influence on the solution, and the time discretization errors are too small for a deep analysis.

This stands in strong contrast to the dynamic analysis. The frequency dependency in the applied sinusoidal boundary condition leads to elasto-plastic wave fronts, creating an inhomogeneous stress distribution. The spatial discretization drastically influences the solution until convergence is obtained for a biquadratic mesh consisting of $NE_{\mathrm{R}} = 2$ elements in radial as well as $NE_{\mathrm{Z}} = 15$ elements in axial direction. Within the classical and the variational approach, the displacement field is approximated continuously with the help of biquadratic Lagrange shape functions. For the multifield ansatz, however, the stresses, the plastic strains, and the Lagrange multiplier are approximated discontinuously using biquadratic Lagrange shape functions with Gauss-Legendre quadrature points as supporting positions. For an identical time discretization scheme, the deviations between the classical and the variational approach are smaller than $10^{-2}\%$.

Within both strategies, stiffly accurate diagonally Runge-Kutta schemes and the Newmark method are applied. Furthermore, the time discretization error of the displacement, the stress, and the plastic strain field are evaluated using the h-error and the embedded error estimator. The orders of convergence and consistency are determined. Again, both approaches yield identical results. Applying the h-error estimator for all three fields, the backward Euler scheme almost reaches the theoretical order of one. The DIRK(2) as well as the Newmark method reach a theoretical order of approximately two. Only the DIRK(3) scheme is hardly above order two, although its theoretical order is three. With the embedded error estimator, the achieved orders of consistency are one order lower.

Within the multifield approach, stiffly accurate fully implicit Runge-Kutta schemes of Lobatto IIIC and Radau IIA type with distinct numbers of stages are applied as well. The orders of consistency are calculated for the displacement, the stress, and the plastic strain field exploiting the h-error estimator. If the number of stages is increased, higher orders of consistency are obtained. Moreover, Radau IIA schemes lead to orders of consistency of roughly around five, while Lobatto IIIC methods only reach orders of consistency of about four.

Furthermore, continuous as well as discontinuous Galerkin methods in their one- and two-field formulation with varying polynomial degree are employed. Again, the orders of consistency for the displacement, the stress, and the plastic strain field are determined taking the h-error estimator into account. With increasing polynomial degree, the orders of consistency grow. In the continuous case, the one- and the two-field setting reach similar orders of consistency, which are at best well above four. If discontinuous Galerkin schemes are considered, deviations in the orders of consistency between the single- and the two-field setting are perceptible. The latter implementation reaches orders of consistency well above five, while the one-field setting only reaches orders of consistency well above four.

For all GALERKIN schemes, the residual error estimator is also applied to the displacement, the stress, and the plastic strain field. Therein, however, similar orders of consistency are attained for all polynomial degrees as well as for the one-field and the two-field setting. Only the stress field shows a non-systematic variation of the order of consistency. Hence, the residual error estimator is apparently not capable of estimating orders of consistency.

Additionally, for the fully implicit RUNGE-KUTTA schemes as well as for the GALERKIN methods, the orders of convergence for the displacement, the stress, and the plastic strain field are determined directly using the global h-error estimator. Therein, only orders a little bit higher than two are ascertained. Thus, locally high orders are obtainable but they cannot be preserved globally. Nevertheless, the error level decreases with increasing theoretical order of convergence.

The adaptation of the benchmark problem to small strain dynamic elastoviscoplasticity leads to identical results as in the plastic case. However, the studied variants of time integrators are reduced.

6. Large Strain Elastoplasticity and Viscoplasticity

In **Chapter 4**, a frequently used elastoplastic material model in the small strain regime as well as its viscoplastic extension are described. Furthermore, their numerical implementations are analyzed with the help of a newly created benchmark problem, which is motivated by the integrated thermomechanical forming process of **Chapter 1**. This production sequence, however, is clearly characterized by finite deformations. Hence, the ideas in the small strain regime will be extended in the following sections.

Plastic flow is micromechanically motivated by the movement of dislocations, while elastic properties are accounted to lattice distortions. The explicit consideration of these microstructural effects in the area of finite strains is carried out in (Carstensen et al., 2002; Miehe et al., 2004, 2002; Mielke, 2003; Nemat-Nasser et al., 1980), whereby the mathematical analysis is one of the key aspects. Other approaches adopt a point of view according to which (visco)plastic properties are only modeled by their effects on macroscopic length scales, cf. (Molinari and Ortiz, 2002; Simo, 1998; Simo and Hughes, 1997). In this context, anisotropic behavior is examined in (Schröder et al., 2002; Seitz et al., 2014; Vladimirov et al., 2010), while (Helm, 2006; Reese, 1998; Simo and Miehe, 1992; Stainier and Ortiz, 2010) treat thermomechanical extensions. The determination of plastic effects due to phase transformations is realized in (Mahnken and Schneidt, 2009; Mahnken et al., 2012).

In this thesis, however, one of the simplest finite deformation models is presented, since the aim is not an exact modeling - but to enable the application of higher order accurate time integration methods in finite elasto(visco)plasticity. This classical model can be found, for example, in (Dhondt, 2004; Simo, 1988, 1998; Simo and Miehe, 1992).

6.1. Classical Approach

The kinematics and kinetics of an elasto(visco)plastic material body $\mathcal{B}$ at finite strains can be described by Equations (2.1)-(2.10). Moreover, the balance of linear momentum (2.13) in the reference configuration characterizes its deformation process, resulting from the applied volume forces $\rho_0 \boldsymbol{f}$ or the boundary conditions

$$\boldsymbol{u}(\boldsymbol{X},t) = \boldsymbol{u}^* \qquad \forall \boldsymbol{X} \in \Gamma_{\mathrm{u}}, \qquad\qquad \boldsymbol{F}\cdot\boldsymbol{S}\cdot\boldsymbol{N} = \boldsymbol{T}^* \qquad \forall \boldsymbol{X} \in \Gamma_{\mathrm{t}^*}. \tag{6.1}$$

Therein, the body's boundary $\Gamma = \Gamma_{\mathrm{u}} \cup \Gamma_{\mathrm{t}^*}$ is divided into a part Γ_{u}, where the displacements are prescribed, and a part Γ_{t^*}, where the stresses are known. The necessary initial conditions are denoted as

$$\boldsymbol{u}_1 = \boldsymbol{u}(\boldsymbol{X},t_1) \qquad \forall \boldsymbol{X} \in \Omega, \qquad\qquad \dot{\boldsymbol{u}}_1 = \dot{\boldsymbol{u}}(\boldsymbol{X},t_1) \qquad \forall \boldsymbol{X} \in \Omega.$$

While the balance of linear momentum (2.13) is valid for arbitrary material assumptions, specific ones are introduced throughout the connection between stresses and strains. If elasto(visco)-plastic behavior is considered, two distinct cases - the elastoplastic and the elastoviscoplastic - have to be accounted for. The derivation of the corresponding equations is performed analogously to the small strain case. Within the theory of finite strains, however, a distinction between the reference and a series of current configurations of the material body $\mathcal{B}$ is made, see **Chapter 2**. Hence, the very same material model can be depicted using different quantities associated to

these configurations. It is remarked that all quantities in this chapter are defined on the reference configuration and are expressed depending on material coordinates $\boldsymbol{X}$. Approaches using further configurations can be found in (Hartmann and Bier, 2007; Haupt, 2000; Simo and Miehe, 1992) to name only a few.

6.1.1. Finite Elastoplasticity

The main idea of modeling finite elastoplastic behavior is the same as in the small strain case, see Section 4.1.1. If a continuum mechanical body's stress state reaches a material-dependent threshold, the stresses of the analyzed specimen are limited. Mathematically, this can be expressed by creating the set of admissible stresses

$$\mathcal{S} \coloneqq \{\boldsymbol{S} | f(\boldsymbol{S}, \boldsymbol{C}) \leq 0\},$$

whereby $f(\boldsymbol{S}, \boldsymbol{C})$ represents the yield surface. For negative values, the stress state behaves elastically. If the yield function is equal to zero, plastic properties prevail. Stress states outside the yield surface are not allowed. Within the theory of ideal finite VON MISES plasticity, this yield function is convex concerning the PIOLA-KIRCHHOFF stress tensor $\boldsymbol{S}$, see **Appendix B**, and it can be determined by

$$f(\boldsymbol{S}, \boldsymbol{C}) = \sqrt{[\mathrm{DEV}\,(\boldsymbol{S}) \cdot \boldsymbol{C}] : [\boldsymbol{C} \cdot \mathrm{DEV}\,(\boldsymbol{S})]} - \sqrt{\frac{2}{3}}\sigma_\mathrm{y} \qquad \text{with} \qquad \sigma_\mathrm{y} > 0. \tag{6.2}$$

The deviator with respect to the reference configuration, cf. (Simo, 1988), is defined as

$$\mathrm{DEV}\,(\boldsymbol{S}) = \boldsymbol{S} - \frac{1}{3}\left[\boldsymbol{C} : \boldsymbol{S}\right] \boldsymbol{C}^{-1}. \tag{6.3}$$

For the necessity of special demands on the yield surface see (Simo, 1988, 1998). In general, Equation (6.2) might be enhanced by appropriate hardening variables, cf. (Simo, 1988; Simo and Miehe, 1992). These aspects are neglected in this thesis to keep the model as simple as possible.

The next step is to derive the material laws. The idea is to exploit the dissipation inequality in (2.14) and, hence, to enforce thermodynamic consistency automatically. Therefore, it is assumed that the internal energy of an isotropic elastoplastic body can be stated as

$$e(\boldsymbol{C}, \boldsymbol{C}_\mathrm{p}^{-1}) = \frac{3\kappa + 2\mu}{6}\left[\frac{1}{2}\left[J^2 J_\mathrm{p}^{-1}\right] - \ln(J J_\mathrm{p}^{-1})\right] + \frac{\mu}{2}\left[J^{-\frac{2}{3}} J_\mathrm{p}^{\frac{2}{3}}\left[\boldsymbol{C} : \boldsymbol{C}_\mathrm{p}^{-1}\right] - 3\right], \tag{6.4}$$

following the ansatz in (Simo and Miehe, 1992; Wriggers, 2008) with the LAMÉ parameters κ, μ. Inserting the time derivative of expression (6.4) together with the relationship

$$\frac{\partial e}{\partial \boldsymbol{C}_\mathrm{p}^{-1}} = \boldsymbol{C} \cdot \frac{\partial e}{\partial \boldsymbol{C}} \cdot \boldsymbol{C}_\mathrm{p}, \tag{6.5}$$

into the dissipation inequality in (2.14) yields

$$D_\mathrm{int} = \frac{1}{2}\boldsymbol{S} : \dot{\boldsymbol{C}} - \frac{\partial e}{\partial \boldsymbol{C}} : \dot{\boldsymbol{C}} - \frac{\partial e}{\partial \boldsymbol{C}_\mathrm{p}^{-1}} : \dot{\boldsymbol{C}}_\mathrm{p}^{-1} = \left[\frac{1}{2}\boldsymbol{S} - \frac{\partial e}{\partial \boldsymbol{C}}\right] : \dot{\boldsymbol{C}} - \frac{\partial e}{\partial \boldsymbol{C}} : \left[\boldsymbol{C} \cdot \dot{\boldsymbol{C}}_\mathrm{p}^{-1} \cdot \boldsymbol{C}_\mathrm{p}\right] \geq 0. \tag{6.6}$$

Thereby, the symmetry of the right CAUCHY-GREEN tensor and the plastic right CAUCHY-GREEN tensor is used. For further explanations see **Appendix A**.

In order to guarantee that Inequality (6.6) is always fulfilled, the material laws

$$\boldsymbol{S} \quad = 2\frac{\partial e}{\partial \boldsymbol{C}} = \frac{3\kappa + 2\mu}{6}\left[J^2 J_{\mathrm{p}}^{-1} - 1\right]\boldsymbol{C}^{-1} + \mu J^{-\frac{2}{3}} J_{\mathrm{p}}^{\frac{2}{3}}\left[\boldsymbol{C}_{\mathrm{p}}^{-1} - \frac{1}{3}\left[\boldsymbol{C} : \boldsymbol{C}_{\mathrm{p}}^{-1}\right]\boldsymbol{C}^{-1}\right], \tag{6.7}$$

$$\dot{\boldsymbol{C}}_{\mathrm{p}}^{-1} = -2\lambda\,\boldsymbol{C}^{-1} \cdot \frac{\partial f(\boldsymbol{S},\boldsymbol{C})}{\partial \boldsymbol{S}} \cdot \boldsymbol{C}_{\mathrm{p}}^{-1} = -2\lambda \frac{\mathrm{DEV}\,(\boldsymbol{S}) \cdot \boldsymbol{C} \cdot \boldsymbol{C}_{\mathrm{p}}^{-1}}{\sqrt{[\mathrm{DEV}\,(\boldsymbol{S}) \cdot \boldsymbol{C}] : [\boldsymbol{C} \cdot \mathrm{DEV}\,(\boldsymbol{S})]}} \tag{6.8}$$

are established. The included parameter λ is denoted as consistency parameter, which is associated to the Karush-Kuhn-Tucker conditions

$$\lambda \geq 0, \qquad f(\boldsymbol{S},\boldsymbol{C}) \leq 0, \qquad \lambda f(\boldsymbol{S},\boldsymbol{C}) = 0, \tag{6.9}$$

to enable the distinction between elastic and plastic behavior. If $\lambda = 0$, holds purely elastic properties prevail and $f(\boldsymbol{S},\boldsymbol{C}) < 0$ is true. For $\lambda > 0$ the plastic right Cauchy-Green tensor evolves and plastic effects are prevalent. At the same time, it must be ensured that the stress state lies on the yield surface. Hence, $f(\boldsymbol{S},\boldsymbol{C}) = 0$ is demanded. With the constitutive law in (6.7), the term in brackets in Inequality (6.6) vanishes, while inserting the evolution equation in (6.8) results in

$$D_{\mathrm{int}} = -\frac{\partial e}{\partial \boldsymbol{C}} : \left[\boldsymbol{C} \cdot \dot{\boldsymbol{C}}_{\mathrm{p}}^{-1} \cdot \boldsymbol{C}_{\mathrm{p}}\right] = \lambda \boldsymbol{S} : \frac{\partial f(\boldsymbol{S},\boldsymbol{C})}{\partial \boldsymbol{S}} = \lambda\left[f(\boldsymbol{S},\boldsymbol{C}) + \sqrt{\frac{2}{3}}\sigma_{\mathrm{y}}\right] \geq 0. \tag{6.10}$$

Thereby, the symmetry of the right Cauchy-Green tensor and the Piola-Kirchhoff stress tensor is exploited. Furthermore, the case $\boldsymbol{C} \cdot \mathrm{DEV}\,(\boldsymbol{S}) = \boldsymbol{0}$, is excluded. This is legitimate since a purely elastic behavior still prevails, due to the definition of the yield function (6.2). Hence, the dissipation inequality in (6.6) is always fulfilled. An alternative derivation strategy for the evolution equation in (6.8) is provided if the postulate of maximum plastic work is acknowledged

$$D_{\mathrm{int}} = \sup_{\boldsymbol{S}}\{-\boldsymbol{S} : \frac{1}{2}\left[\boldsymbol{C} \cdot \dot{\boldsymbol{C}}_{\mathrm{p}}^{-1} \cdot \boldsymbol{C}_{\mathrm{p}}\right] | f(\boldsymbol{S},\boldsymbol{C}) \leq 0\}. \tag{6.11}$$

Thus, it is assumed that within all admissible stresses the dissipation in the material reaches a maximum with respect to the stresses $\boldsymbol{S}$. An analogous procedure is carried out in the small strain regime, see Section 4.1.1. Following approaches known from optimization or convex analysis, cf. (Luenberger, 1973; Zeidler, 1985), Expression (6.11) can be restated into a Lagrange function

$$\mathcal{L} = -\boldsymbol{S} : \frac{1}{2}\left[\boldsymbol{C} \cdot \dot{\boldsymbol{C}}_{\mathrm{p}}^{-1} \cdot \boldsymbol{C}_{\mathrm{p}}\right] - \lambda f(\boldsymbol{S},\boldsymbol{C}), \tag{6.12}$$

with the Lagrange multiplier $\lambda \geq 0$ and the yield function $f(\boldsymbol{S},\boldsymbol{C}) \leq 0$ as a considered inequality constraint. The necessary optimality conditions for a stationary point

$$\frac{\partial \mathcal{L}}{\partial \boldsymbol{S}} = 0 \qquad \text{and} \qquad \lambda f(\boldsymbol{S},\boldsymbol{C}) = 0 \tag{6.13}$$

with $\boldsymbol{C} \cdot \mathrm{DEV}\,(\boldsymbol{S}) \neq \boldsymbol{0}$, yield the evolution Equation (6.8) with the Karush-Kuhn-Tucker conditions in (6.9). In general, the standard optimality conditions in (6.13) and, thus, Equation (6.8) are only valid for continuous differentiable functions $f(\boldsymbol{S},\boldsymbol{C})$, cf. (Geiger and Kanzow, 2002). For an extension to the non-differentiable case, the derivative of $f(\boldsymbol{S},\boldsymbol{C})$ is exchanged by the subdifferential, cf. (Clarke, 1990). Here, this generalization is not needed, although the yield function is differentiable everywhere except for $\boldsymbol{C} \cdot \mathrm{DEV}\,(\boldsymbol{S}) = \boldsymbol{0}$. However, at that point, due to the yield function (6.2), only elastic properties prevail, and the rate of plastic strains disappears anyway. To complete the material laws, an appropriate initial condition

$$\boldsymbol{C}_{\mathrm{p},1}^{-1} = \boldsymbol{C}_{\mathrm{p}}^{-1}(t_1) \tag{6.14}$$

has to be chosen for the evolution equation in (6.8).

6.1.2. Finite Viscoplasticity

The previously presented elastoplastic model is characterized by a rate-independent behavior. Hence, on material law level, it does not matter at which speed the deformation process is carried out. To take this aspect into account, a rate-dependent model has to be established. Therefore, a viscoplastic extension of the finite strain elastoplastic model is performed - similar to the small strain case in Section 4.1.2. Hence, it is again assumed that there is a convex elastic set in the stress space defined by the yield function in (6.2). Now, however, appearing stress states are not longer limited to the yield surface and its interior. Correspondingly, viscoplastic properties prevail for stress states lying on the outside of the latter. The internal energy of the analyzed viscoplastic body is supposed to be represented by (6.4). Since thermodynamic consistency is demanded, the dissipation inequality has to be fulfilled and the constitutive equation in (6.7) remains valid, but the index $_{\mathrm{p}}$ therein now refers to viscous relations. To derive the evolution equation, the postulate of maximum plastic work (6.11) has to be adapted by weakening the inherent inequality constraint. This is achieved throughout introducing a penalization term

$$D_{\mathrm{int}} = \sup_{\boldsymbol{S}} \left\{ -\boldsymbol{S} \colon \frac{1}{2} \left[\boldsymbol{C} \cdot \dot{\boldsymbol{C}}_{\mathrm{p}}^{-1} \cdot \boldsymbol{C}_{\mathrm{p}} \right] - \frac{1}{\chi} h\left(f(\boldsymbol{S}, \boldsymbol{C}) \right) \right\}.$$

Therein, the parameter $\chi > 0$ embodies the viscosity parameter, while

$$h\left(f(\boldsymbol{S}, \boldsymbol{C}) \right) \coloneqq \begin{cases} \dfrac{1}{2} \left[f(\boldsymbol{S}, \boldsymbol{C}) \right]^2 & \text{for} \quad f(\boldsymbol{S}, \boldsymbol{C}) \geq 0 \\ 0 & \text{for} \quad f(\boldsymbol{S}, \boldsymbol{C}) < 0 \end{cases}$$

represents a continuous differentiable function. Correspondingly, stress states outside the yield surface are penalized according to their distance and with respect to the viscosity parameter χ. If this parameter tends to zero, the rate-dependent elastoviscoplastic problem degenerates to the rate-independent elastoplastic problem, cf. (Simo and Hughes, 1997). For basic aspects and proofs of general penalty methods see (Alt, 2011; Luenberger, 1973). As a result, the Lagrange function in (6.12) is modified to

$$\mathcal{L} = -\boldsymbol{S} \colon \frac{1}{2} \left[\boldsymbol{C} \cdot \dot{\boldsymbol{C}}_{\mathrm{p}}^{-1} \cdot \boldsymbol{C}_{\mathrm{p}} \right] - \frac{1}{\chi} h\left(f(\boldsymbol{S}, \boldsymbol{C}) \right),$$

with the stationarity condition

$$\frac{\partial \mathcal{L}}{\partial \boldsymbol{S}} = 0.$$

Exploiting the characteristic of the derivative

$$\frac{\partial\, h\left(f(\boldsymbol{S}, \boldsymbol{C}) \right)}{\partial \left(f(\boldsymbol{S}, \boldsymbol{C}) \right)} = \langle f(\boldsymbol{S}, \boldsymbol{C}) \rangle \coloneqq \begin{cases} f(\boldsymbol{S}, \boldsymbol{C}) & \text{for} \quad f(\boldsymbol{S}, \boldsymbol{C}) \geq 0 \\ 0 & \text{for} \quad f(\boldsymbol{S}, \boldsymbol{C}) < 0. \end{cases}$$

yields the evolution equation

$$\dot{\boldsymbol{C}}_{\mathrm{p}}^{-1} = -2\lambda \frac{\mathrm{DEV}\left(\boldsymbol{S} \right) \cdot \boldsymbol{C} \cdot \boldsymbol{C}_{\mathrm{p}}^{-1}}{\sqrt{\left[\mathrm{DEV}\left(\boldsymbol{S} \right) \cdot \boldsymbol{C} \right] \colon \left[\boldsymbol{C} \cdot \mathrm{DEV}\left(\boldsymbol{S} \right) \right]}} \qquad \text{with} \qquad \lambda = \frac{1}{\chi} \langle f(\boldsymbol{S}, \boldsymbol{C}) \rangle. \tag{6.15}$$

While the parameter λ has to be determined separately within the elastoplastic model, it is prescribed at the beginning in the viscous case. Formally, this is the only distinction between both approaches. Hence, the reduced dissipation inequality in (6.6) remains valid, and inserting the evolution equation as well as the Lagrange multiplier in (6.15) proves thermodynamic consistency. By formulating a proper initial condition analogously to Equation (6.14), the finite strain elastoviscoplastic model is completed.

6.1.3. Numerical Realization

In the finite strain regime, elasto(visco)plastic problems include both material and geometric nonlinearities. However, an analytical solution is usually not possible and numerical strategies have to be employed.

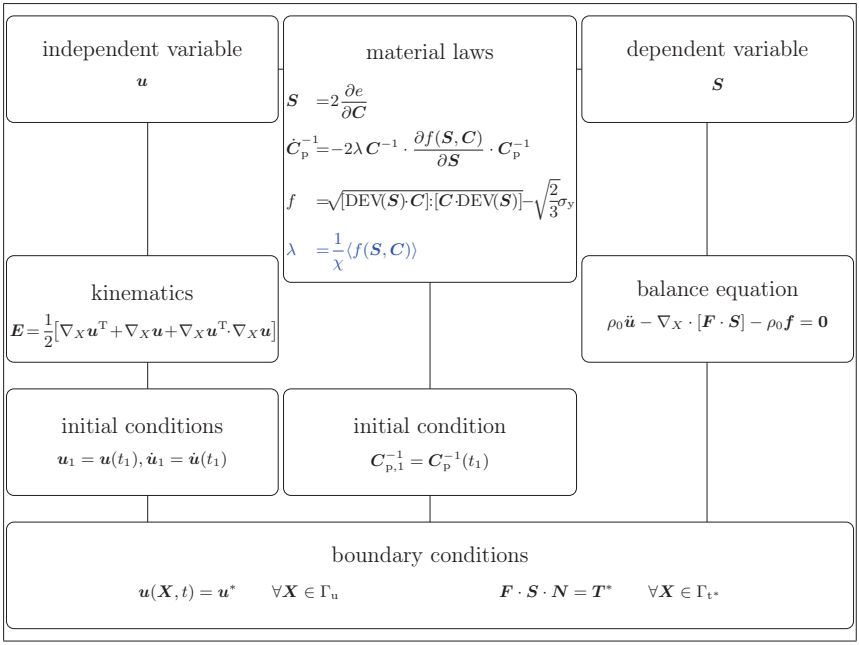

Figure 6.1.: Initial boundary value problem of the classical approach in the finite strain regime with entries in blue referring to expressions needed only in the viscoplastic case

Before the basics described in **Chapter 3** are considered and specified, the complete initial boundary value problem is schematically depicted, see Figure 6.1. It is emphasized that the numerical treatment is always based on a fixed cartesian coordinate system with the space and time-independent unit basis vectors $\boldsymbol{g}_i$ with $i = 1, ..., 3$.

6.1.3.1. Generation of the Weak Formulation

In order to apply the solution strategies presented in **Chapter 3**, the finite elasto(visco)plastic problem has to be recast into an equivalent weak form. This is achieved by applying the principle of virtual work, cf. (Finlayson, 1972; Holzapfel, 2000; Kelly, 2015; Lagrange, 1788; Wriggers, 2008). Thereby, the balance of linear momentum in (2.13) is multiplied with an arbitrary vector-valued test function $\delta\boldsymbol{u}(\boldsymbol{X}) \neq \boldsymbol{0}$ with $\delta\boldsymbol{u}(\boldsymbol{X}) = \boldsymbol{0}$ only on the DIRICHLET boundary Γ_{u}. In the next step, the resulting equation is integrated over the domain Ω of the investigated continuum mechanical body $\mathcal{B}$. The respective NEUMANN boundary condition in $(6.1)_2$ is treated analogously, except that the integration is performed over the boundary Γ_{t^*} of $\mathcal{B}$. The addition of

both expressions leads to

$$\delta W = \int_{\Omega} \delta \boldsymbol{u} \cdot \left[\rho_0 \ddot{\boldsymbol{u}} - \nabla_X \cdot [\boldsymbol{F} \cdot \boldsymbol{S}] - \rho_0 \boldsymbol{f}\right] \, dV + \int_{\Gamma_{t^*}} \delta \boldsymbol{u} \cdot [\boldsymbol{F} \cdot \boldsymbol{S} \cdot \boldsymbol{N} - \boldsymbol{T}^*] \, dA = 0. \tag{6.16}$$

For better clarity, the dependency of the test function on the spatial coordinate $\boldsymbol{X}$ is dropped. In the forthcoming analysis, it will be advantageous to consider the prefix δ not only as an indicator for an arbitrary test function, but as a mathematical operator linked to the GÂTEAUX derivative with respect to the displacement field $\boldsymbol{u}$. Hence, a test function $\delta \boldsymbol{F}$ as virtual counterpart of the deformation gradient can be derived by

$$\delta \boldsymbol{F} = \mathrm{D}_{\mathbf{u}} \boldsymbol{F} = \frac{d}{d\psi} \left[\frac{\partial \left[\boldsymbol{u} + \psi \delta \boldsymbol{u}\right]}{\partial \boldsymbol{X}} + \boldsymbol{I} \right] \Bigg|_{\psi=0} = \nabla_X \delta \boldsymbol{u} = \delta \nabla_X \boldsymbol{u}, \tag{6.17}$$

whereby the commutativity of the GÂTEAUX derivative and the gradient is exploited, cf. (Holzapfel, 2000). A similar procedure can be carried out concerning the virtual GREEN-LAGRANGE strain tensor

$$\delta \boldsymbol{E} = \frac{1}{2} \left[\delta \boldsymbol{F}^{\mathrm{T}} \cdot \boldsymbol{F} + \boldsymbol{F}^{\mathrm{T}} \cdot \delta \boldsymbol{F}\right]. \tag{6.18}$$

Both Definitions (6.17)-(6.18) can be connected, yielding the implications

$$\nabla_X \delta \boldsymbol{u} : [\boldsymbol{F} \cdot \boldsymbol{S}] = \delta \boldsymbol{F} : [\boldsymbol{F} \cdot \boldsymbol{S}] = \left[\boldsymbol{F}^{\mathrm{T}} \cdot \delta \boldsymbol{F}\right] : \boldsymbol{S} = \frac{1}{2} \left[\delta \boldsymbol{F}^{\mathrm{T}} \cdot \boldsymbol{F} + \boldsymbol{F}^{\mathrm{T}} \cdot \delta \boldsymbol{F}\right] : \boldsymbol{S} = \delta \boldsymbol{E} : \boldsymbol{S}. \tag{6.19}$$

In turn, they can be used to reformulate Equation (6.16) into

$$\delta W = \int_{\Omega} \delta \boldsymbol{u} \cdot \rho_0 \ddot{\boldsymbol{u}} \, dV + \int_{\Omega} \delta \boldsymbol{E} : \boldsymbol{S} \, dV - \int_{\Omega} \delta \boldsymbol{u} \cdot \rho_0 \boldsymbol{f} \, dV - \int_{\Gamma_{t^*}} \delta \boldsymbol{u} \cdot \boldsymbol{T}^* \, dA = 0. \tag{6.20}$$

Additionally, the product rule (4.21), the divergence theorem (4.22), and the symmetry of the second PIOLA-KIRCHHOFF tensor $\boldsymbol{S} = \boldsymbol{S}^{\mathrm{T}}$ have to be applied. The DIRICHLET boundary conditions are considered in a strong sense.

Interpreting Equation (6.20) in the context of the general weak form (3.1), it can be recognized that if

$$\delta \mathbf{z}_1 = \begin{bmatrix} \delta \boldsymbol{u} \\ \delta \boldsymbol{E} \end{bmatrix}, \qquad \mathbf{r}_1 = \begin{bmatrix} \rho_0 \ddot{\boldsymbol{u}} - \rho_0 \boldsymbol{f} \\ \boldsymbol{S} \end{bmatrix}, \qquad \mathbf{r}^* = \begin{bmatrix} \mathbf{T}^* \\ \mathbf{0} \end{bmatrix}, \qquad \mathbf{w} = \boldsymbol{u}$$

is set, they are identical. Special care must be taken because the GREEN-LAGRANGE strain tensor and the second PIOLA-KIRCHHOFF stress tensor are not vector-valued, but tensors of second order. Nevertheless, the numerical realization of **Chapter 3** can be applied one-to-one to the weak form (6.20) with the displacement field as the only unknown.

6.1.3.2. Derivation of the Spatial Semidiscrete Equation on Structural Level

In the first step, following the solution procedure in **Chapter 3**, the spatial discretization of the weak form (6.20) is carried out by means of the finite element method. Hereby, only the three-dimensional case will be analyzed since all other possibilities can be considered as special instances. The elasto(visco)plastic body's domain Ω is partitioned following Relation (3.4) into

small elements $\bar{\Omega}^e$. By taking Equation (3.10) into account, the weak form (6.20) is transferred to element level

$$\begin{aligned}\delta W^e = &\int_{\bar{\Omega}^e} \delta \boldsymbol{u}^e(\boldsymbol{X}^e) \cdot \rho_0 \ddot{\boldsymbol{u}}^e(\boldsymbol{X}^e;t)\, d\bar{V}^e + \int_{\bar{\Omega}^e} \left[\boldsymbol{F}^{e,\mathrm{T}}(\boldsymbol{X}^e;t) \cdot \delta \boldsymbol{F}^e(\boldsymbol{X}^e)\right] : \boldsymbol{S}(\boldsymbol{E}^e(\boldsymbol{X}^e;t))\, d\bar{V}^e - \\ &- \int_{\bar{\Omega}^e} \delta \boldsymbol{u}^e(\boldsymbol{X}^e) \cdot \rho_0 \boldsymbol{f}(\boldsymbol{X}^e;t)\, d\bar{V}^e - \int_{\bar{\Gamma}^e_{t^*}} \delta \boldsymbol{u}^e(\boldsymbol{X}^e) \cdot \boldsymbol{T}^*(\boldsymbol{X}^e;t)\, d\bar{A}^e \qquad = 0,\end{aligned} \tag{6.21}$$

whereby Definition (6.18) and the symmetry of the PIOLA-KIRCHHOFF stress tensor are exploited. For a better understanding, the spatial and temporal dependencies are introduced in this reformulation. The geometry is approximated by (3.5), while (3.7)-(3.8) are used for the primary variable and its derivatives. For the test function $\delta \boldsymbol{u}^e(\boldsymbol{X}^e)$, Equation (3.9) is applied. The approximation of the deformation gradient is performed by (3.6) while its virtual counterpart is defined by

$$\delta \boldsymbol{F}^e \approx \sum_{i=1}^{NN} \delta \boldsymbol{u}^{ei} \otimes \nabla_X N^i(\boldsymbol{\xi}).$$

The chosen shape functions are of LAGRANGE type, leading to continuous approximations of the primary variable over element boundaries. Hence, they can be determined by Equation (3.16) together with (3.13). Their derivatives are obtained by evaluating (3.18) together with (3.15). The stress tensor $\boldsymbol{S}$ in (6.21) is not considered as a primary variable. Thus, it can only be approximated indirectly. An explicit explanation is presented in Section 6.1.3.4.

Due to the material and geometric nonlinearities, a nonlinear solution strategy has to be performed. Since the spatial discrete weak form (6.21) only comprises a variational equality, a NEWTON-RAPHSON scheme can be applied as described in Section 3.2.1. Consequently, the linearization in terms of (3.21) and (3.22) is performed, leading to

$$\sum_{i=1}^{NN} \sum_{j=1}^{NN} \delta \boldsymbol{u}^{ei} \cdot \left[\boldsymbol{m}^{eij} \cdot \Delta \ddot{\boldsymbol{u}}^{ej} + \boldsymbol{k}^{eij} \cdot \Delta \boldsymbol{u}^{ej}\right] = \sum_{i=1}^{NN} \delta \boldsymbol{u}^{ei} \cdot \left[\boldsymbol{r}_1^{*,ei} - \boldsymbol{r}_1^{ei}\right], \tag{6.22}$$

with the suitable tangent matrices

$$\begin{aligned}\boldsymbol{m}^{eij} &= \int_{\Omega^e} \rho_0 N^i N^j\, \boldsymbol{I}\, |\boldsymbol{J}^e| dV^e, \\ \boldsymbol{k}^{eij} &= \int_{\Omega^e} \left[\boldsymbol{F}^{e,k} \otimes \nabla_X N^i\right] : \left.\frac{\partial \boldsymbol{S}}{\partial \boldsymbol{E}}\right|_k : \left[\nabla_X N^j \otimes \left[\boldsymbol{F}^{e,k}\right]^{\mathrm{T}}\right] |\boldsymbol{J}^e| dV^e \\ &\quad + \int_{\Omega^e} \nabla_X N^i \cdot \boldsymbol{S}^k \cdot \nabla_X N^j\, \boldsymbol{I}\, |\boldsymbol{J}^e| dV^e,\end{aligned}$$

and the load vectors

$$\begin{aligned}\boldsymbol{r}_1^{*,ei} &= \int_{\Omega^e} N^i\, \rho_0 \boldsymbol{f}^k\, |\boldsymbol{J}^e| dV^e + \int_{\Gamma^e_{t^*}} N^i\, \boldsymbol{T}^{*,k} |\boldsymbol{J}^{e,\mathrm{red}}| dA^e, \\ \boldsymbol{r}_1^{ei} &= \int_{\Omega^e} N^i\, \rho_0 \ddot{\boldsymbol{u}}^{e,k}\, |\boldsymbol{J}^e| dV^e + \int_{\Omega^e} \boldsymbol{F}^{e,k} \cdot \boldsymbol{S}^k \cdot \nabla_X N^i\, |\boldsymbol{J}^e| dV^e.\end{aligned}$$

For the necessary derivatives and the corresponding tensor calculus see **Appendix A**. The appearing integrals are numerically determined using the GAUSS-LEGENDRE quadrature. Afterwards, the individual constituents of (6.22) are assembled according to (3.25) as well as (3.26), yielding the spatial semidiscrete equation

$$\mathbf{M}\Delta\ddot{\mathbf{u}} + \mathbf{K}_1\Delta\mathbf{u} = \mathbf{R}_1^* - \mathbf{R}_1 \tag{6.23}$$

on structural level.

6.1.3.3. Time Discretization on Structural Level

For the complete implementation of the finite elasto(visco)plastic problem, two issues remain unresolved. On the one hand, the material laws have to be accounted for properly while, on the other hand, the time discretization of the balance of linear momentum and the evolution equation has to be carried out. Both aspects, however, cannot be treated separately. By applying a certain time discretization scheme, the semidiscrete Equation (6.23) is evaluated at specific points in time. Hence, the stress tensor and its derivative have to be determined there too. The same is true for (visco)plastic properties, since they are modeled throughout a characteristic stress-strain relationship. Correspondingly, the time discretization of the evolution equation is coupled to the one of the balance of linear momentum. Furthermore, in the elastoplastic case, the yield function has to be fulfilled. Thus, apart from the evolution equation as ordinary differential equation, an algebraic equation has to be solved. In order to ensure that the yield function is not violated at the end of the time step, this point in time has to be explicitly included as solution point, cf. (De Souza Neto et al., 2008; Ellsiepen and Hartmann, 2001; Hairer and Wanner, 2002). This approach will be adopted in the following sections. Moreover, to keep the coupling between the time integration procedure on structural and on integration point level as simple as possible, identical time discretization schemes are applied. To circumvent additional interpolation steps, only the stiffly accurate diagonally implicit RUNGE-KUTTA schemes of Section 3.4.2.2 and the NEWMARK method of Section 3.4.1 are analyzed, cf. (Eidel and Kuhn, 2015). With the latter scheme, Equation (6.23) can be recast, similar to (3.52), into

$$\begin{aligned} \mathbf{K}_{\text{eff}}\Delta\mathbf{u}_{n+1} &= \mathbf{r}_{\text{eff}}, \\ \mathbf{K}_{\text{eff}} &= \frac{1}{\beta\Delta t^2}\mathbf{M}_{n+1} + \mathbf{K}_{1,n+1}, \\ \mathbf{r}_{\text{eff}} &= \mathbf{R}_{1,n+1}^* - \mathbf{R}_{1,n+1} \end{aligned} \tag{6.24}$$

with the parameters in (3.53). Thus, the evaluation is only performed at the end of the time step. Applying stiffly accurate diagonally implicit RUNGE-KUTTA schemes leads to a reformulation

$$\begin{aligned} \mathbf{K}_{\text{eff}}\Delta\mathbf{u}_{ni} &= \mathbf{r}_{\text{eff}}, \\ \mathbf{K}_{\text{eff}} &= \frac{1}{a_{ii}^2\Delta t^2}\mathbf{M}_{ni} + \mathbf{K}_{1,ni}, \\ \mathbf{r}_{\text{eff}} &= \mathbf{R}_{1,ni}^* - \mathbf{R}_{1,ni} \end{aligned} \tag{6.25}$$

as in (3.67) where the parameters are chosen as in Figure 3.13. Consequently, the weak form of the balance equation has to be evaluated at each RUNGE-KUTTA stage.

The literature offers various time integration schemes and distinct combinations of time stepping procedures for structural and integration point level. In (Mohr et al., 2008), GALERKIN time integration schemes are applied to the balance of linear momentum, while the material laws are integrated via an exponential update procedure. This procedure is also followed by (Meng and

Laursen, 2002*a*,*b*; Noels et al., 2008), however, for the time discretization of the balance law, procedures from the energy momentum family are taken into account. A combination of the NEWMARK scheme and the exponential update is performed in (Molinari and Ortiz, 2002). In (Simo and Miehe, 1992), the implicit EULER is exploited on both time integration levels. Quasi-static approaches, where the inertia effects within the balance law are neglected, are carried out in (Hartmann and Bier, 2007; Helm, 2006; Seitz et al., 2014). Thereby, exponential updates as well as RUNGE-KUTTA schemes are used for the material laws.

6.1.3.4. Radial Return Map

The incorporation of elasto(visco)plastic phenomena in the context of the presented numerical strategy requires the time discretization of the evolution equation and a detection strategy for the switching point between elastic and plastic behavior. These two aspects are realized in (Seitz et al., 2014) via an exponential update for the time discretization and a semi-smooth NEWTON process to distinguish between elastic and plastic properties as well as the determination of the corresponding quantities. In (Hartmann, 1993; Hartmann and Bier, 2007), a multilevel NEWTON procedure is developed. Therein, an elastic trial state is defined to determine the switching point. In the case of evolving plastic effects, a local NEWTON-RAPHSON scheme is performed to obtain the respective quantities as well as a consistent linearization for the tangential stiffness matrix. The results are then transferred to the global NEWTON-RAPHSON scheme. Similar predictor-corrector strategies are considered within return mapping procedures as in (Armero, 2006; Auricchio and Taylor, 1999; Meng and Laursen, 2002*b*; Mohr et al., 2008; Schröder et al., 2002; Simo and Miehe, 1992). Thereby, again an elastic trial state is established, and a local NEWTON-RAPHSON scheme is employed to determine the accompanying quantities in the case of plastic behavior. The viscoplastic case is treated analogously. The results are then again transferred to the global NEWTON-RAPHSON scheme.

There are two possible options to determine the derivative of the stress tensor with respect to some strain measures. It might be calculated algorithmically, cf. (Armero, 2006; Auricchio and Taylor, 1999), but there are also analytical approaches, cf. (Armero, 2006; Schröder et al., 2002; Simo and Miehe, 1992). In the following, the procedure presented in (Simo and Hughes, 1997; Simo and Miehe, 1992) with an analytic tangent will be analyzed using, in accordance with Equation (6.25) and (6.24), stiffly accurate diagonally implicit RUNGE-KUTTA schemes (DIRK) as well as the NEWMARK method. This approach is selected due to its simplicity and its analogy to the small strain case, see Section 4.1.3.4. Additionally, in much the same way as for small deformations, the viscoplastic and the plastic model will be partly treated together due to their similar mathematical structure.

Before the different time integration schemes are applied, some reformulations are performed. On the one hand, the evolution equation in (6.8) and (6.15) is recast into

$$\dot{\boldsymbol{C}}_{\mathrm{p}}^{-1} = -\frac{2\lambda J^{\frac{2}{3}}\sqrt{[\mathrm{DEV}\,(\boldsymbol{S})\cdot\boldsymbol{C}]:\,[\boldsymbol{C}\cdot\mathrm{DEV}\,(\boldsymbol{S})]}}{\mu}\boldsymbol{C}^{-1}\cdot\boldsymbol{N}_{\mathrm{p}}\cdot\boldsymbol{N}_{\mathrm{p}} - \frac{2\lambda\mathrm{Tr}\left(\boldsymbol{C}_{\mathrm{p}}^{-1}\right)}{3}\boldsymbol{C}^{-1}\cdot\boldsymbol{N}_{\mathrm{p}} \quad (6.26)$$

with

$$\boldsymbol{N}_{\mathrm{p}} = \frac{\boldsymbol{C}\cdot\mathrm{DEV}\,(\boldsymbol{S})}{\sqrt{[\mathrm{DEV}\,(\boldsymbol{S})\cdot\boldsymbol{C}]:\,[\boldsymbol{C}\cdot\mathrm{DEV}\,(\boldsymbol{S})]}},$$

exploiting the split of the inverse plastic right CAUCHY-GREEN tensor into a deviatoric and a spherical part. Following the course of action in (Simo and Miehe, 1992), the first term in (6.26) is neglected further on. On the other hand, the stress tensor of Equation (6.7) is expressed by

$$\boldsymbol{S} = \frac{3\kappa+2\mu}{6}\left[J^2-1\right]\boldsymbol{C}^{-1} + \mathrm{DEV}\,(\boldsymbol{S}) \qquad \text{with} \qquad \mathrm{DEV}\,(\boldsymbol{S}) = \mu J^{-\frac{2}{3}}\mathrm{DEV}\left(\boldsymbol{C}_{\mathrm{p}}^{-1}\right). \quad (6.27)$$

Therefore, the definition of the deviator with respect to the reference configuration (6.3) is used, and the plastic flow is assumed to be isochoric with $J_{\mathrm{p}} = 1$, cf. (Simo and Hughes, 1997; Simo and Miehe, 1992). Apparently, the stress tensor depends on the plastic right CAUCHY-GREEN tensor and the right CAUCHY-GREEN tensor. The tangential stiffness matrix, however, is influenced by the derivative of the stress tensor with respect to the GREEN-LAGRANGE strain tensor. Hence, the relationship

$$\frac{\partial \boldsymbol{S}}{\partial \boldsymbol{E}} = 2\frac{\partial \boldsymbol{S}}{\partial \boldsymbol{C}}$$

is of great importance.

It is emphasized that the stresses and their derivatives need to be determined only at the GAUSS-LEGENDRE integration points, since this numerical integration procedure is employed to evaluate the integrals of the weak form in (6.22). The same holds for the plastic quantities. However, they are not updated within the global iteration scheme and, hence, the iteration index k is dropped.

6.1.3.4.1. Finite Elastoplasticity: NEWMARK's Method and DIRK Schemes

If diagonally implicit RUNGE-KUTTA schemes or the NEWMARK method are used for the time discretization of the linearized semidiscrete form in (6.23), it is necessary to evaluate the stress relation in (6.27) at each stage t_{ni} or at the end of the time step t_{n+1}

$$\boldsymbol{S}^{k}_{ni/n+1} = \frac{3\kappa + 2\mu}{6}\left[\left[J^{e,k}_{ni/n+1}\right]^2 - 1\right]\left[\boldsymbol{C}^{e,k}_{ni/n+1}\right]^{-1} + \mu\left[J^{e,k}\right]^{-\frac{2}{3}}_{ni/n+1}\mathrm{DEV}\left(\boldsymbol{C}^{-1}_{\mathrm{p},ni/n+1}\right). \quad (6.28)$$

Applying the same time integration methods to the evolution equation in (6.26) yields

$$\boldsymbol{C}^{-1}_{\mathrm{p},ni} = \tilde{\boldsymbol{C}}^{-1}_{\mathrm{p},ni} + \Delta t\; a_{ii}\,\dot{\boldsymbol{C}}^{-1}_{\mathrm{p},ni} \qquad \text{with} \qquad \tilde{\boldsymbol{C}}^{-1}_{\mathrm{p},ni} = \boldsymbol{C}^{-1}_{\mathrm{p},n} + \Delta t\sum_{j=1}^{i-1} a_{ij}\,\dot{\boldsymbol{C}}^{-1}_{\mathrm{p},nj}, \quad (6.29)$$

analogously to Equation (3.64) with (3.65) for stiffly accurate diagonally implicit RUNGE-KUTTA schemes. Using Equation (3.50) of the NEWMARK method, whereby the included second time derivatives are neglected, results in

$$\boldsymbol{C}^{-1}_{\mathrm{p},n+1} = \tilde{\boldsymbol{C}}^{-1}_{\mathrm{p},n} + \Delta t\,\frac{\beta}{\gamma}\dot{\boldsymbol{C}}^{-1}_{\mathrm{p},n+1} \qquad \text{with} \qquad \tilde{\boldsymbol{C}}^{-1}_{\mathrm{p},n} = \boldsymbol{C}^{-1}_{\mathrm{p},n} + \Delta t\frac{\gamma-\beta}{\gamma}\dot{\boldsymbol{C}}^{-1}_{\mathrm{p},n}. \quad (6.30)$$

Comparing Equations $(6.29)_1$ and $(6.30)_1$ enables the general formulation

$$\boldsymbol{C}^{-1}_{\mathrm{p},ni/n+1} = \tilde{\boldsymbol{C}}^{-1}_{\mathrm{p},ni/n} + \Delta t\;\Theta\;\dot{\boldsymbol{C}}^{-1}_{\mathrm{p},ni/n+1} \qquad \text{with} \qquad \Theta = \begin{cases} a_{ii} & \text{for DIRK} \\ \dfrac{\beta}{\gamma} & \text{for NEWMARK.} \end{cases} \quad (6.31)$$

By combining the general Relationship (6.31) and the evolution equation in (6.26) determined at t_{ni} or t_{n+1}

$$\boldsymbol{C}^{-1}_{\mathrm{p},ni/n+1} = \tilde{\boldsymbol{C}}^{-1}_{\mathrm{p},ni/n+1} - \frac{2}{3}\Delta t\Theta\,\lambda_{ni/n+1}\mathrm{Tr}\left(\boldsymbol{C}^{-1}_{\mathrm{p},ni/n+1}\right)\left[\boldsymbol{C}^{e,k}_{ni/n+1}\right]^{-1}\cdot\boldsymbol{N}^{k}_{\mathrm{p}} \quad (6.32)$$

can be obtained. Taking the trace of (6.32) leads to the identity

$$\mathrm{Tr}\left(\boldsymbol{C}^{-1}_{\mathrm{p},ni}\right) = \mathrm{Tr}\left(\tilde{\boldsymbol{C}}^{-1}_{\mathrm{p},ni}\right). \quad (6.33)$$

Furthermore, inserting Equations (6.32) and (6.33) in (6.28) enables the definition of a trial state

$$\begin{aligned}\mathrm{DEV}\left(\boldsymbol{S}^{k,\mathrm{trial}}_{ni/n+1}\right) &:= \mu\left[J^{e,k}_{ni/n+1}\right]^{-\frac{2}{3}}\mathrm{DEV}\left(\tilde{\boldsymbol{C}}^{-1}_{\mathrm{p},ni/n}\right) = \\ &= \mu\left[J^{e,k}_{ni/n+1}\right]^{-\frac{2}{3}}\Big[\mathrm{DEV}\left(\boldsymbol{C}^{-1}_{\mathrm{p},ni/n+1}\right) + \frac{2}{3}\Delta t\Theta\,\lambda_{ni/n+1}\mathrm{Tr}\left(\tilde{\boldsymbol{C}}^{-1}_{\mathrm{p},ni/n}\right)\left[\boldsymbol{C}^{e,k}_{ni/n+1}\right]^{-1}\cdot\boldsymbol{N}^{k}_{\mathrm{p}}\Big],\end{aligned} \tag{6.34}$$

which depends on the actual total deformation state, but only on previous plastic strains. By computing the yield function (6.2) at this state

$$f^{\mathrm{trial}}(\boldsymbol{S}^{k,\mathrm{trial}}_{ni/n+1}, \boldsymbol{C}^{e,k}_{ni/n+1}) = \sqrt{\left[\mathrm{DEV}(\boldsymbol{S}^{k,\mathrm{trial}}_{ni/n+1})\cdot\boldsymbol{C}^{e,k}_{ni/n+1}\right]:\left[\boldsymbol{C}^{e,k}_{ni/n+1}\cdot\mathrm{DEV}(\boldsymbol{S}^{k,\mathrm{trial}}_{ni/n+1})\right]} - \sqrt{\frac{2}{3}}\sigma_{\mathrm{y}} \tag{6.35}$$

with $\sigma_{\mathrm{y}} > 0$, a criterion for the switching point between elastic and plastic behavior is established. If the trial yield function $f^{\mathrm{trial}}(\boldsymbol{S}^{k,\mathrm{trial}}_{ni/n+1}, \boldsymbol{C}^{e,k}_{ni/n+1})$ is smaller than zero, elastic properties prevail. Otherwise, plastic characteristics have to be admitted. A multiplication of Equation (6.34) with $\boldsymbol{C}^{e,k}_{ni/n+1}$ leads, together with the second summand in Relation (6.28), to

$$\sqrt{\left[\mathrm{DEV}(\boldsymbol{S}^{k,\mathrm{trial}}_{ni/n+1})\cdot\boldsymbol{C}^{e,k}_{ni/n+1}\right]:\left[\boldsymbol{C}^{e,k}_{ni/n+1}\cdot\mathrm{DEV}(\boldsymbol{S}^{k,\mathrm{trial}}_{ni/n+1})\right]}\boldsymbol{N}^{k,\mathrm{trial}}_{\mathrm{p}} = \tag{6.36}$$

$$= \sqrt{\left[\mathrm{DEV}(\boldsymbol{S}^{k}_{ni/n+1})\cdot\boldsymbol{C}^{e,k}_{ni/n+1}\right]:\left[\boldsymbol{C}^{e,k}_{ni/n+1}\cdot\mathrm{DEV}(\boldsymbol{S}^{k}_{ni/n+1})\right]}\boldsymbol{N}^{k}_{\mathrm{p}} + \frac{2}{3}\Delta t\Theta\lambda_{ni/n+1}\mu\left[J^{e,k}_{ni/n+1}\right]^{-\frac{2}{3}}\mathrm{Tr}\left(\tilde{\boldsymbol{C}}^{-1}_{\mathrm{p},ni/n}\right)\boldsymbol{N}^{k}_{\mathrm{p}}$$

with

$$\boldsymbol{N}^{k,\mathrm{trial}}_{\mathrm{p}} = \frac{\boldsymbol{C}^{e,k}_{ni/n+1}\cdot\mathrm{DEV}\left(\boldsymbol{S}^{k,\mathrm{trial}}_{ni/n+1}\right)}{\sqrt{\left[\mathrm{DEV}(\boldsymbol{S}^{k,\mathrm{trial}}_{ni/n+1})\cdot\boldsymbol{C}^{e,k}_{ni/n+1}\right]:\left[\boldsymbol{C}^{e,k}_{ni/n+1}\cdot\mathrm{DEV}(\boldsymbol{S}^{k,\mathrm{trial}}_{ni/n+1})\right]}}$$

and

$$\boldsymbol{N}^{k}_{\mathrm{p}} = \frac{\boldsymbol{C}^{e,k}_{ni/n+1}\cdot\mathrm{DEV}\left(\boldsymbol{S}^{k}_{ni/n+1}\right)}{\sqrt{\left[\mathrm{DEV}(\boldsymbol{S}^{k}_{ni/n+1})\cdot\boldsymbol{C}^{e,k}_{ni/n+1}\right]:\left[\boldsymbol{C}^{e,k}_{ni/n+1}\cdot\mathrm{DEV}(\boldsymbol{S}^{k}_{ni/n+1})\right]}}.$$

By comparing the left and right side of Equation (6.36), the additional relationships regarding the trial state

$$\boldsymbol{N}^{k,\mathrm{trial}}_{\mathrm{p}} = \boldsymbol{N}^{k}_{\mathrm{p}} \tag{6.37}$$

$$\sqrt{\left[\mathrm{DEV}(\boldsymbol{S}^{k,\mathrm{trial}}_{ni/n+1})\cdot\boldsymbol{C}^{e,k}_{ni/n+1}\right]:\left[\boldsymbol{C}^{e,k}_{ni/n+1}\cdot\mathrm{DEV}(\boldsymbol{S}^{k,\mathrm{trial}}_{ni/n+1})\right]} = \tag{6.38}$$

$$= \sqrt{\left[\mathrm{DEV}(\boldsymbol{S}^{k}_{ni/n+1})\cdot\boldsymbol{C}^{e,k}_{ni/n+1}\right]:\left[\boldsymbol{C}^{e,k}_{ni/n+1}\cdot\mathrm{DEV}(\boldsymbol{S}^{k}_{ni/n+1})\right]} + \frac{2}{3}\Delta t\Theta\,\lambda_{ni/n+1}\mu\left[J^{e,k}_{ni/n+1}\right]^{-\frac{2}{3}}\mathrm{Tr}\left(\tilde{\boldsymbol{C}}^{-1}_{\mathrm{p},ni/n}\right)$$

are generated. On the one hand, these expressions can be exploited to formulate the evolution equation in (6.32) solely in terms of quantities with respect to the trial state. On the other hand, the yield function in (6.2) can be reformulated into

$$\begin{aligned}f(\boldsymbol{S}^{k,\mathrm{trial}}_{ni/n+1}, \boldsymbol{C}^{e,k}_{ni/n+1}) = &\sqrt{\left[\mathrm{DEV}(\boldsymbol{S}^{k,\mathrm{trial}}_{ni/n+1})\cdot\boldsymbol{C}^{e,k}_{ni/n+1}\right]:\left[\boldsymbol{C}^{e,k}_{ni/n+1}\cdot\mathrm{DEV}(\boldsymbol{S}^{k,\mathrm{trial}}_{ni/n+1})\right]} - \\ &- \frac{2}{3}\Delta t\Theta\,\lambda_{ni/n+1}\mu\left[J^{e,k}_{ni/n+1}\right]^{-\frac{2}{3}}\mathrm{Tr}\left(\tilde{\boldsymbol{C}}^{-1}_{\mathrm{p},ni/n}\right) - \sqrt{\frac{2}{3}}\sigma_{\mathrm{y}} = 0.\end{aligned}$$

Therein, it is taken into account that, at each stage t_{ni} or at the end of the time step t_{n+1} where plastic deformation take place, the corresponding stress state has to lie on the yield surface. Hence, a closed form statement for the LAGRANGE multiplier

$$\lambda_{ni/n+1} = \frac{\sqrt{\left[\mathrm{DEV}(\boldsymbol{S}^{k,\mathrm{trial}}_{ni/n+1})\cdot\boldsymbol{C}^{e,k}_{ni/n+1}\right]:\left[\boldsymbol{C}^{e,k}_{ni/n+1}\cdot\mathrm{DEV}(\boldsymbol{S}^{k,\mathrm{trial}}_{ni/n+1})\right]} - \sqrt{\frac{2}{3}}\sigma_{\mathrm{y}}}{\frac{2}{3}\mu\,\Delta t\Theta\left[J^{e,k}_{ni/n+1}\right]^{-\frac{2}{3}}\mathrm{Tr}\left(\tilde{\boldsymbol{C}}^{-1}_{\mathrm{p},ni/n}\right)} \tag{6.39}$$

can be derived.

Thus, for stiffly accurate diagonal implicit RUNGE-KUTTA schemes or the NEWMARK method, the radial return map can be stated as follows: In the first step, the trial state in (6.34) is determined with current total deformations and previous plastic strains. The obtained quantity is used to determine the value of the trial yield function in (6.35). If $f^{\mathrm{trial}}(\boldsymbol{S}^{k,\mathrm{trial}}_{ni/n+1}, \boldsymbol{C}^{e,k}_{ni/n+1}) < 0$ holds, elastic properties are predicted and the plastic strains, the stress state, and the algorithmic constitutive tensor can be determined by

$$\begin{aligned}
\boldsymbol{C}^{-1}_{\mathrm{p},ni/n+1} &= \tilde{\boldsymbol{C}}^{-1}_{\mathrm{p},ni/n},\\
\boldsymbol{S}^{k}_{ni/n+1} &= \frac{3\kappa+2\mu}{6}\left[\left[J^{e,k}_{ni/n+1}\right]^{2}-1\right]\left[\boldsymbol{C}^{e,k}_{ni/n+1}\right]^{-1} + \mu\left[J^{e,k}_{ni/n+1}\right]^{-\frac{2}{3}}\mathrm{DEV}\left(\tilde{\boldsymbol{C}}^{-1}_{\mathrm{p},ni/n}\right),\\
\mathbb{G} &= \left.\frac{\partial \boldsymbol{S}_{ni/n+1}}{\partial \boldsymbol{C}^{e}_{ni/n+1}}\right|_{k},
\end{aligned} \tag{6.40}$$

whereby the general constitutive tensor $\mathbb{G}$ is determined in **Appendix A**.
For values $f^{\mathrm{trial}}(\boldsymbol{S}^{k,\mathrm{trial}}_{ni/n+1}, \boldsymbol{C}^{e,k}_{ni/n+1}) \geq 0$, the trial stress state lies outside the yield surface and plastic effects are predicted. The real stress state is calculated by projecting the trial state back onto the yield surface, cf. (Simo and Hughes, 1997). Consequently, the plastic strains, the stress state, and the algorithmic constitutive tensor can be calculated by

$$\begin{aligned}
\lambda_{ni/n+1} &= \frac{\sqrt{\left[\mathrm{DEV}(\boldsymbol{S}^{k,\mathrm{trial}}_{ni/n+1})\cdot\boldsymbol{C}^{e,k}_{ni/n+1}\right]:\left[\boldsymbol{C}^{e,k}_{ni/n+1}\cdot\mathrm{DEV}(\boldsymbol{S}^{k,\mathrm{trial}}_{ni/n+1})\right]} - \sqrt{\frac{2}{3}}\sigma_{\mathrm{y}}}{\frac{2}{3}\mu\,\Delta t\Theta\left[J^{e,k}_{ni/n+1}\right]^{-\frac{2}{3}}\mathrm{Tr}\left(\tilde{\boldsymbol{C}}^{-1}_{\mathrm{p},ni/n}\right)},\\
\boldsymbol{C}^{-1}_{\mathrm{p},ni/n+1} &= \tilde{\boldsymbol{C}}^{-1}_{\mathrm{p},ni/n} - \frac{2}{3}\Delta t\Theta\,\lambda_{ni/n+1}\frac{\mathrm{Tr}\left(\tilde{\boldsymbol{C}}^{-1}_{\mathrm{p},ni/n}\right)\mathrm{DEV}\left(\boldsymbol{S}^{k,\mathrm{trial}}_{ni/n+1}\right)}{\sqrt{\left[\mathrm{DEV}(\boldsymbol{S}^{k,\mathrm{trial}}_{ni/n+1})\cdot\boldsymbol{C}^{e,k}_{ni/n+1}\right]:\left[\boldsymbol{C}^{e,k}_{ni/n+1}\cdot\mathrm{DEV}(\boldsymbol{S}^{k,\mathrm{trial}}_{ni/n+1})\right]}},\\
\boldsymbol{S}^{k}_{ni/n+1} &= \frac{3\kappa+2\mu}{6}\left[\left[J^{e,k}_{ni/n+1}\right]^{2}-1\right]\left[\boldsymbol{C}^{e,k}_{ni/n+1}\right]^{-1} + \mu\left[J^{e,k}_{ni/n+1}\right]^{-\frac{2}{3}}\mathrm{DEV}\left(\boldsymbol{C}^{-1}_{\mathrm{p},ni/n+1}\right),\\
\mathbb{G} &= \left.\frac{\partial \boldsymbol{S}_{ni/n+1}}{\partial \boldsymbol{C}^{e}_{ni/n+1}}\right|_{k}
\end{aligned}$$

and the terms in **Appendix A**.

insert initial conditions $\mathbf{u}_1, \dot{\mathbf{u}}_1, \ddot{\mathbf{u}}_1$

loop over time steps $n = 1, ..., NT$

loop over stages $i = 1, ..., s$ || for NEWMARK $s = 1$

loop over iteration k while $\eta_\mathrm{u} > \eta$

loop over elements $e = 1, ..., NE$

loop over GAUSSpoints $l_n = 1, ..., NG$ with $n = 1, ..., ND$

Radial Return Map (including time discretization)

$$\mathrm{DEV}\left(\boldsymbol{S}^{k,\mathrm{trial}}_{ni/n+1}\right) = \mu \left[J^{e,k}_{ni/n+1}\right]^{-\frac{2}{3}} \mathrm{DEV}\left(\tilde{\boldsymbol{C}}^{-1}_{\mathrm{p},ni/n}\right)$$

if $f^{\mathrm{trial}}(\boldsymbol{S}^{k,\mathrm{trial}}_{ni/n+1}, \boldsymbol{C}^{e,k}_{ni/n+1}) < 0$

$$\boldsymbol{S}^{k}_{ni/n+1} = \frac{3\kappa + 2\mu}{6}\left[\left[J^{e,k}_{ni/n+1}\right]^2 - 1\right]\left[\boldsymbol{C}^{e,k}_{ni/n+1}\right]^{-1} + \mu\left[J^{e,k}_{ni/n+1}\right]^{-\frac{2}{3}} \mathrm{DEV}\left(\tilde{\boldsymbol{C}}^{-1}_{\mathrm{p},ni/n}\right)$$

$$\mathbb{G} = \left.\frac{\partial \boldsymbol{S}_{ni/n+1}}{\partial \boldsymbol{C}^{e}_{ni/n+1}}\right|_k$$

else

$$\boldsymbol{C}^{-1}_{\mathrm{p},ni/n+1} = \tilde{\boldsymbol{C}}^{-1}_{\mathrm{p},ni/n} - \frac{2}{3}\frac{\Delta t \Theta\, \lambda_{ni/n+1} \mathrm{Tr}\left(\tilde{\boldsymbol{C}}^{-1}_{\mathrm{p},ni/n}\right) \mathrm{DEV}\left(\boldsymbol{S}^{k,\mathrm{trial}}_{ni/n+1}\right)}{\sqrt{\left[\mathrm{DEV}(\boldsymbol{S}^{k,\mathrm{trial}}_{ni/n+1}) \cdot \boldsymbol{C}^{e,k}_{ni/n+1}\right] : \left[\boldsymbol{C}^{e,k}_{ni/n+1} \cdot \mathrm{DEV}(\boldsymbol{S}^{k,\mathrm{trial}}_{ni/n+1})\right]}}$$

$$\boldsymbol{S}^{k}_{ni/n+1} = \frac{3\kappa + 2\mu}{6}\left[\left[J^{e,k}_{ni/n+1}\right]^2 - 1\right]\left[\boldsymbol{C}^{e,k}_{ni/n+1}\right]^{-1} + \mu\left[J^{e,k}_{ni/n+1}\right]^{-\frac{2}{3}} \mathrm{DEV}\left(\boldsymbol{C}^{-1}_{\mathrm{p},ni/n+1}\right)$$

$$\mathbb{G} = \left.\frac{\partial \boldsymbol{S}_{ni/n+1}}{\partial \boldsymbol{C}^{e}_{ni/n+1}}\right|_k$$

elastoplastic case

$$\lambda_{ni/n+1} = \frac{f^{\mathrm{trial}}(\boldsymbol{S}^{k,\mathrm{trial}}_{ni/n+1}, \boldsymbol{C}^{e,k}_{ni/n+1})}{\frac{2}{3}\mu\, \Delta t \Theta \left[J^{e,k}_{ni/n+1}\right]^{-\frac{2}{3}} \mathrm{Tr}\left(\tilde{\boldsymbol{C}}^{-1}_{\mathrm{p},ni/n}\right)}$$

viscoplastic case

$$\lambda_{ni/n+1} = \frac{f^{\mathrm{trial}}(\boldsymbol{S}^{k,\mathrm{trial}}_{ni/n+1}, \boldsymbol{C}^{e,k}_{ni/n+1})}{\chi + \frac{2}{3}\mu\, \Delta t \Theta \left[J^{e,k}_{ni/n+1}\right]^{-\frac{2}{3}} \mathrm{Tr}\left(\tilde{\boldsymbol{C}}^{-1}_{\mathrm{p},ni/n}\right)}$$

next GAUSSpoint l_n

assembly of structural entries $\mathbf{M}_{ni/n+1}, \mathbf{K}_{1,ni/n+1}, \mathbf{R}^{*}_{1,ni/n+1}, \mathbf{R}_{1,ni/n+1}$

next element e

generate effective quantities $\mathbf{K}_{\mathrm{eff}}, \mathbf{r}_{\mathrm{eff}}$

solve effective system of equations $\mathbf{K}_{\mathrm{eff}} \Delta \mathbf{u}_{ni/n+1} = \mathbf{r}_{\mathrm{eff}}$

update primary variables & derivatives $\mathbf{u}^{k+1}_{ni/n+1} = \Delta \mathbf{u}_{ni/n+1} + \mathbf{u}^{k}_{ni/n+1}, \ddot{\mathbf{u}}^{k+1}_{ni/n+1}, \dot{\mathbf{u}}^{k+1}_{ni/n+1}$

validate convergence $\eta_\mathrm{u} \leq \eta$

next iteration k

next stage i

update time step end values $\mathbf{u}_{n+1}, \dot{\mathbf{u}}_{n+1}, \ddot{\mathbf{u}}_{n+1}$

next time step n

Figure 6.2.: Classical algorithm scheme for finite elasto(visco)plasticity involving DIRK schemes and the NEWMARK method

6.1.3.4.2. Finite Viscoplasticity: NEWMARK's Method and DIRK Schemes

If viscoplastic effects are considered - instead of elastoplastic ones - the derivations in (6.28)-(6.38) can be applied identically. In the elastic case for negative values of the trial yield function, even Equation (6.40) remains valid. However, for values $f^{\text{trial}}(\boldsymbol{S}^{k,\text{trial}}_{ni/n+1}, \boldsymbol{C}^{e,k}_{ni/n+1}) \geq 0$, the LAGRANGE multiplier has to be determined following Equation $(6.15)_2$. Together with the Definition (6.38), this results in

$$\lambda_{ni/n+1} = \frac{\sqrt{\left[\text{DEV}(\boldsymbol{S}^{k,\text{trial}}_{ni/n+1})\cdot\boldsymbol{C}^{e,k}_{ni/n+1}\right]:\left[\boldsymbol{C}^{e,k}_{ni/n+1}\cdot\text{DEV}(\boldsymbol{S}^{k,\text{trial}}_{ni/n+1})\right]} - \sqrt{\frac{2}{3}}\sigma_{\text{y}}}{\chi + \frac{2}{3}\mu\,\Delta t\Theta\left[J^{e,k}_{ni/n+1}\right]^{-\frac{2}{3}}\text{Tr}\left(\tilde{\boldsymbol{C}}^{-1}_{\text{p},ni/n}\right)}.$$

Apparently, the elastoplastic model is obtained for $\chi = 0$. Ultimately, the viscoplastic strains, the stress state, and the algorithmic constitutive tensor can be determined by

$$\begin{aligned}
\boldsymbol{C}^{-1}_{\text{p},ni/n+1} &= \tilde{\boldsymbol{C}}^{-1}_{\text{p},ni/n} - \frac{2}{3}\Delta t\Theta\,\lambda_{ni/n+1}\frac{\text{Tr}\left(\tilde{\boldsymbol{C}}^{-1}_{\text{p},ni/n}\right)\text{DEV}\left(\boldsymbol{S}^{k,\text{trial}}_{ni/n+1}\right)}{\sqrt{\left[\text{DEV}(\boldsymbol{S}^{k,\text{trial}}_{ni/n+1})\cdot\boldsymbol{C}^{e,k}_{ni/n+1}\right]:\left[\boldsymbol{C}^{e,k}_{ni/n+1}\cdot\text{DEV}(\boldsymbol{S}^{k,\text{trial}}_{ni/n+1})\right]}},\\
\boldsymbol{S}^{k}_{ni/n+1} &= \frac{3\kappa+2\mu}{6}\left[\left[J^{e,k}_{ni/n+1}\right]^{2}-1\right]\left[\boldsymbol{C}^{e,k}_{ni/n+1}\right]^{-1} + \mu\left[J^{e,k}_{ni/n+1}\right]^{-\frac{2}{3}}\text{DEV}\left(\boldsymbol{C}^{-1}_{\text{p},ni/n+1}\right),\\
\mathbb{G} &= \left.\frac{\partial\boldsymbol{S}_{ni/n+1}}{\partial\boldsymbol{C}^{e}_{ni/n+1}}\right|_{k.}
\end{aligned}$$

Figure 6.2 shows an algorithmic implementation of the general finite elastoplastic and viscoplastic problem concerning stiffly accurate diagonally implicit RUNGE-KUTTA schemes and the NEWMARK method.

6.2. The Principle of JOURDAIN for a Variational Multifield Approach

For the small strain regime, two distinct approaches concerning the implementation of elasto-(visco)plastic models are presented in **Chapter 4**. The classical ansatz is based on an implicit coupling between material laws and the balance equation, leading to a system of nested time integration schemes in conjunction with specific projection algorithms. In contrast, the multifield approach rests on the idea of treating material laws and the balance law equivalently, so that an explicit coupling between them is established and the number of primary variables is extended. This strategy enables the application of arbitrary time integration schemes suitable for differential algebraic systems. The underlying background is built up by taking the principle of virtual power as a variational principle and adapting it to dissipative phenomena.

Both kinds of formulations can be transferred to the finite strain regime. While the classical approach is elaborated in Section 6.1, the variational setting is derived further on. Distinct aspects in this direction can be found in the literature. The idea of deducing finite elastoplastic models by means of unified functionals is demonstrated in (Hackl, 1997). In (Miehe et al., 2004, 2002; Mosler and Bruhns, 2010; Ortiz and Stainier, 1999), the modeling and implementation of material laws is based on extremum principles related to dissipative potentials, whereby the concept of a dissipative potential within the finite strain regime was already established by (Halphen and Nguyen, 1975). Mathematical considerations concerning these variational methods are analyzed in (Carstensen et al., 2002; Mielke, 2003, 2004).

6.2.1. The Principle of Virtual Power for Finite Elastoplasticity

Following the procedure in Section 4.2.1.1, the variational multifield approach for finite elastoplasticity can be derived. In the first step, it is ascertained that the balance of energy of a continuum mechanical body $\mathcal{B}$ can be formulated by

$$P = \dot{K} + \dot{E} + P^* + D = 0, \tag{6.41}$$

stating that the power within a system is equal to zero. The included quantities are furthermore assumed to be defined by

$$\dot{K} = \int_\Omega \rho_0 \ddot{\boldsymbol{u}} \cdot \dot{\boldsymbol{u}} \, dV, \tag{6.42}$$

$$\dot{E} = \int_\Omega \dot{e}(\boldsymbol{C}, \boldsymbol{C}_\mathrm{p}^{-1}) \, dV = \int_\Omega \left[\frac{\partial e}{\partial \boldsymbol{C}} : \dot{\boldsymbol{C}} + \frac{\partial e}{\partial \boldsymbol{C}_\mathrm{p}^{-1}} : \dot{\boldsymbol{C}}_\mathrm{p}^{-1} \right] dV, \tag{6.43}$$

$$P^* = -\int_\Omega \rho_0 \dot{\boldsymbol{u}} \cdot \boldsymbol{f} \, dV - \int_{\Gamma_{t^*}} \dot{\boldsymbol{u}} \cdot \boldsymbol{t}^* \, dA, \tag{6.44}$$

$$D = \int_\Omega -\boldsymbol{S} : \frac{1}{2} \left[\boldsymbol{C} \cdot \dot{\boldsymbol{C}}_\mathrm{p}^{-1} \cdot \boldsymbol{C}_\mathrm{p} \right] dV - \int_\Omega \lambda f(\boldsymbol{S}, \boldsymbol{C}) \, dV \qquad \text{with } \lambda \geq 0. \tag{6.45}$$

Therein, Ω denotes the domain comprised by the elastoplastic body and Γ_{t^*} embodies the part of its boundary, where external boundary forces operate on. While the term for the time derivative of the kinetic energy $\dot{K}$ is identical to the one of the small strain regime in (4.48), the volume-specific energy e is stated as in the classical approach in Equation (6.4). Thus, the corresponding derivatives

$$\frac{\partial e}{\partial \boldsymbol{C}} = \frac{3\kappa + 2\mu}{12} \left[J^2 J_\mathrm{p}^{-1} - 1 \right] \boldsymbol{C}^{-1} + \frac{1}{2} \mu J^{-\frac{2}{3}} J_\mathrm{p}^{\frac{2}{3}} \left[\boldsymbol{C}_\mathrm{p}^{-1} - \frac{1}{3} \left[\boldsymbol{C} : \boldsymbol{C}_\mathrm{p}^{-1} \right] \boldsymbol{C}^{-1} \right],$$

$$\frac{\partial e}{\partial \boldsymbol{C}_\mathrm{p}^{-1}} = \frac{3\kappa + 2\mu}{12} \left[J^2 J_\mathrm{p}^{-1} - 1 \right] \boldsymbol{C}_\mathrm{p} + \frac{1}{2} \mu J^{-\frac{2}{3}} J_\mathrm{p}^{\frac{2}{3}} \left[\boldsymbol{C} - \frac{1}{3} \left[\boldsymbol{C} : \boldsymbol{C}_\mathrm{p}^{-1} \right] \boldsymbol{C}_\mathrm{p} \right]$$

are obtained, whereby again an isochoric plastic flow with $J_\mathrm{p} = 1$ is assumed, cf. (Simo and Miehe, 1992). The variable P^* represents the power due to external forces and D the dissipation pseudopotential. Another possible formulation of the dissipation potential is stated in (Schröder and Kuhl, 2013) - but, due to its dependence on quantities of the current configuration, this conception seems to be ineffective.

Moreover, it is supposed that an elastoplastic body strives for a state in which the balance of energy reaches a stationary point and, at the same time, the VON MISES yield function in (6.2) is fulfilled. Henceforth, the balance of energy in (6.41) is assumed to hold - and it is also considered as a rate-type functional that has to be stationary. The stationarity problem

$$\operatorname*{stat}_{\dot{\boldsymbol{u}}, \dot{\boldsymbol{C}}_\mathrm{p}^{-1}} \sup_{\boldsymbol{S}} \inf_{\lambda \geq 0} P(\dot{\boldsymbol{u}}, \dot{\boldsymbol{C}}_\mathrm{p}^{-1}, \boldsymbol{S}, \lambda), \tag{6.46}$$

is the consequence, which is the finite strain extension of the procedure described in Section 4.2.1.1. In the next step, the inequality constraint in (6.46) is incorporated into the stationarity problem

$$\operatorname*{stat}_{\dot{\boldsymbol{u}}, \dot{\boldsymbol{C}}_\mathrm{p}^{-1}} \sup_{\boldsymbol{S}} \inf_{\lambda \geq 0} P(\dot{\boldsymbol{u}}, \dot{\boldsymbol{C}}_\mathrm{p}^{-1}, \boldsymbol{S}, \lambda) = \operatorname*{stat}_{\dot{\boldsymbol{u}}, \dot{\boldsymbol{C}}_\mathrm{p}^{-1}} \sup_{\boldsymbol{S}} \inf_{\lambda} \left[\dot{K} + \dot{E} + P^* - \int_\Omega \boldsymbol{S} : \frac{1}{2} \left[\boldsymbol{C} \cdot \dot{\boldsymbol{C}}_\mathrm{p}^{-1} \cdot \boldsymbol{C}_\mathrm{p} \right] + \lambda f(\boldsymbol{S}, \boldsymbol{C}) - \psi_\mathrm{I}(\lambda) dV \right]. \tag{6.47}$$

In order to determine the solution of Problem (6.47), the course of action in (Burger, 2003; Rockafellar, 1970; Zeidler, 1985) is followed to define the stationarity condition

$$0 \in \partial P(\dot{\boldsymbol{u}}, \dot{\boldsymbol{C}}_{\mathrm{p}}^{-1}, \boldsymbol{S}, \lambda) \coloneqq \partial_{\dot{\boldsymbol{u}}} P + \partial_{\dot{\boldsymbol{C}}_{\mathrm{p}}^{-1}} P + \partial_{\boldsymbol{S}} P + \partial_{\lambda} P, \tag{6.48}$$

where the operator $\partial_{(\bullet)}$ represents the sub- or superdifferential with regard to the respective quantity. Together with the definition of the sub- or superdifferential in (4.55) and their link to the GÂTEAUX derivative in (4.56), an evaluation of (6.48) yields:

$$\int_{\Omega} \rho_0\, \delta\dot{\boldsymbol{u}} \cdot \ddot{\boldsymbol{u}}\, dV + \int_{\Omega} \frac{\partial e}{\partial \boldsymbol{C}} : \delta\dot{\boldsymbol{C}}\, dV - \int_{\Omega} \rho_0\, \delta\dot{\boldsymbol{u}} \cdot \boldsymbol{f}\, dV - \int_{\Gamma_{t^*}} \delta\dot{\boldsymbol{u}} \cdot \boldsymbol{T}^*\, dA = 0, \tag{6.49}$$

$$\int_{\Omega} \left[\frac{\partial e}{\partial \boldsymbol{C}_{\mathrm{p}}^{-1}} - \frac{1}{2} \boldsymbol{C}^{\mathrm{T}} \cdot \boldsymbol{S} \cdot \boldsymbol{C}_{\mathrm{p}}^{\mathrm{T}} \right] : \delta\dot{\boldsymbol{C}}_{\mathrm{p}}^{-1}\, dV = 0, \tag{6.50}$$

$$\int_{\Omega} \left[\lambda\, f(\delta\boldsymbol{S}, \boldsymbol{C}) - \lambda\, f(\boldsymbol{S}, \boldsymbol{C})\right]\, dV + \int_{\Omega} \frac{1}{2} \boldsymbol{C} \cdot \dot{\boldsymbol{C}}_{\mathrm{p}}^{-1} \cdot \boldsymbol{C}_{\mathrm{p}} : \left[\delta\boldsymbol{S} - \boldsymbol{S}\right]\, dV \geq 0, \tag{6.51}$$

$$\int_{\Omega} \left[\psi_{\mathrm{I}}(\delta\lambda) - \psi_{\mathrm{I}}(\lambda)\right]\, dV - \int_{\Omega} f(\boldsymbol{S}, \boldsymbol{C})\, \left[\delta\lambda - \lambda\right]\, dV \geq 0. \tag{6.52}$$

Although the weak forms in (6.49)-(6.52) are completely different to the weak form of the classical approach in (6.20), identical strong forms can be derived. Following the statements in Section 4.2.1.1, Inequality (6.52) yields the KARUSH-KUHN-TUCKER conditions as in Equation (6.9)

$$\lambda \geq 0, \qquad f(\boldsymbol{S}, \boldsymbol{C}) \leq 0, \qquad \lambda f(\boldsymbol{S}, \boldsymbol{C}) = 0. \tag{6.53}$$

Inequality (6.51) can be transferred to the inclusion

$$\frac{1}{2} \boldsymbol{C} \cdot \dot{\boldsymbol{C}}_{\mathrm{p}}^{-1} \cdot \boldsymbol{C}_{\mathrm{p}} \in -\lambda \partial_{\boldsymbol{S}} f(\boldsymbol{S}, \boldsymbol{C}).$$

If furthermore the KARUSH-KUHN-TUCKER conditions in (6.53), the properties of the yield function in (6.2), and some basic tensor calculus are taken into account, the evolution equation

$$\dot{\boldsymbol{C}}_{\mathrm{p}}^{-1} = -2\lambda\, \boldsymbol{C}^{-1} \cdot \frac{\partial f(\boldsymbol{S}, \boldsymbol{C})}{\partial \boldsymbol{S}} \cdot \boldsymbol{C}_{\mathrm{p}}^{-1},$$

is obtained. Therein, the previously needed superdifferential is replaced by the respective gradient. This is possible, since at the point $\sqrt{\left[\mathrm{DEV}\left(\boldsymbol{S}\right) \cdot \boldsymbol{C}\right] : \left[\boldsymbol{C} \cdot \mathrm{DEV}\left(\boldsymbol{S}\right)\right]} = 0$, where the superdifferential can have multiple values, the LAGRANGE multiplier is always zero. The same expression for the evolution of plastic strains is used in the classical approach in (6.8). Equation (6.50) can be converted into its strong counterpart by exploiting that the test function $\delta\dot{\boldsymbol{C}}_{\mathrm{p}}^{-1}$ is arbitrary but non-zero. The connection between the derivatives of the internal energy in (6.5) as well as the symmetry of the plastic right CAUCHY-GREEN tensor and the right CAUCHY-GREEN tensor lead to the constitutive law

$$S = 2\boldsymbol{C}^{-1} \cdot \frac{\partial e}{\partial \boldsymbol{C}_{\mathrm{p}}^{-1}} \cdot \boldsymbol{C}_{\mathrm{p}}^{-1} = 2\frac{\partial e}{\partial \boldsymbol{C}} \tag{6.54}$$

already known from Equation (6.7). The nonlinear balance of linear momentum in (2.13) and the corresponding NEUMANN boundary condition in $(6.1)_2$ can be derived from Equation (6.49).

Therefore, the identity of the GÂTEAUX derivatives $\delta\dot{\boldsymbol{C}} = 2\,\delta\dot{\boldsymbol{E}}$ has to be inserted together with the constitutive equation in (6.54). Furthermore, the symmetry of the second PIOLA-KIRCHHOFF stress tensor and the Relationship (6.19) are equally needed, as well as the divergence theorem in (4.22) and the product rule in (4.21). Thus, both the variational and the classical approach are based on the same strong formulations concerning the balance equation and the material laws.

By considering some ideas used to deduce these strong forms, the weak forms in (6.49)-(6.52) can be simplified. The definition of the indicator function in (4.53), the constitutive law in (6.54), and the property that the product of the yield function's superdifferential and the LAGRANGE multiplier is always single-valued lead to the set of equations

$$\int_{\Omega} \rho_0\,\delta\boldsymbol{u}\cdot\ddot{\boldsymbol{u}}\,dV + \int_{\Omega} \frac{\partial e}{\partial \boldsymbol{C}} : \delta\dot{\boldsymbol{C}}\,dV - \int_{\Omega} \rho_0\,\delta\boldsymbol{u}\cdot\boldsymbol{f}\,dV - \int_{\Gamma_{t^*}} \delta\boldsymbol{u}\cdot\boldsymbol{T}^*\,dA = 0, \tag{6.55}$$

$$\int_{\Omega} \left[2\frac{\partial e}{\partial \boldsymbol{C}} - \boldsymbol{S}\right] : \delta\dot{\boldsymbol{C}}_{\mathrm{p}}^{-1}\,dV = 0, \tag{6.56}$$

$$\int_{\Omega} \left[\left[\frac{1}{2}\boldsymbol{C}\cdot\dot{\boldsymbol{C}}_{\mathrm{p}}^{-1}\cdot\boldsymbol{C}_{\mathrm{p}} + \lambda\frac{\partial f(\boldsymbol{S},\boldsymbol{C})}{\partial \boldsymbol{S}}\right] : \delta\boldsymbol{S}\right] dV = 0, \tag{6.57}$$

$$\int_{\Omega} f(\boldsymbol{S},\boldsymbol{C})\,[\delta\lambda - \lambda]\;dV \leq 0 \tag{6.58}$$

with $\delta\lambda \geq 0, \lambda \geq 0$ and $\sqrt{[\mathrm{DEV}\,(\boldsymbol{S})\cdot\boldsymbol{C}] : [\boldsymbol{C}\cdot\mathrm{DEV}\,(\boldsymbol{S})]} \neq 0$. In the forthcoming analysis, Equation (6.57) will be changed to the form

$$\int_{\Omega} \left[\frac{3}{2}\dot{\boldsymbol{C}}_{\mathrm{p}}^{-1} + \lambda\mathrm{Tr}\left(\boldsymbol{C}_{\mathrm{p}}^{-1}\right)\frac{\mathrm{DEV}\,(\boldsymbol{S})}{\sqrt{[\mathrm{DEV}\,(\boldsymbol{S})\cdot\boldsymbol{C}] : [\boldsymbol{C}\cdot\mathrm{DEV}\,(\boldsymbol{S})]}}\right] : \delta\boldsymbol{S}\,dV = 0, \tag{6.59}$$

which is deduced in Section 6.1.3.4 and is based on the formulation of (Simo and Miehe, 1992). Throughout this, the same material model as in the conventional approach is generated, and a comparison between the classical and the variational procedure by means of numerical examples is enabled.

Hence, a variational multifield approach of the ideal elastoplastic problem similar to the small strain case is established. The next step is to generate its viscoplastic extension.

6.2.2. The Principle of Virtual Power for Finite Elastoviscoplasticity

In order to incorporate viscoplastic effects in the multifield approach presented above the dissipation pseudopotential in (6.45) has to be regularized. This is done in accordance with the classical approach in Section 6.1.2, leading to

$$D = \int_{\Omega} -\boldsymbol{S} : \frac{1}{2}\left[\boldsymbol{C}\cdot\dot{\boldsymbol{C}}_{\mathrm{p}}^{-1}\cdot\boldsymbol{C}_{\mathrm{p}}\right] - \frac{1}{\chi}h\left(f(\boldsymbol{S},\boldsymbol{C})\right)dV.$$

The variable χ therein represents a viscosity parameter, while the function $h\left(f(\boldsymbol{S},\boldsymbol{C})\right)$ is continuously differentiable, as defined in (4.16). By performing these adaptations, viscoplastic phenomena are modeled, since stress states outside the yield surface are tolerated but penalized.

The time derivatives of the kinetic energy and the internal energy as well as the power of external forces are identical to the terms stated in (6.42)-(6.44). Furthermore, the stationarity of the balance of energy (6.41) is assumed to derive the variational multifield approach for an elastoviscoplastic continuum. Thus, the physical state where the total power including dissipative effects reaches a stationary point is the preferable one. The corresponding mathematical demand is the inclusion

$$0 \in \partial P(\dot{\boldsymbol{u}}, \dot{\boldsymbol{C}}_{\mathrm{p}}^{-1}, \boldsymbol{S}) \coloneqq \partial_{\dot{\boldsymbol{u}}} P + \partial_{\dot{\boldsymbol{C}}_{\mathrm{p}}^{-1}} P + \partial_{\boldsymbol{S}} P,$$

which results in the general weak form

$$\int_{\Omega} \rho_0 \, \delta\dot{\boldsymbol{u}} \cdot \ddot{\boldsymbol{u}} \, dV + \int_{\Omega} \frac{\partial e}{\partial \boldsymbol{C}} : \delta\dot{\boldsymbol{C}} \, dV - \int_{\Omega} \rho_0 \, \delta\dot{\boldsymbol{u}} \cdot \boldsymbol{f} \, dV - \int_{\Gamma_{t^*}} \delta\dot{\boldsymbol{u}} \cdot \boldsymbol{T}^* \, dA = 0, \tag{6.60}$$

$$\int_{\Omega} \left[2\frac{\partial e}{\partial \boldsymbol{C}} - \boldsymbol{S} \right] : \delta\dot{\boldsymbol{C}}_{\mathrm{p}}^{-1} \, dV = 0, \tag{6.61}$$

$$\int_{\Omega} \left[\frac{3}{2}\dot{\boldsymbol{C}}_{\mathrm{p}}^{-1} + \frac{1}{\chi} \langle f(\boldsymbol{S}, \boldsymbol{C}) \rangle \mathrm{Tr}\left(\boldsymbol{C}_{\mathrm{p}}^{-1}\right) \frac{\mathrm{DEV}\left(\boldsymbol{S}\right)}{\sqrt{\left[\mathrm{DEV}\left(\boldsymbol{S}\right) \cdot \boldsymbol{C}\right] : \left[\boldsymbol{C} \cdot \mathrm{DEV}\left(\boldsymbol{S}\right)\right]}} \right] : \delta\boldsymbol{S} \, dV = 0, \tag{6.62}$$

whereby $\langle f(\boldsymbol{S}, \boldsymbol{C}) \rangle$ denotes the ramp function defined in (4.17). For the derivation of Equation (6.62), a reformulation as in Equation (6.59) is taken into account additionally. Compared to the elastoplastic case of the previous Section 6.2.1, Equations (6.60)-(6.61) remain unaltered. Hence, they embody, analogously, the balance of linear momentum, the accompanying NEUMANN boundary condition, and the constitutive law as their strong counterparts. By considering that the virtual stresses $\delta\boldsymbol{S}$ are arbitrary but non-zero, Relation (6.62) can be transformed into the simplified strong form known from the standard ansatz in Section 6.1.3.4. The viscoplastic multifield approach is thus governed by the same equations as the classical procedure of Section 6.1.2, but it possesses a completely different weak form.

6.2.3. Implementation Strategy for Multifield Finite Elastoplasticity

Although the classical and the variational ansatz for finite elastoplasticity are characterized by the same set of equations, differences prevail: While the displacement field is the only unknown quantity in the standard approach, the multifield procedure considers the plastic CAUCHY-GREEN tensor, the second PIOLA-KIRCHHOFF stress tensor, and the LAGRANGE multiplier as additional primary variables. An altered initial boundary value problem, as depicted in Figure 6.3, is the consequence, wherein the material laws are considered as balance equations. With this reinterpretation, a single level time integration for all unknown field variables is enabled, paving the way for the application of higher order accurate time integrators. To solve this altered initial boundary value problem, the methods discussed in **Chapter 3** are applied as described in the subsequent sections.

6.2.3.1. Weak Formulation of Multifield Finite Elastoplasticity

The classical scheme towards finite elastoplasticity is based on a local formulation of the material laws and the balance of linear momentum. In a further step, an integral representation of the latter is elaborated to enable the usage of the finite element method as one part of the solution strategy. The equations prescribing material properties maintain their local character and are never formulated in a weak sense.

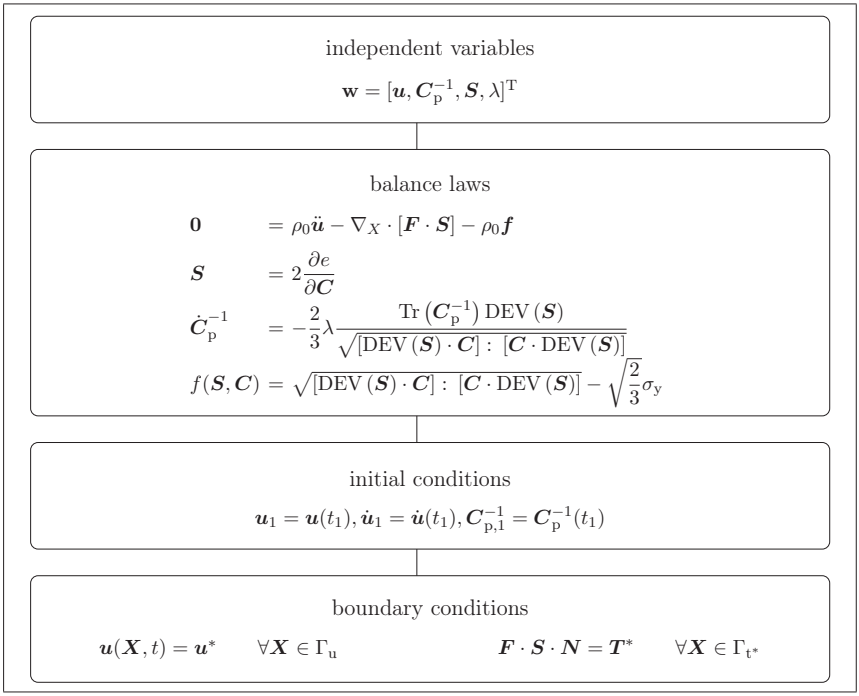

Figure 6.3.: Initial boundary value problem of the variational approach for finite elastoplasticity

In contrast, the point of departure of the multifield scheme is to require that the rate-type functional, derived from the balance of energy, has a stationary point. Consequently, an elastoplastic continuum is directly portrayed by means of weak formulations, consisting of the balance law and the material equations. Hence, no additional step has to be carried out to embed the variational approach consisting of Equations (6.55)-(6.56) and (6.58)-(6.59) in the solution strategy of **Chapter 3**. A comparison to the general weak form (3.1)-(3.2) yields the relations

$$\delta \mathbf{z}_1 = \begin{bmatrix} \delta \dot{\boldsymbol{u}} \\ \delta \dot{\mathbf{C}} \\ \delta \dot{\mathbf{C}}_{\mathrm{p}}^{-1} \\ \delta \mathbf{S} \end{bmatrix}, \quad \mathbf{r}_1 = \begin{bmatrix} \rho_0 \ddot{\boldsymbol{u}} - \rho_0 \boldsymbol{f} \\ \dfrac{\partial e}{\partial \boldsymbol{C}} \\ 2\dfrac{\partial e}{\partial \boldsymbol{C}} - \boldsymbol{S} \\ \dfrac{3}{2}\dot{\boldsymbol{C}}_{\mathrm{p}}^{-1} + \dfrac{\lambda \mathrm{Tr}\left(\boldsymbol{C}_{\mathrm{p}}^{-1}\right) \mathrm{DEV}\left(\boldsymbol{S}\right)}{\sqrt{[\mathrm{DEV}\left(\boldsymbol{S}\right) \cdot \boldsymbol{C}] : [\boldsymbol{C} \cdot \mathrm{DEV}\left(\boldsymbol{S}\right)]}} \end{bmatrix}, \quad r_2 = f(\boldsymbol{S}, \boldsymbol{C}),$$
$$\mathbf{r}^* = \begin{bmatrix} \mathbf{T}^* \\ \mathbf{0} \\ \mathbf{0} \\ \mathbf{0} \end{bmatrix}, \quad \mathbf{w} = \begin{bmatrix} \boldsymbol{u} \\ \boldsymbol{C}_{\mathrm{p}}^{-1} \\ \boldsymbol{S} \\ \lambda \end{bmatrix}. \tag{6.63}$$

The entries of the general weak form's quantities consist of a mixture of tensor-, vector-, and scalar-valued functions, so that their connection has to be defined properly.

6.2.3.2. Spatial Semidiscrete Linearized System of Equations

To solve a finite elastoplastic problem based on the weak forms (3.1)-(3.2) with the quantities specified in (6.63), the semi-smooth NEWTON procedure described in **Chapter 3** is applied. Therefore, the most general three-dimensional case is assumed. The spatial discretization is performed using the finite element method, partitioning the body's domain into subdomains $\bar{\Omega}^e$ fulfilling Equation (3.4). Thus, the geometry can be approximated continuously exploiting Relation (3.5) together with the LAGRANGE shape functions N^i derived in (3.16) as well as (3.13). Identical shape functions are considered to interpolate the displacement field, its time derivatives, and the corresponding test function $\delta\dot{\boldsymbol{u}}^e$ following Equations (3.7)-(3.9). The approximation of the test function $\delta\dot{\boldsymbol{C}}$ is not needed explicitly since the corresponding expression in Equation (6.55) can be reformulated by

$$\delta\dot{\boldsymbol{C}}\colon\frac{\partial e}{\partial\boldsymbol{C}}=2\delta\dot{\boldsymbol{E}}\colon\frac{\partial e}{\partial\boldsymbol{C}}=\left[\delta\dot{\boldsymbol{F}}^{\mathrm{T}}\cdot\boldsymbol{F}+\boldsymbol{F}^{\mathrm{T}}\cdot\delta\dot{\boldsymbol{F}}\right]\colon\frac{\partial e}{\partial\boldsymbol{C}}=2\left[\boldsymbol{F}^{\mathrm{T}}\cdot\delta\dot{\boldsymbol{F}}\right]\colon\frac{\partial e}{\partial\boldsymbol{C}}. \tag{6.64}$$

Therein, the symmetry of the derivative is exploited - as well as the fact that the variation is only calculated with respect to rate expressions. Hence, the deformation gradient and its virtual rate have to be approximated. This is achieved by Equation (3.6) as well as by

$$\delta\dot{\boldsymbol{F}}^e\approx\sum_{i=1}^{NN}\delta\dot{\boldsymbol{u}}^{ei}\otimes\nabla_X N^i(\boldsymbol{\xi}), \tag{6.65}$$

together with the derivatives of the LAGRANGE shape functions in (3.18) and (3.15). The plastic right CAUCHY-GREEN tensor, the second PIOLA-KIRCHHOFF stress tensor, the LAGRANGE multiplier, and the associated test functions are also approximated by $(3.7)_1$. However, discontinuities are allowed and LAGRANGE shape functions $\bar{N}^i$ are taken into account, which are constructed using $(3.13)_1$ and (3.16). The supporting points, however, are chosen to be equal to the GAUSS-LEGENDRE quadrature points, see Table 3.1, which are also used later on for the numerical integration of the weak forms. These kinds of shape functions enable jumps of the interpolated quantities between neighboring elements, whereby the same properties as in the classical approach are maintained. In the next step, the included inequality is reformulated into an equality by means of a nonlinear complementarity function as in (3.31). Thus, a system of nonlinear equations is obtained. Afterwards, a semi-smooth NEWTON method is generated. This includes the appropriate linearization of all apparent equations and the introduction of an active set strategy to account for the case distinction contained in the complementarity function. The result is the linearized semidiscrete form

$$\begin{aligned}
&\sum_{\substack{i,j=1\\ l,n\in\mathcal{A}^k}}^{NN}\begin{bmatrix}\delta\dot{\boldsymbol{u}}^{ei}\\ \delta\dot{\boldsymbol{C}}_{\mathrm{p}}^{-1,ei}\\ \delta\boldsymbol{S}^{ei}\\ \delta\lambda^{el}\end{bmatrix}\circ\left(\begin{bmatrix}\boldsymbol{m}_{\mathrm{uu}}^{eij}&\boldsymbol{0}&\boldsymbol{0}&\boldsymbol{0}\\ \boldsymbol{0}&\boldsymbol{0}&\boldsymbol{0}&\boldsymbol{0}\\ \boldsymbol{0}&\boldsymbol{0}&\boldsymbol{0}&\boldsymbol{0}\\ \boldsymbol{0}&\boldsymbol{0}&\boldsymbol{0}&0\end{bmatrix}\circ\begin{bmatrix}\Delta\ddot{\boldsymbol{u}}^{ej}\\ \Delta\ddot{\boldsymbol{C}}_{\mathrm{p}}^{-1,ej}\\ \Delta\ddot{\boldsymbol{S}}^{ej}\\ \Delta\ddot{\lambda}^{en}\end{bmatrix}+\begin{bmatrix}\boldsymbol{0}&\boldsymbol{0}&\boldsymbol{0}&\boldsymbol{0}\\ \boldsymbol{0}&\boldsymbol{0}&\boldsymbol{0}&\boldsymbol{0}\\ \boldsymbol{0}&\boldsymbol{d}_{\mathrm{sp}}^{eij}&\boldsymbol{0}&\boldsymbol{0}\\ \boldsymbol{0}&\boldsymbol{0}&\boldsymbol{0}&0\end{bmatrix}\circ\begin{bmatrix}\Delta\dot{\boldsymbol{u}}^{ej}\\ \Delta\dot{\boldsymbol{C}}_{\mathrm{p}}^{-1,ej}\\ \Delta\dot{\boldsymbol{S}}^{ej}\\ \Delta\dot{\lambda}^{en}\end{bmatrix}+\right.\\
&\left.+\begin{bmatrix}\boldsymbol{k}_{\mathrm{uu}}^{eij}&\boldsymbol{k}_{\mathrm{up}}^{eij}&\boldsymbol{0}&\boldsymbol{0}\\ \boldsymbol{k}_{\mathrm{pu}}^{eij}&\boldsymbol{k}_{\mathrm{pp}}^{eij}&\boldsymbol{k}_{\mathrm{ps}}^{eij}&\boldsymbol{0}\\ \boldsymbol{k}_{\mathrm{su}}^{eij}&\boldsymbol{k}_{\mathrm{sp}}^{eij}&\boldsymbol{k}_{\mathrm{ss}}^{eij}&\boldsymbol{k}_{\mathrm{s}\lambda}^{ein}\\ \boldsymbol{k}_{\lambda\mathrm{u}}^{elj}&\boldsymbol{0}&\bar{\boldsymbol{k}}_{\lambda\mathrm{s}}^{elj}&0\end{bmatrix}\circ\begin{bmatrix}\Delta\boldsymbol{u}^{ej}\\ \Delta\boldsymbol{C}_{\mathrm{p}}^{-1,ej}\\ \Delta\boldsymbol{S}^{ej}\\ \Delta\lambda^{en}\end{bmatrix}\right]=\sum_{\substack{i=1\\ l\in\mathcal{A}^k}}^{NN}\begin{bmatrix}\delta\dot{\boldsymbol{u}}^{ei}\\ \delta\dot{\boldsymbol{C}}_{\mathrm{p}}^{-1,ei}\\ \delta\boldsymbol{S}^{ei}\\ \delta\lambda^{el}\end{bmatrix}\circ\begin{bmatrix}\boldsymbol{r}_{\mathrm{u}}^{*,ei}-\boldsymbol{r}_{\mathrm{u}}^{ei}\\ -\boldsymbol{r}_{\mathrm{p}}^{ei}\\ -\boldsymbol{r}_{\mathrm{s}}^{ei}\\ -r_{\lambda}^{el}\end{bmatrix}\\
&\qquad\qquad\lambda^{en,k+1}=0\qquad\qquad\forall\,n\in\mathcal{I}^k.
\end{aligned} \tag{6.66}$$

The indices l, n therein are introduced to distinguish between element nodes characterized by plastic or elastic effects. Nodes inheriting plastic properties are gathered in the active set $\mathcal{A}^k$, while the inactive set $\mathcal{I}^k$ contains all elastic nodes. These sets are updated after each iteration k with

$$\begin{aligned} \mathcal{A}^{k+1} &:= \{l | \lambda^{el,k+1} + c\, r_\lambda^{el,k+1} > 0\}, \\ \mathcal{I}^{k+1} &:= \{l | \lambda^{el,k+1} + c\, r_\lambda^{el,k+1} \leq 0\}, \end{aligned} \tag{6.67}$$

where $c > 0$ is assumed. Furthermore, the following abbreviations are used:

$$\boldsymbol{m}_{\mathrm{uu}}^{eij} = \int_{\Omega^e} \rho_0 N^i N^j \, \boldsymbol{I} \, |\boldsymbol{J}^e| dV^e, \qquad \boldsymbol{d}_{\mathrm{sp}}^{eij} = \frac{3}{2} \int_{\Omega^e} \bar{N}^i \, \mathbb{I} \, \bar{N}^j \, |\boldsymbol{J}^e| dV^e,$$

$$\boldsymbol{k}_{\mathrm{ps}}^{eij} = -\int_{\Omega^e} \bar{N}^i \, \mathbb{I} \, \bar{N}^j \, |\boldsymbol{J}^e| dV^e, \qquad \boldsymbol{k}_{\mathrm{pu}}^{eij} = \int_{\Omega^e} \bar{N}^i \frac{\partial}{\partial \boldsymbol{C}^e} \left[4 \frac{\partial e}{\partial \boldsymbol{C}^e} \right] \Big|_k : \left[\nabla_X N^j \otimes \boldsymbol{F}^{e,k,\mathrm{T}} \right] |\boldsymbol{J}^e| dV^e,$$

$$\boldsymbol{k}_{\mathrm{pp}}^{eij} = \int_{\Omega^e} \bar{N}^i \frac{\partial}{\partial \boldsymbol{C}_{\mathrm{p}}^{-1,e}} \left[2 \frac{\partial e}{\partial \boldsymbol{C}^e} \right] \Big|_k \bar{N}^j |\boldsymbol{J}^e| dV^e, \qquad \boldsymbol{k}_{\mathrm{up}}^{eij} = \int_{\Omega^e} \left[\boldsymbol{F}^{e,k} \otimes \nabla_X N^i \right] : \frac{\partial}{\partial \boldsymbol{C}_{\mathrm{p}}^{-1,e}} \left[2 \frac{\partial e}{\partial \boldsymbol{C}^e} \right] \Big|_k \bar{N}^j |\boldsymbol{J}^e| dV^e,$$

$$\boldsymbol{k}_{\lambda \mathrm{s}}^{elj} = -\int_{\Omega^e} \bar{N}^l \frac{\partial f(\boldsymbol{S}^e, \boldsymbol{C}^e)}{\partial \boldsymbol{S}^e} \Big|_k \bar{N}^j \, |\boldsymbol{J}^e| dV^e, \qquad \boldsymbol{k}_{\lambda \mathrm{u}}^{elj} = -2 \int_{\Omega^e} \bar{N}^l \frac{\partial f(\boldsymbol{S}^e, \boldsymbol{C}^e)}{\partial \boldsymbol{C}^e} \Big|_k : \left[\nabla_X N^j \otimes \boldsymbol{F}^{e,k,\mathrm{T}} \right] |\boldsymbol{J}^e| dV^e$$

$$\boldsymbol{k}_{\mathrm{s}\lambda}^{ein} = \int_{\Omega^e} \bar{N}^i \frac{\mathrm{Tr}\left(\left[\boldsymbol{C}_{\mathrm{p}}^{e,k} \right]^{-1} \right) \mathrm{DEV}\left(\boldsymbol{S}^{e,k} \right)}{\sqrt{\left[\mathrm{DEV}\left(\boldsymbol{S}^{e,k} \right) \cdot \boldsymbol{C}^{e,k} \right] : \left[\boldsymbol{C}^{e,k} \cdot \mathrm{DEV}\left(\boldsymbol{S}^{e,k} \right) \right]}} \bar{N}^n \, |\boldsymbol{J}^e| dV^e,$$

$$\boldsymbol{k}_{\mathrm{ss}}^{eij} = \int_{\Omega^e} \bar{N}^i \lambda^{e,k} \frac{\partial}{\partial \boldsymbol{S}^e} \left[\frac{\mathrm{Tr}\left(\boldsymbol{C}_{\mathrm{p}}^{-1,e} \right) \mathrm{DEV}\left(\boldsymbol{S}^e \right)}{\sqrt{\left[\mathrm{DEV}\left(\boldsymbol{S}^e \right) \cdot \boldsymbol{C}^e \right] : \left[\boldsymbol{C}^e \cdot \mathrm{DEV}\left(\boldsymbol{S}^e \right) \right]}} \right] \Big|_k \bar{N}^j \, |\boldsymbol{J}^e| dV^e,$$

$$\boldsymbol{k}_{\mathrm{sp}}^{eij} = \int_{\Omega^e} \bar{N}^i \lambda^{e,k} \frac{\partial}{\partial \boldsymbol{C}_{\mathrm{p}}^{-1,e}} \left[\frac{\mathrm{Tr}\left(\boldsymbol{C}_{\mathrm{p}}^{-1,e} \right) \mathrm{DEV}\left(\boldsymbol{S}^e \right)}{\sqrt{\left[\mathrm{DEV}\left(\boldsymbol{S}^e \right) \cdot \boldsymbol{C}^e \right] : \left[\boldsymbol{C}^e \cdot \mathrm{DEV}\left(\boldsymbol{S}^e \right) \right]}} \right] \Big|_k \bar{N}^j \, |\boldsymbol{J}^e| dV^e,$$

$$\boldsymbol{k}_{\mathrm{uu}}^{eij} = \int_{\Omega^e} \left[\boldsymbol{F}^{e,k} \otimes \nabla_X N^i \right] : 4 \frac{\partial^2 e}{\partial \boldsymbol{C}^e \partial \boldsymbol{C}^e} \Big|_k : \left[\nabla_X N^j \otimes \boldsymbol{F}^{e,k,\mathrm{T}} \right] |\boldsymbol{J}^e| dV^e + \int_{\Omega^e} \nabla_X N^i \cdot 2 \frac{\partial e}{\partial \boldsymbol{C}^e} \Big|_k \cdot \nabla_X N^j \, \boldsymbol{I} \, |\boldsymbol{J}^e| dV^e,$$

$$\boldsymbol{k}_{\mathrm{su}}^{eij} = \int_{\Omega^e} \bar{N}^i \lambda^{e,k} \frac{\partial}{\partial \boldsymbol{C}^e} \left[\frac{2 \mathrm{Tr}\left(\boldsymbol{C}_{\mathrm{p}}^{-1,e} \right) \mathrm{DEV}\left(\boldsymbol{S}^e \right)}{\sqrt{\left[\mathrm{DEV}\left(\boldsymbol{S}^e \right) \cdot \boldsymbol{C}^e \right] : \left[\boldsymbol{C}^e \cdot \mathrm{DEV}\left(\boldsymbol{S}^e \right) \right]}} \right] \Big|_k : \left[\nabla_X N^j \otimes \boldsymbol{F}^{e,k,\mathrm{T}} \right] |\boldsymbol{J}^e| dV^e,$$

$$\boldsymbol{r}_{\mathrm{s}}^{ei} = \int_{\Omega^e} \bar{N}^i \left[\frac{3}{2} \left[\dot{\boldsymbol{C}}_{\mathrm{p}}^{e,k} \right]^{-1} + \lambda^{e,k} \frac{\mathrm{Tr}\left(\left[\boldsymbol{C}_{\mathrm{p}}^{e,k} \right]^{-1} \right) \mathrm{DEV}\left(\boldsymbol{S}^{e,k} \right)}{\sqrt{\left[\mathrm{DEV}\left(\boldsymbol{S}^{e,k} \right) \cdot \boldsymbol{C}^{e,k} \right] : \left[\boldsymbol{C}^{e,k} \cdot \mathrm{DEV}\left(\boldsymbol{S}^{e,k} \right) \right]}} \right] |\boldsymbol{J}^e| dV^e,$$

$$\boldsymbol{r}_{\mathrm{p}}^{ei} = \int_{\Omega^e} \bar{N}^i \left[2 \frac{\partial e}{\partial \boldsymbol{C}^e} \Big|_k - \boldsymbol{S}^{e,k} \right] |\boldsymbol{J}^e| dV^e, \qquad \boldsymbol{r}_{\mathrm{u}}^{*,ei} = \int_{\Omega^e} N^i \, \rho_0 \boldsymbol{f} \, |\boldsymbol{J}^e| dV^e + \int_{\Gamma_{t^*}^e} N^i \, \boldsymbol{T}^* |\boldsymbol{J}^{e,\mathrm{red}}| dA^e,$$

$$r_\lambda^{el} = -\int_{\Omega^e} \bar{N}^i \, f(\boldsymbol{S}^{e,k}, \boldsymbol{C}^{e,k}) |\boldsymbol{J}^e| dV^e, \qquad \boldsymbol{r}_{\mathrm{u}}^{ei} = \int_{\Omega^e} N^i \rho_0 \ddot{\boldsymbol{u}}^{e,k} \, |\boldsymbol{J}^e| dV^e + \int_{\Omega^e} \boldsymbol{F}^{e,k} \cdot 2 \frac{\partial e}{\partial \boldsymbol{C}^e} \Big|_k \cdot \nabla_X N^i |\boldsymbol{J}^e| dV^e.$$

The appearing integrals are assumed to be determined numerically using the Gauss-Legendre quadrature, leading to quantities which are characterized by distinct tensor orders. Since the

primary variables and the corresponding test functions in (6.66) are scalar- as well as, vector- and tensor-valued, distinct types of products have to be considered to establish their relationships correctly. This special property is emphasized by the '$\circ$'-operator.

In order to solve the finite elastoplastic problem based on Equations (6.66) as well as (6.67) with conventional routines, a realignment of the tensor-valued primary variables and test functions into vector-valued ones has to be performed. All other affected entries in Equation (6.66) have to be transformed in a suitable manner too. Moreover, the element-expressions are extended to the structural level using the assembly operators in (3.25) - (3.26) as well as (3.34), resulting in the global system of equations

$$\mathbf{M}\Delta\ddot{\mathbf{w}} + \mathbf{D}\Delta\dot{\mathbf{w}} + \mathbf{K}\Delta\mathbf{w} = \mathbf{R}_1^* - \mathbf{R}_1, \tag{6.68}$$

$$\mathbf{w}^{k+1} = \Delta\mathbf{w} + \mathbf{w}^k, \tag{6.69}$$

$$\lambda^{i,k+1} = 0 \qquad \forall i \in \mathcal{I}^k, \tag{6.70}$$

$$\mathcal{A}^{k+1} := \{i | \lambda^{ei,k+1} + c\, r_\lambda^{ei,k+1} > 0\}, \tag{6.71}$$

$$\mathcal{I}^{k+1} := \{i | \lambda^{ei,k+1} + c\, r_\lambda^{ei,k+1} \leq 0\}. \tag{6.72}$$

For explicit realizations of the sorting see Section 7.2. Furthermore, it is emphasized that in Equation (6.68) only the active entries of the assembled parts of $\boldsymbol{k}_{\lambda\mathrm{u}}^{elj}, \boldsymbol{k}_{\lambda\mathrm{s}}^{elj}, \boldsymbol{k}_{\mathrm{s}\lambda}^{ein}$ and r_λ^{el} are taken into account.

6.2.3.3. Time discretization on Structural Level

The final aspect within the multifield implementation strategy of the finite elastoplastic problem is its temporal integration. Therefore, all methods included in Section 3.4 can be applied directly to the semidiscrete linearized forms in (6.68)-(6.72). However, an extension to even more arbitrary time integration schemes has to be carried out with care. An analysis of Equation (6.66) reveals, that there are algebraic equations inherent. For a proper solution strategy, their exact fulfillment at the end of the time step is of great importance, cf. (Ellsiepen and Hartmann, 2001; Hairer and Wanner, 2002). All time integration methods presented in this thesis take this into account. Another demanding task for the time integration scheme is the adequate consideration of the active set strategy. Despite these limitations, a larger variety of time discretization procedures can simply be applied to this multifield ansatz than to the conventional approach in Section 6.1.3.3. In the latter, the difficulty of taking algebraic equations into account also persists due to the yield function. Furthermore, an appropriate coupling strategy is needed to connect the time integration of the material laws to the one applied to the balance of linear momentum. Within the multifield approach, this coupling is realized automatically, due to its structure.

6.2.4. Implementation Strategy for Multifield Finite Viscoplasticity

In the classical approach in Section 6.1.3, similar numerical realizations are used for the treatment of finite elastoplastic and finite viscoplastic deformations. The main difference between both procedures lies in the determination of the LAGRANGE multiplier and, hence, affects only the evaluation of the material laws on integration point level. The generation of the weak form as well as its discretization, however, remain completely unchanged. In order to consider finite viscoplastic effects in a variational multifield setting, the system of equations compared to the

elastoplastic case is modified, see Sections 6.2.1 and 6.2.2. The LAGRANGE multiplier is no longer regarded as an unknown quantity, and the altered initial boundary value problem in Figure 6.4 is the consequence. Nevertheless, also in the viscoplastic formulation, all field variables can be temporally discretized simultaneously using higher order accurate schemes. The initial bound-

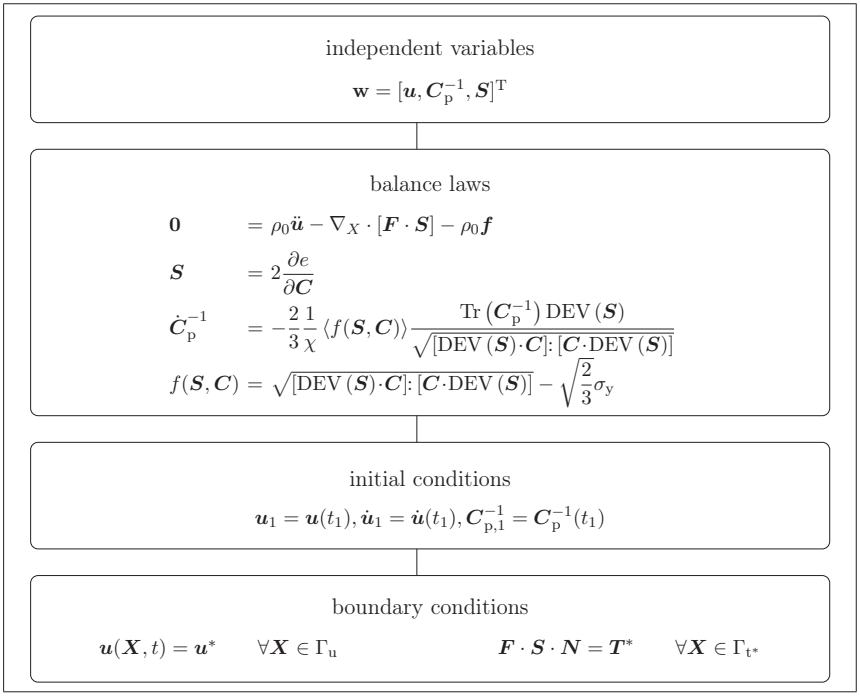

Figure 6.4.: Initial boundary value problem of the variational approach for viscoplasticity in the finite strain regime

ary value problem's detailed solution strategy is described in the subsequent sections, whereby the fundamentals are explained in **Chapter 3**.

6.2.4.1. Weak Formulation of Multifield Finite Viscoplasticity

As in the finite elastoplastic multifield case, its viscoplastic adaptation is based on a weak formulation. This stands in strong contrast to the classical approach, where the first step of the numerical solution procedure is the generation of a weak form. Within the variational framework, Equations (6.60)-(6.62) can hence be directly embedded into the solution strategy of **Chapter 3** by comparing the distinct entries to the general weak form in (3.1). As a consequence, the

following relations are obtained:

$$\delta\mathbf{z}_1 = \begin{bmatrix} \delta\dot{\boldsymbol{u}} \\ \delta\dot{\boldsymbol{C}} \\ \delta\dot{\boldsymbol{C}}_{\mathrm{p}}^{-1} \\ \delta\boldsymbol{S} \end{bmatrix}, \qquad \mathbf{r}_1 = \begin{bmatrix} \rho_0\ddot{\boldsymbol{u}} - \rho_0\boldsymbol{f} \\ \dfrac{\partial e}{\partial \boldsymbol{C}} \\ 2\dfrac{\partial e}{\partial \boldsymbol{C}} - \boldsymbol{S} \\ \dfrac{3}{2}\dot{\boldsymbol{C}}_{\mathrm{p}}^{-1} + \dfrac{1}{\chi}\left\langle f(\boldsymbol{S},\boldsymbol{C})\right\rangle \mathrm{Tr}\left(\boldsymbol{C}_{\mathrm{p}}^{-1}\right) \dfrac{\mathrm{DEV}\left(\boldsymbol{S}\right)}{\sqrt{[\mathrm{DEV}\left(\boldsymbol{S}\right)\cdot\boldsymbol{C}]\colon[\boldsymbol{C}\cdot\mathrm{DEV}\left(\boldsymbol{S}\right)]}} \end{bmatrix},$$

$$\mathbf{r}^* = \begin{bmatrix} \mathbf{T}^* \\ \mathbf{0} \\ \mathbf{0} \\ \mathbf{0} \end{bmatrix}, \qquad \mathbf{w} = \begin{bmatrix} \boldsymbol{u} \\ \boldsymbol{C}_{\mathrm{p}}^{-1} \\ \boldsymbol{S} \end{bmatrix}.$$

Special care has to be taken concerning their multiplicative connections, since tensor- and vector-valued terms are prevalent. Nonetheless, as opposed to the elastoplastic multifield approach in Section 6.2.1, the viscoplastic ansatz does not contain an inequality, so that the standard NEWTON-RAPHSON scheme suffices as solution strategy.

6.2.4.2. Spatial Semidiscrete Linearized System of Equations

As discussed in **Chapter 3**, the first step to solve the finite viscoplastic problem in (6.60)-(6.62) is to carry out a spatial discretization. This is done on the basis of an arbitrary three-dimensional continuum mechanical body representing the most general case. The finite element method is used to partition the body's domain, fulfilling Equation (3.4), into subdomains $\bar{\Omega}^e$. The subdomains' geometry is approximated continuously by Equation (3.5) together with the LAGRANGE shape functions derived in (3.16) as well as in (3.13). The same shape functions N^i are exploited to approximate, together with Equations (3.7)-(3.9), the displacement field, its time derivatives, and the corresponding test function. For the test function $\delta\dot{\boldsymbol{C}}$ the Relations (6.64) - (6.65) are taken into account as well as the derivatives of the LAGRANGE shape functions in (3.18) and (3.15). In contrast to that, the plastic right CAUCHY-GREEN tensor, the second PIOLA-KIRCHHOFF stress tensor, and the associated test functions are approximated discontinuously by $(3.7)_1$ with the LAGRANGE shape functions $\bar{N}^i$. Again, Equations $(3.13)_1$ and (3.16) are employed to generate them. However, the necessary supporting points are chosen to be identical to the GAUSS-LEGENDRE quadrature points, see Table 3.1. Due to this selection, the approximated quantities may perform jumps across element boundaries. These assumptions are identical to those taken into account in the finite elastoplastic case in Section 6.2.3.2.

The next step within the solution strategy requires an appropriate linearization as derived in Equation (3.21), resulting in

$$\begin{aligned} \sum_{i,j=1}^{NN} \begin{bmatrix} \delta\dot{\boldsymbol{u}}^{ei} \\ \delta\dot{\boldsymbol{C}}_{\mathrm{p}}^{-1,ei} \\ \delta\mathbf{S}^{ei} \end{bmatrix} \circ \left(\begin{bmatrix} \boldsymbol{m}_{\mathrm{uu}}^{eij} & \mathbf{0} & \mathbf{0} \\ \mathbf{0} & \mathbf{0} & \mathbf{0} \\ \mathbf{0} & \mathbf{0} & \mathbf{0} \end{bmatrix} \circ \begin{bmatrix} \Delta\ddot{\boldsymbol{u}}^{ej} \\ \Delta\ddot{\boldsymbol{C}}_{\mathrm{p}}^{-1,ej} \\ \Delta\ddot{\mathbf{S}}^{ej} \end{bmatrix} + \begin{bmatrix} \mathbf{0} & \mathbf{0} & \mathbf{0} \\ \mathbf{0} & \mathbf{0} & \mathbf{0} \\ \mathbf{0} & \boldsymbol{d}_{\mathrm{sp}}^{eij} & \mathbf{0} \end{bmatrix} \circ \begin{bmatrix} \Delta\dot{\boldsymbol{u}}^{ej} \\ \Delta\dot{\boldsymbol{C}}_{\mathrm{p}}^{-1,ej} \\ \Delta\dot{\mathbf{S}}^{ej} \end{bmatrix} + \right. \\ \left. + \begin{bmatrix} \boldsymbol{k}_{\mathrm{uu}}^{eij} & \boldsymbol{k}_{\mathrm{up}}^{eij} & \mathbf{0} \\ \boldsymbol{k}_{\mathrm{pu}}^{eij} & \boldsymbol{k}_{\mathrm{pp}}^{eij} & \boldsymbol{k}_{\mathrm{ps}}^{eij} \\ \boldsymbol{k}_{\mathrm{su}}^{eij} & \boldsymbol{k}_{\mathrm{sp}}^{eij} & \boldsymbol{k}_{\mathrm{ss}}^{eij} \end{bmatrix} \circ \begin{bmatrix} \Delta\boldsymbol{u}^{ej} \\ \Delta\boldsymbol{C}_{\mathrm{p}}^{-1,ej} \\ \Delta\mathbf{S}^{ej} \end{bmatrix} \right] = \sum_{i=1}^{NN} \begin{bmatrix} \delta\dot{\boldsymbol{u}}^{ei} \\ \delta\dot{\boldsymbol{C}}_{\mathrm{p}}^{-1,ei} \\ \delta\mathbf{S}^{ei} \end{bmatrix} \circ \begin{bmatrix} \boldsymbol{r}_{\mathrm{u}}^{*,ei} - \boldsymbol{r}_{\mathrm{u}}^{ei} \\ -\boldsymbol{r}_{\mathrm{p}}^{ei} \\ -\boldsymbol{r}_{\mathrm{s}}^{ei} \end{bmatrix}. \end{aligned} \tag{6.73}$$

Therein, the following abbreviations are used:

$$\boldsymbol{m}_{\mathrm{uu}}^{eij} = \int_{\Omega^e} \rho_0 N^i N^j \, \boldsymbol{I} \, |\boldsymbol{J}^e| dV^e,$$

$$\boldsymbol{d}_{\mathrm{sp}}^{eij} = \frac{3}{2} \int_{\Omega^e} \bar{N}^i \, \mathbb{I} \, \bar{N}^j \, |\boldsymbol{J}^e| dV^e,$$

$$\boldsymbol{k}_{\mathrm{pu}}^{eij} = \int_{\Omega^e} \bar{N}^i \frac{\partial}{\partial \boldsymbol{C}^e} \left[4 \frac{\partial e}{\partial \boldsymbol{C}^e} \right] \Big|_k : \left[\nabla_X N^j \otimes \boldsymbol{F}^{e,k,\mathrm{T}} \right] |\boldsymbol{J}^e| dV^e,$$

$$\boldsymbol{k}_{\mathrm{ps}}^{eij} = - \int_{\Omega^e} \bar{N}^i \, \mathbb{I} \, \bar{N}^j \, |\boldsymbol{J}^e| dV^e,$$

$$\boldsymbol{k}_{\mathrm{up}}^{eij} = \int_{\Omega^e} \left[\boldsymbol{F}^{e,k} \otimes \nabla_X N^i \right] : \frac{\partial}{\partial \boldsymbol{C}_{\mathrm{p}}^{-1,e}} \left[2 \frac{\partial e}{\partial \boldsymbol{C}^e} \right] \Big|_k \bar{N}^j |\boldsymbol{J}^e| dV^e,$$

$$\boldsymbol{k}_{\mathrm{pp}}^{eij} = \int_{\Omega^e} \bar{N}^i \frac{\partial}{\partial \boldsymbol{C}_{\mathrm{p}}^{-1,e}} \left[2 \frac{\partial e}{\partial \boldsymbol{C}^e} \right] \Big|_k \bar{N}^j |\boldsymbol{J}^e| dV^e,$$

$$\boldsymbol{k}_{\mathrm{ss}}^{eij} = \int_{\Omega^e} \bar{N}^i \frac{\partial}{\partial \boldsymbol{S}^e} \left[\frac{1}{\chi} \langle f(\boldsymbol{S}^e, \boldsymbol{C}^e) \rangle \frac{\mathrm{Tr}\left(\boldsymbol{C}_{\mathrm{p}}^{-1,e}\right) \mathrm{DEV}\left(\boldsymbol{S}^e\right)}{\sqrt{[\mathrm{DEV}\left(\boldsymbol{S}^e\right) \cdot \boldsymbol{C}^e] : [\boldsymbol{C}^e \cdot \mathrm{DEV}\left(\boldsymbol{S}^e\right)]}} \right] \Big|_k \bar{N}^j |\boldsymbol{J}^e| dV^e,$$

$$\boldsymbol{k}_{\mathrm{sp}}^{eij} = \int_{\Omega^e} \bar{N}^i \frac{1}{\chi} \langle f(\boldsymbol{S}^{e,k}, \boldsymbol{C}^{e,k}) \rangle \frac{\partial}{\partial \boldsymbol{C}_{\mathrm{p}}^{-1,e}} \left[\frac{\mathrm{Tr}\left(\boldsymbol{C}_{\mathrm{p}}^{-1,e}\right) \mathrm{DEV}\left(\boldsymbol{S}^e\right)}{\sqrt{[\mathrm{DEV}\left(\boldsymbol{S}^e\right) \cdot \boldsymbol{C}^e] : [\boldsymbol{C}^e \cdot \mathrm{DEV}\left(\boldsymbol{S}^e\right)]}} \right] \Big|_k \bar{N}^j \, |\boldsymbol{J}^e| dV^e,$$

$$\boldsymbol{k}_{\mathrm{uu}}^{eij} = \int_{\Omega^e} \left[\boldsymbol{F}^{e,k} \otimes \nabla_X N^i \right] : 4 \frac{\partial e^2}{\partial \boldsymbol{C}^e \partial \boldsymbol{C}^e} \Big|_k : \left[\nabla_X N^j \otimes \boldsymbol{F}^{e,k,\mathrm{T}} \right] |\boldsymbol{J}^e| dV^e + \int_{\Omega^e} \nabla_X N^i \cdot \boldsymbol{S}^{e,k} \cdot \nabla_X N^j \, \boldsymbol{I} \, |\boldsymbol{J}^e| dV^e,$$

$$\boldsymbol{k}_{\mathrm{su}}^{eij} = \int_{\Omega^e} \bar{N}^i \frac{\partial}{\partial \boldsymbol{C}^e} \left[\frac{1}{\chi} \langle f(\boldsymbol{S}^e, \boldsymbol{C}^e) \rangle \frac{2 \mathrm{Tr}\left(\boldsymbol{C}_{\mathrm{p}}^{-1,e}\right) \mathrm{DEV}\left(\boldsymbol{S}^e\right)}{\sqrt{[\mathrm{DEV}\left(\boldsymbol{S}^e\right) \cdot \boldsymbol{C}^e] : [\boldsymbol{C}^e \cdot \mathrm{DEV}\left(\boldsymbol{S}^e\right)]}} \right] \Big|_k : \left[\nabla_X N^j \otimes \boldsymbol{F}^{e,k,\mathrm{T}} \right] |\boldsymbol{J}^e| dV^e,$$

$$\boldsymbol{r}_{\mathrm{s}}^{ei} = \int_{\Omega^e} \bar{N}^i \left[\frac{3}{2} \left[\dot{\boldsymbol{C}}_{\mathrm{p}}^{e,k} \right]^{-1} + \frac{1}{\chi} \langle f(\boldsymbol{S}^{e,k}, \boldsymbol{C}^{e,k}) \rangle \frac{\mathrm{Tr}\left(\left[\boldsymbol{C}_{\mathrm{p}}^{e,k} \right]^{-1} \right) \mathrm{DEV}\left(\boldsymbol{S}^{e,k} \right)}{\sqrt{\left[\mathrm{DEV}\left(\boldsymbol{S}^{e,k} \right) \cdot \boldsymbol{C}^{e,k} \right] : \left[\boldsymbol{C}^{e,k} \cdot \mathrm{DEV}\left(\boldsymbol{S}^{e,k} \right) \right]}} \right] |\boldsymbol{J}^e| dV^e,$$

$$\boldsymbol{r}_{\mathrm{p}}^{ei} = \int_{\Omega^e} \bar{N}^i \left[2 \frac{\partial e}{\partial \boldsymbol{C}^e} \Big|_k - \boldsymbol{S}^{e,k} \right] |\boldsymbol{J}^e| dV^e,$$

$$\boldsymbol{r}_{\mathrm{u}}^{*,ei} = \int_{\Omega^e} N^i \, \rho_0 \boldsymbol{f} \, |\boldsymbol{J}^e| dV^e + \int_{\Gamma_{t^*}^e} N^i \, \boldsymbol{T}^* |\boldsymbol{J}^{e,\mathrm{red}}| dA^e,$$

$$\boldsymbol{r}_{\mathrm{u}}^{ei} = \int_{\Omega^e} N^i \, \rho_0 \ddot{\boldsymbol{u}}^{e,k} \, |\boldsymbol{J}^e| dV^e + \int_{\Omega^e} \boldsymbol{F}^{e,k} \cdot 2 \frac{\partial e}{\partial \boldsymbol{C}^e} \Big|_k \cdot \nabla_X N^i \, |\boldsymbol{J}^e| dV^e.$$

The included integrals are calculated numerically with the help of a Gauss-Legendre quadrature. However, care has to be taken since the different entries of Equation (6.73) are vector- and tensor-valued, so that their appropriate multiplicative connection is established by the '$\circ$'-operator. In order to be able to solve this finite viscoplastic problem with conventional solvers, a realignment of the tensor-valued primary variables and test functions into vector-valued ones has to be performed. All other affected entries have to be transformed in a suitable manner too. Moreover, the elemental expressions are extended to the structural level using the assembly operators in (3.25) - (3.26), resulting in the global system of equations

$$\mathbf{M} \Delta \ddot{\mathbf{w}} + \mathbf{D} \Delta \dot{\mathbf{w}} + \mathbf{K} \Delta \mathbf{w} = \mathbf{R}_1^* - \mathbf{R}_1, \tag{6.74}$$

$$\mathbf{w}^{k+1} = \Delta \mathbf{w} + \mathbf{w}^k.$$

6.2.4.3. Time discretization on Structural Level

Before the unknown primary variables of the linear semidiscrete system of Equations (6.74) can be calculated, a time integration procedure has to be applied. This can be done in accordance with Section 3.4 using the described methods. However, it should be emphasized that the system of Equations (6.74) contains algebraic equations, although the yield surface is no longer included as an inequality constraint as in the elastoplastic case. Therefore, special demands are made on the time discretization schemes, since the algebraic equations have to be fulfilled at the end of the time step, cf. (Ellsiepen and Hartmann, 2001; Hairer and Wanner, 2002). All time integration methods presented in this thesis take this into account. In the variational approach, a greater variety of time discretization schemes can be applied in a simpler manner than in the case of the conventional scheme. Therein, the time integration methods of the balance law and of the material laws have to be coupled exploiting specific strategies. In the multifield approach, this is not necessary.

6.3. Summary

The general elasto(visco)plastic problem is defined to enable a uniform numerical treatment of distinct material formulations considering inelastic effects. This chapter brings this concept to life. Herein, widespread models for elastoplasticity as well as for viscoplasticity in the finite strain context are presented and integrated into this systematic framework. For the derivation and the implementation of these material laws, two approaches are followed.

The classical ansatz is based on the balance of linear momentum as balance equation, describing the movement of general continuum mechanical bodies. The equations describing the corresponding (visco)plastic material behavior are settled on a multiplicative split of the deformation gradient and exploit the fact that the dissipation inequality in the reference configuration has to be fulfilled. While plastic properties are characterized by a rate-independent formulation, viscoplastic features are controlled by the speed of the deformation process. For sufficiently slow displacement rates, both models yield identical results. Hence, viscoplasticity can be considered as a regularization of plasticity. The numerical realization within the classical approach focusses on the weak formulation of the balance of linear momentum. A comparison with the general elasto(visco)plastic problem enables a solution strategy as mentioned in **Chapter 3**. Only the embedding of the material laws leads to a deviation. The material laws are exclusively evaluated at integration point level and, thus, require a special treatment. Their time integration is coupled to the one of the balance of linear momentum by exploiting a radial return map algorithm together with diagonally implicit Runge-Kutta schemes as well as the Newmark method.

In contrast to this course of action, an enhanced variational multifield approach is developed. It is founded on the principle of Jourdain, wherein the stationarity conditions of a rate-type functional are calculated. As a result, the balance of linear momentum and the material laws are formulated in a weak sense. Hence, it is not necessary to incorporate a distinction between the balance law and the material expressions in the solution procedure, allowing for a direct application of the schemes established in **Chapter 3**. Due to the equal treatment of both types of formulations, the number of unknowns is increased - but a variety of higher order accurate time integrators can be applied directly to all field variables. The limitation to diagonally implicit Runge-Kutta schemes or the Newmark method and the necessity of special projection strategies is neutralized, although the considered material models are identical to those of the classical approach.

With the approaches presented in this chapter, a straightforward extension of the small strain procedures depicted in **Chapter 4** is accomplished, whereby the derivation and the implemen-

tation strategies remain identical. The result is that - within the variational multifield approach, not only in the small strain regime but also within finite strains - a variety of distinct classes of higher order accurate time discretization schemes can be applied.

7. Deformation of an Axisymmetric Steel Shaft in Finite Strain (Visco)plasticity

As in the small strain case, both the classical and the variational approach are compared in the finite strain regime - with regard to their applicability, their solution accuracy, and their convergence behavior. Therefore, the dynamic benchmark problem established in Section 5.2 is extended appropriately. The quasi-static analyses carried out in the same **Chapter 5** are not transferred to finite deformations, since no further insight can be gained and since the focus lies on implementing higher order accurate time integration schemes.

The thermomechanical deformation process depicted in **Chapter 1** served as motivation to construct a benchmark problem for small strain dynamic elasto(visco)plasticity. Due to the appearing large deformations, the enhancement to the finite strain regime is closely related. In order to generate a corresponding benchmark problem as a real extension to the small strain case, the essential parameters of the problem statement in Section 5.2 are maintained. This includes that the process-inherent thermal effects are neglected. Hence, the forging process of the steel shaft is again modeled exploiting an axisymmetric ansatz, leading to a displacement field solely characterized by its radial and axial components $\boldsymbol{u}(\boldsymbol{X}) = [u_{\mathrm{R}}, u_{\mathrm{Z}}]$. Due to the introduction of polar coordinates and their position-dependent basis vectors, the material deformation tensor is expressed in an echo of Equation (5.3) by

$$\boldsymbol{F} = \begin{bmatrix} F_{\mathrm{RR}} & 0 & F_{\mathrm{RZ}} \\ 0 & F_{\Phi\Phi} & 0 \\ F_{\mathrm{ZR}} & 0 & F_{\mathrm{ZZ}} \end{bmatrix} = \begin{bmatrix} 1 + \dfrac{\partial u_{\mathrm{R}}}{\partial R} & 0 & \dfrac{\partial u_{\mathrm{R}}}{\partial Z} \\ 0 & 1 + \dfrac{u_{\mathrm{R}}}{R} & 0 \\ \dfrac{\partial u_{\mathrm{Z}}}{\partial R} & 0 & 1 + \dfrac{\partial u_{\mathrm{Z}}}{\partial Z} \end{bmatrix}, \tag{7.1}$$

while, in accordance with Equation (5.4), the second PIOLA-KIRCHHOFF tensor can be restated into

$$\boldsymbol{S} = \begin{bmatrix} S_{\mathrm{RR}} & 0 & S_{\mathrm{RZ}} \\ 0 & S_{\Phi\Phi} & 0 \\ S_{\mathrm{RZ}} & 0 & S_{\mathrm{ZZ}} \end{bmatrix}. \tag{7.2}$$

For additional information concerning polar coordinates see **Appendix C**. The respective model specifications concerning the material parameters, geometric aspects, and load conditions, are chosen as shown in Figure 5.6.

7.1. Classical Approach towards the Dynamic Analysis of Finite Elastoplasticity

In order to solve the finite strain variant of the dynamic benchmark problem using the classical approach described in Section 6.1, the tangential quantities in Equation (6.22) have to be adapted. This is crucial to take the example's axisymmetric nature into account. Moreover, it is convenient to reduce the computational effort by exchanging the tensor calculus by matrix vector

multiplications. In this context, the greatest modifications have to be performed with regard to the tangential stiffness matrix. Therefore, the deformation tensor in (7.1) is exploited to form the right CAUCHY-GREEN tensor and the GREEN-LAGRANGE strain tensor of Equation (2.3). The existence of zero entries and prevailing symmetry aspects can then be employed to generate the vector-valued quantities

$$\overline{\overline{\mathbf{C}}} = \begin{bmatrix} C_{\mathrm{RR}} \\ C_{\Phi\Phi} \\ C_{\mathrm{ZZ}} \\ C_{\mathrm{RZ}} \end{bmatrix}, \qquad \overline{\overline{\mathbf{E}}} = \begin{bmatrix} E_{\mathrm{RR}} \\ E_{\Phi\Phi} \\ E_{\mathrm{ZZ}} \\ E_{\mathrm{RZ}} \end{bmatrix}, \qquad \overline{\overline{\mathbf{F}}} = \begin{bmatrix} F_{\mathrm{RR}} \\ F_{\Phi\Phi} \\ F_{\mathrm{ZZ}} \\ F_{\mathrm{RZ}} \\ F_{\mathrm{ZR}} \end{bmatrix}. \tag{7.3}$$

The reformulation of the second PIOLA-KIRCHHOFF stress tensor is twofold. On the one hand, a vector-valued quantity is of interest - while, on the other hand, a matrix-like expression is needed

$$\overline{\overline{\mathbf{S}}} = \begin{bmatrix} S_{\mathrm{RR}} \\ S_{\Phi\Phi} \\ S_{\mathrm{ZZ}} \\ 2S_{\mathrm{RZ}} \end{bmatrix}, \qquad \overline{\overline{\mathbf{S}}} = \begin{bmatrix} S_{\mathrm{RR}} & 0 & 0 & S_{\mathrm{RZ}} & 0 \\ 0 & S_{\Phi\Phi} & 0 & 0 & 0 \\ 0 & 0 & S_{\mathrm{ZZ}} & 0 & S_{\mathrm{RZ}} \\ S_{\mathrm{RZ}} & 0 & 0 & S_{\mathrm{ZZ}} & 0 \\ 0 & 0 & S_{\mathrm{RZ}} & 0 & S_{\mathrm{RR}} \end{bmatrix}. \tag{7.4}$$

In accordance with the small strain case, the algorithmic constitutive tensor $\mathbb{G}$ can be recast into

$$\overline{\overline{\mathbf{G}}} = \begin{bmatrix} G_{\mathrm{RRRR}} & G_{\mathrm{RR}\Phi\Phi} & G_{\mathrm{RRZZ}} & 2G_{\mathrm{RRRZ}} \\ G_{\Phi\Phi\mathrm{RR}} & G_{\Phi\Phi\Phi\Phi} & G_{\Phi\Phi\mathrm{ZZ}} & 2G_{\Phi\Phi\mathrm{RZ}} \\ G_{\mathrm{ZZRR}} & G_{\mathrm{ZZ}\Phi\Phi} & G_{\mathrm{ZZZZ}} & 2G_{\mathrm{ZZRZ}} \\ 2G_{\mathrm{RZRR}} & 2G_{\mathrm{RZ}\Phi\Phi} & 2G_{\mathrm{RZZZ}} & 4G_{\mathrm{RZRZ}} \end{bmatrix}. \tag{7.5}$$

Additionally, the restructuring of the terms related to shape functions has to be performed. For this purpose, the abbreviations

$$\mathbf{B}^i_{\mathrm{g}} = \begin{bmatrix} \dfrac{\partial N^i}{\partial R} & \dfrac{N^i}{R} & 0 & \dfrac{\partial N^i}{\partial Z} & 0 \\ 0 & 0 & \dfrac{\partial N^i}{\partial Z} & 0 & \dfrac{\partial N^i}{\partial R} \end{bmatrix}^{\mathrm{T}}, \quad \mathbf{B}^i_{\mathrm{m}} = \begin{bmatrix} F_{\mathrm{RR}}\dfrac{\partial N^i}{\partial R} & F_{\Phi\Phi}\dfrac{N^i}{R} & F_{\mathrm{RZ}}\dfrac{\partial N^i}{\partial Z} & \dfrac{1}{2}\left[F_{\mathrm{RR}}\dfrac{\partial N^i}{\partial Z} + F_{\mathrm{RZ}}\dfrac{\partial N^i}{\partial R}\right] \\ F_{\mathrm{ZR}}\dfrac{\partial N^i}{\partial R} & 0 & F_{\mathrm{ZZ}}\dfrac{\partial N^i}{\partial Z} & \dfrac{1}{2}\left[F_{\mathrm{RR}}\dfrac{\partial N^i}{\partial Z} + F_{\mathrm{RZ}}\dfrac{\partial N^i}{\partial R}\right] \end{bmatrix}^{\mathrm{T}} \tag{7.6}$$

are introduced.

Concerning the tangential mass matrix, only the unity matrix's dimension has to be reduced, in contrast to the general three-dimensional case, since the axisymmetric displacement vector only consists of two unknowns. Within the load vector, the volume forces and the surface forces can be neglected due to the displacement based load. Thus, for Equation (6.22) the adapted tangential quantities

$$\mathbf{m}^{eij} = \int_{\Omega^e} N^i N^j \, \mathbf{I} \, |\boldsymbol{J}^e| dV^e, \tag{7.7}$$

$$\mathbf{k}^{eij} = \int_{\Omega^e} \left[\mathbf{B}^i_{\mathrm{m}}\right]^{\mathrm{T}} \, 2\,\overline{\overline{\mathbf{G}}}^k \, \mathbf{B}^j_{\mathrm{m}} \, |\boldsymbol{J}^e| dV^e + \int_{\Omega^e} \left[\mathbf{B}^i_{\mathrm{g}}\right]^{\mathrm{T}} \, \overline{\overline{\mathbf{S}}}^k \, \mathbf{B}^j_{\mathrm{g}} \, |\boldsymbol{J}^e| dV^e, \tag{7.8}$$

$$\mathbf{r}^{ei}_1 = \int_{\Omega^e} N^i \, \rho_0 \ddot{\boldsymbol{u}}^{e,k} \, |\boldsymbol{J}^e| dV^e + \int_{\Omega^e} \left[\mathbf{B}^i_{\mathrm{m}}\right]^{\mathrm{T}} \, \overline{\overline{\mathbf{S}}}^k \, |\boldsymbol{J}^e| dV^e \tag{7.9}$$

are obtained.

7.2. Variational Approach towards the Dynamic Analysis of Finite Elastoplasticity

In order to simulate the dynamic benchmark problem of finite elastoplasticity also using the multifield setting, similar simplifications as in the classical approach have to be considered. Therefore, the tangential quantities included in Equation (6.66) are reformulated into

$$\mathbf{m}_{\mathrm{uu}}^{eij} = \int_{\Omega^e} \rho_0 N^i N^j \, \boldsymbol{I} \, |\boldsymbol{J}^e| dV^e, \qquad \mathbf{d}_{\mathrm{sp}}^{eij} = \frac{3}{2} \int_{\Omega^e} \bar{N}^i \bar{\bar{\mathbf{I}}} \bar{N}^j \, |\boldsymbol{J}^e| dV^e, \qquad \mathbf{k}_{\mathrm{pu}}^{eij} = \int_{\Omega^e} \bar{N}^i 4 \overline{\overline{\mathbf{G}}}_1^{e,k} \mathbf{B}_{\mathrm{m}}^j |\boldsymbol{J}^e| dV^e, \tag{7.10}$$

$$\mathbf{k}_{\mathrm{ps}}^{eij} = -\int_{\Omega^e} \bar{N}^i \bar{\bar{\mathbf{I}}} \bar{N}^j \, |\boldsymbol{J}^e| dV^e, \qquad \mathbf{k}_{\mathrm{up}}^{eij} = \int_{\Omega^e} \left[\mathbf{B}_{\mathrm{m}}^i\right]^{\mathrm{T}} 2 \overline{\overline{\mathbf{G}}}_2^{e,k} \bar{N}^j |\boldsymbol{J}^e| dV^e, \qquad \mathbf{k}_{\mathrm{pp}}^{eij} = \int_{\Omega^e} \bar{N}^i 2 \overline{\overline{\mathbf{G}}}_2^{e,k} \bar{N}^j |\boldsymbol{J}^e| dV^e, \tag{7.11}$$

$$\mathbf{k}_{\mathrm{uu}}^{eij} = \int_{\Omega^e} \left[\mathbf{B}_{\mathrm{g}}^i\right]^{\mathrm{T}} \overline{\overline{\boldsymbol{S}}}^{e,k} \mathbf{B}_{\mathrm{g}}^j |\boldsymbol{J}^e| dV^e + \int_{\Omega^e} \left[\mathbf{B}_{\mathrm{m}}^i\right]^{\mathrm{T}} 4 \overline{\overline{\mathbf{G}}}_1^{e,k} \mathbf{B}_{\mathrm{m}}^j |\boldsymbol{J}^e| dV^e, \tag{7.12}$$

$$\mathbf{k}_{\mathrm{sp}}^{eij} = \int_{\Omega^e} \bar{N}^i \lambda^{e,k} 2 \overline{\overline{\mathbf{G}}}_8^{e,k} \bar{N}^j |\boldsymbol{J}^e| dV^e, \qquad \mathbf{k}_{\mathrm{su}}^{eij} = \int_{\Omega^e} \bar{N}^i \lambda^{e,k} 2 \overline{\overline{\mathbf{G}}}_9^{e,k} \mathbf{B}_{\mathrm{m}}^j |\boldsymbol{J}^e| dV^e, \qquad \mathbf{k}_{\lambda\mathrm{s}}^{elj} = -\int_{\Omega^e} \bar{N}^l \overline{\overline{\mathbf{G}}}_6^{e,k,\mathrm{T}} \bar{N}^j |\boldsymbol{J}^e| dV^e,$$

$$\mathbf{k}_{\lambda\mathrm{u}}^{elj} = -\int_{\Omega^e} 2 \bar{N}^l \overline{\overline{\mathbf{G}}}_7^{e,k,\mathrm{T}} \mathbf{B}_{\mathrm{m}}^j |\boldsymbol{J}^e| dV^e, \qquad \mathbf{k}_{\mathrm{ss}}^{eij} = \int_{\Omega^e} \bar{N}^i \lambda^{e,k} \overline{\overline{\mathbf{G}}}_5^{e,k} \bar{N}^j \, |\boldsymbol{J}^e| dV^e, \qquad \mathbf{k}_{\mathrm{s}\lambda}^{ein} = \int_{\Omega^e} \bar{N}^i \overline{\overline{\mathbf{G}}}_4^{e,k} \bar{N}^n |\boldsymbol{J}^e| dV^e,$$

while the load vectors can be recast into

$$\mathbf{r}_{\mathrm{p}}^{ei} = \int_{\Omega^e} \bar{N}^i \left[2 \overline{\overline{\mathbf{G}}}_{11}^{e,k} - \overline{\overline{\mathbf{S}}}^{e,k}\right] |\boldsymbol{J}^e| dV^e, \qquad \mathbf{r}_{\mathrm{u}}^{ei} = \int_{\Omega^e} N^i \, \rho_0 \ddot{\boldsymbol{u}}^{e,k} |\boldsymbol{J}^e| dV^e + \int_{\Omega^e} \boldsymbol{F}^{e,k} \overline{\overline{\mathbf{S}}}^{e,k} \nabla_X N^i |\boldsymbol{J}^e| dV^e, \tag{7.13}$$

$$\mathbf{r}_{\mathrm{s}}^{ei} = \int_{\Omega^e} \bar{N}^i \left[\frac{3}{2} \overline{\overline{\mathbf{G}}}_{10}^{e,k} + \lambda^{e,k} \overline{\overline{\mathbf{G}}}_4^{e,k}\right] |\boldsymbol{J}^e| dV^e, \quad r_\lambda^{el} = -\int_{\Omega^e} \bar{N}^i f(\boldsymbol{S}^{e,k}; \boldsymbol{C}^{e,k}) |\boldsymbol{J}^e| dV^e.$$

Here, it is a useful feature that no volume forces or surface loads are applied - only internal forces. Furthermore, the axisymmetric properties reduce the inherited unity matrix $\mathbf{I}$ to a two-dimensional one and allow the tensor-valued quantities to be recast into matrix or vector formulations

$$\overline{\overline{\mathbf{G}}}_1 = \begin{bmatrix} \frac{\partial}{\partial C_{\mathrm{RR}}}\left[\frac{\partial e}{\partial C_{\mathrm{RR}}}\right] & \frac{\partial}{\partial C_{\Phi\Phi}}\left[\frac{\partial e}{\partial C_{\mathrm{RR}}}\right] & \frac{\partial}{\partial C_{\mathrm{ZZ}}}\left[\frac{\partial e}{\partial C_{\mathrm{RR}}}\right] & 2\frac{\partial}{\partial C_{\mathrm{RZ}}}\left[\frac{\partial e}{\partial C_{\mathrm{RR}}}\right] \\ \frac{\partial}{\partial C_{\mathrm{RR}}}\left[\frac{\partial e}{\partial C_{\Phi\Phi}}\right] & \frac{\partial}{\partial C_{\Phi\Phi}}\left[\frac{\partial e}{\partial C_{\Phi\Phi}}\right] & \frac{\partial}{\partial C_{\mathrm{ZZ}}}\left[\frac{\partial e}{\partial C_{\Phi\Phi}}\right] & 2\frac{\partial}{\partial C_{\mathrm{RZ}}}\left[\frac{\partial e}{\partial C_{\Phi\Phi}}\right] \\ \frac{\partial}{\partial C_{\mathrm{RR}}}\left[\frac{\partial e}{\partial C_{\mathrm{ZZ}}}\right] & \frac{\partial}{\partial C_{\Phi\Phi}}\left[\frac{\partial e}{\partial C_{\mathrm{ZZ}}}\right] & \frac{\partial}{\partial C_{\mathrm{ZZ}}}\left[\frac{\partial e}{\partial C_{\mathrm{ZZ}}}\right] & 2\frac{\partial}{\partial C_{\mathrm{RZ}}}\left[\frac{\partial e}{\partial C_{\mathrm{ZZ}}}\right] \\ 2\frac{\partial}{\partial C_{\mathrm{RR}}}\left[\frac{\partial e}{\partial C_{\mathrm{RZ}}}\right] & 2\frac{\partial}{\partial C_{\Phi\Phi}}\left[\frac{\partial e}{\partial C_{\mathrm{RZ}}}\right] & 2\frac{\partial}{\partial C_{\mathrm{ZZ}}}\left[\frac{\partial e}{\partial C_{\mathrm{RZ}}}\right] & 4\frac{\partial}{\partial C_{\mathrm{RZ}}}\left[\frac{\partial e}{\partial C_{\mathrm{RZ}}}\right] \end{bmatrix},$$

$$\overline{\overline{\mathbf{G}}}_2 = \begin{bmatrix} \frac{\partial}{\partial C_{\mathrm{p,RR}}^{-1}}\left[\frac{\partial e}{\partial C_{\mathrm{RR}}}\right] & \frac{\partial}{\partial C_{\mathrm{p},\Phi\Phi}^{-1}}\left[\frac{\partial e}{\partial C_{\mathrm{RR}}}\right] & \frac{\partial}{\partial C_{\mathrm{p,ZZ}}^{-1}}\left[\frac{\partial e}{\partial C_{\mathrm{RR}}}\right] & 2\frac{\partial}{\partial C_{\mathrm{p,RZ}}^{-1}}\left[\frac{\partial e}{\partial C_{\mathrm{RR}}}\right] \\ \frac{\partial}{\partial C_{\mathrm{p,RR}}^{-1}}\left[\frac{\partial e}{\partial C_{\Phi\Phi}}\right] & \frac{\partial}{\partial C_{\mathrm{p},\Phi\Phi}^{-1}}\left[\frac{\partial e}{\partial C_{\Phi\Phi}}\right] & \frac{\partial}{\partial C_{\mathrm{p,ZZ}}^{-1}}\left[\frac{\partial e}{\partial C_{\Phi\Phi}}\right] & 2\frac{\partial}{\partial C_{\mathrm{p,RZ}}^{-1}}\left[\frac{\partial e}{\partial C_{\Phi\Phi}}\right] \\ \frac{\partial}{\partial C_{\mathrm{p,RR}}^{-1}}\left[\frac{\partial e}{\partial C_{\mathrm{ZZ}}}\right] & \frac{\partial}{\partial C_{\mathrm{p},\Phi\Phi}^{-1}}\left[\frac{\partial e}{\partial C_{\mathrm{ZZ}}}\right] & \frac{\partial}{\partial C_{\mathrm{p,ZZ}}^{-1}}\left[\frac{\partial e}{\partial C_{\mathrm{ZZ}}}\right] & 2\frac{\partial}{\partial C_{\mathrm{p,RZ}}^{-1}}\left[\frac{\partial e}{\partial C_{\mathrm{ZZ}}}\right] \\ 2\frac{\partial}{\partial C_{\mathrm{p,RR}}^{-1}}\left[\frac{\partial e}{\partial C_{\mathrm{RZ}}}\right] & 2\frac{\partial}{\partial C_{\mathrm{p},\Phi\Phi}^{-1}}\left[\frac{\partial e}{\partial C_{\mathrm{RZ}}}\right] & 2\frac{\partial}{\partial C_{\mathrm{p,ZZ}}^{-1}}\left[\frac{\partial e}{\partial C_{\mathrm{RZ}}}\right] & 4\frac{\partial}{\partial C_{\mathrm{p,RZ}}^{-1}}\left[\frac{\partial e}{\partial C_{\mathrm{RZ}}}\right] \end{bmatrix},$$

$$\bar{\bar{\mathbf{I}}} = \begin{bmatrix} I_{\mathrm{RRRR}} & I_{\mathrm{RR\Phi\Phi}} & I_{\mathrm{RRZZ}} & 2I_{\mathrm{RRRZ}} \\ I_{\mathrm{\Phi\Phi RR}} & I_{\mathrm{\Phi\Phi\Phi\Phi}} & I_{\mathrm{\Phi\Phi ZZ}} & 2I_{\mathrm{\Phi\Phi RZ}} \\ I_{\mathrm{ZZRR}} & I_{\mathrm{ZZ\Phi\Phi}} & I_{\mathrm{ZZZZ}} & 2I_{\mathrm{ZZRZ}} \\ 2I_{\mathrm{RZRR}} & 2I_{\mathrm{RZ\Phi\Phi}} & 2I_{\mathrm{RZZZ}} & 4I_{\mathrm{RZRZ}} \end{bmatrix}, \qquad \boldsymbol{G}_3 = \frac{\mathrm{Tr}\left([\boldsymbol{C}_\mathrm{p}]^{-1}\right)\mathrm{DEV}\left(\boldsymbol{S}\right)}{\sqrt{[\mathrm{DEV}\left(\boldsymbol{S}\right)\cdot\boldsymbol{C}]\colon[\boldsymbol{C}\cdot\mathrm{DEV}\left(\boldsymbol{S}\right)]}}, \qquad \bar{\bar{\mathbf{G}}}_4 = \begin{bmatrix} G_{3,\mathrm{RR}} \\ G_{3,\mathrm{\Phi\Phi}} \\ G_{3,\mathrm{ZZ}} \\ 2G_{3,\mathrm{RZ}} \end{bmatrix},$$

$$\bar{\bar{\mathbf{G}}}_5 = \begin{bmatrix} \frac{\partial G_{3,\mathrm{RR}}}{\partial S_{\mathrm{RR}}} & \frac{\partial G_{3,\mathrm{RR}}}{\partial S_{\mathrm{\Phi\Phi}}} & \frac{\partial G_{3,\mathrm{RR}}}{\partial S_{\mathrm{ZZ}}} & 2\frac{\partial G_{3,\mathrm{RR}}}{\partial S_{\mathrm{RZ}}} \\ \frac{\partial G_{3,\mathrm{\Phi\Phi}}}{\partial S_{\mathrm{RR}}} & \frac{\partial G_{3,\mathrm{\Phi\Phi}}}{\partial S_{\mathrm{\Phi\Phi}}} & \frac{\partial G_{3,\mathrm{\Phi\Phi}}}{\partial S_{\mathrm{ZZ}}} & 2\frac{\partial G_{3,\mathrm{\Phi\Phi}}}{\partial S_{\mathrm{RZ}}} \\ \frac{\partial G_{3,\mathrm{ZZ}}}{\partial S_{\mathrm{RR}}} & \frac{\partial G_{3,\mathrm{ZZ}}}{\partial S_{\mathrm{\Phi\Phi}}} & \frac{\partial G_{3,\mathrm{ZZ}}}{\partial S_{\mathrm{ZZ}}} & 2\frac{\partial G_{3,\mathrm{ZZ}}}{\partial S_{\mathrm{RZ}}} \\ 2\frac{\partial G_{3,\mathrm{RZ}}}{\partial S_{\mathrm{RR}}} & 2\frac{\partial G_{3,\mathrm{RZ}}}{\partial S_{\mathrm{\Phi\Phi}}} & 2\frac{\partial G_{3,\mathrm{RZ}}}{\partial S_{\mathrm{ZZ}}} & 4\frac{\partial G_{3,\mathrm{RZ}}}{\partial S_{\mathrm{RZ}}} \end{bmatrix}, \quad \bar{\bar{\mathbf{G}}}_6 = \begin{bmatrix} \frac{\partial f(\boldsymbol{S},\boldsymbol{C})}{\partial S_{\mathrm{RR}}} \\ \frac{\partial f(\boldsymbol{S},\boldsymbol{C})}{\partial S_{\mathrm{\Phi\Phi}}} \\ \frac{\partial f(\boldsymbol{S},\boldsymbol{C})}{\partial S_{\mathrm{ZZ}}} \\ 2\frac{\partial f(\boldsymbol{S},\boldsymbol{C})}{\partial S_{\mathrm{RZ}}} \end{bmatrix}, \quad \bar{\bar{\mathbf{G}}}_7 = \begin{bmatrix} \frac{\partial f(\boldsymbol{S},\boldsymbol{C})}{\partial C_{\mathrm{RR}}} \\ \frac{\partial f(\boldsymbol{S},\boldsymbol{C})}{\partial C_{\mathrm{\Phi\Phi}}} \\ \frac{\partial f(\boldsymbol{S},\boldsymbol{C})}{\partial C_{\mathrm{ZZ}}} \\ 2\frac{\partial f(\boldsymbol{S},\boldsymbol{C})}{\partial C_{\mathrm{RZ}}} \end{bmatrix},$$

$$\bar{\bar{\mathbf{G}}}_8 = \begin{bmatrix} \frac{\partial G_{3,\mathrm{RR}}}{\partial C^{-1}_{\mathrm{p,RR}}} & \frac{\partial G_{3,\mathrm{RR}}}{\partial C^{-1}_{\mathrm{p,\Phi\Phi}}} & \frac{\partial G_{3,\mathrm{RR}}}{\partial C^{-1}_{\mathrm{p,ZZ}}} & 2\frac{\partial G_{3,\mathrm{RR}}}{\partial C^{-1}_{\mathrm{p,RZ}}} \\ \frac{\partial G_{3,\mathrm{\Phi\Phi}}}{\partial C^{-1}_{\mathrm{p,RR}}} & \frac{\partial G_{3,\mathrm{\Phi\Phi}}}{\partial C^{-1}_{\mathrm{p,\Phi\Phi}}} & \frac{\partial G_{3,\mathrm{\Phi\Phi}}}{\partial C^{-1}_{\mathrm{p,ZZ}}} & 2\frac{\partial G_{3,\mathrm{\Phi\Phi}}}{\partial C^{-1}_{\mathrm{p,RZ}}} \\ \frac{\partial G_{3,\mathrm{ZZ}}}{\partial C^{-1}_{\mathrm{p,RR}}} & \frac{\partial G_{3,\mathrm{ZZ}}}{\partial C^{-1}_{\mathrm{p,\Phi\Phi}}} & \frac{\partial G_{3,\mathrm{ZZ}}}{\partial C^{-1}_{\mathrm{p,ZZ}}} & 2\frac{\partial G_{3,\mathrm{ZZ}}}{\partial C^{-1}_{\mathrm{p,RZ}}} \\ 2\frac{\partial G_{3,\mathrm{RZ}}}{\partial C^{-1}_{\mathrm{p,RR}}} & 2\frac{\partial G_{3,\mathrm{RZ}}}{\partial C^{-1}_{\mathrm{p,\Phi\Phi}}} & 2\frac{\partial G_{3,\mathrm{RZ}}}{\partial C^{-1}_{\mathrm{p,ZZ}}} & 4\frac{\partial G_{3,\mathrm{RZ}}}{\partial C^{-1}_{\mathrm{p,RZ}}} \end{bmatrix}, \quad \bar{\bar{\mathbf{G}}}_9 = \begin{bmatrix} \frac{\partial G_{3,\mathrm{RR}}}{\partial C_{\mathrm{RR}}} & \frac{\partial G_{3,\mathrm{RR}}}{\partial C_{\mathrm{\Phi\Phi}}} & \frac{\partial G_{3,\mathrm{RR}}}{\partial C_{\mathrm{ZZ}}} & 2\frac{\partial G_{3,\mathrm{RR}}}{\partial C_{\mathrm{RZ}}} \\ \frac{\partial G_{3,\mathrm{\Phi\Phi}}}{\partial C_{\mathrm{RR}}} & \frac{\partial G_{3,\mathrm{\Phi\Phi}}}{\partial C_{\mathrm{\Phi\Phi}}} & \frac{\partial G_{3,\mathrm{\Phi\Phi}}}{\partial C_{\mathrm{ZZ}}} & 2\frac{\partial G_{3,\mathrm{\Phi\Phi}}}{\partial C_{\mathrm{RZ}}} \\ \frac{\partial G_{3,\mathrm{ZZ}}}{\partial C_{\mathrm{RR}}} & \frac{\partial G_{3,\mathrm{ZZ}}}{\partial C_{\mathrm{\Phi\Phi}}} & \frac{\partial G_{3,\mathrm{ZZ}}}{\partial C_{\mathrm{ZZ}}} & 2\frac{\partial G_{3,\mathrm{ZZ}}}{\partial C_{\mathrm{RZ}}} \\ 2\frac{\partial G_{3,\mathrm{RZ}}}{\partial C_{\mathrm{RR}}} & 2\frac{\partial G_{3,\mathrm{RZ}}}{\partial C_{\mathrm{\Phi\Phi}}} & 2\frac{\partial G_{3,\mathrm{RZ}}}{\partial C_{\mathrm{ZZ}}} & 4\frac{\partial G_{3,\mathrm{RZ}}}{\partial C_{\mathrm{RZ}}} \end{bmatrix},$$

$$\bar{\bar{\mathbf{G}}}_{10} = \begin{bmatrix} \dot{C}^{-1}_{\mathrm{p,RR}} \\ \dot{C}^{-1}_{\mathrm{p,\Phi\Phi}} \\ \dot{C}^{-1}_{\mathrm{p,ZZ}} \\ 2\dot{C}^{-1}_{\mathrm{p,RZ}} \end{bmatrix}, \qquad \bar{\bar{\mathbf{G}}}_{11} = \begin{bmatrix} \frac{\partial e}{\partial C_{\mathrm{RR}}} \\ \frac{\partial e}{\partial C_{\mathrm{\Phi\Phi}}} \\ \frac{\partial e}{\partial C_{\mathrm{ZZ}}} \\ 2\frac{\partial e}{\partial C_{\mathrm{RZ}}} \end{bmatrix}.$$

Apart from these terms, the expressions in (7.3)-(7.6) are taken into account. Concerning the spatial approximation of the distinct fields, different shape functions are chosen. While N^i represent continuous approximations with LAGRANGE shape functions, $\bar{N}^i$ characterize discontinuous ones. With these modifications at hand, a numerical comparison between the classical and the multifield approach can be carried out with the help of the dynamic benchmark problem.

7.3. Classical vs. Variational Approach of Finite Elastoplasticity

In accordance with the small strain regime for both approaches, an exemplary mesh consisting of $NE_\mathrm{R} = 2$ and $NE_\mathrm{Z} = 15$ biquadratic elements in $\boldsymbol{g}_\mathrm{R}$- as well as in $\boldsymbol{g}_\mathrm{Z}$-direction is taken into account. The displacement field is approximated continuously using biquadratic LAGRANGE shape functions. Within the variational approach, the stresses, the plastic strains, and the LAGRANGE multiplier are approximated using biquadratic LAGRANGE shape functions which are based on the GAUSS-LEGENDRE quadrature points in Table 3.1. Thus, the realization of spatial discontinuities over element boundaries is enabled. For the time discretization, the DIRK(3) scheme with a time step size of $\Delta t = 1 \cdot 10^{-5}$s is applied. For this case, exemplary solutions are listed in **Appendix E**.

In the first step, the finite strain solution obtained by the classical setting is opposed to the corresponding small strain result. In Figure 7.1, the temporal progress of the material characterizing quantities is analyzed at evaluation point ①.

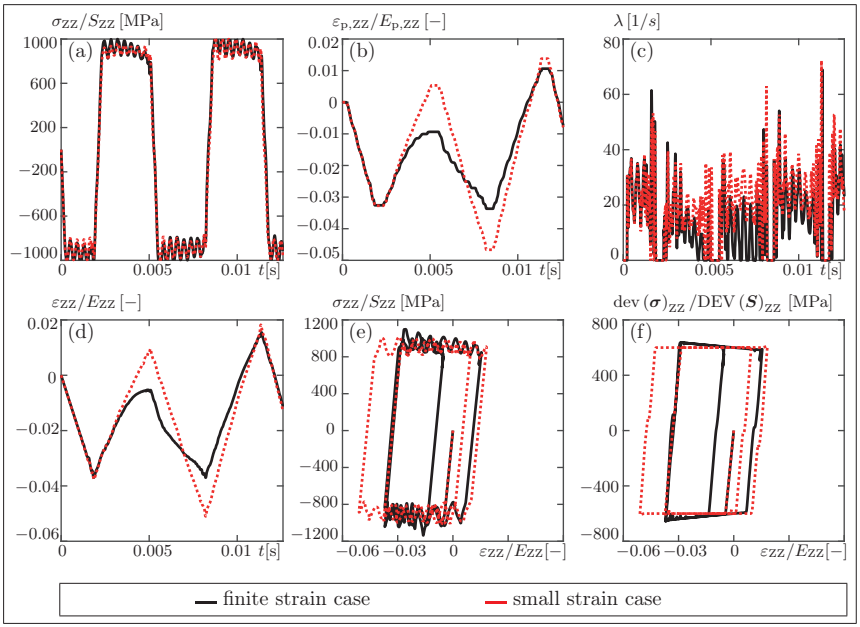

Figure 7.1.: Evaluation for $NE_R = 2, NE_Z = 15$ at point ① for the small strain case (red) and the finite strain case (black): (a) Stress-time diagram, (b) Plastic strain-time diagram, (c) LAGRANGE multiplier-time diagram, (d) Strain-time diagram, (e) Stress-strain diagram, (f) Deviatoric stress-strain diagram

Figure 7.1 (a) shows the evolution of the stress component σ_{ZZ} and the part S_{ZZ} of the second PIOLA-KIRCHHOFF stress tensor over time. The temporal progress of the plastic strains $\varepsilon_{p,ZZ}/E_{p,ZZ}$, the LAGRANGE multiplier and the strains ε_{ZZ}/E_{ZZ} is depicted in Figure 7.1 (b)-(d). Figure 7.1 (e) portrays the stress-strain diagram of the ZZ-components within both regimes. The corresponding deviatoric stress evolution can be observed in Figure 7.1 (f). While the stresses only exhibit minor differences between the small and the finite strain regime, remarkable deviations can be observed for the strain equivalent quantities and the LAGRANGE multiplier, although the biggest depicted strains do not exceed 5%. The considered nonlinearities are clearly mirrored in the total and plastic strain courses in Figure 7.1 (b) and (d), demonstrating the necessity of finite strain models. Identical graphs as obtained by the classical finite strain approach are achieved within the variational setting. Thereby, the maximum deviation in the displacement, the stress, and the plastic strain field is of about 0.005% compared to the classical approach.

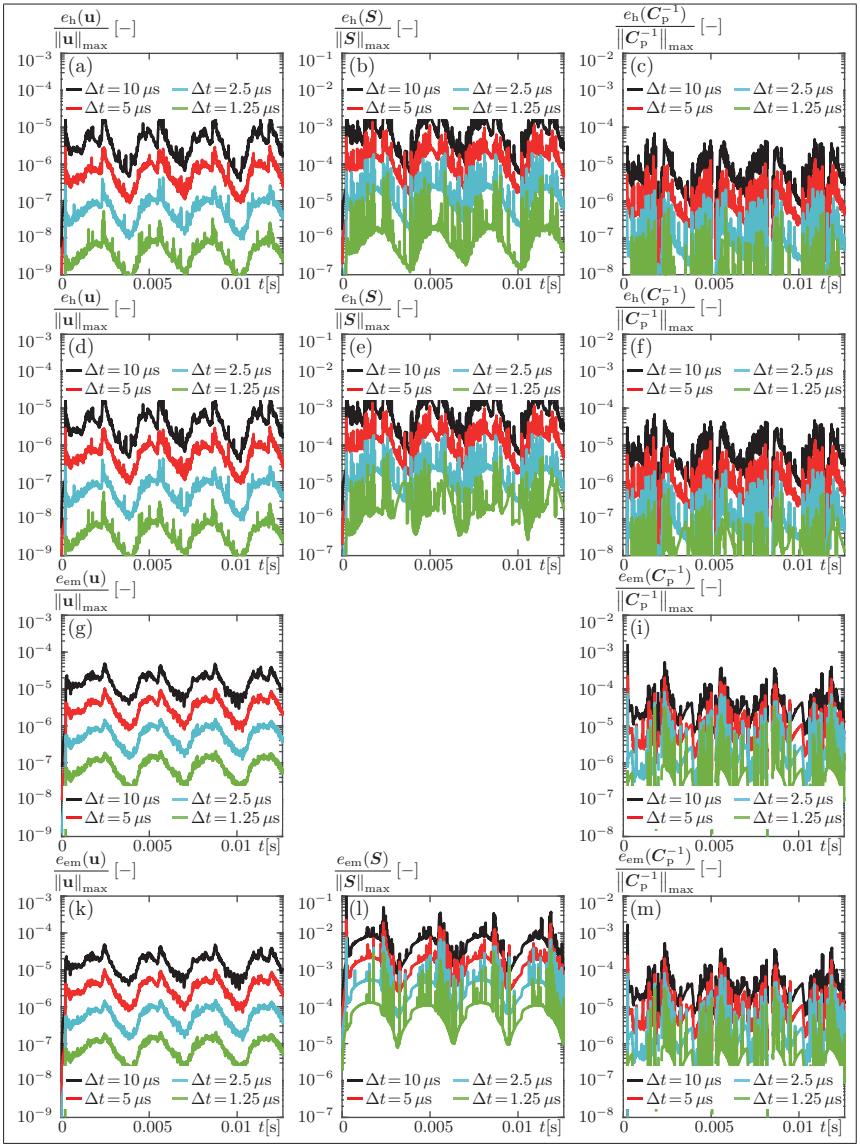

Figure 7.2.: Local time discretization error of the h- and the embedded method for the displacement, the plastic strain, and the stress field within the conventional and the multifield approach: (a)-(c) h-error DIRK(3) conventional, (d)-(f) h-error DIRK(3) multifield, (g)-(i) embedded error DIRK(3) conventional, (k)-(m) embedded error DIRK(3) multifield

In the next step, the time discretization error of both finite strain schemes related to the DIRK(3) method is compared. Distinct error curves for various time step sizes are depicted in Figure 7.2. Figure 7.2 (a)-(c) show the h-error of the displacement field, the second PIOLA-KIRCHHOFF stresses and the plastic CAUCHY-GREEN strains for the conventional approach. Figure 7.2(d)-(f) yield the graphs for the corresponding quantities in the multifield approach. For all error estimations, it can be observed that the error always decreases for a decreasing time step size. While a comparison between both settings of the quantities linked to the displacement field results in no differences, the course of the h-error of the stresses and the plastic strains diverges. This phenomenon can also be seen in Table 7.1 within the orders of consistency determined by local error estimates. For the stresses and the plastic strains, the multifield approach leads to consistency rates which are one order lower than within the conventional ansatz. For the embedded error, however, these differences do not appear. The accompanying graphs for the conventional approach can be seen in Figure 7.2 (g)-(i). The multifield setting is evaluated in Figure 7.2 (k)-(m). A portray of the stress field's embedded error in the conventional approach is missing, since no time discretization of the stress field is performed there.

The benefit of the multifield approach, however, is the simple applicability of higher order accurate schemes as already shown in the small strain context in **Chapter 5**. Hence, another implementation strategy for the DIRK(3) method can be followed. Therein, a reformulated diagonally implicit RUNGE-KUTTA scheme (rDIRK(3)) is created, resulting in a solution procedure where all stages of one time step are solved simultaneously as it is the case within fully implicit RUNGE-KUTTA methods. In the DIRK(3) method, in contrast, each stage is solved one after another, exploiting the information of previous stages. This is also the implemented form used within the classical approach. The resulting h-error curves for the displacement, the stress, and the plastic strain field of the reformulated rDIRK(3) scheme are illustrated in Figure 7.3 (g)-(i). Comparing those to the graphs of the conventional approach in Figure 7.2 (a)-(c), demonstrates that the discrepancies disappear and the reduction of the order of consistency of the multifield approach is cured, cf. Table 7.1. Correspondingly, within the multifield approach the DIRK(3) method suffers from order reduction phenomena while the rDIRK(3) scheme does not. In the small strain regime, this kind of order reduction cannot be observed, see Section 5.2.2. Despite, the orders of convergence determined by the global h-error are identical for all methods.

Table 7.1.: Estimation of the order of consistency/convergence for finite strain plasticity

	$q_{\mathrm{h}}(\mathbf{u})$	$q_{\mathrm{h}}(\boldsymbol{C}_{\mathrm{p}}^{-1})$	$q_{\mathrm{h}}(\boldsymbol{S})$	$q_{\mathrm{r}}(\mathbf{u})/$ $q_{\mathrm{emb}}(\mathbf{u})$	$q_{\mathrm{r}}(\boldsymbol{C}_{\mathrm{p}}^{-1})/$ $q_{\mathrm{emb}}(\boldsymbol{C}_{\mathrm{p}}^{-1})$	$q_{\mathrm{r}}(\boldsymbol{S})/$ $q_{\mathrm{emb}}(\boldsymbol{S})$	$q_{\mathrm{h}}^{\mathrm{glob}}(\mathbf{u})$	$q_{\mathrm{h}}^{\mathrm{glob}}(\boldsymbol{C}_{\mathrm{p}}^{-1})$	$q_{\mathrm{h}}^{\mathrm{glob}}(\boldsymbol{S})$
DIRK(3) CON	2.46	2.59	2.37	1.66	1.36	–	2.38	2.23	2.12
DIRK(3) MULTI	2.45	1.59	1.54	1.66	1.33	1.05	2.41	2.22	2.12
rDIRK(3)	2.46	2.59	2.38	1.66	1.36	1.08	2.41	2.23	2.12
LOBATTO IIIC(2)	1.53	1.50	1.37	–	–	–	1.90	1.81	1.24
RADAU IIA(2)	2.57	2.59	2.50	–	–	–	2.55	2.37	2.27
$\mathrm{cG}_1(2)$	2.57	2.49	2.50	0.99	2.62	0.03	2.55	2.37	2.27
$\mathrm{dG}_1(2)$	3.43	3.51	3.36	1.00	2.63	2.71	2.20	2.39	2.79

In addition to the diagonal implicit RUNGE-KUTTA schemes, further more general higher order accurate time integrators are analyzed in the multifield framework. Figure 7.3 shows the h-method error curves for the displacement field, the second PIOLA-KIRCHHOFF stresses, and the

plastic CAUCHY-GREEN strains for the fully implicit RUNGE-KUTTA schemes LOBATTO IIIC(2) and RADAU IIA(2). Again, it can be observed that the error decreases with decreasing time step sizes, while the error in the stress field is higher than in the displacement and in the plastic strain field. The obtained orders of consistency are listed in Table 7.1. It can be noticed that the theoretical orders are not obtained and the highest order of consistency lies well below three, however, these discrepancies are identical to those of the small strain case. The orders of convergence determined by global error estimates are listed in Table 7.1, too. For the RADAU IIA(2) scheme, their range is similar to the orders of consistency. For the LOBATTO IIIC(2) method, the orders of convergence are even higher than the orders of consistency.

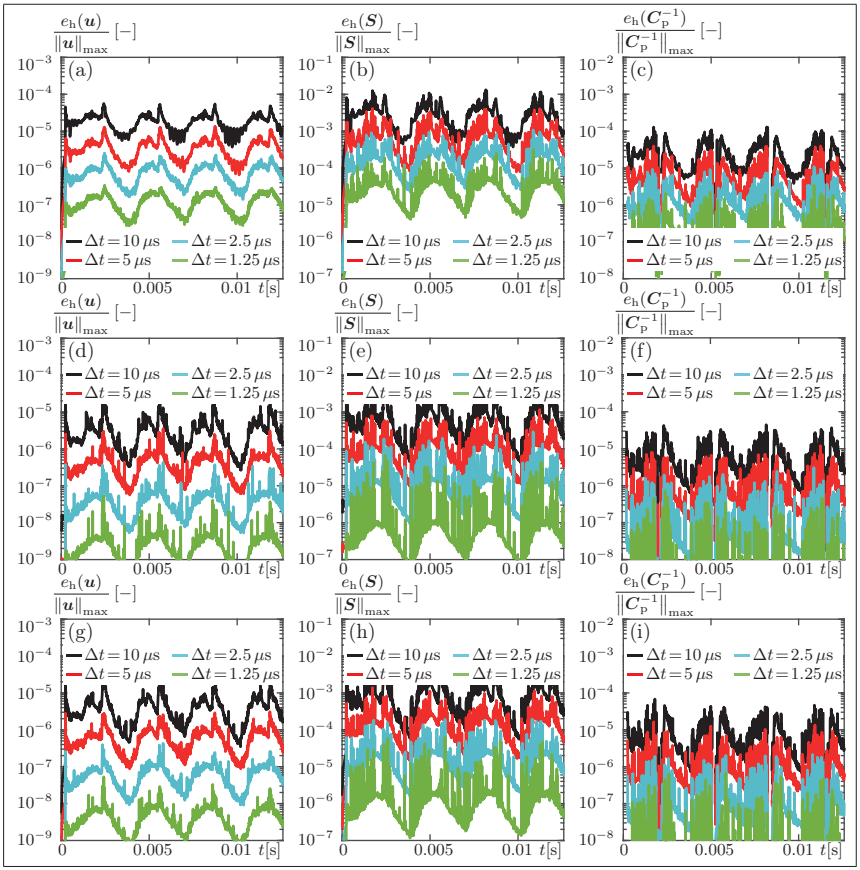

Figure 7.3.: Local time discretization error of the h-method for the displacement, the plastic strain, and the stress field for distinct time integration methods within the multifield approach: (a)-(c) LOBATTO IIIC(2), (d)-(f) RADAU IIA(2), (g)-(i) rDIRK(3)

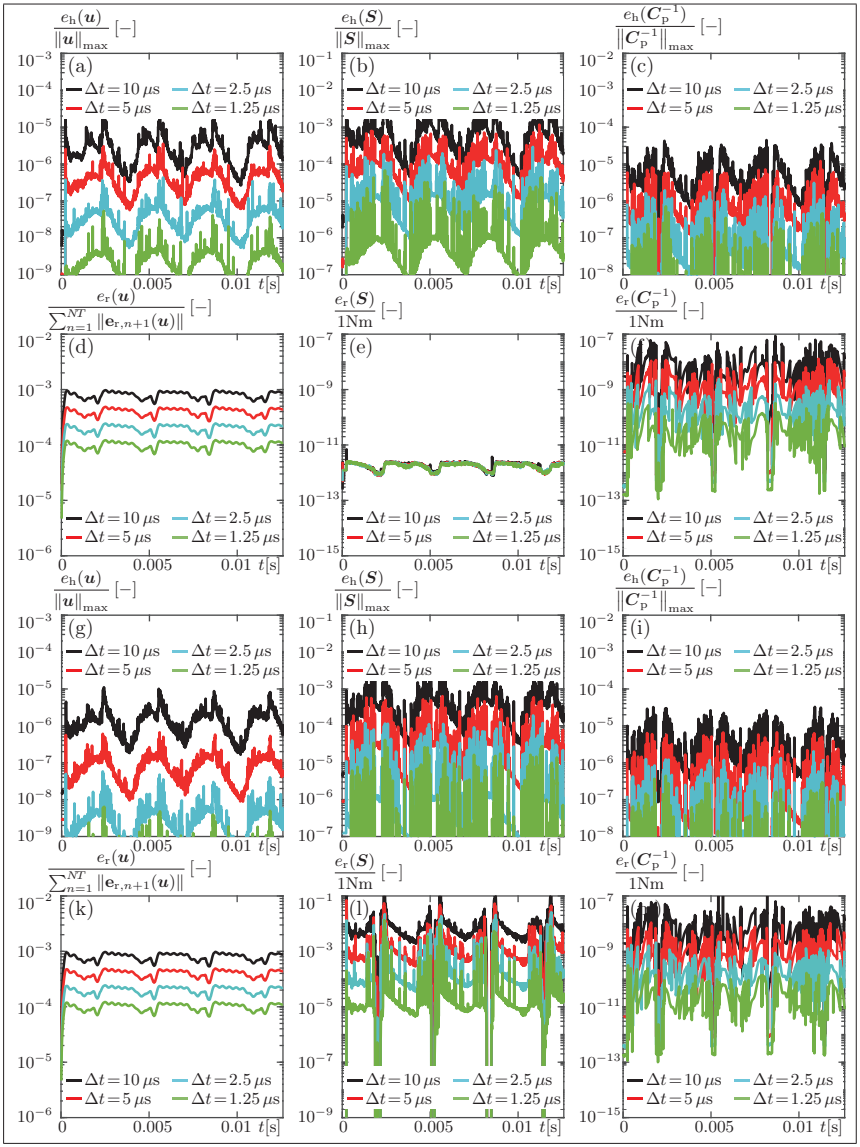

Figure 7.4.: Local time discretization error of the h- and the residual method for the displacement, the plastic strain, and the stress field for distinct time integration methods within the multifield approach: (a)-(c) h-error $\mathrm{cG}_1(2)$, (d)-(f) residual error $\mathrm{cG}_1(2)$, (g)-(i) h-error $\mathrm{dG}_1(2)$, (k)-(m) residual error $\mathrm{dG}_1(2)$

Figure 7.4 (a)-(c) show the h-error curves of the the displacement field, the second PIOLA-KIRCHHOFF stresses and the plastic CAUCHY-GREEN strains for the continuous GALERKIN method in the one-field setting. Figure 7.4 (d)-(f) depict the corresponding residual error curves. Figure 7.4 (g)-(i) and (k)-(m) show the analogous curves for the discontinuous GALERKIN method in the one-field setting. Both schemes are based on a polynomial degree of two. Except for the residual error of the stress field within the continuous GALERKIN scheme, all error curves decrease with decreasing time step size. The achieved orders of consistency and convergence are listed in Table 7.1. While the continuous GALERKIN scheme reaches orders of consistency well above two for the h-error, the discontinuous approach reaches orders well above three. With increasing order of consistency, the error level decreases. The corresponding orders of convergence, however, are all just well above order two. Comparing Table 7.1 to its counterpart in the small strain regime, Table 5.3 shows huge similarities. Only the orders of consistency for the residual error of the stress and the plastic strain field diverge drastically.

Because of the high computational effort, all other time integrators applied within the small strain regime are not analyzed in the finite strain case. However, due to the substantial analogies demonstrated, comparable results are expected.

7.4. Classical Approach towards the Dynamic Analysis of Finite Elastoviscoplasticity

Analogously to the small strain case, the viscoplastic regularization is taken into account within the conventional approach also in the finite strain regime. The numerical analysis is carried out concerning the same dynamic example as in elastoplasticity, see Section 7.3. Thus, the terms in Equations (7.1)-(7.9) remain valid. Only the algorithmic constitutive tensor $\mathbb{G}$ is subject to changes due to the viscoplastic adaptation, see Section 6.1.2. To ensure a comparability between the elastoplastic and the viscoplastic approach, the same biquadratic spatial mesh consisting of $NE_{\mathrm{R}} = 2$ as well as $NE_{\mathrm{Z}} = 15$ elements and the identical LAGRANGE approximations as within the elastoplastic model are chosen. The viscosity parameter $\chi = 0.001$ Ns/mm^2 is selected to be small. The suitability of this choice is demonstrated in Figure 7.5.

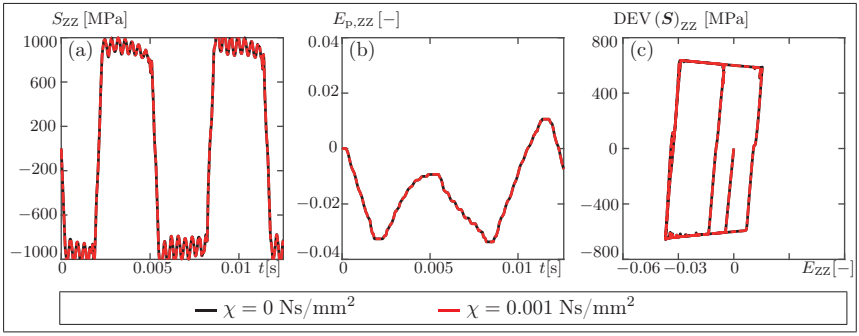

Figure 7.5.: Comparison of the elastoplastic and the viscoplastic model at evaluation point ①: (a) Stress-time diagram, (b) Plastic strain-time diagram, (c) Deviatoric stress-strain diagram

Therein, the evolution of the axial component of the stress and the plastic strain for both the elastoplastic and the viscoplastic model is portrayed over time at evaluation point ①. Addi-

tionally, the deviatoric stress strain diagram is illustrated. For the time discretization of both models, a DIRK(3) scheme with a time step size $\Delta t = 1 \cdot 10^{-5}\,\mathrm{s}$ is applied. This demonstrates that the results of both models are identical. A more precise examination serves to determine the maximal absolute deviations of the stress, the displacement, as well as the plastic strain field. Their relation to the elastoplastic approach reveals that values greater than 0.2% are not obtained.

7.5. Variational Approach for the Dynamic Analysis of Finite Elastoviscoplasticity

In order to investigate the effect of higher order accurate time integrators in the context of finite elastoviscoplasticity, the multifield approach is also analyzed within this dynamic benchmark problem. Due to the axisymmetric characteristics, a recast of the formulations in (6.73) is carried out. Therefore, the terms (7.10)-(7.13) of the elastoplastic case can be exploited because of their identity. Additionally, the quantities

$$\mathbf{k}_{\mathrm{sp}}^{eij} = \int_{\Omega^e} \bar{N}^i \frac{1}{\chi} \langle f(\boldsymbol{S}^{e,k}, \boldsymbol{C}^{e,k}) \rangle \overline{\overline{\mathbf{G}}}_8^{e,k} \bar{N}^j |\boldsymbol{J}^e| dV^e, \qquad \mathbf{k}_{\mathrm{su}}^{eij} = \int_{\Omega^e} 2\bar{N}^i \overline{\overline{\mathbf{G}}}_{12}^{e,k} \mathbf{B}_{\mathrm{in}}^j |\boldsymbol{J}^e| dV^e,$$

$$\mathbf{k}_{\mathrm{ss}}^{eij} = \int_{\Omega^e} \bar{N}^i \overline{\overline{\mathbf{G}}}_{13}^{e,k} \bar{N}^j \, |\boldsymbol{J}^e| dV^e,$$

$$\mathbf{r}_{\mathrm{s}}^{ei} = \int_{\Omega^e} \bar{N}^i \left[\frac{3}{2} \overline{\overline{\mathbf{G}}}_{10}^{e,k} + \frac{1}{\chi} \langle f(\boldsymbol{S}^{e,k}, \boldsymbol{C}^{e,k}) \rangle \overline{\overline{\mathbf{G}}}_4^{e,k} \right] |\boldsymbol{J}^e| dV^e$$

together with the abbreviations

$$\overline{\overline{\mathbf{G}}}_{12} = \begin{bmatrix} \frac{\partial \left[\frac{1}{\chi} \langle f(\boldsymbol{S},\boldsymbol{C}) \rangle G_{3,\mathrm{RR}} \right]}{\partial C_{\mathrm{RR}}} & \frac{\partial \left[\frac{1}{\chi} \langle f(\boldsymbol{S},\boldsymbol{C}) \rangle G_{3,\mathrm{RR}} \right]}{\partial C_{\Phi\Phi}} & \frac{\partial \left[\frac{1}{\chi} \langle f(\boldsymbol{S},\boldsymbol{C}) \rangle G_{3,\mathrm{RR}} \right]}{\partial C_{\mathrm{ZZ}}} & 2\frac{\partial \left[\frac{1}{\chi} \langle f(\boldsymbol{S},\boldsymbol{C}) \rangle G_{3,\mathrm{RR}} \right]}{\partial C_{\mathrm{RZ}}} \\ \frac{\partial \left[\frac{1}{\chi} \langle f(\boldsymbol{S},\boldsymbol{C}) \rangle G_{3,\Phi\Phi} \right]}{\partial C_{\mathrm{RR}}} & \frac{\partial \left[\frac{1}{\chi} \langle f(\boldsymbol{S},\boldsymbol{C}) \rangle G_{3,\Phi\Phi} \right]}{\partial C_{\Phi\Phi}} & \frac{\partial \left[\frac{1}{\chi} \langle f(\boldsymbol{S},\boldsymbol{C}) \rangle G_{3,\Phi\Phi} \right]}{\partial C_{\mathrm{ZZ}}} & 2\frac{\partial \left[\frac{1}{\chi} \langle f(\boldsymbol{S},\boldsymbol{C}) \rangle G_{3,\Phi\Phi} \right]}{\partial C_{\mathrm{RZ}}} \\ \frac{\partial \left[\frac{1}{\chi} \langle f(\boldsymbol{S},\boldsymbol{C}) \rangle G_{3,\mathrm{ZZ}} \right]}{\partial C_{\mathrm{RR}}} & \frac{\partial \left[\frac{1}{\chi} \langle f(\boldsymbol{S},\boldsymbol{C}) \rangle G_{3,\mathrm{ZZ}} \right]}{\partial C_{\Phi\Phi}} & \frac{\partial \left[\frac{1}{\chi} \langle f(\boldsymbol{S},\boldsymbol{C}) \rangle G_{3,\mathrm{ZZ}} \right]}{\partial C_{\mathrm{ZZ}}} & 2\frac{\partial \left[\frac{1}{\chi} \langle f(\boldsymbol{S},\boldsymbol{C}) \rangle G_{3,\mathrm{ZZ}} \right]}{\partial C_{\mathrm{RZ}}} \\ 2\frac{\partial \left[\frac{1}{\chi} \langle f(\boldsymbol{S},\boldsymbol{C}) \rangle G_{3,\mathrm{RZ}} \right]}{\partial C_{\mathrm{RR}}} & 2\frac{\partial \left[\frac{1}{\chi} \langle f(\boldsymbol{S},\boldsymbol{C}) \rangle G_{3,\mathrm{RZ}} \right]}{\partial C_{\Phi\Phi}} & 2\frac{\partial \left[\frac{1}{\chi} \langle f(\boldsymbol{S},\boldsymbol{C}) \rangle G_{3,\mathrm{RZ}} \right]}{\partial C_{\mathrm{ZZ}}} & 4\frac{\partial \left[\frac{1}{\chi} \langle f(\boldsymbol{S},\boldsymbol{C}) \rangle G_{3,\mathrm{RZ}} \right]}{\partial C_{\mathrm{RZ}}} \end{bmatrix},$$

$$\overline{\overline{\mathbf{G}}}_{13} = \begin{bmatrix} \frac{\partial \left[\frac{1}{\chi} \langle f(\boldsymbol{S},\boldsymbol{C}) \rangle G_{3,\mathrm{RR}} \right]}{\partial S_{\mathrm{RR}}} & \frac{\partial \left[\frac{1}{\chi} \langle f(\boldsymbol{S},\boldsymbol{C}) \rangle G_{3,\mathrm{RR}} \right]}{\partial S_{\Phi\Phi}} & \frac{\partial \left[\frac{1}{\chi} \langle f(\boldsymbol{S},\boldsymbol{C}) \rangle G_{3,\mathrm{RR}} \right]}{\partial S_{\mathrm{ZZ}}} & 2\frac{\partial \left[\frac{1}{\chi} \langle f(\boldsymbol{S},\boldsymbol{C}) \rangle G_{3,\mathrm{RR}} \right]}{\partial S_{\mathrm{RZ}}} \\ \frac{\partial \left[\frac{1}{\chi} \langle f(\boldsymbol{S},\boldsymbol{C}) \rangle G_{3,\Phi\Phi} \right]}{\partial S_{\mathrm{RR}}} & \frac{\partial \left[\frac{1}{\chi} \langle f(\boldsymbol{S},\boldsymbol{C}) \rangle G_{3,\Phi\Phi} \right]}{\partial S_{\Phi\Phi}} & \frac{\partial \left[\frac{1}{\chi} \langle f(\boldsymbol{S},\boldsymbol{C}) \rangle G_{3,\Phi\Phi} \right]}{\partial S_{\mathrm{ZZ}}} & 2\frac{\partial \left[\frac{1}{\chi} \langle f(\boldsymbol{S},\boldsymbol{C}) \rangle G_{3,\Phi\Phi} \right]}{\partial S_{\mathrm{RZ}}} \\ \frac{\partial \left[\frac{1}{\chi} \langle f(\boldsymbol{S},\boldsymbol{C}) \rangle G_{3,\mathrm{ZZ}} \right]}{\partial S_{\mathrm{RR}}} & \frac{\partial \left[\frac{1}{\chi} \langle f(\boldsymbol{S},\boldsymbol{C}) \rangle G_{3,\mathrm{ZZ}} \right]}{\partial S_{\Phi\Phi}} & \frac{\partial \left[\frac{1}{\chi} \langle f(\boldsymbol{S},\boldsymbol{C}) \rangle G_{3,\mathrm{ZZ}} \right]}{\partial S_{\mathrm{ZZ}}} & 2\frac{\partial \left[\frac{1}{\chi} \langle f(\boldsymbol{S},\boldsymbol{C}) \rangle G_{3,\mathrm{ZZ}} \right]}{\partial S_{\mathrm{RZ}}} \\ 2\frac{\partial \left[\frac{1}{\chi} \langle f(\boldsymbol{S},\boldsymbol{C}) \rangle G_{3,\mathrm{RZ}} \right]}{\partial S_{\mathrm{RR}}} & 2\frac{\partial \left[\frac{1}{\chi} \langle f(\boldsymbol{S},\boldsymbol{C}) \rangle G_{3,\mathrm{RZ}} \right]}{\partial S_{\Phi\Phi}} & 2\frac{\partial \left[\frac{1}{\chi} \langle f(\boldsymbol{S},\boldsymbol{C}) \rangle G_{3,\mathrm{RZ}} \right]}{\partial S_{\mathrm{ZZ}}} & 4\frac{\partial \left[\frac{1}{\chi} \langle f(\boldsymbol{S},\boldsymbol{C}) \rangle G_{3,\mathrm{RZ}} \right]}{\partial S_{\mathrm{RZ}}} \end{bmatrix}$$

have to be taken into account. With these modifications at hand, a numerical comparison between the classical and the multifield approach as well as an investigation of the functionality of various time integration schemes can be performed.

7.6. Classical vs. Variational Approach of Finite Elastoviscoplasticity

Exploiting the relations in Section 7.5 as well as 7.4 allows to evaluate the finite strain elastoviscoplastic benchmark problem within the classical and the multifield approach. As spatial discretization, a biquadratic mesh consisting of $NE_{\mathrm{R}} = 2$ as well as $NE_{\mathrm{Z}} = 15$ elements is used together with a continuous approximation of the displacement field taking biquadratic LAGRANGE shape functions into account. For the variational approach, additional discontinuous approximations are established for the stresses and the strains, whereby LAGRANGE shape functions with GAUSS-LEGENDRE quadrature points serve as a basis. In a first step, both strategies are compared applying a DIRK(3) scheme with a time step size $\Delta t = 1 \cdot 10^{-5}\,\mathrm{s}$. The maximum deviation in the displacement, the stress, and the plastic strain field lies at about 0.0001% compared to the classical approach, so that both solutions can be considered as identical.

In a further step, the applied DIRK(3) time discretization scheme is analyzed in detail. The corresponding h-error curves of the displacement field, the second PIOLA-KIRCHHOFF stresses, and the plastic CAUCHY-GREEN strains are depicted in Figure 7.6 (a)-(c) for the conventional and in Figure 7.6 (d)-(f) for the multifield approach. Additionally, Figure 7.6 (g)-(i) and (k)-(m) show the results for the embedded error estimator. A portrait of the stress field's embedded error in the conventional approach is missing, since no time discretization of the stress field is performed there. It can be seen that the error decreases for all graphs with decreasing time step size. Furthermore, the error of the stress field is higher than for the plastic strain and the displacement field. If the h-error of the second PIOLA-KIRCHHOFF stresses and the plastic CAUCHY-GREEN strains of the distinct approaches are opposed directly, it becomes apparent that discrepancies prevail. These can also be recognized within the orders of consistency in Table 7.2. While the conventional ansatz reaches orders of consistency well above two, the multifield setting does not even come close. This phenomenon is already known from the elastoplastic model in the finite strain regime in Section 7.3. Therein, the staggered DIRK(3) scheme is exchanged by its reformulated rDIRK(3) counterpart in order to cure this problem. Following the same idea in the elastoviscoplastic case yields the same result. The order reduction is cancelled out. The linked plots can be observed in Figure 7.7 (g)-(f). The orders of convergence determined by the global h-error, also listed in Table 7.2, do not have this characteristic. There, the orders of the three methods are almost identical. With this analysis, it is demonstrated that, despite the higher numerical effort of the multifield approach, higher or equivalent orders of consistency compared to the classical ansatz are not necessarily obtained.

Table 7.2.: Estimation of the order of consistency/convergence for finite strain viscoplasticity

	$q_{\mathrm{h}}(\mathbf{u})$	$q_{\mathrm{h}}(\boldsymbol{C}_{\mathrm{p}}^{-1})$	$q_{\mathrm{h}}(\boldsymbol{S})$	$q_{\mathrm{r}}(\mathbf{u})/$ $q_{\mathrm{emb}}(\mathbf{u})$	$q_{\mathrm{r}}(\boldsymbol{C}_{\mathrm{p}}^{-1})/$ $q_{\mathrm{emb}}(\boldsymbol{C}_{\mathrm{p}}^{-1})$	$q_{\mathrm{r}}(\boldsymbol{S})/$ $q_{\mathrm{emb}}(\boldsymbol{S})$	$q_{\mathrm{h}}^{\mathrm{glob}}(\mathbf{u})$	$q_{\mathrm{h}}^{\mathrm{glob}}(\boldsymbol{C}_{\mathrm{p}}^{-1})$	$q_{\mathrm{h}}^{\mathrm{glob}}(\boldsymbol{S})$
DIRK(3) CON	2.46	2.36	2.22	1.66	1.36	–	2.40	2.23	2.12
DIRK(3) MULTI	2.46	1.53	1.50	1.68	1.33	1.03	2.38	2.22	2.12
rDIRK(3)	2.46	2.36	2.23	1.67	1.36	1.08	2.43	2.23	2.12
LOBATTO IIIC(2)	1.54	1.50	1.38	–	–	–	1.91	1.82	1.26
RADAU IIA(2)	2.57	2.56	2.40	–	–	–	2.56	2.38	2.27
$\mathrm{cG}_1(2)$	2.57	2.27	2.40	1.00	2.00	0.77	2.56	2.38	2.27
$\mathrm{dG}_1(2)$	3.42	3.33	3.21	1.00	1.82	2.69	2.27	2.44	2.79

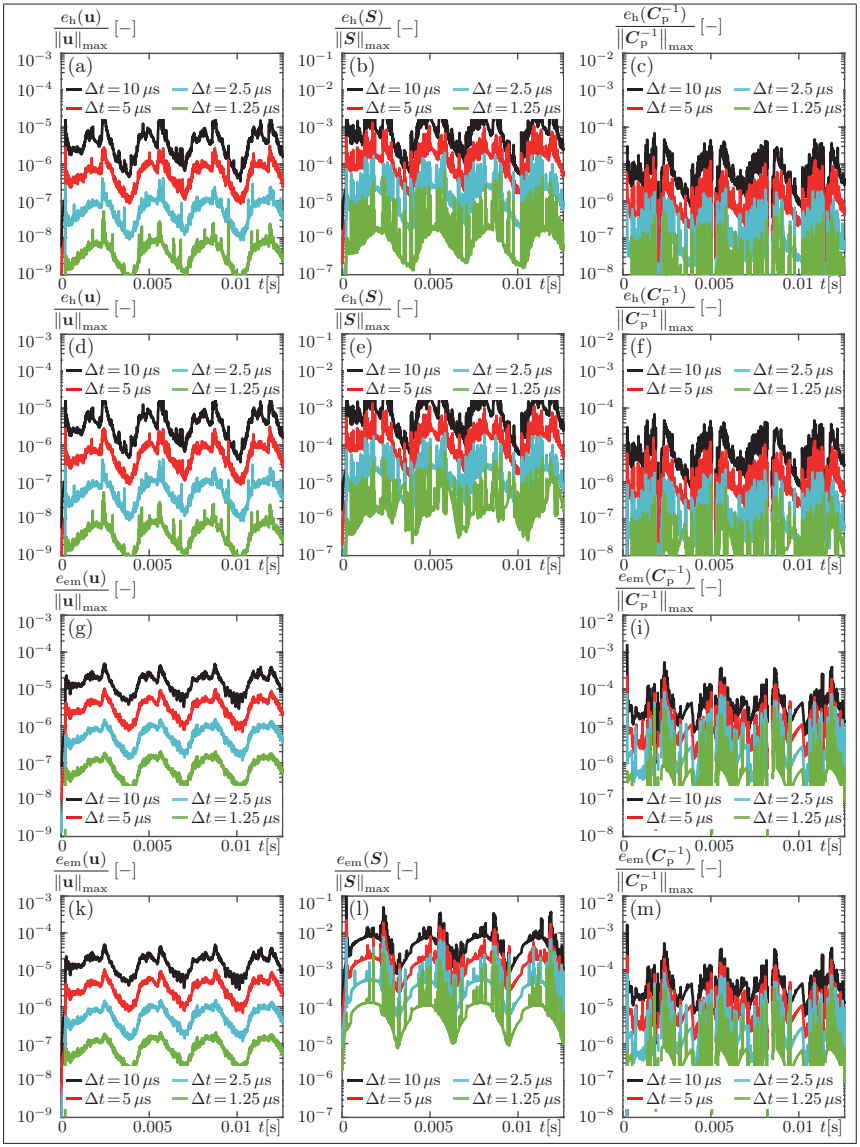

Figure 7.6.: Local time discretization error of the h- and the embedded method for the displacement, the viscoplastic strain, and the stress field within conventional and multifield elastoviscoplasticity: (a)-(c) h-error DIRK(3) conventional, (d)-(f) h-error DIRK(3) multifield, (g)-(i) embedded error DIRK(3) conventional, (k)-(m) embedded error DIRK(3) multifield

However, the multifield setting is derived to enable the application of further higher order accurate schemes. Figure 7.7 (a)-(c) show the time discretization h-error results of the displacement field, the stresses, and the plastic strains for the fully implicit Lobatto IIIC(2) and in Figure 7.7 (d)-(f) for the Radau IIA(2) scheme.

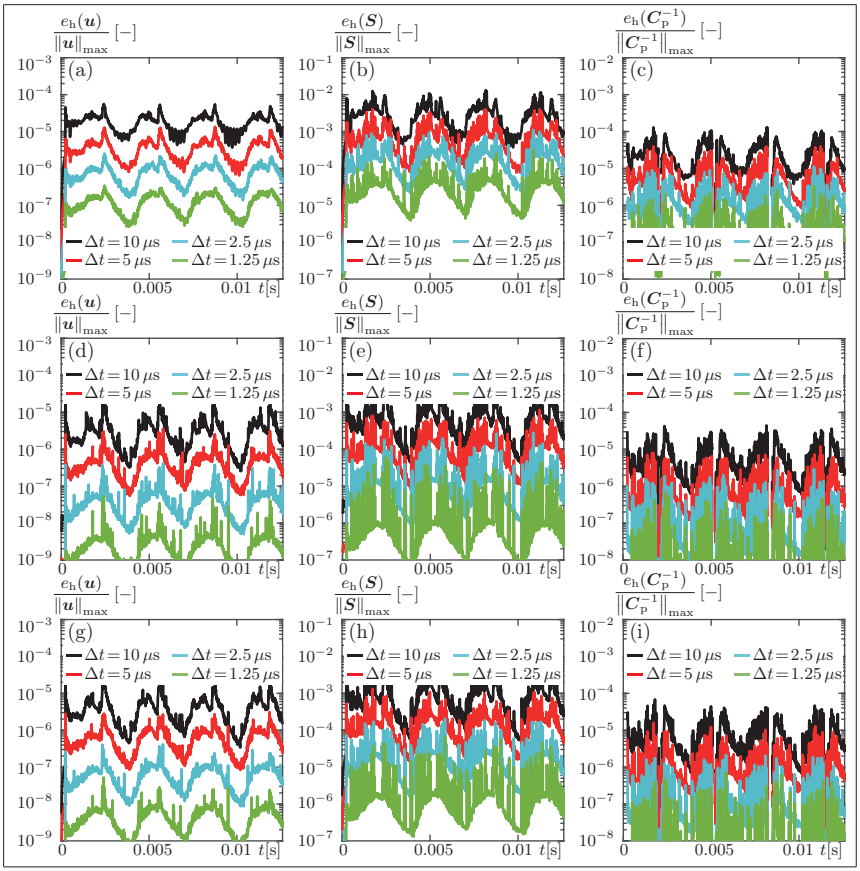

Figure 7.7.: Local time discretization error of the h-method for the displacement, the viscoplastic strain, and the stress field for distinct time integration methods within multifield elastoviscoplasticity: (a)-(c) Lobatto IIIC(2), (d)-(f) Radau IIA(2), (g)-(i) rDIRK(3)

Figure 7.8 (a)-(c) and Figure 7.8 (g)-(i) illustrate the respective curves for the continuous as well as the discontinuous Galerkin $cG_1(2)$ and $dG_1(2)$ method. Additionally, the residual error estimates are exemplified in Figure 7.8 (d)-(f) and (k)-(m). For all curves in the mentioned figures, the error decreases with decreasing time step size. This is also the case for the residual error of the stress field within the continuous Galerkin scheme. In the finite strain

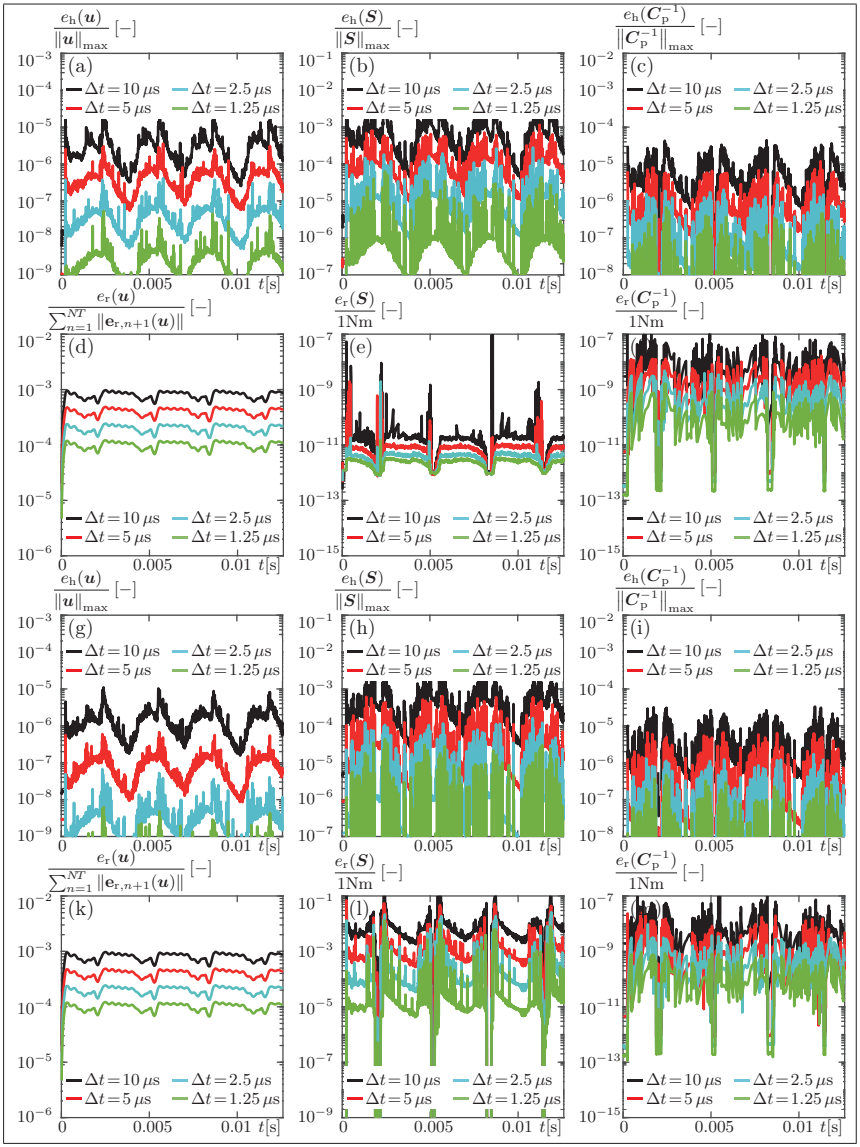

Figure 7.8.: Local time discretization error of the h- and the residual method for the displacement, the viscoplastic strain, and the stress field for distinct time integration methods within multifield elastoviscoplasticity: (a)-(c) h-error $\mathrm{cG}_1(2)$, (d)-(f) residual error $\mathrm{cG}_1(2)$, (g)-(i) h-error $\mathrm{dG}_1(2)$, (k)-(m) residual error $\mathrm{dG}_1(2)$

elastoplastic model, a distinct behavior is observed. The orders of consistency and convergence of the displacement field, the stresses, and the plastic strains shown in Table 7.2, are almost identical to those determined in the finite elastoplastic context. The discontinuous GALERKIN scheme yields, with well above three, the highest order of consistency concerning the h-error. All other methods result in orders of consistency well above two. Only the LOBATTO IIIC(2) scheme hardly reaches orders of consistency of two. If the global h-error is considered, however, the highest results are orders well above two. Once again, the viscoplastic regularization hence has no improving effect on the time discretization error.

7.7. Summary

The derivation of novel numerical approaches is only one side of the coin. Their application and validation are other aspects to be considered. To take this into account, **Chapter 7** adapts the dynamic benchmark problem of Section 5.2 to the finite strain regime with an elastoplastic as well as an elastoviscoplastic variant. It is founded on the displacement-driven deformation process modeled in **Chapter 5** for small strains and thus represents its straightforward extension within the geometrically nonlinear theory. The high dynamic characteristic of the chosen benchmark problem demands the utilization and enables the evaluation of distinct time integrators also within finite strains.

As a starting point, the classical approach is used for the elastoplastic problem. The obtained solution is compared to the small strain case, yielding small deviations concerning the stresses but large ones considering the strains and the LAGRANGE multiplier. Hence, a geometrically nonlinear analysis should even be performed for strains smaller than 5%.

The variational multifield ansatz is equally employed within the elastoplastic benchmark problem. For the same mesh, a corresponding approximation quality and the identical time discretization scheme with fixed time step size, the differences related to the classical strategy do not exceed 0.005%. However, if the orders of consistency determined by the local h-error are compared, dissimilarities prevail. Within the multifield approach, diagonally implicit RUNGE-KUTTA schemes can be applied in a monolithic and a staggered fashion. If the latter implementation is followed for a DIRK(3) scheme, the orders of consistency of the stresses and the plastic strains do not reach two, despite the fact that the classical approach yields an order of almost three. If a monolithic treatment is employed, the orders of consistency of all field variables within both approaches are identical. Thus, even with the higher numerical effort within the multifield procedure, a lower order of consistency is the result. The orders of convergence directly determined by the global h-error, however, are always the same. The same statement holds for the orders of consistency estimated by the embedded error.

Nevertheless, the benefit of the multifield approach is that further time integrators can be applied. For the elastoplastic variant of the benchmark problem, the fully implicit RUNGE-KUTTA schemes, LOBATTO IIIC(2) and RADAU IIA(2), as well as a continuous GALERKIN and a discontinuous GALERKIN method in the one-field setting are adapted. With the latter time discretization scheme, the h-error estimator even leads to orders of consistency well above three for all field variables. With increasing order of consistency, the error level of the local h-error decreases. Additionally, GALERKIN procedures possess a residual error estimator. Within this elastoplastic problem, however, this error estimator cannot be used to determine the order of consistency, since distinct solutions are obtained for all field variables. Its usage for a time adaptive scheme is, hence, also questionable. Despite the variety of time integrators used within the multifield approach, the orders of convergence attained are far away from three.

In the viscoplastic benchmark problem, equivalent investigations are performed, whereby a small viscosity parameter is assumed. The obtained results are indistinguishable to those of the plastic problem. Hence, the regularization has no positive effect.

8. Conclusion

In the preceding thesis, a novel ansatz towards small and finite strain elasto(visco)plasticity is derived, enabling a straightforward application of higher order accurate time integration schemes. Furthermore, the advantages of fully coupled implicit RUNGE-KUTTA schemes, diagonally implicit RUNGE-KUTTA schemes, the NEWMARK method, and continuous as well as discontinuous GALERKIN methods are analyzed.

As a motivation, the integrated forming process of (Steinhoff et al., 2009) is taken into account. The appearing elasto(visco)plastic effects are modeled by widespread continuum mechanical approaches in the small and the finite strain regime, stated for example in (Simo, 1998; Simo and Hughes, 1997). In order to permit an integral treatment of the distinct formulations, a general elasto(visco)plastic problem is created. Additionally, the focus is on the corresponding numerical implementation. In this thesis, two main approaches are described. The necessary theoretical background concerning the nonlinear solution strategies as well as the spatial and temporal discretization is stated in the context of the general elasto(visco)plastic problem. In order to enable the investigation of higher order accurate time integrators, these two approaches are substantiated and utilized within suitable benchmark problems for the small and the finite strain case of elasto(visco)plasticity.

The first procedure uses the finite element method for the spatial discretization of the balance of linear momentum. The (visco)plastic constitutive laws are incorporated on integration point level by exploiting the radial return map algorithm. The resulting system of nonlinear equations is solved by a NEWTON-RAPHSON scheme. This treatment contributes to an imminent multilevel time integration, due to the separate time discretization of the balance equation and the material laws. Here, only diagonally implicit RUNGE-KUTTA schemes or the NEWMARK method are applied. This classical course of action is followed to generate reference solutions.

The multifield approach is derived to establish a simple algorithmic treatment for different classes of higher order accurate time integrators. The procedure's corner stones are installed by exploiting the principle of virtual power to deduce the necessary fundamental equations. In contrast to the classical procedure, the constitutive laws and the balance of linear momentum are gathered in a system of equations, so that this time both types of formulations can be spatially discretized by the finite element method. Hence, the (visco)plastic quantities are no longer solved on integration point level but by means of a nodal basis. This concept permits a single-level time integration for all unknown quantities and, thus, enables the applicability of higher order accurate time integration schemes like fully implicit RUNGE-KUTTA schemes or GALERKIN methods to the balance equation and the constitutive laws at the same time. In this context, the algorithmic treatment of RADAU IIA, LOBATTO IIIC as well as of continuous and discontinuous GALERKIN schemes founded on RADAU and LOBATTO integration rules are elaborated. In some cases, however, this implementation strategy involves a semi-smooth NEWTON scheme.

To validate the implementation of the classical and the multifield procedure, a rectangular strip with a hole in the plane strain case is calculated, and the obtained results are compared to the literature, cf. (Stein, 2003). The influence of different time integrators is determined by a dynamic benchmark problem in the small and the finite strain regime, explicitly derived for this purpose. It embodies, drawing on the forging process of (Steinhoff et al., 2009), an axisymmetric model of a steel shaft with an inhomogeneous time-dependent boundary condition. The time integrators' characteristics are evaluated using various local as well as global error formulations

for the displacement, the plastic strain, and the stress field. With their help, the orders of consistency and of convergence are estimated, respectively.

Considering only small strains, it can be observed that identical results are achieved for the dynamic benchmark problem, within the classical and the multifield approach, for time integrators that are applied to both procedures. Hence, in these cases, the multifield approach has no advantages at all compared to the classical approach. Indeed, it is characterized by a greater numerical effort. Nevertheless, the derivation of the multifield approach is inevitable. It allows for a consistent application of higher order accurate fully implicit RUNGE-KUTTA or GALERKIN schemes, whose implementation in the classical approach is accompanied by a series of difficulties, cf. (Alberty and Carstensen, 2002; Büttner and Simeon, 2002; Eidel and Kuhn, 2015).

Independent of the chosen procedure, time integrator, or error estimator, a decreasing time step size leads to a decreasing error level within the displacement, the plastic strain, and the stress field. For an elastoplastic material model, the best order of consistency is about $q_\mathrm{h} = 5.32$ for all analyzed field variables obtained by the two-field discontinuous GALERKIN scheme with polynomial order $\bar{p}_\mathrm{t} = 3$. Following the argumentations in (Strehmel et al., 2012), the order of consistency is identical to the order of convergence. Within small strain elastoplasticity, however, this line of reasoning is apparently not applicable. Estimating the order of convergence directly by evaluating the global h-error leads to orders of at best 2.51 for the RADAU IIA(3) or the continuous $\mathrm{cG}_1(2)$ method. The two-field discontinuous GALERKIN scheme with polynomial order three solely attains first order convergence. Accordingly, the theoretical orders of convergence are not accessed. Similar properties are reported in (Büttner and Simeon, 2002; Eidel and Kuhn, 2015; Grafenhorst et al., 2017). The explanations of the reasons given therein include non-smooth strain paths as well as missing switching point determination strategies. However, as demonstrated in (Eidel and Kuhn, 2015), the latter are only able to partly cure the order reduction phenomenon - and the non-smoothness can merely be seen as half of the truth. If a viscoplastic regularization is analyzed instead of an ideal elastoplastic material model, identical orders of consistency and convergence are obtained within the preceding dynamic benchmark problem. Thus, not even a smoothening of the problem formulation leads to better orders of convergence. The same observation is reported in (Hartmann and Bier, 2007). Hence, the identification of the sources of order reduction in elasto(visco)plasticity is not completed, (Grafenhorst et al., 2017). A deeper mathematical analysis is necessary - but this is beyond the scope of this thesis. Despite the lack of orders of convergence well above two, the implementation of higher order accurate schemes still has its benefits. The mean error level decreases with increasing theoretical order of convergence.

Apart from the h-error, which is mainly used to estimate order properties, this thesis also investigates the local embedded as well as the local residual error if applicable. Both proposals intend to generate numerically cheap error estimates for adaptive schemes. Their suitability is determined in the context of the dynamic benchmark problem. Thereby, it is noticed that, for both error estimates, the error decreases with decreasing time step size. However, only with the embedded error different orders of consistency are obtained for procedures inheriting distinct theoretical orders of convergence. The residual error results in identical orders of convergence, although opposing polynomial degrees are taken into account. Its applicability to p-adaptivity has, hence, to be investigated separately.

In the finite strain regime, analogous analyzes are performed as for the small strain case - with the consequence that similar conclusions can be drawn. Again, a dynamic benchmark problem is calculated. Only the extent of the applied time discretization schemes is reduced. However, for the methods used for the small and the finite strain regime, the orders of convergence and consistency are similar for both the elastoplastic and the elastoviscoplastic case. Small differences

only appear for the residual error estimators and the DIRK(3) scheme. The staggered implementation of the third order diagonally implicit RUNGE-KUTTA method in the elasto(visco)plastic multifield approach suffers from order reduction phenomena in the second PIOLA-KIRCHHOFF stresses and the plastic CAUCHY-GREEN strains. The displacement field remains unaffected. A reformulation of this time discretization scheme into a monolithic method cures the problem of order reduction. Nevertheless, this represents a further inconvenience of the multifield setting. In the finite strain regime, it is characterized, apart from a higher numerical effort by additional order reduction phenomena. In general, however, the applicability of higher order accurate schemes are still to be considered as an advantage.

9. Outlook

The conclusions drawn in the previous chapter open up space for a bunch of further possible investigations and improvements. First, a profound mathematical analysis of the general elasto(visco)plastic problem, focussing on the phenomenon of order reduction, should be carried out. Although this thesis covers a successful implementation of a multifield approach towards elasto(visco)plasticity in the small as well as the finite strain regime - thus including the usage of higher order time integrators of GALERKIN and RUNGE-KUTTA type - only orders of convergence of at best 2.51 are reached for representative examples. Hence, it is an essential goal to determine why locally obtained orders of consistency up to 5.32 cannot be transferred to the global error characteristics, even though the applicability of RUNGE-KUTTA schemes in the context of differential-algebraic systems is shown in (Hairer and Wanner, 2002; Strehmel et al., 2012) without order reduction. Even if a viscoplastic regularization is carried out, no enhancements are achieved - neither in the small nor in the finite strain regime. The question whether strategies to resolve the elastoplastic switching point precisely will cure this problem, as demonstrated in (Eidel and Kuhn, 2015) for some cases, comes along with that.

Despite the lack of higher orders of convergence, the multifield approach and the implemented time discretization schemes permit a significant reduction of the error level compared to the classical approach. The price for this benefit, however, is an increased numerical effort. The quantification of its actual amount in dependence of the obtained accuracy is still an open task which has to be performed before the efficiency of the multifield approach can be assessed. This fact is accompanied by striving for embedding methods to accelerate the variational approach. An investigation of distinct nonlinear complementarity functions to find a procedure leading to a reduced number of semi-smooth NEWTON iterations is one possibility, cf. (Geiger and Kanzow, 2002; Seitz et al., 2014). Another alternative enhancement of the multifield approach may be the contraction of the resulting system of linear equations by applying static condensation, cf. (Hüeber and Wohlmuth, 2005; Schröder and Kuhl, 2015*b*). Following the procedure in (Hüeber and Wohlmuth, 2005) would lead to the requirement that special shape functions have to be chosen to ensure a fast and easy static condensation. In the multifield context, however, a prescribed choice of shape functions for certain unknowns can lead to difficulties. On the one hand, the problem formulation itself may require special concurrent properties on the shape functions, cf. (Comi and Perego, 1995), while, on the other hand, stability aspects may urge for certain limitations, cf. (Braess, 2010). Hence, the investigation of distinct combinations of approximations for the different field variables considering various topics is of increased interest.

Concerning the stability of the general variational elasto(visco)plastic problem, the contemplation of the shape functions only comprises a small part of the necessary analysis. A variety of distinct aspects has to be taken into account as well. This includes, for example, mathematical topics such as existence and uniqueness of solutions. For these investigations, a closer look at the structure of the multifield approach would be inevitable. Due to the application of the principle of virtual power for derivation, an extremum principle with side conditions is involved. As a consequence, the problem formulation exhibits saddle-point-like characteristics. One question arising in this context would be whether the obtained similarities are linked to single- or multifold generalized saddle point problems, cf. (Ciarlet Jr. et al., 2003; Walkington and Howell, 2011). Another one is concerned with solvability conditions, which affect the variational approach at different sides. At first, the corresponding stationarity problem should be analyzed using methods of functional or convex analysis to characterize its existence and

uniqueness properties, cf. (Zeidler, 1985). In a further step, the results should be associated to the weak forms, which should be examined with respect to these topics as well. This implies aspects such as the necessity and the applicability of the continuity, the definiteness, or the inf-sup condition, cf. (Boffi et al., 2013; Braess, 2010; Brezzi and Bathe, 1990). Then, the same study should be performed with regard to the spatially discretized problem - leading, amongst other things, to mathematically sound assumptions for the shape functions of the distinct field variables. An additional point of interest in the scope of the previously described examinations is the consideration of the dynamic behavior. This thesis takes almost entirely inertia effects into account. Their contribution to solvability arguments should be reviewed, likewise. A possible approach could be based on a series of time incremental problem formulations, cf. (Han and Reddy, 1999; Mielke, 2004).

This way of proceeding requires the utilization of a time discretization scheme as it is the case within the solution strategy of the general elasto(visco)plastic problem. Hence, the imposing question is how the solvability conditions are influenced by the time integrator in question - and whether there are certain stability criteria which have to be fulfilled for dynamic elasto(visco)plasticity. The order reduction phenomenon observed for higher order time discretization schemes may be analyzed in this context, too. In order to carry out these studies, a profound understanding of the distinct time integrators involved in this thesis is necessary. While Runge-Kutta schemes have been examined widely and a general framework is established , cf. (Butcher, 2008; Hairer and Wanner, 2002; Strehmel et al., 2012), Galerkin methods in time are rarely investigated and mostly by means of special cases, cf. (Matthies and Schieweck, 2011; Thomée, 1997). For the shape functions and quadrature rules applied in this thesis, no theoretical background for the determination of the procedures' order of convergence could be found. Furthermore, there is a lack of mathematical theory regarding the question how the incorporated weighting has to be chosen to create Galerkin schemes with good convergence. Examples with distinct weighting matrices together with an adaptation of a Gauss-Legendre quadrature can be found in (Carstens, 2013; Gleim and Kuhl, 2013) in the context of diffusion and elastic problems. A direct transfer of these methods to the elasto(visco)plastic case, however, comes along with further investigations regarding the treatment of differential algebraic systems within the Galerkin theory. Within the Gauss-Legendre quadrature, the supporting points do not lie at the end of the interval, hence, the system matrices and loads are not explicitly evaluated at the end of the time step. In the multifield approach, this leads to the fact that the semi-smooth Newton procedure has to be extended by a projection step and the consistency condition is no longer fulfilled at the end of the time step. A similar practice is carried out in (Simo and Govindjee, 1991). Nonetheless, the benefit of such formulations still has to be explored.

But apart from investigations of numerical or mathematical nature, aspects of modeling should be examined as well. In order to keep the derivation of the multifield approach and the implementation of higher order accurate time integration schemes as simple as possible, only elementary material models are considered. Hardening mechanisms as well as thermal effects are consistently neglected. Their integration in the variational approach is, hence, of great importance. Compared to the classical approach, this adaptation will be accompanied by large changes in the code and an even higher numerical effort, since the material equations are defined on structural level. Strategies to accelerate the multifield approach will thus gain more significance. This could also imply the application of adaptive space and time discretization schemes, along with new effective error estimators. One example could be a residual error estimator for fully implicit Runge-Kutta schemes.

A. Tensor Calculus

This chapter provides the fundamental aspects of tensor algebra and analysis, which are needed for the understanding of this thesis. For further detailed explanations see (De Boer, 1982; Ehlers, 2009; Holzapfel, 2000; Talpaert, 2002; Wriggers, 2008) and the references therein. In the course of this chapter, four distinct groups of quantities and their respective notations will be distinguished.

1. zeroth order tensors, scalars	a, b, c
2. first order tensors, vectors	$\boldsymbol{a}, \boldsymbol{b}, \boldsymbol{b}$
3. second order tensors	$\boldsymbol{A}, \boldsymbol{B}, \boldsymbol{C}$
4. third order tensors	$\underline{\boldsymbol{A}}, \underline{\boldsymbol{B}}, \underline{\boldsymbol{C}}$
5. fourth order tensors	$\mathbb{A}, \mathbb{B}, \mathbb{C}$

Table A.1.: Exemplified notations

These types of notations cannot be extended to the rest of the thesis. Therein, the different quantities are generally denoted using designations common in the literature. The distinction between the tensor orders is accomplished due to the physical or numerical interpretation and application. Furthermore, uppercase bold-face Latin letters are considered, which always refer to specially assembled arrays.

The order of the tensor indicates how many unit basis vectors $\boldsymbol{g}_i$ with $i = 1, ..., 3$ are needed to define the corresponding tensor. If no further information is given, always a cartesian basis is considered. Thus, the variants in Table A.1 can be expressed by

$$
\begin{aligned}
a &= a, \\
\boldsymbol{a} &= \sum_{i=1}^{3} a_i \, \boldsymbol{g}_i && = a_i \, \boldsymbol{g}_i, \\
\boldsymbol{A} &= \sum_{i=1}^{3} \sum_{j=1}^{3} A_{ij} \, \boldsymbol{g}_i \otimes \boldsymbol{g}_j && = A_{ij} \, \boldsymbol{g}_i \otimes \boldsymbol{g}_j, \\
\underline{\boldsymbol{A}} &= \sum_{i=1}^{3} \sum_{j=1}^{3} \sum_{k=1}^{3} A_{ijk} \, \boldsymbol{g}_i \otimes \boldsymbol{g}_j \otimes \boldsymbol{g}_k && = A_{ijk} \, \boldsymbol{g}_i \otimes \boldsymbol{g}_j \otimes \boldsymbol{g}_k, \\
\mathbb{A} &= \sum_{i=1}^{3} \sum_{j=1}^{3} \sum_{k=1}^{3} \sum_{l=1}^{3} A_{ijkl} \, \boldsymbol{g}_i \otimes \boldsymbol{g}_j \otimes \boldsymbol{g}_k \otimes \boldsymbol{g}_l = A_{ijkl} \, \boldsymbol{g}_i \otimes \boldsymbol{g}_j \otimes \boldsymbol{g}_k \otimes \boldsymbol{g}_l,
\end{aligned}
\tag{A.1}
$$

where the operator $\otimes$ denotes the dyadic product. It is defined by its property

$$(\boldsymbol{a} \otimes \boldsymbol{b})\boldsymbol{c} = (\boldsymbol{b} \cdot \boldsymbol{c})\boldsymbol{a}$$

for arbitrary vectors $\boldsymbol{a}, \boldsymbol{b}, \boldsymbol{c}$ with the dot operator $\cdot$ referring to the standard scalar product of

vectors, cf. (De Boer, 1982; Holzapfel, 2000). Hence, it is in general not commutative

$$\boldsymbol{a} \otimes \boldsymbol{b} \neq \boldsymbol{b} \otimes \boldsymbol{a}.$$

Since all appearing sums in (A.1) have the same limits, they are dropped for simplification. This fact is denoted as the summation convention of Einstein. In the following sections, various useful relationships for the calculation with tensors are presented. For the necessary proofs see the special literature, e. g. (De Boer, 1982; Talpaert, 2002).

A.1. Tensor Algebra

Important arithmetic operations for first order tensors are:

$$\boldsymbol{a} + \boldsymbol{b} = \boldsymbol{b} + \boldsymbol{a}, \tag{A.2}$$
$$[\boldsymbol{a} + \boldsymbol{b}] + \boldsymbol{c} = \boldsymbol{a} + [\boldsymbol{b} + \boldsymbol{c}], \tag{A.3}$$
$$\boldsymbol{a} - \boldsymbol{a} = \boldsymbol{0}. \tag{A.4}$$

Taking also scalars into account yields

$$[ab]\,\boldsymbol{a} = a\,[b\boldsymbol{a}], \tag{A.5}$$
$$[a + b]\,\boldsymbol{a} = a\,\boldsymbol{a} + b\,\boldsymbol{a}, \tag{A.6}$$
$$a\,[\boldsymbol{a} + \boldsymbol{b}] = a\,\boldsymbol{a} + a\,\boldsymbol{b}. \tag{A.7}$$

For the inner product, the properties

$$\begin{aligned} \boldsymbol{a} \cdot \boldsymbol{b} &= \boldsymbol{b} \cdot \boldsymbol{a}, \\ \boldsymbol{a} \cdot [a\,\boldsymbol{b} + b\,\boldsymbol{c}] &= a\,[\boldsymbol{a} \cdot \boldsymbol{b}] + b\,[\boldsymbol{b} \cdot \boldsymbol{c}], \\ \boldsymbol{a} \cdot \boldsymbol{a} > 0 \quad \Leftrightarrow \quad \boldsymbol{a} \neq \boldsymbol{0} \quad \text{and} \quad \boldsymbol{a} \cdot \boldsymbol{a} = 0 \quad &\Leftrightarrow \quad \boldsymbol{a} = \boldsymbol{0}. \end{aligned}$$

are valid. Applying the scalar product to the basis vectors

$$\boldsymbol{g}_i \cdot \boldsymbol{g}_j = \delta_{ij} = \begin{cases} 1 & \text{if} \quad i = j \\ 0 & \text{if} \quad i \neq j \end{cases}$$

results in the definition of the Kronecker delta δ_{ij}. For second order tensors, Equations (A.2)-(A.7) can be adapted identically. Moreover, the dot product between a first and a second order tensor can be defined by

$$\boldsymbol{A} \cdot \boldsymbol{b} = A_{ij} b_k\, \boldsymbol{g}_i \otimes \boldsymbol{g}_j \cdot \boldsymbol{g}_k = A_{ij} b_k \delta_{jk}\, \boldsymbol{g}_i = A_{ij} b_j\, \boldsymbol{g}_i, \tag{A.8}$$

while the double contraction is determined using

$$\boldsymbol{A} : \boldsymbol{B} = A_{ij} B_{kl}\, \boldsymbol{g}_i \otimes \boldsymbol{g}_j : \boldsymbol{g}_k \otimes \boldsymbol{g}_l = A_{ij} B_{kl} \delta_{jl} \delta_{ik} = A_{ij} B_{ij}. \tag{A.9}$$

This proceeding can be adapted to define the Frobenius norm

$$\|\boldsymbol{A}\| = \sqrt{\boldsymbol{A} : \boldsymbol{A}}. \tag{A.10}$$

A change in the sorting of the basis vectors of a second order tensor $\boldsymbol{A}$ leads to the transpose tensor

$$\boldsymbol{A}^{\mathrm{T}} = A_{ij}\, \boldsymbol{g}_j \otimes \boldsymbol{g}_i. \tag{A.11}$$

If

$$\boldsymbol{A}^{\mathrm{T}} = \boldsymbol{A} \tag{A.12}$$

holds, the tensor $\boldsymbol{A}$ is called symmetric. Of special importance in the context of second order tensors is the symmetric unity tensor

$$\boldsymbol{I} = \delta_{ij}\boldsymbol{g}_i \otimes \boldsymbol{g}_j = \boldsymbol{g}_i \otimes \boldsymbol{g}_i = \boldsymbol{I}^{\mathrm{T}}.$$

With its help, the inverse of the second order tensor $\boldsymbol{A}$ is established

$$\boldsymbol{A} \cdot \boldsymbol{A}^{-1} = \boldsymbol{I}.$$

Additionally, performing the double contraction as in Equation (A.9) yields the definition of the trace operator $\mathrm{tr}\,(\bullet)$

$$\mathrm{tr}\,(\boldsymbol{A}) = \boldsymbol{A} \colon \boldsymbol{I} = A_{ij}\delta_{kl}\boldsymbol{g}_i \otimes \boldsymbol{g}_j \colon \boldsymbol{g}_k \otimes \boldsymbol{g}_l = A_{ij}\delta_{kl}\delta_{jl}\delta_{ik} = A_{ii}.$$

This enables the split of an arbitrary tensor $\boldsymbol{A}$ into a deviatoric $\mathrm{dev}\,(\boldsymbol{A})$ and a volumetric part $\mathrm{sph}\,(\boldsymbol{A})$

$$\boldsymbol{A} = \mathrm{dev}\,(\boldsymbol{A}) + \mathrm{sph}\,(\boldsymbol{A})$$

with

$$\mathrm{sph}\,(\boldsymbol{A}) = \frac{1}{3}\mathrm{tr}\,(\boldsymbol{A})\,\boldsymbol{I}, \qquad \mathrm{dev}\,(\boldsymbol{A}) = \boldsymbol{A} - \frac{1}{3}\mathrm{tr}\,(\boldsymbol{A})\,\boldsymbol{I}$$

as well as the properties

$$\mathrm{tr}\,(\mathrm{dev}\,(\boldsymbol{A})) = 0, \qquad \mathrm{dev}\,(\mathrm{tr}\,(\boldsymbol{A})\,\boldsymbol{I}) = \boldsymbol{0}.$$

In the finite strain case, see **Chapter 2**, it is useful to consider a second deviatoric operator and a second trace operator

$$\mathrm{DEV}\,(\boldsymbol{A}) = \boldsymbol{A} - \frac{1}{3}\left[\boldsymbol{C} \colon \boldsymbol{A}\right]\boldsymbol{C}^{-1}, \qquad \mathrm{Tr}\,(\boldsymbol{A}) = \boldsymbol{C} \colon \boldsymbol{A}.$$

The idea thereby is to exploit the transformation properties between the current and the reference configuration

$$\mathrm{dev}\left(\boldsymbol{F} \cdot \boldsymbol{A} \cdot \boldsymbol{F}^{\mathrm{T}}\right) = \boldsymbol{F} \cdot \mathrm{DEV}\,(\boldsymbol{A}) \cdot \boldsymbol{F}^{\mathrm{T}}, \qquad \mathrm{tr}\left(\boldsymbol{F} \cdot \boldsymbol{A} \cdot \boldsymbol{F}^{\mathrm{T}}\right) = \mathrm{Tr}\,(\boldsymbol{A}).$$

Another important operator in the context of second order tensors is the determinant $\det\,(\bullet)$ and the corresponding relations

$$\det\,(\boldsymbol{A} \cdot \boldsymbol{B}) = \det\,\boldsymbol{A} \cdot \det\,\boldsymbol{B}, \qquad \det\,\boldsymbol{A} = \det\,\boldsymbol{A}^{\mathrm{T}}, \qquad \det\,\boldsymbol{A}\det\,\boldsymbol{A}^{-1} = 1.$$

Since third order tensors are of secondary interest in this thesis, it is only emphasized that the Relations (A.2)-(A.7) are applicable, too. The last category of tensors treated in this section are those of fourth order. They also follow the rules in Equations (A.2)-(A.7). Moreover, analogously to Equations (A.8) as well as (A.9), they can be part of a single and a double contraction. As examples, the fourth and second order tensors

$$\mathbb{A} \cdot \boldsymbol{B} = A_{ijkl}B_{mn}\,\boldsymbol{g}_i \otimes \boldsymbol{g}_j \otimes \boldsymbol{g}_k \otimes \boldsymbol{g}_l \cdot \boldsymbol{g}_m \otimes \boldsymbol{g}_n = A_{ijkl}B_{ln}\,\boldsymbol{g}_i \otimes \boldsymbol{g}_j \otimes \boldsymbol{g}_k \otimes \boldsymbol{g}_n,$$
$$\mathbb{A} \colon \boldsymbol{B} = A_{ijkl}B_{mn}\,\boldsymbol{g}_i \otimes \boldsymbol{g}_j \otimes \boldsymbol{g}_k \otimes \boldsymbol{g}_l \colon \boldsymbol{g}_m \otimes \boldsymbol{g}_n = A_{ijkl}B_{kl}\,\boldsymbol{g}_i \otimes \boldsymbol{g}_j$$

are obtained. Acknowledging the idea of changing basis vectors as in Equation (A.11) generates a series of possibilities. The most important ones are

$$\begin{aligned}
\mathbb{A}^{\mathrm{T}} &= A_{ijkl}\, \boldsymbol{g}_k \otimes \boldsymbol{g}_l \otimes \boldsymbol{g}_i \otimes \boldsymbol{g}_j, \\
\mathbb{A}^{\overset{12}{\mathrm{T}}} &= A_{ijkl}\, \boldsymbol{g}_j \otimes \boldsymbol{g}_i \otimes \boldsymbol{g}_k \otimes \boldsymbol{g}_l, \\
\mathbb{A}^{\overset{23}{\mathrm{T}}} &= A_{ijkl}\, \boldsymbol{g}_i \otimes \boldsymbol{g}_k \otimes \boldsymbol{g}_j \otimes \boldsymbol{g}_l, \\
\mathbb{A}^{\overset{24}{\mathrm{T}}} &= A_{ijkl}\, \boldsymbol{g}_i \otimes \boldsymbol{g}_l \otimes \boldsymbol{g}_k \otimes \boldsymbol{g}_j,
\end{aligned}$$

whereby all others can be constructed similarly. These expressions can even be applied to third order tensors. The benefit of such symmetry conditions is demonstrated in the recast

$$[\boldsymbol{a} \otimes \boldsymbol{b}] : \mathbb{A} = \boldsymbol{a} \cdot [\boldsymbol{b} \cdot \mathbb{A}], \qquad \text{if } \mathbb{A} = \mathbb{A}^{\overset{12}{\mathrm{T}}}.$$

An example of a fourth order tensor is the special unity tensor

$$\mathbb{I} = \frac{1}{2}[\delta_{ik}\delta_{jl} + \delta_{il}\delta_{jk}]\, \boldsymbol{g}_i \otimes \boldsymbol{g}_j \otimes \boldsymbol{g}_k \otimes \boldsymbol{g}_l,$$

with its symmetrizing effect

$$\boldsymbol{A} : \mathbb{I} = \frac{1}{2}\left[\boldsymbol{A} + \boldsymbol{A}^{\mathrm{T}}\right] = \frac{1}{2}\left[\boldsymbol{A} + \boldsymbol{A}^{\mathrm{T}}\right]^{\mathrm{T}}.$$

A.2. Tensor Analysis

In the field of material theory and its numerical implementation, apart from purely algebraic manipulations of different tensorial quantities, the introduction and analysis of tensor functions is inevitable. A tensor function or a tensor field is a scalar-, vector-, or tensor-valued function depending on one or more tensorial quantities, cf. (De Boer, 1982; Holzapfel, 2000). Certain interest lies in the derivatives of these functions with respect to the tensorial quantities. As examples, the following relationships can be considered, cf. (Ehlers, 2009; Holzapfel, 2000):

$$\begin{aligned}
\frac{\partial \boldsymbol{A}}{\partial \boldsymbol{A}} &= \mathbb{I}, \text{with } \boldsymbol{A} = \boldsymbol{A}^{\mathrm{T}} \\
\frac{\partial\, \boldsymbol{A}}{\partial \boldsymbol{A}} &= [\boldsymbol{I} \otimes \boldsymbol{I}]^{\overset{23}{\mathrm{T}}}, & \frac{\partial\, \boldsymbol{A}^{\mathrm{T}}}{\partial \boldsymbol{A}} &= [\boldsymbol{I} \otimes \boldsymbol{I}]^{\overset{24}{\mathrm{T}}}, \\
\frac{\partial [a\, \boldsymbol{a}]}{\partial \boldsymbol{b}} &= \boldsymbol{a} \otimes \frac{\partial a}{\partial \boldsymbol{b}} + a \frac{\partial \boldsymbol{a}}{\partial \boldsymbol{b}}, & \frac{\partial [a\, \boldsymbol{A}]}{\partial \boldsymbol{B}} &= \boldsymbol{A} \otimes \frac{\partial a}{\partial \boldsymbol{B}} + a \frac{\partial \boldsymbol{A}}{\partial \boldsymbol{B}}, \\
\frac{\partial \operatorname{tr}(\boldsymbol{A})}{\partial \boldsymbol{A}} &= \boldsymbol{I}, & \frac{\partial\, [\boldsymbol{A} \cdot \boldsymbol{B}]}{\partial \boldsymbol{A}} &= \left[\boldsymbol{I} \otimes \boldsymbol{B}^{\mathrm{T}}\right]^{\overset{23}{\mathrm{T}}}, \\
\frac{\partial\, [\boldsymbol{A} \cdot \boldsymbol{B}]}{\partial \boldsymbol{B}} &= [\boldsymbol{A} \otimes \boldsymbol{I}]^{\overset{23}{\mathrm{T}}}, & \frac{\partial\, \left[\boldsymbol{A}^{\mathrm{T}} \cdot \boldsymbol{A}\right]}{\partial \boldsymbol{A}} &= \left[\boldsymbol{A}^{\mathrm{T}} \otimes \boldsymbol{I}\right]^{\overset{23}{\mathrm{T}}} + [\boldsymbol{I} \otimes \boldsymbol{A}]^{\overset{24}{\mathrm{T}}}, \\
\frac{\partial\, \left[\boldsymbol{A} \cdot \boldsymbol{A}^{\mathrm{T}}\right]}{\partial \boldsymbol{A}} &= [\boldsymbol{A} \otimes \boldsymbol{I}]^{\overset{24}{\mathrm{T}}} + [\boldsymbol{I} \otimes \boldsymbol{A}]^{\overset{23}{\mathrm{T}}}, & \frac{\partial\, [\boldsymbol{A} \cdot \boldsymbol{B} \cdot \boldsymbol{C}]}{\partial \boldsymbol{B}} &= \left[\boldsymbol{A} \otimes \boldsymbol{C}^{\mathrm{T}}\right]^{\overset{23}{\mathrm{T}}},
\end{aligned}$$

$$\frac{\partial\,[\boldsymbol{A}\cdot\boldsymbol{b}]}{\partial\boldsymbol{B}} = \left[\left[\frac{\partial\boldsymbol{A}}{\partial\boldsymbol{B}}\right]^{\overset{24}{\mathrm{T}}}\right]^{\overset{23}{\mathrm{T}}}\cdot\boldsymbol{b}+\boldsymbol{A}\cdot\frac{\partial\boldsymbol{b}}{\partial\boldsymbol{B}}, \qquad \frac{\partial\,[\boldsymbol{A}\cdot\boldsymbol{b}]}{\partial\boldsymbol{A}} = [\boldsymbol{I}\otimes\boldsymbol{I}]\cdot\boldsymbol{b},$$

$$\frac{\partial\,[\boldsymbol{B}\cdot\boldsymbol{A}\cdot\boldsymbol{b}]}{\partial\boldsymbol{A}} = [\boldsymbol{B}\otimes\boldsymbol{I}]\cdot\boldsymbol{b}, \qquad \frac{\partial\,\boldsymbol{A}^{-1}}{\partial\boldsymbol{A}} = -\left[\boldsymbol{A}^{-1}\otimes\boldsymbol{A}^{-\mathrm{T}}\right]^{\overset{23}{\mathrm{T}}},$$

$$\frac{\partial[\boldsymbol{A}\colon\boldsymbol{B}]}{\partial\boldsymbol{C}} = \left[\frac{\partial\boldsymbol{A}}{\partial\boldsymbol{C}}\right]^{\mathrm{T}}\colon\boldsymbol{B}+\left[\frac{\partial\boldsymbol{B}}{\partial\boldsymbol{C}}\right]^{\mathrm{T}}\colon\boldsymbol{A}, \qquad \frac{\partial\sqrt{\det\boldsymbol{A}}}{\partial\boldsymbol{A}} = \frac{1}{2}\sqrt{\det(\boldsymbol{A})}\boldsymbol{A}^{-1},$$

$$\frac{\partial\,[\boldsymbol{A}\cdot\boldsymbol{B}]}{\partial\boldsymbol{C}} = \left[\left[\frac{\partial\boldsymbol{A}}{\partial\boldsymbol{C}}\right]^{\overset{24}{\mathrm{T}}}\cdot\boldsymbol{B}\right]^{\overset{24}{\mathrm{T}}}+\left[\left[\frac{\partial\boldsymbol{B}}{\partial\boldsymbol{C}}\right]^{\overset{14}{\mathrm{T}}}\cdot\boldsymbol{A}^{\mathrm{T}}\right]^{\overset{14}{\mathrm{T}}}.$$

Therein, it is assumed that all appearing expressions depend on the respective tensorial quantities. If the derivative is carried out with respect to a location vector $\boldsymbol{x}$ or $\boldsymbol{X}$, see **Chapter 2**, particular operators can be defined. For the following derivations in this section, only cartesian coordinate systems will be admitted. An introduction towards cylindrical coordinates is given in **Appendix C**. For an arbitrary scalar-valued function f

$$\nabla_x f = \frac{\partial f}{\partial\boldsymbol{x}} = \frac{\partial f}{\partial x_i}\boldsymbol{g}_i, \qquad \nabla_X f = \frac{\partial f}{\partial\boldsymbol{X}} = \frac{\partial f}{\partial X_i}\boldsymbol{g}_i$$

are achieved introducing the NABLA operators

$$\nabla_x = \boldsymbol{g}_1\frac{\partial}{\partial x_1}+\boldsymbol{g}_2\frac{\partial}{\partial x_2}+\boldsymbol{g}_3\frac{\partial}{\partial x_3}, \qquad \nabla_X = \boldsymbol{g}_1\frac{\partial}{\partial X_1}+\boldsymbol{g}_2\frac{\partial}{\partial X_2}+\boldsymbol{g}_3\frac{\partial}{\partial X_3}. \tag{A.13}$$

Their application to first and second order tensor functions permits a supplementary variety. While their dyadic use leads to the gradient operators

$$\nabla_x\boldsymbol{a}=[\nabla_x\otimes\boldsymbol{a}]^{\mathrm{T}}=\frac{\partial a_i}{\partial x_j}\boldsymbol{g}_i\otimes\boldsymbol{g}_j, \qquad \nabla_X\boldsymbol{a}=[\nabla_X\otimes\boldsymbol{a}]^{\mathrm{T}}=\frac{\partial a_i}{\partial X_j}\boldsymbol{g}_i\otimes\boldsymbol{g}_j, \tag{A.14}$$

$$\nabla_x\boldsymbol{A}=[\nabla_x\otimes\boldsymbol{A}]^{\overset{13}{\mathrm{T}}}=\frac{\partial A_{ij}}{\partial x_k}\boldsymbol{g}_i\otimes\boldsymbol{g}_j\otimes\boldsymbol{g}_k, \qquad \nabla_X\boldsymbol{A}=[\nabla_X\otimes\boldsymbol{A}]^{\overset{13}{\mathrm{T}}}=\frac{\partial A_{ij}}{\partial X_k}\boldsymbol{g}_i\otimes\boldsymbol{g}_j\otimes\boldsymbol{g}_k, \tag{A.15}$$

the divergence operators

$$\nabla_x\cdot\boldsymbol{a}=\frac{\partial a_i}{\partial x_j}\boldsymbol{g}_i\cdot\boldsymbol{g}_j=\frac{\partial a_i}{\partial x_i}, \qquad \nabla_X\cdot\boldsymbol{a}=\frac{\partial a_i}{\partial X_j}\boldsymbol{g}_i\cdot\boldsymbol{g}_j=\frac{\partial a_i}{\partial X_i}, \tag{A.16}$$

$$\nabla_x\cdot\boldsymbol{A}=\frac{\partial A_{ij}}{\partial x_k}\boldsymbol{g}_i\otimes\boldsymbol{g}_j\cdot\boldsymbol{g}_k=\frac{\partial A_{ij}}{\partial x_j}\boldsymbol{g}_i, \qquad \nabla_X\cdot\boldsymbol{A}=\frac{\partial A_{ij}}{\partial X_k}\boldsymbol{g}_i\otimes\boldsymbol{g}_j\cdot\boldsymbol{g}_k=\frac{\partial A_{ij}}{\partial X_j}\boldsymbol{g}_i \tag{A.17}$$

are constructed using the dot product. The deformation gradient $\boldsymbol{F}=\nabla_X\boldsymbol{x}$, see **Chapter 2**, can be considered as a special case of Term $(\mathrm{A.14})_2$. Moreover, the expressions in (A.14)-(A.17)

can be linked by applying the chain rule or the product rule as well as the deformation gradient $\boldsymbol{F}$

$$
\begin{aligned}
\nabla_x \cdot \boldsymbol{A} \quad &= \frac{\partial A_{ij}}{\partial X_k} \frac{\partial X_l}{\partial x_m} [\boldsymbol{g}_i \otimes \boldsymbol{g}_j \otimes \boldsymbol{g}_k \cdot \boldsymbol{g}_l] \cdot \boldsymbol{g}_m = \frac{\partial A_{ij}}{\partial X_k} \frac{\partial X_k}{\partial x_j} \boldsymbol{g}_i \qquad = \nabla_X \boldsymbol{A} : \boldsymbol{F}^{-\mathrm{T}}, \\
\nabla_X \boldsymbol{A} \quad &= \frac{\partial A_{ij}}{\partial x_l} \frac{\partial x_m}{\partial X_k} \boldsymbol{g}_i \otimes \boldsymbol{g}_j \otimes \boldsymbol{g}_l \cdot \boldsymbol{g}_m \otimes \boldsymbol{g}_k = \frac{\partial A_{ij}}{\partial x_l} \frac{\partial x_l}{\partial X_k} \boldsymbol{g}_i \otimes \boldsymbol{g}_j \otimes \boldsymbol{g}_k \quad = \nabla_x \boldsymbol{A} \cdot \boldsymbol{F}, \\
\nabla_x \cdot [\boldsymbol{A} \cdot \boldsymbol{B}] &= \frac{\partial [A_{ij} B_{jk}]}{\partial x_k} \boldsymbol{g}_i \qquad = \frac{\partial A_{ij}}{\partial x_k} B_{jk} \boldsymbol{g}_i + \frac{\partial B_{jk}}{\partial x_k} A_{ij} \boldsymbol{g}_i = \nabla_x \boldsymbol{A} : \boldsymbol{B} + \boldsymbol{A} \cdot [\nabla_x \cdot \boldsymbol{B}], \\
\nabla_X \cdot [\boldsymbol{A} \cdot \boldsymbol{B}] &= \frac{\partial [A_{ij} B_{jk}]}{\partial X_k} \boldsymbol{g}_i \qquad = \frac{\partial A_{ij}}{\partial X_k} B_{jk} \boldsymbol{g}_i + \frac{\partial B_{jk}}{\partial X_k} A_{ij} \boldsymbol{g}_i = \nabla_X \boldsymbol{A} : \boldsymbol{B} + \boldsymbol{A} \cdot [\nabla_X \cdot \boldsymbol{B}], \\
\nabla_X \cdot [\boldsymbol{A} \cdot \boldsymbol{b}] &= \frac{\partial [A_{ij} b_j]}{\partial X_i} \qquad = \frac{\partial A_{ij}}{\partial X_i} b_j + \frac{\partial b_j}{\partial X_i} A_{ij} \qquad = [\nabla_X \cdot \boldsymbol{A}^{\mathrm{T}}] \cdot \boldsymbol{b} + \boldsymbol{A}^{\mathrm{T}} : \nabla_X \boldsymbol{b}.
\end{aligned}
\tag{A.18}
$$

For further connections see (Ehlers, 2009; Holzapfel, 2000; Kelly, 2015).

A.3. Applications

For the mathematical formulations of the distinct elasto(visco)plastic problems, the tensor calculus is essential. If the numerical implementation is performed using Newton-like procedures, tangential matrices have to be determined, see Section 3.2. This can be accomplished numerically, cf. (Wriggers, 2008), or explicitly by exploiting the rules listed in **Appendix A.2**. In this thesis, the explicit fashion is chosen. Thus, in the following, the derivatives needed for the tangential quantities of the distinct models and approaches are illustrated.

A.3.1. Small Strain Elasto(visco)plasticity - Classical Approach

In the classical approach towards small strain elasto(visco)plasticity, the only unknowns are the displacements, see **Chapter 4**. Hence, the tangential stiffness matrix is the only nonlinear expression that has to be linearized in the context of Newton-like procedures. Conventionally, this implies that, in each iteration and for all required points in time, the derivative of the stress tensor is calculated with respect to the strain tensor, see Section 4.1.3.2. In the purely elastic case, this results in the constitutive tensor $\mathbb{C}_{\mathrm{e}}$. For the plastic or viscoplastic case, the following essential derivatives are elaborated, whereby the spatial as well as temporal dependencies will be dropped for simplicity.

Derivatives in Plasticity with Stiffly Accurate DIRK Schemes or the Newmark Method

The basis for the tangential stiffness matrix in elastoplasticity is the derivative of the stress tensor

$$
\left. \frac{\partial \boldsymbol{\sigma}_{ni/n+1}}{\partial \boldsymbol{\varepsilon}^{e}_{ni/n+1}} \right|_k = \frac{\partial \mathrm{sph}\left(\boldsymbol{\sigma}^{k}_{ni/n+1}\right)}{\partial \boldsymbol{\varepsilon}^{e,k}_{ni/n+1}} + \frac{\partial \mathrm{dev}\left(\boldsymbol{\sigma}^{k}_{ni/n+1}\right)}{\partial \boldsymbol{\varepsilon}^{e,k}_{ni/n+1}}
\tag{A.19}
$$

together with the definitions of the individual quantities in (4.30)-(4.38) and (4.41). Exploiting

the relations in **Appendix A.1** and **Appendix A.2** yields the necessary derivatives

$$\frac{\partial \mathrm{sph}\left(\boldsymbol{\sigma}^{k}_{ni/n+1}\right)}{\partial \boldsymbol{\varepsilon}^{e,k}_{ni/n+1}} = \frac{3\kappa + 2\mu}{3} \boldsymbol{I} \otimes \boldsymbol{I}, \tag{A.20}$$

$$\frac{\partial \mathrm{dev}\left(\boldsymbol{\sigma}^{\mathrm{trial},k}_{ni/n+1}\right)}{\partial \boldsymbol{\varepsilon}^{e,k}_{ni/n+1}} = 2\mu \left[\mathbb{I} - \frac{1}{3} \boldsymbol{I} \otimes \boldsymbol{I}\right], \tag{A.21}$$

$$\frac{\partial \left[\lambda_{ni/n+1} \boldsymbol{n}^{k}_{\mathrm{p}}\right]}{\partial \boldsymbol{\varepsilon}^{e,k}_{ni/n+1}} = \boldsymbol{n}^{k}_{\mathrm{p}} \otimes \frac{\partial \lambda_{ni/n+1}}{\partial \boldsymbol{\varepsilon}^{e}_{ni/n+1}} + \lambda_{ni/n+1} \frac{\partial \boldsymbol{n}^{k}_{\mathrm{p}}}{\partial \boldsymbol{\varepsilon}^{e,k}_{ni/n+1}}, \tag{A.22}$$

$$\frac{\partial \boldsymbol{n}^{k}_{\mathrm{p}}}{\partial \boldsymbol{\varepsilon}^{e,k}_{ni/n+1}} = -\frac{2\mu}{\left\| \mathrm{dev}\left(\boldsymbol{\sigma}^{k,\mathrm{trial}}_{ni/n+1}\right)\right\|} \boldsymbol{n}^{k}_{\mathrm{p}} \otimes \boldsymbol{n}^{k}_{\mathrm{p}} + \frac{2\mu}{\left\| \mathrm{dev}\left(\boldsymbol{\sigma}^{k,\mathrm{trial}}_{ni/n+1}\right)\right\|} \left[\mathbb{I} - \frac{1}{3} \boldsymbol{I} \otimes \boldsymbol{I}\right], \tag{A.23}$$

$$\frac{\partial \lambda_{ni/n+1}}{\partial \boldsymbol{\varepsilon}^{e,k}_{ni/n+1}} = \frac{1}{\Delta t\, \Theta} \boldsymbol{n}^{k}_{\mathrm{p}} \tag{A.24}$$

and the algorithmic constitutive tensor

$$\mathbb{G} = \frac{3\kappa + 2\mu}{3} \boldsymbol{I} \otimes \boldsymbol{I} + \left[2\mu - \frac{4\mu^2\, \Delta t\, \Theta \lambda_{ni/n+1}}{\left\| \mathrm{dev}\left(\boldsymbol{\sigma}^{k,\mathrm{trial}}_{ni/n+1}\right)\right\|}\right] \left[\mathbb{I} - \frac{1}{3} \boldsymbol{I} \otimes \boldsymbol{I} - \boldsymbol{n}^{k}_{\mathrm{p}} \otimes \boldsymbol{n}^{k}_{\mathrm{p}}\right].$$

Derivatives in Viscoplasticity with Stiffly Accurate DIRK Schemes or the Newmark Method

If, instead of the elastoplastic problem, the viscoplastic problem is considered within the classical approach, the necessary derivatives are identical to those in Equations (A.19)-(A.23). Only the Lagrange multiplier is determined alternatively - leading to the derivative

$$\frac{\partial \lambda_{ni/n+1}}{\partial \boldsymbol{\varepsilon}^{e,k}_{ni/n+1}} = \frac{2\mu}{\chi + 2\mu\, \Delta t\, \Theta} \boldsymbol{n}^{k}_{\mathrm{p}}$$

and the algorithmic constitutive tensor

$$\mathbb{G} = \frac{3\kappa + 2\mu}{3} \boldsymbol{I} \otimes \boldsymbol{I} + \left[2\mu - \frac{4\mu^2\, \Delta t\, \Theta \lambda_{ni/n+1}}{\left\| \mathrm{dev}\left(\boldsymbol{\sigma}^{k,\mathrm{trial}}_{ni/n+1}\right)\right\|}\right] \left[\mathbb{I} - \frac{1}{3} \boldsymbol{I} \otimes \boldsymbol{I}\right] -$$

$$-2\mu \left[\frac{2\mu \Delta t\, \Theta}{\chi + 2\mu \Delta t\, \Theta} + \frac{2\mu\, \Delta t\, \Theta \lambda_{ni/n+1}}{\left\| \mathrm{dev}\left(\boldsymbol{\sigma}^{k,\mathrm{trial}}_{ni/n+1}\right)\right\|}\right] \boldsymbol{n}^{k}_{\mathrm{p}} \otimes \boldsymbol{n}^{k}_{\mathrm{p}}.$$

A.3.2. Small Strain Elasto(visco)plasticity - Variational Approach

Within the variational approach of small strain elasto(visco)plasticity, the displacements, the plastic strains, the stresses, and the Lagrange multiplier embody the unknown primary variables. Hence, if Newton-like procedures are applied as solution strategies, a linearization with respect to all these quantities has to be performed. In the conventional ansatz, the linearization demands that a proper time discretization scheme is chosen beforehand, to establish the

coupling between the balance law and the material equations. In the multifield approach, the time integration can be carried out afterwards, due to the equivalence of the distinct types of equations. In the following, the derivatives of the elastoplastic and the viscoplastic case will thus be listed without paying attention to the point in time where an evaluation is taking place.

Derivatives in Variational Elastoplasticity

The starting points for the linearization of the multifield elastoplastic model are the weak forms in (4.66)-(4.69) in their spatially discretized setting on element level. Furthermore, the tensor calculus introduced in **Appendix A.1-Appendix A.2** is applied. In the following, the essential derivatives are summarized

$$\mathrm{D}^k_{\ddot{\boldsymbol{u}}^e}\ddot{\boldsymbol{u}}^{e,k} = \boldsymbol{I} \;:\Delta\ddot{\boldsymbol{u}}^e, \qquad \mathrm{D}^k_{\boldsymbol{\sigma}^e}\boldsymbol{\sigma}^{e,k} = \boldsymbol{I} \;:\Delta\boldsymbol{\sigma}^e, \tag{A.25}$$

$$\mathrm{D}^k_{\boldsymbol{\varepsilon}^e}\left[\mathbb{C}_\mathrm{e}:\left[\boldsymbol{\varepsilon}^{e,k}-\boldsymbol{\varepsilon}^{e,k}_\mathrm{p}\right]\right] = \mathbb{C}_\mathrm{e}:\Delta\boldsymbol{\varepsilon}^e, \qquad \mathrm{D}^k_{\boldsymbol{\varepsilon}^e_\mathrm{p}}\left[\mathbb{C}_\mathrm{e}:\left[\boldsymbol{\varepsilon}^{e,k}-\boldsymbol{\varepsilon}^{e,k}_\mathrm{p}\right]\right] = -\mathbb{C}_\mathrm{e}:\Delta\boldsymbol{\varepsilon}^e_\mathrm{p}, \tag{A.26}$$

$$\mathrm{D}^k_{\dot{\boldsymbol{\varepsilon}}^e_\mathrm{p}}\dot{\boldsymbol{\varepsilon}}^{e,k}_\mathrm{p} = \boldsymbol{I} \;:\Delta\dot{\boldsymbol{\varepsilon}}^{\,e}_\mathrm{p}, \tag{A.27}$$

$$\mathrm{D}^k_{\lambda^e}\left[\left.\frac{\partial f(\boldsymbol{\sigma}^e)}{\partial\boldsymbol{\sigma}^e}\right|_k\lambda^{e,k}\right] = \frac{\operatorname{dev}\left(\boldsymbol{\sigma}^{e,k}\right)}{\left\|\operatorname{dev}\left(\boldsymbol{\sigma}^{e,k}\right)\right\|}\Delta\lambda^e,$$

$$\mathrm{D}^k_{\boldsymbol{\sigma}^e}\left[\left.\frac{\partial f(\boldsymbol{\sigma}^e)}{\partial\boldsymbol{\sigma}^e}\right|_k\lambda^{e,k}\right] = \lambda^{e,k}\left[-\frac{\operatorname{dev}\left(\boldsymbol{\sigma}^{e,k}\right)\otimes\operatorname{dev}\left(\boldsymbol{\sigma}^{e,k}\right)}{\left\|\operatorname{dev}\left(\boldsymbol{\sigma}^{e,k}\right)\right\|^3}+\frac{1}{\left\|\operatorname{dev}\left(\boldsymbol{\sigma}^{e,k}\right)\right\|}\left[\mathbb{I}-\frac{1}{3}\boldsymbol{I}\otimes\boldsymbol{I}\right]\right]:\Delta\boldsymbol{\sigma}^e,$$

whereby the spatial as well as temporal dependencies are dropped for simplicity.

Derivatives in Variational Viscoplasticity

Within the variational viscoplastic approach, the weak forms in (4.70)-(4.72) in their spatially discretized setting on element level have to be linearized. Hence, the Equations (A.25)-(A.27) must be considered, too. Furthermore, the penalization function substituting the Lagrange multiplier has to be accounted for

$$\mathrm{D}^k_{\boldsymbol{\sigma}^e}\left[\frac{1}{\chi}\langle f(\boldsymbol{\sigma}^{e,k})\rangle\left.\frac{\partial f(\boldsymbol{\sigma}^e)}{\partial\boldsymbol{\sigma}^e}\right|_k\right] = \frac{1}{\chi}\langle f(\boldsymbol{\sigma}^{e,k})\rangle\left[\frac{-\operatorname{dev}\left(\boldsymbol{\sigma}^{e,k}\right)\otimes\operatorname{dev}\left(\boldsymbol{\sigma}^{e,k}\right)}{\left\|\operatorname{dev}\left(\boldsymbol{\sigma}^{e,k}\right)\right\|^3}+\frac{1}{\left\|\operatorname{dev}\left(\boldsymbol{\sigma}^{e,k}\right)\right\|}\left[\mathbb{I}-\frac{1}{3}\boldsymbol{I}\otimes\boldsymbol{I}\right]\right]:\Delta\boldsymbol{\sigma}^e +$$

$$+\frac{1}{2\chi}\left[\left[1+\frac{f(\boldsymbol{\sigma}^{e,k})}{|f(\boldsymbol{\sigma}^{e,k})|}\right]\frac{\operatorname{dev}\left(\boldsymbol{\sigma}^{e,k}\right)}{\left\|\operatorname{dev}\left(\boldsymbol{\sigma}^{e,k}\right)\right\|}\otimes\frac{\operatorname{dev}\left(\boldsymbol{\sigma}^{e,k}\right)}{\left\|\operatorname{dev}\left(\boldsymbol{\sigma}^{e,k}\right)\right\|}\right]:\Delta\boldsymbol{\sigma}^e.$$

A.3.3. Finite Strain Elasto(visco)plasticity - Classical Approach

Within the finite strain regime, a series of tensor operations has to be performed on distinct levels. While in the small strain regime elasto(visco)plastic problems are solely characterized by material nonlinearities, finite deformations involve geometric nonlinearities as well. This leads to a profound application of tensor calculus already in the area of model derivation. Further usage is made in the field of numerical implementation.

Tensor Operations in the Context of the Finite Elasto(visco)plastic Model Derivation

In order to establish the elasto(visco)plastic material laws, the relationships between various derivatives of the internal energy are necessary

$$\frac{\partial e}{\partial \boldsymbol{C}} = \frac{\partial e}{\partial \hat{\boldsymbol{C}}_\mathrm{e}} : \frac{\partial \hat{\boldsymbol{C}}_\mathrm{e}}{\partial \boldsymbol{C}}, \qquad \frac{\partial e}{\partial \boldsymbol{C}} = \boldsymbol{F}_\mathrm{p}^{-1} \cdot \frac{\partial e}{\partial \hat{\boldsymbol{C}}_\mathrm{e}} \cdot \boldsymbol{F}_\mathrm{p}^{-\mathrm{T}},$$

$$\frac{\partial e}{\partial \boldsymbol{F}_\mathrm{p}^{-1}} = \frac{\partial e}{\partial \hat{\boldsymbol{C}}_\mathrm{e}} : \frac{\partial \hat{\boldsymbol{C}}_\mathrm{e}}{\partial \boldsymbol{F}_\mathrm{p}^{-1}}, \qquad \frac{\partial e}{\partial \boldsymbol{F}_\mathrm{p}^{-1}} = 2\boldsymbol{C} \cdot \boldsymbol{F}_\mathrm{p}^{-1} \cdot \frac{\partial e}{\partial \hat{\boldsymbol{C}}_\mathrm{e}},$$

$$\frac{\partial e}{\partial \boldsymbol{F}_\mathrm{p}^{-1}} = \frac{\partial e}{\partial \boldsymbol{C}_\mathrm{p}^{-1}} : \frac{\partial \boldsymbol{C}_\mathrm{p}^{-1}}{\partial \boldsymbol{F}_\mathrm{p}^{-1}}, \qquad \frac{\partial e}{\partial \boldsymbol{F}_\mathrm{p}^{-1}} = 2\frac{\partial e}{\partial \boldsymbol{C}_\mathrm{p}^{-1}} \cdot \boldsymbol{F}_\mathrm{p}^{-1}.$$

With the balance of linear momentum and the material laws at hand, the numerical solution procedure of an elasto(visco)plastic problem can be started. If general NEWTON schemes are used in this context, a linearization process has to be carried out due to the material and geometric nonlinearities.

Linearization of the Weak Form of the Finite Elasto(visco)plastic Model

In this thesis, the finite element method is generally, used for the spatial resolution of the primary variables' course. Hence, as a starting point, the nonlinear weak form of the balance of linear momentum is obtained. It has to be linearized before a conventional linear equation solver can be applied. Therefore, the following steps are performed

$$\mathrm{D}^k_{\ddot{\boldsymbol{u}}^e} \ddot{\boldsymbol{u}}^{e,k} = \boldsymbol{I} : \Delta \ddot{\boldsymbol{u}}^e, \tag{A.28}$$

$$\mathrm{D}^k_{\boldsymbol{F}^e} \left[\left[\boldsymbol{F}^{e,\mathrm{T}} \cdot \delta \boldsymbol{F}^e \right] : \boldsymbol{S} \right] \Big|_k = \mathrm{D}^k_{\boldsymbol{F}^e} \left[\left[\delta \boldsymbol{F}^e \cdot \boldsymbol{F}^{e,\mathrm{T}} \right] : \boldsymbol{S} \right] \Big|_k =$$

$$= \left[\boldsymbol{F}^{e,k,\mathrm{T}} \cdot \delta \boldsymbol{F}^{e,k} \right] : \frac{\partial \boldsymbol{S}}{\partial \boldsymbol{E}} \Big|_k : \left[\Delta \boldsymbol{F}^{e,\mathrm{T}} \cdot \boldsymbol{F}^{e,k} \right] + \left[\delta \boldsymbol{F}^{e,k,\mathrm{T}} \cdot \Delta \boldsymbol{F}^e \right] : \boldsymbol{S}^k. \tag{A.29}$$

Furthermore, a series of derivations has to be performed to obtain the tangential stiffness matrix.

Derivatives in Finite Elastoplasticity with Stiffly Accurate DIRK Schemes and the NEWMARK method

The application of diagonal implicit RUNGE-KUTTA schemes or the NEWMARK method leads in the general elastoplastic case to the stress tensor of Equation (6.28) consisting of a volumetric part $\boldsymbol{S}^{k,\mathrm{vol}}_{ni/n+1}$ and a deviatoric part. The latter can be divided into

$$\mathrm{DEV}\left(\boldsymbol{S}^k_{ni/n+1}\right) = \mathrm{DEV}\left(\boldsymbol{S}^{k,\mathrm{trial}}_{ni/n+1}\right) + \mathrm{DEV}\left(\boldsymbol{S}^{k,\mathrm{plas}}_{ni/n+1}\right). \tag{A.30}$$

The trial state therein is defined by

$$\mathrm{DEV}\left(\boldsymbol{S}^{k,\mathrm{trial}}_{ni/n+1}\right) = \mu \left[J^{e,k}_{ni/n+1} \right]^{-\frac{2}{3}} \mathrm{DEV}\left(\tilde{\boldsymbol{C}}^{-1}_{\mathrm{p},ni/n} \right), \tag{A.31}$$

which is used to define the attached expression

$$\boldsymbol{B}^{k,\mathrm{trial}}_1 = \sqrt{\left[\mathrm{DEV}(\boldsymbol{S}^{k,\mathrm{trial}}_{ni/n+1}) \cdot \boldsymbol{C}^{e,k}_{ni/n+1} \right] : \left[\boldsymbol{C}^{e,k}_{ni/n+1} \cdot \mathrm{DEV}(\boldsymbol{S}^{k,\mathrm{trial}}_{ni/n+1}) \right]}. \tag{A.32}$$

If plastic deformations occur

$$\begin{aligned}\mathrm{DEV}\left(\boldsymbol{S}^{k,\mathrm{plas}}_{ni/n+1}\right)&=-\frac{2}{3}\Delta t\Theta\,\lambda_{ni/n+1}\mu\frac{\left[J^{e,k}_{ni/n+1}\right]^{-\frac{2}{3}}\mathrm{Tr}\left(\tilde{\boldsymbol{C}}^{-1}_{\mathrm{p},ni/n}\right)\mathrm{DEV}\left(\boldsymbol{S}^{k,\mathrm{trial}}_{ni/n+1}\right)}{\boldsymbol{B}^{k,\mathrm{trial}}_{1}}=\\&=\left[\frac{\sqrt{\frac{2}{3}}y}{\boldsymbol{B}^{k,\mathrm{trial}}_{1}}-1\right]\mathrm{DEV}\left(\boldsymbol{S}^{k,\mathrm{trial}}_{ni/n+1}\right)\end{aligned}\tag{A.33}$$

has to be considered together with the LAGRANGE multiplier of Equation (6.39). To determine the tangential stiffness matrix, the stress tensor's derivative with respect to the right CAUCHY-GREEN tensor has to be calculated. Hence, with the expressions in **Appendix A.2**, the following terms are obtained:

$$\begin{aligned}\left.\frac{\partial\boldsymbol{S}^{\mathrm{vol}}_{ni/n+1}}{\partial\boldsymbol{C}^{e}_{ni/n+1}}\right|_k&=\frac{3\kappa+2\mu}{6}\left[J^{e,k}_{ni/n+1}\right]^2\left[\left[\boldsymbol{C}^{e,k}_{ni/n+1}\right]^{-1}\otimes\left[\boldsymbol{C}^{e,k}_{ni/n+1}\right]^{-1}\right]-\\&-\frac{3\kappa+2\mu}{6}\left[\left[J^{e,k}_{ni/n+1}\right]^2-1\right]\left[\left[\boldsymbol{C}^{e,k}_{ni/n+1}\right]^{-1}\otimes\left[\boldsymbol{C}^{e,k}_{ni/n+1}\right]^{-1}\right]^{\overset{23}{\mathrm{T}}},\end{aligned}\tag{A.34}$$

$$\begin{aligned}\left.\frac{\partial\mathrm{DEV}\left(\boldsymbol{S}^{\mathrm{trial}}_{ni/n+1}\right)}{\partial\boldsymbol{C}^{e}_{ni/n+1}}\right|_k&=\frac{1}{3}\mu\left[J^{e,k}_{ni/n+1}\right]^{-\frac{2}{3}}\mathrm{Tr}\left(\tilde{\boldsymbol{C}}^{-1}_{\mathrm{p},ni/n}\right)\left[\left[\left[\boldsymbol{C}^{e,k}_{ni/n+1}\right]^{-1}\otimes\left[\boldsymbol{C}^{e,k}_{ni/n+1}\right]^{-1}\right]^{\overset{23}{\mathrm{T}}}+\right.\\&\left.+\frac{1}{3}\left[\left[\boldsymbol{C}^{e,k}_{ni/n+1}\right]^{-1}\otimes\left[\boldsymbol{C}^{e,k}_{ni/n+1}\right]^{-1}\right]\right]-\\&-\frac{1}{3}\mu\left[J^{e,k}_{ni/n+1}\right]^{-\frac{2}{3}}\left[\tilde{\boldsymbol{C}}^{-1}_{\mathrm{p},ni/n}\otimes\left[\boldsymbol{C}^{e,k}_{ni/n+1}\right]^{-1}+\left[\boldsymbol{C}^{e,k}_{ni/n+1}\right]^{-1}\otimes\tilde{\boldsymbol{C}}^{-1}_{\mathrm{p},ni/n}\right],\end{aligned}\tag{A.35}$$

$$\begin{aligned}\left.\frac{\partial\mathrm{DEV}\left(\boldsymbol{S}^{\mathrm{plas}}_{ni/n+1}\right)}{\partial\boldsymbol{C}^{e}_{ni/n+1}}\right|_k&=\mathrm{DEV}\left(\boldsymbol{S}^{k,\mathrm{trial}}_{ni}\right)\otimes\frac{\partial}{\partial\boldsymbol{C}^{e}_{ni/n+1}}\left[\sqrt{\frac{2}{3}}y\frac{1}{\boldsymbol{B}^{k,\mathrm{trial}}_{1}}-1\right]\Bigg|_k+\\&+\left[\sqrt{\frac{2}{3}}y\frac{1}{\boldsymbol{B}^{k,\mathrm{trial}}_{1}}-1\right]\left.\frac{\partial\mathrm{DEV}\left(\boldsymbol{S}^{\mathrm{trial}}_{ni/n+1}\right)}{\partial\boldsymbol{C}^{e}_{ni/n+1}}\right|_k=\\&=\frac{-\sqrt{\frac{2}{3}}y\,\mathrm{DEV}\left(\boldsymbol{S}^{k,\mathrm{trial}}_{ni/n+1}\right)\otimes\boldsymbol{B}^{k,\mathrm{trial}}_{2}}{[\boldsymbol{B}^{k,\mathrm{trial}}_{1}]^3}+\\&+\frac{-\sqrt{\frac{2}{3}}y\,\mathrm{DEV}\left(\boldsymbol{S}^{k,\mathrm{trial}}_{ni/n+1}\right)\otimes\left[\boldsymbol{B}^{k,\mathrm{trial}}_{3}:\left.\frac{\partial\mathrm{DEV}(\boldsymbol{S}^{\mathrm{trial}}_{ni/n+1})}{\partial\boldsymbol{C}^{e}_{ni/n+1}}\right|_k\right]}{[\boldsymbol{B}^{k,\mathrm{trial}}_{1}]^3}+\\&+\left[\sqrt{\frac{2}{3}}y\frac{1}{\boldsymbol{B}^{k,\mathrm{trial}}_{1}}-1\right]\left.\frac{\partial\mathrm{DEV}\left(\boldsymbol{S}^{\mathrm{trial}}_{ni/n+1}\right)}{\partial\boldsymbol{C}^{e}_{ni/n+1}}\right|_{k.}\end{aligned}\tag{A.36}$$

Additionally, the abbreviations

$$\boldsymbol{B}^{k,\mathrm{trial}}_{2}=\mathrm{DEV}(\boldsymbol{S}^{k,\mathrm{trial}}_{ni/n+1})\cdot\boldsymbol{C}^{e,k}_{ni/n+1}\cdot\mathrm{DEV}(\boldsymbol{S}^{k,\mathrm{trial}}_{ni/n+1}),\tag{A.37}$$

$$\boldsymbol{B}^{k,\mathrm{trial}}_{3}=\left[\boldsymbol{C}^{e,k}_{ni/n+1}\cdot\mathrm{DEV}(\boldsymbol{S}^{k,\mathrm{trial}}_{ni/n+1})\cdot\boldsymbol{C}^{e,k}_{ni/n+1}\right],\tag{A.38}$$

are taken into account.

Derivatives in Finite Viscoplasticity with Stiffly Accurate DIRK Schemes and the Newmark method

In the case of viscoplastic deformations, the Relations (A.30)-(A.31) can still be applied. Hence, also the derivatives in (A.34) and (A.35) remain valid. However, the Lagrange multiplier is modified - yielding

$$\mathrm{DEV}(\boldsymbol{S}^{k,\mathrm{plas}}_{ni/n+1}) = \frac{\bar{\mu}}{\chi+\bar{\mu}} \left[\frac{\sqrt{\frac{2}{3}}y}{\boldsymbol{B}^{k,\mathrm{trial}}_{1}} - 1 \right] \mathrm{DEV}(\boldsymbol{S}^{k,\mathrm{trial}}_{ni/n+1})$$

with

$$\bar{\mu} = \frac{2}{3}\mu\, \Delta t \Theta \left[J^{e,k}_{ni/n+1} \right]^{-\frac{2}{3}} \mathrm{Tr}\left(\tilde{\boldsymbol{C}}^{-1}_{\mathrm{p},ni/n} \right).$$

Thus, the derivative (A.36) has to be adapted to

$$\begin{aligned}
\left.\frac{\partial \mathrm{DEV}\left(\boldsymbol{S}^{\mathrm{plas}}_{ni/n+1}\right)}{\partial \boldsymbol{C}^{e}_{ni/n+1}}\right|_{k} = {} & \frac{-\sqrt{\frac{2}{3}}y\, \mathrm{DEV}\left(\boldsymbol{S}^{k,\mathrm{trial}}_{ni/n+1}\right) \frac{\bar{\mu}}{\chi+\bar{\mu}} \otimes \boldsymbol{B}^{k,\mathrm{trial}}_{2}}{[\boldsymbol{B}^{k,\mathrm{trial}}]^{3}} + \\
& + \frac{-\sqrt{\frac{2}{3}}y\, \mathrm{DEV}\left(\boldsymbol{S}^{k,\mathrm{trial}}_{ni/n+1}\right) \frac{\bar{\mu}}{\chi+\bar{\mu}} \otimes \left[\boldsymbol{B}^{k,\mathrm{trial}}_{3} : \left.\frac{\partial \mathrm{DEV}(\boldsymbol{S}^{\mathrm{trial}}_{ni/n+1})}{\partial \boldsymbol{C}^{e}_{ni/n+1}}\right|_{k} \right]}{[\boldsymbol{B}^{k,\mathrm{trial}}]^{3}} + \\
& + \frac{\bar{\mu}}{\chi+\bar{\mu}} \left[\frac{\sqrt{\frac{2}{3}}y}{\boldsymbol{B}^{k,\mathrm{trial}}} - 1 \right] \left.\frac{\partial \mathrm{DEV}\left(\boldsymbol{S}^{\mathrm{trial}}_{ni/n+1}\right)}{\partial \boldsymbol{C}^{e}_{ni/n+1}}\right|_{k} + \\
& + \left[\sqrt{\frac{2}{3}}y \frac{1}{\boldsymbol{B}^{k,\mathrm{trial}}} - 1 \right] \mathrm{DEV}\left(\boldsymbol{S}^{k,\mathrm{trial}}_{ni/n+1}\right) \otimes \frac{\frac{2}{3}\Delta t \Theta \chi\, \mathrm{DEV}\left(\boldsymbol{S}^{k,\mathrm{trial}}_{ni/n+1}\right)}{[\chi+\bar{\mu}]^{2}}.
\end{aligned}$$

A.3.4. Finite Strain Elasto(visco)plasticity - Variational Approach

The multifield ansatz towards finite strain plasticity is based on the weak formulation of the balance of linear momentum and the material laws. As main ingredients for an accurate solution strategy in this thesis, the finite element method is applied together with a series of distinct time integration schemes. Moreover, Newton-like procedures are exploited to convert the obtained systems of nonlinear equations into linear ones. Therefore, various derivatives have to be calculated. In the classical approach to (visco)plasticity, their evaluation at a specific point in time is necessary to couple the material laws to the balance of linear momentum. Within the variational ansatz, this is superfluous, since an explicit link between the different equations prevails. In the following, the derivatives are thus presented without an index indicating the considered point in time. Furthermore, the isochoric flow property with $J_{\mathrm{p}} = 1$, cf. (Simo and Hughes, 1997; Simo and Miehe, 1992), is exploited.

Derivatives in Variational Finite Elastoplasticity

The solution process of the multifield approach towards finite elastoplasticity rests on a semi-smooth NEWTON procedure. This includes a number of linearizations on element level exploiting the GÂTEAUX derivative in (3.22) and the generalized gradient in (3.32).

$$\mathrm{D}^k_{\boldsymbol{F}^e}\left[\left[\boldsymbol{F}^{e,\mathrm{T}}\cdot\delta\dot{\boldsymbol{F}}^e\right]:\frac{\partial e}{\partial\boldsymbol{C}^e}\right]\Big|_k = \left[\boldsymbol{F}^{\mathrm{e,k,T}}\cdot\delta\dot{\boldsymbol{F}}^{e,k}\right]:2\frac{\partial^2 e}{\partial\left[\boldsymbol{C}^e\right]^2}\Big|_k:\left[\Delta\boldsymbol{F}^{e,k,\mathrm{T}}\cdot\boldsymbol{F}^{e,k}\right]+ \\ +\left[\delta\dot{\boldsymbol{F}}^{e,k,\mathrm{T}}\cdot\Delta\boldsymbol{F}^{e,k}\right]:\frac{\partial e}{\partial\boldsymbol{C}^e}\Big|_k, \tag{A.39}$$

$$\mathrm{D}^k_{\ddot{\boldsymbol{u}}^e}\ddot{\boldsymbol{u}}^{e,k} = \boldsymbol{I}:\Delta\ddot{\boldsymbol{u}}, \qquad \mathrm{D}^k_{\boldsymbol{F}^e}\frac{\partial e}{\partial\boldsymbol{C}^e}\Big|_k = 2\frac{\partial^2 e}{\partial\left[\boldsymbol{C}^e\right]^2}\Big|_k:\left[\Delta\boldsymbol{F}^{e,k,\mathrm{T}}\cdot\boldsymbol{F}^{e,k}\right], \tag{A.40}$$

$$\mathrm{D}^k_{\boldsymbol{S}^e}\boldsymbol{S}^{e,k} = \boldsymbol{I}:\Delta\boldsymbol{S}^e, \qquad \mathrm{D}^k_{\boldsymbol{C}_\mathrm{p}^{e,-1}}\frac{\partial e}{\partial\boldsymbol{C}^e}\Big|_k = 2\frac{\partial^2 e}{\partial\boldsymbol{C}^e\partial\boldsymbol{C}_\mathrm{p}^{e,-1}}\Big|_k:\Delta\boldsymbol{C}_\mathrm{p}^{e,-1}, \tag{A.41}$$

$$\mathrm{D}^k_{\dot{\boldsymbol{C}}_\mathrm{p}^{e,-1}}\left[\dot{\boldsymbol{C}}_\mathrm{p}^{e,k,-1}\right]=\boldsymbol{I}:\Delta\dot{\boldsymbol{C}}_\mathrm{p}^{e,-1}, \qquad \mathrm{D}^k_{\boldsymbol{S}^e}f(\boldsymbol{C}^{e,k},\boldsymbol{S}^{e,k})=\frac{\partial f(\boldsymbol{C}^e,\boldsymbol{S}^e)}{\partial\boldsymbol{S}^e}\Big|_k:\Delta\boldsymbol{S}^e, \tag{A.42}$$

The introduction of the abbreviation

$$\boldsymbol{B}_1=\sqrt{\left[\mathrm{DEV}(\boldsymbol{S})\cdot\boldsymbol{C}\right]:\left[\boldsymbol{C}\cdot\mathrm{DEV}(\boldsymbol{S})\right]}, \tag{A.43}$$

in analogy to (A.32) results in further derivatives

$$\mathrm{D}^k_{\boldsymbol{F}^e}f(\boldsymbol{C}^{e,k},\boldsymbol{S}^{e,k}) = 2\frac{\partial f(\boldsymbol{C}^e,\boldsymbol{S}^e)}{\partial\boldsymbol{C}^e}\Big|_k:\left[\Delta\boldsymbol{F}^{e,k,\mathrm{T}}\cdot\boldsymbol{F}^{e,k}\right],$$

$$\mathrm{D}^k_{\lambda^e}\left[\lambda^e\frac{\mathrm{Tr}\left(\boldsymbol{C}_\mathrm{p}^{e,-1}\right)\mathrm{DEV}\left(\boldsymbol{S}^e\right)}{\boldsymbol{B}_1^e}\right]\Big|_k = \frac{\mathrm{Tr}\left(\left[\boldsymbol{C}_\mathrm{p}^{e,k}\right]^{-1}\right)\mathrm{DEV}\left(\boldsymbol{S}^{e,k}\right)}{\boldsymbol{B}_1^{e,k}}\Delta\lambda^e,$$

$$\mathrm{D}^k_{\boldsymbol{C}_\mathrm{p}^{e,-1}}\left[\lambda^e\frac{\mathrm{Tr}\left(\boldsymbol{C}_\mathrm{p}^{e,-1}\right)\mathrm{DEV}\left(\boldsymbol{S}^e\right)}{\boldsymbol{B}_1^e}\right]\Big|_k = \left[\lambda^{e,k}\frac{\mathrm{DEV}\left(\boldsymbol{S}^{e,k}\right)}{\boldsymbol{B}_1^{e,k}}\otimes\boldsymbol{C}^{e,k}\right]:\Delta\boldsymbol{C}_\mathrm{p}^{e,-1},$$

$$\mathrm{D}^k_{\boldsymbol{F}^e}\left[\lambda^e\frac{\mathrm{Tr}\left(\boldsymbol{C}_\mathrm{p}^{e,-1}\right)\mathrm{DEV}\left(\boldsymbol{S}^e\right)}{\boldsymbol{B}_1^e}\right]\Big|_k = \left[\frac{2\lambda^{e,k}\mathrm{DEV}\left(\boldsymbol{S}^{e,k}\right)}{\boldsymbol{B}_1^{e,k}}\otimes\left[\boldsymbol{C}^{e,k}\right]_\mathrm{p}^{-1}\right]:\left[\Delta\boldsymbol{F}^{e,k,\mathrm{T}}\cdot\boldsymbol{F}^{e,k}\right]+ \\ +\lambda^{e,k}\mathrm{Tr}\left(\left[\boldsymbol{C}_\mathrm{p}^{e,k}\right]^{-1}\right)\frac{\partial}{\partial\boldsymbol{C}^e}\left[\frac{2\mathrm{DEV}\left(\boldsymbol{S}^e\right)}{\boldsymbol{B}_1^e}\right]\Big|_k:\left[\Delta\boldsymbol{F}^{e,k,\mathrm{T}}\cdot\boldsymbol{F}^{e,k}\right],$$

$$\mathrm{D}^k_{\boldsymbol{S}^e}\left[\lambda^e\frac{\mathrm{Tr}\left(\boldsymbol{C}_\mathrm{p}^{e,-1}\right)\mathrm{DEV}\left(\boldsymbol{S}^e\right)}{\boldsymbol{B}_1^e}\right]\Big|_k = \lambda^{e,k}\mathrm{Tr}\left(\left[\boldsymbol{C}_\mathrm{p}^{e,k}\right]^{-1}\right)\frac{\partial}{\partial\boldsymbol{S}^e}\left[\frac{\mathrm{DEV}\left(\boldsymbol{S}^e\right)}{\boldsymbol{B}_1^e}\right]\Big|_k:\Delta\boldsymbol{S}^e.$$

Within these expressions, further derivations have to be performed:

$$\left.\frac{\partial^2 e}{\partial \left[\boldsymbol{C}^e\right]^2}\right|_k = \frac{3\kappa+2\mu}{12}\left[\left[J^{e,k}\right]^2\left[\boldsymbol{C}^{e,k}\right]^{-1}\otimes\left[\boldsymbol{C}^{e,k}\right]^{-1} - \left[\left[J^{e,k}\right]^2-1\right]\left[\left[\boldsymbol{C}^{e,k}\right]^{-1}\otimes\left[\boldsymbol{C}^{e,k}\right]^{-1}\right]^{23}_{\mathrm{T}}\right] -$$

$$-\frac{1}{6}\mu\left[J^{e,k}\right]^{-\frac{2}{3}}\left[\left[\boldsymbol{C}_{\mathrm{p}}^{e,k}\right]^{-1}\otimes\left[\boldsymbol{C}^{e,k}\right]^{-1} + \left[\boldsymbol{C}^{e,k}\right]^{-1}\otimes\left[\boldsymbol{C}_{\mathrm{p}}^{e,k}\right]^{-1}\right]+$$

$$+\frac{1}{6}\mu\left[J^{e,k}\right]^{-\frac{2}{3}}\left[\boldsymbol{C}^{e,k}:\left[\boldsymbol{C}_{\mathrm{p}}^{e,k}\right]^{-1}\right]\left[\left[\left[\boldsymbol{C}^{e,k}\right]^{-1}\otimes\left[\boldsymbol{C}^{e,k}\right]^{-1}\right]^{23}_{\mathrm{T}}+\frac{1}{3}\left[\boldsymbol{C}^{e,k}\right]^{-1}\otimes\left[\boldsymbol{C}^{e,k}\right]^{-1}\right],$$

$$\left.\frac{\partial^2 e}{\partial \boldsymbol{C}^e \partial \boldsymbol{C}_{\mathrm{p}}^{e,-1}}\right|_k = \frac{3\kappa+2\mu}{24}\left[J^{e,k}\right]^2\left[\boldsymbol{C}^{e,k}\right]^{-1}\otimes\boldsymbol{C}_{\mathrm{p}}^{e,k} + \frac{1}{18}\mu\left[J^{e,k}\right]^{-\frac{2}{3}}\left[\boldsymbol{C}^{e,k}:\left[\boldsymbol{C}_{\mathrm{p}}^{e,k}\right]^{-1}\right]\left[\left[\boldsymbol{C}^{e,k}\right]^{-1}\otimes\boldsymbol{C}_{\mathrm{p}}^{e,k}\right]+$$

$$+\frac{1}{2}\mu\left[J^{e,k}\right]^{-\frac{2}{3}}\left[\left[\left[\boldsymbol{C}_{\mathrm{p}}^{e,k}\right]^{-1}\otimes\left[\boldsymbol{C}_{\mathrm{p}}^{e,k}\right]^{-1}\right]^{23}_{\mathrm{T}}-\frac{1}{3}\left[\left[\boldsymbol{C}_{\mathrm{p}}^{e,k}\right]^{-1}\otimes\boldsymbol{C}_{\mathrm{p}}^{e,k}+\left[\boldsymbol{C}^{e,k}\right]^{-1}\otimes\boldsymbol{C}^{e,k}\right]\right],$$

$$\left.\frac{\partial}{\partial\boldsymbol{C}^e}\left[\frac{\mathrm{DEV}\left(\boldsymbol{S}^e\right)}{\boldsymbol{B}_1^e}\right]\right|_k = \left[\boldsymbol{S}^{e,k}-\frac{1}{3}\left[\boldsymbol{C}^{e,k}:\boldsymbol{S}^{e,k}\right]\left[\boldsymbol{C}^{e,k}\right]^{-1}\right]\otimes\frac{\left[\frac{1}{3}\left[\boldsymbol{C}^{e,k}:\boldsymbol{S}^{e,k}\right]\boldsymbol{S}^{e,k}-\boldsymbol{S}^{e,k}\cdot\boldsymbol{C}^{e,k}\boldsymbol{S}^{e,k}\right]}{[\boldsymbol{B}_1^{e,k}]^3}+$$

$$+\frac{1}{\boldsymbol{B}_1^{e,k}}\left[-\frac{1}{3}\left[\boldsymbol{C}^{e,k}\right]^{-1}\otimes\boldsymbol{S}^{e,k}+\frac{1}{3}\left[\boldsymbol{C}^{e,k}:\boldsymbol{S}^{e,k}\right]\left[\left[\boldsymbol{C}^{e,k}\right]^{-1}\otimes\left[\boldsymbol{C}^{e,k}\right]^{-1}\right]^{23}_{\mathrm{T}}\right],$$

$$\left.\frac{\partial}{\partial\boldsymbol{S}^e}\left[\frac{\mathrm{DEV}\left(\boldsymbol{S}^e\right)}{\boldsymbol{B}_1^e}\right]\right|_k = \left[\boldsymbol{S}^{e,k}-\frac{1}{3}\left[\boldsymbol{C}^{e,k}:\boldsymbol{S}^{e,k}\right]\left[\boldsymbol{C}^{e,k}\right]^{-1}\right]\otimes\frac{\left[\frac{1}{3}\left[\boldsymbol{C}^{e,k}:\boldsymbol{S}^{e,k}\right]\boldsymbol{C}^{e,k}-\boldsymbol{C}^{e,k}\cdot\boldsymbol{S}^{e,k}\cdot\boldsymbol{C}^{e,k}\right]}{[\boldsymbol{B}_1^{e,k}]^3}+$$

$$+\frac{1}{\boldsymbol{B}_1^{e,k}}\left[\mathbb{I}-\frac{1}{3}\left[\left[\boldsymbol{C}^{e,k}\right]^{-1}\otimes\boldsymbol{C}^{e,k}\right]\right],$$

$$\left.\frac{\partial f(\boldsymbol{C}^e,\boldsymbol{S}^e)}{\partial\boldsymbol{S}^e}\right|_k = \frac{\boldsymbol{C}^{e,k}\cdot\boldsymbol{S}^{e,k}\cdot\boldsymbol{C}^{e,k}-\frac{1}{3}\left[\boldsymbol{C}^{e,k}:\boldsymbol{S}^{e,k}\right]\boldsymbol{C}^{e,k}}{\boldsymbol{B}_1^{e,k}},$$

$$\left.\frac{\partial f(\boldsymbol{C}^e,\boldsymbol{S}^e)}{\partial\boldsymbol{C}^e}\right|_k = \frac{\boldsymbol{S}^{e,k}\cdot\boldsymbol{C}^{e,k}\cdot\boldsymbol{S}^{e,k}-\frac{1}{3}\left[\boldsymbol{C}^{e,k}:\boldsymbol{S}^{e,k}\right]\boldsymbol{S}^{e,k}}{\boldsymbol{B}_1^{e,k}}.$$

Derivatives in Variational Finite Viscoplasticity

In contrast to the elastoplastic multifield approach, the viscoplastic ansatz can be solved by an ordinary Newton-Raphson scheme. This is grounded in the lack of a variational inequality in the model formulation. Nevertheless, a series of Gâteaux derivatives as in (3.22) has to be

determined during the solution process. While Equations (A.39)-(A.42) remain unchanged

$$
\begin{aligned}
\mathrm{D}^{k}_{\boldsymbol{C}_{\mathrm{p}}^{e,-1}}\left[\frac{1}{\chi}\frac{\mathrm{Tr}\left(\boldsymbol{C}_{\mathrm{p}}^{e,-1}\right)\boldsymbol{B}_{4}^{e}}{\boldsymbol{B}_{1}^{e}}\right]\Big|_{k} &= \left[\frac{1}{\chi}\frac{\boldsymbol{B}_{4}^{e,k}}{\boldsymbol{B}_{1}^{e,k}}\otimes\boldsymbol{C}^{e,k}\right]:\Delta\boldsymbol{C}_{\mathrm{p}}^{e,-1},\\
\mathrm{D}^{k}_{\boldsymbol{F}^{e}}\left[\frac{1}{\chi}\frac{\mathrm{Tr}\left(\boldsymbol{C}_{\mathrm{p}}^{e,-1}\right)\boldsymbol{B}_{4}^{e}}{\boldsymbol{B}_{1}^{e}}\right]\Big|_{k} &= \left[\frac{2\chi^{-1}\boldsymbol{B}_{4}^{e,k}}{\boldsymbol{B}_{1}^{e,k}}\otimes\left[\boldsymbol{C}_{\mathrm{p}}^{e,k}\right]^{-1}\right]:\left[\Delta\boldsymbol{F}^{e,k,\mathrm{T}}\cdot\boldsymbol{F}^{e,k}\right]+\\
&\quad+\mathrm{Tr}\left(\left[\boldsymbol{C}_{\mathrm{p}}^{e,k}\right]^{-1}\right)\frac{\partial}{\partial\boldsymbol{C}^{e}}\left[\frac{2\chi^{-1}\boldsymbol{B}_{4}^{e}}{\boldsymbol{B}_{1}^{e}}\right]\Big|_{k}:\left[\Delta\boldsymbol{F}^{e,k,\mathrm{T}}\cdot\boldsymbol{F}^{e,k}\right],\\
\mathrm{D}^{k}_{\boldsymbol{S}^{e}}\left[\frac{1}{\chi}\frac{\mathrm{Tr}\left(\boldsymbol{C}_{\mathrm{p}}^{e,-1}\right)\boldsymbol{B}_{4}^{e}}{\boldsymbol{B}_{1}^{e}}\right]\Big|_{k} &= \mathrm{Tr}\left(\left[\boldsymbol{C}_{\mathrm{p}}^{e,k}\right]^{-1}\right)\frac{\partial}{\partial\boldsymbol{S}^{e}}\left[\frac{1}{\chi}\frac{\boldsymbol{B}_{4}^{e}}{\boldsymbol{B}_{1}^{e}}\right]\Big|_{k}:\Delta\boldsymbol{S}^{e},\\
\frac{\partial}{\partial\boldsymbol{C}^{e}}\left[\frac{1}{\chi}\frac{\boldsymbol{B}_{4}^{e}}{\boldsymbol{B}_{1}^{e}}\right]\Big|_{k} &= \frac{1}{2\chi}\frac{\mathrm{DEV}\left(\boldsymbol{S}^{e,k}\right)}{\boldsymbol{B}_{1}^{e,k}}\otimes\left[\frac{\partial f(\boldsymbol{S}^{e},\boldsymbol{C}^{e})}{\partial\boldsymbol{C}^{e}}\Big|_{k}+\frac{f(\boldsymbol{S}^{e},\boldsymbol{C}^{e})}{|f(\boldsymbol{S}^{e},\boldsymbol{C}^{e})|}\frac{\partial f(\boldsymbol{S}^{e},\boldsymbol{C}^{e})}{\partial\boldsymbol{C}^{e}}\Big|_{k}\right]+\\
&\quad+\frac{1}{\chi}\langle f(\boldsymbol{S}^{e,k},\boldsymbol{C}^{e,k})\rangle\frac{\partial}{\partial\boldsymbol{C}^{e}}\left[\frac{\mathrm{DEV}\left(\boldsymbol{S}^{e}\right)}{\boldsymbol{B}_{1}^{e}}\right]\Big|_{k},\\
\frac{\partial}{\partial\boldsymbol{S}^{e}}\left[\frac{1}{\chi}\frac{\boldsymbol{B}_{4}^{e}}{\boldsymbol{B}_{1}^{e}}\right]\Big|_{k} &= \frac{1}{2\chi}\frac{\mathrm{DEV}\left(\boldsymbol{S}^{e,k}\right)}{\boldsymbol{B}_{1}^{e,k}}\otimes\left[\frac{\partial f(\boldsymbol{S}^{e},\boldsymbol{C}^{e})}{\partial\boldsymbol{S}^{e}}\Big|_{k}+\frac{f(\boldsymbol{S}^{e},\boldsymbol{C}^{e})}{|f(\boldsymbol{S}^{e},\boldsymbol{C}^{e})|}\frac{\partial f(\boldsymbol{S}^{e},\boldsymbol{C}^{e})}{\partial\boldsymbol{S}^{e}}\Big|_{k}\right]+\\
&\quad+\frac{1}{\chi}\langle f(\boldsymbol{S}^{e},\boldsymbol{C}^{e})\rangle\frac{\partial}{\partial\boldsymbol{S}^{e}}\left[\frac{\mathrm{DEV}\left(\boldsymbol{S}^{e}\right)}{\boldsymbol{B}_{1}^{e}}\Big|_{k}\right].
\end{aligned}
$$

have to be considered additionally together with the abbreviation

$$\boldsymbol{B}_{4} = \langle f(\boldsymbol{S},\boldsymbol{C})\rangle\mathrm{DEV}\left(\boldsymbol{S}\right).$$

B. Convexity of the Yield Function in Finite Strain (Visco)plasticity

A function $k(x)$ defined on a proper vector space X is called convex if

$$k(cx_1 + (1-c)x_2) \leq ck(x_1) + (1-c)k(x_2) \tag{B.1}$$

holds for $\forall x_1, x_2$ in X and $0 \leq c \leq 1$. To prove the convexity of the yield function in (6.2) with respect to the second PIOLA-KIRCHHOFF stress tensor $\boldsymbol{S}$, Equation (6.2) is reformulated applying the definition of the right CAUCHY-GREEN tensor and the FROBENIUS norm (A.10), leading to

$$f(\boldsymbol{S},\boldsymbol{F}) = \sqrt{[\mathrm{DEV}\,(\boldsymbol{S})\cdot\boldsymbol{C}]:\,[\boldsymbol{C}\cdot\mathrm{DEV}\,(\boldsymbol{S})]} - \sqrt{\frac{2}{3}}\sigma_{\mathrm{y}} = \left\| \boldsymbol{F}\cdot\boldsymbol{S}\cdot\boldsymbol{F}^{\mathrm{T}} - \frac{1}{3}\left[\boldsymbol{F}\cdot\boldsymbol{S}\cdot\boldsymbol{F}^{\mathrm{T}}\right]:\boldsymbol{I} \right\| - \sqrt{\frac{2}{3}}\sigma_{\mathrm{y}}. \tag{B.2}$$

Exploiting the left hand side of Relation (B.1) together with the triangle inequality yields the convexity of the yield function

$$\begin{aligned} f(c\boldsymbol{S}_1+[1-c]\boldsymbol{S}_2,\boldsymbol{F}) = & \left\| \boldsymbol{F}\cdot[c\boldsymbol{S}_1+[1-c]\boldsymbol{S}_2]\cdot\boldsymbol{F}^{\mathrm{T}} - \frac{1}{3}\left[\boldsymbol{F}\cdot[c\boldsymbol{S}_1+[1-c]\,\boldsymbol{S}_2]\cdot\boldsymbol{F}^{\mathrm{T}}\right]:\boldsymbol{I} \right\| - \sqrt{\frac{2}{3}}\sigma_{\mathrm{y}} = \\ & \leq c \left\| \boldsymbol{F}\cdot\boldsymbol{S}_1\cdot\boldsymbol{F}^{\mathrm{T}} - \frac{1}{3}\left[\boldsymbol{F}\cdot\boldsymbol{S}_1\cdot\boldsymbol{F}^{\mathrm{T}}\right]:\boldsymbol{I} \right\| - c\sqrt{\frac{2}{3}}\sigma_{\mathrm{y}} + \\ & + [1-c] \left\| \boldsymbol{F}\cdot\boldsymbol{S}_2\cdot\boldsymbol{F}^{\mathrm{T}} - \frac{1}{3}\left[\boldsymbol{F}\cdot\boldsymbol{S}_2\cdot\boldsymbol{F}^{\mathrm{T}}\right]:\boldsymbol{I} \right\| - [1-c]\sqrt{\frac{2}{3}}\sigma_{\mathrm{y}} = \\ & = cf(\boldsymbol{S}_1,\boldsymbol{F}) + [1-c]f(\boldsymbol{S}_2,\boldsymbol{F}). \end{aligned}$$

C. Polar Coordinates

For some applications it is recommendable to formulate the model problem using cylindrical coordinates instead of cartesian ones. Due to the tensor notation in use this change of basis leads to no modifications in terms of the general continuum mechanical aspects or the material modeling. However, care has to be taken if an explicit evaluation has to be carried out. The same is true in the field of numerical implementation. To demonstrate the differences between the two basis systems, their relation is derived. In order to do so, a continuum mechanical body $\mathcal{B}$ in the reference configuration is considered, which is generated by rotating an arbitrary plane geometry in the $\boldsymbol{g}_1 - \boldsymbol{g}_3$ plane around the $\boldsymbol{g}_3$-axis. As an example, a rectangle leading to a cylinder can be taken into account, see Figure C.1.

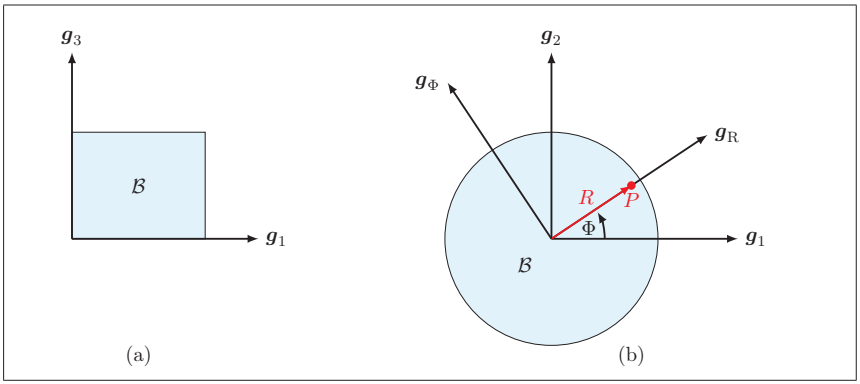

Figure C.1.: Definition of cylindrical coordinates: (a) Geometry in the $\boldsymbol{g}_1 - \boldsymbol{g}_3$ plane, (b) Geometry rotated around the $\boldsymbol{g}_3$-axis

To describe the location of an arbitrary point P within this material body $\mathcal{B}$ a cartesian coordinate system with the orthogonal basis vectors $\boldsymbol{g}_1, \boldsymbol{g}_2, \boldsymbol{g}_3$ can be introduced, leading to the location vector $\boldsymbol{X} = [X_1, X_2, X_3]$. On the contrary, a cylindrical coordinate system with the orthogonal basis vectors $\boldsymbol{g}_\mathrm{R}, \boldsymbol{g}_\Phi, \boldsymbol{g}_\mathrm{Z}$ can be exploited, creating the location vector $\boldsymbol{X} = [R, \Phi, Z]$, cf. (Kreißig and Benedix, 2002; Specht, 2005). Thereby, the identity of the $\boldsymbol{g}_3$ and the $\boldsymbol{g}_\mathrm{Z}$ axis is assumed. Furthermore, it is stipulated that the point P lies on the $\boldsymbol{g}_\mathrm{R}$-axis, which is rotated by an angle Φ around the $\boldsymbol{g}_\mathrm{Z}$ direction with respect to the $\boldsymbol{g}_1$ axis, see Figure C.1. This yields the relations

$$\boldsymbol{g}_1 = \boldsymbol{g}_\mathrm{R}\cos(\Phi) - \boldsymbol{g}_\Phi \sin(\Phi) \qquad \boldsymbol{g}_2 = \boldsymbol{g}_\mathrm{R}\sin(\Phi) + \boldsymbol{g}_\Phi \cos(\Phi) \qquad \boldsymbol{g}_3 = \boldsymbol{g}_\mathrm{Z} \tag{C.1}$$

$$\boldsymbol{g}_R = \boldsymbol{g}_1\cos(\Phi) + \boldsymbol{g}_2 \sin(\Phi) \qquad \boldsymbol{g}_\Phi = -\boldsymbol{g}_1 \sin(\Phi) + \boldsymbol{g}_2 \cos(\Phi) \qquad \boldsymbol{g}_3 = \boldsymbol{g}_\mathrm{Z}. \tag{C.2}$$

Analogously, the coordinates of point P

$$X_1 = R\cos(\Phi) \qquad X_2 = R\sin(\Phi) \qquad X_3 = Z \tag{C.3}$$

$$R = \sqrt{[X_1]^2 + [X_2]^2} \qquad \Phi = \arctan\left(\frac{X_2}{X_1}\right) \qquad Z = X_3 \tag{C.4}$$

can be established. An important difference between both coordinate systems is that, while the cartesian one is fix, the cylindrical one depends on the investigated position. With a modification in the angle Φ, a change in the basis vectors $\boldsymbol{g}_\mathrm{R}$ and $\boldsymbol{g}_\Phi$ is implied, (Kelly, 2015). Hence, the derivatives

$$\frac{\partial \boldsymbol{g}_\mathrm{R}}{\partial \Phi} = \boldsymbol{g}_\Phi \qquad \frac{\partial \boldsymbol{g}_\Phi}{\partial \Phi} = -\boldsymbol{g}_\mathrm{R} \tag{C.5}$$

can be determined. These expressions gain special importance for the gradient of a vector- or tensor field. Therefore, in a first step the Nabla Operator $(A.13)_2$ in cartesian coordinates is transformed to the cylindrical system:

$$\nabla_R = \boldsymbol{g}_\mathrm{R}\frac{\partial}{\partial R} + \boldsymbol{g}_\Phi\frac{1}{R}\frac{\partial}{\partial \Phi} + \boldsymbol{g}_\mathrm{Z}\frac{\partial}{\partial Z}. \tag{C.6}$$

This is accomplished by inserting the chain rules

$$\begin{aligned}
\frac{\partial}{\partial X_1} &= \frac{\partial R}{\partial X_1}\frac{\partial}{\partial R} + \frac{\partial \Phi}{\partial X_1}\frac{\partial}{\partial \Phi} + \frac{\partial Z}{\partial X_1}\frac{\partial}{\partial Z} \\
\frac{\partial}{\partial X_2} &= \frac{\partial R}{\partial X_2}\frac{\partial}{\partial R} + \frac{\partial \Phi}{\partial X_2}\frac{\partial}{\partial \Phi} + \frac{\partial Z}{\partial X_2}\frac{\partial}{\partial Z} \\
\frac{\partial}{\partial X_3} &= \frac{\partial R}{\partial X_3}\frac{\partial}{\partial R} + \frac{\partial \Phi}{\partial X_3}\frac{\partial}{\partial \Phi} + \frac{\partial Z}{\partial X_3}\frac{\partial}{\partial Z}
\end{aligned}$$

together with the definitions (C.1) and (C.5) as well as the derivatives

$$\frac{\partial R}{\partial X_1} = \frac{X_1}{R} \qquad \frac{\partial R}{\partial X_2} = \frac{X_2}{R} \qquad \frac{\partial R}{\partial X_3} = 0 \tag{C.7}$$

$$\frac{\partial \Phi}{\partial X_1} = -\frac{X_2}{R^2} \qquad \frac{\partial \Phi}{\partial X_2} = \frac{X_1}{R^2} \qquad \frac{\partial \Phi}{\partial X_3} = 0 \tag{C.8}$$

$$\frac{\partial Z}{\partial X_1} = 0 \qquad \frac{\partial Z}{\partial X_2} = 0 \qquad \frac{\partial Z}{\partial X_3} = 1. \tag{C.9}$$

into the definition of the Nabla Operator $(A.13)_2$.

Applying the Nabla Operator (C.6) to a vector field as in $(A.14)_2$, results in

$$\begin{aligned}
\nabla_R \boldsymbol{a} &= \left[\left[\boldsymbol{g}_\mathrm{R}\frac{\partial}{\partial R} + \boldsymbol{g}_\Phi\frac{1}{R}\frac{\partial}{\partial \Phi} + \boldsymbol{g}_\mathrm{Z}\frac{\partial}{\partial Z}\right] \otimes [a_\mathrm{R}\boldsymbol{g}_\mathrm{R} + a_\Phi\boldsymbol{g}_\Phi + a_\mathrm{Z}\boldsymbol{g}_\mathrm{Z}]\right]^\mathrm{T} = \\
&= \begin{bmatrix}
\dfrac{\partial a_\mathrm{R}}{\partial R} & \dfrac{1}{R}\dfrac{\partial a_\mathrm{R}}{\partial \Phi} - \dfrac{a_\Phi}{R} & \dfrac{\partial a_\mathrm{R}}{\partial Z} \\
\dfrac{\partial a_\Phi}{\partial R} & \dfrac{1}{R}\dfrac{\partial a_\Phi}{\partial \Phi} + \dfrac{a_\mathrm{R}}{R} & \dfrac{\partial a_\Phi}{\partial Z} \\
\dfrac{\partial a_\mathrm{Z}}{\partial R} & \dfrac{1}{R}\dfrac{\partial a_\mathrm{Z}}{\partial \Phi} & \dfrac{\partial a_\mathrm{Z}}{\partial Z}
\end{bmatrix}.
\end{aligned} \tag{C.10}$$

A similar procedure is performed to adapt the divergence operator of $(A.16)_2$ to polar coordinates, yielding

$$\begin{aligned}\nabla_R \cdot \boldsymbol{a} &= \left[\boldsymbol{g}_{\mathrm{R}}\frac{\partial}{\partial R} + \boldsymbol{g}_{\Phi}\frac{1}{R}\frac{\partial}{\partial \Phi} + \boldsymbol{g}_{\mathrm{Z}}\frac{\partial}{\partial Z}\right] \cdot \left[a_{\mathrm{R}}\boldsymbol{g}_{\mathrm{R}} + a_{\Phi}\boldsymbol{g}_{\Phi} + a_{\mathrm{Z}}\boldsymbol{g}_{\mathrm{Z}}\right] = \\ &= \frac{\partial a_{\mathrm{R}}}{\partial R} + \frac{a_{\mathrm{R}}}{R} + \frac{1}{R}\frac{\partial a_{\Phi}}{\partial \Phi} + \frac{\partial a_{\mathrm{Z}}}{\partial Z}.\end{aligned} \tag{C.11}$$

For higher order tensors, the procedure has to be carried out analogously. To derive equivalent equations to (C.10) as well as (C.11), but considering the current configuration of the material body $\mathcal{B}$, the location vector $\boldsymbol{x}$ has to be expressed using cartesian as well as polar coordinates. For this purpose, the same suppositions as for the reference configuration are employed, but the location vector is denoted as $\boldsymbol{x} = [x_1, x_2, x_3] = [r, \phi, z]$ in the respective bases, cf. (Wu et al., 1992). Henceforth, Equations (C.1)-(C.11) have to be rewritten accordingly, generating

$$\begin{aligned}\nabla_r \boldsymbol{a} &= \left[\left[\boldsymbol{g}_{\mathrm{r}}\frac{\partial}{\partial r} + \boldsymbol{g}_{\phi}\frac{1}{r}\frac{\partial}{\partial \phi} + \boldsymbol{g}_{\mathrm{z}}\frac{\partial}{\partial z}\right] \otimes \left[a_{\mathrm{r}}\boldsymbol{g}_{\mathrm{r}} + a_{\phi}\boldsymbol{g}_{\phi} + a_{\mathrm{z}}\boldsymbol{g}_{\mathrm{z}}\right]\right]^{\mathrm{T}} = \\ &= \begin{bmatrix} \dfrac{\partial a_{\mathrm{r}}}{\partial r} & \dfrac{1}{r}\dfrac{\partial a_{\mathrm{r}}}{\partial \phi} - \dfrac{a_{\phi}}{r} & \dfrac{\partial a_{\mathrm{r}}}{\partial z} \\ \dfrac{\partial a_{\phi}}{\partial r} & \dfrac{1}{r}\dfrac{\partial a_{\phi}}{\partial \phi} + \dfrac{a_{\mathrm{r}}}{r} & \dfrac{\partial a_{\phi}}{\partial z} \\ \dfrac{\partial a_{\mathrm{z}}}{\partial r} & \dfrac{1}{r}\dfrac{\partial a_{\mathrm{z}}}{\partial \phi} & \dfrac{\partial a_{\mathrm{z}}}{\partial z} \end{bmatrix}.\end{aligned}$$

and

$$\begin{aligned}\nabla_r \cdot \boldsymbol{a} &= \left[\boldsymbol{g}_{\mathrm{r}}\frac{\partial}{\partial r} + \boldsymbol{g}_{\Phi}\frac{1}{r}\frac{\partial}{\partial \Phi} + \boldsymbol{g}_{\mathrm{z}}\frac{\partial}{\partial z}\right] \cdot \left[a_{\mathrm{r}}\boldsymbol{g}_{\mathrm{r}} + a_{\Phi}\boldsymbol{g}_{\Phi} + a_{\mathrm{z}}\boldsymbol{g}_{\mathrm{z}}\right] = \\ &= \frac{\partial a_{\mathrm{r}}}{\partial r} + \frac{a_{\mathrm{r}}}{r} + \frac{1}{r}\frac{\partial a_{\phi}}{\partial \phi} + \frac{\partial a_{\mathrm{z}}}{\partial z}.\end{aligned}$$

For higher order tensors and for the derivation of the Relationships (A.18), the application of the polar Nabla operator has to be carried out analogously.

D. Nodal Solutions for a Rectangular Strip with a Hole in Plane Strain Case

In the course of the investigations performed in (Stein, 2003) concerning the analysis of methods aimed at solving elastoplastic problems, different benchmark problems are treated. One example is a rectangular strip with a hole in the plane strain case. For this problem, a list of nodal solutions is published in (Stein, 2003), which were generated using a spatial mesh consisting of $65,536$ Q2/P1 elements and 205 load steps. An abbreviated version is depicted in Table D.1 and Table D.2. These reference solutions are compared to the solutions obtained exploiting the classical and the variational approach established in this thesis. Thereby, it is emphasized that the difference between the latter two methods is smaller than $4 \cdot 10^{-4}\%$. Thus, in view of the results, no distinction is made.

Table D.1.: Exemplary solutions for the displacement field

t^*[N/mm^2]	u_1(①)[mm]		u_2(②)[mm]		u_1(③)[mm]	
	reference solution	classical/ variational approach	reference solution	classical/ variational approach	reference solution	classical/ variational approach
100.00	$4.7312 \cdot 10^{-04}$	$4.7311 \cdot 10^{-04}$	$4.6559 \cdot 10^{-03}$	$4.6559 \cdot 10^{-03}$	$1.7057 \cdot 10^{-03}$	$1.7057 \cdot 10^{-03}$
175.00	$8.2765 \cdot 10^{-04}$	$8.2764 \cdot 10^{-04}$	$8.1479 \cdot 10^{-03}$	$8.1479 \cdot 10^{-03}$	$2.9850 \cdot 10^{-03}$	$2.9850 \cdot 10^{-03}$
200.00	$9.3757 \cdot 10^{-04}$	$9.3780 \cdot 10^{-04}$	$9.3143 \cdot 10^{-03}$	$9.3143 \cdot 10^{-03}$	$3.4103 \cdot 10^{-03}$	$3.4103 \cdot 10^{-03}$
225.00	$1.0284 \cdot 10^{-03}$	$1.0293 \cdot 10^{-03}$	$1.0485 \cdot 10^{-02}$	$1.0485 \cdot 10^{-02}$	$3.8336 \cdot 10^{-03}$	$3.8336 \cdot 10^{-03}$
250.00	$1.0927 \cdot 10^{-03}$	$1.0947 \cdot 10^{-03}$	$1.1661 \cdot 10^{-02}$	$1.1661 \cdot 10^{-02}$	$4.2544 \cdot 10^{-03}$	$4.2545 \cdot 10^{-03}$
275.00	$1.1247 \cdot 10^{-03}$	$1.1285 \cdot 10^{-03}$	$1.2844 \cdot 10^{-02}$	$1.2844 \cdot 10^{-02}$	$4.6722 \cdot 10^{-03}$	$4.6723 \cdot 10^{-03}$
300.00	$1.1200 \cdot 10^{-03}$	$1.1258 \cdot 10^{-03}$	$1.4034 \cdot 10^{-02}$	$1.4034 \cdot 10^{-02}$	$5.0867 \cdot 10^{-03}$	$5.0869 \cdot 10^{-03}$
325.00	$1.0761 \cdot 10^{-03}$	$1.0827 \cdot 10^{-03}$	$1.5232 \cdot 10^{-02}$	$1.5232 \cdot 10^{-02}$	$5.4973 \cdot 10^{-03}$	$5.4975 \cdot 10^{-03}$
350.00	$9.8518 \cdot 10^{-04}$	$9.9275 \cdot 10^{-04}$	$1.6441 \cdot 10^{-02}$	$1.6440 \cdot 10^{-02}$	$5.9032 \cdot 10^{-03}$	$5.9034 \cdot 10^{-03}$
400.00	$9.9872 \cdot 10^{-04}$	$1.0068 \cdot 10^{-03}$	$1.9123 \cdot 10^{-02}$	$1.9122 \cdot 10^{-02}$	$6.6019 \cdot 10^{-03}$	$6.6023 \cdot 10^{-03}$
412.50	$1.0693 \cdot 10^{-03}$	$1.0769 \cdot 10^{-03}$	$1.9948 \cdot 10^{-02}$	$1.9947 \cdot 10^{-02}$	$6.7130 \cdot 10^{-03}$	$6.7135 \cdot 10^{-03}$
425.00	$1.1983 \cdot 10^{-03}$	$1.2031 \cdot 10^{-03}$	$2.0944 \cdot 10^{-02}$	$2.0943 \cdot 10^{-02}$	$6.7555 \cdot 10^{-03}$	$6.7562 \cdot 10^{-03}$
437.50	$1.4408 \cdot 10^{-03}$	$1.4350 \cdot 10^{-03}$	$2.2310 \cdot 10^{-02}$	$2.2307 \cdot 10^{-02}$	$6.6502 \cdot 10^{-03}$	$6.6514 \cdot 10^{-03}$
450.00	$1.9071 \cdot 10^{-03}$	$1.8748 \cdot 10^{-03}$	$2.4585 \cdot 10^{-02}$	$2.4579 \cdot 10^{-02}$	$6.1802 \cdot 10^{-03}$	$6.1827 \cdot 10^{-03}$
425.00	$1.7888 \cdot 10^{-03}$	$1.7565 \cdot 10^{-03}$	$2.3421 \cdot 10^{-02}$	$2.3415 \cdot 10^{-02}$	$5.7537 \cdot 10^{-03}$	$5.7562 \cdot 10^{-03}$
400.00	$1.6705 \cdot 10^{-03}$	$1.6382 \cdot 10^{-03}$	$2.2257 \cdot 10^{-02}$	$2.2251 \cdot 10^{-02}$	$5.3273 \cdot 10^{-03}$	$5.3298 \cdot 10^{-03}$
375.00	$1.5522 \cdot 10^{-03}$	$1.5199 \cdot 10^{-03}$	$2.1093 \cdot 10^{-02}$	$2.1087 \cdot 10^{-02}$	$4.9009 \cdot 10^{-03}$	$4.9034 \cdot 10^{-03}$
350.00	$1.4340 \cdot 10^{-03}$	$1.4016 \cdot 10^{-03}$	$1.9929 \cdot 10^{-02}$	$1.9923 \cdot 10^{-02}$	$4.4744 \cdot 10^{-03}$	$4.4769 \cdot 10^{-03}$
325.00	$1.3157 \cdot 10^{-03}$	$1.2834 \cdot 10^{-03}$	$1.8765 \cdot 10^{-02}$	$1.8759 \cdot 10^{-02}$	$4.0480 \cdot 10^{-03}$	$4.0505 \cdot 10^{-03}$
300.00	$1.1974 \cdot 10^{-03}$	$1.1651 \cdot 10^{-03}$	$1.7601 \cdot 10^{-02}$	$1.7595 \cdot 10^{-02}$	$3.6216 \cdot 10^{-03}$	$3.6241 \cdot 10^{-03}$
275.00	$1.0791 \cdot 10^{-03}$	$1.0468 \cdot 10^{-03}$	$1.6437 \cdot 10^{-02}$	$1.6431 \cdot 10^{-02}$	$3.1951 \cdot 10^{-03}$	$3.1976 \cdot 10^{-03}$
250.00	$9.6084 \cdot 10^{-04}$	$9.2853 \cdot 10^{-04}$	$1.5273 \cdot 10^{-02}$	$1.5267 \cdot 10^{-02}$	$2.7687 \cdot 10^{-03}$	$2.7712 \cdot 10^{-03}$

Table D.1 – *Continued on next page*

Table D.1 – *Continued from previous page*

225.00	$8.4256 \cdot 10^{-04}$	$8.1026 \cdot 10^{-04}$	$1.4109 \cdot 10^{-02}$	$1.4103 \cdot 10^{-02}$	$2.3423 \cdot 10^{-03}$	$2.3448 \cdot 10^{-03}$
200.00	$7.2428 \cdot 10^{-04}$	$6.9198 \cdot 10^{-04}$	$1.2945 \cdot 10^{-02}$	$1.2939 \cdot 10^{-02}$	$1.9158 \cdot 10^{-03}$	$1.9183 \cdot 10^{-03}$
175.00	$6.0600 \cdot 10^{-04}$	$5.7370 \cdot 10^{-04}$	$1.1781 \cdot 10^{-02}$	$1.1775 \cdot 10^{-02}$	$1.4894 \cdot 10^{-03}$	$1.4919 \cdot 10^{-03}$
150.00	$4.8772 \cdot 10^{-04}$	$4.5542 \cdot 10^{-04}$	$1.0617 \cdot 10^{-02}$	$1.0611 \cdot 10^{-02}$	$1.0630 \cdot 10^{-03}$	$1.0655 \cdot 10^{-03}$
125.00	$3.6942 \cdot 10^{-04}$	$3.3713 \cdot 10^{-04}$	$9.4532 \cdot 10^{-03}$	$9.4472 \cdot 10^{-03}$	$6.3653 \cdot 10^{-04}$	$6.3903 \cdot 10^{-04}$
100.00	$2.5196 \cdot 10^{-04}$	$2.1957 \cdot 10^{-04}$	$8.2887 \cdot 10^{-03}$	$8.2826 \cdot 10^{-03}$	$2.1036 \cdot 10^{-04}$	$2.1286 \cdot 10^{-04}$
75.00	$1.3803 \cdot 10^{-04}$	$1.0549 \cdot 10^{-04}$	$7.1228 \cdot 10^{-03}$	$7.1168 \cdot 10^{-03}$	$-2.1520 \cdot 10^{-04}$	$-2.1270 \cdot 10^{-04}$
50.00	$2.9997 \cdot 10^{-05}$	$-2.9802 \cdot 10^{-06}$	$5.9551 \cdot 10^{-03}$	$5.9491 \cdot 10^{-03}$	$-6.3994 \cdot 10^{-04}$	$-6.3746 \cdot 10^{-04}$
25.00	$-7.0368 \cdot 10^{-05}$	$-1.0347 \cdot 10^{-04}$	$4.7854 \cdot 10^{-03}$	$4.7793 \cdot 10^{-03}$	$-1.0637 \cdot 10^{-03}$	$-1.0612 \cdot 10^{-03}$
0.00	$-1.6094 \cdot 10^{-04}$	$-1.9412 \cdot 10^{-04}$	$3.6132 \cdot 10^{-03}$	$3.6072 \cdot 10^{-03}$	$-1.4864 \cdot 10^{-03}$	$-1.4839 \cdot 10^{-03}$
−25.00	$-2.3980 \cdot 10^{-04}$	$-2.7302 \cdot 10^{-04}$	$2.4383 \cdot 10^{-03}$	$2.4323 \cdot 10^{-03}$	$-1.9078 \cdot 10^{-03}$	$-1.9054 \cdot 10^{-03}$
−100.00	$-3.8748 \cdot 10^{-04}$	$-4.2513 \cdot 10^{-04}$	$-1.1051 \cdot 10^{-03}$	$-1.1107 \cdot 10^{-03}$	$-3.1635 \cdot 10^{-03}$	$-3.1612 \cdot 10^{-03}$
−125.00	$-4.0298 \cdot 10^{-04}$	$-4.4328 \cdot 10^{-04}$	$-2.2931 \cdot 10^{-03}$	$-2.2986 \cdot 10^{-03}$	$-3.5789 \cdot 10^{-03}$	$-3.5767 \cdot 10^{-03}$
−150.00	$-4.0055 \cdot 10^{-04}$	$-4.4362 \cdot 10^{-04}$	$-3.4849 \cdot 10^{-03}$	$-3.4902 \cdot 10^{-03}$	$-3.9925 \cdot 10^{-03}$	$-3.9904 \cdot 10^{-03}$
−175.00	$-3.7947 \cdot 10^{-04}$	$-4.2502 \cdot 10^{-04}$	$-4.6807 \cdot 10^{-03}$	$-4.6858 \cdot 10^{-03}$	$-4.4043 \cdot 10^{-03}$	$-4.4022 \cdot 10^{-03}$
−200.00	$-3.3917 \cdot 10^{-04}$	$-3.8729 \cdot 10^{-04}$	$-5.8810 \cdot 10^{-03}$	$-5.8860 \cdot 10^{-03}$	$-4.8140 \cdot 10^{-03}$	$-4.8120 \cdot 10^{-03}$
−225.00	$-2.8108 \cdot 10^{-04}$	$-3.3215 \cdot 10^{-04}$	$-7.0870 \cdot 10^{-03}$	$-7.0919 \cdot 10^{-03}$	$-5.2211 \cdot 10^{-03}$	$-5.2191 \cdot 10^{-03}$
−250.00	$-2.2723 \cdot 10^{-04}$	$-2.8206 \cdot 10^{-04}$	$-8.3060 \cdot 10^{-03}$	$-8.3107 \cdot 10^{-03}$	$-5.6223 \cdot 10^{-03}$	$-5.6204 \cdot 10^{-03}$
−275.00	$-2.0393 \cdot 10^{-04}$	$-2.6214 \cdot 10^{-04}$	$-9.5553 \cdot 10^{-03}$	$-9.5591 \cdot 10^{-03}$	$-6.0103 \cdot 10^{-03}$	$-6.0088 \cdot 10^{-03}$
−300.00	$-2.1097 \cdot 10^{-04}$	$-2.7384 \cdot 10^{-04}$	$-1.0850 \cdot 10^{-02}$	$-1.0852 \cdot 10^{-02}$	$-6.3790 \cdot 10^{-03}$	$-6.3782 \cdot 10^{-03}$
−325.00	$-2.5838 \cdot 10^{-04}$	$-3.2528 \cdot 10^{-04}$	$-1.2210 \cdot 10^{-02}$	$-1.2211 \cdot 10^{-02}$	$-6.7202 \cdot 10^{-03}$	$-6.7197 \cdot 10^{-03}$
−350.00	$-3.5820 \cdot 10^{-04}$	$-4.3164 \cdot 10^{-04}$	$-1.3672 \cdot 10^{-02}$	$-1.3672 \cdot 10^{-02}$	$-7.0189 \cdot 10^{-03}$	$-7.0190 \cdot 10^{-03}$
−400.00	$-8.7048 \cdot 10^{-04}$	$-9.5740 \cdot 10^{-04}$	$-1.7267 \cdot 10^{-02}$	$-1.7266 \cdot 10^{-02}$	$-7.3458 \cdot 10^{-03}$	$-7.3462 \cdot 10^{-03}$
−412.50	$-1.1177 \cdot 10^{-03}$	$-1.2030 \cdot 10^{-03}$	$-1.8472 \cdot 10^{-02}$	$-1.8469 \cdot 10^{-02}$	$-7.3052 \cdot 10^{-03}$	$-7.3060 \cdot 10^{-03}$
−425.00	$-1.4405 \cdot 10^{-03}$	$-1.5167 \cdot 10^{-03}$	$-1.9933 \cdot 10^{-02}$	$-1.9930 \cdot 10^{-02}$	$-7.1616 \cdot 10^{-03}$	$-7.1629 \cdot 10^{-03}$
−437.50	$-1.8542 \cdot 10^{-03}$	$-1.9130 \cdot 10^{-03}$	$-2.1810 \cdot 10^{-02}$	$-2.1805 \cdot 10^{-02}$	$-6.8510 \cdot 10^{-03}$	$-6.8529 \cdot 10^{-03}$
−450.00	$-2.3814 \cdot 10^{-03}$	$-2.4182 \cdot 10^{-03}$	$-2.4444 \cdot 10^{-02}$	$-2.4434 \cdot 10^{-02}$	$-6.2376 \cdot 10^{-03}$	$-6.2413 \cdot 10^{-03}$
−425.00	$-2.2632 \cdot 10^{-03}$	$-2.3000 \cdot 10^{-03}$	$-2.3280 \cdot 10^{-02}$	$-2.3270 \cdot 10^{-02}$	$-5.8111 \cdot 10^{-03}$	$-5.8149 \cdot 10^{-03}$
−400.00	$-2.1449 \cdot 10^{-03}$	$-2.1817 \cdot 10^{-03}$	$-2.2116 \cdot 10^{-02}$	$-2.2106 \cdot 10^{-02}$	$-5.3847 \cdot 10^{-03}$	$-5.3884 \cdot 10^{-03}$
−375.00	$-2.0266 \cdot 10^{-03}$	$-2.0634 \cdot 10^{-03}$	$-2.0952 \cdot 10^{-02}$	$-2.0942 \cdot 10^{-02}$	$-4.9583 \cdot 10^{-03}$	$-4.9620 \cdot 10^{-03}$
−350.00	$-1.9083 \cdot 10^{-03}$	$-1.9451 \cdot 10^{-03}$	$-1.9788 \cdot 10^{-02}$	$-1.9778 \cdot 10^{-02}$	$-4.5318 \cdot 10^{-03}$	$-4.5356 \cdot 10^{-03}$
−325.00	$-1.7900 \cdot 10^{-03}$	$-1.8268 \cdot 10^{-03}$	$-1.8624 \cdot 10^{-02}$	$-1.8614 \cdot 10^{-02}$	$-4.1054 \cdot 10^{-03}$	$-4.1091 \cdot 10^{-03}$
−300.00	$-1.6718 \cdot 10^{-03}$	$-1.7086 \cdot 10^{-03}$	$-1.7460 \cdot 10^{-02}$	$-1.7450 \cdot 10^{-02}$	$-3.6790 \cdot 10^{-03}$	$-3.6827 \cdot 10^{-03}$
−275.00	$-1.5535 \cdot 10^{-03}$	$-1.5903 \cdot 10^{-03}$	$-1.6296 \cdot 10^{-02}$	$-1.6286 \cdot 10^{-02}$	$-3.2525 \cdot 10^{-03}$	$-3.2563 \cdot 10^{-03}$
−250.00	$-1.4352 \cdot 10^{-03}$	$-1.4720 \cdot 10^{-03}$	$-1.5132 \cdot 10^{-02}$	$-1.5123 \cdot 10^{-02}$	$-2.8261 \cdot 10^{-03}$	$-2.8298 \cdot 10^{-03}$
−225.00	$-1.3169 \cdot 10^{-03}$	$-1.3537 \cdot 10^{-03}$	$-1.3968 \cdot 10^{-02}$	$-1.3959 \cdot 10^{-02}$	$-2.3997 \cdot 10^{-03}$	$-2.4034 \cdot 10^{-03}$
−200.00	$-1.1986 \cdot 10^{-03}$	$-1.2355 \cdot 10^{-03}$	$-1.2804 \cdot 10^{-02}$	$-1.2795 \cdot 10^{-02}$	$-1.9732 \cdot 10^{-03}$	$-1.9770 \cdot 10^{-03}$
−175.00	$-1.0804 \cdot 10^{-03}$	$-1.1172 \cdot 10^{-03}$	$-1.1640 \cdot 10^{-02}$	$-1.1631 \cdot 10^{-02}$	$-1.5468 \cdot 10^{-03}$	$-1.5505 \cdot 10^{-03}$
−150.00	$-9.6208 \cdot 10^{-04}$	$-9.9890 \cdot 10^{-04}$	$-1.0476 \cdot 10^{-02}$	$-1.0467 \cdot 10^{-02}$	$-1.1204 \cdot 10^{-03}$	$-1.1241 \cdot 10^{-03}$
−125.00	$-8.4378 \cdot 10^{-04}$	$-8.8060 \cdot 10^{-04}$	$-9.3123 \cdot 10^{-03}$	$-9.3027 \cdot 10^{-03}$	$-6.9393 \cdot 10^{-04}$	$-6.9767 \cdot 10^{-04}$
−100.00	$-7.2632 \cdot 10^{-04}$	$-7.6305 \cdot 10^{-04}$	$-8.1477 \cdot 10^{-03}$	$-8.1381 \cdot 10^{-03}$	$-2.6776 \cdot 10^{-04}$	$-2.7150 \cdot 10^{-04}$
−75.00	$-6.1239 \cdot 10^{-04}$	$-6.4897 \cdot 10^{-04}$	$-6.9819 \cdot 10^{-03}$	$-6.9723 \cdot 10^{-03}$	$1.5779 \cdot 10^{-04}$	$1.5406 \cdot 10^{-04}$
−50.00	$-5.0437 \cdot 10^{-04}$	$-5.4051 \cdot 10^{-04}$	$-5.8142 \cdot 10^{-03}$	$-5.8046 \cdot 10^{-03}$	$5.8253 \cdot 10^{-04}$	$5.7882 \cdot 10^{-04}$

Table D.1 – *Continued on next page*

Table D.1 – *Continued from previous page*

−25.00	$-4.0402 \cdot 10^{-04}$	$-4.4004 \cdot 10^{-04}$	$-4.6444 \cdot 10^{-03}$	$-4.6348 \cdot 10^{-03}$	$1.0063 \cdot 10^{-03}$	$1.0026 \cdot 10^{-03}$
0.00	$-3.1351 \cdot 10^{-04}$	$-3.4944 \cdot 10^{-04}$	$-3.4722 \cdot 10^{-03}$	$-3.4627 \cdot 10^{-03}$	$1.4290 \cdot 10^{-03}$	$1.4253 \cdot 10^{-03}$

Table D.2.: Exemplary solutions for the stress field

t^*[N/mm^2]	σ_{33}(④)[N/mm^2]		σ_{11}(⑤)[N/mm^2]	
	reference solution	classical/ variational approach	reference solution	classical/ variational approach
100.00	$3.0796 \cdot 10^2$	$3.0860 \cdot 10^2$	$-4.0299 \cdot 10^0$	$-4.0375 \cdot 10^0$
175.00	$5.0755 \cdot 10^2$	$5.0731 \cdot 10^2$	$-7.0549 \cdot 10^0$	$-7.0682 \cdot 10^0$
200.00	$5.1188 \cdot 10^2$	$5.1195 \cdot 10^2$	$-8.1055 \cdot 10^0$	$-8.1205 \cdot 10^0$
225.00	$5.1508 \cdot 10^2$	$5.1524 \cdot 10^2$	$-9.2310 \cdot 10^0$	$-9.2471 \cdot 10^0$
250.00	$5.1717 \cdot 10^2$	$5.1726 \cdot 10^2$	$-1.0447 \cdot 10^1$	$-1.0464 \cdot 10^1$
275.00	$5.1844 \cdot 10^2$	$5.1844 \cdot 10^2$	$-1.1766 \cdot 10^1$	$-1.1783 \cdot 10^1$
300.00	$5.1918 \cdot 10^2$	$5.1904 \cdot 10^2$	$-1.3199 \cdot 10^1$	$-1.3215 \cdot 10^1$
325.00	$5.1963 \cdot 10^2$	$5.1935 \cdot 10^2$	$-1.4755 \cdot 10^1$	$-1.4773 \cdot 10^1$
350.00	$5.1988 \cdot 10^2$	$5.1952 \cdot 10^2$	$-1.6466 \cdot 10^1$	$-1.6487 \cdot 10^1$
400.00	$5.2007 \cdot 10^2$	$5.1967 \cdot 10^2$	$-2.5751 \cdot 10^1$	$-2.5753 \cdot 10^1$
412.50	$5.2008 \cdot 10^2$	$5.1970 \cdot 10^2$	$-3.2869 \cdot 10^1$	$-3.2764 \cdot 10^1$
425.00	$5.2008 \cdot 10^2$	$5.1975 \cdot 10^2$	$-5.1517 \cdot 10^1$	$-5.0898 \cdot 10^1$
437.50	$5.2008 \cdot 10^2$	$5.1978 \cdot 10^2$	$-5.4243 \cdot 10^1$	$-5.3654 \cdot 10^1$
450.00	$5.2008 \cdot 10^2$	$5.1969 \cdot 10^2$	$-5.2568 \cdot 10^1$	$-5.1398 \cdot 10^1$
425.00	$4.4309 \cdot 10^2$	$4.4254 \cdot 10^2$	$-5.1560 \cdot 10^1$	$-5.0389 \cdot 10^1$
400.00	$3.6610 \cdot 10^2$	$3.6539 \cdot 10^2$	$-5.0553 \cdot 10^1$	$-4.9380 \cdot 10^1$
375.00	$2.8910 \cdot 10^2$	$2.8824 \cdot 10^2$	$-4.9545 \cdot 10^1$	$-4.8370 \cdot 10^1$
350.00	$2.1211 \cdot 10^2$	$2.1109 \cdot 10^2$	$-4.8538 \cdot 10^1$	$-4.7361 \cdot 10^1$
325.00	$1.3512 \cdot 10^2$	$1.3394 \cdot 10^2$	$-4.7530 \cdot 10^1$	$-4.6351 \cdot 10^1$
300.00	$5.8129 \cdot 10^1$	$5.6784 \cdot 10^1$	$-4.6523 \cdot 10^1$	$-4.5342 \cdot 10^1$
275.00	$-1.8863 \cdot 10^1$	$-2.0367 \cdot 10^1$	$-4.5515 \cdot 10^1$	$-4.4333 \cdot 10^1$
250.00	$-9.5855 \cdot 10^1$	$-9.7518 \cdot 10^1$	$-4.4508 \cdot 10^1$	$-4.3323 \cdot 10^1$
225.00	$-1.7284 \cdot 10^2$	$-1.7467 \cdot 10^2$	$-4.3500 \cdot 10^1$	$-4.2314 \cdot 10^1$
200.00	$-2.4983 \cdot 10^2$	$-2.5182 \cdot 10^2$	$-4.2493 \cdot 10^1$	$-4.1304 \cdot 10^1$
175.00	$-3.2683 \cdot 10^2$	$-3.2897 \cdot 10^2$	$-4.1485 \cdot 10^1$	$-4.0295 \cdot 10^1$
150.00	$-4.0382 \cdot 10^2$	$-4.0612 \cdot 10^2$	$-4.0478 \cdot 10^1$	$-3.9286 \cdot 10^1$
125.00	$-4.6613 \cdot 10^2$	$-4.6636 \cdot 10^2$	$-3.9470 \cdot 10^1$	$-3.8276 \cdot 10^1$
100.00	$-4.8090 \cdot 10^2$	$-4.8202 \cdot 10^2$	$-3.8452 \cdot 10^1$	$-3.7256 \cdot 10^1$
75.00	$-4.9339 \cdot 10^2$	$-4.9449 \cdot 10^2$	$-3.7410 \cdot 10^1$	$-3.6213 \cdot 10^1$
50.00	$-5.0275 \cdot 10^2$	$-5.0374 \cdot 10^2$	$-3.6338 \cdot 10^1$	$-3.5139 \cdot 10^1$
25.00	$-5.0950 \cdot 10^2$	$-5.1010 \cdot 10^2$	$-3.5229 \cdot 10^1$	$-3.4029 \cdot 10^1$
0.00	$-5.1394 \cdot 10^2$	$-5.1418 \cdot 10^2$	$-3.4081 \cdot 10^1$	$-3.2879 \cdot 10^1$
−25.00	$-5.1666 \cdot 10^2$	$-5.1666 \cdot 10^2$	$-3.2889 \cdot 10^1$	$-3.1684 \cdot 10^1$

Table D.2 – *Continued on next page*

Table D.2 – *Continued from previous page*

-100.00	$-5.1953 \cdot 10^{2}$	$-5.1925 \cdot 10^{2}$	$-2.9012 \cdot 10^{1}$	$-2.7807 \cdot 10^{1}$
-125.00	$-5.1979 \cdot 10^{2}$	$-5.1944 \cdot 10^{2}$	$-2.7611 \cdot 10^{1}$	$-2.6407 \cdot 10^{1}$
-150.00	$-5.1993 \cdot 10^{2}$	$-5.1954 \cdot 10^{2}$	$-2.6153 \cdot 10^{1}$	$-2.4949 \cdot 10^{1}$
-175.00	$-5.2000 \cdot 10^{2}$	$-5.1959 \cdot 10^{2}$	$-2.4634 \cdot 10^{1}$	$-2.3430 \cdot 10^{1}$
-200.00	$-5.2004 \cdot 10^{2}$	$-5.1961 \cdot 10^{2}$	$-2.3047 \cdot 10^{1}$	$-2.1841 \cdot 10^{1}$
-225.00	$-5.2006 \cdot 10^{2}$	$-5.1963 \cdot 10^{2}$	$-2.1371 \cdot 10^{1}$	$-2.0165 \cdot 10^{1}$
-250.00	$-5.2007 \cdot 10^{2}$	$-5.1964 \cdot 10^{2}$	$-1.9455 \cdot 10^{1}$	$-1.8250 \cdot 10^{1}$
-275.00	$-5.2008 \cdot 10^{2}$	$-5.1965 \cdot 10^{2}$	$-1.6919 \cdot 10^{1}$	$-1.5725 \cdot 10^{1}$
-300.00	$-5.2008 \cdot 10^{2}$	$-5.1967 \cdot 10^{2}$	$-1.3407 \cdot 10^{1}$	$-1.2240 \cdot 10^{1}$
-325.00	$-5.2008 \cdot 10^{2}$	$-5.1970 \cdot 10^{2}$	$-8.3747 \cdot 10^{0}$	$-7.2317 \cdot 10^{0}$
-350.00	$-5.2008 \cdot 10^{2}$	$-5.1976 \cdot 10^{2}$	$-5.8370 \cdot 10^{-1}$	$4.8530 \cdot 10^{-1}$
-400.00	$-5.2008 \cdot 10^{2}$	$-5.2015 \cdot 10^{2}$	$4.9090 \cdot 10^{1}$	$4.8841 \cdot 10^{1}$
-412.50	$-5.2008 \cdot 10^{2}$	$-5.2029 \cdot 10^{2}$	$5.7428 \cdot 10^{1}$	$5.6738 \cdot 10^{1}$
-425.00	$-5.2008 \cdot 10^{2}$	$-5.2036 \cdot 10^{2}$	$5.6882 \cdot 10^{1}$	$5.6939 \cdot 10^{1}$
-437.50	$-5.2008 \cdot 10^{2}$	$-5.2030 \cdot 10^{2}$	$5.6364 \cdot 10^{1}$	$5.5974 \cdot 10^{1}$
-450.00	$-5.2008 \cdot 10^{2}$	$-5.2006 \cdot 10^{2}$	$5.4813 \cdot 10^{1}$	$5.3559 \cdot 10^{1}$
-425.00	$-4.4309 \cdot 10^{2}$	$-4.4291 \cdot 10^{2}$	$5.3806 \cdot 10^{1}$	$5.2550 \cdot 10^{1}$
-400.00	$-3.6610 \cdot 10^{2}$	$-3.6576 \cdot 10^{2}$	$5.2798 \cdot 10^{1}$	$5.1540 \cdot 10^{1}$
-375.00	$-2.8910 \cdot 10^{2}$	$-2.8861 \cdot 10^{2}$	$5.1791 \cdot 10^{1}$	$5.0531 \cdot 10^{1}$
-350.00	$-2.1211 \cdot 10^{2}$	$-2.1146 \cdot 10^{2}$	$5.0783 \cdot 10^{1}$	$4.9521 \cdot 10^{1}$
-325.00	$-1.3512 \cdot 10^{2}$	$-1.3431 \cdot 10^{2}$	$4.9776 \cdot 10^{1}$	$4.8512 \cdot 10^{1}$
-300.00	$-5.8131 \cdot 10^{1}$	$-5.7158 \cdot 10^{1}$	$4.8768 \cdot 10^{1}$	$4.7503 \cdot 10^{1}$
-275.00	$1.8860 \cdot 10^{1}$	$1.9993 \cdot 10^{1}$	$4.7761 \cdot 10^{1}$	$4.6493 \cdot 10^{1}$
-250.00	$9.5851 \cdot 10^{1}$	$9.7144 \cdot 10^{1}$	$4.6753 \cdot 10^{1}$	$4.5484 \cdot 10^{1}$
-225.00	$1.7284 \cdot 10^{2}$	$1.7430 \cdot 10^{2}$	$4.5746 \cdot 10^{1}$	$4.4474 \cdot 10^{1}$
-200.00	$2.4983 \cdot 10^{2}$	$2.5145 \cdot 10^{2}$	$4.4738 \cdot 10^{1}$	$4.3465 \cdot 10^{1}$
-175.00	$3.2683 \cdot 10^{2}$	$3.2860 \cdot 10^{2}$	$4.3731 \cdot 10^{1}$	$4.2456 \cdot 10^{1}$
-150.00	$4.0382 \cdot 10^{2}$	$4.0575 \cdot 10^{2}$	$4.2723 \cdot 10^{1}$	$4.1446 \cdot 10^{1}$
-125.00	$4.6613 \cdot 10^{2}$	$4.6598 \cdot 10^{2}$	$4.1716 \cdot 10^{1}$	$4.0437 \cdot 10^{1}$
-100.00	$4.8090 \cdot 10^{2}$	$4.8165 \cdot 10^{2}$	$4.0698 \cdot 10^{1}$	$3.9417 \cdot 10^{1}$
-75.00	$4.9339 \cdot 10^{2}$	$4.9412 \cdot 10^{2}$	$3.9656 \cdot 10^{1}$	$3.8374 \cdot 10^{1}$
-50.00	$5.0275 \cdot 10^{2}$	$5.0337 \cdot 10^{2}$	$3.8583 \cdot 10^{1}$	$3.7300 \cdot 10^{1}$
-25.00	$5.0950 \cdot 10^{2}$	$5.0972 \cdot 10^{2}$	$3.7475 \cdot 10^{1}$	$3.6189 \cdot 10^{1}$
0.00	$5.1393 \cdot 10^{2}$	$5.1381 \cdot 10^{2}$	$3.6327 \cdot 10^{1}$	$3.5039 \cdot 10^{1}$

E. Nodal Solutions for the Dynamic Benchmark Problem

This chapter lists exemplary values for the strain field, the stresses, the plastic strains, and the LAGRANGE multiplier for the displacement-driven deformation of an axisymmetric steel shaft in small and finite strain elastoplasticity. They are determined using the conventional approach for small and finite strain elastoplasticity together with the DIRK(3) method and a time step size of $\Delta t = 1 \cdot 10^{-5}$s. The solutions for the multifield approaches as well as for the viscoplastic adaptations with $\chi = 0.001$ Ns/mm^2 are not shown explicitly due to the huge similarities.

Table E.1.: Exemplary solutions for the strain, the stress, the LAGRANGE multiplier, and the plastic strain field at evolution point ① for small strain elastoplasticity

u_Z[mm]	$\varepsilon_{ZZ}(①)$[-]	$\sigma_{ZZ}(①)$[N/mm^2]	$\varepsilon_{p,ZZ}(①)$[-]	$\lambda(①)$[1/s]
0.0000	0.0000	0.0000	0.0000	0.0000
-0.2989	-0.0030	-600.0000	0.0000	0.0000
-0.5910	-0.0060	-1011.5965	-0.0009	15.1283
-0.8699	-0.0090	-870.0603	-0.0046	35.9829
-1.1293	-0.0120	-873.1094	-0.0076	17.5264
-1.3633	-0.0150	-973.2176	-0.0101	29.3150
-1.5667	-0.0180	-812.2761	-0.0140	23.4950
-1.7348	-0.0210	-963.2054	-0.0162	23.8073
-1.8641	-0.0240	-893.9042	-0.0196	36.9014
-1.9514	-0.0271	-853.0823	-0.0228	19.9340
-1.9950	-0.0303	-990.9310	-0.0254	20.8121
-1.9937	-0.0324	-796.5242	-0.0284	34.3352
-1.9477	-0.0358	-890.1490	-0.0313	39.9873
-1.8579	-0.0361	-671.4195	-0.0327	0.0000
-1.7264	-0.0333	-113.6446	-0.0327	0.0000
-1.5561	-0.0300	556.8003	-0.0327	0.0000
-1.3509	-0.0274	897.0199	-0.0319	19.1284
-1.1154	-0.0255	876.8880	-0.0299	37.1075
-0.8548	-0.0238	837.5331	-0.0280	17.9959
-0.5750	-0.0215	928.1603	-0.0261	20.0362
-0.2822	-0.0185	852.1704	-0.0228	28.0723
0.0168	-0.0160	930.2361	-0.0207	16.1889
0.3155	-0.0133	930.0613	-0.0179	28.8722
0.6071	-0.0117	867.8574	-0.0160	13.2575
0.8850	-0.0095	941.4862	-0.0142	20.6775
1.1431	-0.0073	866.1839	-0.0116	14.3288
1.3755	-0.0055	906.2744	-0.0100	13.0075
1.5771	-0.0033	910.1963	-0.0078	21.2658

Table E.1 – *Continued on next page*

Table E.1 – *Continued from previous page*

1.7432	-0.0013	865.6619	-0.0056	14.2728
1.8701	0.0007	925.7299	-0.0040	11.1963
1.9551	0.0024	862.3757	-0.0019	21.8332
1.9961	0.0041	867.6291	-0.0003	1.6708
1.9923	0.0064	921.2012	0.0018	3.6235
1.9438	0.0082	852.1891	0.0039	14.0364
1.8516	0.0090	739.9943	0.0053	0.0000
1.7179	0.0055	40.8023	0.0053	0.0000
1.5455	0.0028	-500.7802	0.0053	0.0000
1.3385	-0.0009	-938.5350	0.0038	20.4099
1.1014	-0.0028	-921.9784	0.0018	25.5279
0.8395	-0.0062	-826.7332	-0.0020	21.2573
0.5588	-0.0090	-999.2352	-0.0040	26.2449
0.2656	-0.0120	-828.1474	-0.0078	29.6963
-0.0336	-0.0149	-913.7364	-0.0103	13.2967
-0.3321	-0.0175	-938.7406	-0.0128	23.9929
-0.6231	-0.0201	-804.6280	-0.0161	23.5509
-0.9001	-0.0235	-971.2926	-0.0187	26.2951
-1.1569	-0.0269	-870.6547	-0.0225	31.8593
-1.3877	-0.0297	-889.3909	-0.0253	14.5961
-1.5873	-0.0326	-954.8881	-0.0278	26.5994
-1.7513	-0.0353	-828.5083	-0.0311	22.0102
-1.8760	-0.0378	-939.1455	-0.0331	13.3265
-1.9585	-0.0403	-869.9944	-0.0359	22.1292
-1.9971	-0.0428	-846.8255	-0.0385	8.9222
-1.9908	-0.0456	-938.1260	-0.0409	3.4168
-1.9398	-0.0478	-794.2501	-0.0439	19.1472
-1.8452	-0.0498	-631.5134	-0.0467	0.0000
-1.7092	-0.0466	12.2701	-0.0467	0.0000
-1.5348	-0.0439	554.7917	-0.0467	0.0000
-1.3259	-0.0397	927.7298	-0.0443	14.5836
-1.0873	-0.0368	914.8764	-0.0414	32.0225
-0.8242	-0.0326	844.8506	-0.0368	21.5269
-0.5427	-0.0290	1012.4285	-0.0341	27.0321
-0.2489	-0.0255	836.6737	-0.0297	30.2398
0.0504	-0.0221	945.1646	-0.0268	15.3505
0.3487	-0.0189	944.5911	-0.0237	33.1567
0.6390	-0.0156	833.4138	-0.0198	25.1670
0.9151	-0.0120	992.9657	-0.0169	30.5769
1.1706	-0.0083	879.0420	-0.0127	33.3000
1.3997	-0.0052	914.9478	-0.0098	19.1886
1.5975	-0.0022	960.1204	-0.0070	29.6703
1.7594	0.0007	833.6431	-0.0035	22.6071

Table E.1 – *Continued on next page*

Table E.1 – *Continued from previous page*

1.8818	0.0034	953.7643	-0.0014	16.2789
1.9619	0.0061	866.3420	0.0017	26.4644
1.9979	0.0089	859.5879	0.0046	10.9190
1.9891	0.0119	933.9341	0.0072	24.6871
1.9356	0.0145	786.2009	0.0106	17.3495
1.8387	0.0167	590.0253	0.0138	0.0000
1.7004	0.0136	-31.8564	0.0138	0.0000
1.5240	0.0108	-603.8524	0.0138	0.0000
1.3133	0.0061	-941.7573	0.0108	8.1423
1.0731	0.0029	-888.5935	0.0074	40.0490
0.8089	-0.0015	-855.0086	0.0027	25.8542
0.5265	-0.0053	-997.5802	-0.0003	28.6482
0.2322	-0.0090	-827.8482	-0.0049	29.2595
-0.0672	-0.0127	-957.8640	-0.0079	18.1727

Table E.2.: Exemplary solutions for the strain, the stress, the LAGRANGE multiplier, and the plastic strain field at evolution point ① for finite strain elastoplasticity

u_Z[mm]	$E_{ZZ}(①)$[-]	$S_{ZZ}(①)$[N/mm^2]	$E_{p,ZZ}(①)$[-]	$\lambda(①)$[1/s]
0.0000	0.0000	0.0000	0.0000	0.0000
-0.2989	-0.0030	-603.5160	0.0000	0.0000
-0.5910	-0.0061	-1023.5293	-0.0009	15.0718
-0.8699	-0.0091	-888.4206	-0.0047	36.0906
-1.1293	-0.0122	-891.3157	-0.0077	17.9402
-1.3633	-0.0153	-1006.4801	-0.0101	29.2807
-1.5667	-0.0185	-842.9667	-0.0139	24.4065
-1.7348	-0.0217	-998.9709	-0.0162	22.9538
-1.8641	-0.0250	-954.2680	-0.0195	36.6020
-1.9514	-0.0283	-894.2506	-0.0228	19.7516
-1.9950	-0.0314	-1042.5791	-0.0250	16.4727
-1.9937	-0.0348	-897.3134	-0.0287	39.2595
-1.9477	-0.0382	-946.5712	-0.0315	50.2580
-1.8579	-0.0379	-629.9781	-0.0326	0.0000
-1.7264	-0.0351	-63.0727	-0.0326	0.0000
-1.5561	-0.0315	642.4008	-0.0326	0.0000
-1.3509	-0.0288	969.2134	-0.0316	11.8408
-1.1154	-0.0268	922.3756	-0.0297	32.8555
-0.8548	-0.0252	871.2768	-0.0280	15.6484
-0.5750	-0.0228	993.1647	-0.0265	24.6745
-0.2822	-0.0198	875.5723	-0.0232	27.2347
0.0168	-0.0178	967.9392	-0.0218	9.7754
0.3155	-0.0154	960.9982	-0.0196	22.5655

Table E.2 – *Continued on next page*

Table E.2 – *Continued from previous page*

0.6071	-0.0142	873.6825	-0.0180	11.5156
0.8850	-0.0124	985.7770	-0.0169	17.4634
1.1431	-0.0108	864.1490	-0.0148	11.7949
1.3755	-0.0095	926.7186	-0.0139	5.1844
1.5771	-0.0083	926.6588	-0.0128	15.4189
1.7432	-0.0074	847.7580	-0.0115	4.6208
1.8701	-0.0067	937.1158	-0.0113	4.1576
1.9551	-0.0062	835.8275	-0.0104	9.5253
1.9961	-0.0059	842.6958	-0.0100	0.0000
1.9923	-0.0057	863.2811	-0.0100	1.0160
1.9438	-0.0054	797.3776	-0.0094	9.8504
1.8516	-0.0056	759.0233	-0.0094	0.0000
1.7179	-0.0090	76.7003	-0.0094	0.0000
1.5455	-0.0118	-488.4606	-0.0094	0.0000
1.3385	-0.0155	-1044.7133	-0.0103	16.9011
1.1014	-0.0179	-1009.7869	-0.0127	36.4348
0.8395	-0.0199	-856.0199	-0.0154	7.5890
0.5588	-0.0216	-1065.5392	-0.0159	10.2538
0.2656	-0.0227	-838.8846	-0.0181	17.4227
-0.0336	-0.0242	-912.1285	-0.0191	1.3692
-0.3321	-0.0254	-979.1755	-0.0199	19.4784
-0.6231	-0.0265	-791.1451	-0.0218	7.4777
-0.9001	-0.0277	-980.1612	-0.0220	0.2150
-1.1569	-0.0292	-871.6930	-0.0239	21.7284
-1.3877	-0.0305	-861.2630	-0.0251	0.0000
-1.5873	-0.0313	-987.5613	-0.0252	9.0612
-1.7513	-0.0323	-803.1236	-0.0270	7.6793
-1.8760	-0.0330	-921.8597	-0.0271	0.0000
-1.9585	-0.0341	-900.7152	-0.0282	17.4527
-1.9971	-0.0354	-816.0989	-0.0297	0.1182
-1.9908	-0.0366	-951.1507	-0.0301	1.4568
-1.9398	-0.0383	-830.2712	-0.0322	2.1164
-1.8452	-0.0387	-562.5971	-0.0337	0.0000
-1.7092	-0.0352	131.3981	-0.0337	0.0000
-1.5348	-0.0326	639.0492	-0.0337	0.0000
-1.3259	-0.0288	993.7726	-0.0318	11.9438
-1.0873	-0.0262	1044.8267	-0.0298	27.4832
-0.8242	-0.0226	878.0510	-0.0258	22.6801
-0.5427	-0.0196	1062.3861	-0.0240	10.8997
-0.2489	-0.0170	899.2932	-0.0209	26.3927
0.0504	-0.0143	928.0104	-0.0186	9.1694
0.3487	-0.0121	998.1378	-0.0168	22.1185
0.6390	-0.0092	838.5533	-0.0134	23.9891

Table E.2 – *Continued on next page*

Table E.2 – *Continued from previous page*

0.9151	-0.0062	989.5759	-0.0112	22.1034
1.1706	-0.0031	924.6983	-0.0079	32.0135
1.3997	-0.0006	890.3888	-0.0053	13.4837
1.5975	0.0019	992.9828	-0.0034	21.3140
1.7594	0.0040	843.3404	-0.0006	19.7878
1.8818	0.0060	937.6860	0.0009	9.8965
1.9619	0.0078	899.9491	0.0030	21.4590
1.9979	0.0096	832.1313	0.0051	16.9579
1.9891	0.0113	922.0275	0.0064	24.2247
1.9356	0.0135	822.8865	0.0092	23.2706
1.8387	0.0149	822.6814	0.0106	0.0000
1.7004	0.0114	121.5125	0.0106	0.0000
1.5240	0.0086	-438.9167	0.0106	0.0000
1.3133	0.0053	-889.6594	0.0095	15.0077
1.0731	0.0029	-946.8217	0.0073	42.0122
0.8089	-0.0005	-790.1569	0.0031	30.6060
0.5265	-0.0043	-1027.2081	0.0004	24.0935
0.2322	-0.0077	-876.8850	-0.0038	35.9840
-0.0672	-0.0116	-914.2330	-0.0074	23.1742

Bibliography

Abramowitz, M. and Stegun, I. A. (1972), *Handbook of Mathematical Functions With Formulas, Graphs, and Mathematical Tables*, U.S. Department of Commerce. National Bureau of Standards. Applied Mathematics Series 55.

Ainsworth, M. and Craig, A. (1997), 'A posteriori error estimation in finite element method', *Numerische Mathematik* **60**, 429–463.

Ainsworth, M. and Oden, J. T. (1997), 'A posteriori error estimation in finite element analysis', *Computer Methods in Applied Mechanics and Engineering* **142**, 1–88.

Alberty, J. and Carstensen, C. (2000), 'Numerical analysis of time-depending primal elastoplasticity with hardening', *Journal on Numerical Analysis* **37**, 1271–1294.

Alberty, J. and Carstensen, C. (2002), 'Discontinuous Galerkin time discretization in elastoplasticity: motivation, numerical algorithms, and applications', *Computer Methods in Applied Mechanics and Engineering* **191**, 4949–4968.

Alberty, J., Carstensen, C. and Zarrabi, D. (1999), 'Adaptive numerical analysis in primal elastoplasticity with hardening', *Computer Methods in Applied Mechanics and Engineering* **171**, 175–204.

Alexander, R. (1977), 'Diagonally implicit Runge-Kutta methods for stiff O.D.E.'s', *Journal on Numerical Analysis* **14**, 1006–1021.

Alt, W. (2011), *Nichtlineare Optimierung. Eine Einführung in Theorie, Verfahren und Anwendungen*, Vieweg+Teubner Verlag.

Altenbach, H. (2012), *Kontinuumsmechanik*, Springer Verlag.

Anzellotti, G. and Luckhaus, S. (1987), 'Dynamical evolution of elasto-perfectly plastic bodies', *Applied Mathematics and Optimization* **15**, 121–140.

Argyris, J. H. and Scharpf, D. W. (1969), 'Finite Elements in Time and Space', *Nuclear Engineering and Design* **10**, 456–464.

Armero, F. (2006), 'Energy-dissipative momentum-conserving time-stepping algorithms for finite strain multiplicative plasticity', *Computer Methods in Applied Mechanics and Engineering* **195**, 4862–4889.

Arnold, D. N., Falk, R. S. and Winther, R. (2007), 'Mixed Finite Element Methods for Linear Elasticity with Weakly Imposed Symmetry', *Mathematics of Computation* **76**, 1699–1723.

Ascher, U. M. and Petzold, L. R. (1998), *Computer Methods for Ordinary Differential Equations and Differential-Algebraic Equations*, Society for Industrial and Applied Mathematics.

Auricchio, F. and Taylor, R. (1999), 'A return-map algorithm for general associative isotropic elasto-plastic material in large deformation regimes', *International Journal of Plasticity* **15**, 1359–1378.

Aziz, A. K. and Monk, P. (1989), 'Continuous Finite Elements in Space and Time for the Heat Equation', *Mathematics of Computation* **52**, 255–274.

Babuška, I. and Miller, A. (1987), 'A feedback finite element method with a posteriori error estimation: Part I. The finite element method and some basic properties of the a posteriori error estimator', *Computer Methods in Applied Mechanics and Engineering* **61**, 1–40.

Babuška, I. and Rheinboldt, W. C. (1978), 'Error estimates for adaptive finite element computations', *Journal on Numerical Analysis* **15**, 736–754.

Babuška, I. and Strouboulis, T. (2001), *The Finite Element Method and its Reliability*, Oxford Science Publications.

Backman, M. E. (1964), 'Form for the Relation Between Stress and Finite Elastic and Plastic Strains under Impulse Loading', *Journal of Applied Physics* **35**, 2524–2533.

Bangerth, W. and Rannacher, R. (2003), *Adaptive Finite Element Methods for Differential Equations*, Birkhäuser.

Bär, S. and Groß, M. (2016), 'Variational integration in endochronic theory for small strain elastoplastodynamics', *Proceedings in Applied Mathematics and Mechanics* **16**, 255–256.

Bargel, H.-J. and Schulze, G. (2005), *Werkstoffkunde*, Springer Verlag.

Bathe, K.-J. (2002), *Finite-Elemente-Methoden*, Springer-Verlag.

Bishop, J. F. W. and Hill, R. (1951), 'A theory of the plastic distortion of a polycrystalline aggregate under combined stresses', *The London, Edinburgh and Dublin Philosophical Magazine and Journal of Science* **42**, 414–427.

Boffi, D., Brezzi, F. and Fortin, M. (2013), *Mixed Finite Element Methods and Applications*, Springer Verlag.

Bonet, J. and Wood, R. D. (2009), *Nonlinear Continuum Mechanics for Finite Element Analysis*, Cambridge University Press.

Borri, M., Mello, F. and Atluri, S. N. (1990), 'Variational approaches for dynamics and time-finite-elements: numerical studies', *Computational Mechanics* **7**, 49–76.

Botasso, C. L. (1997), 'A new look at finite elements in time: a variational interpretation of Runge-Kutta methods', *Applied Numerical Mathematics* **25**, 355–368.

Botasso, C. L. and Ragazzi, A. (2000), 'Finite Element and Runge-Kutta Methods for Boundary-Value and Optimal Control Problems', *Journal for Guidance, Control, and Dynamics* **23**, 749–750.

Braess, D. (2010), *Finite Elemente. Theorie, schnelle Löser und Anwendungen in der Elastizitätstheorie*, Springer Verlag.

Bremer, H. (1993), 'Das Jourdainsche Prinzip', *Zeitschrift für angewandte Mathematik und Mechanik* **73**, 184–187.

Brezzi, F. and Bathe, K.-J. (1990), 'A Discourse on the Stability Conditions for Mixed Finite Element Formulations', *Computer Methods in Applied Mechanics and Engineering* **82**, 27–57.

Brezzi, F. and Fortin, M. (1991), *Mixed and Hybrid Finite Element Methods*, Springer Verlag.

Buliga, M. (2009), 'Hamiltonian inclusions with convex dissipation with a view towards applications', *Annals of the Academy of Romanian Scientists. Series on Mathematics and its Applications* **1**, 228–251.

Burger, M. (2003), 'Infinite-dimensional Optimization and Optimal Design', Lecture Notes, 285J, Department of Mathematics,UCLA.

Butcher, J. C. (1963), 'Coefficients for the study of Runge-Kutta integration processes', *Journal of Australian Mathematical Society* **3**, 185–201.

Butcher, J. C. (1964), 'Implicit Runge-Kutta Processes', *Mathematics of Computation* **18**, 50–64.

Butcher, J. C. (1996), 'A history of Runge-Kutta methods', *Applied Numerical Mathematics* **20**, 247–260.

Butcher, J. C. (2008), *Numerical Methods for Ordinary Differential Equations*, John Wiley & Sons.

Butcher, J. C. and Wanner, G. (1996), 'Runge-Kutta methods: some historical notes', *Applied Numerical Mathematics* **22**, 113–151.

Büttner, J. and Simeon, B. (2002), 'Runge-Kutta methods in elastoplasticity', *Applied Numerical Mathematics* **41**, 443–458.

Capurso, M. and Maier, G. (1970), 'Incremental elastoplastic analysis and quadratic optimization', *Meccanica* **5**, 107–116.

Carstens, S. (2013), 'Diskontinuierliche Galerkin-Verfahren in Raum und Zeit zur Simulation von Transportprozessen', PhD Thesis, Universität Kassel.

Carstensen, C. (1997), 'Domain Decomposition for a Non-smooth Convex Minimization Problem and its Application to Plasticity', *Numerical Linear Algebra with Applications* **4**, 177–190.

Carstensen, C., Hackl, K. and Mielke, A. (2002), 'Nonconvex Potentials and Microstructures in Finite-Strain Plasticity', *Proceedings of the Royal Society A. Mathematical, Physical and Engineering Sciences.* **458**, 299–317.

Casey, J. (1985), 'Approximate Kinematical Relations in Plasticity', *International Journal of Solids and Structures* **21**, 671–682.

Casey, J. and Nagdhi, P. M. (1980), 'A remark on the Use of the Decomposition $\boldsymbol{F} = \boldsymbol{F}_{\mathrm{e}}\boldsymbol{F}_{\mathrm{p}}$ in Plasticity', *Journal of Applied Mechanics* **47**, 672–673.

Casey, J. and Naghdi, P. (1988), 'On the relationship between the Eulerian and Lagrangian descriptions of finite rigid plasticity', *Archive for Rational Mechanics and Analysis* **102**, 351–375.

Cash, J. R. (1979), 'Diagonally Implicit Runge-Kutta Formulae with Error Estimates', *IMA Journal of Applied Mathematics* **24**, 293–301.

Casio Computer Co. LTD, . (2016), 'Nodes and Weights of Gaussian Quadrature Calculator'. **URL:** *http://keisan.casio.com/exec/system/1329114617*

Chaboche, J. (2008), 'A review of some plasticity and viscoplasticity constitutive theories', *International Journal of Plasticity* **24**, 1642–1693.

Chakrabarty, J. (2000), *Applied Plasticity*, Springer-Verlag.

Chelmiński, K. (2001), 'Coercive approximation of viscoplasticity and plasticity', *Asymptotic Analysis* **26**, 105–133.

Christensen, P. W. (2002), 'A nonsmooth Newton method for elastoplastic problems', *Computer Methods in Applied Mechanics and Engineering* **191**, 1189–1219.

Chung, J. and Hulbert, G. M. (1993), 'A Time Integration Algorithm for Structural Dynamics with Improved Numerical Dissipation: The Generalized-α Method', *Journal of Applied Mechanics* **60**, 371–375.

Ciarlet Jr., P., Huang, J. and Zou, J. (2003), 'Some observations on generalized saddle-point problems', *Journal on Matrix Analysis and Application* **25**, 224–236.

Ciarlet, P. G. (1978), *The Finite Element Method for Elliptic Problems*, North-Holland Publishing Company.

Clarke, F. H. (1990), *Optimization and Nonsmooth Analysis*, Society for Industrial and Applied Mathematics.

Cockburn, B., Karniadakis, G. E. and Shu, C.-W. (2000), Discontinuous Galerkin Methods. Theory, Computation and Applications, *in* Griebel, M., Keyes, D. E., Nieminen, R. M., Roose, D. and Schlick, T., eds, 'Lecture Notes in Computational Science and Engineering 11', Springer Verlag.

Comi, C. and Perego, U. (1991), 'A variationally consistent generalized variable formulation of the elastoplastic rate problem', *Rendiconti Lincei Matematica e Applicazioni* **2**, 177–190.

Comi, C. and Perego, U. (1995), 'A unified approach for variationally consistent finite elements in elastoplasticity', *Computer Methods in Applied Mechanics and Engineering* **121**, 323–344.

Cristescu, N. (1967), *Dynamic Plasticity*, North-Holland.

De Boer, R. (1982), *Vektor- und Tensorrechnung für Ingenieure*, Springer Verlag.

De Borst, R. and Mühlhaus, H.-B. (1992), 'Gradient-dependent plasticity: formulation and algorithmic aspects', *International Journal for Numerical Methods in Engineering* **35**, 521–539.

De Souza Neto, E., Perić, D. and Owen, D. (2008), *Computational methods for plasticity*, John Wiley & Sons.

Dhondt, G. (2004), *The finite element method for three-dimensional thermomechanical applications*, John Wiley & Sons.

Dormand, J. R. and Prince, P. J. (1980), 'A family of embedded Runge-Kutta formulae', *Journal of Computational and Applied Mathematics* **6**, 19–26.

Dür, M. and Martin, A. (2005), 'Einführung in die Optimierung', Vorlesungsskript, TU Darmstadt.

Duvaut, G. and Lions, J. L. (1972), *Inequalities in Mechanics and Physics*, Springer Verlag.

Ebobisse, F. and Reddy, B. D. (2004), 'Some mathematical problems in perfect plasticity', *Computer Methods in Applied Mechanics and Engineering* **193**, 5071–5094.

Ehlers, W. (2009), 'Ergänzungen zu den Vorlesungen Technische Mechanik und Höhere Mechanik', Vorlesungsskript, Universität Stuttgart.

Eidel, B. and Kuhn, C. (2011), 'Order reduction in computational inelasticity: Why it happens and how to overcome it - The ODE-case of viscoelasticity', *International Journal for Numerical Methods in Engineering* **87**, 1046–1073.

Eidel, B. and Kuhn, C. (2015), 'Is there an order-barrier $p \leq 2$ for time integration in computational elasto-plasticity?'.

El Hajj, A., Ibrahim, H. and Monneau, R. (2009), 'Dislocation dynamics: from microscopic models to macroscopic crystal plasticity', *Continuum Mechanics and Thermodynamics* **21**, 109–123.

Ellsiepen, P. (1999), 'Zeit- und ortsadaptive Verfahren angewandt auf Mehrphasenprobleme poröser Medien', PhD Thesis, Universität Stuttgart.

Ellsiepen, P. and Hartmann, S. (2001), 'Remarks on the interpretation of current non-linear finite element analyses as differential-algebraic equations', *International Journal for Numerical Methods in Engineering* **51**, 679–707.

Eriksson, K., Estep, D., Hansbo, P. and Johnson, C. (2005), *Computational Differential Equations*, Studentlitteratur.

Estep, D. J. and Stuart, A. M. (2001), 'The Dynamical Behavior of the Discontinuous Galerkin Method and Related Difference Schemes', *Mathematics of Computation* **71**, 1075–1103.

Euler, L. (1894), Methode Curven zu finden, denen eine Eigenschaft im höchsten oder geringsten Grade zukommt oder Lösung des isoperimetrischen Problems, wenn es im weitesten Sinne des Wortes aufgefasst wird., *in* Stäckel, P., ed., 'Ostwalds Klassiker der exakten Wissenschaften Nr. 46', Verlag von Wilhelm Engelmann.

Eve, R. A., Reddy, B. D. and Rockafellar, R. T. (1990), 'An internal variable theory of elastoplasticity based on the maximum plastic work inequality', *Quarterly of Applied Mathematics* **48**, 59–83.

Facchinei, F. and Pang, J.-S. (2003), *Finite-Dimensional Variational Inequalities and Complementarity Problems. Vol. II*, Springer-Verlag.

Fehlberg, E. (1970), 'Klassische Runge-Kutta-Formeln vierter und niedrigerer Ordnung mit Schrittweiten-Kontrolle und ihre Anwendung auf Wärmeleitungsprobleme', *Computing* **6**, 61–71.

Finlayson, B. A. (1972), *The Method of Weighted Residuals and Variational Principles*, Society for Industrial and Applied Mathematics.

Finlayson, B. A. and Scriven, L. E. (1966), 'On the Search for Variational Principles', *International Journal of Heat and Mass Transfer* **10**, 799–821.

Fleischer, J. (2014), 'Intrinsische Hybridverbunde für Leichtbautragstrukturen - Grundlage der Fertigung, Charakterisierung und Auslegung. DFG SPP 1712'.

Fried, I. (1969), 'Finite Element Analysis of Time-Dependent Phenomena', *American Institute of Aeronautics and Astronautics Journal* **6**, 1170–1173.

Gautschi, W. (1999), 'Orthogonal Polynomials and Quadrature', *Electronic Transactions on Numerical Analysis* **9**, 65–76.

Geiger, C. and Kanzow, C. (2002), *Theorie und Numerik restringierter Optimierungsaufgaben*, Springer-Verlag.

Germain, P. (1972), 'Sur l'application de la méthode des puissances virtuelles en mécanique des milieux continus', *Comptes rendus hebdomadaires des séances de l'Académie des sciences. Séries A et B, Sciences mathématiques et Sciences* **274**, 1051–1055.

Germain, P. (1973), 'The method of virtual power in continuum mechanics. Part 2: Microstructure', *SIAM Journal on Applied Mathematics* **25**, 556–576.

Gleim, T. (2010), 'Entwicklung von residualen Fehlerschätzern, Fehlerindikatoren und Methoden der adaptiven Zeitschrittweitensteuerung für Galerkin-Zeitintegrationsverfahren', Master Thesis, Universität Kassel.

Gleim, T. (2016), 'Simulation of Manufacturing Sequences of Functionally Graded Structures', PhD Thesis, Universität Kassel.

Gleim, T. and Kuhl, D. (2013), 'Higher order accurate discontinuous and continuous p-Galerkin methods for linear elastodynamics', *Zeitschrift für angewandte Mathematik und Mechanik* **93**, 177–194.

Gleim, T., Schröder, B. and Kuhl, D. (2015), 'Nonlinear thermo-electromagnetic analysis of inductive heating processes', *Archive of Applied Mechanics* **85**, 1055–1073.

Gleim, T., Schröder, B. and Kuhl, D. (2017), 'Simulation of manufacturing sequences using higher order accurate Runge-Kutta time integration schemes', *AIP Conference Proceedings* **1863**.

Göldner, H., Sähn, S., Altenbach, J., Eschke, K. and Garz, K. F. (1991), *Lehrbuch Höhere Festigkeitslehre*, Fachbuchverlag GmbH.

Grafenhorst, M., Rang, J. and Hartmann, S. (2017), 'Time-Adaptive Finite Element Simulations of Dynamical Problems for Temperature-Dependent Materials', *Journal of Mechanics of Materials and Structures* **12**, 57–91.

Grätsch, T. and Bathe, K.-J. (2005), 'A posteriori error estimation techniques in practical finite element analysis', *Computers and Structures* **83**, 235–265.

Green, A. E. and Nagdhi, P. M. (1965), 'A General Theory of an Elastic-Plastic Continuum', *Archive for Rational Mechanics and Analysis* **18**, 251–281.

Grinfeld, P. (2013), *Introduction to Tensor Analysis and the Calculus of Moving Surfaces*, Springer Verlag.

Hackl, K. (1997), 'Generalized standard media and variational principles in classical and finite strain elastoplasticity', *Journal of the Mechanics and Physics of Solids* **45**, 667–688.

Hager, C. and Wohlmuth, B. I. (2009), 'Nonlinear complementarity functions for plasticity problems with frictional contact', *Computer Methods in Applied Mechanics and Engineering* **198**, 3411–3427.

Hairer, E., Nørsett, S. and Wanner, G. (2008), *Solving Ordinary Differential Equations I. Non-stiff Problems.*, Springer-Verlag.

Hairer, E. and Wanner, G. (2002), *Solving Ordinary Differential Equations II. Stiff and Differential-Algebraic Problems.*, Springer-Verlag.

Halphen, B. and Nguyen, Q. (1975), 'Sur les matériaux standards généralisés', *Journal de Mécanique* **14**, 39–63.

Hamilton, W. R. (1834), 'On a general method in dynamics; by which the study of the motions of all free systems of attracting or repelling points is reduced to the search and differentiation of one central relation, or characteristic function', *Philosophical Transactions* **124**, 247–308.

Hamilton, W. R. (1835), 'Second essay on a general method in dynamics.', *Philosophical Transactions* **125**, 95–144.

Han, W. and Reddy, B. D. (1999), *Plasticity. Mathematical Theory and Numerical Analysis*, Springer Verlag.

Hartmann, S. (1993), 'Lösung von Randwertaufgaben der Elastoplastizität. Ein Finite Element Konzept für nichtlineare kinematische Verfestigung bei kleinen und finiten Verzerrungen', PhD Thesis, Universität Gesamthochschule Kassel.

Hartmann, S. (2005), 'A remark on the application of the Newton-Raphson method in non-linear finite element analysis', *Computational Mechanics* **36**, 100–116.

Hartmann, S. (2008), 'Introduction to Theory of Materials', Lecture Notes, University of Kassel.

Hartmann, S. and Bier, W. (2007), 'High-order time integration applied to metal powder plasticity', *International Journal of Plasticity* **24**, 17–54.

Hartmann, S., Lührs, G. and Haupt, P. (1997), 'An efficient stress algorithm with applications in viscoplasticity and plasticity', *International Journal for Numerical Methods in Engineering* **40**, 991–1013.

Haupt, P. (2000), *Continuum Mechanics and Theory of Materials*, Springer-Verlag.

Helm, D. (2006), 'Stress computation in finite thermoviscoplasticity', *International Journal of Plasticity* **22**, 1699–1727.

Hesthaven, J. S. and Wartburton, T. (2000), *Nodal Discontinuous Galerkin Methods*, Springer Verlag.

Heun, K. (1900), 'Neue Methode zur approximativen Integration der Differentialgleichungen einer unabhängigen Veränderlichen', *Zeitschrift für Mathematik und Physik* **45**, 23–38.

Hilber, H. M., Hughes, T. J. R. and Taylor, R. L. (1977), 'Improved numerical dissipation for time integration algorithms in structural dynamics', *Earthquake Engineering and Structural Dynamics* **5**, 283–292.

Hildebrand, F. E. (2013), 'Variational Multifield Modeling of the Formation and Evolution of Laminate Microstructures', PhD Thesis, Universität Stuttgart.

Hill, R. (1983), *The mathematical theory of plasticity*, Oxford at the Clarendon Press.

Hintermüller, M. (2010), 'Semismooth Newton Methods and Applications', Oberwolfach-Seminar on "Mathematics of PDE-Contrained Optimization" at Mathematisches Forschungsinstitut in Oberwolfach.

Hintermüller, M., Ito, K. and Kunish, K. (2003), 'The Primal-Dual Active Set Strategy as a Semismooth Newton Method', *Journal on Optimization* **13**, 865–888.

Holzapfel, G. (2000), *Nonlinear Solid Mechanics*, John Wiley & Sons.

Huang, H. and Costanzo, F. (2002), 'On the use of space-time finite elements in the solution of elasto-dynamic problems with strain discontinuities', *Computer Methods in Applied Mechanics and Engineering* **191**, 5315–5343.

Hüeber, S. and Wohlmuth, B. I. (2005), 'A primal-dual active set strategy for non-linear multibody contact problems', *Computer Methods in Applied Mechanics and Engineering* **194**, 3147–3166.

Hughes, T. J. R. (1983), Analysis of Transient Algorithms with Particular Reference to Stability Behavior, *in* Belytschko, T. and Hughes, T. J. R., eds, 'Computational Methods for Transient Analysis', North-Holland Publishing Company.

Hughes, T. J. R. (2000), *The Finite Element Method. Linear Static and Dynamic Finite Element Analysis*, Dover Publications, INC.

Hughes, T. J. R. and Hulbert, G. M. (1988), 'Space-Time Finite Element Methods for Elastodynamics: Formulations and Error Estimates', *Computer Methods in Applied Mechanics and Engineering* **66**, 339–363.

Hulber, G. M. and Hughes, T. J. R. (1990), 'Space-Time Finite Element Methods for Second-Order Hyperbolic Equations', *Computer Methods in Applied Mechanics and Engineering* **84**, 327–348.

Hulbert, G. M. (1992), 'Time Finite Element Methods for Structural Dynamics', *International Journal for Numerical Methods in Engineering* **33**, 307–331.

Hulme, B. L. (1972*a*), 'Discrete Galerkin and Related One-Step Methods for Ordinary Differential Equations', *Mathematics of Computation* **26**, 881–891.

Hulme, B. L. (1972*b*), 'One-Step Piecewise Polynomial Galerkin Methods for Initial Value Problems', *Mathematics of Computation* **26**, 415–426.

Ito, K. and Kunisch, K. (2008), *Lagrange Multiplier Approach to Variational Problems and Applications*, Society for Industrial and Applied Mathematics.

Jeltsch-Fricker, R. (2007), 'Variationsrechnung', Vorlesungsskript, Universität Kassel.

Johnson, C. (1976), 'Existence theorems for plasticity problems', *Journal de Mathématiques pures et appliquées* **55**, 431–444.

Johnson, C. (1988), 'Error estimates and adaptive time-step control for a class of one-step methods for stiff ordinary differential equations', *Journal on Numerical Analysis* **25**, 908–926.

Jourdain, P. E. B. (1909), 'Note on an Analogue of Gauß' Principle of Least Constraints', *Quarterly Journal of Pure and Applied Mathematics* **40**, 153–157.

Junker, P., Makowski, J. and Hackl, K. (2013), 'The principle of the minimum of the dissipation potential for non-isothermal processes', *Continuum Mechanics and Thermodynamics* .

Kanzow, C. (2007), 'Nichtlineare Gleichungssysteme', Vorlesungsskript, Julius-Maximilians-Universität Würzburg.

Kelly, P. (2015), *Mechanics Lecture Notes Part III: Foundations of Continuum Mechanics*, Faculty of Engineering, University of Auckland.

Kim, J., Dargush, G. F. and Ju, Y. K. (2013), 'Extended framework of Hamilton's principle for continuum dynamics', *International Journal of Solids and Structures* **50**, 3418–3429.

Kizio, S. (2008), 'Adaptive Finite-Elemente-Algorithmen in der Strukturdynamik', PhD Thesis, Universität Fridericiana zu Karlsruhe.

Kleiber, M. (1975), 'Kinematics of deformation processes in materials subjected to finite elastic-plastic strains', *International Journal of Engineering Science* **13**, 513–525.

Kolsky, H. (1963), *Stress Waves in Solids*, Dover Publications, Inc.

Kreißig, R. and Benedix, U. (2002), *Höhere Technische Mechanik*, Springer Verlag.

Krieg, R. D. and Krieg, D. B. (1977), 'Accuracies of Numerical Solution Methods for the Elastic-Perfectly Plastic Model', *Journal of Pressure Vessel Technology* **99**, 510–515.

Kröner, E. and Teodosiu, C. (1974), Lattice defect approach to plasticity and viscoplasticity, *in* Sawczuk, A., ed., 'Problems of Plasticity. Papers contributed to the International Symposium on Foundations of Plasticity', Noordhoff International Publishing.

Kuhl, D. (2004), 'Modellierung und Simulation von Mehrfeldproblemen der Strukturmechanik', Habilitation Thesis, Ruhr-Universität Bochum.

Kutta, W. (1901), 'Beitrag zur Näherungsweisen Integration totaler Diffrentialgleichungen', PhD Thesis, Karl Ludwig Maximilian Universität München.

Lagrange, J. L. (1788), *Méchanique Analitique*, de l' Académie des Sciences de Paris.

Lagrange, J. L. (1894), Versuch einer neuen Methode um die Maxima und Minima unbestimmter Integralformeln zu bestimmen., *in* Stäckel, P., ed., 'Ostwalds Klassiker der exakten Wissenschaften Nr. 47', Verlag von Wilhelm Engelmann.

Lambermont, J. and Lebon, G. (1972), 'A Rather General Variational Principle for Purely Dissipative Non-Stationary Processes', *Annalen der Physik. 7. Folge* **28**, 15–30.

Lee, E. H. (1969), 'Elastic-Plastic Deformation at Finite Strains', *Journal of Applied Mechanics* **36**, 1–6.

Lee, E. H. and Germain, P. (1974), Elastic-plastic theory at finite strain, *in* Sawczuk, A., ed., 'Problems of Plasticity. Papers contributed to the International Symposium on Foundations of Plasticity', Noordhoff International Publishing.

Lee, E. H. and Liu, D. T. (1967), 'Finite-Strain Elastic-Plastic Theory with Application to Plane-Wave Analysis', *Journal of Applied Physics* **38**, 19–27.

Leine, R. I. and Aeberhard, U. (2008), 'A weak form of Hamilton's principle as variational inequality', *Proceedings of the sixth EUROMECH Nonlinear Dynamics Conference* .

Lemaitre, J. and Chaboche, J.-L. (1990), *Mechanics of solid materials*, Cambridge University Press.

Li, X. D., Zeng, L. F. and Wiberg, N.-E. (1993), 'A simple local error estimator and an adaptive time-stepping procedure for direct integration in dynamic analysis', *Communications in Numerical Methods in Engineering* **9**, 273–292.

Liewald, M. (2012), 'Fügen durch plastische Deformation. DFG SPP 1640'.

Lubliner, J. (2006), *Plasticity Theory*, Pearson Education, Inc.

Luenberger, D. G. (1973), *Introduction to linear and nonlinear programming*, Addison-Wesley Publishing Company.

Macneal, R. H. (1994), *Finite Elements: Their Design and Performance*, Marcel Dekker, Inc.

Mahnken, R. and Schneidt, A. (2009), 'A thermodynamic framework and numerical aspects for transformation-induced plasticity at large strains', *Archive of Applied Mechanics* **80**, 229–253.

Mahnken, R., Schneidt, A. and Antretter, T. (2009), 'Macro modelling and homogenization for transformation induced plasticity of a low-alloy steel', *International Journal of Plasticity* **25**, 183–204.

Mahnken, R., Schneidt, A., Tschumak, S. and Maier, H. (2011), 'On the simulation of austenite to bainite phase transformation', *Computational Material Science* **50**, 1823–1829.

Mahnken, R. and Wilmanns, S. (2011), 'A projected Newton algorithm for simulation of multi-variant textured polycrystalline shape memory alloys', *Computational Material Science* **50**, 2535–2548.

Mahnken, R., Wolff, M., Schneidt, A. and Böhm, M. (2012), 'Multi-phase transformations at large strains - Thermodynamic framework and simulation', *International Journal of Plasticity* **39**, 1–26.

Marcal, P. V. and King, I. P. (1967), 'Elasto-plastic analysis of two-dimensional stress systems by finite element method', *International Journal of Mechanical Sciences* **9**, 142–155.

Matthies, G. and Schieweck, F. (2011), 'Higher order variational time discretizations for nonlinear systems of ordinary differential equations', Preprint No. 23/2011, Fakultät für Mathematik, Otto-von-Guericke Universität Magdeburg.

Maugin, G. A. (1980), 'The Method of Virtual Power in Continuum Mechanics: Application to Coupled Fields', *Acta Mechanica* **35**, 1–70.

Maugin, G. A. (1992), *The thermomechanics of plasticity and fracture*, Cambridge University Press.

Meister, A. (2010), *Skriptum zur Vorlesung Numerik II*, Fachbereich Mathematik Universität Kassel.

Meng, X. N. and Laursen, T. A. (2002*a*), 'Energy consistent algorithms for dynamic finite deformation plasticity', *Computer Methods in Applied Mechanics and Engineering* **191**, 1639–1675.

Meng, X. N. and Laursen, T. A. (2002*b*), 'On energy consistency of large deformation plasticity models, with application to the design of unconditionally stable time integrators', *Finite Elements in Analysis and Design* **38**, 949–963.

Miehe, C. (1995), 'A theory of large-strain isotropic thermoplasticity based on metric transformation tensors', *Archive of Applied Mechanics* **66**, 45–64.

Miehe, C. (2002), 'Strain-driven homogenization of inelastic microstructures and composites based on an incremental variational formulation', *International Journal for Numerical Methods in Engineering* **55**, 1285–1322.

Miehe, C. (2011), 'A multi-field incremental variational framework for gradient-extended standard dissipative solids', *Journal of Mechanics and Physics of Solids* **59**, 898–923.

Miehe, C. (2012), 'Mixed variational principles for the evolution problem of gradient-extended dissipative solids', *GAMM-Mitteilungen* **35**, 8–25.

Miehe, C., Lambrecht, M. and Gürses, E. (2004), 'Analysis of material instabilities in inelastic solids by incremental energy minimization and relaxation methods: evolving deformation microstructures in finite plasticity', *Journal of the Mechanics and Physics of Solids* **52**, 2725–2769.

Miehe, C., Schotte, J. and Lambrecht, M. (2002), 'Homogenization of inelastic solid materials at finite strains based on incremental minimization principles. Application to the texture analysis of polycristals.', *Journal of the Mechanics and Physics of Solids* **50**, 2123–2167.

Mielke, A. (2003), 'Energetic formulation of multiplicative elasto-plasticity using dissipation distances', *Continuum Mechanics and Thermodynamics* **15**, 351–382.

Mielke, A. (2004), A new approach to elasto-plasticity using energy and dissipation functionals, *in* Hill, J. M. and Moore, R., eds, 'ICIAM 2003. Applied Mathematics Entering the 21^{st} Century', The Society for Industrial and Applied Mathematics.

Mielke, A., Paoli, L., Petrov, A. and Stefanelli, U. (2010), 'Error estimates for space-time discretizations of a rate-independent variational inequality', *SIAM Journal on Numerical Analysis* **48**, 1625–1646.

Mohr, R., Menzel, A. and Steinmann, P. (2008), 'A consistent time FE-method for large strain elasto-plasto-dynamics', *Computer Methods in Applied Mechanics and Engineering* **197**, 3024–3044.

Molinari, J. F. and Ortiz, M. (2002), 'Three-dimensional adaptive meshing by subdivision and edge-collapse in finite-deformation dynamic-plasticity problems with application to adiabatic shear banding', *International Journal for Numerical Methods in Engineering* **53**, 1101–1126.

Monk, P. (1993), 'An analysis of Nédélec's method for the spatial discretization of Maxwell's equations', *Journal of Computational and Applied Mathematics* **47**, 101–121.

Moon, F. C. (1998), *Applied Dynamics*, John Wiley & Sons, Inc.

Moreau, J. J. (1970), 'Sur le lois de frottement, de placticité et de viscosité', *Comptes rendus hebdomadaires des séances de l'Académie des sciences. Séries A et B, Sciences mathématiques et Sciences* **271**, 608–611.

Moreau, J. J. (1976), Application of convex analysis to the treatment of elastoplastic systems, *in* 'Applications of methods of functional analysis to problems in mechanics', Springer.

Mosler, J. and Bruhns, O. (2010), 'On the implementation of rate-independent standard dissipative solids at finite strain - Variational constitutive updates', *Computer Methods in Applied Mechanics and Engineering* **199**, 417–429.

Mühlhaus, H.-B. and Aifantis, E. C. (1991), 'A variational principle for gradient plasticity', *International Journal of Solids and Structures* **28**, 845–857.

Naghdi, P. (1990), 'A critical review of the state of finite plasticity', *Journal of Applied Mathematics and Physics* **41**, 315–394.

Nemat-Nasser, S. (1982), 'On Finite Deformation Elasto-Plasticity', *International Journal for Solids and Structures* **18**, 857–872.

Nemat-Nasser, S., Mehrabadi, M. M. and Iwakuma, T. (1980), On Certain Macroscopic and Microscopic Aspects of Plastic Flow of Ductile Materials, *in* 'Three-Dimensional Constitutive Relations and Ductile Fracture', North-Holland.

Neundorf, W. (2013), *Numerik gewöhnlicher Differentialgleichungen mit Computeralgebrasystemen*, Universitätsverlag Ilmenau.

Newmark, N. M. (1959), 'A Method of Computation for Structural Dynamics', *ASCE Journal of the Engineering Mechanics Division* **85**, 67–94.

Noels, L., Stainier, L. and Ponthot, J.-P. (2008), 'A first-order energy-dissipative momentum-conserving scheme for elasto-plasticity using the variational updates formulation', *Computer Methods in Applied Mechanics and Engineering* **197**, 706–726.

Oden, J. T. (1969), 'A General Theory of Finite Elements. II Applications', *International Journal of Numerical Methods in Engineering* **1**, 247–259.

Ortiz, M., Pinsky, P. M. and Taylor, R. L. (1983), 'Operator split methods for the numerical solution of the elastoplastic dynamic problem', *Computer Methods in Applied Mechanics and Engineering* **39**, 137–157.

Ortiz, M. and Stainier, L. (1999), 'The variational formulation of viscoplastic constitutive updates', *Computer Methods in Applied Mechanics and Engineering* **171**, 419–444.

Ostwald, R., Bartel, T. and Menzel, A. (2010), 'A computational micro-sphere model applied to the simulation of phase-transformations', *Zeitschrift für Angewandte Mathematik und Mechanik* **90**, 605–622.

Ottosen, N. and Petersson, H. (1992), *Introduction to the Finite Element Method*, Prentice Hall.

Pamin, J. K. (1994), 'Gradient-Dependent Plasticity in Numerical Simulation of Localization Phenomena', PhD Thesis, Technische Universiteit Delft.

Piedbœuf, J.-C. (1993), 'Kane's equations or Jourdain's principle', *Proceedings of 36th Midwest Symposium on Circuits and Systems* **2**, 1471–1474.

Pinsky, P. M. (1987), 'A finite element formulation for elastoplasticity based on a three-field variational equation', *Computer Methods in Applied Mechanics and Engineering* **61**, 41–60.

Popp, A., Gee, M. W. and Wall, W. A. (2009), 'A finite deformation mortar contact formulation using primal-dual active set strategy', *International Journal of Numerical Methods in Engineering* **79**, 1354–1391.

Prothero, A. and Robinson, A. (1974), 'On the Stability and Accuracy of One-Step Methods for Solving Stiff Systems of Ordinary Differential Equations', *Mathematics of Computation* **28**, 145–162.

Qi, L. and Sun, J. (1993), 'A nonsmooth version of Newton's method', *Mathematical Programming* **58**, 353–367.

Quint, K. (2011), 'Thermomechanically Coupled Processes for Functionally Graded Materials', PhD Thesis, TU Clausthal.

Reddy, B. and Martin, J. (1994), 'Internal variable formulations of problems in elastoplasticity: Constitutive and algorithmic aspects', *Applied Mechanics Review* **47**, 429–456.

Reese, S. (1998), 'Multiplicative Thermo-Viscoplasticity: A Thermodynamic Model and its Finite Element Implementation', *Technische Mechanik* **18**, 209–216.

Reese, S. (2008), 'Entwicklung neuer Technologien zur numerischen Simulation quasistatisch-dynamisch kombinierter Umformverfahren. DFG 81609791'.

Repin, S. I. and Xanthis, L. S. (1996), 'A posteriori error estimaton for elasto-plastic problems based on duality theory', *Computer Methods in Applied Mechanics and Engineering* **138**, 317–339.

Rockafellar, R. T. (1970), *Convex Analysis*, Princeton University Press.

Rockafellar, R. T. (2001), Convex Analysis in the Calculus of Variations, *in* Hadjisavvas, N. and Pardalos, P. M., eds, 'Advances in Convex Analysis and Global Optimization', Kluwer Academic Publishers.

Rose, E. (2007), 'Implizite Runge-Kutta-Verfahren und ihre Anwendung auf Steuerungsprobleme', PhD Thesis, Universität Bayreuth.

Runge, C. (1895), 'Ueber die numerische Auflösung von Differentialgleichungen', *Mathematische Annalen* **46**, 167–178.

Schäuble, A.-K. (2013), 'Isogeometric Galerkin Finite Elements in Time and Space', Master Thesis, Universität Stuttgart.

Schieweck, F. (2009), 'A-stable discontinuous Galerkin-Petrov time discretization of higher order', *Journal of Numerical Mathematics* **18**, 25–57.

Schmidt, M. (2001), 'Adaptive Finite-Elemente-Methoden für elastoplastische Deformationen. Algorithmen und Visualisierungen.', PhD Thesis, Universität Hannover.

Schöberl, J. and Zaglmayr, S. (2005), 'High order Nédélec elements with local complete sequence properties', *The International Journal for Computation and Mathematics in Electrical and Electronic Engineering* **24**, 374–384.

Schreiber, L. (1997), 'Einführung in die Plastizitätstheorie', Skript zur Vorlesung, Universität Kassel.

Schröder, A. and Wiedemann, S. (2011), 'Error estimates in elastoplasticity using a mixed method', *Applied Numerical Mathematics* **61**, 1031–1045.

Schröder, B. and Kuhl, D. (2013), Time-adaptive computation of finite thermoviscoplastic structures, *in* Heim, H.-P., Biermann, D. and Homberg, W., eds, 'Functionally Graded Materials in Industrial Mass Production', Verlag Wissenschaftliche Scripten.

Schröder, B. and Kuhl, D. (2015*a*), 'Small strain plasticity: classical versus multifield formulation', *Archive of Applied Mechanics* **85**, 1127–1145.

Schröder, B. and Kuhl, D. (2015*b*), 'Static condensation within the context of multifield elastoplasticity', *Proceedings in Applied Mathematics and Mechanics* **15**, 423–424.

Schröder, B. and Kuhl, D. (2016), 'A semi-smooth Newton method for dynamic multifield plasticity', *Proceedings in Applied Mathematics and Mechanics* **16**, 767–768.

Schröder, B. and Kuhl, D. (2018), 'Time Discretization Error Analysis in Multifield Plasticity', *Proceedings of 6th European Conference on Computational Mechanics* .

Schröder, J., Gruttmann, F. and Löblein, J. (2002), 'A simple orthotropic finite elasto-plasticity model based on generalized stress-strain measures', *Computational Mechanics* **30**, 48–64.

Schwarz, A., Schröder, J. and Starke, G. (2009), 'Least-squares mixed finite elements for small strain elasto-viscoplasticity', *International Journal for Numerical Methods in Engineering* **77**, 1351–1370.

Seitz, A., Popp, A. and Wall, W. A. (2014), 'A semi-smooth Newton method for orthotropic plasticity and frictional contact at finite strains', *Computer Methods in Applied Mechanics and Engineering* **285**, 228–254.

Simo, J. C. (1988), 'A framework for finite strain elastoplasticity based on maximum plastic dissipation and the multiplicative decomposition: part I. Continuum formulation', *Computer Methods in Applied Mechanics and Engineering* **66**, 199–219.

Simo, J. C. (1998), *Numerical Analysis and Simulation of Plasticity*, Elsevier.

Simo, J. C. and Govindjee, S. (1991), 'Non-linear B-stability and symmetry preserving return mapping algorithms for plasticity and viscoplasticity', *International Journal for Numerical Methods in Engineering* **31**, 151–176.

Simo, J. C. and Hughes, T. J. R. (1997), *Computational Inelasticity*, Springer Verlag.

Simo, J. C., Kennedy, J. G. and Govindjee, S. (1988), 'Non-smooth multisurface plasticity and viscoplasticity. Loading/unloading conditions and numerical algorithms.', *International Journal for Numerical Methods in Engineering* **26**, 2161–2185.

Simo, J. C., Kennedy, J. and Taylor, R. (1989), 'Complementary mixed finite element formulations for elastoplasticity', *Computer Methods in Applied Mechanics and Engineering* **74**, 177–206.

Simo, J. C. and Ortiz, M. (1985), 'A unified approach to finite deformation elastoplastic analysis based on the use of hyperelastic constitutive equations', *Computer Methods in Applied Mechanics and Engineering* **49**, 221–245.

Simo, J. and Miehe, C. (1992), 'Associative coupled thermoplasticity at finite strains: Formulation, numerical analysis and implementation', *Computer Methods in Applied Mechanics and Engineering* **98**, 41–104.

Specht, E. (2005), 'Einführung in die Vektoranalysis'.

Stainier, L. (2013), A Variational Approach to Modeling Coupled Thermo-Mechanical Nonlinear Dissipative Behaviors, *in* Bordas, S., ed., 'Advances in Applied Mechanics', Vol. 46, Elsevier.

Stainier, L. and Ortiz, M. (2010), 'Study and validation of a variational theory of thermo-mechanical coupling in finite visco-plasticity', *International Journal of Solids and Structures* **47**, 705–715.

Stangenberg, F., Breitenbücher, R., Bruhns, O. T., Hartmann, D., Höffer, R., Kuhl, D. and Meschke, G. (2009), *Lifetime-Oriented Structural Design Concepts*, Springer Verlag.

Stein, E. (2003), *Error-controlled Adaptive Finite Elements in Solid Mechanics*, John Wiley & Sons, Inc.

Steinhoff, K., Weidig, U. and Saba, N. (2009), Investigation of Plastic Forming Under the Influence of Locally and Temporally Variable Temperature and Stress States, *in* Steinhoff, K., Maier, H. and Biermann, D., eds, 'Functionally Graded Materials in Industrial Mass Production', Verlag Wissenschaftliche Scripten, Auerbach.

Strehmel, K., Weiner, R. and Podhaisky, H. (2012), *Numerik gewöhnlicher Differentialgleichungen*, Springer Spektrum.

Stroud, A. H. (1974), *Numerical Quadrature and Solution of Ordinary Differential Equations*, Springer-Verlag.

Suquet, P.-M. (1978), Existence and Regularity of Solutions for Plasticity Problems, *in* Nemat-Nasser, S., ed., 'Variational Methods in the Mechanics of Solids', Pergamon Press.

Svendsen, B. (2007), 'A logarithmic-exponential backward-Euler-based split of the flow rule for anisotropic inelastic behaviour at small elastic strain', *International Journal for Numerical Methods in Engineering* **70**, 496–504.

Szabó, B. and Babuška, I. (1991), *Finite Element Analysis*, John Wiley & Sons, Inc.

Talpaert, Y. R. (2002), *Tensor Analysis and Continuum Mechanics*, Springer Science+Business Media Dordrecht.

Thomée, V. (1997), *Galerkin Finite Element Methods for Parabolic Problems*, Springer Verlag.

Tonti, E. (1984), 'Variational Formulation for Every Nonlinear Problem', *International Journal of Engineering Science* **22**, 1343–1371.

Tsakmakis, C. (1994), 'Methoden zur Darstellung inelastischen Materialverhaltens bei kleinen Deformationen', PhD Thesis, Universität Kassel.

Tsakmakis, C. (1996*a*), 'Kinematic hardening rules in finite plasticity. Part I: A constitutive approach', *Continuum Mechanics and Thermodynamics* **8**, 215–231.

Tsakmakis, C. (1996*b*), 'Kinematic hardening rules in finite plasticity. Part II: Some examples', *Continuum Mechanics and Thermodynamics* **8**, 233–246.

Turner, M. J., Clough, R. W., Martin, H. C. and Topp, L. J. (1956), 'Stiffness and Deflection Analysis of Complex Structures', *Journal of the Aeronautical Sciences* **23**, 805–823.

Ueberhuber, C. W. (1997), *Numerical Computation 2. Methods, Software, and Analysis*, Springer-Verlag.

Vladimirov, I., Pietryga, M. and Reese, S. (2010), 'Anisotropic finite elastoplasticity with nonlinear kinematic and isotropic hardening and application to sheet metal forming', *International Journal of Plasticity* **26**, 659–687.

Walkington, N. J. and Howell, J. S. (2011), 'Inf-Sup Conditions for Twofold Saddle Point Problems', *Numerische Mathematik* **118**, 663–690.

Weisstein, E. W. (2016), 'Radau Quadrature'.
URL: *http://mathworld.wolfram.com/RadauQuadrature.html*

Welschinger, F. R. (2011), 'A Variational Framework for Gradient-Extended Dissipative Continua. Application to Damage Mechanics, Fracture, and Plasticity', PhD Thesis, Universität Stuttgart.

Wiberg, N.-E., Li, X. D. and Abdulwahab, F. (1996), 'Adaptive Finite Element Procedures in Elasticity and Plasticity', *Engineering with Computers* **12**, 120–414.

Wieners, C. (1999), 'Multigrid Methods for Prandtl-Reuss Plasticity', *Numerical Linear Algebra with Applications* **6**, 457–478.

Wieners, C. (2007), 'Nonlinear solution methods for infinitesimal perfect plasticity', *Zeitschrift für angewandte Mathematik und Mechanik* **87**, 643–660.

Wilkins, M. L. (1963), 'Calculation of elastic-plastic flow'.

Wood, D. S. (1952), 'On Longitudinal Plane Waves of Elastic-Plastic Strain in Solids', *Journal of Applied Mechanics* **19**, 521–525.

Wood, W. L., Bossak, M. and Zienkiewicz, O. C. (1980), 'An α modification of newmark's method', *International Journal for Numerical Methods in Engineering* **15**, 1562–1566.

Wriggers, P. (2008), *Nonlinear Finite Element Methods*, Springer-Verlag.

Wriggers, P., Miehe, C., Kleiber, M. and Simo, J. (1992), 'On the coupled thermomechanical treatment of necking problems via finite element methods', *International Journal for Numerical Methods in Engineering* **33**, 869–883.

Wu, C. S., Budhu, M. and El-Kholy, S. (1992), 'Finite strain elastic closed form solutions for some axisymmetric problems', *Acta Mechanica* **97**, 1–22.

Xiao, T., Bruhns, O. T. and Meyers, A. (2006), 'Elastoplasticity beyond small deformations', *Acta Mechanica* **182**, 31–111.

Yunt, K. (2014), 'On the Relation of the Principle of Maximum Dissipation to the Principles of Jourdain and Gauss for Rigid Body Systems', *Journal of Computational and Nonlinear Dynamics* **9**, 1–11.

Zeidler, E. (1985), *Nonlinear Functional Analysis and its Applications III*, Springer Verlag.

Zhao, S. and Wei, G. W. (2013), 'A unified discontinuous Galerkin framework for time integration', *Mathematical Methods in Applied Sciences* **37**, 1042–1071.

Zienkiewicz, O. C. (1984), *Methode der finiten Elemente*, Carl Hanser Verlag.

Zienkiewicz, O. C. and Xie, Y. M. (1991), 'A simple error estimator and adaptive time stepping procedure for dynamic analysis', *Earthquake Engineering and Structural Dynamics* **20**, 871–887.

Zienkiewicz, O. and Taylor, R. (2000), *The Finite Element Method*, Butterworth Heinemann.

Zienkiewicz, O., Valliappan, S. and King, P. (1969), 'Elasto-plastic Solutions of Engineering Problems. 'Initial Stress', Finite Element Approach', *International Journal for Numerical Methods in Engineering* **1**, 75–100.

Schriftenreihe Institut für Baustatik und Baudynamik
Series Institute of Structural Mechanics

2013-1 Sönke Carstens: Modellbildung und numerische Mechanik tensegrer Strukturen. Dissertation. Fachgebiet Baumechanik/Baudynamik

2013-2 Sandra Carstens: Diskontinuierliche Galerkin-Verfahren in Raum und Zeit zur Simulation von Transportprozessen. Dissertation. Fachgebiet Baumechanik/ Baudynamik

2013-3 Wagner Fleming Petri: Static and Dynamic Crack Propagation in Brittle Materials with XFEM. Dissertation. Fachgebiet Baumechanik/Baudynamik

2016-4 Tobias Gleim: Simulation of Manufacturing Sequences of Functionally Graded Structures. Dissertation. Fachgebiet Baumechanik/Baudynamik

2017-5 Florian Niederhöfer: Eine Methode zur Kopplung von molekular- und kontinuumsmechanischen Modellen unter Einsatz von Translations- und Rotationsfreiheitsgraden – Die virtuelle Projektionsmethode. Dissertation. Fachgebiet Baustatik

2019-1 Torsten Hartkorn: Entwicklung und Untersuchung von Methoden zur Simulation umströmter funktionaler Strukturen

2019-2 Bettina Schröder: Consistent Higher Order Accurate Time Discretization Methods for Inelastic Material Models

ISBN 978-3-7376-0772-8

kassel university press

The present thesis investigates the usage of higher order accurate time integrators together with appropriate error estimators for small and finite dynamic (visco)plasticity. Therefore, a general (visco)plastic problem is defined which serves as a basis to create closed-form solution strategies. A classical access towards small and finite (visco)plasticity is integrated into this concept. This approach is based on the idea, that the balance of linear momentum is formulated in a weak sense and the material laws are included indirectly. Thus, separate time discretizations are implemented and an appropriate coupling between them is necessary. Limitations for the usage of time integrators are the consequence. In contrast, an alternative multifield formulation is derived, adapting the principle of Jourdain. The idea is to assume that the balance of energy - taking into account a pseudopotential representing dissipative effects – resembles a rate-type functional, whose stationarity condition leads to the equations describing small or finite dynamic (visco)plasticity. Accordingly, the material laws and the balance of linear momentum can be solved on the same level and only one single time discretization has to be performed. A greater freedom in the choice of time integrators is obtained and the application of higher order accurate schemes - such as Newmark's method, fully implicit as well as diagonally implicit Runge-Kutta schemes, and continuous as well as discontinuous Galerkin methods - is facilitated. An analysis and a comparison of the classical and the multifield formulation is accomplished by means of distinct examples. In this context, a dynamic benchmark problem is developed, which allows to focus on the effect of different time integrators. For this investigation, a variety of time discretization error estimators are formulated, evaluated, and compared.